NIST Technical Note 1524

Trapped Ions and Laser Cooling, VI

Edited by

James C. Bergquist
John J. Bollinger
Wayne M. Itano
David J. Wineland

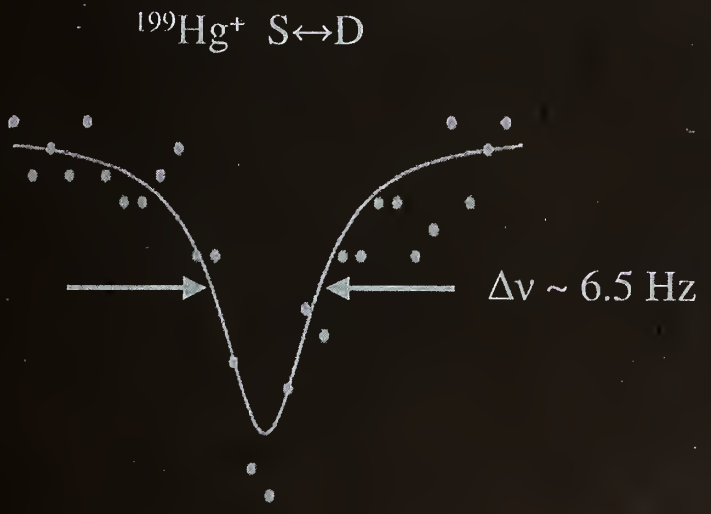

ν_0 = 1 064 721 609 899 143 Hz

Selected publications of the Ion Storage Group
NIST Time and Frequency Division

National Institute of Standards and Technology
Technology Administration, U.S. Department of Commerce

NIST Technical Note 1524

Trapped Ions and Laser Cooling, VI

Selected publications of the Ion Storage Group NIST Time and Frequency Division

Edited by

James C. Bergquist
John J. Bollinger
Wayne M. Itano
David J. Wineland

Time and Frequency Division
Physics Laboratory
National Institute of Standards and Technology
325 Broadway
Boulder, Colorado 80305

February 2002

U.S. Department of Commerce
Donald L. Evans, Secretary

Technology Administration
Phillip J. Bond, Under Secretary of Commerce for Technology

National Institute of Standards and Technology
Arden L. Bement, Jr., Director

National Institute of Standards and Technology Technical Note 1524
Natl. Inst. Stand. Technol. Tech. Note 1524, 208 pages (February 2002)
CODEN: NTNOEF

U.S. GOVERNMENT PRINTING OFFICE
WASHINGTON: 2002

For sale by the Superintendent of Documents, U.S. Government Printing Office
Internet: bookstore.gpo.gov Phone: (202) 512-1800 Fax: (202) 512-2250
Mail: Stop SSOP, Washington, DC 20402-0001

CONTENTS

LASER-COOLED NON-NEUTRAL PLASMAS

QUANTUM MECHANICS AND QUANTUM METROLOGY

ADDITIONAL PUBLICATIONS

The following publications were published during the period between January 1999 and October 2001 but are not included in this Technical Note.

1. "$^{199}Hg^{+}$ optical frequency standard: Progress report," J.J. Rafac B.C. Young, F.C. Cruz, J.A. Beall, J.C. Bergquist, W.M. Itano, and D.J. Wineland, Proc., 1999 IEEE Int. Frequency Control Symp. IEEE catalog number 99CH36313, Piscataway, NJ: IEEE (1999), pp. 676-681.

2. "High-accuracy frequency standards using laser-cooled $^{199}Hg^{+}$ ions," D.J. Berkeland, J.D. Miller, J.C. Bergquist, W.M. Itano, and D.J. Wineland, Gravitational Waves and Experimental Gravity, J. Trân Thanh Vân, J. Dumarchez, S. Reynaud, C. Salomon, S. Thorsett, and J.Y. Vinet, eds., Proc., XXXIVth Rencontres de Moriond Les Arcs, Hanoi, Vietnam: World Publishers (2000), pp. 371-378.

3. "Primary atomic frequency standards at NIST," D.B. Sullivan, J.C. Bergquist, J.J. Bollinger, R.E. Drullinger, W.M. Itano, S.R. Jefferts, W.D. Lee, D. Meekhof, T.E. Parker, F.L. Walls, and D.J. Wineland, J. Res. Natl. Inst. Stand. Technol. **106**, 47-63 (2001).

4. "A compact femtosecond-laser-based optical clockwork," S.A. Diddams, Th. Udem, K.R. Vogel, C.W. Oates, E.A. Curtis, R.W. Windeler, A. Bartels, J.C. Bergquist, and L. Hollberg, Proc., SPIE 4269 (2001).

5. "Crystalline order in strongly coupled ion plasmas," T.B. Mitchell, J.J. Bollinger, X.-P. Huang, W.M. Itano, J.N. Tan, B.M. Jelenkovic, and D.J. Wineland, Non-neutral Plasma Physics III, J.J. Bollinger, R.L. Spencer, and R.C. Davidson, eds., Proc., AIP Conf. 498, Melville, NY: AIP Press (1999), pp. 353-366.

6. Non-neutral plasma physics, III, J.J. Bollinger, R.L. Spencer, and R.C. Davidson, eds., Proc., AIP Conf. 498, Melville, NY: AIP Press (1999).

7. "Crystalline order in strongly coupled plasmas," J.J. Bollinger, T.B. Mitchell, X.-P. Huang, W.M. Itano, J.N. Tan, B.M. Jelenković, and D.J. Wineland, Trapped Charged Particles and Fundamental Physics, D.H.E. Dubin and D. Schneider, eds., Proc., AIP Conf. 457 Woodbury, NY: AIP Press (1999), pp. 295-304.

8. "Atomic ion crystals in non-neutral plasmas," J.J. Bollinger, T. Mitchell, X.-P. Huang, W.M. Itano, J.N. Tan, B.M. Jelenković, and D.J. Wineland, Atomic Physics 16, W.E. Baylis and G.W.F. Drake, eds., Proc., AIP Conf. 477 Woodbury, NY: AIP Press (1999), pp. 87-99.

9. "Negative Poisson's ratios for extreme states of matter," R.H. Baughman, S.O. Dantas, S. Stafström, A.A. Zakhidov, T.B. Mitchell, and D.H.E. Dubin, Science **288**, 2018-2022 (2000).

10. "A laser-cooled positron plasma," B.M. Jelenković, J.J. Bollinger, A.B. Newbury, T.B. Mitchell, and W.M. Itano, New Directions in Antimatter Physics and Chemistry, C. Surko and F. Gianturco, eds., The Netherlands: Kluwer Academic Publishers (2001), pp. 1-20.

11. "Conference report: Workshop on non-neutral plasmas," J.J. Bollinger and J. Fajans, Comments on Plasma Physics and Controlled Fusion, **18**(6), 411-422 (1999).

12. "Crystalline plasma," W.M. Itano, McGraw-Hill Yearbook of Science and Technology, 2001, New York, NY: McGraw-Hill (2000), p. 116-118.

13. "Quantum logic with a few trapped ions," C. Monroe, W.M. Itano, D. Kielpinski, B.E. King, D. Leibfried, C.J. Myatt, Q.A. Turchette, D.J. Wineland, and C.S. Wood, Trapped Charged Particles and Fundamental Physics, D.H.E. Dubin and D. Schneider, eds., Proc., AIP Conf. 457, Woodbury, NY: AIP Press (1999), pp.

378-387.

14. "Searches for anomalous interactions using trapped ions," D.J. Wineland, J.J. Bollinger, W.M. Itano, J.C. Bergquist, C. Monroe, CPT and Lorentz Symmetry, V. Alan Kostelecký, ed., Singapore: World Scientific (1999), pp. 87-93.

15. "Decay of quantum superpositions into engineered reservoirs," C.J. Myatt, B.E. King, Q.A. Turchette, C.A. Sackett, D. Kielpinski, W.M. Itano, C. Monroe, and D.J. Wineland, Laser Spectroscopy, XIV International Conf., R. Blatt, J. Eschner, D. Leibfried, and F. Schmidt-Kaler, eds., Singapore: World Scientific (1999), pp. 237-245.

16. "Decoherence of motional states of trapped ions," C.J. Myatt, B.E. King, Q.A. Turchette, C.A. Sackett, D. Kielpinski, W.M. Itano, C. Monroe, and D.J. Wineland, J. Mod. Op. **47**, 2181-2186 (2000).

17. "Computing with atoms and molecules?" C. Monroe and D. J. Wineland, Science Spectra **23**, 72-79 (2000).

18. "Superposition and quantum measurement of trapped atoms," D. J. Wineland, C. R. Monroe, C. Sackett, D. Kielpinski, M. Rowe, V. Meyer, and W. Itano, Ann. Phys. (Leipzig) **9**, 851-854 (2000).

19. "Sub-systems for optical frequency measurements: application to the 282 nm $^{199}Hg^{+}$ transition and the 657 nm Ca line," B. Frech, J.S. Wells, C.W. Oates, J. Mitchell, Y.-P. Lan, T. Kurosu, L. Zink, L. Hollberg, T. Zibrova, B.C. Young, and J.C. Bergquist, IEEE Trans. Ultrason. Ferroelectr. Freq. Control 47, 513-517 (2000).

20. "Atom cooling, trapping, and quantum manipulation," C.E. Wieman, D.E. Pritchard, and D.J. Wineland, Rev. Mod. Phys. Centenary **71**, S253-S262 (1999); in More things in heaven and earth: A celebration of physics at the millennium, Ben Bederson, ed., Springer, NY (1999), pp. 426-441.

PREFACE

This collection of papers represents the work of the Ion Storage Group, Time and Frequency Division, National Institute of Standards and Technology, from January 1999 to October 2001. It follows the similar collections of papers contained in the previous Tech Notes:

NBS Technical Note 1086, *Trapped Ions and Laser Cooling I* (June 1985)
NIST Technical Note 1324, *Trapped Ions and Laser Cooling II* (September 1988)
NIST Technical Note 1353, *Trapped Ions and Laser Cooling III* (April 1992)
NIST Technical Note 1380, *Trapped Ions and Laser Cooling IV* (February 1996)
NIST Technical Note 1523, *Trapped Ions and Laser Cooling V* (January 2001)

Papers listed on page vi were published during the period from January 1999 to October 2001, but are not included here. Copies can be obtained on request. We hope this collection of papers will be useful to our colleagues in this and related fields.

We acknowledge our ion-trap/laser-cooling colleagues whose contributions made this work possible. These include Jim Beall, Dana Berkeland, Flavio Cruz, Ann Curtis, Scott Diddams, Bob Drullinger, Dan Dubin, Rich Fox, Leo Hollberg, Pei Huang, Steve Jefferts, Brana Jelenković, David Kielpinski, Brad King, Brian King, Chris Langer, David Lee, Didi Leibfried, Dawn Meekhof, Volker Meyer, John Miller, Travis Mitchell, Chris Myatt, Amy Newbury, Chris Oates, Rob Rafac, Mary Rowe, Cass Sackett, Joseph Tan, Quentin Turchette, Thomas Udem, Kurt Vogel, Joe Wells, Chris Wood, Brent Young, and in particular, Chris Monroe (now at University of Michigan). We gratefully acknowledge the support of the U.S. Office of Naval Research (ONR), the U.S. Army Research Office (ARO), the U.S. National Security Agency (NSA), the U.S. Advanced Research and Development Activity (ARDA), the U.S. National Reconnaissance Organization (NRO), and Timing Solutions, Inc. We thank Eyvon Petty and Edie DeWeese for assembling this collection.

James C. Bergquist
John J. Bollinger
Wayne M. Itano
David J. Wineland

Boulder, Colorado
December 2001

Lasers for an Optical Frequency Standard using Trapped Hg^+ Ions[1]

Brenton C. Young, Flavio C. Cruz,[2] Dana J. Berkeland,[3] Robert J. Rafac, James C. Bergquist, Wayne M. Itano, and David J. Wineland

National Institute of Standards and Technology, Boulder, Colorado 80303

Abstract. We are developing an optical frequency standard based on the narrow 281.5 nm transition of trapped $^{199}Hg^+$ ions. A major step toward the completion of this standard is the construction of an isolated high-finesse Fabry-Pérot cavity to stabilize the local oscillator. The cavity system that we have assembled has enabled the creation of an optical frequency source with good short-term stability. Eventually, this frequency source will derive long-term stability from a lock to the Hg^+ transition. We have recently demonstrated an improved linewidth of 0.6 Hz (40 s averaging time) for a 563 nm dye laser locked to our stable cavity. Additionally, we are developing solid-state laser replacements for gas and dye lasers presently used for driving 194 nm and 281.5 nm Hg^+ transitions.

INTRODUCTION

The next major advance for frequency standards probably lies in the development of optical frequency standards. Optical frequency standards are attractive since the potential fractional frequency instability of a quantum system is inversely proportional to the transition frequency. Because optical frequencies are approximately 10^5 times higher than the 9.2 GHz microwave transition used in cesium standards, much higher fractional stability might be achieved in a given measurement time.

In the 1970s, Dehmelt noted that single trapped and laser-cooled ions might be nearly ideal references for optical frequency and time standards [1,2]. High resolution is possible because perturbations can be made small and interrogation times long [1–4]. In addition, laser cooling considerably reduces first- and second-order Doppler shifts [5,6].

Several groups are developing optical frequency standards based on a variety of ions [7–20]. Among proposed standards that use trapped and laser-cooled ions, $^{199}Hg^+$ ions are attractive because they offer both a suitable microwave and optical transition. Figure 1(a) shows the $^{199}Hg^+$ electric dipole transitions at 194 nm used for laser cooling, optical pumping, and detection, and the electric quadrupole transition at 281.5 nm that is the reference for the optical frequency standard. Our group has recently demonstrated an accurate microwave frequency standard based on the 40.5 GHz. $F = 0 \rightarrow F = 1$, ground-state hyperfine splitting in trapped and cooled $^{199}Hg^+$ ions [21]. We expect to achieve significant gains in statistical precision, and likely in accuracy, for an optical frequency standard that interrogates the ultraviolet transition, with a frequency over 25 000 times that of the microwave frequency standard.

The optical standard is based on the $^2S_{1/2} \rightarrow {}^2D_{5/2}$, 281.5 nm electric-quadrupole transition [20]. An optical oscillator locked to this transition can have a fractional frequency instability approximately equal to 1×10^{-15} at 1 s even for a single laser-cooled ion. However, reaching such low instabilities requires a laser (local oscillator) whose frequency fluctuations are less than approximately 1 Hz during time intervals as long as a few seconds.

One of the main technical difficulties of working with Hg^+ is the development of reliable and economical ultraviolet laser sources. Recent advances in solid-state lasers have made possible optical sources at these

---

[1] Work of the U.S. Government, not subject to U.S. copyright.

[2] Present address: Universidade Estadual de Campinas, Campinas, SP, 13083-970, Brazil.

[3] Present address: Los Alamos National Laboratory, Los Alamos, NM 87545.

CP457, *Trapped Charged Particles and Fundamental Physics*
edited by Daniel H. E. Dubin and Dieter Schneider

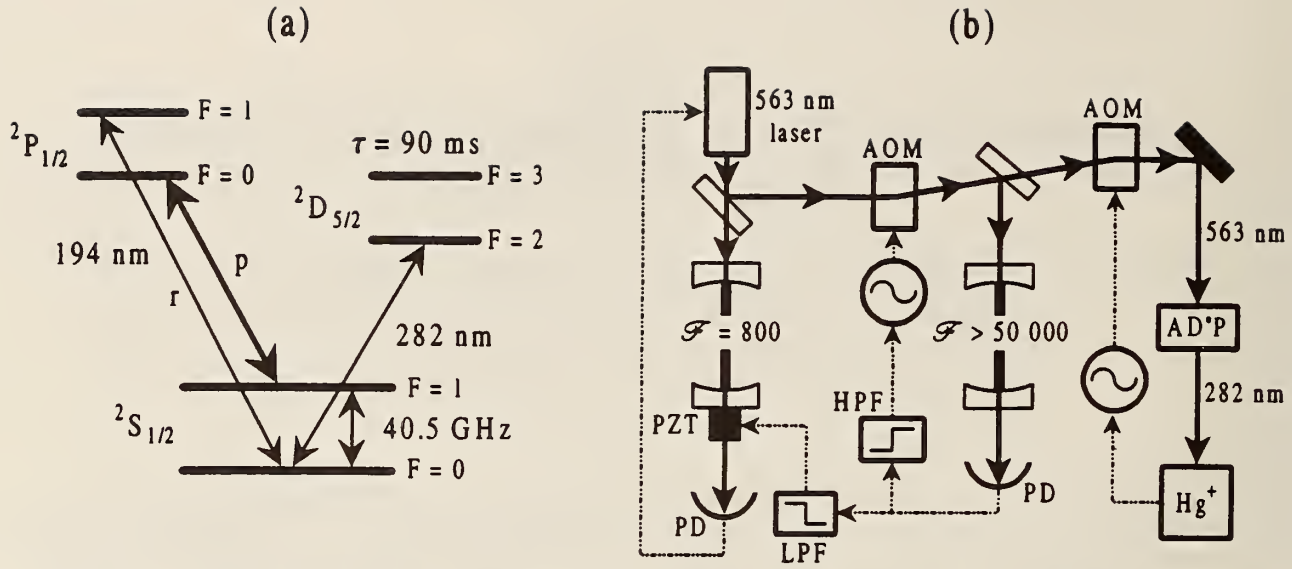

FIGURE 1. (a) Energy level diagram of $^{199}Hg^+$. We cool the ions using the $^2S_{1/2} \rightarrow {}^2P_{1/2}$ transitions at 194 nm. Because the $^2P_{1/2}$, F=0 $\rightarrow {}^2S_{1/2}$, F=0 transition is forbidden, transition p is a cycling transition. A second laser on transition r repumps atoms that decayed to $^2S_{1/2}$, F=0 after off-resonant excitation to $^2P_{1/2}$, F=1 by the first laser. (b) Simplified schematic of the proposed optical frequency standard. A dye laser is prestabilized to a Fabry-Pérot cavity ($\mathcal{F}$ = 800). Further stabilization to a much higher finesse cavity ($\mathcal{F}$ > 50000), and eventually to a narrow transition of trapped Hg^+ ion(s) should provide a highly stable frequency source. Solid lines denote optical paths and dotted lines represent electrical connections. AD*P, deuterated ammonium dihydrogen phosphate crystal for frequency doubling, AOM, acousto-optic modulator; $\mathcal{F}$, finesse; HPF, high-pass filter; LPF, low-pass filter; PD, photodiode, PZT, piezoelectric transducer.

wavelengths with lower initial costs and operating costs, higher reliability and efficiency, and lower intrinsic noise than for Ar^+ and dye lasers. Consequently, we are developing solid-state replacements for our present laser systems.

OVERVIEW OF THE OPTICAL FREQUENCY STANDARD

Figure 1(b) shows a simplified diagram of our proposed optical frequency standard. When interrogating a narrow atomic resonance, the laser must have a frequency width narrower than the transition linewidth to prevent the frequency instability of the laser from limiting the performance of the frequency standard. Consequently, one of the major steps in the development of the optical frequency standard is the construction of an optical local oscillator with sufficient spectral purity. For the 1.7 Hz linewidth $^{199}Hg^+$ transition, the stability of the standard will not be significantly degraded if the laser linewidth is below 1 Hz for interrogation times as long as a few seconds.

A central component of this system is a high-finesse ($\mathcal{F}$ > 50000) Fabry-Pérot cavity [20], which is described in detail in a later section. We use a dye laser at 563 nm as the optical source that is locked to this reference cavity. (The light is frequency-doubled to 281.5 nm in a crystal close to the Hg^+ trap.) Not shown in Fig. 1(b) is an iodine reference cell that we use to locate the Hg^+ transition whenever changes are made to the high-finesse reference cavity.

Rather than locking the laser directly to the high-finesse cavity, we first prestabilize it to a cavity with a finesse of approximately 800 using a Pound-Drever-Hall FM lock [22]. This prestabilization provides several advantages, including an increased locking range, a higher loop bandwidth for the lock, and improved versatility and tunability of the laser. An intracavity electro-optic modulator (EOM) in the dye laser provides high-frequency correction of laser frequency noise. A piezoelectric transducer (PZT) behind one of the dye-laser cavity mirrors eliminates long-term frequency drifts between the dye laser and the cavity. A loop bandwidth

of approximately 2 MHz in this prestabilization stage narrows the dye laser short-term ($\tau < 1$ s) linewidth to approximately 1 kHz.

An optical fiber delivers light from the dye-laser table to a vibrationally isolated table that supports the high-finesse cavity. An acousto-optic modulator (AOM) mounted on the isolated table shifts the frequency of the incoming light to match a cavity resonance. Again, we implement the lock using the Pound-Drever-Hall technique. The feedback loop performs corrections at low frequencies by adjusting a PZT on the prestabilization cavity, and at higher frequencies as high as approximately 90 kHz by varying the AOM drive frequency. With the lock enabled, the light entering the cavity has a spectral width less than 1 Hz, as we demonstrate later.

Finally, the frequency-stabilized light is transported to the table holding a cryogenic Hg^+ trap. The 563 nm radiation is frequency-doubled to 281.5 nm and is focused onto the trapped ion(s). The final AOM in Fig. 1(b) shifts the frequency of the light to match the ion transition. We plan to interrogate the transition using the Ramsey technique [23], with a Ramsey time of approximately 30 ms. A digital servo loop will adjust the AOM frequency to step between both sides of the central fringe, and will periodically record the values of the center frequency [20].

SOLID-STATE LASERS

The inherent frequency stability of solid-state lasers makes them attractive for metrological applications and precision spectroscopy. In addition, a solid-state laser can be compact, reliable, and long-lived. Reliable, commercial diode lasers do not yet exist in the uv, near the transitions needed for the Hg^+ system, but high-power, near-infrared diode lasers are available. Consequently, some groups have frequency-quadrupled the output of near-infrared diode lasers that oscillate at a single frequency and in a single spatial mode to obtain cw, single-frequency uv sources [24,25]. An alternative approach is to frequency-quadruple the output of a cw, solid-state laser that is pumped with high-power multimode diode lasers, as has been done using Nd:YAG and Nd:YVO_4 lasers [26,27]. We have taken this latter approach in developing an all-solid-state laser for driving the $^{199}Hg^+$ $S-D$ transition at 281.5 nm. The solid-state generation of 194 nm radiation for the cooling transition employs a diode-pumped solid-state laser in addition to sum-frequency mixing. These two laser systems are described in the following subsections.

Nd:FAP laser

For the 281.5 nm light source, we plan to replace a dye laser and its multiline Ar^+ pump laser with a frequency-doubled Nd^{3+}-doped fluorapatite (Nd:FAP) laser [28]. Nd:FAP has a lasing transition at 1.126 μm that, when frequency-quadrupled, coincides with the Hg^+ transition at 281.5 nm. The major difficulty in designing this laser is that Nd:FAP has a much stronger transition nearby at 1.063 μm [29] that must be suppressed by the laser optics. With 680 mW of diode pump light at 808 nm, the Nd:FAP output power is approximately 90 mW at 1.126 μm. Frequency doubling in $KNbO_3$ gives approximately 5 mW at 563 nm.

For the second stage of harmonic generation, we use deuterated ammonium dihydrogen phosphate (AD*P) to frequency-double 563 nm radiation to 281.5 nm [30]. Since less than 1 pW can be enough to saturate the narrow $S-D$ transition [30], we simply frequency-double the radiation at 563 nm in a single-pass configuration. approximately 25 nW is generated at 281.5 nm for 5 mW of input power at 563 nm.

Because the free-running frequency instability of this laser is dominated by low-frequency acoustical and mechanical noise, only a moderate-speed servo system is needed to lock the laser frequency tightly to the resonance of a high-finesse cavity [20,31]. In addition, since the frequency of the Nd:FAP laser is quadrupled to reach the atomic transition, this facilitates the first steps in a frequency chain from the optical to the microwave. We have demonstrated tunability of this laser through the Hg^+ transition. Poor stability of the pump-diode output mode, however, has forced us to use the original dye laser source for the experimental work described in the remainder of this paper.

Yb:YAG laser

Currently, the 194 nm cooling light is generated using a single-mode Ar^+ laser at 515 nm that is frequency-doubled in β-barium borate (BBO) to 257 nm and is then sum-frequency mixed in BBO with a diode source at

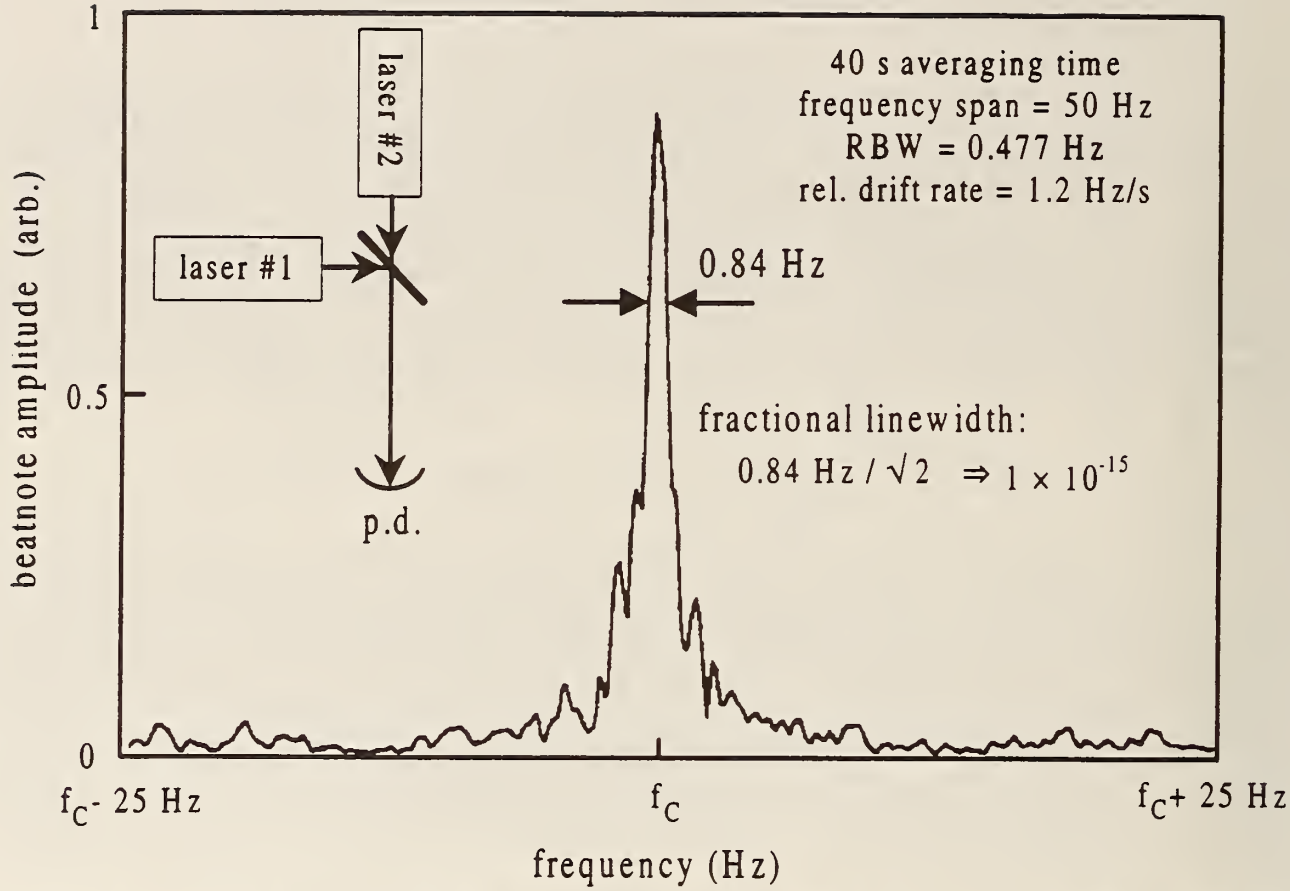

FIGURE 2. Amplitude spectrum of the beat note between two laser beams stabilized to two independent cavities. The dashed line shows the -3 dB level. The averaging time is 40 s. A nearly uniform relative cavity drift of 1.2 Hz/s is suppressed by mixing the beat note with a swept synthesizer.

792 nm to produce light at 194 nm [32]. We plan to replace the Ar^+ laser with a Yb:YAG laser at 1.03 μm [33]. With 3 W of diode pump power at 941 nm, the Yb:YAG output power is 1.2 W at 1.03 μm. We have frequency-doubled the Yb:YAG laser output in $KNbO_3$ to obtain over 400 mW at 515 nm, which should be sufficient power to replace the Ar^+ laser. At high optical powers, the frequency-doubling conversion efficiency is limited by losses from blue-light-induced infrared absorption [34]. We anticipate achieving a better conversion efficiency by frequency-doubling with lithium triborate (LBO) instead of $KNbO_3$.

HIGH-FINESSE REFERENCE CAVITY

To achieve a laser linewidth of <1 Hz for the source driving the Hg^+ ion transition, we start with a high-finesse cavity that has intrinsically low sensitivity to temperature variations, and then take great care to protect it from environmental perturbations. The separation of the cavity mirrors is set by optically contacting the mirrors to the ends of a hollow cylinder made from a low-thermal-expansion material. The mirror substrates are made of the same material as the cylinder. The cavity is supported inside an evacuated chamber by two thin wires. Keeping the cavity under vacuum both avoids pressure shifts of the cavity resonance and thermally insulates it from the environment. The temperature of the vacuum chamber is held near 30 °C, which is the point of zero coefficient of expansion for the cavity material. We protect the cavity from seismic noise by mounting it on a passively isolated optical table. The table is suspended by strands of surgical tubing approximately 3 m long. The fundamental vibrational mode of the suspension has a frequency of ≈0.3 Hz, which provides an isolation from floor noise that exceeds a factor of 50 in noise amplitude already at 3 Hz (some

viscous damping is used). To prevent the coupling of acoustic noise into the cavity, we enclose the optical table in a wooden box lined internally with lead foam [35].

The intracavity light heats the mirror coatings, thereby shifting the cavity resonance. To hold this shift at a reasonable value, we couple only approximately 100 μW of 563 nm light into the cavity. Furthermore, controlling the optical power in the cavity stabilizes this power shift. Active control of the rf power driving the AOM stabilizes the output power from the cavity to $\approx$0.1%.

To characterize the cavity's short-term stability performance without referencing to Hg^+, we constructed a second cavity and isolated table similar to that described above. Figure 2 shows the spectrum of the beat note between two independent laser beams stabilized to the two cavities. A nearly uniform relative cavity drift of $\approx$1 Hz/s is suppressed by mixing the beat note with a swept synthesizer. The width of the spectrum at its half-power point is 0.8 Hz (40 s averaging time). This implies that at least one of the lasers has a frequency width less than 0.6 Hz at 563 nm, corresponding to a fractional linewidth of only 1×10^{-15}. This is roughly 40 times better than previous results with only one cavity well isolated from vibrations [20], and may represent the smallest fractional linewidth ever recorded in the optical regime.

CONCLUSIONS

We have demonstrated an optical local oscillator suitable for development of a Hg^+ optical frequency standard at 281.5 nm. The frequency source has a linewidth of less than 0.6 Hz at 563 nm (40 s averaging time), corresponding to a fractional linewidth of 1×10^{-15}. We have described work on solid-state laser replacements for gas and dye lasers presently used in the trapped Hg^+ work. Future work will involve collaboration with other researchers at NIST and JILA to develop a frequency chain for translating the frequency and the stability of our standard into the microwave regime. This work is supported by ONR and NIST.

REFERENCES

1. Dehmelt, H. G., *Bull. Am. Phys. Soc.* 18, 1521 (1973).
2. Dehmelt, H. G., *IEEE Trans. Instrum. Meas.* **IM-31**, 83–87 (1982).
3. Wineland, D. J., *et al.*, *J. Phys. (Paris)* **42**, C8-307–C8-313 (1981).
4. Fisk, P. T. H., *Rep. Prog. Phys.* **60**, 761–817 (1997).
5. Wineland, D., and Dehmelt, H., *Bull. Am. Phys. Soc.* **20**, 637 (1975).
6. Wineland, D. J., and Itano, W. M., *Phys. Today* **40**, 34–40 (1987).
7. Bergquist, J. C., ed., *Proceedings of the Fifth Symposium on Frequency Standards and Metrology*, Singapore: World Scientific, 1996.
8. Sugiyama, K., Sasaki, K., Wakita, A., and Yoda, J., "Progress toward high-resolution spectroscopy of the $^2S_{1/2}$-$^2D_{5/2}$ transition of laser-cooled trapped Yb^+," in *International Workshop on Current Topics of Laser Technology*, 1998, p. 56.
9. Taylor, P., Roberts, M., Barwood, G. P., and Gill, P., *Opt. Lett.* **23**, 298–300 (1998).
10. Engelke, D., and Tamm, C., *Europhys. Lett.* **33**, 347–352 (1996).
11. Barwood, G. P., *et al.*, *Opt. Commun.* **151**, 50–55 (1998).
12. Bernard, J. E., Marmet, L., and Madej, A. A., *Opt. Commun.* **150**, 170–174 (1998).
13. Madej, A. A., *et al.*, "Precision absolute frequency measurements with single atoms of Ba^+ and Sr^+," in *Proceedings of the Fifth Symposium on Frequency Standards and Metrology*, 1996, pp. 165–170.
14. Urabe, S., *et al.*, *Appl. Phys. B* **67**, 223–227 (1998).
15. Knoop, M., Vedel, M., and Vedel, F., *Phys. Rev. A* **58**, 264–269 (1998).
16. Fermigier, B., *et al.*, *Opt. Commun.* **153**, 73–77 (1998).
17. Peik, E., *et al.*, "Towards an optical clock with a laser-cooled indium ion," in *International Workshop on Current Topics of Laser Technology*, 1998, pp. 23–24.
18. Nagourney, W., Burt, E., and Dehmelt, H. G., "Optical frequency standard using individual indium ions," in *Proceedings of the Fifth Symposium on Frequency Standards and Metrology*, 1996, pp. 341–346.
19. Yu, N., Dehmelt, H., and Nagourney, W., *Proc. Natl. Acad. Sci. U.S.A.* **89**, 7289 (1992).
20. Bergquist, J. C., Itano, W. M., and Wineland, D. J., "Laser stabilization to a single ion," in *Frontiers in Laser Spectroscopy*, 1994, pp. 359–376.
21. Berkeland, D. J., *et al.*, *Phys. Rev. Lett.* **80**, 2089–2092 (1998).
22. Drever, R. W. P., *et al.*, *Appl. Phys. B* **31**, 97–105 (1983).
23. Ramsey, N. F., *Phys. Rev.* **78**, 695–699 (1950).

24. Zimmermann, C., Vuletic, V., Hemmerich, A., and Hänsch, T. W., *Appl. Phys. Lett.* **66**, 2318–2320 (1995).
25. Matsubara, K., *et al.*, *Appl. Phys. B* **67**, 1–4 (1998).
26. Hollemann, G., Peik, E., and Walther, H., *Opt. Lett.* **19**, 192–194 (1994).
27. Kondo, K., *et al.*, *Opt. Lett.* **23**, 195–197 (1998).
28. Cruz, F. C., Young, B. C., and Bergquist, J. C., "Diode-pumped Nd:FAP laser at 1.126 μm: a possible local oscillator for a Hg^+ optical frequency standard," *Appl. Opt.* (to be published).
29. Ohlmann, R. C., Steinbruegge, K. B., and Mazelsky, R., *Appl. Opt.* **7**, 905–914 (1968).
30. Bergquist, J. C., Hulet, R. G., Itano, W. M., and Wineland, D. J., *Phys. Rev. Lett.* **57**, 1699–1702 (1986).
31. Zhu, M., and Hall, J. L., "Frequency stabilization of tunable lasers," in *Atomic, Molecular, and Optical Physics: Electromagnetic Radiation*, 1997, pp. 103–136.
32. Berkeland, D. J., Cruz, F. C., and Bergquist, J. C., *Appl. Opt.* **36**, 4159–4162 (1997).
33. Fan, T. Y., and Ochoa, J., *IEEE Photon. Technol. Lett.* **7**, 1137–1138 (1995).
34. Mabuchi, H., Polzik, E. S., and Kimble, H. J., *J. Opt. Soc. Am. B* **11**, 2023–2029 (1994).
35. Hils, D., Faller, J. E., and Hall, J. L., *Rev. Sci. Instrum.* **57**, 2532–2534 (1986).

High-Resolution, High-Accuracy Spectroscopy of Trapped Ions *

D.J. Berkeland[1], J.D. Miller[2], F.C. Cruz[3], B.C. Young, R.J. Rafac, X.P. Huang[4], W.M. Itano, J.C. Bergquist and D.J. Wineland

National Institute of Standards and Technology (NIST), 325 Broadway, Boulder Colorado 80303

Abstract. Microwave spectroscopy using trapped and cooled ions can achieve precision and accuracy comparable to the best cesium frequency standards. We discuss standards based on $^{199}Hg^{+}$ ions trapped in linear Paul traps: the Jet Propulsion Laboratory (JPL) standard, which uses up to 10^7 atoms confined near the trap axis, and the recently evaluated NIST standard, which uses approximately ten ions laser cooled and crystalized on the trap axis. We consider future directions in trapped ion frequency standard work, including the use of entangled states for achieving higher precision, and progress on trapped ion optical frequency standards. Finally, we discuss scientific and technical applications of extremely stable frequency standards.

INTRODUCTION

Precise and accurate atomic spectroscopy can rigorously test theories of atomic structure, quantum electrodynamics [1] and other fundamental physics [2,3], determine fundamental constants [4], and provide time and frequency standards [3]. Precise and accurate spectroscopy has two basic requirements. First, the measurement must reach the desired precision in a reasonable averaging time. This requires a good signal to noise ratio and a narrow transition. Second, systematic frequency shifts and broadening mechanisms of the atomic transition being studied must be either very small, or stable and very well measured.

As seen at this conference, many experiments with cooled and trapped ions and with laser-cooled neutral atoms can satisfy these requirements. Here we limit our discussion to precision experiments using trapped and cooled ions [5]. The

*) Work performed at NIST is supported by the Office for Naval Research and the Army Research Office. Work of U.S. Government; not subject to U.S. copyright.

1) Los Alamos National Laboratory, P23, MS H803, Los Alamos, NM

2) KLA-Tencor Corp., 1701 Directors Blvd., Suite 1000, Austin, TX 78744

3) Universidade Estadual de Campinas, UNICAMP-IFGW-DEQ, CP.6165 Campinas, SP, 13083-970, Brazil

4) Colorado MED-Tech-RELA, Inc., 6175 Longbow Dr., Boulder, CO 80301

systematic shifts of atomic transition frequencies in these systems can be small and well-characterized. For example, Stark shifts are small since $< \mathbf{E} > = 0$ and $< E^2 >$ is small when the ions are cold. The magnetic field can be small and easy to characterize because the ions occupy a small volume. The corresponding Zeeman shift is typically small because usually transitions with only a second-order field dependence are used. Because background gas pressure can be negligible, collisional shifts and broadening can be small. The ions can be cooled using either buffer-gas cooling or laser cooling [6], reducing Doppler shifts. The statistical precision can be high if large numbers of ions are stored, or if the shot noise limit is reached. Finally, free precession times of several minutes have been reported [7,8], giving extremely narrow transition linewidths.

The statistical precision of a frequency standard can be predicted quantitatively for various cases. For example, if an atomic transition is probed using the Ramsey technique [9] and the measurement precision is limited only by quantum fluctuations in the atomic state populations [10], the fractional precision of the frequency measurement is given by [11]

$$\frac{\Delta\omega_{measured}}{\omega_0} \equiv \sigma_y(\tau) = \frac{1}{\omega_0\sqrt{NT_R}}\,\tau^{-1/2}. \qquad (1)$$

Here, ω_0 is the transition angular frequency, $\Delta\omega_{measured}$ is the precision with which the frequency is measured, and the Allan deviation $\sigma_y(\tau)$ is related to the fractional frequency instability. N is the number of atoms used, T_R is the free precession time between the two $\pi/2$ Rabi pulses, and τ ($> T_R$) is the averaging time of the measurement. Ideally, N, T_R, and τ are large, although various experimental constraints may limit these values.

Table 1 compares these parameters for two types of microwave frequency standards—those based on ions confined in an rf Paul trap and those based on a pulsed fountain of cesium atoms [12]. The number N of atoms used in the trapped ion standards is limited in part by the second-order Doppler shift due to micromotion. This motion is driven by the trap's rf electromagnetic fields, and becomes greater as the Coulomb repulsion between the ions forces them further from the field nodal point or line [13]. Thus there is a trade-off between using very large N but with a substantial Doppler shift, or a negligible Doppler shift but smaller N. In the Cs fountain standard, N is limited in part by collisional shifts. For laser-cooled trapped ion standards, T_R is limited by the time the ions remain cold in the absence of cooling radiation. In a fountain standard it is limited to about 1 s by the maximum practical height the atoms can be tossed (about one meter). Finally, the averaging time τ is not fundamentally limited in either type of standard.

Ions in Penning traps have been used previously to realize the first laser-cooled frequency standard [7,16]. An important limitation to accuracy in those experiments was the uncertainty in the second-order Doppler shift due to the overall rotational motion of the ion cloud. This motion can now be precisely controlled [17], and it should therefore be possible to realize an rf or microwave frequency

TABLE 1. Example parameters for trapped ion and cesium fountain microwave frequency standards.

Parameter	Ions	Cs
$\omega_0/(2\pi)$	40.5 GHz ($^{199}Hg^+$)	9.2 GHz
N	$\approx$ 10 [14] to 10^7 [15]	10^4 to 10^6
T_R	Up to 600 s [7,8]	$\sim$ 1 s

standard with accuracy comparable to what is possible with Paul traps [18]. To date, the highest accuracies and stabilities have been obtained in linear Paul traps; therefore, we highlight this work below.

Figure 1 shows a schematic diagram of a linear Paul trap [19–21]. In this trap, the ions are confined axially by the two cylindrical sections (endcaps) held at static potential U_0. The shape of these endcaps is not critical, and axial confinement can be produced by thin conducting rods located on the trap axis at both ends of the trap [15], by small rings [20] or by segmented electrodes [21]. Two of the long, thin rods of Fig. 1 are held at ground potential, while the other two are held at an rf potential. This gives an oscillating electric potential that traps the ions in a radial quadratic pseudopotential [22]. The advantage of the linear trap is that many ions can be confined near or on the electric field nodal line, where Doppler shifts from micromotion are minimized.

MICROWAVE SPECTROSCOPY

Microwave spectroscopy with clouds of trapped ions has been used for many years in atomic structure measurements [23]. Some recent experiments report measurements of g factors [24] and hyperfine constants [25–29]. Because ion traps can use small samples, they are well-suited for measurements of hyperfine anomalies using different isotopes, some of which are radioactive [25,26,29].

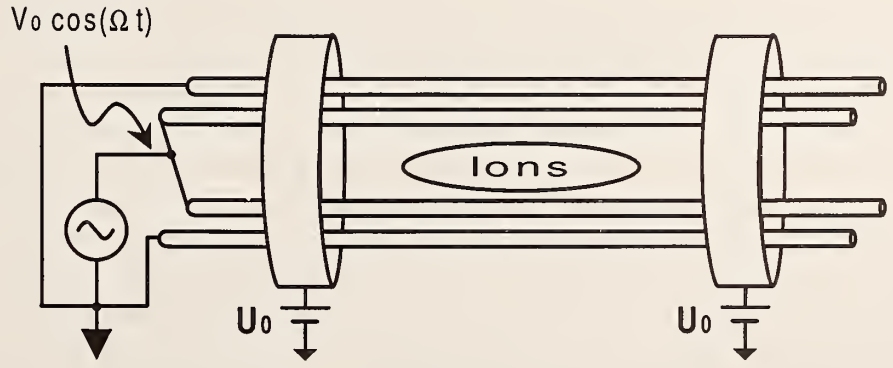

FIGURE 1. Schematic diagram of a linear Paul trap.

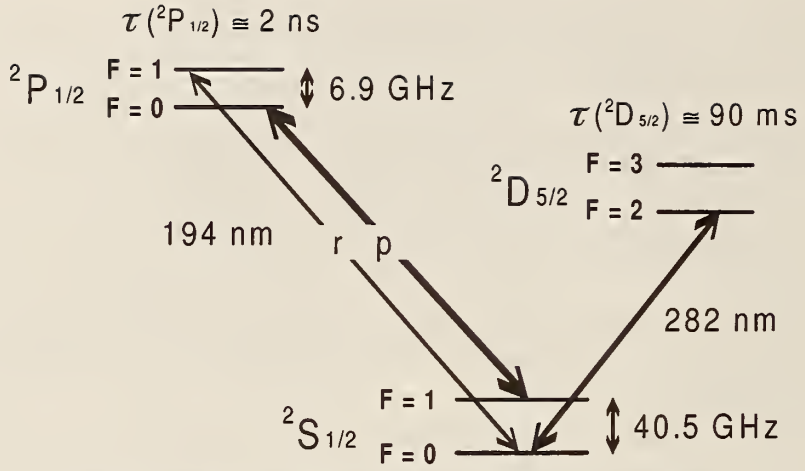

FIGURE 2. Partial energy level diagram of $^{199}Hg^{+}$.

Taking advantage of the precision and accuracy offered by the ground state hyperfine transition of trapped ions, several groups are working on atomic frequency standards based on $^{113}Cd^{+}$ ($\omega_0 = 2\pi \times 15.2$ GHz) [27,30] and $^{171}Yb^{+}$ ($\omega_0 = 2\pi \times 12.6$ GHz) [20,31–33]. Here we describe microwave frequency standards based on trapped $^{199}Hg^{+}$ ions [14,15,34]. Figure 2 shows a partial energy level diagram of this atom. The electric dipole transitions at 194 nm are used for state preparation and detection, and can be used for laser cooling. The ground state hyperfine splitting frequency is $2\pi \times 40.5$ GHz, the highest of routinely trapped ions. The $\Delta m_F = 0$ hyperfine transition dependends only quadratically on the magnetic field, when the field is near zero.

At JPL, much work has been done with clouds of $^{199}Hg^{+}$ ions in a linear Paul trap [15,34]. The methods and performance of the Commonwealth Scientific and Industrial Research Organization (CSIRO) experiments on $^{171}Yb^{+}$ are similar [20]. The four trap rods of the JPL linear ion trap standard (LITS) in reference [15] are evenly spaced on a circle of 1 cm radius, with two endcap rods on the trap axis 7.5 cm apart. This trap confines clouds of up to 10^7 ions, which are cooled with a helium buffer gas. States are prepared and detected with a ^{202}Hg lamp, which emits broad-line radiation that partially overlaps the resonances of the two $^2S_{1/2}, F = 1 \rightarrow {}^2P_{1/2}$, $F = 0, 1$ transitions. Because the $^2P_{1/2}, F = 1$ state can decay to the $^2S_{1/2}, F = 0$ state, illuminating the ions with the lamp radiation pumps them into the $^2S_{1/2}$ $F = 0$ state in preparation for the Ramsey interrogation. At the end of the Ramsey interrogation, the lamp radiation is returned to the ions, and the detected fluorescence indicates how many ions are in the $^2S_{1/2}$ $F = 1$ state. Because the ions scatter only a few photons before optically pumping out of the $^2S_{1/2}$ $F = 1$ state, and because only a small fraction of the scattered photons are detected, the state detection efficiency is much less than unity, so the state measurements are not quantum noise limited and Eq. (1) is not applicable. However, because N is large, this device is very stable. With a Ramsey time T_R of

8 s, LITS has recently demonstrated an instability of $\sigma_y(\tau) = 3 \times 10^{-14}\ \tau^{-1/2}$ [35]. At CSIRO, a similar standard using clouds of laser-cooled $^{171}Yb^+$ ions in a linear trap has $\sigma_y(\tau) = 4.7 \times 10^{-14}\ \tau^{-1/2}$ [20].

Although these standards are very stable, the second-order Doppler shift from the ion motion is substantial (about 9×10^{-13}). At NIST, the goal is to develop a frequency standard that is both stable and accurate. We use a linear trap such as that shown in Fig. 1, with the endcaps approximately 4 mm apart and the 0.2 mm radius rods on a 0.64 mm radius [36]. Approximately ten ions are used, and they are laser cooled so that they crystalize along the nodal line of the rf electric field, near the trap axis. Using a small number of ions sacrifices precision according to Eq. (1), but greatly reduces Doppler shifts. Groups at CSIRO [37] and the Communications Research Laboratory (CRL) [38] have also crystalized laser-cooled ions in linear Paul traps in order to improve the accuracy of their frequency standards.

The NIST standard has other advantages. The trap is enclosed in a copper container that forms the bottom of a liquid helium reservoir [36]. Because of the cryogenic environment, the pressure of background neutral mercury atoms is negligible. This is critical because the background mercury pressure leads to ion loss, presumably due to dimer formation. This ion loss limits the storage time of trapped ions in a room temperature trap to about ten minutes. At 4 K, the ions can be trapped for days at a time without loss. Also, in the 4 K environment the pressure of all other background gases is negligible, with the possible exception of helium. This greatly reduces collisional shifts and heating from collisions. Additionally, the black body shift, which is already over two orders of magnitude smaller than in cesium at room temperature [39], is dramatically reduced. To ensure that the ions are on the nodal line, we minimize the micromotion observed in three non-coplanar directions [13]. Because the rf electric field at the site of the ions in minimized, the rf heating while the cooling lasers are off during the free precession time T_R is minimized. Finally, laser cooling (instead of buffer gas cooling) significantly reduces Doppler shifts; we have measured the second-order Doppler shift to be less than 3×10^{-17} [14].

The steps in operating the frequency standard are as follows. We Doppler cool the ions by using radiation from a primary laser whose frequency is slightly red-detuned from transition p (see Fig. 2). Although this is a cycling transition, the laser weakly couples the $S_{1/2}$, $F = 1$ state to the $P_{1/2}$, $F = 1$ state, which decays to the $S_{1/2}$, $F = 0$ state. To optically pump the ions out of this state, we overlap a less intense repumping laser beam with the primary laser beam to drive the r transition. After a Doppler cooling period of 200 to 300 ms, we pump the ions into the $S_{1/2}$, $F = 0$ state with high efficiency by applying only the primary laser for 10 ms. Then we drive the microwave transition using the Ramsey method, with a free precession time T_R of 2 to 100 s. After this, to determine the ensemble average of the $S_{1/2}$, $F = 1$ state populations, we again apply only the primary laser for about 10 ms. If an ion is found to be in the $F = 1$ state, it will scatter

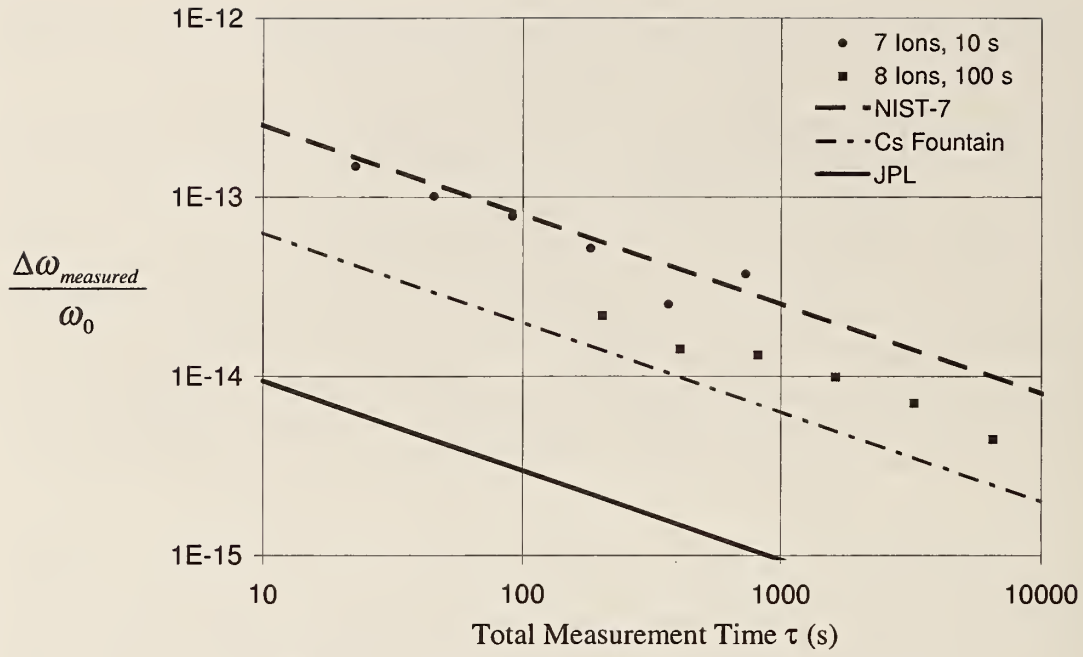

FIGURE 3. Stabilities of several standards.

approximately 10,000 photons before being optically pumped into the $S_{1/2}$, $F = 0$ state. Otherwise, the atoms scatter only a few photons in the same time interval, due to the off-resonant $S_{1/2}$, $F = 0$ to $P_{1/2}$, $F = 1$ transition. Our detection signal is the observed fluorescence from all of the ions. Repeating this measurement process and scanning the microwave frequency produces a Ramsey fringe pattern. We lock the frequency to the central Ramsey fringe by stepping the frequency from one side of the fringe to the other, while a digital servo works to keep the detection signal constant at each step.

Figure 3 shows the instability $\sigma_y(\tau)$ of the microwave oscillator when it is locked to the central Ramsey fringe with $T_R = 10$ s and $T_R = 100$ s. For $T_R = 100$ s, the instability is $\sigma_y(\tau) = 3.3 \times 10^{-13}\, \tau^{-1/2}$. The measured instability of the standard is consistently twice that expected from Eq. (1), due to fluctuations of the laser intensity at the site of the ions. The figure also shows the stability of the cesium beam standard NIST-7 ($8 \times 10^{-13}\ \ \tau^{-1/2}$) [40] and the Paris cesium fountain standard ($2 \times 10^{-13}\ \ \tau^{-1/2}$) [12]. The instabilities of these three standards are comparable, while that of the JPL $^{199}Hg^+$ standard is significantly better ($\sigma_y(\tau) = 3 \times 10^{-14}\, \tau^{-1/2}$).

The accuracy of the JPL standard is limited by the second-order Doppler shift to around 10^{-13} [41]. The other standards in Fig. 3 have significantly greater accuracy, and the accuracies of these standards are comparable. The fractional accuracy of NIST-7 is 5×10^{-15}, limited by the distributed cavity phase shift [42]. This high accuracy corresponds to splitting the central Ramsey fringe to about a part in 10^6. A natural next step toward a more accurate frequency standard is to reduce the

linewidth. The cesium fountain frequency standard does this by increasing the Ramsey free precession time T_R. In this standard, the accuracy is currently limited by black body and collisional shifts to 1.4×10^{-15} [43]. The accuracy of the NIST $^{199}Hg^+$ standard is 3.4×10^{-15}, and is limited by uncertainties in the Zeeman shift [14]. The dominant shift is caused by asymmetries in currents running through the trap electrodes, which cause a net rf magnetic field at the site of the ions.

The trapped ion and cesium fountain standard are both emerging technologies that promise even higher accuracy. At NIST we have constructed a new, smaller trap, which we will run with lower trap drive frequency Ω. Less rf potential is needed for the same radial confinement in the trap, reducing the currents in the trap rods and, from scaling arguments, the associated magnetic field at the site of the ions. Also, we have improved our magnetic shielding to reduce fluctuations in the ambient magnetic field. We expect that the next generation of this standard will be accurate to approximately 10^{-16}.

FUTURE DIRECTIONS

One way to reduce the instability $\sigma_y(\tau)$ of a standard is to increase the transition frequency ω_0. Therefore, many groups are working on optical frequency standards. The laser-cooled stored ion efforts include trapped $^{172}Yb^+$ at 411 nm [44] and 3.43 μm [45], $^{171}Yb^+$ at 435 nm [46], $^{88}Sr^+$ at 674 nm [47,48], $^{138}Ba^+$ at 12.5 μm [49], $^{40}Ca^+$ at 729 nm [50–52], $^{115}In^+$ at 237 nm [53,54], and $^{199}Hg^+$ at 282 nm [55].

Earlier work at NIST using $^{199}Hg^+$ in a room temperature trap produced a narrow transition with structure due to Rabi oscillations [55]. The width of the central feature was about 40 Hz at 563 nm. Our pursuit of higher resolution and a study of systematic effects was hampered by the the limited lifetime of the ion in the room temperature trap. However, we have now built a second cryogenic system that will provide long ion lifetimes and more detailed investigations of this transition. Also, we have recently made substantial improvements in the laser system; the laser linewidth in about a one minute averaging time is now less than one hertz at 563 nm [56].

For the absolute frequency of a transition to be determined, ω_0 must be compared to an accepted frequency standard. We are now comparing the frequency of the 282 nm transition to a that of the narrow $^1S_0 - ^3P_1$ intercombination line of Ca at 657 nm [57,58] by mixing a CO overtone line with the fundamental 563 nm light [59]. The NIST Ca standard has been compared to the Physikalisch-Technische Bundesanstalt (PTB) Ca standard, which has in turn been compared to the 9.2 GHz line in Cs [60]. In other laboratories, the absolute frequency of the $^{88}Sr^+$ S to D transition at 674 nm has been measured with a frequency chain [48]. Interferometric measurements have also been made on this transition [61] and on the S to D transition at 411 nm in $^{172}Yb^+$ [44], with frequency chain measurements in progress [62].

Another way to reduce $\sigma_y(\tau)$ is by using entangled states [63,64]. Consider

an atomic system with two states labeled $\uparrow$ and $\downarrow$, separated by frequency ω_0. We use the spin 1/2 analog for these two states [65], so the total angular momentum for N ions is given by $\mathbf{J} = \sum_{i=1}^{N} \mathbf{S_i}$, where $\mathbf{S_i}$ is the spin of the ith atom ($S_i = 1/2$). For uncorrelated atoms, the Ramsey spectrum is given by $< J_z > = N \cos((\omega_0 - \omega)\, T_R)$. The best possible uncertainty in the measured value of ω_0 is the shot noise limit of $\Delta\omega_0 = 1/\sqrt{NT_R\tau}$ [10]. This uncertainty can be reduced if we use an entangled state in the following way. Suppose that the N-atom state at the beginning of the free precession time is given by

$$(e^{\frac{-iN\omega_0 t}{2}} |\uparrow_1\uparrow_2 \ldots \uparrow_N> + e^{\frac{+iN\omega_0 t}{2}} |\downarrow_1\downarrow_2 \ldots \downarrow_N>)/\sqrt{2}. \qquad (2)$$

After the free precession time, a $\pi/2$ Rabi pulse is applied as in usual Ramsey spectroscopy. The signal is obtained by measuring an operator that is the product of the z-components of the Pauli spin matrices, $O = \prod_{i=1}^{N} (\sigma_z)_i$. This gives a signal $\langle O \rangle = (-1)^N \cos(N\ (\omega_0 - \omega)\ T_R)$, where ω is the frequency of the applied radiation. The uncertainty in ω_0 is now given by the exact Heisenberg limit $\Delta\omega_0 = 1/N\sqrt{T\tau}$ [63]. This method results in a factor of N decrease in the averaging time τ required to achieve a given precision. Although similar precision gains can be made by increasing N, the optimal value of N in high accuracy ion trap standards might be limited by other experimental constraints, thereby making entangled state spectroscopy advantageous.

APPLICATIONS

Improved frequency standards benefit communications and navigation [66,67] and help in determining some fundamental physical constants [68]. Another possible application of improved frequency standards is in detecting the stochastic background of gravitational radiation [69,70]. This background is similar to the observed cosmic microwave background at 4 K, but has not been detected. Estimates for the density ρ of these gravitational waves vary by many orders of magnitude and are extremely model dependent. A limit on ρ may be determined by timing the bursts of light emitted by pulsars, which are more stable for long times than the best clocks on earth [71]. If gravitational radiation present at the pulsar location is not correlated with the gravitational radiation present at earth, clocks at the two locations will become decorrelated after some time τ_d, and the measured instability $\sigma_y(\tau)$ of the pulsar bursts will begin to increase with averaging time $\tau > \tau_d$. For example, using the estimates from [72], timing measurements from the pulsar J1713+0747 should destabilize at $\tau = \tau_d \sim 2$ y and $\sigma_y(\tau_d) \sim 10^{-14}$ [73]. However, because the current global time scale is stable at only the 10^{-14} level on a time scale of about one year, any observed destabilization could also be from the long-term drifts in the terrestrial time scale. Better clocks are thus required to verify or reject these theories.

Another scientific application of better frequency standards is the laboratory measurement of possible changes in fundamental constants, such

as the fine structure constant α. Nonlaboratory measurements include estimates from Sm isotope distributions at the Oklo mine, giving $-6.7 \times 10^{-17}/\text{year} < \dot{\alpha}/\alpha < 5.0 \times 10^{-17}/\text{year}$ [74]. However, this measurement assumes a linear change in α over time and is model dependent. Laboratory measurements can in principle detect nonlinear changes in α over a relatively short time. Because the hyperfine splitting frequency depends nonlinearly on the nuclear charge Z and on α, comparing the frequency of the hyperfine constant in hydrogen A_H to that of another alkali A_{Alkali} gives $\dot{\alpha}/\alpha$ according to [75]

$$\frac{d}{dt} \ln \frac{A_{Alkali}}{A_H} = \alpha \frac{d}{d\alpha} \ln \left(F_{rel}(\alpha Z)\right) \left(\frac{1}{\alpha} \frac{d\alpha}{dt}\right), \tag{3}$$

where $F_{rel}(\alpha Z)$ is the Casimir correction factor [76]. Recently, the hyperfine structure frequency of $^{199}Hg^{+}$ has been compared to that of hydrogen for 140 days to obtain $|\dot{\alpha}/\alpha| \leq 3.7 \times 10^{-14}/\text{year}$ [75]. Optical atomic transition measurements have also been proposed for detecting changes in α [77]. Clearly, any improvement in the precision of laboratory frequency standards would tighten the limits on $\dot{\alpha}/\alpha$.

SUMMARY

Trapped and cooled ions are particularly suitable systems for precise and accurate spectroscopy. Frequency standards using trapped ions have stabilities and accuracies that are comparable to those of the best of Cs standards and are expected to continue to improve. Some directions toward improving trapped ion frequency standards use optical transitions and entangled states. In addition to improving technological applications, better frequency standards can test fundamental physics.

ACKNOWLEDGEMENTS

We thank Lute Maleki, Travis Mitchell, John Prestage, Don Sullivan and Matt Young for valuable comments on this manuscript.

REFERENCES

1. T. Kinoshita, editor, *Quantum Electrodynamics*, World Scientific, 1990.
2. L. Maleki, editor, *Proceedings of the Workshop on the Scientific Applications of Clocks in Space*, 1997, JPL Publication 97-15.
3. J. Bergquist, editor, *Proceedings of the 5th Symposium on Frequency Standards and Metrology*, Singapore, 1996, World Scientific.
4. B. W. Petley, *The Fundamental Physical Constants and the Frontier of Measurement*, A. Higler, Bristol, England, 1988.
5. P. T. H. Fisk, **60**, 761 (1997).

6. W. M. Itano, J. C. Bergquist, J. J. Bollinger, and D. J. Wineland, **59**, 106 (1995).
7. J. J. Bollinger, D. J. Heinzen, W. M. Itano, S. L. Gilbert, and D. J. Wineland, **40**, 126 (1991).
8. P. T. H. Fisk et al., 44, 113 (1995).
9. N. F. Ramsey, *Molecular Beams*, Oxford University Press, 1956.
10. W. M. Itano et al., Phys. Rev. A **47**, 3554 (1993).
11. D. J. Wineland et al., High Accuracy Spectroscopy of Stored Ions, in *Proceedings of the 4th Symposium on Frequency Standards*, edited by A. Demarchi, pages 71–76, Heidelberg, 1989, Springer-Verlag.
12. A. Clairon et al., Preliminary Accuracy Evaluation of a Cesium Fountain Frequency Standard, In Bergquist [3], pages 49–59.
13. D. J. Berkeland, J. D. Miller, J. C. Bergquist, W. M. Itano, and D. J. Wineland, J. Appl. Phys. **83**, 5025 (1998).
14. D. J. Berkeland, J. D. Miller, J. C. Bergquist, W. M. Itano, and D. J. Wineland, Phys. Rev. Lett. **80**, 2089 (1998).
15. R. Tjoelker, J. D. Prestage, and L. Maleki, Record Frequency Stability with Mercury in a Linear Ion Trap, In Bergquist [3], pages 33–38.
16. J. J. Bollinger, J. D. Prestage, W. M. Itano, and D. J. Wineland, Phys. Rev. Lett. **54**, 1000 (1985).
17. X. P. Huang, J. J. Bollinger, T. B. Mitchell, and W. M. Itano, Phys. Rev. Lett. **80**, 73 (1998).
18. J. N. Tan, J. J. Bollinger, and D. J. Wineland, 44, 144 (1995).
19. J. D. Prestage, G. J. Dick, and L. Maleki, J. Appl. Phys. **66**, 1013 (1989).
20. P. T. H. Fisk, M. J. Sellars, M. A. Lawn, and C. Coles, **44**, 344 (1997).
21. M. G. Raizen, J. M. Gilligan, J. C. Bergquist, W. M. Itano, and D. J. Wineland, **39**, 233 (1992).
22. W. Paul, Rev. Mod. Phys. **62**, 531 (1990).
23. G. Werth, Hyperfine Interactions **99**, 3 (1996).
24. K. H. Knöll et al., Phys. Rev. A **54**, 1199 (1996).
25. K. Enders et al., Phys. Rev. A **56**, 265 (1997).
26. M. Wada et al., **626**, 365c (1997).
27. U. Tanaka et al., Phys. Rev. A **53**, 3982 (1996).
28. F. Arbes, M. Benzing, T. Gudjons, F. Kurth, and G. Werth, **31**, 27 (1994).
29. H. Sunaoshi et al., Hyperfine Interactions **78**, 241 (1993).
30. K. Matsubara et al., **67**, 1 (1998).
31. C. Tamm, D. Schnier, and A. Bauch, **60**, 19 (1995).
32. V. Enders et al., **24**, 325 (1993).
33. D. J. Seidel, A. Williams, R. W. Berends, and L. Maleki, The Development of the Ytterbium Ion Frequency Standard, in *1992 IEEE Frequency Control Symposium*, pages 70–75, New York, 1992, IEEE.
34. J. D. Prestage, R. L. Tjoelker, G. J. Dick, and L. Maleki, **39**, 221 (1992).
35. L. Maleki, MS 298-100, JPL, 4800 Oak Grove Drive, Pasadena, CA 91109, private communication.
36. M. E. Poitzsch, J. C. Bergquist, W. M. Itano, and D. J. Wineland, Rev. Sci. Instrum. **67**, 129 (1996).

37. P. T. H. Fisk, National Measurement Laboratory, CSIRO Division of Telecommunications and Industrial Physics, PO Box 218, Lindfield NSW 2070, Sydney, Australia, private communication.
38. U. Tanaka, Kansai Research Center, Communications Research Laboratory, 588-2, Iwaoka, Nishi-ku, Kobe 651-24, Japan, private communication.
39. W. M. Itano, L. L. Lewis, and D. J. Wineland, Phys. Rev. A **23**, 1233 (1982).
40. W. D. Lee, J. H. Shirley, J. P. Lowe, and R. E. Drullinger, 44, 120 (1995).
41. R. Tjoelker, J. D. Prestage, and L. Maleki, Long Term Stability of Hg^+ Trapped Ion Frequency Standards, in *Proceedings of the 1993 IEEE International Frequency Control Symposium*, pages 132–138, Piscataway, NJ, 1993.
42. R. E. Drullinger, J. H. Shirley, and W. Lee, NIST-7, the U.S. Primary Frequency Standard: New Evaluation Techniques, in *28th Annual PTTI Application and Planning Meeting*, pages 255–264, 1997.
43. A. Clairon, 1998, Presented at the 1998 Conference on Precision Electromagnetic Measurements.
44. P. Taylor et al., Phys. Rev. A **56**, 2699 (1997).
45. P. Taylor, M. Roberts, G. P. Barwood, and P. Gill, **23**, 298 (1998).
46. C. Tamm and D. Engelke, Optical Frequency Standard Investigations on Trapped ^{171}Yb Ions, In Bergquist [3], pages 283–288.
47. G. P. Barwood, P. Gill, G. Huang, H. A. Klein, and W. R. C. Rowley, **151**, 50 (1998).
48. A. A. Madej, these proceedings.
49. A. A. Madej, K. J. Siemsen, B. G. Whitford, J. E. Bernard, and L. Marmet, Precision Absolute Frequency Measurements with Single Atoms of Ba^+ and Sr^+, In Bergquist [3], pages 165–170.
50. S. Urabe, M. Watanabe, H. Imago, K. Hayasaka, and U. Tanaka, Observation of Doppler sidebands of a laser-cooled Ca^+ ion by using a low temperature-operated laser diode, in *Internation Workshop on Current Topics of Laser Technology*, page 55, Tokyo, 1998, Communications Research Laboratory.
51. M. Knoop, M. Vedel, and F. Vedel, 4, 1639 (1994).
52. F. Plumelle, M. Desaintfuscien, and M. Houssin, **42**, 462 (1993).
53. E. Peik, G. Hollemann, J. Abel, J. v. Zanthier, and H. Walther, Single-ion Spectroscopy of Indium: Towards a Group-III Monoion Oscillator, In Bergquist [3], pages 376–379.
54. W. Nagourney, E. Burt, and H. G. Dehmelt, Optical Frequency Standard Using Individual Indium Ions, In Bergquist [3], pages 341–346.
55. J. C. Bergquist, W. M. Itano, and D. J. Wineland, Laser Stabilization to a Single Ion, in *Frontier in Laser Spectroscopy*, edited by T. Hänsch and M. Inguscio, pages 359–376, North Holland, 1994.
56. B. C. Young, F. C. Cruz, and J. C. Bergquist, in preparation.
57. F. Riehle et al., Optical Frequency Standard Based on Laser-cooled Ca Atoms, In Bergquist [3], pages 277–282.
58. A. S. Zibrov et al., **59**, 327 (1994).
59. B. Frech et al., in preparation.
60. H. Schnatz, B. Lipphardt, J. Helmcke, R. Riehle, and G. Zinner, Phys. Rev. Lett. **76**, 18 (1996).

61. G. P. Barwood et al., 44, 117 (1995).
62. S. N. Lea and P. Gill, Proposed Infra-red to Visible Frequency Chain at NPL, In Bergquist [3], pages 507–508.
63. J. J. Bollinger, W. M. Itano, D. J. Wineland, and D. J. Heinzen, Phys. Rev. A **54**, R4649 (1996).
64. D. J. Wineland et al., NIST J. Res. **103**, 259 (1998).
65. R. P. Feynman, F. L. Vernon, and R. W. Hellwarth, J. Appl. Phys. **28**, 49 (1957).
66. H. Hellwig, **40**, 538 (1993).
67. J. R. Vig, **40**, 522 (1993).
68. B. W. Petley, Proc. IEEE **79**, 1070 (1993).
69. S. Detweiler, Astrophys. J. **234**, 1100 (1979).
70. K. S. Thorne, *300 Years of Gravitation*, pages 330–458, Cambridge University Press, Cambridge, 1987.
71. J. H. Taylor, Proc. IEEE **79**, 1054 (1991).
72. T. Vachaspati and A. Vilenkin, **31**, 3052 (1985).
73. R. S. Foster, F. Camilo, and A. Wolszczan, High-precision Metrology from Pulsar J1713+0747, in *Marcel Grossmann Conference on General Relativity*, 1995.
74. T. Damour and F. Dyson, **480**, 37 (1996).
75. J. D. Prestage, R. L. Tjoelker, G. J. Dick, and L. Maleki, Phys. Rev. Lett. **74**, 3511 (1995).
76. H. B. G. Casimir, *On the Interaction between Atomic Nuclei and Electrons*, page 54, San Francisco, 1963.
77. V. A. Dzuba, V. V. Flambaum, and J. K. Webb, Space-time Variation of Physical Constants and Relativistic Corrections in Atoms, 1998, submitted to Phys. Rev. Lett.; preprint physics/9802029 on http://xxx.lanl.gov.

Hg^+ OPTICAL FREQUENCY STANDARD: RECENT PROGRESS*

B. C. YOUNG, R. J. RAFAC, J. A. BEALL, F. C. CRUZ,†
W. M. ITANO, D. J. WINELAND, AND J. C. BERGQUIST
National Institute of Standards and Technology, 325 Broadway, Boulder, CO 80303, USA
E-mail: byoung@boulder.nist.gov

We report progress toward an optical frequency standard based on the 1.7 Hz linewidth $^2S_{1/2} \rightarrow {}^2D_{5/2}$ transition of a single trapped $^{199}Hg^+$ ion. We have constructed an isolated, high-finesse, Fabry-Pérot cavity for stabilization of the optical local oscillator. A 563 nm source frequency-locked to this cavity has a linewidth less than 0.16 Hz for averaging times up to 20 s. The measured fractional frequency instability is 3×10^{-16} at 1 s. A simple scheme allows the transport of this light through an optical fiber with negligible degradation of its spectral purity. We have constructed small cryogenic linear traps that are designed to provide confinement in the Lamb-Dicke regime for the optical transition.

1 Introduction

Neutral-atom and trapped-ion frequency standards based on microwave transitions have achieved fractional inaccuracies[1,2] near 10^{-15} and fractional frequency instabilities[1,3,4] near $4 \times 10^{-14} \tau^{-1/2}$, where τ is the measurement averaging time. Some of these microwave standards now have reached (or nearly reached) the theoretical performance limit set by quantum projection noise. For an atomic standard based on an ensemble of N uncorrelated atoms that are interrogated by Ramsey's separated oscillatory field method,[5] quantum projection noise limits the fractional frequency instability to[6]

$$\frac{\Delta\omega}{\omega_0} \approx \sigma_y(\tau) = \frac{1}{\omega_0 \sqrt{N T_R \tau}}, \tag{1}$$

where $\sigma_y(\tau)$ is the two-sample Allan deviation, ω_0 is the frequency of the clock transition, and T_R is the Ramsey interrogation time.

The next major advance for frequency standards probably lies in the development of standards based on long-lived optical transitions. Because optical frequencies are $\approx 10^5$ times higher than the 9.2 GHz microwave transition used in cesium standards, higher fractional stability can be achieved in a

†PRESENT ADDRESS: UNIVERSIDADE ESTADUAL DE CAMPINAS, CAMPINAS, SP, 13083-970, BRAZIL.

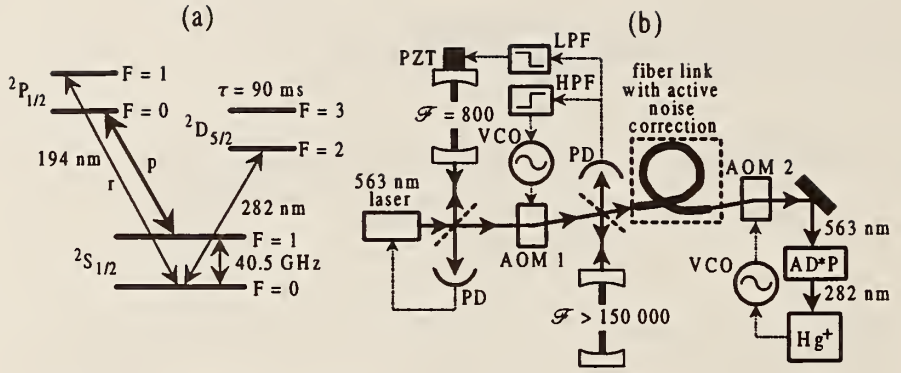

Figure 1. (a) Simplified energy-level diagram for $^{199}Hg^+$. We cool the ions using the $^2S_{1/2} \rightarrow {}^2P_{1/2}$ transitions at 194 nm. Transition p is a cycling transition. A second laser on transition r repumps atoms in $^2S_{1/2}$, F=0 back into $^2S_{1/2}$, F=1. The microwave clock transition is at 40.5 GHz, and the optical clock transition is at 282 nm. (b) Simplified schematic of the proposed optical frequency standard. A dye laser is prestabilized to a Fabry-Pérot cavity ($\mathcal{F}$ = 800). Further stabilization to a much higher finesse cavity ($\mathcal{F}$ > 150 000), and eventually to a narrow transition of a trapped Hg^+ ion should provide a highly stable frequency source. Solid lines denote optical paths and dotted lines represent electrical connections. AD*P, deuterated ammonium dihydrogen phosphate crystal for frequency doubling; AOM, acousto-optic modulator; $\mathcal{F}$, finesse; HPF, high-pass filter; LPF, low-pass filter; PD, photodiode; PZT, piezoelectric transducer; VCO, voltage-controlled oscillator.

given measurement time even for a smaller number of atoms. Single trapped and laser-cooled ions might be nearly ideal references for optical frequency and time standards.[7,8] High resolution is possible because perturbations can be made small and interrogation times long.[7,8,9,10] In addition, laser cooling considerably reduces first- and second-order Doppler shifts.[11] Several groups are developing optical frequency standards based on a variety of ions.[12] We are developing an optical frequency standard using $^{199}Hg^+$ ions, which are attractive because they offer both microwave and optical transitions suitable for frequency standards.[2,13] Figure 1(a) shows the $^{199}Hg^+$ electric dipole transitions at 194 nm used for laser cooling, optical pumping, and detection, and the 1.7 Hz linewidth electric quadrupole transition at 281.5 nm that is the reference for the optical frequency standard. For a single Hg^+ ion and T_R = 30 ms, Eq. (1) gives a quantum-projection-noise limit of $\sigma_y(\tau) \approx 10^{-15}\tau^{-1/2}$. Reaching such low instabilities requires a laser whose frequency fluctuations are $\lesssim$1 Hz during time intervals as long as a few seconds.

2 Overview of the Optical Frequency Standard

Figure 1(b) shows a simplified diagram of our proposed optical frequency standard.[13] A critical component is the high-finesse ($\mathcal{F} > 150\,000$) Fabry-Pérot cavity, which is described in Sec. 3.1. A dye laser at 563 nm is prestabilized to a cavity with a finesse $\mathcal{F} \approx 800$ using a Pound–Drever–Hall FM lock.[14] A feedback loop bandwidth of ≈2 MHz narrows the dye laser short-term (<1 s) linewidth to ≈1 kHz. An optical fiber (not shown) delivers light from the dye-laser table to a vibrationally isolated table that supports the high-finesse cavity. An acousto-optic modulator (AOM) mounted on the isolated table shifts the frequency of the incoming light to match a cavity resonance. A second FM lock performs corrections at frequencies as high as ≈90 kHz by varying the AOM drive frequency and at low frequencies by adjusting a PZT on the prestabilization cavity. With the lock enabled, the light entering the high-finesse cavity has a subhertz spectral width (see Sec. 3.2).

Finally, the frequency-stabilized light couples through an optical fiber to the table holding a cryogenic Hg^+ trap. A simple feedback loop actively reduces the frequency-noise contributions to the light from the fiber (see Sec. 3.3). The 563 nm radiation is frequency-doubled to 281.5 nm and is focused onto the trapped ion. AOM 2 in Fig. 1(b) shifts the frequency of the light to match the ion transition. We plan to interrogate the transition using the Ramsey technique[5] with a Ramsey time $T_R \approx 30$ ms. A digital servo loop will adjust the AOM frequency to step between both sides of the central fringe, and will periodically record the values of the center frequency.[13]

3 Laser Frequency Stabilization

The frequencies of several types of lasers have been locked to resonances of Fabry–Pérot cavities with imprecisions less than 0.1 Hz,[15] but the frequency instabilities of the cavity resonances were orders of magnitude greater. Previously, the narrowest published visible-laser linewidth was 10 Hz for a 1 s averaging time.[16] Recently we achieved a linewidth of 0.6 Hz for averaging times up to 32 s.[17] Here we report a linewidth <0.16 Hz for averaging times up to 20 s. These improvements arose chiefly from better isolation of the cavities from mechanical vibrations.

3.1 High-Finesse Reference Cavity

The high-finesse reference cavity should be insensitive to and/or well-protected from environmental perturbations.[17] The cavity spacer and mirror

substrates are composed of ULE,[18,19] a low-thermal-expansion material. The cavity is supported inside an evacuated chamber by an aluminum V-block with four Viton contact points. We protect the cavity from vibrational noise by mounting the vacuum chamber on a passively isolated optical table. Dashpots filled with grease at each corner of the table provide viscous damping. To reduce the coupling of acoustic noise into the cavity, we enclose the optical table in a wooden box lined internally with lead foam.[20] Active servo control of the optical power transmitted through the cavity stabilizes the frequency shift caused by mirror heating.

3.2 Measurement of Cavity Stability

To characterize the cavity's stability, we constructed a second cavity and mounted it on a second, independent, vibrationally isolated table.[17] A laser beam is frequency-locked to each of the cavities. Some light from one of these beams propagates from one isolated platform to the other. There, it heterodynes with light from the beam that is stabilized to the second cavity, providing a measure of the relative frequency deviations between the two cavities. We mix the beat note ($\nu \approx 400$ MHz) with a linearly swept rf source, which translates the beat-note frequency lower to facilitate high-resolution analysis and removes a fairly uniform frequency drift ($\lesssim 2$ Hz/s). We also can remove Doppler-shifts of the beat frequency caused by relative motion of the isolated platforms,[13,17] but that correction is usually unnecessary.

In the frequency domain, a fast Fourier transform (FFT) spectrum analyzer measures the spectrum of the beat note, as shown in Fig. 2. The width of the spectrum at its half-power point is 0.22 Hz (20 s averaging time). The 0.19 Hz resolution bandwidth of the spectrum analyzer makes a sizable contribution to this frequency width. However, we conservatively estimate the laser linewidth by omitting the bandwidth correction. We infer that at least one of the beams has a linewidth <0.16 Hz at 563 nm for averaging times up to 20 s. This fractional linewidth of 3×10^{-16} is nearly two orders of magnitude smaller than published results for other stabilized lasers, and may represent the smallest fractional linewidth ever measured in the optical regime.

For time-domain analysis, we first frequency-divide the beat signal by a factor of 20, and then mix the signal down to dc.[17] The frequency division permits a simple conversion from mixer output amplitude to relative laser phase $\Delta\phi$ by allowing the in-quadrature condition $(\Delta\phi/20 - \pi/2) \ll 1$ to persist for several seconds. From a time record of $\Delta\phi$ we compute $\sigma_y(\tau)$ for $\tau \leq 2.5$ s. For $\tau \geq 0.5$ s, we perform time-domain measurements using an automated dual-mixer time-difference measurement system.[21] Figure 3 shows

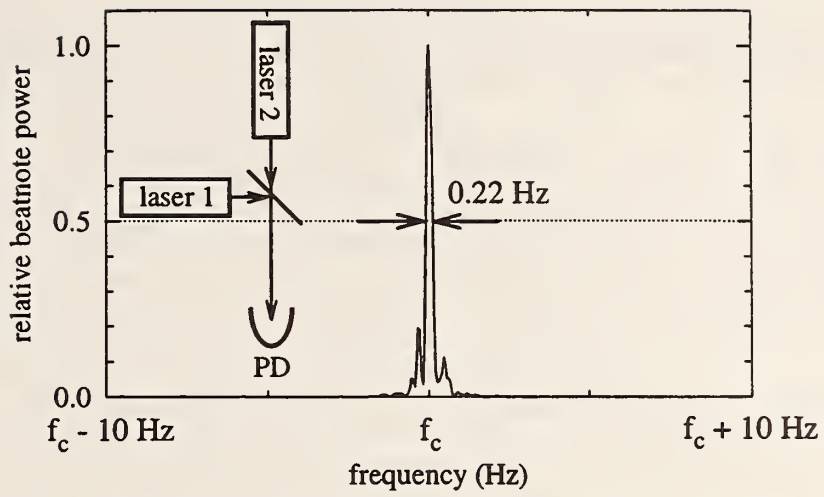

Figure 2. Power spectrum of the beat note between two 563 nm laser beams stabilized to two independent cavities. The dashed line shows the -3 dB level. The resolution bandwidth of the spectrum analyzer is 0.19 Hz, and the averaging time is 20 s. A nearly uniform relative cavity drift of 0.4 Hz/s is suppressed by mixing the beat note with a swept frequency synthesizer. PD, photodiode.

the Allan deviations determined using these two measurement techniques, alongside the reported $\sigma_y(\tau)$ for other stable laser systems. For 30 ms $< \tau <$ 100 s, the Allan deviation of our laser is approximately an order of magnitude less than that of any other stable lasers.

3.3 Reduction of Optical Fiber Noise

Optical fibers are convenient for transporting light and avoiding alignment instabilities. Unfortunately, fibers add considerable frequency noise to the light.[27] A high-performance fiber-noise cancellation scheme using two AOMs has been demonstrated.[27] Since we need multiple fiber links with limited table space and wish to conserve optical power, we implemented a simpler scheme using a single AOM, as shown in Fig. 4.

The stabilized light propagates through the optical fiber and then an AOM. Some of this light retroreflects back through the AOM and the fiber, where it heterodynes with a sample of the input light. A phase-locked loop servos the AOM deflection frequency so that the beat signal is phase-coherent with a stable rf reference signal at 160 MHz. Thus, the phase-locked loop

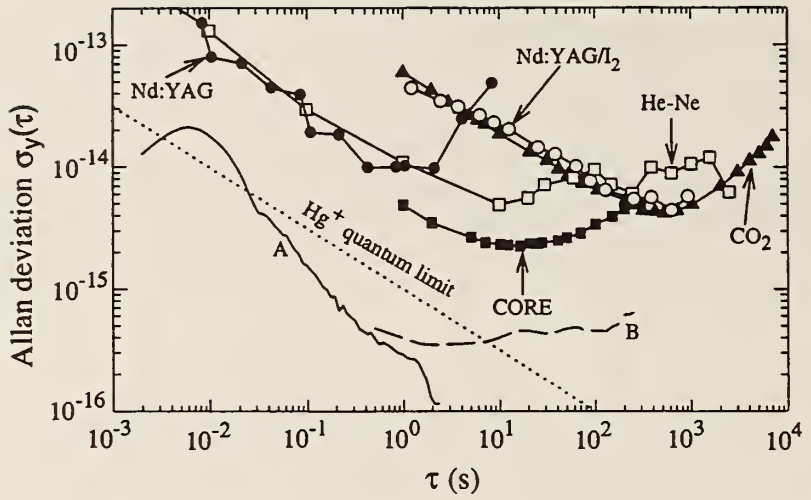

Figure 3. Allan deviation curves for stabilized lasers. We calculate $\sigma_y(\tau)$ for one of our sources from an analog-to-digital sample of the beat signal (curve A) and using a dual-mixer measurement system (curve B). (We remove a linear relative cavity drift of 2.4 Hz/s.) The dotted line shows the quantum noise limit for a Hg^+ optical frequency standard ($N = 1$ and $T_R = 30$ ms). Results for other stabilized lasers: (Nd:YAG) Nd:YAG lasers locked to Fabry–Pérot cavities[22]; (Nd:YAG/I_2) iodine-stabilized Nd:YAG lasers[23]; (He–Ne) methane-stabilized He–Ne lasers[24]; (CO_2) CO_2 lasers[25] locked to OsO_4; (CORE) Nd:YAG lasers locked to cryogenic resonator oscillators.[26]

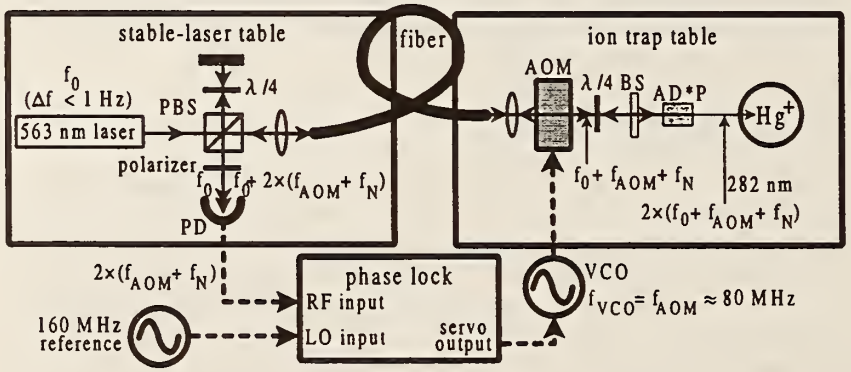

Figure 4. Fiber-noise cancellation scheme. A phase-locked loop controls the deflection frequency f_{AOM} of an AOM to suppress the frequency noise f_N on the light caused by the optical fiber. BS, beam splitter; PBS, polarizing beam splitter.

impresses noise on the AOM frequency that nearly cancels the noise put on the light by the fiber. Consequently, light that only single-passes both the fiber and the AOM has a frequency precisely 80 MHz different from the incident light, maintaining its high spectral purity.

Unfortunately, the ≈80 MHz AOM also amplitude-modulates the light at a frequency nearly degenerate with our 160 MHz signal. This modulation component, which is about 24 dB below the signal power, limits the fiber-noise cancellation. Additionally, we retroreflect light through the fiber using linear polarization orthogonal to the incident light polarization, rather than identical linear polarization. This conserves optical power, but there may be a difference between the noise contributions on the two passes through the fiber, again limiting the accuracy of the noise cancellation.

We test the capability of our scheme to transport light without significant spectral broadening by using a fiber link similar to that in Fig. 4, except that both fiber ends are mounted on a single optical table. We verify the noise correction by heterodyning the single-passed light with some incident light. The spectral purity of the 80 MHz beat signal indicates the accuracy of the fiber-noise cancellation. When the phase lock is disabled, the frequency excursions of the beat note are ≈20 kHz; when enabled, the phase lock largely eliminates the fiber noise. We perform time-domain characterization of the 80 MHz beat signal as described in Sec. 3.2. The Allan deviation corresponding to the residual fiber noise (see Fig. 5) is ≈10 times less than $\sigma_y(\tau)$ for the laser light.

4 Single-Ion Frequency Reference

The high vapor pressure of Hg^+ at room temperature combined with our desire for ion storage times of several days has guided us toward cryogenic traps. Cryogenic operation introduces a host of challenges, most prominently the accumulation and "freezing out" of patches of charge on the trap electrodes during the loading process. The resulting stray electric fields can add enough additional bias to prevent the trapping of ions. Therefore, heaters must be incorporated into the trap structure so that its temperature may be elevated enough to permit the dissipation of any charge accumulated during the time the Hg oven and ionizing electron beam are activated. After loading, the trap is returned to cryogenic operation without further evidence of fluctuating bias fields.

We are experimenting with a number of heated trap structures, which, so far, are all variations of a linear rf Paul trap geometry.[28] For use in the optical frequency standard, it is critical that the trap provide tight confine-

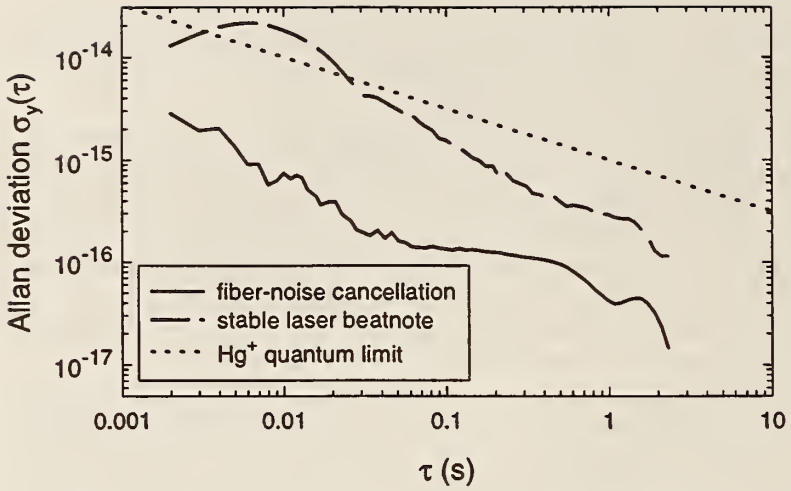

Figure 5. Fractional frequency instability introduced by our fiber link with fiber-noise cancellation. The Allan deviation measured for the incident laser light is ≈10 times larger than the instability introduced by the actively corrected fiber link.

ment satisfying the Lamb-Dicke criterion that the ion's maximum excursions $|\Delta r| < \lambda/2\pi \approx 45$ nm.[29,30] Otherwise, the transition strength of the optical carrier sensitively depends on the vibrational amplitude of the trapped ion, and fluctuations in transition strength result when the mean excitation number of the harmonic motion is large or changing. Presently, we have trapped and cooled ions to crystallization in one trap that does not satisfy the Lamb-Dicke criterion. We recently constructed a smaller trap that should yield stronger confinement. In the future, we may employ lithographic traps similar to those used in our group for quantum-state engineering investigations, but modified for cryogenic operation.

5 Conclusions

We have demonstrated a laser suitable for precision spectroscopy and for optical frequency standards. It has a linewidth of less than 0.16 Hz at 563 nm for averaging times up to 20 s. Its fractional frequency instability is 3×10^{-16} at 1 s. We have assembled a new cryogenic Hg^+ trap that should provide Lamb-Dicke confinement. When tight confinement is demonstrated, we will frequency-lock our stable laser to the ion.[13] If a simple frequency synthesis

scheme connecting the optical transition to microwave frequencies[31,32] proves feasible, we anticipate a time standard with an inaccuracy near 10^{-18}, and stability surpassing the best present-day clocks.

Acknowledgments

We thank C. N. Man for use of her high-finesse cavity design and R. Lalezari, M. Lauer, and D. Willis of Research Electro-Optics for its fabrication; W. D. Lee and C. Nelson for use of their digital servo software in stabilizing one of our isolation tables; F. Walls for assistance with the dual-mixer measurement system; and J. Wells, S. Jefferts, M. Young, and M. Lombardi for useful comments on the manuscript. This work is supported by the Office of Naval Research, the Army Research Office, and the National Institute of Standards and Technology.

References

1. A. G. Mann *et al.*, in *Proceedings of the 1998 IEEE International Frequency Control Symposium* (IEEE, New York, 1998), pp. 13–17.
2. D. J. Berkeland *et al.*, Phys. Rev. Lett. **80**, 2089 (1998).
3. P. T. H. Fisk, M. J. Sellars, M. A. Lawn, and C. Coles, IEEE Trans. Ultrason. Ferroelectr. Freq. Control **44**, 344 (1997).
4. J. D. Prestage, R. L. Tjoelker, and L. Maleki, in *Trapped Charged Particles and Fundamental Physics*, AIP Conference Proceedings 457, edited by D. H. E. Dubin and D. Schneider (AIP, New York, 1999), pp. 357–364.
5. N. F. Ramsey, Phys. Rev. **78**, 695 (1950).
6. W. M. Itano *et al.*, Phys. Rev. A **47**, 3554 (1993).
7. H. G. Dehmelt, Bull. Am. Phys. Soc. **18**, 1521 (1973).
8. H. G. Dehmelt, IEEE Trans. Instrum. Meas. **IM-31**, 83 (1982).
9. D. J. Wineland *et al.*, J. Phys. (Paris) **42**, C8 (1981).
10. P. T. H. Fisk, Rep. Prog. Phys. **60**, 761 (1997).
11. D. J. Wineland and W. M. Itano, Phys. Today **40**, 34 (1987).
12. J. C. Bergquist, ed., *Proceedings of the Fifth Symposium on Frequency Standards and Metrology* (World Scientific, Singapore, 1996); see also *Proceedings of the 1999 European Frequency and Time Forum*, to be published.
13. J. C. Bergquist, W. M. Itano, and D. J. Wineland, in *Frontiers in Laser Spectroscopy*, proceedings of the International School of Physics "Enrico Fermi": Course 120, edited by T. W. Hänsch and M. Inguscio (North-Holland, Amsterdam, 1994), pp. 359–376.

14. R. W. P. Drever *et al.*, Appl. Phys. B **31**, 97 (1983).
15. Ch. Salomon, D. Hils, and J. L. Hall, J. Opt. Soc. Am. B **5**, 1576 (1988).
16. J. Dirscherl, B. Neizert, T. Wegener, and H. Walther, Opt. Commun. **91**, 131 (1992).
17. B. C. Young, F. C. Cruz, W. M. Itano, and J. C. Bergquist, Phys. Rev. Lett. **82**, 3799 (1999).
18. Commercial products are identified in order to adequately specify the experimental procedure. Such identification does not imply recommendation or endorsement by the National Institute of Standards & Technology.
19. S. F. Jacobs, Opt. Acta **33**, 1377 (1986).
20. D. Hils, J. E. Faller, and J. L. Hall, Rev. Sci. Instrum. **57**, 2532 (1986).
21. S. Stein *et al.*, in *Proceedings, 36th Annual Frequency Control Symposium* (U.S. Army Electronics Command, Ft. Monmouth, NJ, 1982), pp. 314–320.
22. N. M. Sampas, E. K. Gustafson, and R. L. Byer, Opt. Lett. **18**, 947 (1993).
23. J. L. Hall *et al.*, in *1998 Conference on Precision Electromagnetic Measurements Digest*, edited by T. L. Nelson (IEEE, New York, 1998), pp. 151–152.
24. S. N. Bagayev, A. K. Dmitriyev, P. V. Pokasov, and B. N. Skvortsov, in *Proceedings of the Fifth Symposium on Frequency Standards and Metrology*, edited by J. C. Bergquist (World Scientific, Singapore, 1996), pp. 289–296.
25. O. Acef, Opt. Commun. **134**, 479 (1997).
26. S. Seel *et al.*, Phys. Rev. Lett. **78**, 4741 (1997).
27. L.-S. Ma, P. Jungner, J. Ye, and J. L. Hall, Opt. Lett. **19**, 1777 (1994).
28. M. E. Poitzsch, J. C. Bergquist, W. M. Itano, and D. J. Wineland, Rev. Sci. Instrum. **67**, 129 (1996).
29. R. H. Dicke, Phys. Rev. **89**, 472 (1953).
30. J. C. Bergquist, W. M. Itano, and D. J. Wineland, Phys. Rev. A **36**, 428 (1987).
31. Th. Udem, J. Reichert, R. Holzwarth, and T. W. Hänsch, Phys. Rev. Lett. **82**, 3568 (1999).
32. B. Frech *et al.*, "Sub-systems for optical frequency measurements: Application to the 282 nm $^{199}Hg^{+}$ transition and the 657 nm Ca line," in *Proceedings of the 1999 European Frequency and Time Forum*, to be published.

Sub-dekahertz Ultraviolet Spectroscopy of $^{199}Hg^+$

R. J. Rafac, B. C. Young,* J. A. Beall, W. M. Itano, D. J. Wineland, and J. C. Bergquist
National Institute of Standards and Technology, Boulder, Colorado 80303
(Received 8 May 2000)

Using a laser that is frequency locked to a Fabry-Pérot étalon of high finesse and stability, we probe the $5d^{10}6s\,^2S_{1/2}(F = 0) \leftrightarrow 5d^9 6s^2\,^2D_{5/2}(F = 2)$ $\Delta m_F = 0$ electric-quadrupole transition of a single laser-cooled $^{199}Hg^+$ ion stored in a cryogenic radio-frequency ion trap. We observe Fourier-transform limited linewidths as narrow as 6.7 Hz at 282 nm (1.06×10^{15} Hz), yielding a line $Q \approx 1.6 \times 10^{14}$. We perform a preliminary measurement of the $5d^9 6s^2\,^2D_{5/2}$ electric-quadrupole shift due to interaction with the static fields of the trap, and discuss the implications for future trapped-ion optical frequency standards.

PACS numbers: 32.30.Jc, 06.30.Ft, 32.80.Pj, 42.62.Fi

Precision spectroscopy has held an enduring place in physics, particularly in the elucidation of atomic structure and the measurement of fundamental constants, in the development of accurate clocks, and for fundamental tests of physical laws. Two ingredients of paramount importance are high accuracy, that is, the uncertainty in systematic frequency shifts must be small, and high signal-to-noise ratio, since the desired measurement precision must be reached in a practical length of time. In this paper, we report the measurement of an optical absorption line in a single laser-cooled $^{199}Hg^+$ ion at a frequency $\nu_0 = 1.06 \times 10^{15}$ Hz (wavelength ≈ 282 nm) for which a linewidth $\Delta\nu = 6.7$ Hz is observed, yielding the highest $Q \equiv \nu_0/\Delta\nu$ ever achieved for optical (or lower frequency) spectroscopy. We also report a preliminary measurement of the interaction of the upper state electric-quadrupole moment with the static field gradients of the ion trap, which is expected to contribute the largest uncertainty for a frequency standard based on this system.

In spectroscopy and for clocks, fluctuations in frequency measurement are usually expressed fractionally: $\sigma_y(\tau) = \Delta\nu_{\rm meas}(\tau)/\nu_0$, where τ is the total measurement time. When the stability is limited by quantum fluctuations in state detection, $\sigma_y(\tau) = C(2\pi\nu_0)^{-1}(N\tau_{\rm probe}\tau)^{-1/2}$, where N is the number of atoms, $\tau_{\rm probe}$ is the transition probe time (typically limited by the excited-state lifetime or the stability of the local oscillator), and C is a constant of order unity that depends on the method of interrogation. For many decades, the highest accuracies and the greatest stabilities have been achieved by locking a microwave oscillator to a hyperfine transition in an atomic ground state [1–5]. Since the fractional instability $\sigma_y(\tau)$ is inversely proportional to the transition frequency, greater stability can be attained using transitions at higher frequencies such as those in the optical region of the electromagnetic spectrum. Only recently have lasers of sufficient spectral purity become available to probe the narrow resonances provided by transitions between long-lived atomic states [6–12]. The stable laser source of Refs. [6,11] and the relative freedom from environmental perturbation afforded by ion trapping enable the high resolution reported here. Combined with novel, highly compact, and accurate laser frequency measurement schemes [13,14], a trapped-ion optical frequency standard would appear to have significant advantages over present-day atomic clocks.

A partial energy-level diagram of $^{199}Hg^+$ is shown in Fig. 1. The 282 nm radiation used to drive the $2S_{1/2} \leftrightarrow {}^2D_{5/2}$ transition is produced in a nonlinear crystal as the second harmonic of a dye laser oscillating at 563 nm. The frequency of the dye laser radiation is electronically served to match a longitudinal mode of a high-finesse Fabry-Pérot cavity that is temperature controlled and supported on an isolation platform [6,11]. The stabilized laser light is sent through an optical fiber to the table holding the ion trap. Unavoidable mechanical vibration of this fiber broadens the laser spectrum by nearly 1 kHz. The fiber-induced phase noise is sensed and removed using a method [11] similar to that described in Ref. [15]. Finally, the frequency of the 563 nm light is referenced to the electric-quadrupole transition by first frequency shifting in an acousto-optic modulator (AOM) and then frequency doubling in a single pass through a deuterated ammonium dihydrogen phosphate crystal.

The design of the linear cryogenic ion trap used in these measurements borrows heavily from our previous work

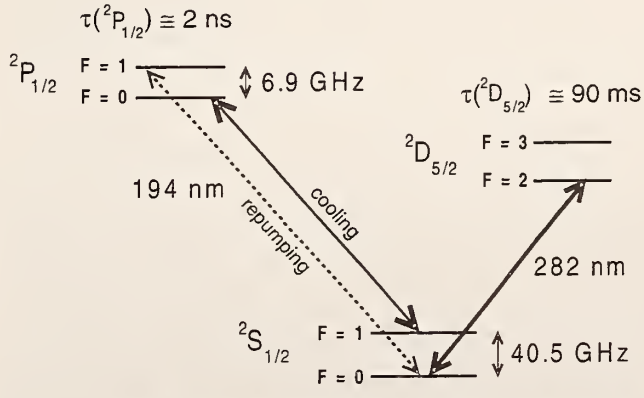

FIG. 1. Partial energy level diagram of $^{199}Hg^+$ with the transitions of interest indicated.

 0031-9007/00/85(12)/2462(4)$15.00

[4,16,17]. A single ^{199}Hg atom from a thermal source is ionized by an electron beam and trapped in the harmonic pseudopotential formed by the rf and static potentials of a linear quadrupole trap. The trap operates in analogy to a quadrupole mass filter having its ends "plugged" with static fields. The trap electrodes are constructed from Au-metallized alumina tubes 530 μm in diameter. The electrode axes are held parallel and coincident with the vertices of a square of side 1.37 mm by an alumina structure that facilitates electrical connection and mounting in the vacuum chamber.

One pair of diagonally opposite electrodes is segmented by laser micromachining prior to metallization to permit application of the axially confining static potential. The remaining pair of electrodes is driven by a cryogenic copper helical resonator coupled to a 8.6 MHz signal source. Under typical operating conditions, a single $^{199}Hg^+$ ion exhibits secular motion at 1.45, 1.86, and 1.12 MHz in the x, y, and z (axial) directions, respectively, as inferred from the vibrational sideband spectrum of the ion [18]. In addition, biasing electrodes are mounted outside the trap rods to cancel any stray static electric fields that may be present.

Previous experiments using ^{199}Hg were performed at room temperature and at a pressure of approximately 10^{-7} Pa [19]. Under those conditions, the background gas pressure was large enough that the ion would be lost due to chemical reaction after only a few minutes. To circumvent this, the ion trap is housed in a liquid He vacuum Dewar like that described in [17]. Engineering particulars of the liquid He cryostat allow low-frequency ($<$100 Hz) vibratory motion of the trap structure relative to the optical table. Uncorrected, these vibrations contribute 50–1000 Hz of Doppler broadening to the laser line. We eliminate the majority of this broadening using an additional stage of Doppler cancellation, where the correction signal is derived from optical heterodyne detection of a motion-sensing beam reflected from a mirror rigidly affixed to the trap [19]. The resulting cancellation is not ideal, because the sensing beam is steered by additional optical elements and its path deviates slightly from overlap with the probe beam near the trap. Measurements indicate that this optical path difference can contribute as much as 2 Hz to the spectral width of the 282 nm probe laser in the reference frame of the ion.

The ion is laser cooled to near the 1.7 mK Doppler limit by driving the $5d^{10}6s\,^2S_{1/2}(F = 1) \leftrightarrow 5d^{10}6p\,^2P_{1/2}(F = 0)$ cycling transition at 194 nm (Fig. 1) [18]. Because of weak off-resonant pumping to the $^2S_{1/2}(F = 0)$ state, we employ a second 194 nm source phase locked to the first with a 47 GHz offset that returns the ion to the ground-state $F = 1$ hyperfine level. We tolerate the complication of hyperfine structure, since only isotopes with nonzero nuclear spin can have first-order magnetic-field-insensitive transitions that provide immunity from fluctuations of the ambient field. This significantly relaxes the requirements for control and/or shielding of environmental magnetic sources.

We monitor the ion and deduce its electronic state using light scattered from the cooling transition. Fluorescence at 194 nm is collected by a five-element uv-grade fused silica $f/1$ objective located inside the cryostat. The scattered light is imaged outside the Dewar, spatially filtered with a 75 μm aperture, and relayed with a second lens to an imaging photomultiplier tube having $\approx$5% quantum efficiency at 194 nm. Transitions to the $^2D_{5/2}$ state are detected using the technique of "electron shelving," which infers the presence of the atom in the metastable level through the absence of scattering from the strong laser-cooling transition [18,20]. A metastable-state detection efficiency near unity can be achieved, because the absorption of a single 282 nm photon suppresses scattering of many photons from the 194 nm transition for a period determined by the lifetime of the $^2D_{5/2}$ state. The radiation from the 194 and 282 nm sources is admitted to the trap sequentially using mechanical shutters and an AOM, which prevents broadening of the quadrupole transition by the cooling radiation. Typical count rates are 2000 Hz for a single ion cycling at the half-power point of the cooling transition, compared to only 20 Hz combined laser scatter and photomultiplier thermal background when the ion is shelved in the metastable level.

Spectra of the recoilless "carrier" component of the $^2S_{1/2}(F = 0) \leftrightarrow {}^2D_{5/2}(F = 2)$ $\Delta m_F = 0$ transition were obtained for a range of probe times and laser intensities by laser cooling for 30 ms, preparing the ion in the $F = 0$ ground state by blocking the repumping laser, and then interrogating the quadrupole transition. The spectra are built up from multiple bidirectional scans of the 282 nm probe laser frequency. Since the frequency drift of the probe laser is not precisely compensated, nor is it constant, we incorporate a locking step in between pairs of positive- and negative-going frequency sweeps about the center of the quadrupole resonance. In the locking sequence, we step the frequency of the probe laser alternately to the approximate half maximum on either side of the quadrupole resonance, probe for a fixed time τ_{servo}, and then look for transitions to the $^2D_{5/2}$ level. Typically, 48 measurements are made on each side of the resonance during each lock cycle. The asymmetry between the number of quantum jumps detected on the high- and low-frequency sides of the resonance is used to correct the frequency of a synthesizer used to compensate for cavity drift. In this fashion, variations in the frequency of the 282 nm laser for times exceeding several seconds are reduced. Using the locking step alone with $\tau_{\text{servo}} = 40$ ms, the error signal from the lock indicates a fractional frequency instability $\sigma_y(\tau) = 1.5 \times 10^{-15}$ for times comparable to the length of the combined servo and scanning cycle (15–60 s). This is worse than the quantum-projection-noise-limited stability ($\approx 5 \times 10^{-16}$) but is consistent with fluctuating quadratic Zeeman shifts arising from variations in the ambient magnetic field. The trap was not magnetically shielded during the measurements reported here.

Spectra are plotted in Fig. 2 for a variety of probe times $\tau_{\text{probe}} = 20$–120 ms, with $\tau_{\text{servo}} = \tau_{\text{probe}}$. The

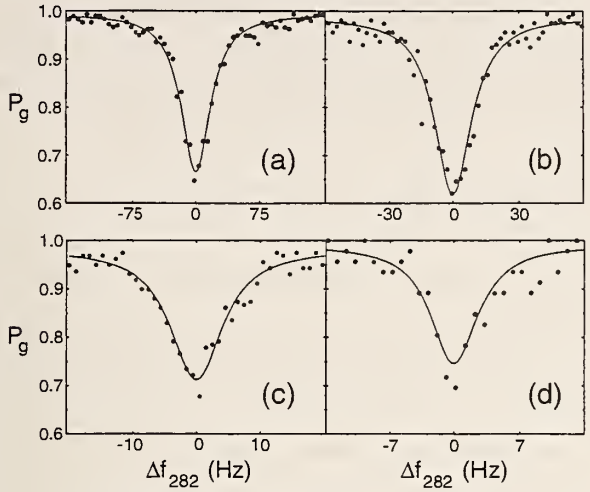

FIG. 2. Quantum-jump absorption spectra of the $^2S_{1/2}(F = 0) \leftrightarrow {}^2D_{5/2}(F = 2)$ $\Delta m_F = 0$ electric-quadrupole transition. Δf_{282} is the frequency of the 282 nm probe laser detuning, and P_g is the probability of finding the atom in the ground state. The four plots correspond to excitation with 282 nm pulses of different lengths: (a) 20 ms (averaged over 292 sweeps), (b) 40 ms (158 sweeps), (c) 80 ms (158 sweeps), and (d) 120 ms (46 sweeps). The linewidths are consistent with the Fourier-transform limit of the pulse at 40(2), 20(1), 10(1), and 6(1) Hz.

linewidths of all the spectra are transform limited by the finite probe time, decreasing to 6.7 Hz in the uv at 120 ms, the longest time used. The carrier transition amplitude is a function of the initial value of the vibrational quantum number n [see, for example, Eq. (31) of Ref. [21]]. Since for our trapping parameters $\langle n \rangle \approx 35$ at the Doppler cooling limit, it is not possible to transfer the electron to the $^2D_{5/2}$ state with unit probability. The observed signals are in good agreement with the theoretical expectation, and the signal loss for $\tau_{\text{probe}} = 120$ ms [Fig. 2(d)] is consistent with applying the probe for a time that exceeds the natural lifetime of the $^2D_{5/2}$ state by 33%. This result corresponds to a fractional frequency resolution of 6.3×10^{-15}, which we believe is the smallest reported for excitation with an optical or microwave source. The result is surpassed only by Mössbauer spectroscopy in ZnO, where a fractional linewidth of 2.5×10^{-15} was achieved using a nuclear source of 93 keV gamma rays [22], which is not practical for use in an atomic clock. The measurements reported here illustrate the potential of a single-ion optical frequency standard and confirm the phase stability of our probe laser system, validating the results of the heterodyne comparison of the two reference cavities [6,11]. An excellent review of the performance of similar systems can be found in Ref. [12].

Figure 3 shows a typical power-broadened spectrum with consequent Rabi "sidebands," using $\tau_{\text{probe}} = 10$ ms and $\tau_{\text{servo}} = 40$ ms. A least-squares fit to the data indicates that it is consistent with a pulse area of $2.41(7)\pi$ (relative to $n \approx 0$) and a mean vibrational quantum number $\langle n \rangle = 73(9)$. This is twice the value of $\langle n \rangle$ expected at

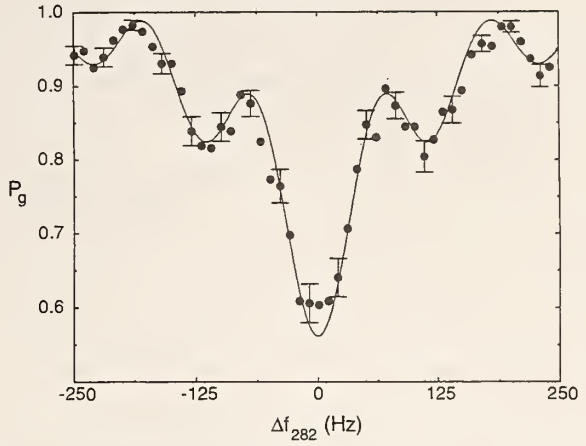

FIG. 3. Quantum-jump absorption spectrum of the power-broadened electric-quadrupole transition. Δf_{282} is the frequency of the 282 nm probe laser detuning, and P_g is the probability of finding the atom in the ground state. The data are averaged over 348 frequency sweeps with $\tau_{\text{probe}} = 10$ ms and $\tau_{\text{servo}} = 40$ ms. The solid line is a least-squares fit to a Rabi line profile with pulse area $2.41(7)\pi$ and $\langle n \rangle = 73(9)$. The quantum-projection-noise-limited uncertainty is indicated by representative error bars plotted every third point.

the Doppler cooling limit; the larger result is likely due to saturation of the cooling transition.

In Fig. 4 we plot the central three Ramsey fringes of a time-domain separated-oscillatory-fields interrogation of the $^2S_{1/2} \leftrightarrow {}^2D_{5/2}$ transition with 5 ms pulses separated by a 20 ms free-precession interval. In operation as a frequency standard, the Ramsey method offers 1.6× reduction in linewidth (and a corresponding increase in stability) for an equivalent measurement period.

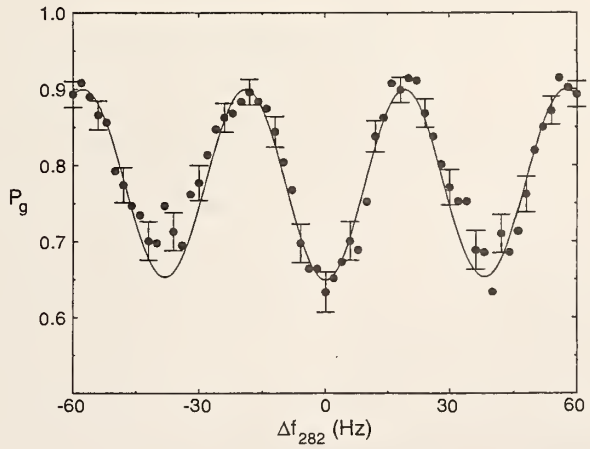

FIG. 4. The central three fringes obtained by time-domain Ramsey interrogation of the electric-quadrupole transition. Δf_{282} is the frequency of the 282 nm probe laser detuning, and P_g is the probability of finding the atom in the ground state. The data are averaged over 328 frequency sweeps with $\tau_{\text{servo}} = 40$ ms. The solid line is the expected Ramsey signal for 5 ms pulses separated by 20 ms of free precession; the ≈10% background arises primarily from suboptimal setting of the discriminator levels in our detection electronics. The quantum-projection-noise-limited uncertainty is indicated by representative error bars plotted every third point.

It should be possible to reduce the uncertainties of all systematic shifts in this system including the second-order Doppler (time-dilation) shift and static or dynamic Zeeman and Stark shifts to values approaching 10^{-18}. The electric-quadrupole shift of the $^2D_{5/2}F = 2$ $(m_F = 0)$ state arising from coupling with the static potentials of the trap is expected to be the limiting systematic contribution in future measurements of the absolute value of the $^2S_{1/2} \leftrightarrow {}^2D_{5/2}$ transition frequency, because of the difficulty in determining with certainty the magnitude and configuration of the static fields of the trap. In principle, it is possible to eliminate this shift by measuring the quadrupole transition frequencies for each of three mutually orthogonal orientations of a quantizing magnetic field of constant magnitude; the mean value is then the unperturbed $^2S_{1/2} \leftrightarrow {}^2D_{5/2}$ transition frequency. We follow this procedure for several values of the total magnetic induction and for all possible directions in a suitable coordinate system (e.g., [1 1 1], [1 −1 −1], [−1 −1 1], where [1 1 1] is elevated 45° from the trap axis and 45° from the vertical plane). Using the ion as a magnetometer, the magnitude of the field produced by three sets of coils is calibrated by the measurement of the frequency of the $F = 0 \rightarrow 2$ $(\Delta m_F = 2)$ magnetic field-dependent electric-quadrupole transition. For an ideal linear trap with secular frequencies $\omega_x = \omega_y$ and $\omega_z = 2\pi$ (1 MHz), we calculate a shift that varies between +7.5 and −15 Hz depending on field orientation. The estimate of the atomic quadrupole moment is based on Hartree-Fock wave functions for the ground state of Hg^+, which yield the matrix element $\langle 5d|r^2|5d\rangle = 6.61 \times 10^{-21}$ m^2 [23]. In our apparatus we observe shifts departing from the mean frequency by +12(7), +9(13), and −27(7) Hz for the three field orientations at 282 nm, in reasonable agreement with the simple model. The quoted uncertainties arise from imprecision in our ability to set the absolute magnitude and direction of the magnetic induction. Thus the fractional frequency uncertainty is of the order of 10^{-14}, and we might reduce this below 10^{-15} in the present apparatus with straightforward improvements to the magnetic shielding and control. Uncertainties approaching 10^{-18} should be obtainable through stringent control of magnetic fields in combination with a spherical rf quadrupole trap geometry that does not rely on static potentials for confinement. Greater resolution and accuracy might be more readily achieved using a different type of transition, e.g., the weak hyperfine-induced electric-dipole transitions like those between the low-lying $^1S_0$ and $^3P_0$ states of the singly ionized species of the Group IIIA elements of the periodic table [12,24,25], particularly in cases where first-order magnetic-field independent transitions are available (albeit at nonzero field) [26].

This research was partially supported by the Office of Naval Research and through a Cooperative Research and Development agreement with Timing Solutions, Corp., Boulder, Colorado. We would like to thank C. Oates, J. Ye, and D. Sullivan for their careful reading of this manuscript.

*Present address: Jet Propulsion Laboratory, Pasadena, CA 91109.

[1] A. Clairon *et al.*, in *Proceedings of the 5th Symposium on Frequency Standards and Metrology* (World Scientific, Singapore, 1996), pp. 49–59.
[2] R. L. Tjoelker *et al.*, in *Proceedings of the 5th Symposium on Frequency Standards and Metrology* (Ref. [1]), pp. 33–38.
[3] P. T. H. Fisk *et al.*, IEEE Trans. Ultrason. Ferroelectr. Freq. Control **44**, 344 (1997).
[4] D. J. Berkeland *et al.*, Phys. Rev. Lett. **80**, 2089 (1998).
[5] S. R. Jefferts *et al.* (to be published).
[6] B. C. Young *et al.*, Phys. Rev. Lett. **82**, 3799 (1999).
[7] Ch. Salomon *et al.*, J. Opt. Soc. Am. B **5**, 1576 (1988).
[8] N. M. Sampas *et al.*, Opt. Lett. **18**, 947 (1993).
[9] O. Acef, Opt. Commun. **134**, 479 (1997).
[10] S. Seel *et al.*, Phys. Rev. Lett. **78**, 4741 (1997).
[11] B. C. Young *et al.*, in *Proceedings of the 14th International Conference Laser Spectroscopy* (World Scientific, Singapore, 1999), pp. 61–70.
[12] A. A. Madej and J. E. Bernard, in "Frequency Measurement and Control," edited by Andre N. Luiten, Springer Topics in Applied Physics (Springer-Verlag, Berlin, to be published).
[13] J. Reichert *et al.*, Phys. Rev. Lett. **84**, 3232 (2000).
[14] S. A. Diddams *et al.* (to be published).
[15] L.-S. Ma *et al.*, Opt. Lett. **19**, 1777 (1994).
[16] M. G. Raizen *et al.*, J. Mod. Opt. **39**, 233 (1992).
[17] M. E. Poitzsch *et al.*, Rev. Sci. Instrum. **67**, 129 (1996).
[18] J. C. Bergquist *et al.*, Phys. Rev. A **36**, 428 (1987).
[19] J. C. Bergquist *et al.*, in *Frontiers in Laser Spectroscopy*, Proceedings of the International School of Physics "Enrico Fermi," Course CXX (North-Holland, Amsterdam, 1994), p. 359.
[20] H. G. Dehmelt, Bull. Am. Phys. Soc. **20**, 60 (1975); J. Phys. (Paris) Colloq. **42**, C8-299 (1980).
[21] D. J. Wineland and W. M. Itano, Phys. Rev. A **20**, 1521 (1979).
[22] G. J. Perlow *et al.*, J. Phys. (Paris) Colloq. **35**, C6-197 (1974).
[23] A. D. McLean and R. S. McLean, At. Data Nucl. Data Tables **26**, 197 (1981).
[24] H. G. Dehmelt, IEEE Trans. Instrum. Meas. **31**, 83 (1982).
[25] E. Peik *et al.*, in *Proceedings of the 13th European Frequency and Time Forum and the 1999 IEEE Frequency Control Symposium, Besançon, France* (Institute of Electrical and Electronics Engineers, Piscataway, NJ, 1999), pp. 682–685.
[26] D. J. Wineland and W. M. Itano, Bull. Am. Phys. Soc. **27**, 864 (1982).

Volume 105, Number 6, November–December 2000
Journal of Research of the National Institute of Standards and Technology

[J. Res. Natl. Inst. Stand. Technol. **105**, 829–837 (2000)]

External-Field Shifts of the $^{199}Hg^{+}$ Optical Frequency Standard

Volume 105 Number 6 November–December 2000

Wayne M. Itano

National Institute of Standards and Technology,
Boulder, CO 80305

itano@boulder.nist.gov

Frequency shifts of the $^{199}Hg^{+}$ $5d^{10}6s\ ^2S_{1/2}$ ($F = 0$, $M_F = 0$) to $5d^96s^2\ ^2D_{5/2}$ ($F = 2$, $M_F = 0$) electric-quadrupole transition at 282 nm due to external fields are calculated, based on a combination of measured atomic parameters and *ab initio* calculations. This transition is under investigation as an optical frequency standard. The perturbations calculated are the quadratic Zeeman shift, the scalar and tensor quadratic Stark shifts, and the interaction between an external electric field gradient and the atomic quadrupole moment. The quadrupole shift is likely to be the most difficult to evaluate in a frequency standard and may have a magnitude of about 1 Hz for a single ion in a Paul trap.

Key words: atomic polarizabilities; electric quadrupole interaction; mercury ion; optical frequency standards; Stark shift; Zeeman shift.

Accepted: November 1, 2000

Available online: http://www.nist.gov/jres

1. Introduction

It has long been recognized that a frequency standard could be based on the 282 nm transition between the ground $5d^{10}6s\ ^2S_{1/2}$ level and the metastable $5d^96s^2\ ^2D_{5/2}$ level of Hg^+ [1]. The lifetime of the upper level is 86(3) ms [2], so the ratio of the natural linewidth $\Delta\nu$ to the transition frequency ν_0 is 2×10^{-15}. (Unless otherwise noted, all uncertainties given in this paper are standard uncertainties, i.e., one standard deviation estimates.) Doppler broadening can be avoided if the transition is excited with two counter-propagating photons, as originally proposed by Bender et al. [1] and subsequently demonstrated by Bergquist et al. [3]. However, optical Stark shifts are greatly reduced if the transition is driven instead with a single photon by the electric-quadrupole interaction. In this case, Doppler broadening can be eliminated if the ion is confined to dimensions much less than the optical wavelength, as was first demonstrated by Bergquist et al. [4].

Recently, the ($F = 0$, $M_F = 0$) to ($F = 2$, $M_F = 0$) hyperfine component of the $^{199}Hg^{+}$ $5d^{10}6s\ ^2S_{1/2}$ to $5d^96s^2\ ^2D_{5/2}$ single-photon transition has been observed with a linewidth of only 6.7 Hz by Rafac et al. [5]. A laser servo-locked to this transition is an extremely stable and reproducible frequency reference. New developments in optical frequency metrology [6, 7] may soon make this system practical as an atomic frequency standard or clock.

While the ($F = 0$, $M_F = 0$) to ($F = 2$, $M_F = 0$) hyperfine component has no linear Zeeman shift, it does have a quadratic Zeeman shift that must be accounted for. In addition, there is a second-order Stark shift and a shift due to the interaction between the electric-field gradient and the atomic electric-quadrupole moment. None of these shifts has yet been measured accurately, so it is useful to have calculated values, even if they are not very precise. Also, it is useful to know the functional form of

the perturbation, even if the magnitude is uncertain. For example, the quadrupole shift can be eliminated by averaging the transition frequency over three mutually orthogonal magnetic-field orientations, independent of the orientation of the electric-field gradient.

2. Methods and Notation

The quadratic Zeeman shift can be calculated if the hyperfine constants and electronic and nuclear g-factors are known. Similarly, the quadratic Stark effect can be calculated from a knowledge of the electric-dipole oscillator strengths. The quadrupole shift depends on the atomic wavefunctions. Some of these parameters have been measured, such as the hyperfine constants and some of the oscillator strengths. There are also published calculations for some of the oscillator strengths.

Here, we estimate, by the use of the Cowan atomic-structure codes, values for parameters for which there are neither measured values nor published calculations. The Cowan codes are based on the Hartree-Fock approximation with some relativistic corrections [8]. The odd-parity configurations included in the calculation were $5d^{10}np$ ($n = 6,7,8,9$), $5d^{10}5f$, $5d^96s6p$, $5d^96s7p$, $5d^96s5f$, and $5d^86s^26p$. The even-parity configurations were $5d^{10}ns$ ($n = 6,7,8,9,10$), $5d^{10}nd$ ($n = 6,7,8,9$), $5d^96s^2$, $5d^96s7s$, $5d^96s6d$, and $5d^96p^2$. Recently, Sansonetti and Reader have made new measurements of the spectrum of Hg^+ and classified many new lines [9]. They also carried out a least-squares adjustment of the energy parameters that enter the Cowan-code calculations in order to match the observed energy levels. We use these adjusted parameters in our Cowan-code calculations.

As one test of this method of calculation, we estimated the weakly allowed 10.7 μm $5d^{10}6p\ ^2P_{1/2}$ to $5d^96s^2\ ^2D_{3/2}$ electric-dipole decay rate. This decay is allowed only because of configuration mixing, since it requires two electrons to change orbitals. The calculation shows the decay to be due mostly to mixing between the $5d^{10}6p$ and $5d^96s6p$ configurations. The calculated rate is 111 s^{-1}; the measured rate is 52(16) s^{-1} [2]. Another test is the electric-quadrupole decay rate of the $5d^96s^2\ ^2D_{5/2}$ level to the ground level. The calculated rate is 12.6 s^{-1}, and the measured rate is 11.6(0.4) s^{-1}. Similar calculations have been carried out by Wilson [10].

Let H_0 be the atomic Hamiltonian, exclusive of the hyperfine and external field effects, which are treated as perturbations. For convenience, we denote the eigenstates of H_0 corresponding to the electronic levels $5d^{10}6s\ ^2S_{1/2}$ and $5d^96s^2\ ^2D_{5/2}$ having J_z eigenvalue M_J by $|S\ 1/2\ M_J\rangle$ and $|D\ 5/2\ M_J\rangle$, respectively.

The corresponding eigenvalues of H_0 are denoted $W(S, 1/2)$ and $W(D, 5/2)$. An arbitrary eigenstate of H_0 with eigenvalue $W(\gamma, J)$ and electronic angular momentum J is denoted $|\gamma\ J\ M_J\rangle$. Since $^{199}Hg^+$ has in addition a nuclear angular momentum I, where $I = 1/2$, the complete state designation is $|\gamma\ JFM_F\rangle$, where F is the total angular momentum, and M_F is the eigenvalue of F_z.

3. Quadratic Zeeman Shift

In order to calculate the energy shifts due to the hyperfine interaction and to an external magnetic field $\boldsymbol{B} \equiv B\hat{z}$, we define effective Hamiltonian operators H'_S and H'_D that operate within the subspaces of hyperfine sublevels associated with the electronic levels $5d^{10}6s\ ^2S_{1/2}$ and $5d^96s^2\ ^2D_{5/2}$, respectively:

$$H'_S = hA_S \boldsymbol{I}\cdot\boldsymbol{J} + g_J(S)\mu_B \boldsymbol{J}\cdot\boldsymbol{B} + g'_I\mu_B \boldsymbol{I}\cdot\boldsymbol{B}, \quad (1)$$

$$H'_D = hA_D \boldsymbol{I}\cdot\boldsymbol{J} + g_J(D)\mu_B \boldsymbol{J}\cdot\boldsymbol{B} + g'_I\mu_B \boldsymbol{I}\cdot\boldsymbol{B}, \quad (2)$$

where A_S and A_D are the dipole hyperfine constants, $g_J(S)$ and $g_J(D)$ are the electronic g-factors, g'_I is the nuclear g-factor, h is the Planck constant, and μ_B is the Bohr magneton. All of the parameters entering H'_S and H'_D are known from experiments, although a more accurate measurement of $g_J(D)$ would be useful. The ground-state hyperfine constant A_S has been measured in a $^{199}Hg^+$ microwave frequency standard to be 40 507.347 996 841 59 (43) MHz [11]. The excited-state hyperfine constant A_D has been measured recently by an extension to the work described in Ref. [5], in which the difference in the frequencies of the $|S\ 1/2\ 0\ 0\rangle$ to $|D\ 5/2\ 2\ 0\rangle$ and the $|S\ 1/2\ 0\ 0\rangle$ to $|D\ 5/2\ 3\ 0\rangle$ transition frequencies was determined to be $3A_D = 2\ 958.57(12)$ MHz [12], in good agreement with an earlier, less precise measurement by Fabry-Pérot spectroscopy [13]. The ground-state electronic g-factor $g_J(S)$ was measured in $^{198}Hg^+$ by rf-optical double resonance to be 2.003 174 5(74) [14]. The excited-state electronic g-factor $g_J(D)$ was measured in $^{198}Hg^+$ by conventional grating spectroscopy of the 398 nm $5d^{10}6p\ ^2P_{3/2}$ to $5d^96s^2\ ^2D_{5/2}$ line to be 1.198 0(7) [15]. The difference in $g_J(S)$ or $g_J(D)$ between $^{198}Hg^+$ and $^{199}Hg^+$ is estimated to be much less than the experimental uncertainties. The nuclear g-factor g'_I is $-5.422\ 967(9) \times 10^{-4}$ [16]. The measurement was made with neutral ground-state ^{199}Hg atoms, so the diamagnetic shielding factor will be slightly different from that in the ion. However, this is effect is negligible, since the magnitude of g'_I is so small compared to $g_J(S)$ or $g_J(D)$.

The determination of $g_J(\mathrm{D})$ could be improved by measuring the optical-frequency difference between two components of the 282 nm line and the frequency of a ground-state microwave transition at the same magnetic field. Since the uncertainty in the quadratic Zeeman shift is due mainly to the uncertainty in $g_J(\mathrm{D})$, it is useful to see how accurately it can be estimated theoretically. The Landé g-factor for a $^2D_{5/2}$ state, including the correction for the anomalous magnetic moment of the electron, is 1.200 464. The Cowan-code calculation shows that the configuration mixing does not change this value by more than about 10^{-6}, i.e., 1 in the last place. There are several relativistic and diamagnetic corrections that modify $g_J(\mathrm{D})$, one of which, called the Breit-Margenau correction by Abragam and Van Vleck [17], is proportional to the electron mean kinetic energy. The other corrections are more difficult to calculate. The Cowan-code result for the mean kinetic energy of an electron in the $5d$ orbital of the $5d^96s^2$ configuration is $T = 19.32\ hcR_\infty$, where R_∞ is the Rydberg constant. Using this value, we obtain a theoretical value of $g_J(\mathrm{D})$, including the Breit-Margenau correction, of 1.199 85, which disagrees with the the experimental value by 1.85×10^{-3}, which is 2.6 times the estimated experimental uncertainty of Ref. [15]. If we calculate $g_J(\mathrm{D})$ for neutral gold, which is isoelectronic to Hg^+, by the same method, we obtain a value which differs from the accurately measured experimental one [18] by $(7 \pm 2) \times 10^{-5}$. Thus, the error in the calculated value for $g_J(\mathrm{D})$ of $^{199}Hg^+$ might be less than 1×10^{-4}, but it is impossible to be certain of this, since there are uncalculated terms. Measurements of the $^{199}Hg^+$ optical clock frequency at different values of the magnetic field should result in a better experimental value for $g_J(\mathrm{D})$ in the near future.

For low magnetic fields (B less than 1 mT), it is sufficient to calculate the energy levels to second order in B. To this order in B, the energies of the hyperfine-Zeeman sublevels for the ground electronic level are

$$W(\mathrm{S},\ 1/2,\ 0,\ 0,\ B) = W(\mathrm{S},\ 1/2) - \frac{3hA_\mathrm{S}}{4} - \frac{[g_J(\mathrm{S}) - g_I']^2\mu_\mathrm{B}^2B^2}{4hA_\mathrm{S}}, \tag{3}$$

$$W(\mathrm{S},\ 1/2,\ 1,\ 0,\ B) = W(\mathrm{S},\ 1/2) + \frac{hA_\mathrm{S}}{4} + \frac{[g_J(\mathrm{S}) - g_I']^2\mu_\mathrm{B}^2B^2}{4hA_\mathrm{S}}, \tag{4}$$

$$W(\mathrm{S},\ 1/2,\ 1,\ \pm1,\ B) = W(\mathrm{S},\ 1/2) + \frac{hA_\mathrm{S}}{4} \pm \frac{[g_J(\mathrm{S}) + g_I']\mu_\mathrm{B}B}{2}, \tag{5}$$

For the $5d^96s^2\ ^2D_{5/2}$ level we have

$$W(\mathrm{D},\ 5/2,\ 2,\ 0,\ B) = W(\mathrm{D},\ 5/2) - \frac{7hA_\mathrm{D}}{4} - \frac{[g_J(\mathrm{D}) - g_I']^2\mu_\mathrm{B}^2B^2}{12hA_\mathrm{D}}, \tag{6}$$

$$W(\mathrm{D},\ 5/2,\ 2,\ \pm1,\ B) = W(\mathrm{D},\ 5/2) - \frac{7hA_\mathrm{D}}{4} \pm \frac{[7g_J(\mathrm{D}) - g_I']\mu_\mathrm{B}B}{6} - \frac{2[g_J(\mathrm{D}) - g_I']^2\mu_\mathrm{B}^2B^2}{27hA_\mathrm{D}}, \tag{7}$$

$$W(\mathrm{D},\ 5/2,\ 2,\ \pm2,\ B) = W(\mathrm{D},\ 5/2) - \frac{7hA_\mathrm{D}}{4} \pm \frac{[7g_J(\mathrm{D}) - g_I']\mu_\mathrm{B}B}{3} - \frac{5[g_J(\mathrm{D}) - g_I']^2\mu_\mathrm{B}^2B^2}{108hA_\mathrm{D}}, \tag{8}$$

$$W(\mathrm{D},\ 5/2,\ 3,\ 0,\ B) = W(\mathrm{D},\ 5/2) + \frac{5hA_\mathrm{D}}{4} + \frac{[g_J(\mathrm{D}) - g_I']^2\mu_\mathrm{B}^2B^2}{12hA_\mathrm{D}}, \tag{9}$$

$$W(\mathrm{D},\ 5/2,\ 3,\ \pm1,\ B) = W(\mathrm{D},\ 5/2) + \frac{5hA_\mathrm{D}}{4} \pm \frac{[5g_J(\mathrm{D}) + g_I']\mu_\mathrm{B}B}{6} + \frac{2[g_J(\mathrm{D}) - g_I']^2\mu_\mathrm{B}^2B^2}{27hA_\mathrm{D}}, \tag{10}$$

$$W(\mathrm{D},\ 5/2,\ 3,\ \pm2,\ B) = W(\mathrm{D},\ 5/2) + \frac{5hA_\mathrm{D}}{4} \pm \frac{[5g_J(\mathrm{D}) + g_I']\mu_\mathrm{B}B}{3} + \frac{5[g_J(\mathrm{D}) - g_I']^2\mu_\mathrm{B}^2B^2}{108hA_\mathrm{D}}, \tag{11}$$

$$W(\mathrm{D},\ 5/2,\ 3,\ \pm3,\ B) = W(\mathrm{D},\ 5/2) + \frac{5hA_\mathrm{D}}{4} \pm \frac{[5g_J(\mathrm{D}) + g_I']\mu_\mathrm{B}B}{2}. \tag{12}$$

Here, $W(\gamma, J, F, M_F, B)$ denotes the energy of the state $|\gamma JFM_F\rangle$, including the effects of the hyperfine interaction and the magnetic field.

At a value of B of 0.1 mT, the quadratic shift of the $|S\ 1/2\ 0\ 0\rangle$ to $|D\ 5/2\ 2\ 0\rangle$ transition (optical clock transition) is −189.25(28) Hz, where the uncertainty stems mainly from the uncertainty in the experimental value of $g_J(D)$. In practice, the error may be less than this if the magnetic field is determined from the Zeeman splittings within the $|D\ 5/2\ F\ M_F\rangle$ sublevels. The reason is that an error in $g_J(D)$ leads to an error in the value of B inferred from the Zeeman splittings, which partly compensates for the $g_J(D)$ error. If instead we use the calculated value of $g_J(D)$, the quadratic shift for $B = 0.1$ mT is −189.98 Hz, where the uncertainty is difficult to estimate.

4. Quadratic Stark Shift

The theory of the quadratic Stark shift in free atoms has been described in detail by Angel and Sandars [19]. The Stark Hamiltonian is

$$H_E = -\boldsymbol{\mu}\cdot\boldsymbol{E}, \tag{13}$$

where $\boldsymbol{\mu}$ is the electric-dipole moment operator,

$$\boldsymbol{\mu} = -e\sum_i \boldsymbol{r}_i, \tag{14}$$

and $\boldsymbol{E}$ is the applied external electric field. In Eq. (14), $\boldsymbol{r}_i$ is the position operator of the ith electron, measured relative to the nucleus, and the summation is over all electrons.

First consider an atom with zero nuclear spin, such as $^{198}Hg^+$. To second order in the electric field, the Stark shifts of the set of sublevels $|\gamma J M_J\rangle$ depend on two parameters, $\alpha_{scalar}(\gamma, J)$ and $\alpha_{tensor}(\gamma, J)$, called the scalar and tensor polarizabilities. In principle, when both magnetic and electric fields are present but are not parallel, the energy levels are obtained by simultaneously diagonalizing the hyperfine, Zeeman, and Stark Hamiltonians. In practice, the Zeeman shifts are normally much larger than the Stark shifts, so that H_E does not affect the diagonalization. In that case, the energy shift of the state $|\gamma J M_J\rangle$ due to H_E is

$$\Delta W_E(\gamma, J, M_J, \boldsymbol{E}) = -\tfrac{1}{2}\,\alpha_{scalar}(\gamma, J)E^2 - \tfrac{1}{4}\,\alpha_{tensor}(\gamma, J)\,\frac{[3M_J^2 - J(J+1)]}{J(2J-1)}\,(3E_z^2 - E^2). \tag{15}$$

Treating H_E by second-order perturbation theory leads to the following expressions for the polarizabilities [19]:

$$\alpha_{scalar}(\gamma, J) = \frac{8\pi\epsilon_0}{3(2J+1)}\sum_{\gamma' J'}\frac{|\langle\gamma J\|\mu^{(1)}\|\gamma' J'\rangle|^2}{W(\gamma', J') - W(\gamma, J)}, \tag{16}$$

$$\alpha_{tensor}(\gamma, J) = 8\pi\epsilon_0\left[\frac{10J(2J-1)}{3(2J+3)(J+1)(2J+1)}\right]^{1/2} \times \sum_{\gamma' J'}(-1)^{J-J'}\begin{Bmatrix}1 & 1 & 2\\ J & J & J'\end{Bmatrix}\frac{|\langle\gamma J\|\mu^{(1)}\|\gamma' J'\rangle|^2}{W(\gamma', J') - W(\gamma, J)}. \tag{17}$$

The summations are over all levels other than $|\gamma J\rangle$. Equations (16) and (17) can be rewritten in terms of the oscillator strengths $f_{\gamma J,\gamma' J'}$:

$$\alpha_{scalar}(\gamma, J) = \frac{4\pi\epsilon_0 e^2\hbar^2}{m_e}\sum_{\gamma' J'}\frac{f_{\gamma J,\gamma' J'}}{[W(\gamma', J') - W(\gamma, J)]^2}, \tag{18}$$

$$\alpha_{tensor}(\gamma, J) = \frac{4\pi\epsilon_0 e^2\hbar^2}{m_e}\left[\frac{30J(2J-1)(2J+1)}{(2J+3)(J+1)}\right]^{1/2} \times \sum_{\gamma' J'}(-1)^{J-J'}\begin{Bmatrix}1 & 1 & 2\\ J & J & J'\end{Bmatrix}\frac{f_{\gamma J,\gamma' J'}}{[W(\gamma', J') - W(\gamma, J)]^2}, \tag{19}$$

where m_e is the electron mass. The tensor polarizability is zero for levels with $J < 1$, such as the $Hg^+\ 5d^{10}6s\ ^2S_{1/2}$ level.

For an atom with nonzero nuclear spin I, the quadratic Stark shift of the state $|\gamma J F M_F\rangle$ is

$$\Delta W_E(\gamma, J, M_F, \boldsymbol{E}) = -\tfrac{1}{2}\,\alpha_{scalar}(\gamma, J, F)E^2 - \tfrac{1}{4}\,\alpha_{tensor}(\gamma, J, F)\,\frac{[3M_F^2 - F(F+1)]}{F(2F-1)}\,(3E_z^2 - E^2). \tag{20}$$

We make the approximation that hyperfine interaction does not modify the electronic part of the atomic wavefunctions (the IJ-coupling approximation of Angel and Sandars [19]). This approximation is adequate for the present purpose, which is to evaluate the Stark shift of the $^{199}Hg^+$ optical clock transition. Obtaining the differential Stark shift between the hyperfine levels of the ground state, which is significant for the $^{199}Hg^+$ microwave frequency standard [11], requires going to a higher order of perturbation theory [20]. In the IJ-coupling approximation [19],

$$\alpha_{scalar}(\gamma, J, F) = \alpha_{scalar}(\gamma, J), \tag{21}$$

$$\alpha_{tensor}(\gamma, J, F) = (-1)^{I+J+F}\left[\frac{F(2F-1)(2F+1)(2J+3)(2J+1)(J+1)}{(2F+3)(F+1)J(2J-1)}\right]^{1/2} \times\begin{Bmatrix}F & J & I\\ J & F & 2\end{Bmatrix}\alpha_{tensor}(\gamma, J). \tag{22}$$

Equations (18) and (19) were used to evaluate the polarizabilities for the Hg^+ $5d^{10}6s\ ^2S_{1/2}$ and $5d^96s^2\ ^2D_{5/2}$ levels. For the calculation of $\alpha_{scalar}(S, 1/2)$, the oscillator strengths for all electric-dipole transitions connecting the $5d^{10}6s$ configuration to the $5d^{10}np$ ($n = 6,7,8$) and $5d^96s6p$ configurations were included. These were taken from the theoretical work of Brage et al. [21]. The final result is $\alpha_{scalar}(S, 1/2)/(4\pi\epsilon_0) = 2.41 \times 10^{-24}$ cm^3, which compares very well with the value of 2.22×10^{-24} cm^3 obtained by Henderson et al. from a combination of experimental and calculated oscillator strengths [22]. For the calculations of $\alpha_{scalar}(D, 5/2)$ and $\alpha_{tensor}(D, 5/2)$, the oscillator strengths for electric-dipole transitions to the $5d^{10}np$ ($n = 6,7,8$), $5d^{10}5f$, and $5d^96s6p$ configurations were taken from Brage et al. [21]. The oscillator strengths for electric-dipole transitions to the $5d^96s7p$ and $5d^86s^26p$ configurations were taken from the Cowan-code calculations. The results were $\alpha_{scalar}(D, 5/2)/(4\pi\epsilon_0) = 3.77 \times 10^{-24}$ cm^3 and $\alpha_{tensor}(D, 5/2)/(4\pi\epsilon_0) = -0.263 \times 10^{-24}$ cm^3. Evaluating Eq. (22) for $F = 2$ and $F = 3$ in the $5d^96s^2\ ^2D_{5/2}$ level, we obtain $\alpha_{tensor}(D, 5/2, 2) = \frac{4}{5}\alpha_{tensor}(D, 5/2)$ and $\alpha_{tensor}(D, 5/2, 3) = \alpha_{tensor}(D, 5/2)$.

The tensor polarizability is much smaller than the scalar polarizabilities and in any case does not contribute if the external electric field is isotropic, as is the case for the blackbody radiation field. The net shift of the optical clock transition due to the scalar polarizabilities is $\frac{1}{2}[\alpha_{scalar}(S, 1/2) - \alpha_{scalar}(D, 5/2)]E^2$. In frequency units, the shift is $-1.14 \times 10^{-3}\ E^2$ Hz, where E is expressed in V/cm. The error in the coefficient is difficult to estimate, particularly since it is a difference of two quantities of about the same size. However, the total shifts are small for typical experimental conditions. If the electric field is time-dependent, as for the blackbody field, the mean-squared value $\langle E^2 \rangle$ is taken. At a temperature of 300 K, the shift of the optical clock transition due to the blackbody electric field is -0.079 Hz. The mean-squared blackbody field is proportional to the fourth power of the temperature. For a single, laser-cooled ion in a Paul trap, the mean-squared trapping electric fields can be made small enough that the Stark shifts are not likely to be observable [23].

5. Electric Quadrupole Shift

The atomic quadrupole moment is due to a departure of the electronic charge distribution of an atom from spherical symmetry. Atomic quadrupole moments were first measured by the shift in energy levels due to an applied electric-field gradient in atomic-beam resonance experiments [24, 25].

The interaction of the atomic quadrupole moment with external electric-field gradients, for example those generated by the electrodes of an ion trap, is analogous to the interaction of a nuclear quadrupole moment with the electric field gradients due to the atomic electrons. Hence, we can adapt the treatment used for the electric-quadrupole hyperfine interaction of an atom [26]. The Hamiltonian describing the interaction of external electric-field gradients with the atomic quadrupole moment is

$$H_Q = \nabla E^{(2)} \cdot \Theta^{(2)} = \sum_{q=2}^{2} (-1)^q \nabla E_q^{(2)} \Theta_{-q}^{(2)}, \tag{23}$$

where $\nabla E^{(2)}$ is a tensor describing the gradients of the external electric field at the position of the atom, and $\Theta^{(2)}$ is the electric-quadrupole operator for the atom.

Following Ref. [26], we define the components of $\nabla E^{(2)}$ as

$$\nabla E_0^{(2)} = -\frac{1}{2}\frac{\partial E_z}{\partial z}, \tag{24}$$

$$\nabla E_{\pm 1}^{(2)} = \pm\frac{\sqrt{6}}{6}\frac{\partial E_{\pm}}{\partial z} = \pm\frac{\sqrt{6}}{6}\partial_{\pm} E_z, \tag{25}$$

$$\nabla E_{\pm 2}^{(2)} = -\frac{\sqrt{6}}{12}\partial_{\pm} E_{\pm}, \tag{26}$$

where $E_{\pm} \equiv E_x \pm iE_y$ and $\partial_{\pm} \equiv \frac{\partial}{\partial x} \pm i\frac{\partial}{\partial y}$.

The operator components $\Theta_q^{(2)}$ are defined in terms of the electronic coordinate operators as

$$\Theta_0^{(2)} = -\frac{e}{2}\sum_j (3z_j^2 - r_j^2), \tag{27}$$

$$\Theta_{\pm 1}^{(2)} = -e\sqrt{\frac{3}{2}}\sum_j z_j(x_j \pm iy_j), \tag{28}$$

$$\Theta_{\pm 2}^{(2)} = -e\sqrt{\frac{3}{8}}\sum_j (x_j \pm iy_j)^2, \tag{29}$$

where the sums are taken over all the electrons. The quadrupole moment $\Theta(\gamma, J)$ of an atomic level $|\gamma J\rangle$ is defined by the diagonal matrix element in the state with maximum M_J:

$$\Theta(\gamma, J) = \langle \gamma JJ | \Theta_0^{(2)} | \gamma JJ \rangle. \tag{30}$$

This is the definition used by Angel et al. [24].

In order to simplify the form of $\nabla E^{(2)}$, we make a principal-axis transformation as in Ref. [27]. That is, we express the electric potential in the neighborhood of the atom as

$$\Phi(x', y', z') = A[(x'^2 + y'^2 - 2z'^2) + \epsilon(x'^2 - y'^2)]. \quad (31)$$

The principal-axis (primed) frame (x', y', z') is the one in which Φ has the simple form of Eq. (31), while the laboratory (unprimed) frame (x, y, z) is the one in which the magnetic field is oriented along the z axis.

The tensor components of $\nabla \boldsymbol{E}^{(2)}$ in the principal-axis frame are obtained by taking derivatives of $\Phi(x', y', z')$:

$$\nabla E_0^{(2)'} = -2A, \quad (32)$$

$$\nabla E_{\pm 1}^{(2)'} = 0, \quad (33)$$

$$\nabla E_{\pm 2}^{(2)'} = \sqrt{\frac{2}{3}}\,\epsilon A. \quad (34)$$

In the principal-axis frame, H_Q has the simple form

$$H_Q = -2A\Theta_0^{(2)'} + \sqrt{\frac{2}{3}}\,\epsilon A\left(\Theta_2^{(2)'} + \Theta_{-2}^{(2)'}\right). \quad (35)$$

As long as the energy shifts due to H_Q are small relative to the Zeeman shifts, which is the usual case in practice, H_Q can be treated as a perturbation. In that case, it is necessary only to evaluate the matrix elements of H_Q that are diagonal in the basis of states $|\gamma JFM_F\rangle$, where $\boldsymbol{F}$ is the total atomic angular momentum, including nuclear spin $\boldsymbol{I}$, and M_F is the eigenvalue of F_z with respect to the laboratory (not principal-axis) frame. Let $\boldsymbol{\omega}$ denote the set of Euler angles $\{\alpha, \beta, \gamma\}$ that takes the principal-axis frame to the laboratory frame. To be explicit, starting from the principal-axis frame, we rotate the coordinate system about the z axis by α, then about the new y axis by β, and then about the new z axis by γ so that the rotated coordinate system coincides with the laboratory coordinate system. We can set $\gamma = 0$, since the final rotation about the laboratory z axis, which is parallel to $\boldsymbol{B}$, has no effect. The states $|\gamma JFm\rangle'$ defined in the principal-axis frame and the states $|\gamma JF\mu\rangle$ defined in the laboratory frame are related by

$$|\gamma JFm\rangle' = \sum_{\mu} D_{\mu m}^{(F)}(\boldsymbol{\omega})|\gamma JF\mu\rangle, \quad (36)$$

where $D_{\mu m}^{(F)}(\boldsymbol{\omega})$ is a rotation matrix element defined in the passive representation [28, 29]. The inverse relation is

$$|\gamma JF\mu\rangle = \sum_{m} D_{\mu m}^{(F)*}(\boldsymbol{\omega})|\gamma JFm\rangle'. \quad (37)$$

In order to evaluate the diagonal matrix elements of H_Q in the laboratory frame, it is necessary to evaluate matrix elements of the operators $\Theta_q^{(2)'}$, defined in the principal-axis frame. These matrix elements are of the form

$$\langle \gamma JF\mu|\Theta_q^{(2)'}|\gamma JF\mu\rangle$$

$$= \sum_{m'm} D_{\mu m'}^{(F)}(\boldsymbol{\omega}) D_{\mu m}^{(F)*}(\boldsymbol{\omega})\,'\langle \gamma JFm'|\Theta_q^{(2)'}|\gamma JFm\rangle', \quad (38)$$

$$= (\gamma JF\|\Theta^{(2)}\|\gamma JF)\sum_{m'm}(-1)^{F-m'}$$

$$\times\begin{pmatrix} F & 2 & F \\ -m' & q & m \end{pmatrix} D_{\mu m'}^{(F)}(\boldsymbol{\omega}) D_{\mu m}^{(F)*}(\boldsymbol{\omega}), \quad (39)$$

$$= (-1)^{F-\mu-q}(\gamma JF\|\Theta^{(2)}\|\gamma JF)$$

$$\times\sum_{m'm}\begin{pmatrix} F & 2 & F \\ -m' & q & m \end{pmatrix} D_{\mu m'}^{(F)}(\boldsymbol{\omega}) D_{-\mu -m}^{(F)}(\boldsymbol{\omega}), \quad (40)$$

$$= (-1)^{F-\mu-q}(\gamma JF\|\Theta^{(2)}\|\gamma JF)\sum_{K m m' n n'}(2K+1)$$

$$\times\begin{pmatrix} F & 2 & F \\ -m' & q & m \end{pmatrix}\begin{pmatrix} F & F & K \\ \mu & -\mu & n' \end{pmatrix}\begin{pmatrix} F & F & K \\ m' & -m & n \end{pmatrix} D_{n'n}^{(K)*}(\boldsymbol{\omega}), \quad (41)$$

$$= (-1)^{F-\mu-q}(\gamma JF\|\Theta^{(2)}\|\gamma JF)\begin{pmatrix} F & 2 & F \\ -\mu & 0 & \mu \end{pmatrix} D_{0-q}^{(2)*}(\boldsymbol{\omega}), \quad (42)$$

where Eq. (39) follows from the Wigner-Eckart theorem, and Eqs. (40), (41), and (42) follow from Eqs. (4.2.7), (4.3.2), and (3.7.8) of Ref. [28], respectively. The required rotation matrix elements are, from Eq. (4.1.25) of Ref. [28] (with correction of a typographical error),

$$D_{00}^{(2)*}(\boldsymbol{\omega}) = \tfrac{1}{2}(3\cos^2\beta - 1), \quad (43)$$

$$D_{0\pm 2}^{(2)*}(\boldsymbol{\omega}) = \sqrt{\tfrac{3}{8}}\sin^2\beta(\cos 2\alpha \mp i\sin 2\alpha). \quad (44)$$

The 3-j symbol in Eq. (42) is

$$\begin{pmatrix} F & 2 & F \\ -\mu & 0 & \mu \end{pmatrix}$$

$$= (-1)^{F-\mu}\frac{2[3\mu^2 - F(F+1)]}{[(2F+3)(2F+2)(2F+1)2F(2F-1)]^{1/2}}. \quad (45)$$

The diagonal matrix elements of H_Q in the laboratory frame are

$$\langle \gamma JFM_F|H_Q|\gamma JFM_F\rangle$$

$$= \frac{-2[3M_F^2 - F(F+1)]A(\gamma JF\|\Theta^{(2)}\|\gamma JF)}{[(2F+3)(2F+2)(2F+1)2F(2F-1)]^{1/2}}$$

$$\times [(3\cos^2\beta - 1) - \epsilon \sin^2\beta(\cos^2\alpha - \sin^2\alpha)]. \quad (46)$$

It is simple to show, by directly integrating the angular factor in square brackets in Eq. (46), that the average value of the diagonal matrix elements of H_Q, taken over all possible orientations of the laboratory frame with respect to the principal-axis frame, is zero. This also follows directly from the fact that the quantity in square brackets is a linear combination of spherical harmonics. It is less obvious that the average, taken over any three mutually perpendicular orientations of the laboratory z quantization axis, is also zero. This result is proven in Appendix A. This provides a method for eliminating the quadrupole shift from the observed transition frequency. The magnetic field must be oriented in three mutually perpendicular directions with respect to the trap electrodes, which are the source of the external quadrupole field, but with the same magnitude of the magnetic field. The average of the transition frequencies taken under these three conditions does not contain the quadrupole shift.

The reduced matrix element in Eq. (46) is, in the IJ-coupling approximation,

$$(\gamma(IJ)F\|\Theta^{(2)}\|\gamma(IJ)F)$$

$$= (-1)^{I+J+F}(2F+1)\begin{Bmatrix} J & 2 & J \\ F & I & F \end{Bmatrix}\begin{pmatrix} J & 2 & J \\ -J & 0 & J \end{pmatrix}^{-1}\Theta(\gamma, J), \quad (47)$$

where I is included in the state notation in order to specify the order of coupling of I and J. For the particular case of the $^{199}Hg^+$ $5d^96s^2\ ^2D_{5/2}$ level, the reduced matrix elements are

$$(\mathrm{D}\ 5/2\ 2\|\Theta^{(2)}\|\mathrm{D}\ 5/2\ 2) = 2\sqrt{\frac{14}{5}}\,\Theta(\mathrm{D},\ 5/2), \quad (48)$$

$$(\mathrm{D}\ 5/2\ 3\|\Theta^{(2)}\|\mathrm{D}\ 5/2\ 3) = 2\sqrt{\frac{21}{5}}\,\Theta(\mathrm{D},\ 5/2), \quad (49)$$

Since the Cowan-code calculation shows that there is very little configuration mixing in the $^{199}Hg^+$ $5d^96s^2\ ^2D_{5/2}$ level, $\Theta(D,\ 5/2)$ can be reduced to a matrix element involving only the $5d$ orbital:

$$\Theta(D,\ 5/2) = \frac{e}{2}\langle 5d^2 d_{5/2},\ m_j$$

$$= 5/2|3z^2 - r^2|5d^2 d_{5/2},\ m_j = 5/2\rangle, \quad (50)$$

$$= \frac{e}{2}\langle 5d,\ m_l = 2|3z^2 - r^2|5d,\ m_l = 2\rangle, \quad (51)$$

$$= e\sqrt{\frac{4\pi}{5}}\langle 5d,\ m_l = 2|Y_{2,0}(\theta,\ \phi)|5d,\ m_l = 2\rangle, \quad (52)$$

$$= e\sqrt{\frac{4\pi}{5}}\langle 5d|r^2|5d\rangle$$

$$\times \int_0^{2\pi}\int_0^{\pi} Y^*_{2,2}(\theta,\ \phi)Y_{2,0}(\theta,\ \phi)Y_{2,2}(\theta,\phi)\sin\theta\,\mathrm{d}\theta\mathrm{d}\phi, \quad (53)$$

$$= 5e\langle 5d|r^2|5d\rangle\begin{pmatrix} 2 & 2 & 2 \\ -2 & 0 & 2 \end{pmatrix}\begin{pmatrix} 2 & 2 & 2 \\ 0 & 0 & 0 \end{pmatrix}, \quad (54)$$

$$= -\frac{2e}{7}\langle 5d|r^2|5d\rangle. \quad (55)$$

The apparent sign reversal in Eq. (50) relative to Eqs. (27) and (30) is due to the fact that the quadrupole moment is due to a single *hole* in the otherwise filled $5d$ shell rather than to a single *electron*. According to the Cowan-code calculation,

$$\langle 5d|r^2|5d\rangle = 2.324\,a_0^2 = 6.509 \times 10^{-17}\ \mathrm{cm}^2, \quad (56)$$

where a_0 is the Bohr radius.

Since the quadrupole shifts are zero in the $5d^{10}6s\ ^2S_{1/2}$ level, the quadrupole shift of the $^{199}Hg^+$ optical clock transition is due entirely to the shift of the $|\mathrm{D}\ 5/2\ 2\ 0\rangle$ state, and is given by

$$\langle \mathrm{D}\ 5/2\ 2\ 0|H_Q|\mathrm{D}\ 5/2\ 2\ 0\rangle$$

$$= \tfrac{4}{5}A\Theta(\mathrm{D},\ 5/2)[(3\cos^2\beta - 1)$$

$$- \epsilon\sin^2\beta(\cos^2\alpha - \sin^2\alpha)], \quad (57)$$

$$= -\tfrac{8}{35}Ae\langle 5d|r^2|5d\rangle[(3\cos^2\beta - 1)$$

$$- \epsilon\sin^2\beta(\cos^2\alpha - \sin^2\alpha)], \quad (58)$$

$$\approx -3.6 \times 10^{-3}hA[(3\cos^2\beta - 1)$$

$$- \epsilon\sin^2\beta(\cos^2\alpha - \sin^2\alpha)]\mathrm{Hz}, \quad (59)$$

where A is expressed in units of V/cm^2. Thus, for typical values $A \approx 10^3$ V/cm^2 and $|\epsilon| \lesssim 1$, the quadrupole shift is on the order of 1 Hz.

6. Appendix A. Angular Averaging of the Quadrupole Shift

For the purpose of describing the quadrupole shift, the orientation of the laboratory (quantization) axis with respect to the principal-axis frame is defined by the angles β and α. In the principal-axis coordinate system, a unit vector along the laboratory z axis is defined in terms of β and α by

$$\hat{z} = (\sin\beta\cos\alpha,\ \sin\beta\sin\alpha,\ \cos\beta). \tag{60}$$

We wish to show that the angular dependence of the quadrupole shift is such that the diagonal matrix elements given by Eq. (46) average to zero, for $\hat{z}$ along any three mutually perpendicular directions.

An arbitrary set of three mutually perpendicular unit vectors $\boldsymbol{e}_1$, $\boldsymbol{e}_2$, and $\boldsymbol{e}_3$ can be parameterized by the set of angles θ, ϕ, and ψ in the following way:

$$\boldsymbol{e}_1 = (\sin\theta\cos\phi,\ \sin\theta\sin\phi,\ \cos\theta), \tag{61}$$

$$\boldsymbol{e}_2 = (\cos\phi\cos\theta\cos\psi - \sin\phi\sin\psi,\ \sin\phi\cos\theta\cos\psi + \cos\phi\sin\psi,\ -\sin\theta\cos\psi), \tag{62}$$

$$\boldsymbol{e}_3 = (-\cos\phi\cos\theta\sin\psi - \sin\phi\cos\psi,\ -\sin\phi\cos\theta\sin\psi + \cos\phi\cos\psi,\ \sin\theta\sin\psi). \tag{63}$$

It can be verified by direct computation that $\boldsymbol{e}_i \cdot \boldsymbol{e}_j = \delta_{ij}$.

The quadrupole shift can be evaluated for each of these three unit vectors substituted for $\hat{z}$ [Eq. (60)] and the average taken. First consider the average of the quantity $(3\cos^2\beta - 1)$ that appears in Eq. (46): We use the fact that $\cos\beta$ is the third component of $\hat{z}$, so the average is:

$$\langle 3\cos^2\beta - 1\rangle = \cos^2\theta + \sin^2\theta\cos^2\psi + \sin^2\theta\sin^2\psi - 1, \tag{64}$$

$$= \cos^2\theta + \sin^2\theta - 1, \tag{65}$$

$$= 0, \tag{66}$$

for arbitrary θ, ϕ, and ψ. Similarly, the average of the other angle-dependent term in Eq. (46), $\sin^2\beta(\cos^2\alpha - \sin^2\alpha)$, is calculated by making use of the fact that $\sin\beta\cos\alpha$ is the first component of $\hat{z}$, and $\sin\beta\sin\alpha$ is the second:

$$\langle \sin^2\beta(\cos^2\alpha - \sin^2\alpha)\rangle$$

$$= \tfrac{1}{3}[\sin^2\theta\cos^2\phi - \sin^2\theta\sin^2\phi + (\cos\phi\cos\theta\cos\psi - \sin\phi\sin\psi)^2 - (\sin\phi\cos\theta\cos\psi + \cos\phi\sin\psi)^2 + (\cos\phi\cos\theta\sin\psi + \sin\phi\cos\psi)^2 - (\sin\phi\cos\theta\sin\psi - \cos\phi\cos\psi)^2], \tag{67}$$

$$= 0, \tag{68}$$

for arbitrary θ, ϕ, and ψ. Hence, the matrix elements of H_Q given by Eq. (46) average to zero for any three mutually perpendicular orientations of the laboratory quantization axis.

Acknowledgments

We thank Dr. C. J. Sansonetti for making available the results of Ref. [9] prior to publication. We acknowledge financial support from the U.S. Office of Naval Research.

7. References

[1] P. L. Bender, J. L. Hall, R. H. Garstang, F. M. J. Pichanick, W. W. Smith, R. L. Barger, and J. B. West, Bull. Am. Phys. Soc. **21**, 599 (1976).
[2] W. M. Itano, J. C. Bergquist, R. G. Hulet, and D. J. Wineland, Phys. Rev. Lett. **59**, 2732 (1987).
[3] J. C. Bergquist, D. J. Wineland, W. M. Itano, H. Hemmati, H.-U. Daniel, and G. Leuchs, Phys. Rev. Lett. **55**, 1567 (1985).
[4] J. C. Bergquist, W. M. Itano, and D. Wineland, Phys. Rev. A **36**, 428 (1987).
[5] R. J. Rafac, B. C. Young, J. A. Beall, W. M. Itano, D. J. Wineland, and J. C. Bergquist, Phys. Rev. Lett. **85**, 2462 (2000).
[6] J. Reichert, M. Niering, R. Holzwarth, M. Weitz, Th. Udem, and T. W. Hänsch, Phys. Rev. Lett. **84**, 3232 (2000).
[7] S. A. Diddams, D. J. Jones, J. Ye, S. T. Cundiff, J. L. Hall, J. K. Ranka, R. S. Windeler, R. T. Udem, and T. W. Hänsch, Phys. Rev. Lett. **84**, 5102 (2000).
[8] R. D. Cowan, The Theory of Atomic Structure and Spectra, Univ. California Press, Berkeley, CA (1981).
[9] C. J. Sansonetti and J. Reader, Phys. Scripta **63**, 219 (2001).
[10] M. Wilson, Atomic Spectra and Oscillator Strengths for Astrophysics and Fusion Research, J. E. Hansen, ed., North-Holland, Amsterdam (1990).
[11] D. J. Berkeland, J. D. Miller, J. C. Bergquist, W. M. Itano, and D. J. Wineland, Phys. Rev. Lett. **80**, 2089 (1998).
[12] J. C. Bergquist, unpublished experimental results.
[13] O. Loebich and A. Steudel, Z. Phys. **166**, 56 (1961).
[14] W. M. Itano, J. C. Bergquist, and D. J. Wineland, J. Opt. Soc. Am. B **2**, 1392 (1985).
[15] Th. A. M. Van Kleef and M. Fred, Physica **29**, 389 (1963).
[16] B. Cagnac, Ann. Phys. (Paris) **6**, 467 (1961).
[17] A. Abragam and J. H. Van Vleck, Phys. Rev. **92**, 1448 (1953).
[18] W. J. Childs and L. S. Goodman, Phys. Rev. **141**, 176 (1966).
[19] J. R. P. Angel and P. G. H. Sandars, Proc. Roy. Soc. A **305**, 125 (1968).

[20] W. M. Itano, L. L. Lewis, and D. J. Wineland, Phys. Rev. A **25**, 1233 (1982).
[21] T. Brage, C. Proffitt, and D. S. Leckrone, Ap. J. **513**, 524 (1999). (Updated tables of oscillator strengths were taken from the website http://aniara.gsfc.nasa.gov/sam/sam.html.)
[22] M. Henderson, L. J. Curtis, R. Matulioniene, D. G. Ellis, and C. E. Theodosiu, Phys. Rev. A **56**, 1872 (1997).
[23] D. J. Berkeland, J. D. Miller, J. C. Bergquist, W. M. Itano, and D. J. Wineland, J. Appl. Phys. **83**, 5025 (1998).
[24] J. R. P. Angel, P. G. H. Sandars, and G. K. Woodgate, J. Chem. Phys. **47**, 1552 (1967).
[25] P. G. H. Sandars and A. J. Stewart, Atomic Physics 3, S. J. Smith and G. K. Walters, eds., Plenum Press, New York (1973) p. 429.
[26] N. F. Ramsey, Molecular Beams, Oxford Univ. Press, London (1956) Chap. III.
[27] L. S. Brown and G. Gabrielse, Phys. Rev. A **25**, 2423 (1982).
[28] A. R. Edmonds, Angular Momentum in Quantum Mechanics, Princeton Univ. Press (1974). (Earlier printings include some incorrect equations involving the rotation operators. See Ref. [29].)
[29] A. A. Wolf, Am. J. Phys. **37**, 531 (1969).

About the author: *Wayne M. Itano is a physicist in the Time and Frequency Division of the NIST Physics Laboratory. The National Institute of Standards and Technology is an agency of the Technology Administration, U.S. Department of Commerce.*

Direct comparison of two cold-atom-based optical frequency standards by using a femtosecond-laser comb

K. R. Vogel, S. A. Diddams, C. W. Oates, E. A. Curtis, R. J. Rafac, W. M. Itano, J. C. Bergquist, R. W. Fox, W. D. Lee, J. S. Wells, and L. Hollberg

Time and Frequency Division, National Institute of Standards and Technology, Boulder, Colorado 80305-3328

Received August 15, 2000

With a fiber-broadened, femtosecond-laser frequency comb, the 76-THz interval between two laser-cooled optical frequency standards was measured with a statistical uncertainty of 2×10^{-13} in 5 s, to our knowledge the best short-term instability thus far reported for an optical frequency measurement. One standard is based on the calcium intercombination line at 657 nm, and the other, on the mercury ion electric-quadrupole transition at 282 nm. By linking this measurement to the known Ca frequency, we report a new frequency value for the Hg^+ clock transition with an improvement in accuracy of $\sim 10^5$ compared with its best previous measurement.

OCIS codes: 120.3930, 320.7090, 190.4370.

State-of-the-art optical frequency standards based on cold atoms and ions exhibit excellent frequency stability and have the potential for achieving high reproducibility and accuracy. Such frequency references should find application in precise tests of fundamental physics and in next-generation atomic clocks. Incorporating these optical-based standards into a clockwork, however, has proved troublesome because their large frequencies (>300 THz) could not be conveniently converted into countable microwave signals. Several optical-frequency measurements have been made with harmonic chains used to multiply the frequency of the 9.2-GHz cesium microwave standard,[1–6] but these chains are complex and their operation requires significant resources. A paradigm-changing simplification was pioneered by Udem *et al.*[7,8] when they used the wide frequency-domain comb output of a femtosecond (fs) mode-locked laser to measure the absolute frequency of the Cs D_1 line and the hydrogen $1s-2s$ transition,[9] the most accurate measurement to date of an optical frequency. A further refinement, by Diddams *et al.*,[10] expanded the available comb spectrum to an optical octave by broadening the fs-laser output in a microstructure fiber, leading to a direct connection between microwave and optical frequencies. A recent comparison of two independent, fiber-broadened fs laser combs that measured the same frequency interval verified that a precision and reproducibility of $<5.1 \times 10^{-16}$ can be attained with this measurement method.[11]

In this Letter we report a high-precision comparison of two promising cold-atom optical frequency standards by use of a fs-laser frequency comb. One standard is based on a 2-mK collection of $\sim 10^7$ neutral ^{40}Ca atoms, and the other probes a single $^{199}Hg^+$ ion that is laser cooled to near the Doppler limit. At 657 nm, a cw frequency-stabilized diode laser is locked to the central Ramsey–Bordé fringe obtained by four-pulse excitation of the Ca $^1S_0-^3P_1$ intercombination transition ($\nu_{Ca} = 456$ THz, $\Delta\nu = 400$ Hz).[12] This system has demonstrated a frequency instability of $4 \times 10^{-15}\ \tau^{-1/2}$ (τ is the averaging time) when it is probing subkilohertz fringe linewidths.[13] For the present measurements the Ca spectrometer was operated with 2.9-kHz linewidths, which gave an estimated short-term instability of $<2 \times 10^{-14}\ \tau^{-1/2}$. The oscillator in the Hg^+ standard is a frequency-narrowed cw dye laser at 563 nm that has a linewidth of ~0.16 Hz for a 20-s integration time.[14] This light is frequency doubled to 282 nm to interrogate the $^2S_{1/2}-^2D_{5/2}$ electric-quadrupole transition ($\nu_{Hg^+} = 1065$ THz, $\Delta\nu = 1.7$ Hz) of a Hg^+ ion that is confined in a linear, cryogenic, rf ion trap. Rabi linewidths as narrow as 6.7 Hz at 282 nm have been observed with this system.[15] For these measurements the laser was stabilized to the Hg^+ ion with a linewidth of 40 Hz at 282 nm, and the instability under these conditions is estimated to be $<3 \times 10^{-15}\ \tau^{-1/2}$.

The fs-comb frequency measurement system shown in Fig. 1 measures the 76-THz interval between the 657- and the 563-nm light which is transported from each stabilized laser by a 10- and a 130-m optical fiber, respectively. No attempt has been made to actively cancel the fiber-added noise,[14,16] which we measured to average as $<4.4 \times 10^{-14}\ \tau^{-1/2}$ for these optical frequencies. The frequency comb is produced by a Kerr-lens mode-locked Ti:sapphire laser that has a bandwidth of 42 nm (FWHM) centered at 810 nm and operates with a repetition rate of ≈98 MHz. To control the frequency spacing between comb modes we detect the ninth harmonic of the repetition rate with a signal-to-noise ratio (S/N) of >70 dB in a 100-kHz

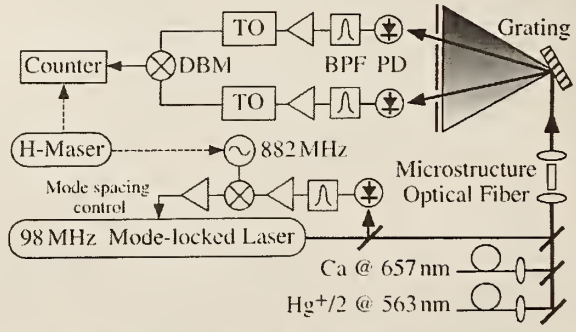

Fig. 1. Block diagram of frequency measurement: DBM, doubly balanced mixer; PD, photodiode; BPF, bandpass filter; TO's, tracking oscillators.

bandwidth (BW) and then mix it with an 882-MHz reference signal from a frequency synthesizer. We phase lock the repetition rate of the mode-locked laser to this reference frequency by using the phase-dependent mixer output to control the horizontal tilt of the high-reflector mirror, which is situated after a dispersion-compensating prism pair.[7–9] The internal clock of the synthesizer is phase locked to a hydrogen maser [H-Maser; $\sigma_y(\tau) \approx 2 \times 10^{-13}\tau^{-1/2}$], whose frequency is known with an uncertainty of $\pm 4 \times 10^{-15}$ by comparison with a Cs primary standard.

To extend the comb bandwidth we launch the fs-laser pulses into a 5 cm-long microstructure optical fiber that has a core diameter of $\approx$1.7 μm and zero group-velocity dispersion near 770 nm.[17] Self-phase modulation and other nonlinearities in the fiber produce an output spectrum from approximately 500 to 1100 nm. The cw light from both stabilized lasers is also coupled into the microstructure fiber to ensure good spatial mode overlap with the fs-laser light. The fiber output is dispersed by an optical grating and imaged onto slits such that only a few modes in the vicinity of the cw light frequencies are selected. A photodiode after each slit detects the rf heterodyne beat note (δ_1, δ_2) between the cw light and a comb mode with a S/N of ~25 dB in a 100-kHz BW, with the background limited by the shot noise of the cw light power. For accurate frequency counting, a tracking oscillator is phase locked to each beat note to provide regenerated signals with >50-dB S/N in a 100-kHz BW. These tracking oscillators consist of a low-phase-noise, voltage-controlled oscillator that is phase locked with an ~100-kHz BW to track the incoming signal in such a way that the broadband, background noise pedestal below the beat note is not reproduced.

In these measurements the comb-mode spacing ν_{rep} is locked tightly to the H-maser frequency, but the offset frequency of the fs-laser comb remains uncontrolled. So, although the comb modes are spaced equidistantly, knowledge of the absolute frequency of an individual comb mode is limited by the frequency jitter of the fs laser (~10 MHz). As we are concerned only with a frequency difference, we can remove this noise that is common to both beat notes by mixing together the correlated signals from the two tracking oscillators.[10] The mixer output is either a stable sum or difference signal $\delta = \delta_1 \pm \delta_2$, which is counted to yield the frequency interval $\Delta\nu = {}^1/_2\,\nu_{Hg^+} - \nu_{Ca} = N\nu_{rep} \pm \delta$. We determined the integer number N and the sign choice for δ unambiguously by comparing $\Delta\nu$ with our previous ±10-MHz measurement of this frequency difference,[18] and we verified our choices by making measurements for different repetition rates.

The inset in Fig. 2 shows a typical time record of the frequency fluctuations of δ, counted with a 5-s gate time. Points that exhibit obvious cycle slip errors, which are due predominantly to a tracking oscillator's losing lock, are eliminated in the data sorting. We calculate the Allan deviation, shown in Fig. 2, for various averaging times by juxtaposing the 5 s gate-time data; the deviation indicates that the measurement precision averages as $(34\ \text{Hz})\tau^{-1/2}$ for the duration of the measurement. Three frequency sources (ν_{Ca}, ν_{Hg^+}, ν_{rep}) contribute to the short-term instability of this measurement, and from these data alone we cannot attribute the noise unambiguously to a specific source. Nonetheless, by assuming that all the noise comes solely from a given source, we can place an upper limit on its short-term Allan deviation. From this datum we infer an upper limit of $\leq 7 \times 10^{-14}\tau^{-1/2}$ for the fractional frequency instability of the two optical standards, although each probably has a significantly better stability.[13–15] Combining the best estimates for the (normalized) instabilities of the microwave and two optical references, as well as for the optical fiber delivery, we arrive at a calculated instability of $3.5 \times 10^{-13}\tau^{-1/2}$ for the 76-THz interval, in good agreement with the measured value of $4.5 \times 10^{-13}\tau^{-1/2}$. There are likely additional degradations of the stability as a result of noise in the microwave detection of the repetition rate and (or) in the synthesizer electronics that multiply the frequency of the H-maser reference.

The results of running the fs-comb measurement system on four separate days over a 6-week period are plotted in Fig. 3 as the frequency offset from the weighted mean, which is $\Delta\nu$ = 76 374 564 455 429 (40) Hz. Each of these points represents the weighted mean of the data runs on an individual day, corrected for the second-order Zeeman shifts for both Ca and Hg^+, which are determined to an uncertainty of $<10^{-14}$ for each day. The Ca system contributes to the majority of the 40-Hz uncertainty; the Hg^+ reference supplies a <10-Hz contribution (at 563 nm), limited by the present measurement of the electric-quadrupole shift.[15] The largest systematic error (~30 Hz) stems from uncertainty in our knowledge of the angular overlap of the counterpropagating probe beams in the Ca spectrometer, which leads to a residual first-order Doppler shift when the cold Ca ensemble has a transverse drift velocity.[4] It is noteworthy that the uncertainties for the data of May 5 and May 25 are dominated by systematic effects. The run-to-run measurements on those days are consistent with ≈10 Hz, as illustrated for the May 25 data in the Fig. 3 inset, which show only the statistical uncertainty for each run. Given the relatively small

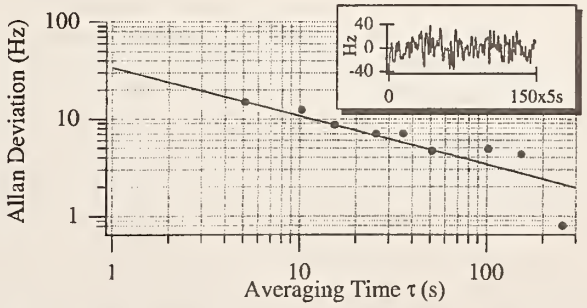

Fig. 2. Allan deviation of a typical measurement record. Curve, $(34\ \text{Hz})\tau^{-1/2}$; inset, the corresponding time record. From these data we place upper limits of $\sigma_y(\tau) \leq 45, 7.4, 6.4 \times 10^{-14}\ \tau^{-1/2}$ for the short-term instability of the microwave reference, ν_{Ca}, and ν_{Hg^+}, respectively.

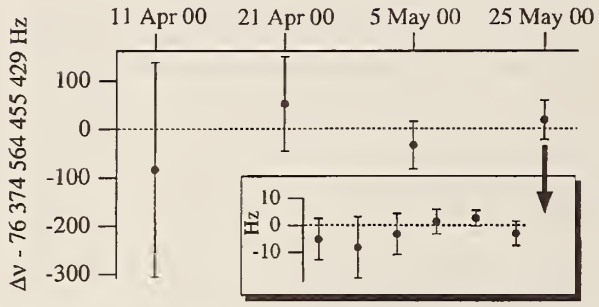

Fig. 3. Frequency deviation (Hz) of $\Delta\nu = {}^1/_2\,\nu_{Hg^+} - \nu_{Ca}$. Each data point is the weighted mean of an individual day's data runs. Inset, data runs for May 25 collected over a 50-min period, with each run averaging 230 s. Error bars in the inset reflect only statistical uncertainties.

statistical contribution (~2 Hz on a given day) to the total uncertainty, we believe that fs-laser-based frequency metrology gives us, for the first time, a practical tool for evaluating systematic shifts at an inaccuracy approaching 10^{-15} for these high-accuracy optical standards.

The uncertainties given for the two optical references were estimated for conditions during these experiments only, and no serious attempt was made to minimize systematic effects. Nevertheless, it is encouraging that our results for the frequency difference have a standard deviation of the mean of 60 Hz over a 6-week period. This consistency shows that all three components, the frequency-measurement system and the two optical standards, are reproducible at this level. Thus we offer an improved value for the Hg^+ clock transition frequency by summing our measured $Hg^+/2$–Ca interval with the absolute frequency of the Ca 657-nm clock transition measured in Ref. 4. We obtain $\nu_{Hg^+} = 2 \times 532\,360\,804\,949\,559\,(124)$ Hz, where the uncertainty is dominated by the 120-Hz uncertainty in the Ca measurement. This is an 80,000-fold improvement over the best previous frequency measurement of the 282-nm clock transition.[18]

Work is currently under way to self-reference the frequency offset of our fs comb,[19] and we anticipate confirmation of the Hg^+ and Ca frequencies with a direct rf-to-optical measurement. In fact, locking a mode of the self-referenced comb to one of the optical standards can achieve an all-optical connection between Hg^+ and Ca that eliminates any dependence on the H-maser microwave reference. This interval measurement should then average at the stability of the optical standards alone, allowing for a more precise determination of systematic shifts. The capability to intercompare three high-performance frequency standards (Hg^+, Ca, and Cs) has powerful advantages, such as permitting absolute frequency stabilities to be determined and the fidelity of fs-comb measurements to be tested. Indeed, an optical clock is realized by the repetition-rate output of an all-optically referenced comb, and microwave sources with frequency instabilities near $10^{-15}\,\tau^{-1/2}$ should be obtainable, provided that the repetition-rate signal can be extracted with a suitably high S/N.

The authors thank J. L. Hall, J. Ye, D. Jones, S. Cundiff, Th. Udem, F. Walls, R. Holzwarth, and T. Hänsch for useful discussions and are especially grateful to J. Ranka and R. Windeler for supplying the microstructure optical fiber. This research was partially supported by the U.S. Office of Naval Research. K. Vogel's e-mail address is kvogel@boulder.nist.gov.

References

1. D. A. Jennings, C. R. Pollock, F. R. Petersen, R. E. Drullinger, K. M. Evenson, J. S. Wells, J. L. Hall, and H. P. Layer, Opt. Lett. **8,** 136 (1983).
2. C. R. Pollock, D. A. Jennings, F. R. Petersen, J. S. Wells, R. E. Drullinger, E. C. Beaty, and K. M. Evenson, Opt. Lett. **8,** 133 (1983).
3. H. Schnatz, B. Lipphardt, J. Helmcke, F. Riehle, and G. Zinner, Phys. Rev. Lett. **76,** 18 (1996).
4. F. Riehle, H. Schnatz, B. Lipphardt, G. Zinner, T. Trebst, T. Binnewies, G. Wilpers, and J. Helmcke, in *Proceedings of the 1999 Joint Meeting of the EFTF–IEEE IFCS* (IEEE, New York, 1999), p. 700.
5. D. Touahri, O. Acef, A. Clairon, J.-J. Zondy, R. Felder, L. Hilico, B. de Beauvoir, F. Biraben, and F. Nez, Opt. Commun. **133,** 471 (1997).
6. J. E. Bernard, A. A. Madej, L. Marmet, B. G. Whitford, K. J. Siemsen, and S. Cundy, Phys. Rev. Lett. **82,** 3228 (1999).
7. Th. Udem, J. Riechert, R. Holzwarth, and T. W. Hänsch, Opt. Lett. **24,** 881 (1999).
8. Th. Udem, J. Reichert, R. Holzwarth, and T. W. Hänsch, Phys. Rev. Lett. **82,** 3568 (1999).
9. M. Niering, R. Holzwarth, J. Reichert, P. Pokasov, Th. Udem, M. Weitz, T. W. Hänsch, P. Lemonde, G. Santarelli, M. Abgrall, P. Laurent, C. Salomon, and A. Clairon, Phys. Rev. Lett. **84,** 5496 (2000).
10. S. A. Diddams, D. J. Jones, J. Ye, S. T. Cundiff, J. L. Hall, J. K. Ranka, R. S. Windeler, R. Holzwarth, Th. Udem, and T. W. Hänsch, Phys. Rev. Lett. **84,** 5102 (2000).
11. R. Holzwarth, Th. Udem, T. W. Hänsch, J. C. Knight, W. J. Wadsworth, and P. St. J. Russell, Phys. Rev. Lett. **85,** 2264 (2000).
12. C. W. Oates, F. Bondu, R. W. Fox, and L. Hollberg, Eur. Phys. J. D **7,** 449 (1999).
13. C. W. Oates, E. A. Curtis, and L. Hollberg, Opt. Lett. **25,** 1603 (2000).
14. B. C. Young, R. J. Rafac, J. A. Beall, F. C. Cruz, W. M. Itano, D. J. Wineland, and J. C. Bergquist, in *Proceedings of XIV International Conference on Laser Spectroscopy* (World Scientific, Singapore, 1999), pp. 61–70.
15. R. J. Rafac, B. C. Young, J. A. Beall, W. M. Itano, D. J. Wineland, and J. C. Bergquist, Phys. Rev. Lett. **85,** 2462 (2000).
16. L.-S. Ma, P. Junger, J. Ye, and J. L. Hall, Opt. Lett. **19,** 1777 (1994).
17. J. K. Ranka, R. S. Windeler, and A. Stentz, Opt. Lett. **25,** 25 (2000).
18. B. Frech, J. S. Wells, C. W. Oates, J. Mitchell, Y.-P. Lan, T. Kurosu, L. Zink, L. Hollberg, T. Zibrova, B. C. Young, and J. C. Bergquist, IEEE Trans. Ultrason. Ferroelectr. Freq. Control **47,** 513 (2000).
19. D. J. Jones, S. A. Diddams, J. K. Ranka, A. Stentz, R. S. Windeler, J. L. Hall, and S. T. Cundiff, Science **288,** 635 (2000).

Time Measurement at the Millennium

The latest clocks use a single ion to measure time with an anticipated precision of one part in 10^{18}.

James C. Bergquist, Steven R. Jefferts, and David J. Wineland

In 1714, stimulated by another naval disaster attributed to inaccurate navigation, the British Parliament passed the Longitude Act. This act created a prize of £20 000—an enormous sum at that time—to be given to the inventor of an accurate method for determining longitude. It had long been realized that longitude could be calculated from the positions of the Sun or stars if the time were known accurately. What was needed was an accurate, seaworthy clock. John Harrison met the challenge by developing a rugged mechanical clock, accurate within a few seconds over several months. After years of bureaucratic foot-dragging, he eventually received the prize.[1]

Navigation has continued to be one of the principal applications of accurate clocks. Indeed, we already take for granted the GPS (Global Positioning System) whose phenomenal navigational accuracy is based on clocks that keep time within 3 nanoseconds. However, navigation has not always provided the stimulus for better clocks. In some cases, such as the development of the atomic clock, navigation was the beneficiary of advances elsewhere in physics.

For modern-day physicists, the pursuit of better clocks provides a natural means for studying various aspects of nature, including the fundamental constants and the interaction of radiation and matter. Those of us who measure time are mindful of the practical applications, but we are also strongly driven by scientific considerations and the desire to apply clocks to other interesting measurements. Perhaps we will one day find that clocks, whose frequencies depend differently on the basic forces, diverge in time, signaling a fundamental change in how we perceive nature.[2]

Although a unit of time can be constructed from other physical constants, time is usually viewed as an arbitrary parameter to describe dynamics. The frequency of any periodic event, such as the mechanical oscillation of a pendulum or the quantum oscillation of an atomic dipole, can be adopted to define the unit of time, the second.

For centuries, the mean solar day served as our unit of time, but Earth's period of rotation is irregular and slowly increasing. In 1956, the International Astronomical Union and the International Committee on Weights and Measures recommended adopting Ephemeris Time—based on Earth's orbital motion around the Sun—as a more accurate and stable basis for the definition of time. Four years later, the two organizations' recommendation was formally ratified by the General Conference on Weights and Measures.

Until the definition of the second in terms of atomic time in 1967, much of the work of the National Bureau of Standards (NBS, the forerunner of NIST—the National Institute of Standards and Technology) and other standards laboratories was devoted to developing reliable secondary standards, such as lumped-element circuits and quartz crystals, whose resonant frequencies could be calibrated relative to Ephemeris Time (1 s was defined as 1/31 556 925.9747 of the year 1900).[1]

Frequencies derived from resonant transitions in atoms or molecules offer important advantages over macroscopic oscillators. Any unperturbed atomic transition is identical from atom to atom, so two clocks based on such a transition should generate the same time. Also, unlike macroscopic devices, atoms do not wear out. And, at least as far as we know, they do not change their properties over time. These features were appreciated by Lord Kelvin, who suggested using transitions in hydrogen as a time-keeping oscillator. However, it wasn't until the mid-20th century that technology made these ideas possible.

The first atomic clock was developed in 1949 by Harold Lyons of NBS, and was based on the inversion transition in ammonia, which occurs at a frequency of about 24 GHz. In the mid-1950s, Louis Essen and John Parry of Britain's National Physical Laboratory made a significantly more stable and accurate atomic clock based on the ground-state hyperfine transition in cesium. As NBS and other national laboratories developed cesium standards, pressure mounted for an atom-based definition of time.

This change occurred in 1967 when, by international agreement, the second was defined as the duration of 9 192 631 770 periods of the radiation corresponding to the transition between the two hyperfine levels of the ground state of the ^{133}Cs atom.[1] This definition made atomic time agree with the second based on Ephemeris Time, to the extent that measurement allowed.

Atomic clock recipe

The basic idea of most atomic clocks is straightforward. First, identify a transition between two nondegenerate eigenstates of an atom. Then, create an ensemble of these atoms—in an atomic beam or storage device, for example. Next, illuminate the atoms with radiation from a tunable source that operates near the transition frequency f_0. Sense and control the frequency where the atoms absorb maximally. When maximal absorption is achieved, count

James Bergquist, Steven Jefferts, *and* David Wineland *all work in the time and frequency division of the National Institute of Standards and Technology in Boulder, Colorado.*

Quantum Limits to Spectroscopy

A resonance curve for N atoms is generated by sweeping the probing radiation's frequency f and recording the outcomes of a meter operator $\tilde{O}$. In a frequency standard, the relevant signal is the change of this measurement outcome with change of frequency—that is, $\partial\langle\tilde{O}\rangle/\partial f$. The uncertainty of a frequency determination is therefore given by $\Delta f_m = \Delta\tilde{O}/|(\partial\tilde{O}/\partial f)|$, where $(\Delta\tilde{O})^2$ is the variance of repeated measurements of $\tilde{O}$.

In Ramsey spectroscopy[4] with separable (unentangled) atoms, the state Ψ after the first $\pi/2$ pulse is as shown below in the upper panel. After the second $\pi/2$ pulse, we measure the number of atoms N_+ in the excited state $|+\rangle$ (that is, $\tilde{O} \equiv \tilde{N}_+$). In this case, $\Delta f_m/f_0 = 1/(2\pi f_0 T N^{1/2})$, the standard quantum limit due to projection noise.[3]

Now suppose we replace the first Ramsey pulse with an operation that creates the (entangled) state Ψ shown in the lower panel. In this case, after the second (normal) $\pi/2$ pulse, we want to measure parity (that is, $\tilde{O} \equiv \tilde{P}_+$; $P_+ = +1$ if the number of $|+\rangle$ atoms is even, and -1 if the number of $|+\rangle$ atoms is odd). For this case, $\Delta f_m/f_0 = 1/(2\pi f_0 T N)$, the Heisenberg limit. This gain in precision is due to the fact that we have created a state where the energy between the two states of the superposition is N times larger than the separable-state case. In practice, this means the time to reach a certain measurement precision would be reduced by the number N of entangled atoms, an important improvement because clock outputs are typically averaged for weeks or months to reduce measurement uncertainty. Experimenters are now beginning to create such states for spectroscopy.

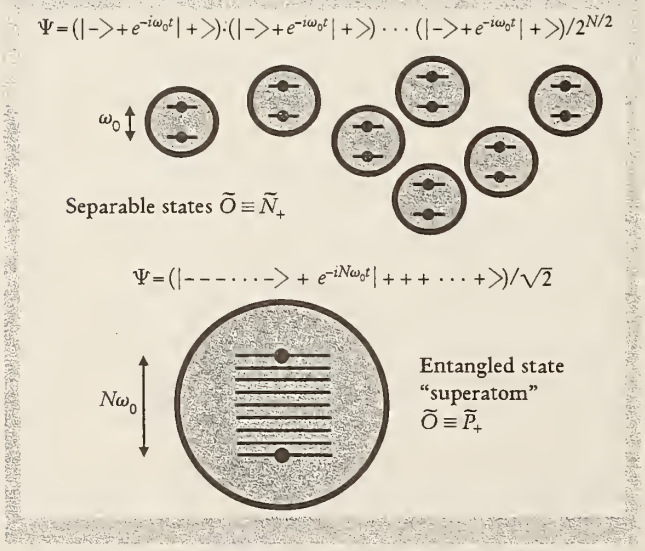

the cycles of the oscillator: A certain number of elapsed cycles generates a standard interval of time.

It is not quite as straightforward to put the recipe into practice. To sense the atomic transition, a difference in populations between the states of the selected transition must already exist or be created. Optimal performance is obtained when all the atoms are prepared in one of the states.

Changes to the difference in state populations caused by the tunable "clock" radiation can be probed by a number of schemes. For example, changes in state populations could be detected by absorption of the clock radiation (as was done in the first ammonia clock) or by looking at state-sensitive light scattering. If a number of absorption measurements are performed for a range of frequencies of the clock oscillator, an absorption feature, or resonance curve, can be recorded.

Because the degree of absorption is not very sensitive to small changes in frequency of the oscillator near the center of the resonance curve, the atoms are usually irradiated at two frequencies near the maximum slopes of the curve on opposite sides of its center. If the resonance curve is symmetric and the two frequencies are adjusted so that the absorptions on opposite sides of the resonance are the same, then the arithmetic mean of the two frequencies corresponds to the condition for maximum absorption. In practice, the determination of the frequency corresponding to maximum absorption is limited by noise. With care, we can reduce electronic and other sources of noise so that the measurement precision is limited only by what is known as quantum projection noise.[3]

Quantum projection noise can be viewed as arising from the statistical nature of projecting a superposition of two states into one state when a measurement is made. Whenever an atom is prepared in a coherent superposition of two states, any single attempt to measure the state composition will reveal only one of the states, not a mixture. The average of repeated measurements (or over many atoms in an atomic ensemble) will produce the desired point on the resonance curve with a precision that increases as the square root of the number of measurements (or as the square root of the number of atoms in the ensemble; see the adjacent box). This quantum measurement noise limits our ability to steer the average frequency of the oscillator to the center of the atomic resonance.

The fractional frequency uncertainty $\Delta f_m/f_0$ of our measurement can be expressed as

$$\frac{\Delta f_m}{f_0} = \frac{C}{2\pi f_0 T\sqrt{NM}} = \frac{C}{2\pi f_0\sqrt{NT\tau}},$$

where C is a constant of order unity; T is the interrogation time (that is, the time during which the clock radiation is applied before each measurement); N is the number of atoms; and M is the total number of measurements. In the last expression, τ is the total measurement time (over many measurements), and we have assumed that the time between interrogations is small compared to T. The stability of the clock is maximized when $\Delta f_m/f_0$ is minimized. Clearly, it is important to use a high transition frequency, a large number of atoms, and a long interrogation time.

With this prescription in mind, the makers of atomic clocks seek an atomic transition for which $\Delta f_m/f_0$ can be made small enough that the desired measurement precision is reached in a practical length of time. Equally important is the degree to which the measured frequency matches the unperturbed resonance frequency f_0 of the atom. Accuracy is maximized when the uncertainty Δf_a of deviations from the ideal are minimized, or the fractional frequency inaccuracy $\Delta f_a/f_0$ is minimized. For that reason, stable and accurate atomic clocks use an atom for which the environmental perturbations to the measured transition frequency are small or easily accounted for. Environmental perturbations can include frequency shifts to the clock transition caused by magnetic fields or collisions between the atoms.

Frequency shifts due to the atoms' motion can also Doppler-broaden and shift the observed absorption feature. Trapping the atoms eliminates the first-order Doppler shift (proportional to velocity) because the mean velocity of a trapped atom is zero. However, care must be taken that the trapping fields do not uncontrollably perturb the atom's frequency.

Cooling the atoms suppresses both Doppler broadening

and the second-order Doppler or time-dilation shift. With the simplest form of laser cooling, Doppler cooling,[4] temperatures around 0.001 K can be reached, which are sufficient to suppress the time-dilation shift to about 1 part in 10^{18} (see the article by Wineland and Wayne Itano, PHYSICS TODAY, June 1987, page 34). However, deeper cooling is needed to prevent an untrapped sample of atoms from spreading during the application of the radiation (see the article by Claude Cohen-Tannoudji and Bill Phillips, PHYSICS TODAY, October 1990, page 33).

Cesium clocks

Even without cooling or trapping, the ground-state hyperfine transition in cesium exhibits many of the desired attributes for making an atomic clock. The resonance frequency is high, the perturbations to the hyperfine energy can be made relatively small, and first-order Doppler shifts can be largely eliminated.[4] NIST (and earlier NBS) and the national laboratories of many countries worldwide have constructed a series of cesium clocks, called primary frequency standards. In most instances, each successive standard has provided a more accurate realization of the definition of the second.

Unfortunately, the hyperfine structure of cesium is not a simple two-level system. Each hyperfine level is composed of several magnetic substates whose degeneracies are removed in the presence of an external magnetic field. Most cesium clocks, including the first six primary standards at NBS, are atomic beam devices that use magnets to reject all magnetic substates except for the $F = 4$, $m_F = 0$ and $F = 3$, $m_F = 0$ hyperfine states. The transition frequency between these two states (corrected to zero field) is used as the best approximation of the second because it is the least sensitive to the applied magnetic field.

Although magnetically selected atomic-beam clocks are simple and rugged, their accuracy and stability suffer, in part, from inefficient state selection and short interrogation times (limited by the time of flight of the thermal atoms through the apparatus).

Around 1950, Alfred Kastler developed the concept of optical pumping and proposed using it to perform state preparation and detection. Optical pumping has been used in rubidium atomic standards for many years,[4] but became practical for cesium beam standards only with the development of solid-state lasers in the late 1970s. Optical state preparation and detection of the ground-state hyperfine levels can produce thermal beams with larger useable beam flux and correspondingly smaller $\Delta f_m/f_0$ than the magnetically selected beam clocks. It also avoids the B-field inhomogeneity associated with magnetic state selection.

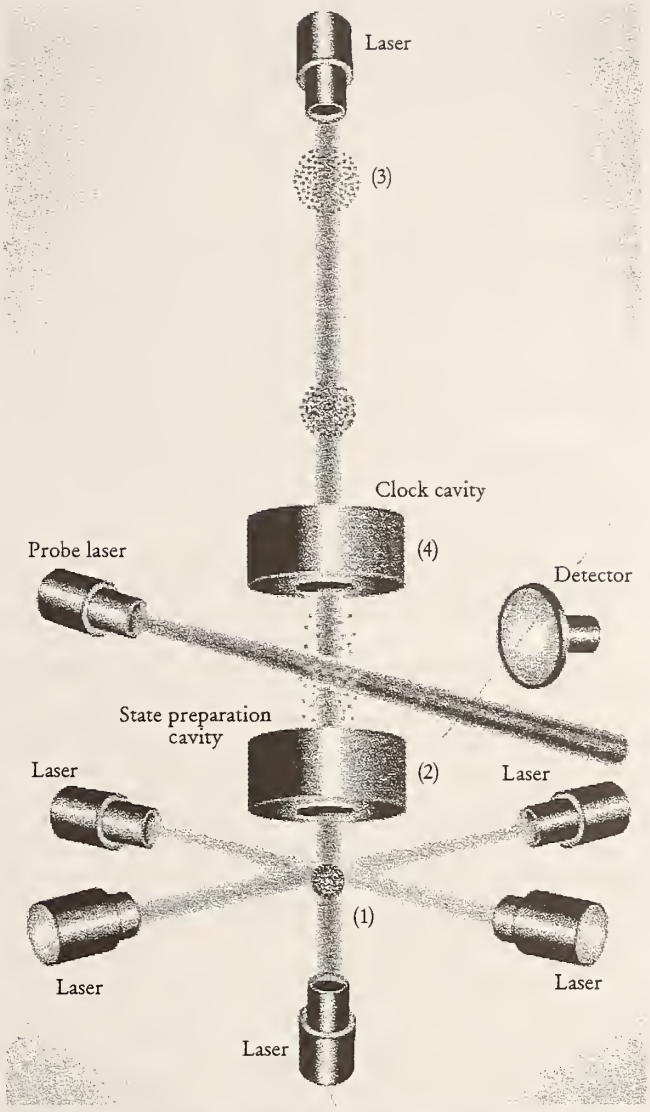

FIGURE 1. A SCHEMATIC VIEW of a cesium fountain frequency standard. A sample of 10^7 cesium atoms is first cooled to 1 μK at the intersection of the laser beams (1) and then launched upward at low velocity through the state preparation (2) and clock (4) cavities. The atoms reach apogee (3) and, about 1 s later, fall back through the clock cavity (4). Light scattered by the probe laser is used to measure the number of atoms that changed their hyperfine state as a result of the interaction with the microwaves.

The first optically pumped cesium standard at NIST, NIST-7, became the US time and frequency standard in 1993. In NIST-7, atoms from a thermal source first pass through a laser beam that optically pumps all atoms into the $F = 3$ hyperfine level. The atoms next transit a 1-meter-long region in which the clock radiation is applied. Finally, any atoms making the clock transition into the $F = 4$ level are detected by state-sensitive fluorescence in a second region crossed by another laser beam. The mean interrogation time of the atoms in NIST-7 is about 7 ms, which produces a resonance linewidth of about 70 Hz. This standard, which remains in operation today, attains values of $\Delta f_m/f_0$ of about 5×10^{-15} for $\tau \approx 1$ day.

Had atomic cesium clocks reached their stability and accuracy limit by the mid-1990s? Not quite! Already in the mid-1950s, Jerrold Zacharias had suggested a vertical geometry, or atom fountain, as a way to reach higher resolution (see the letter by Robert Naumann and Henry Stroke, PHYSICS TODAY, May 1996, page 89). He reasoned that if the atoms were launched vertically, then the slower atoms emerging from the oven would be decelerated, stopped by gravity, and fall back toward the source. The speed of most of the atoms in the thermal distribution emitted by the source would carry them to the top of the apparatus, where they would simply stick. If the beam tube is a few meters long, the mean transit time for the returning atoms is about 1 s, and the measured width of the hyperfine resonance about 1 Hz. Zacharias built a fountain apparatus, but saw no signal and abandoned the experiment. It was later determined that the faster atoms collide with the slower atoms and scatter them out of the beam.

Laser cooling brought life back to the fountain concept because all the atoms in the beam could be slowed. In the late 1980s, Steven Chu's group at Stanford University

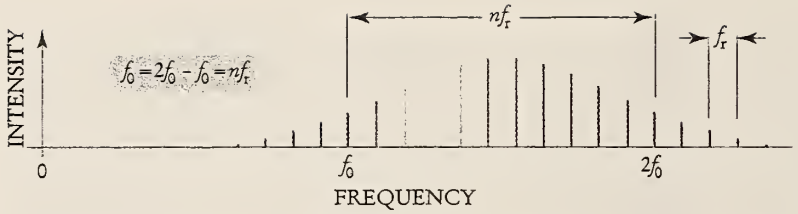

FIGURE 2. THE BASIC CONCEPT of the optical frequency divider. If an integer number n of phase-coherent frequencies, equidistantly spaced by f_r, can be made to precisely span the frequency interval $f_0 \rightarrow 2f_0$, then the frequency f_0 can be directly measured by measuring f_r because $f_0 = 2f_0 - f_0 = nf_r$. Pulsed lasers can now produce a comb of equally spaced spectral components, or teeth, that straddle an octave in the visible region of the spectrum, making possible the conversion of any optical frequency to a countable radio or microwave frequency.

succeeded in using laser-cooled sodium atoms to demonstrate the first fountain clock.[5] In 1991, a group led by André Clairon and Christophe Salomon at the Laboratoire Primaire du Temps et des Fréquences in Paris built the first cesium frequency standard configured as a fountain.[6] Now, many laboratories have built, or are building, cesium fountain clocks—including NIST, which put one into operation in 1998.[7]

The NIST cesium fountain, NIST-F1 (see figure 1), uses six laser beams tuned near the D_2, $F = 4 \rightarrow F' = 5$ cycling transition ($\lambda = 852$ nm) to laser-cool an approximately spherical sample of about 10^7 cesium atoms in optical molasses. The atoms in the $F = 3$ hyperfine ground state are not cooled in the molasses and are lost from the sample. The remaining ball of cold atoms is then launched vertically at a velocity of about 4 m s^{-1} by inducing a frequency difference between the vertical beams that causes the cold atom reference frame to move upward. The atoms drift upward through a microwave state preparation cavity whose frequency is adjusted to cause essentially all of the atoms in the $F = 4$, $m_F = 0$ state to undergo a transition to the $F = 3$, $m_F = 0$ state. When the atoms exit this cavity they are irradiated by a pulse of light that is tuned to resonance with the D_2, $F = 4 \rightarrow F' = 5$ transition. Any $F = 4$ atoms remaining in the sample are pushed aside by the absorbed photons, leaving only the $F = 3$, $m_F = 0$ atoms.

The ascending ball of atoms next transits a second microwave cavity, where the atoms are irradiated by the clock radiation. As the atoms continue upward, they exit the upper microwave cavity and enter a drift region. Approximately $\frac{1}{2}$ s after launch, their motion is arrested by gravity, and they start to fall. The descending atoms reenter the microwave cavity, where they experience a second dose of the clock radiation. This method of excitation—two pulses of radiation separated by a drift region (or simply by time)—is termed the Ramsey method after its inventor, Norman Ramsey.[4] Finally, the atoms enter the detection region, where the population of atoms in $F = 4$ is determined optically (the number of atoms remaining in $F = 3$ is also measured for normalization). Then, when another ball of atoms is cooled and launched, the clock cycle is repeated.

In NIST-F1, where the noise is dominated by the short-term frequency fluctuations of the microwave source and not by quantum projection noise, $\Delta f_m/f_0$ reaches about 2×10^{-15} for $\tau = 1$ day. The quantum noise limit for a cesium fountain is below this value. By using a more stable microwave source and a larger number of atoms, the Paris group demonstrated that it was possible to operate at the quantum projection noise limit reaching about 6×10^{-16} for $\tau = 5.5$ hours.[3]

With values of $\Delta f_a/f_0$ approaching 10^{-15}, the cesium fountain standards are currently the world's most accurate clocks. Their largest source of uncertainty arises from collisions between the cold cesium atoms, which cause a density- (and temperature-) dependent shift of the hyperfine frequency. Unfortunately, then, a compromise must be made between stability and accuracy.

But it is possible to increase both the stability and accuracy at the same time—by increasing the interrogation time and lowering the atomic thermal velocity. These two avenues are difficult to pursue in the presence of gravity, so, with NASA's support, NIST, along with the Jet Propulsion Laboratory and the University of Colorado, is currently constructing a laser-cooled cesium clock for flight aboard the microgravity environment of the International Space Station. The project, known as PARCS (Primary Atomic Reference Clock in Space) combines the traditional beam geometry with the cold source of the atomic fountain. The European Space Agency has a similar effort, ACES (Atomic Clock Ensemble in Space). In the absence of gravity, it will be possible to make short beam tubes and still achieve long interrogation times by launching slowly moving samples of cold atoms. PARCS is projected to attain $\Delta f_a/f_0$ of about 5×10^{-17}, due in part to a lower collisional shift and extraordinarily long (by terrestrial standards for neutral beams) interrogation times of up to 10 s.

Long interrogation times can also be obtained by atom trapping.[4] Neutral atoms can be trapped by a number of means, including magnetic or optical-dipole forces. These traps rely on trading an atom's kinetic energy for internal energy. Unfortunately, this exchange of energy typically perturbs the clock transition so that high accuracy is precluded. However, traps for atomic ions act directly on the charge and, thus, cause minimal perturbations to the internal structure.[8] Because trapping times can be extremely long, very high resolutions can be obtained and linewidths less than 0.001 Hz have been observed. (An atomic fountain would have to be a few 100 km tall to achieve the same resolution.) For high accuracies, relatively small numbers of trapped ions are desirable, which partially offsets the advantages of long interrogation times. Nevertheless, trapped-ion clocks based on microwave hyperfine transitions have achieved stabilities and accuracies comparable to those of cesium fountain clocks.[9]

Optical frequency standards

Perhaps the most promising route to better clocks is to use optical transitions, simply because clock stability is proportional to frequency f_0. As early as the 1960s, shortly after the demonstration of the first working laser, researchers began to investigate optical atomic and molecular transitions that might be suitable references for clocks.[10] However, an enormous barrier loomed: No practical device was fast enough to count the optical cycles to generate a unit of time.

Recently that stumbling block was all but eliminated with the demonstration—by Theodor Hänsch and his group in Garching, Germany, and by John Hall, Steven Cundiff, and their group in Boulder—that pulsed lasers can span an octave from the infrared to the ultraviolet with a grid of equidistant marker frequencies that are all phase coherent (ref. 11 and PHYSICS TODAY, June 1999, page 19). As depicted in figure 2, the spectrum of the pulse train from a mode-locked femtosecond laser corresponds to

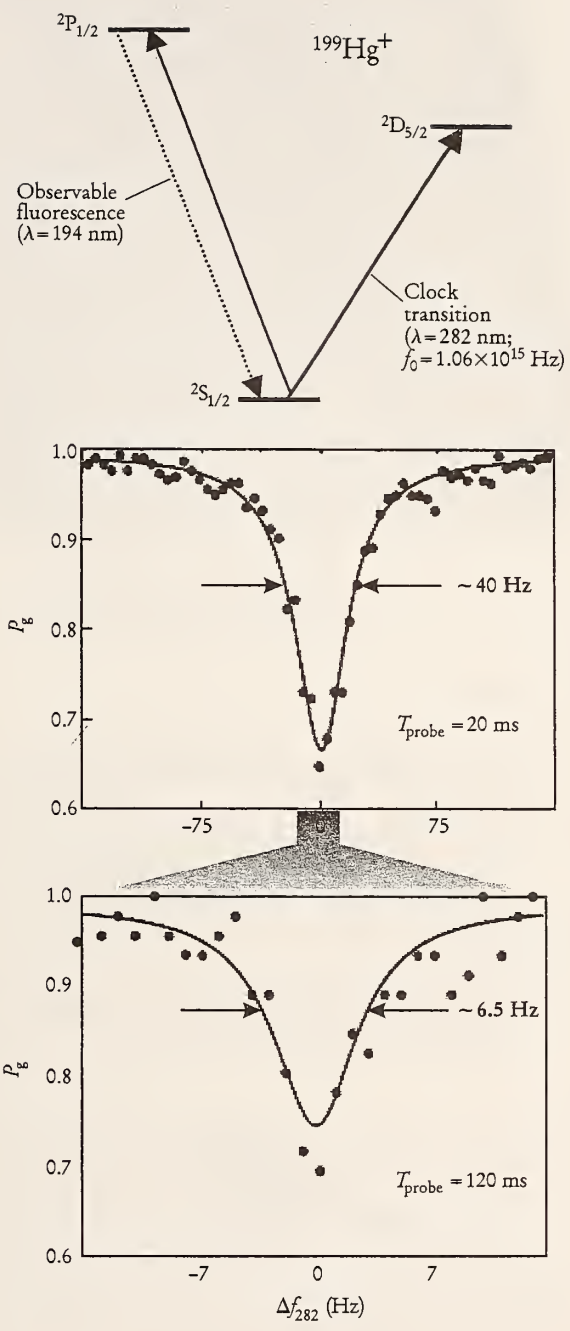

FIGURE 3. SINGLE $^{199}Hg^+$ ION OPTICAL CLOCK. Partial energy-level diagram of $^{199}Hg^+$ is shown in the upper panel. Cooling, state preparation, and state detection are done on the strongly allowed $^2S_{1/2} \rightarrow {}^2P_{1/2}$ transition at 194 nm. Any clock transition to the $^2D_{5/2}$ level at 282 nm (the allowed electric-quadrupole transition) is marked by the abrupt cessation of scattered 194-nm fluorescence photons. Absorption spectra of the $^2S_{1/2}(F = 0) \rightarrow {}^2D_{5/2}(F = 2)$, $\Delta m_F = 0$ clock transition are shown in the middle and bottom panels. Δf_{282} is the frequency of the 282 nm probe laser detuning and P_g is the probability of finding the atom in the ground state subsequent to the application of the clock radiation. In the middle panel, the signal is averaged over 292 sweeps; in the bottom, 46 sweeps are made. The observed linewidths are consistent with the Fourier-transform limit of the interrogation times. The laser oscillator is then steered to coincide with the center of the resonance curve. (Adapted from ref. 16.)

a comb of phase-locked frequency components whose spacing is precisely given by the pulse repetition rate f_r. Frequency fluctuations of the pulsed laser can be suppressed, for example, by locking one tooth of the comb to the frequency f_0 of a stable laser and locking another tooth to the harmonic $2f_0$ of the stable laser.[12] In this case, the frequency position of each tooth in the comb and the spacing between teeth is fixed with a stability and accuracy given by the stabilized laser. If a microwave or radio frequency oscillator is then locked to the pulse repetition rate, its frequency will exhibit the same stability and accuracy as the stabilized reference laser. Moreover, when f_r is compared to a cesium standard, the absolute frequency $f_0 = nf_r$ of the optical standard can be determined (n is an integer that can be determined from a relatively crude measurement of $\lambda = c/f_0$).

A powerful technique for approximating a nearly ideal optical atomic reference system has been the coupling of ion-storage devices with laser cooling.[8,10,13] For example, it is now possible to suspend a single ion in an ultrahigh vacuum, reduce its kinetic energy to the zero-point state, and localize its position to submicrometer dimensions. Such conditions provide a significant decoupling of the internal states of the ion from perturbations caused by collisions and second-order Doppler shifts.

Although a single trapped ion possesses the intrinsic advantages of a nearly isolated quantum system, detecting the absorption of single photons at the clock transition remains a challenge. The quantum projection noise limit can be obtained only if each clock transition is observed.[3,8,13] These transitions are observed by a double-resonance technique, which is very similar to the detection scheme used in the atomic fountains. There, the absorption of a single clock photon is indicated by the presence or absence of scattered light on a strongly allowed transition (usually the laser-cooling transition) that shares a common level with the clock transition, as shown in figure 3. Extremely weak, dipole-forbidden transitions, as well as weakly allowed dipole transitions, have been detected with efficiencies approaching unity. Many of the single-ion systems presently under investigation promise instabilities and inaccuracies approaching 10^{-18} (refs. 8, 13).

A final ingredient needed for the optimal realization of an optical frequency and time standard is a laser whose linewidth is narrower than that of the atomic resonance. This is a stringent requirement. If the width of the atomic resonance is 1 Hz, then the laser linewidth must be less than 1 Hz for the interrogation time. Typically, the frequency of the laser is prestabilized to the resonance of a single longitudinal mode of a high-finesse, stable reference cavity that is well isolated from external perturbances.[14] Many groups have demonstrated subhertz relative stabilization of their laser source to such a reference cavity, but the absolute frequency stability of the stabilized laser can be only as good as the absolute frequency (mechanical) stability of the reference cavity. To ensure that the frequency of a visible laser does not change by more than 1 Hz, the length of a meter-long cavity must not change by more than 1 femtometer, the size of an atomic nucleus!

A number of evacuated, temperature-stabilized and vibrationally isolated reference cavity laser systems have been built over the years specifically to probe narrow

atomic resonances. Laser linewidths of a few hundred hertz have been observed by several groups. Although extremely narrow by most standards, these line widths would limit the performance of a clock based on a 1-Hz-wide atomic resonance. At NIST in Boulder, we were recently able to achieve subhertz linewidths, principally by better isolating our cavities. Measurements of the beat frequency between two independent, cavity-stabilized laser systems revealed their linewidths to be below 0.2 Hz at an oscillation frequency of 530 THz ($\lambda = 563$ nm) for averaging times up to 20 s.[15]

As an example of an optical clock, the harmonic radiation at 282 nm generated by one of these lasers was applied to the electric-quadrupole allowed, S–D clock-transition in $^{199}Hg^+$. In work completed last year, we obtained a linewidth of approximately 6.7 Hz, which was the transform limit of the interrogation time.[16] At 120 ms, the interrogation period was 33% longer than the natural lifetime. We used a stabilized, self-referenced, pulsed laser to measure the frequency of the S–D clock transition in $^{199}Hg^+$ with an uncertainty $\Delta f_m/f_0 < 10^{-14}$ (ref. 17). A single tooth of the pulsed laser ($f_r \sim 1$ GHz) was locked to the Hg^+-stabilized laser to produce an all-optical time and frequency standard based on a single stored $^{199}Hg^+$ ion. We expect $\Delta f_m/f_0$ and $\Delta f_a/f_0$ to reach at least 10^{-17} for $\tau \geq 10^4$ s. Similar strategies based on narrow optical transitions in other atomic and ionic systems are being pursued at many laboratories worldwide. The clock generation of the future may have arrived with the millennium.

The NIST ion-clock work is supported by the Office of Naval Research.

References

1. D. Howse, *Greenwich Time*, Oxford U. Press, Oxford, England (1980). J. Jespersen, J. Fitz-Randolph, *From Sundials to Atomic Clocks*, US Government Printing Office, Washington, DC (1999).
2. T. Damour, A. M. Polyakov, *Nucl. Phys. B* **423**, 532 (1994). S. Karshenboim, *Can. J. Phys.* **78**, 639 (2000).
3. W. M. Itano et al., *Phys. Rev. A* **47**, 3554 (1993). G. Santarelli et al., *Phys Rev. Lett.* **82**, 4619 (1999).
4. W. M. Itano, N. Ramsey, *Scientific American* **269** (1), 56 (1993).
5. M. A. Kasevich et al., *Phys. Rev. Lett.* **63**, 612 (1989).
6. A. Clairon et al., *Europhys. Lett.* **16**, 165 (1991).
7. S. R. Jefferts et al., *Metrologia* (in press).
8. H. G. Dehmelt, *IEEE Trans. Instrum. Meas.* **IM-31**, 83 (1982). D. J. Wineland, *Science* **226**, 395 (1985).
9. P. T. H. Fisk, *Rep. Prog. Phys.* **60**, 761 (1997). J. D. Prestage et al. in *Frequency Measurement and Control*, A. N. Luiten, ed., Springer-Verlag, New York (2000). D. J. Berkeland et al., *Phys. Rev. Lett.* **80**, 2089 (1998).
10. See, for example, Proceedings of the 3rd Symposium on Frequency Standards and Metrology, *J. Phys. Colloq.* **42** (1981). Proceedings of the 5th Symposium on Frequency Standards and Metrology, J. C. Bergquist, ed., World Scientific, Singapore (1996).
11. J. Reichert et al., *Phys. Rev. Lett.* **84**, 3232 (2000). D. J. Jones et al., *Science* **288**, 635 (2000). S. A. Diddams et al., *Phys. Rev. Lett.* **84**, 5102 (2000).
12. J. Ye et al. *Opt. Lett.* **25**, 1675 (2000).
13. A. A. Madej, J. E. Bernard, in *Frequency Measurement and Control*, A. N. Luiten, ed., Springer-Verlag, New York (2000).
14. J. L. Hall, M. S. Taubman, Jun Ye, in *Handbook of Optics*, 2nd edition, vol. 4, Chap. 27, McGraw-Hill, New York (2000), and references therein.
15. B. C. Young et al., *Phys. Rev. Lett.* **82**, 3799 (1999). B. C. Young et al., in *Laser Spectroscopy*, XIV International Conf., Innsbruck, June 1999, R. Blatt, J. Eschner, D. Leibfried, F. Schmidt-Kaler, eds., World Scientific, Singapore (1999), p. 61.
16. R. J. Rafac et al., *Phys. Rev. Lett.* **85**, 2462 (2000).
17. Th. Udem et al., preprint at http://xxx.lanl.gov/physics/0101029 ■

Sub-dekahertz spectroscopy of $^{199}Hg^{+}$[†]

J.C. Bergquist*[a], R.J. Rafac[a], B.C. Young[b], J.A. Beall[a], W.M. Itano[a], and D.J. Wineland[a]
[a]National Institute of Standards and Technology, MS 847, 325 Broadway, Boulder, CO 80305
[b]Jet Propulsion Laboratory, MS 298-100, 4800 Oak Grove Drive, Pasadena, CA 91109

ABSTRACT

Using a laser that is frequency-locked to a Fabry-Pérot etalon of high finesse and stability, we probed the $5d^{10}6s\ ^2S_{1/2}$ ($F = 0$, $m_F = 0$) $\leftrightarrow$ $5d^9 6s^2\ ^2D_{5/2}$ ($F = 2$, $m_F = 0$) electric-quadrupole transition of a single laser-cooled $^{199}Hg^+$ ion stored in a cryogenic radio-frequency ion trap. We observed Fourier-transform limited linewidths as narrow as 6.7 Hz at 282 nm (1.06×10^{15} Hz). The functional form and estimated values of some of the frequency shifts of the $^2S_{1/2} \leftrightarrow {}^2D_{5/2}$ "clock" transition (including the quadrupole shift), which have been calculated using a combination of measured atomic parameters and *ab initio* calculations, are given.

Keywords: Lasers, atomic spectroscopy, cooling and trapping, atomic frequency standards, optical clocks.

1. Introduction

For spectroscopy and clocks, fluctuations in frequency measurement are expressed fractionally as $\sigma_y(\tau) = \Delta\nu_{meas}(\tau)/\nu_0$, where τ is the total measurement time. When the measured stability is limited by quantum fluctuations in state detection, $\sigma_y(\tau) = C(2\pi\nu_0)^{-1}(N\,\tau_{probe}\,\tau)^{-1/2}$, where C is a constant of order unity, N is the number of atoms, and τ_{probe} is the interrogation time. For atomic clocks, the highest accuracies and the greatest stabilities have been achieved by locking a microwave oscillator to a hyperfine transition in the electronic ground state (see, for example, the contribution by A. Clairon in these Proceedings). Since the fractional frequency instability $\sigma_y(\tau)$ of a frequency and time standard is inversely proportional to its frequency, a promising route to realizing clocks with stability significantly higher than present-day standards is to use optical frequencies. However, there are significant obstacles that so far have thwarted the development of an optical clock. Principal among these are the requirements of a spectrally pure and stable laser, a narrow reference transition that can be probed with a high signal-to-noise (S/N) ratio, and a device fast enough to count optical frequencies. If high accuracy is also desired, then either perturbations to the reference transition must be small or the uncertainty in measuring the frequency shifts of the reference transition in the perturbed system must be small.

Recently, the major technical barriers to the development of an optical clock were eliminated. Two years ago, lasers suitable for probing sub-hertz atomic linewidths were demonstrated,[1,2] and in the past year, precision, optical-frequency measuring devices based on mode-locked femtosecond lasers have emerged.[3,4,5] It has long been recognized that a frequency and time standard based on an optical transition in a single ion that is tightly confined in a benign environment and virtually at rest could be made both highly stable *and accurate*.[6] In this paper, we summarize the measurement of the $5d^{10}6s\ ^2S_{1/2}$ ($F = 0$, $m_F = 0$) $\leftrightarrow$ $5d^9 6s^2\ ^2D_{5/2}$ ($F = 2$, $m_F = 0$) electric-quadrupole-allowed transition ($\lambda \approx 282$ nm) in a single, laser-cooled $^{199}Hg^+$ ion for which a linewidth $\Delta\nu \approx 6.7$ Hz is observed.[7] The frequency of a laser can be locked to this transition to provide an extremely stable and reproducible frequency reference. Elsewhere[8] (and in these Proceedings: see S.A. Diddams *et al.*, "A compact femtosecond-laser-based optical clockwork") we report an absolute measurement of the frequency ν_0 of this $^2S_{1/2} \leftrightarrow {}^2D_{5/2}$ "clock" transition, $\nu_0 = 1\ 064\ 721\ 609\ 899\ 143(10)$ Hz, which represents the most precise measurement of an optical frequency ever made. We also report recent calculations[9] of perturbations to the ($F = 0$, $m_F = 0$) to ($F = 2$, $m_F = 0$) hyperfine component of the $^2S_{1/2} \leftrightarrow {}^2D_{5/2}$ transition that include the quadratic Zeeman shift, the scalar and tensor quadratic Stark shifts, and the interaction between an external static electric field gradient and the atomic quadrupole moment. The quadrupole shift is likely to be the most difficult to evaluate in such a frequency standard and may have a magnitude as large as 1 Hz for a single ion in a spherical rf quadrupole trap.

*email: berky@boulder.nist.gov

2. Spectroscopy of $^{199}Hg^{+}$

2.1 The atomic system, probe laser, and trap

A partial energy-level diagram of $^{199}Hg^{+}$ is shown in Fig. 1. The 282 nm radiation used to drive the S-D clock transition is produced in a nonlinear crystal as the second harmonic of a dye laser oscillating at 563 nm. The frequency of the dye-laser's radiation is made to match the resonance of a single longitudinal mode of a high-finesse Fabry-Pérot cavity that is temperature-controlled and supported on an isolation platform.[1,2] The frequency-stabilized laser light is sent through a single-mode optical fiber to the table holding the ion trap. Mechanical and acoustical vibrations of the fiber broaden the laser spectrum by about 1 kHz. The phase and frequency noise caused by the journey through the fiber is sensed and removed using a method[2] that is similar to that described in references 10 and 11. Finally, the frequency of the 563 nm light is shifted away from the cavity resonance and on to the ion resonance by passing the 563 nm radiation through an acousto-optic crystal and then doubling the frequency of the shifted light by harmonic generation in a deuterated ammonium-dihydrogen-phosphate crystal.

Two types of cryogenic ion traps have been used in our most recent measurements; a linear quadrupole trap[7] and a spherical Paul trap.[8] For both systems, a single mercury ion is loaded into the trap by ionizing a mercury atom from a thermal source with a pulsed electron beam. Under typical operating conditions, the radial secular frequency of the trapped ion varies between 1.2 and 1.5 MHz. Biasing electrodes are mounted outside the trap electrodes to cancel any stray static electric fields that may be present. Since the electrodes in both traps are gold coated and can be heated, oxidation is precluded and any charging of the electrodes is minimized.

The ion is laser-cooled to near the 1.7 mK Doppler limit by driving the $5d^{10}6s\ ^2S_{1/2}\ (F = 1) \leftrightarrow 5d^{10}6p\ ^2P_{1/2}\ (F = 0)$ cycling transition at 194 nm (Fig. 1). Because of weak off-resonant pumping into the $^2S_{1/2}\ (F = 0)$ state, we employ a second 194 nm source, phase-locked to the first with a 47 GHz offset, that returns the ion to the ground state $F = 1$ hyperfine level. We tolerate the complication of a re-pumper, since only isotopes with nonzero nuclear spin can have transitions that are first-order insensitive to magnetic field fluctuations. This provides immunity from fluctuations of the ambient field and significantly relaxes the requirements for control and shielding of the magnetic environment. Previous experiments using mercury were performed at room temperature and at a pressure of approximately 10^{-7} Pa.[10] Under those conditions, the background gas pressure was large enough that when the ion was irradiated with the 194 nm light, it would be lost due to chemical reaction after a few minutes. Partly as a means to help reduce this loss, the ion trap is now housed in a vacuum system held at liquid-helium temperature. Single ion hold times have now exceeded 100 days, and any loss of an ion has been caused either by a deliberate or accidental action of the operator. Vibrations of the supported trap structure relative to the optical table are sensed and removed with an additional stage of Doppler cancellation, where the correction signal is derived from optical heterodyne detection of a motion-sensing beam reflected from a mirror that is rigidly fixed to the trap support structure.[7,10] The cancellation is not ideal, because the sensing beam is steered by additional optical elements and its path deviates slightly from overlap with the probe beam near the trap. Measurements indicate that this optical path difference can contribute as much as 2 Hz to the spectral width of the 282 nm probe laser in the reference frame of the ion.

We monitor the ion and deduce its electronic state using light scattered from the cooling transition. Fluorescence at 194 nm is collected by a five-element *f*/1 objective located inside the cryostat. The scattered light is imaged outside the dewar, spatially filtered, and then relayed with a second lens to either an imaging tube or to a side-on photomultiplier tube. Transitions to the D state are detected using the technique of "electron shelving," which infers the presence of the atom in the metastable level through the absence of scattering from the strong laser-cooling transition.[6,12,13] Radiation from the 194 and 282 nm sources is admitted to the trap sequentially to prevent broadening of the quadrupole transition by the cooling radiation. Typical count rates using the more efficient photomultiplier tube are 12 000 Hz for a single ion when the frequency of the 194 nm source is detuned below resonance with the cooling transition by about ½ the natural linewidth. The background rate is only about 25 Hz when the ion is shelved in the metastable level. Hence, each clock transition to the D level can be detected in only a few milliseconds with near unit efficiency.

Spectra of the recoilless component of the $^2S_{1/2}\ (F = 0, m_F = 0) \leftrightarrow {}^2D_{5/2}\ (F = 2, m_F = 0)$ clock transition were obtained for a range of probe times and laser intensities by laser cooling for a short period, preparing the ion in the $F = 0$ ground state by blocking the repumping laser, and then interrogating the quadrupole transition. The spectra are built up from multiple bi-directional scans of the 282 nm probe-laser frequency. Since the frequency of the probe laser can drift, we incorporate a locking step in between pairs of positive- and negative-going frequency sweeps through the quadrupole resonance. During the locking sequence, we step the frequency of the probe laser alternately to the maximum slope on either side of the S-D

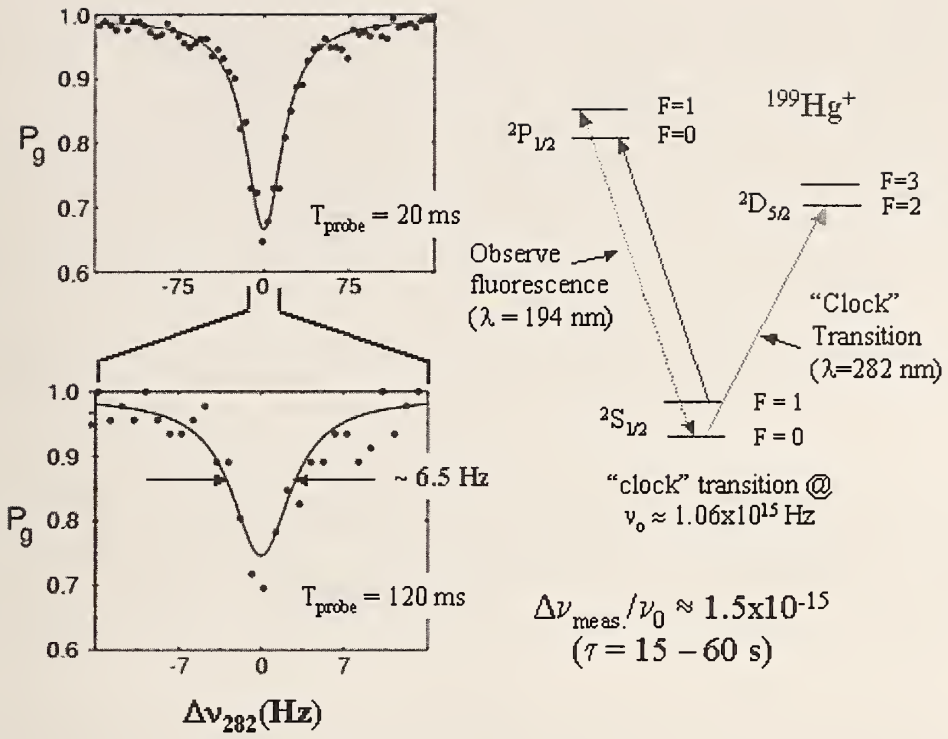

Figure 1: The simplified optical level diagram of $^{199}Hg^+$is depicted on the right. Quantum-jump absorption spectra of the $^2S_{1/2}$ ($F = 0$, $m_F = 0$) ↔ $^2D_{5/2}$ ($F = 2$, $m_F = 0$) clock transition for two different probe times are shown on the left. $\Delta\nu_{282}$ is the frequency detuning of the 282 nm probe laser, and P_g is the probability of finding the atom in the ground state after the probe radiation is applied. In the top spectrum (averaged over 292 sweeps), the probe-pulse period was 20 ms; in the bottom spectrum (averaged over 46 sweeps), the probe period was 120 ms. The observed linewidths are consistent with the Fourier-transform limit of the probe period at 40(2) Hz and 6(1) Hz respectively.

quadrupole resonance, probe for a fixed time τ_{servo}, and then look for transitions to the D level. Typically, we make 48 measurements on each side of the resonance during each lock cycle before steering the mean frequency of the 282 nm radiation to line center. Our servo is a simple integrator that works to minimize the asymmetry between the number of detected transitions on the high- and low-frequency sides of the resonance. In this fashion, variations in the frequency of the 282 nm laser for times exceeding several seconds are reduced.

Two examples of the spectra are plotted in Fig. 1. The probe time for the lower resolution spectrum is 20 ms and the probe time for the higher resolution signal is 120 ms. In both cases, the linewidths are transform limited by the finite probe time at 40(2) Hz and 6(1) Hz, respectively. The carrier transition amplitude is a function of the vibrational quantum number n.[14] For the spectra shown in Fig. 1, the trapping parameters gave $\langle n \rangle \approx 35$ at the Doppler cooling limit ($\langle n \rangle \approx 20$ for the spherical trap at the Doppler cooling limit). Hence, it is not possible to transfer the electron to the D level with unit probability. The observed signals are in good agreement with the theoretical expectation, and the signal loss for τ_{probe} = 120 ms is consistent with applying the probe time for a period that exceeds the natural lifetime of the $^2D_{5/2}$ state by 33 %. In future experiments, we plan to reduce $\langle n \rangle$ to less than 1 toward improving the signal amplitude and S/N ratio.

3. External field shifts to the quadrupole transition

While the $^2S_{1/2}$ ($F = 0$, $m_F = 0$) ↔ $^2D_{5/2}$ ($F = 2$, $m_F = 0$) hyperfine component has no linear Zeeman shift, it does have a quadratic Zeeman shift. In addition, there is a second-order Stark shift and a shift due to the interaction between a static electric-field gradient and the D-state atomic electric-quadrupole moment. None of these shifts has yet been measured accurately but their values have recently been calculated by one of us.[9] While these values may be imprecise, it is useful to know the functional form of the perturbation. For example, the quadrupole shift can be eliminated by averaging the S-D

transition frequency over three mutually orthogonal magnetic-field orientations, independent of the orientation of the electric-field gradient, and is zero in lowest order for the $^2S_{1/2}$ ($F = 2$, $m_F = 0$) $\leftrightarrow$ $^2D_{3/2}$ ($F = 0$, $m_F = 0$) hyperfine component in $^{201}Hg^+$.

The quadratic Zeeman shift can be calculated if the hyperfine constants and electronic and nuclear g-factors are known. Similarly, the quadratic Stark shift can be calculated from a knowledge of the electric-dipole oscillator strengths. The quadrupole shift depends on the atomic wavefunctions. Some of these parameters have been measured, such as the hyperfine constants and some of the oscillator strengths. In Ref. 9, values for parameters for which there are neither measured values nor published calculations are estimated using the Cowan atomic-structure codes.[15] The Cowan codes are based on the Hartree-Fock approximation with some relativistic corrections. The odd-parity configurations used in these calculations were $5d^{10}np$ (n = 6,7,8,9), $5d^{10}5f$, $5d^96s6p$, $5d^96s7p$, $5d^96s5f$, and $5d^86s^26p$. The even-parity configurations were $5d^{10}ns$ (n = 6,7,8,9,10), $5d^{10}nd$ (n = 6,7,8,9), $5d^96s^2$, $5d^96s7s$, $5d^96s6d$, and $5d^96p^2$. Recently, Sansonnetti and Reader have made new measurements of the spectrum of Hg^+ and classified many new lines.[16] They also carried out a least-squares adjustment of the energy parameters in order to match the observed energy levels. Those adjusted parameters were used for the calculations in Ref. 9.

3.1 Quadratic Zeeman shift

In order to calculate the energy shifts due to the hyperfine interaction and to an external magnetic field $\boldsymbol{B} \equiv B\hat{\mathbf{z}}$, we define effective Hamiltonian operators H_S and H_D that operate within the subspaces of hyperfine levels associated with the electronic levels $5d^{10}6s\ ^2S_{1/2}$ and $5d^96s^2\ ^2D_{5/2}$ respectively:

$$H_S = hA_S\boldsymbol{I}\cdot\boldsymbol{J} + g_J(S)\mu_B\boldsymbol{J}\cdot\boldsymbol{B} + g'_I\mu_B\boldsymbol{I}\cdot\boldsymbol{B}$$

$$H_D = hA_D\boldsymbol{I}\cdot\boldsymbol{J} + g_J(D)\mu_B\boldsymbol{J}\cdot\boldsymbol{B} + g'_I\mu_B\boldsymbol{I}\cdot\boldsymbol{B},$$

where A_S and A_D are the dipole hyperfine constants, $g_J(S)$ and $g_J(D)$ are the electronic g-factors, g'_I is the nuclear g-factor, h is the Planck constant, and μ_B is the Bohr magneton. All of the parameters entering H_S and H_D are known from experiments, although a more accurate measurement of the excited-state electronic g-factor would improve our estimate of the quadratic Zeeman shift of the $^2D_{5/2}$ level. So far, the best determination of $g_J(D)$ (= 1.1980(7)) is derived from a conventional grating spectroscopic measurement of the $5d^96p\ ^2P_{3/2}$ to $5d^96s^2\ ^2D_{5/2}$ at 398 nm in $^{198}Hg^+$.[17] The difference in $g_J(S)$ or $g_J(D)$ between $^{198}Hg^+$ and $^{199}Hg^+$ is estimated to be much less than the experimental uncertainties. The determination of $g_J(D)$ could be improved by measuring the optical frequency difference between two components of the 282 nm line and the frequency of a ground-state hyperfine transition at the same magnetic field. Since the uncertainty in the quadratic Zeeman shift is due mainly to the uncertainty in $g_J(D)$, it is useful to improve the experimental value and/or make an accurate theoretical estimate. The Cowan-code calculation gives a theoretical value of $g_J(D)$ of 1.19985,[9] which disagrees with the present experimental value by about 2.6 times the stated measurement uncertainty. From a similar comparison of the calculated value of $g_J(D)$ for neutral gold (which is isoelectronic to Hg^+) to its accurately measured experimental value, we might expect that the error in the calculated value of $g_J(D)$ of $^{199}Hg^+$ to be less than 1×10^{-4}. However, uncalculated terms may decrease the theoretical precision.

For low magnetic fields (< 1 mT), it is sufficient to calculate the energies of the Zeeman sub-levels of the $^2S_{1/2}$ ground electronic level and those of the $^2D_{5/2}$ electronic level to second order in B. For a magnetic field value of 0.1 mT, the quadratic shift of the $^2S_{1/2}$ ($F = 0$, $m_F = 0$) $\leftrightarrow$ $^2D_{5/2}$ ($F = 2$, $m_F = 0$) clock transition is −189.25(28) Hz, where the uncertainty is dominated by the uncertainty in the experimental value of $g_J(D)$. If instead we use the calculated value of $g_J(D)$, the quadratic shift for B = 0.1 mT is −189.98 Hz, where the uncertainty may be less than 0.02 Hz but is difficult to estimate.[9]

3.2 Quadratic Stark shift

The theory of the quadratic Stark shift in free atoms has been described thoroughly by Angel and Sandars.[18] The Stark Hamiltonian is

$$H_E = -\boldsymbol{\mu}\cdot\boldsymbol{E},$$

where $\boldsymbol{\mu}$ is the electric-dipole moment operator,

$$\boldsymbol{\mu} = -e\sum\boldsymbol{r}_i,$$

and E is the applied external electric field. In the latter expression, r_i is the position operator of the ith electron, measured relative to the nucleus, and the summation is over all electrons. For an atom with zero nuclear spin, and to second order in the electric field, the Stark shift of the set of sublevels $|\gamma JM_J\rangle$ depend on two parameters, $\alpha_{scalar}(\gamma, J)$ and $\alpha_{tensor}(\gamma, J)$, called the scalar and tensor polarizabilities. Here, γ designates the electronic level, J the electronic angular momentum, and M_J is the eigenvalue of J_z. In principle, when both magnetic and electric fields are present but not parallel, the energy shifts of the levels are obtained by simultaneously diagonalizing the hyperfine, Zeeman, and Stark Hamiltonians. In practice, the Zeeman shifts normally dominate the Stark shifts, so H_E does not affect the diagonalization. We also note that the tensor polarizability is zero for levels with $J < 1$, such as the ground electronic level in Hg^+. For an atom with nonzero nuclear spin I, we make the approximation that the hyperfine interaction does not modify the electronic part of the atomic wavefunctions . This approximation is adequate for the evaluation of the Stark shift of the S-D optical clock transition in $^{199}Hg^+$.

In Ref. 9, the polarizabilities for the Hg^+ $5d^{10}6s\ ^2S_{1/2}$ and $5d^96s^2\ ^2D_{5/2}$ levels were evaluated. The tensor polarizability is much smaller than the scalar polarizabilities and, in any case, contributes nothing if the external field, such as the blackbody radiation field, is isotropic. The net shift of the optical clock transition due to the scalar polarizabilities is $\frac{1}{2}[\alpha_{scalar}(S,1/2) - \alpha_{tensor}(D,5/2)]E^2$. In frequency units, the shift is $-1.14 \times 10^{-3}\ E^2$ Hz, where E is expressed in V/cm. The error in the coefficient is difficult to estimate, particularly since it is a difference of two quantities of nearly equal magnitude. However, the total shift of either state is small for typical experimental conditions. If the electric field is time dependent, as for the blackbody field, the mean square value of the field is taken. At a temperature of 300 K, the shift of the S-D clock transition due to the blackbody field is –0.079 Hz. Since the blackbody electric field is proportional to the fourth power of the temperature, in our cryogenic environment the Stark shift due to blackbody radiation is negligible. Finally, for a single, laser-cooled ion in a Paul trap, the mean square trapping fields at the site of the ion can be made small enough that the Stark shifts are not likely to be observable.[19]

3.3 Electric quadrupole shift

The atomic quadrupole moment arises from the departure of the electronic charge distribution of an atom from spherical symmetry. The interaction of the atomic quadrupole moment with external field gradients, such as those that might be generated by the electrodes of an ion trap, is analogous to the interaction of a nuclear quadrupole moment with the electric field gradients due to the atomic electrons. The Hamiltonian describing the interaction of external electric-field gradients with the atomic quadrupole moment is

$$H_Q = \nabla E^{(2)} \cdot \Theta^{(2)},$$

where $\nabla E^{(2)}$ is a tensor describing the gradients of the external electric field at the position of the ion, and $\Theta^{(2)}$ is the electric-quadrupole operator for the atom. As long as the energy shifts due to H_Q are small relative to the Zeeman shifts, which is usually the case in practice, H_Q can be treated as a perturbation. In that case, it is necessary only to evaluate the matrix elements of H_Q that are diagonal in the basis states $|\gamma JFM_F\rangle$, where F is the total atomic angular momentum, including the nuclear spin I, and M_F is the eigenvalue of F_z with respect to the laboratory frame, where the magnetic field is oriented along the z axis. The diagonal matrix elements of H_Q in the laboratory frame are[9]

$$\langle \gamma JFM_F | H_Q | \gamma JFM_F \rangle =$$

$$\frac{-2[3M_F^2 - F(F+1)]A(\gamma JF\|\Theta^{(2)}\|\gamma JF)}{[(2F+3)(2F+2)(2F+1)2F(2F-1)]^{1/2}}[(3\cos^2\beta - 1) - \varepsilon \sin^2\beta(\cos^2\alpha - \sin^2\alpha)]. \qquad (1)$$

It is relatively straightforward to show, by directly integrating the angular factor in square brackets in the above equation, that the average value of the diagonal matrix elements of H_Q, taken over all possible orientations of the laboratory frame with respect to the principal-axis frame,[20] is zero. It is less obvious, but nevertheless true, that the average taken over *any* three mutually perpendicular orientations of the laboratory z quantization axis is also zero.[9] This provides a method for eliminating the quadrupole shift from the observed transition frequency. The magnetic field, with constant magnitude, must be oriented in three mutually orthogonal directions; the average of the clock transition frequencies taken under these three conditions does not contain the quadrupole shift.

The reduced matrix element in Eq.(1) is, in the IJ-coupling approximation,

$$(\gamma(IJ)F\|\Theta^{(2)}\|\gamma(IJ)F) = (-1)^{I+J+F}(2F+1)\begin{Bmatrix} J & 2 & J \\ F & I & F \end{Bmatrix}\begin{pmatrix} J & 2 & J \\ -J & 0 & J \end{pmatrix}^{-1}\Theta(\gamma,J),$$

where I is included in the state notation in order to specify the order of coupling of I and J. For the particular case of the $^{199}Hg^+$ $5d^9 6s^2\,{}^2D_{5/2}$ level, the reduced matrix elements are

$$(D\,5/2\,2\|\Theta^{(2)}\|D\,5/2\,2) = 2\sqrt{\frac{14}{5}}\Theta(D,5/2),$$

$$(D\,5/2\,3\|\Theta^{(2)}\|D\,5/2\,3) = 2\sqrt{\frac{21}{5}}\Theta(D,5/2).$$

Since the Cowan-code calculation shows that there is very little mixing in the $^{199}Hg^+$ $5d^9 6s^2\,{}^2D_{5/2}$ level, Θ(D,5/2) can be reduced to a matrix element involving only the $5d$ orbital:[9]

$$\Theta(D,5/2) = \frac{e}{2} < 5d^2 d_{5/2}, m_j = 5/2\left|3z^2 - r^2\right|5d^2 d_{5/2}, m_j = 5/2 >,$$

$$= -\frac{2e}{7} < 5d\left|r^2\right|5d >.$$

In this case, the matrix element is negative because the quadrupole moment is due to a single *hole* in the otherwise filled $5d$ shell rather than to a single electron. Again, according to the Cowan-code calculation,

$$< 5d\left|r^2\right|5d >= 2.324\, a_0^2 = 6.509\times10^{-17}\ \mathrm{cm}^2,$$

where a_0 is the Bohr radius. Since the quadrupole shifts are zero in the $5d^{10}6s\,{}^2S_{5/2}$ level, the quadrupole shift of the $^{199}Hg^+$ optical clock transition is due entirely to the shift of the |D 5/2 2 0> state, and is given by

$$\begin{aligned} < \mathrm{D}\,5/2\,2\,0\left|H_Q\right|\mathrm{D}\,5/2\,2\,0 >&= \frac{4}{5}A\Theta(\mathrm{D},5/2)[(3\cos^2\beta - 1) - \varepsilon\sin^2\beta(\cos^2\alpha - \sin^2\alpha)], \\ &= -\frac{8}{35}Ae < 5d\left|r^2\right|5d >[(3\cos^2\beta - 1) - \varepsilon\sin^2\beta(\cos^2\alpha - \sin^2\alpha)], \\ &\approx -3.6\times10^{-3}\,hA[(3\cos^2\beta - 1) - \varepsilon\sin^2\beta(\cos^2\alpha - \sin^2\alpha)]\ \mathrm{Hz}, \end{aligned}$$

where A is expressed in units of V/cm^2. Thus, for typical values $A \approx 10^3$ V/cm^2 and $|\varepsilon| \le 1$, the quadrupole shift is on the order of 1 Hz.[9] We also note that states with zero total angular momentum have no quadrupole shift. Thus, the $^2S_{1/2}$ ($F = 2$, $m_F = 0$) $\leftrightarrow$ $^2D_{3/2}$ ($F = 0$, $m_F = 0$) hyperfine component in $^{201}Hg^+$, for which the nuclear spin I is 3/2, has no quadrupole shift. Similar strategies to eliminate the quadrupole shift could be used on other potential optical-clock ions such as Ca^+, Sr^+, Ba^+, and Yb^+.

ACKNOWLEDGMENTS

We acknowledge the support of the Office of Naval Research. This work was also supported through a Cooperative Research and Development Agreement with Timing Solutions, Corp., Boulder, Colorado. We thank Dr. C.J. Sansonetti for making available his results (Ref. 16) prior to their publication. We would also like to thank R. Drullinger, M. Lombardi, and D. Smith for their careful reading of this manuscript.

REFERENCES

[†] Work of U.S. government. Not subject to U.S. copyright.

1. B.C. Young, F.C. Cruz, W.M. Itano, and J.C. Bergquist, "Visible lasers with subhertz linewidths," *Phys. Rev. Lett.* **82**, pp. 3799-3802, 1999.

2. B.C. Young, R.J. Rafac, J.A. Beall, F.C. Cruz, W.M. Itano, D.J. Wineland, and J.C. Bergquist, "Hg^+ optical frequency standard: recent progress," in *Laser Spectroscopy XIV International Conference*, ed. by R. Blatt, J. Eschner, D. Leibfried, and F. Schmidt-Kaler (World Scientific, Singapore, 1999) pp. 61-70.

3. Th. Udem, J. Reichert, R. Holzwarth, and T.W. Hänsch, "Absolute optical frequency measurement of the cesium D_1 line with a mode-locked laser," *Phys. Rev. Lett.***82**, pp. 3568-3571, 1999.

4. D.J. Jones, S.A. Diddams, J.K. Ranka, A. Stentz, R.S. Windeler, J.L. Hall, and S.T. Cundiff, "Carrier-envelope phase control of femtosecond mode-locked lasers and direct optical frequency synthesis, " *Science* **288**, pp. 635-639, 2000.

5. S.A. Diddams, D.J. Jones, J. Ye, S.T. Cundiff, J.L. Hall, J.K. Ranka, R.S. Windeler, R. Holzwarth, Th. Udem, and T. W. Hänsch, "Direct link between microwave and optical frequencies with a 300 THz femtosecond laser comb," *Phys. Rev. Lett.* **84**, pp. 5102-5105, 2000.

6. H.G. Dehmelt, "Coherent spectroscopy on single atomic system at rest in free space II," *J. Phys. (Paris) Colloq.* **42**, pp. C8-299 to C8-305, 1981.

7. R.J. Rafac, B.C. Young, J.A. Beall, W.M. Itano, D.J. Wineland, and J.C. Bergquist, "Sub-dekahertz ultraviolet spectroscopy of $^{199}Hg^+$," *Phys. Rev. Lett.* **85**, pp. 2462-2465, 2000.

8. Th. Udem, S.A. Diddams, K.R. Vogel, C.W. Oates, E.A. Curtis, W.D. Lee, W.M. Itano, R.E. Drullinger, J.C. Bergquist, and L. Hollberg, "Absolute Frequency Measurements of the Hg^+ and Ca optical clock transitions with a femtosecond laser," submitted to *Phys. Rev. Lett.*

9. W.M. Itano, "External-field shifts of the $^{199}Hg^+$ optical frequency standard," *J. Res. NIST*, in press, 2001.

10. J.C. Bergquist, W.M. Itano, and D.J. Wineland, "Laser stabilization to a single ion," in *Frontiers in laser spectroscopy, proceedings of the international school of physics "Enrico Fermi": course 120*, ed. by T.W. Hänsch, and M. Inguscio (North-Holland, Amsterdam, 1994), pp. 359-376.

11. L.S. Ma, P. Jungner, J. Ye, and J.L. Hall, "Delivering the same optical frequency at two places: accurate cancellation of phase noise introduced by an optical fiber or other time-varying path," *Opt. Lett.* **19**, pp. 1777-1779, 1994.

12. H.G. Dehmelt, "Proposed $10^{14}\ \Delta\nu < \nu$ laser fluorescence spectroscopy on Tl^+ mono-ion oscillator," *Bull. Am. Phys. Soc.* **20**, p. 60, 1975.

13. J.C. Bergquist, W.M. Itano, and D.J. Wineland, "Recoilless optical absorption and Doppler sidebands of a single trapped ion," *Phys. Rev. A* **36**, pp. 428-430, 1987.

14. D.J. Wineland and W.M. Itano, "Laser cooling of atoms," *Phys. Rev. A* **20**, pp. 1521-1540, 1979.

15. R.D. Cowan, *The theory of atomic structure and spectra,* Univ. California Press, Berkeley, CA, 1981.

16. C.J. Sansonetti and J. Reader, "Spectrum and energy levels of singly-ionized mercury (HgII)," *Phys. Scripta*, (in press).

17. Th. A.M. Van Kleef and M Fred, "Zeeman effect measurements in neutral and singly ionized mercury," *Physica* **29**, pp. 389-404, 1963.

18. J.R.P. Angel and P.G.H. Sandars, "The hyperfine structure Stark effect: I. Theory," *Proc. Roy. Soc. A* **305**, pp. 125-138, 1968.

19. D.J. Berkeland, J.D. Miller, J.C. Bergquist, W.M. Itano, and D.J. Wineland, "Minimization of ion micromotion in a Paul trap," *J. Appl. Phys.* **83**, pp. 5025-5033, 1998.

20. L.S. Brown and G. Gabrielse, "Precision spectroscopy of a charged particle in an imperfect Penning trap," *Phys. Rev. A* **25,** 2423-2425, 1982.

Absolute Frequency Measurements of the Hg^+ and Ca Optical Clock Transitions with a Femtosecond Laser

Th. Udem,* S. A. Diddams, K. R. Vogel, C. W. Oates, E. A. Curtis, W. D. Lee, W. M. Itano, R. E. Drullinger, J. C. Bergquist, and L. Hollberg

Time and Frequency Division, National Institute of Standards and Technology, 325 Broadway, Boulder, Colorado 80305

(Received 4 January 2001)

The frequency comb created by a femtosecond mode-locked laser and a microstructured fiber is used to phase coherently measure the frequencies of both the Hg^+ and Ca optical standards with respect to the SI second. We find the transition frequencies to be $f_{Hg} = 1\,064\,721\,609\,899\,143(10)$ Hz and $f_{Ca} = 455\,986\,240\,494\,158(26)$ Hz, respectively. In addition to the unprecedented precision demonstrated here, this work is the precursor to all-optical atomic clocks based on the Hg^+ and Ca standards. Furthermore, when combined with previous measurements, we find no time variations of these atomic frequencies within the uncertainties of $|(\partial f_{Ca}/\partial t)/f_{Ca}| \leq 8 \times 10^{-14}$ yr^{-1} and $|(\partial f_{Hg}/\partial t)/f_{Hg}| \leq 30 \times 10^{-14}$ yr^{-1}.

DOI: 10.1103/PhysRevLett.86.4996 PACS numbers: 06.30.Ft, 32.30.Jc, 32.80.Pj

Optical standards based on a single ion or a collection of laser-cooled atoms are emerging as the most stable and accurate frequency sources of any sort [1–5]. However, because of their high frequencies (~500 THz), it has proven difficult to count cycles as required for building an optical clock and comparing to the cesium microwave standard. Only recently, a reliable and convenient optical clockwork fast enough to count optical oscillations has been realized [6–8]. Here, we report an optical clockwork based on a single femtosecond laser that phase coherently divides down the visible radiation of the Hg^+ and Ca optical frequency standards to a countable radio frequency. By this means we determine the absolute frequencies of these optical transitions with unparalleled precision in terms of the SI second as realized at National Institute of Standards and Technology (NIST) [9]. Indeed, for the Hg^+ standard, the statistical uncertainty in the measurement is essentially limited by our knowledge of the SI second at $\sim 2 \times 10^{-15}$. The high precision and high demonstrated stability of the standards [1,4] combined with the straightforward femtosecond-laser-based clockwork suggest Hg^+ and Ca as excellent references for future all-optical clocks. Additionally, the comparison of atomic frequencies over time provides constraints on the possible time variation of fundamental constants. When combined with previous measurements, the current level of precision allows us to place the tightest constraint yet on the possible variation of optical frequencies with respect to the cesium standard.

The Hg^+ and Ca systems have recently been described elsewhere [1,4,10,11], so we summarize only the basic features. The heart of the mercury optical frequency standard is a single, laser-cooled $^{199}Hg^+$ ion that is stored in a cryogenic, radio frequency spherical Paul trap. The $^2S_{1/2}(F = 0, M_F = 0) \leftrightarrow {}^2D_{5/2}(F = 2, M_F = 0)$ electric-quadrupole transition at 282 nm [Fig. 1(a)] provides the reference for the optical standard [1]. We lock the frequency-doubled output of a well-stabilized 563 nm dye laser to the center of the quadrupole resonance by irradiating the Hg^+ ion alternately at two frequencies near the maximum slope of the resonance signal and on opposite sides of its center. Transitions to the metastable $^2D_{5/2}$ state are detected with near unit efficiency since the absorption of a single 282 nm photon suppresses the scattering of many 194 nm photons on the strongly allowed $^2S_{1/2} - {}^2P_{1/2}$ transition [12,13]. Because the fractional frequency instability of the probe laser is $\leq 10^{-15}$ for measurement times $0.1\ \text{s} < t < 10\ \text{s}$ [11], usually 48 measurements are made on each side of the resonance prior to correcting the average frequency of the 282 nm source. The resonance probe period was either 10 or 20 ms, but each measurement cycle was longer by the time used (for example) for state preparation (15 ms) and detection (10 ms), as well as the decay time ($\tau_D \approx 90$ ms) of the metastable state if an excitation was made. A new interrogation cycle is begun when the 194 nm fluorescence intensity rises above a preset threshold level. This reduces dead time, since it would otherwise be necessary to wait more than the lifetime of

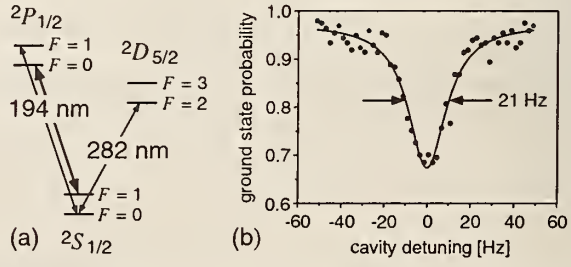

FIG. 1. (a) Partial level scheme for $^{199}Hg^+$. The 194 nm radiation is used for Doppler cooling, state preparation, and detection. The 282 nm transition from the ground state $^2S_{1/2}(F = 0, M_F = 0)$ to the metastable $^2D_{5/2}(F = 2, M_F = 0)$ state provides the reference for the optical clock frequency. (b) A typical spectrum of the 282 nm clock transition obtained under lock conditions is shown. Here, the excitation pulse length was 20 ms, and the measured linewidth is Fourier transform limited to about 20 Hz at 563 nm (40 Hz at 282 nm).

the metastable state to ensure that the ion has returned to the ground state. If an asymmetry between the number of excitations detected on the high- and low-frequency sides is found, then the frequency of the probe radiation is adjusted to minimize the asymmetry. In this way, we steer the frequency of the 282 nm source to the center of the $S - D$ quadrupole resonance with an uncertainty that is less than 2×10^{-15} for averaging times $\tau \leq 30$ s and that decreases as $\tau^{-1/2}$ for $\tau > 30$ s [14]. In Fig. 1(b) we show an example of a normalized spectrum that was obtained from multiple bidirectional scans through the resonance during the lockup, where the probe time was 20 ms.

The calcium standard is based on a collection of $\sim 10^7$ laser-cooled ^{40}Ca atoms held in a magneto-optic trap. The 423 nm $^1S_0 \leftrightarrow {}^1P_1$ transition is used for Doppler cooling and trapping the atoms to a residual temperature of ~ 2 mK, while the 657 nm $^1S_0(M_J = 0) \leftrightarrow {}^3P_1(M_J = 0)$ clock transition (400 Hz natural linewidth) is used for the frequency standard [Fig. 2(a)]. We excite the clock transition with a four-pulse Bordé-Ramsey sequence (pulse duration = 1.5 μs) with light from a continuous wave (cw) frequency-stabilized diode laser. Using a shelving detection technique similar to that employed in the Hg^+ system, near-resonant 423 nm pulses (5 μs duration) are used before and after the 657 nm excitation to determine the fraction of atoms transferred from the ground state. Figure 2(b) shows Bordé-Ramsey fringes taken at a resolution of 960 Hz. This system has demonstrated a fractional frequency instability of $4 \times 10^{-15}\tau^{-1/2}$, when probing subkilohertz linewidths [4]. For the measurements presented here the Ca spectrometer was operated with linewidths ranging from 0.96 to 11.55 kHz which are integer subharmonics of the recoil splitting.

The recent introduction of mode-locked lasers to optical frequency metrology greatly simplifies the task of optical frequency measurements [6–8,15–17]. The spectrum emitted by a mode-locked laser consists of a comb of regular spaced continuous waves that are separated by the pulse repetition rate f_r. The frequency of the nth mode of the comb is given by $f_n = nf_r + f_o$ [18,19], where f_o is the frequency offset common to all modes that is caused by the difference between the group and the phase velocity inside the laser cavity. Whereas f_r can be measured by direct detection of the laser output with a photodiode, f_o is measured by heterodyning the harmonic of a mode $f_n = nf_r + f_o$ from the infrared wing of the comb with a mode $f_{2n} = 2nf_r + f_o$ from the blue side of the comb [7,8]. While an octave spanning comb can be produced directly from a mode-locked laser [20], launching the longer pulses from a commercially available femtosecond laser into an air-silica microstructure fiber [21,22] also produces a frequency comb that spans an octave. Via nonlinear processes in the fiber, additional equally spaced and phase-coherent modes are added to the comb. It has been demonstrated that this process of spectral broadening preserves the uniformity of spacing and spectral fidelity of the comb to at least a few parts in 10^{16} [8].

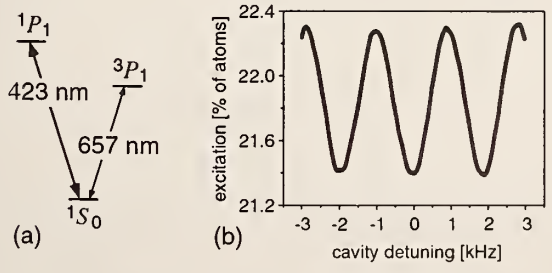

FIG. 2. (a) Simplified diagram of the relevant energy levels in the Ca standard. (b) Optical Bordé-Ramsey fringes with a 960 Hz (FWHM) resolution. The total averaging time to generate this figure was 20 s.

We couple approximately 200 mW average power from a femtosecond Ti:sapphire ring laser ($f_r \approx 1$ GHz) [23] into a 15 cm piece of a microstructure fiber that has a 1.7 μm core and a group velocity dispersion that vanishes near 770 nm [21]. This power is sufficient to increase the spectral width of the laser from 13 THz to more than 300 THz, spanning from ~ 520 to ~ 1170 nm. The infrared part of the comb from the fiber ($\lambda \approx 1060$ nm) is split off by a dichroic mirror and frequency doubled into the green portion of the visible spectrum with a 2 mm long $KNbO_3$ crystal. Following an adjustable delay line that matches the optical path lengths, the frequency-doubled light is spatially combined with the green part of the original comb using a polarizing beam splitter. A second rotatable polarizer projects the polarization of the combined beams onto a common axis so that they can interfere on a photodiode. This polarizer is also used to adjust the relative power of the two beams for optimum signal-to-noise ratio in the heterodyne signal. A small grating prior to the photodiode helps to select only that part of the frequency comb that matches the frequency-doubled light, thereby reducing noise from unwanted comb lines [19]. We phase lock both f_o and f_r to synthesized frequencies derived from a cavity-tuned hydrogen maser. Control of f_r is achieved with a cavity folding mirror that is mounted on a piezotransducer, while f_o is controlled by adjusting the 532 nm pump beam intensity with an electro-optic modulator [8]. When f_o and f_r are both phase locked, the frequency of every mode in the comb is known with the same precision as the reference maser.

The cw light from the Hg^+ (563 nm) and Ca (657 nm) spectrometers is transferred to the mode-locked laser system via two single mode optical fibers that are 180 m and 10 m long, respectively. Approximately 2 mW of cw light from each fiber is mode matched with the appropriate spectral region of the frequency comb to generate a beat signal f_b with a nearby mode. This beat note is amplified and measured with a radio frequency counter. The optical frequency is then expressed as $f_{\text{opt}} = f_o + mf_r + f_b$, where m is a large integer uniquely determined for each system from previous coarse measurements of f_{opt}.

We detect cycle slips in both of the phase locks by monitoring f_r and f_o with additional counters [24]. We selectively discard any measurement of f_{opt} for which the measured f_o or f_r deviate from the expected value by more than $1/\tau_{\text{gate}}$, where τ_{gate} is the counter gate time in seconds. We avoid miscounts of f_b by using an auxiliary counter to record the ratio r between f_b and $f_b/4$, where the division by 4 is implemented digitally. Any measurements of f_b where the auxiliary counter gives a result that does not satisfy $(r - 4)f_b < 10/\tau_{\text{gate}}$ are discarded. We rely on the assumption that the two counters recording f_b and r, if in agreement, do not make the *same* mistake. For each data point the three additional counters (f_r, f_o, and r) are started before the counting of f_b and operated with 50 ms longer gate times to ensure temporal overlap.

Figure 3 summarizes the frequency measurements of Hg^+ made between 16 August and 31 August 2000, and Fig. 4 summarizes the Ca measurements made from 26 October to 17 November 2000. All measurements are corrected for the second-order Zeeman shift and for the offset of the reference maser frequency. The uncertainty for the Zeeman correction is $<1 \times 10^{-15}$ for the Hg^+ system and $<2.5 \times 10^{-15}$ in the Ca system. The frequency of the maser is calibrated by comparing to the local NIST time scale (5 hydrogen masers and 3 commercial cesium clocks), which in turn is calibrated by the local cesium fountain standard (NIST-F1 [9]), as well as international cesium standards. This resulted in a fractional uncertainty in the frequency of the reference maser of about 1.8×10^{-15} for the measurements.

The weighted mean of our measurements of the Hg^+ clock transition is $f_{\text{Hg}} = 1\,064\,721\,609\,899\,143$ Hz, where the statistical uncertainty of 2.4 Hz is near the fractional frequency instability of the reference maser ($\sim 2 \times 10^{-13}$ at 1 s, decreasing to $\sim 4 \times 10^{-16}$ at a few days). We have not yet made a full evaluation of the systematic uncertainties of the Hg^+ standard; however, we believe that 10 Hz is a conservative upper bound for the total systematic uncertainty. The largest systematic uncertainty is due to the interaction between the atomic quadrupole moment of the $^2D_{5/2}$ state and a static electric field gradient. In the currently used spherical Paul trap, no static field gradient is deliberately applied. A potential difference between the ring and the end cap electrodes of as large as 0.5 V due to contact potentials or stray charges, for example, would result in a quadrupole shift of only 1 Hz [25]. The magnetic field is evaluated before and after each run by measuring the frequency of one or more of the magnetic field dependent electric-quadrupole transitions. This results in an uncertainty of the second-order Zeeman shift of the clock transition of less than 0.5 Hz. The accuracy of this calibration has been verified by varying the magnitude of the magnetic field for successive runs. The blackbody radiation shift of the clock transition would be -0.08 Hz at 300 K and is considerably lower in the cryogenic trap environment of approximately 4 K. At the Doppler cooling limit, the second-order Doppler shift due to thermal motion is -0.003 Hz. Finally, the second-order Doppler shift due to residual micromotion caused by the trapping field is estimated to have a magnitude no greater than 0.1 Hz. We anticipate that the uncertainties of all systematic shifts in the Hg^+ system can be reduced to values approaching 1×10^{-18} [1,25].

For the Ca data shown (Fig. 4), an additional correction is applied each day to account for a frequency shift caused by residual phase chirping on the optical Ramsey pulses produced by amplitude modulating an acousto-optic modulator (AOM). The phase chirping produced a resolution dependent frequency shift on the order of 100 Hz for 11.5 kHz wide fringes but only 10 Hz for 0.96 kHz

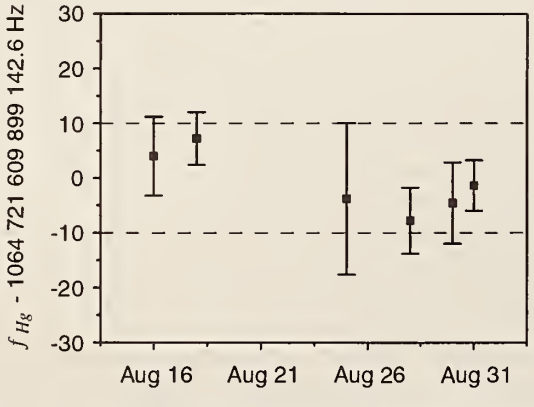

FIG. 3. A chronological record of the average daily frequency of the $^{199}Hg^+$ clock transition measured on six days over a 15 day period representing 21 651 s of total measurement time. The error bars represent statistical fluctuations. The dashed lines represent an estimated systematic uncertainty of ± 10 Hz in the Hg^+ system in the absence of a full evaluation.

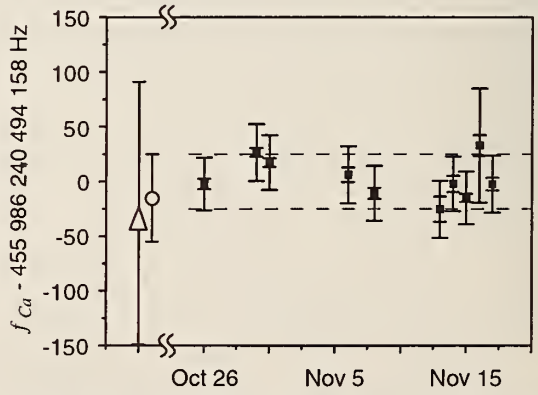

FIG. 4. The filled squares are the measured Ca frequencies on ten days over a 23 day period representing 38 787 s of total measurement time. The inner and outer error bars for each day represent the statistical and total uncertainties, respectively. The dashed lines show the 26 Hz systematic uncertainty assigned to the mean. The open triangle is the Physikalisch-Technische Bundesananstalt (PTB) measurement reported in Ref. [26], and the open circle is the Ca frequency calculated from the present Hg^+ result and our previous measurement of the 76 THz gap between Ca and Hg^+ [27].

wide fringes. On each day, the Ca frequency was measured for ~30 min at each of several fringe resolutions, and the zero intercept of a linear fit to the data was used as the corrected frequency. On the last three days of measurements, we were able to reduce this shift by a factor of ~3 with improvements to the rf pulses that drive the AOM's. With horizontal beams we can achieve <20 Hz gravity-induced frequency shift, which can be readily quantified and eliminated simply by reversing the pulse sequence. The statistical uncertainty for each day's measurement (typically 8 Hz) is smaller than the uncontrolled systematic uncertainties in the Ca frequency. The largest systematic uncertainty stems from incomplete knowledge of the angular overlap of the counterpropagating beams in the Ca spectrometer, combined with a transverse drift velocity of the cold Ca ensemble. This leads to a residual first-order Doppler shift with a magnitude <15 Hz (except on 16 November 2000, where a large drift velocity led to a ~52 Hz uncertainty). Other significant uncertainties include our lack of knowledge or control of electronic offsets and baseline asymmetries (<12 Hz), wave front curvature (<10 Hz), and cold-atom collisional shifts (<10 Hz). Taking all known systematic uncertainties in quadrature gives a confidence level of ~26 Hz for the measured mean value as indicated by the dashed lines in Fig. 4. Again, for the Ca measurement we find that the stability is limited by the maser.

Figure 4 also shows the good agreement between our measurement and the most recent value measured with a harmonic frequency chain [26], which provides a degree of confidence in the reproducibility of the Ca standards. An additional measure of the Ca frequency can be made by using the present absolute measurement of Hg^+ and our earlier measurement of the 76 374 564 455 429(40) Hz gap between $f_{Hg}/2$ and the Ca standard [27]. This yields a value $f_{Ca} = 455\,986\,240\,494\,143(40)$ Hz in good agreement with the present absolute measurement of f_{Ca}.

Finally, these results also provide data on the relative time variability of atomic frequencies. Karshenboim has recently reviewed the implications of such comparisons and their contribution toward constraining the possible time variation of fundamental constants [28]. In this regard Hg^+ and Ca are two of the most interesting cases to study. Comparing our present measurement of f_{Ca} to measurements made by PTB in 1997 [26] gives $(\partial f_{Ca}/\partial t)/f_{Ca} = (+2 \pm 8) \times 10^{-14}\ \mathrm{yr}^{-1}$. Similarly, combining this result with our May 2000 measurement of f_{Hg} with respect to f_{Ca} [27] provides an initial baseline constraint on the time variation of f_{Hg} of $(\partial f_{Hg}/\partial t)/f_{Hg} = (-7 \pm 30) \times 10^{-14}\ \mathrm{yr}^{-1}$. Here we use the defined unit of time based on the frequency of the Cs hyperfine interval and assume that any time dependence is slow and dominantly linear over the relevant time scale. At our present level of precision we find no evidence of any relative time variation between these three frequency standards, two optical and one microwave.

The authors are most grateful to T. Parker for providing the crucial maser calibration and to A. Bartels of Giga-Optics GmbH for his valuable assistance with the femtosecond laser. We are also indebted to R. Windeler of Lucent Technologies for providing the microstructure optical fiber. We further acknowledge many illuminating discussions with D. Wineland, J. Hall, S. Karshenboim, and F. Walls. This work was partially supported by the Office of Naval Research and through a cooperative research and development agreement with Timing Solutions, Inc., Boulder, CO.

Note added.—Since the submission of this work a new measurement of the Ca clock transition was conducted at PTB with a femtosecond system similar to the one described here [29]. Although less precise, this most recent PTB measurement is in agreement with the value we report.

*Present address: Max-Planck-Institut für Quantenoptik, Hans-Kopfermann-Strasse 1, 85748 Garching, Germany.

[1] R. Rafac *et al.*, Phys. Rev. Lett. **85**, 2462 (2000).
[2] J. E. Bernard *et al.*, Phys. Rev. Lett. **82**, 3228 (1999).
[3] H. Schnatz *et al.*, Phys. Rev. Lett. **76**, 18 (1996).
[4] C. W. Oates *et al.*, Opt. Lett. **25**, 1603 (2000).
[5] J. von Zanthier *et al.*, Opt. Lett. **25**, 1729 (2000).
[6] S. A. Diddams *et al.*, Phys. Rev. Lett. **84**, 5102 (2000).
[7] D. J. Jones *et al.*, Science **228**, 635 (2000).
[8] R. Holzwarth *et al.*, Phys. Rev. Lett. **85**, 2264 (2000).
[9] S. R. Jefferts *et al.* (to be published); S. R. Jefferts *et al.*, in *Proceedings of the IEEE International Frequency Control Symposium* (IEEE, Piscataway, NJ, 2000), pp. 714–717.
[10] C. W. Oates *et al.*, J. Phys. D **7**, 449 (1999).
[11] B. Young *et al.*, Phys. Rev. Lett. **82**, 3799 (1999).
[12] H. Dehmelt, Bull. Am. Phys. Soc. **20**, 60 (1975).
[13] J. C. Bergquist *et al.*, Phys. Rev. A **36**, 428 (1987).
[14] D. J. Wineland *et al.*, *The Hydrogen Atom*, edited by T. W. Hänsch (Springer, Berlin, Heidelberg, 1989), pp. 123–133.
[15] Th. Udem *et al.*, Phys. Rev. Lett. **82**, 3568 (1999).
[16] J. Reichert *et al.*, Phys. Rev. Lett. **84**, 3232 (2000).
[17] M. Niering *et al.*, Phys. Rev. Lett. **84**, 5496 (2000).
[18] A. I. Ferguson, J. N. Eckstein, and T. W. Hänsch, Appl. Phys. **18**, 257 (1979).
[19] J. Reichert *et al.*, Opt. Commun. **172**, 59 (1999).
[20] R. Ell *et al.*, Opt. Lett. **26**, 373 (2001).
[21] J. K. Ranka *et al.*, Opt. Lett. **25**, 25 (2000).
[22] W. J. Wadsworth *et al.*, Electron. Lett. **36**, 53 (2000).
[23] A. Bartels, T. Dekorsy, and H. Kurz, Opt. Lett. **24**, 996 (1999).
[24] Th. Udem *et al.*, Opt. Lett. **23**, 1387 (1998).
[25] W. M. Itano, J. Res. Natl. Inst. Stand. Technol. **105**, 829 (2000).
[26] F. Riehle *et al.*, in *Proceedings of the Joint European Frequency and Time Forum and the IEEE International Frequency Control Symposium* (IEEE, Piscataway, NJ, 1999), pp. 700–705.
[27] K. R. Vogel *et al.*, Opt. Lett. **26**, 102 (2001).
[28] S. Karshenboim, Can. J. Phys. **78**, 639 (2000).
[29] J. Stenger *et al.*, Phys. Rev. A **63**, 021802 (2001).

An Optical Clock Based on a Single Trapped $^{199}Hg^{+}$ Ion

S. A. Diddams,[1]* Th. Udem,[1]† J. C. Bergquist,[1] E. A. Curtis,[1,2] R. E. Drullinger,[1] L. Hollberg,[1] W. M. Itano,[1] W. D. Lee,[1] C. W. Oates,[1] K. R. Vogel,[1] D. J. Wineland[1]

Microwave atomic clocks have been the de facto standards for precision time and frequency metrology over the past 50 years, finding widespread use in basic scientific studies, communications, and navigation. However, with its higher operating frequency, an atomic clock based on an optical transition can be much more stable. We demonstrate an all-optical atomic clock referenced to the 1.064-petahertz transition of a single trapped $^{199}Hg^{+}$ ion. A clockwork based on a mode-locked femtosecond laser provides output pulses at a 1-gigahertz rate that are phase-coherently locked to the optical frequency. By comparison to a laser-cooled calcium optical standard, an upper limit for the fractional frequency instability of 7×10^{-15} is measured in 1 second of averaging—a value substantially better than that of the world's best microwave atomic clocks.

Since the development of the first atomic clocks around 1950, it was recognized that the stability and accuracy of standards based on atomic transitions would benefit from choosing transition frequencies as high as possible. However, because it was not possible to count cycles of an oscillator at an arbitrarily high frequency in order to generate time, most time standards have been based on hyperfine transitions in atoms that occur at microwave frequencies where the period of one oscillation corresponds to roughly 0.1 to 1 ns. In fact, since 1967 the internationally accepted definition of the second has been based on the 9,192,631,770-Hz ground-state hyperfine transition in Cs, and Cs-based clocks are currently the world's most accurate time standards with a fractional frequency uncertainty of about 1×10^{-15} (*1–4*). Although the stability and accuracy of an optical clock based on a spectrally narrow atomic transition in the visible/ultraviolet (UV) region might be better, the frequency is about 10^{15} Hz, where the period of one oscillation is on the order of 1 fs. Until recently, it was not practical to count such high frequencies without loss of cycles, but the introduction of mode-locked femtosecond lasers has now made it possible to conveniently and accurately divide optical frequencies to countable microwave or radio frequencies (*5–10*). The all-optical atomic clock reported here is based on a single, laser-cooled, trapped $^{199}Hg^{+}$ ion and a femtosecond laser comb that provides the phase-coherent clockwork. Our optical clock demonstrates a fractional frequency instability of $\leq 7 \times 10^{-15}$ with 1 s of averaging—a value substantially better than that of the world's best microwave atomic standards—and promises accuracy that would be difficult to achieve with atomic clocks based on microwave transitions. This optical clock provides two distinct outputs: a comb of stable and accurate optical frequencies throughout the visible and near infrared, and a pulsed electronic signal at 1 GHz that is phase-coherent with the optical frequency comb. The quantum-limited instability of the Hg^{+} ion optical clock is expected to be around $1 \times 10^{-15}\,\tau^{-1/2}$, where τ is the averaging time measured in seconds, with an ultimate fractional frequency uncertainty approaching 10^{-18} (*11*).

Ultrastable and accurate optical metrology tools can be expected to provide an even finer-grained view of the physical world, much as precision spectroscopy in the past 50 years has opened the door to an improved understanding of many fundamental aspects of atoms and molecules (*12*, *13*). Of particular interest will be the continued application of optical frequency standards in spectroscopy and the improved determination of the fine structure constant α and the Rydberg constant R_∞ (*14*). As measurement stability and accuracy improve, metrologists may find themselves in the unique position of being able to observe physical "constants" evolve in time (*15*). Indeed, laboratory tests on the possible divergence of clocks based on different atomic transitions already provide some of the most stringent constraints of the variation of α. Other experiments of fundamental importance for which precision clocks/oscillators are of value include searches for variations in the isotropy of space, a preferred reference frame, and Lorentz and charge-parity-time (CPT) symmetry violation (*16–20*). From a technological standpoint, there is little dispute that stable and accurate microwave atomic clocks have greatly improved navigation and communications. It is likely that optical clocks of the future will have a similarly important impact.

Atomic clock basics. All clocks consist of two major components: some device that produces periodic events or "clock ticks," and some means for counting, accumulating, and displaying each tick. For example, the swing of a pendulum provides the periodic events that are counted, accumulated, and displayed by means of a set of gears driving a pair of clock hands. Similarly, in a quartz watch, the mechanical vibrations of a small quartz crystal are electronically detected, accumulated, and displayed to generate time. Atomic clocks add a third component: the resonance of a well-isolated atomic transition, which is used to control the oscillator frequency. If the frequency of the oscillator is made to match the transition frequency (i.e., the oscillator is locked to the atomic transition frequency) between two nondegenerate and unperturbed atomic states, then the time generated can have improved long-term stability and accuracy. For an atomic clock based on a microwave transition, high-speed electronics count and accumulate a defined number of cycles of the reference oscillator to mark a second of time. The basic concepts are the same for an atomic clock based on an optical transition at a much higher frequency. In this case the oscillator is a laser locked to an optical transition, but no electronic device exists that can count the very fast optical oscillations. For this purpose, a specialized frequency divider (commonly called a frequency chain) is required. Until very recently, optical-to-microwave frequency chains have been complicated, large-scale devices, requiring significant resources for operation (*21*). However, as described below, a femtosecond laser–based clockwork greatly simplifies this problem of directly counting the optical frequency.

All other factors being equal, a higher transition frequency can produce a more stable frequency standard. This is the principal advantage of an optical atomic clock over a microwave clock because the operating frequency is ~100,000 times higher, providing a finer division of time and thus potentially higher precision. This is seen in the Allan deviation $\sigma_y(\tau)$ which provides a convenient measure of the fractional frequency instability of a clock as a function of the averaging time τ (*22*). For an oscillator locked to an atomic transition of frequency ν_0 and linewidth $\Delta\nu$,

$$\sigma_y(\tau) \approx \left\langle \frac{\Delta\nu_{rms}}{\nu_0} \right\rangle_\tau \approx \frac{\Delta\nu}{\pi\nu_0}\sqrt{\frac{T}{\tau N}} \qquad (1)$$

where $\Delta\nu_{rms}$ is the measured frequency fluctuation, N is the number of atoms, and T is the cycle time (i.e., the time required to make a determination of the line center) with $\tau > T$.

[1]Time and Frequency Division, National Institute of Standards and Technology, 325 Broadway, Boulder, CO 80305, USA. [2]Department of Physics, University of Colorado, Boulder, CO 80309, USA.

*To whom correspondence should be addressed. E-mail: sdiddams@boulder.nist.gov

†Present address: Max-Planck-Institut für Quantenoptik, Hans-Kopfermann Strasse 1, 85748, Garching, Germany.

This expression assumes that technical noise is reduced to a sufficiently small level such that the quantum-mechanical atomic projection noise is the dominant stability limit (*23*, *24*). In this limit $\sigma_y(\tau)$ decreases as the square root of the averaging time for all clocks, so a 10-fold decrease in the short-term instability leads to a 100-fold reduction in averaging time τ to reach a given stability and uncertainty. This point is particularly important if one ultimately hopes to reach a fractional frequency uncertainty of 10^{-18}, which is the anticipated level for optical clocks. In this case, $\sigma_y(\tau) \leq 1 \times 10^{-15}\ \tau^{-1/2}$ is clearly desirable to avoid inordinately long averaging times.

Principles of the optical clock. Fundamental ideas and technical developments principally in three areas have brought us to the point where we are now able to demonstrate an optical frequency standard representative of clocks of the future: (i) the idea (*25*, *26*) and demonstration of laser cooling of atoms (*27*, *28*), (ii) the frequency stabilization of lasers (*29*–*32*), and (iii) the concept (*33*) and demonstration (*5*–*10*) that femtosecond mode-locked lasers combined with nonlinear fibers can provide a simple, direct, and phase-coherent connection between radio frequencies and optical frequencies. Although most of these concepts have existed for some time, and preliminary demonstrations of optical clocks have even been made (*34*–*36*), only now have the techniques and tools advanced to the levels required for optical frequency standards to move beyond the benchmark results of the microwave standards. Trapped ions have been laser-cooled into the Lamb-Dicke regime to the zero-point energy limit of a trap potential (*37*), dramatically reducing the Doppler shifts and providing near-stationary, relatively unperturbed atomic references for extended observation times (*11*). Similarly, large numbers of neutral atoms that are suitable references for optical clocks are routinely laser-cooled and then trapped in magneto-optic traps (*38*–*43*). Stabilized lasers have now been demonstrated with linewidths less than 0.2 Hz (*32*, *44*) and with the center frequency reproducibly controlled for extended times at the levels of $|\Delta f/f| < 10^{-15}$ (*45*). And finally, a practical method for measuring optical frequencies based on femtosecond laser technology has been developed (*5*–*8*) and its measurement uncertainty tested to a few parts in 10^{16} (*9*).

These advances are exploited in our optical clock, which consists of a stable continuous wave (CW) laser oscillator that is frequency doubled and locked to a narrow UV transition of a single trapped and laser-cooled $^{199}Hg^+$ ion. Thus stabilized, the frequency of the laser light is coherently divided down to lower frequencies by means of a femtosecond mode-locked laser that ultimately produces an electronic output at a frequency of 1 GHz. A simplified representation of the coherent relation between the optical frequency standard and the microwave pulses is shown in Fig. 1. The envelope of the pulse train is made synchronous with the optical phase of the CW laser with, in our case, ~532,361 optical cycles between pulses (*46*). The pulses thus provide "clock ticks" that are coherently connected to the Hg^+ transition.

The Hg^+ standard and optical clockwork. Figure 2 shows the optical clock in more detail, consisting of the optical frequency standard and the femtosecond laser–based optical clockwork. The $^{199}Hg^+$ optical frequency standard has been described in detail elsewhere (*32*, *45*), so we provide only the most relevant details. The $^2S_{1/2}$ ($F = 0, M_F = 0$) $\leftrightarrow$ $^2D_{5/2}$ ($F = 2, M_F = 0$) electric-quadrupole transition at 282 nm provides the reference for the optical frequency standard. The natural linewidth of the S$\leftrightarrow$D resonance is about 2 Hz at 1.064 PHz, and recently a Fourier-transform–limited linewidth of only 6.7 Hz ($Q = 1.5 \times 10^{14}$) has been observed (*45*). The "local oscillator" for the standard is the output of a well-stabilized 532-THz (563 nm) dye laser (*32*, *44*) that is frequency doubled and locked to the center of the 1.064-PHz (282 nm) S $\leftrightarrow$ D resonance. The short-term (1 to 10 s) fractional frequency instability of the probe laser is $\leq 5 \times 10^{-16}$. This short-term laser instability is low enough that information gathered from probing the ion transition can be integrated for about 10 s before it is used to steer the average laser frequency. The net result is a $\sigma_y(\tau) \leq 2 \times 10^{-15}$ for averaging times up to ~30 s, at which point $\sigma_y(\tau)$ begins to average down as $\tau^{-1/2}$.

The Hg^+ standard provides high accuracy and stability, but for distribution purposes and to realize a countable clock output, we must phase-coherently convert the optical signal to a lower frequency. The clockwork that divides the 1.064-PHz optical frequency to a countable microwave frequency f_r is based on a femtosecond laser and a novel microstructure optical fiber. The Ti:sapphire femtosecond ring laser emits a train of pulses (compressible to ~25-fs duration) at the nominal repetition rate of $f_r = 1$ GHz (*47*). The frequency-domain spectrum of the pulse train is a uniform comb of phase-coherent continuous waves separated by f_r. The frequency of the nth mode of this comb is $f_n = nf_r + f_o$ (*48*, *49*), where f_o is the frequency offset common to all modes that results from the difference between the group- and the phase-velocity inside the laser cavity. If the frequency comb of the laser covers an entire octave, then f_o can be measured by frequency doubling an infrared mode (n) and heterodyning it with an existing mode ($2n$) in the visible portion of the comb (*7*, *9*). The heterodyne signal yields the frequency difference $2(nf_r + f_o) - (2nf_r + f_o) = f_o$. Only recently, with the arrival of microstructure silica fibers (also called photonic crystal fibers), has the required octave-spanning spectrum been attained with high repetition rate, low-power femtosecond lasers (*50*, *51*). The unique dispersion properties of the microstructure fiber provide guidance in a single

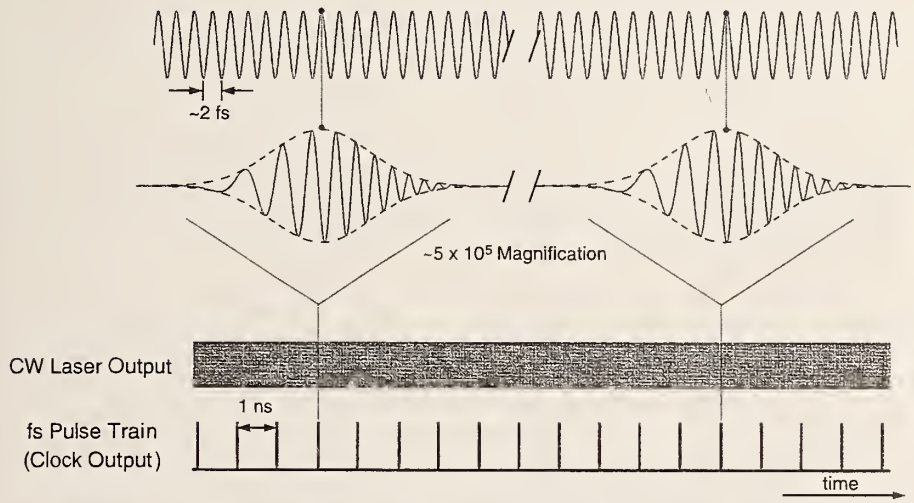

Fig. 1. Illustration of the time-domain relation between the atomically stabilized 532-THz CW laser field and the mode-locked femtosecond laser pulses. The two lines at the bottom show the near delta-function optical pulse train with a f_r = 1-GHz repetition rate and the CW laser output without the optical oscillation resolved. When the system is locked as an optically referenced femtosecond clockwork, the pulse repetition rate is phase-coherently related to the 532-THz CW field. This is indicated schematically in the upper portion of the figure where an expanded view of the lower two traces shows how the phase of the pulse envelope is related to the phase of the CW laser field. The net result is that the frequency of the pulse repetition rate is simply a rational fraction of the Hg^+ transition frequency.

spatial mode (~1.7-μm diameter) with zero group velocity dispersion near 800 nm (*50*). Because temporal spreading of the pulse is minimized, peak intensities in the range of hundreds of GW/cm^2 are maintained over a considerable propagation length, thus providing enhanced spectral broadening due to self-phase modulation. With ~200 mW (average power) coupled into a 15-cm piece of microstructure fiber, the total spectral width is broadened from ~15 to ~300 THz (spanning from ~520 nm to ~1170 nm).

In addition to f_o, a second heterodyne beat f_b is measured between an individual comb element $f_m = mf_r + f_o$ (m is an integer) and the 532-THz local oscillator of the Hg^+ standard. As shown in Fig. 2, two phase-locked loops (PLL) are used to control f_o and f_b, thereby fixing the clock output f_r. PLL-1 forces $f_o = \beta f_r$ by controlling the pump power of the femtosecond laser (*9*). Similarly, PLL-2 changes the cavity length of the femtosecond laser with a piezo-mounted mirror, such that $f_b = \alpha f_r$. The constants α and β are integer ratios implemented with frequency synthesizers that use $f_r/100$ as a reference. In this manner, the frequencies of both PLLs are phase-coherently linked to f_r such that all oscillators used in the clock are referenced to the 532-THz laser oscillator itself. When f_o and f_b are phase-locked, every element of the femtosecond comb, as well as their frequency separation f_r, is phase-coherent with the laser locked to the Hg^+ standard (*52*). With no other frequency reference as an input, we realize all aspects of a high-accuracy, high-stability optical atomic clock: a stable local oscillator (the laser) locked to a narrow atomic reference, and a pulsed microwave output that can be recorded with a counter.

High-stability output. With both PLLs closed, the ~1-GHz microwave output has the value of $f_r = f_{Hg}/(m \pm \alpha \pm \beta)$. If we choose the signs of beats f_o and f_r such that $\alpha = -\beta$, then f_r would be an exact subharmonic of f_{Hg}. The stability of the 532-THz laser (given above) should be transferred to each element of the femtosecond comb, in addition to f_r. We obtain f_r from the bandpass-filtered photocurrent generated with ~5 mW of the broadened comb light incident on a p-i-n photodiode. We have measured the instability of f_r by subtracting it from the output of a synthesizer that is referenced to a hydrogen maser for which $\sigma_y(1\ s) \approx 2.5 \times 10^{-13}$. The stability of this difference frequency is then analyzed with both a high-resolution counter and a dual-mixer time-measurement system (*53*). Both results are consistent with the resolutions of the respective measurements and the maser stability, demonstrating that the 1-s instability of f_r is at least as good as that of the hydrogen maser.

Before we can conclusively state that a microwave signal with stability matching that of the optical standard can be obtained from the optical clock, f_r needs to be compared to an oscillator with stability substantially better than that of the hydrogen maser. This could be either the microwave output of a second optical clock, or the high-stability output of a cryogenic microwave oscillator (*54*). Nonetheless, lacking these we can verify the exceptional stability of the comb in the optical domain and thereby infer the expected stability of f_r. This is done by comparing one element of the optical comb to the Ca optical standard that operates at 456 THz (657 nm). For this measurement the femtosecond comb is phase-locked to the $^{199}Hg^+$ standard as described above. For short averaging times, the femtosecond comb is effectively controlled by the stable Fabry-Perot cavity of the

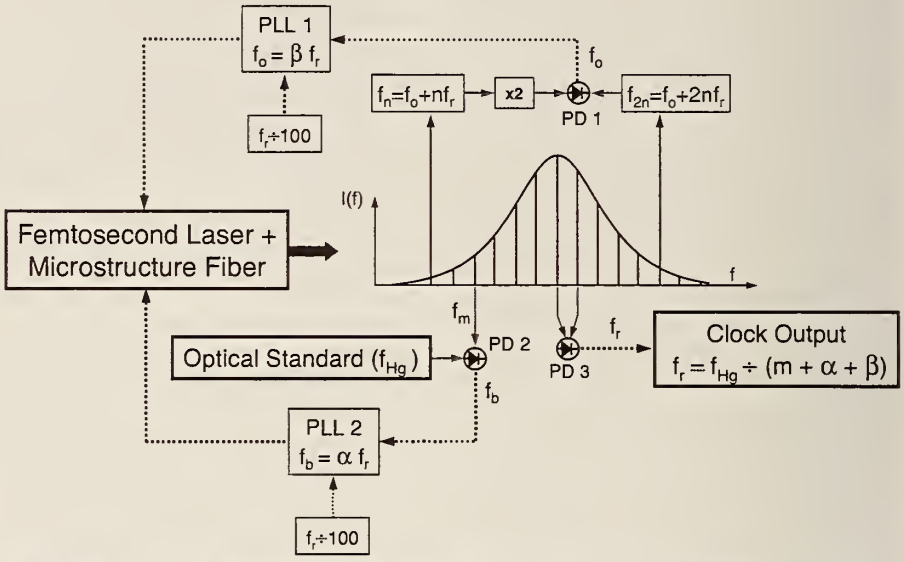

Fig. 2. Schematic of the self-referenced all-optical atomic clock. Solid lines represent optical beams, and dashed lines represent electrical paths. Photodiodes are designated by PD. The femtosecond laser, having repetition rate f_r, combined with the spectral broadening microstructure fiber produces an octave-spanning comb of frequencies in the visible/near infrared, represented by the array of vertical lines in the center of the figure. As shown above this comb, the low-frequency portion of the comb is frequency-doubled and heterodyned against the high-frequency portion in PD 1, yielding the offset frequency f_o that is common to all modes of the comb. Additionally, an individual element of the comb is heterodyned with the optical standard laser oscillator (f_{Hg} = 532 THz) that is locked to the clock transition frequency of a single $^{199}Hg^+$ ion. When detected on PD 2, this yields the beat frequency f_b. Two phase-locked loops (PLL) control f_o and f_b with the result that the spacing (f_r) of the frequency comb is phase-locked to the Hg^+ optical standard. Thus, f_r is the countable microwave output of the clock, which is readily detected by illuminating PD 3 with the broadband spectrum from the frequency comb. See the text for further details.

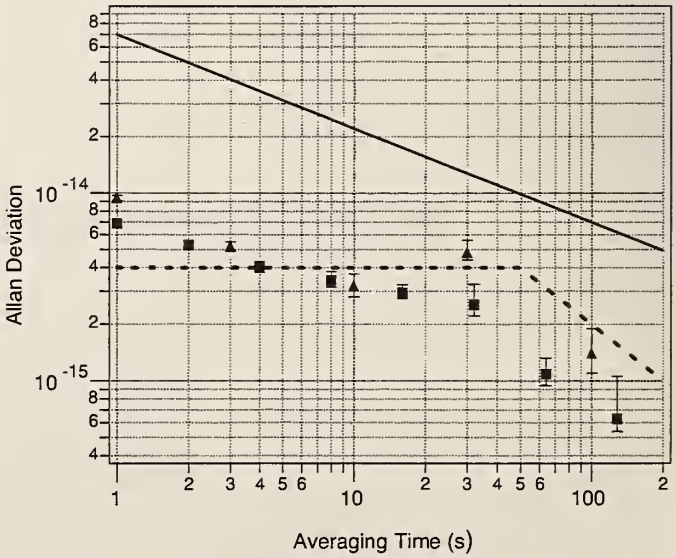

Fig. 3. Measured stability of the heterodyne signal between one element of the femtosecond comb and the Ca optical standard at 456-THz (657 nm). The femtosecond comb is phase-locked to the 532-THz laser oscillator. The black triangles are the stability data without cancellation of the additive fiber noise, which is represented by the dashed line. The red squares are the measured stability with active cancellation of the fiber noise and improved stability in the Ca standard. These results are about an order of magnitude better than the best stability reported with a Cs microwave standard, which is designated by the solid line (*24*).

532-THz laser oscillator, and for $\tau \geq 30$ s the control shifts to the $^{199}Hg^+$ ion. We detect, filter, and count the heterodyne beat signal between a single element of the comb at 456 THz and a frequency-stabilized diode laser locked to the $^1S_0 \leftrightarrow {}^3P_1$ intercombination transition of a laser-cooled ensemble of Ca atoms (*43*, *55*). The Bordé-Ramsey technique (*56*) is used for locking the diode laser to the 456-THz clock transition with resolutions ranging from 0.96 to 11.55 kHz, which are integer subharmonics of the recoil splitting. When the Ca standard is operated with 0.96-kHz resolution, the Allan deviation of the heterodyne signal between the Hg^+-stabilized comb and the Ca standard is shown as the triangles in Fig. 3. For $\tau < 10$ s, the Allan deviation averages down roughly as $9 \times 10^{-15}\ \tau^{-1/2}$, which is consistent with the expected instability of the Ca standard in its present configuration. We also observe a monotonic degradation in the 1-s instability of the heterodyne beat frequency as the stability of the Ca standard is degraded by using lower resolution Ramsey fringes. However, for $\tau > 10$ s, fluctuations introduced by the 180-m-long optical fiber that transmits the 532-THz light to the femtosecond system begin to pose a limitation. We have measured the fiber-induced noise by double-passing the light through the optical fiber, and the average fractional frequency fluctuations are indicated by the dashed line in Fig. 3. Furthermore, for $\tau > 30$ s, the instability of the Hg^+ standard is anticipated to contribute to the measurement at approximately the same level as the Ca standard. Nonetheless, the measured stability improves with averaging to $\sim 1.5 \times 10^{-15}$ at 100 s.

More recently, we have implemented active cancellation (*44*, *57*) of this fiber noise and have further improved the signal-to-noise ratio in the Ca spectroscopy. Data taken under these conditions reveal a fractional frequency instability of 7×10^{-15} at $\tau = 1$ s. These results are plotted as the square data points in Fig. 3. In this case, we cannot place great significance in the stability for $\tau > 1$ s for two reasons. First, the Allan deviation for averaging times $\tau > 1$ s is calculated from the juxtaposition of 1-s averages. Such data analysis is known to result in biases for certain noise processes (*58*). Second, although not generally the case, for this specific data the 532-THz laser oscillator was not locked to the $^{199}Hg^+$ ion, and therefore it was necessary to subtract out the smooth and predictable drift ($\sim$1 Hz/s) of the Fabry-Perot cavity to which this laser is stabilized. However, neither of these affect the measured 1-s Allan deviation, which provides an upper limit for the short-term (1-s) instability of 7×10^{-15} for the optical comb. Again, this 1-s instability is consistent with that of the Ca standard in its present configuration. Similar stability in the $\sim$1-GHz clock output remains to be verified.

Conclusion. We have constructed an optical clock based on the 1.064-PHz (282 nm) electric-quadrupole transition in a laser-cooled, single $^{199}Hg^+$ ion. The optical frequency is phase-coherently divided down to provide a coherent microwave output through the use of a mode-locked femtosecond laser and a microstructured optical fiber. The short-term (1-s) instability of the optical output of the clock is measured against an independent optical standard to be $\leq 7 \times 10^{-15}$. This optically referenced femtosecond comb provides a countable output at 1 GHz, which should ultimately be usable as a higher accuracy reference for time scales, synthesis of frequencies from the radio frequency to the UV, comparison to other atomic standards, and tests of fundamental properties of nature.

References and Notes

1. P. Laurent *et al.*, in *Laser Spectroscopy XIV*, R. Blatt, J. Eschner, D. Leibfried, F. Schmidt-Kaler, Eds. (World Scientific, Singapore, 1999), pp. 41–S0.
2. S. R. Jefferts, D. M. Meekhof, J. H. Shirley, M. Stepanovic, T. E. Parker, in *Proceedings of the 2000 IEEE International Frequency Control Symposium*, Kansas City, 7 to 9 June 2000 (IEEE, Piscataway, NJ, 2000), pp. 714–717.
3. S. Weyers, R. Schröder, A. Bauch, in *Proceedings of the 15th European Frequency and Time Forum*, Neuchâtel, Switzerland, 6 to 8 March 2001 (Fondation Suisse pour la Recherche en Microtechnique, Neuchâtel, Switzerland, in press).
4. S. Weyers, U. Hübner, R. Schröder, Chr. Tamm, A. Bauch, *Metrologia* **38**, 4 (2001).
S. Th. Udem, J. Reichert, R. Holzwarth, T. W. Hänsch, *Phys. Rev. Lett.* **82**, 3S68 (1999).
6. J. Reichert *et al.*, *Phys. Rev. Lett.* **84**, 3232 (2000).
7. D. J. Jones *et al.*, *Science* **288**, 63S (2000).
8. S. A. Diddams *et al.*, *Phys. Rev. Lett.* **84**, 5102 (2000).
9. R. Holzwarth *et al.*, *Phys. Rev. Lett.* **85**, 2264 (2000).
10. J. Stenger *et al.*, *Phys. Rev. A* **63**, 021802R (2001).
11. A. A. Madej, J. E. Bernard, in *Frequency Measurement and Control*, A. N. Luiten, Ed. (Springer-Verlag, Berlin, 2001), pp. 1S3–194.
12. See, for example, J. L. Hall, *Colloques Internationaux du C.N.R.S. No. 217—Méthodes de Spectroscopie Sans Largeur Doppler de Niveaux Excités de Systèmes Moléculaires* (CNRS, Paris, 1974), pp. 105–12S.
13. T. W. Hänsch, A. L. Schawlow, G. W. Series, *Sci. Am.* **240**, 72 (March 1979).
14. See, for example, the contributions of F. Biraben *et al.* (pp. 17–41) and Th. Udem *et al.* (pp. 125–144), in *The Hydrogen Atom: Precision Physics of Simple Atomic Systems*, S. V. Karshenboim, F. S. Pavone, F. Bassani, M. Inguscio, T. W. Hänsch, Eds. (Springer-Verlag, Berlin, 2001).
1S. S. V. Karshenboim, *Can. J. Phys.* **78**, 639 (2000).
16. A. Brillet, J. L. Hall, *Phys. Rev. Lett.* **42**, S49 (1979).
17. M. P. Haugen, C. M. Will, *Phys. Today* **40**, 69 (1987).
18. D. Hils, J. L. Hall, *Phys. Rev. Lett.* **64**, 1697 (1990).
19. V. A. Kostelecky, Ed. *CPT and Lorentz Symmetry* (World Scientific, Singapore, 1999).
20. D. Bear, R. E. Stoner, R. L. Walsworth, V. A. Kostelecky, C. D. Lane, *Phys. Rev. Lett.* **85**, S038 (2000).
21. See, for example, C. O. Weiss, G. Kramer, B. Lipphardt, H. Schnatz, in *Frequency Measurement and Control*, A. N. Luiten, Ed. (Springer-Verlag, Berlin, 2001), pp. 215–247.
22. J. A. Barnes *et al.*, *IEEE Trans. Instrum. Meas.* **20**, 204 (1971).
23. W. M. Itano *et al.*, *Phys. Rev. A* **47**, 3SS4 (1993).
24. G. Santarelli *et al.*, *Phys. Rev. Lett.* **82**, 4619 (1999).
2S. T. W. Hänsch, A. L. Schawlow, *Opt. Commun.* **13**, 68 (197S).
26. D. J. Wineland, H. G. Dehmelt, *Bull. Am. Phys. Soc.* **20**, 637 (197S).
27. D. J. Wineland, W. M. Itano, *Phys. Today* **40**, 34 (1987).
28. C. Cohen-Tannoudji, W. D. Phillips, *Phys. Today* **43**, 33 (1990).
29. J. L. Hall, *Science* **202**, 147 (1978).
30. Ch. Salomon, D. Hils, J. L Hall, *J. Opt. Soc. Am. B*, **8**, 1S76 (1988).
31. S. N. Bagaev, Yu. D. Kolomnikov, V. N. Lisitsyn, V. P. Chebotayev, *IEEE J. Quant. Electr.* **4**, 868 (1968).
32. B. C. Young, F. C. Cruz, W. M. Itano, J. C. Bergquist, *Phys. Rev. Lett.* **82**, 3799 (1999).
33. J. N. Eckstein, A. I. Ferguson, T. W. Hänsch, *Phys. Rev. Lett.* **40**, 847 (1978).
34. V. P. Chebotayev *et al.*, *Appl. Phys. B* **29**, 63 (1982).
3S. C. O. Weiss, G. Kramer, B. Lipphardt, E. Garcia, *IEEE J. Quant. Electr.* **24**, 1970 (1988).
36. J. Ye, J. L Hall, S. A. Diddams, *Opt. Lett.* **25**, 167S (2000).
37. F. Diedrich, J. C. Bergquist, W. M. Itano, D. J. Wineland, *Phys. Rev. Lett.* **62**, 403 (1989).
38. T. Kurosu, F. Shimizu, *Jpn. J. Appl. Phys.* **29**, L2127 (1990).
39. Th. Kisters, K. Zeiske, F. Riehle, J. Helmcke, *Appl. Phys. B* **59**, 89 (1994).
40. F. Ruschewitz *et al.*, *Phys. Rev. Lett.* **80**, 3173 (1998).
41. H. Katori, T. Ido, Y. Isoya, M. Kuwata-Gonokami, *Phys. Rev. Lett.* **82**, 1116 (1999).
42. K. R. Vogel, T. P. Dinneen, A. Gallagher, J. L Hall, in *Proceedings of the Joint Meeting of the European Frequency and Time Forum and the IEEE International Frequency Control Symposium*, Besançon, France, 13 to 16 April 1999 (IEEE, Piscataway, NJ, 1999), pp. 692–69S.
43. C. W. Oates, F. Bondu, R. W. Fox, L. Hollberg, *J. Phys. D* **7**, 449 (1999).
44. B. C. Young *et al.*, in *Laser Spectroscopy XIV*, R. Blatt, J. Eschner, D. Leibfried, F. Schmidt-Kaler, Eds. (World Scientific, Singapore, 1999), pp. 61–70.
4S. R. Rafac, *et al.*, *Phys. Rev. Lett.* **85**, 2462 (2000).
46. The coherent relation between the pulse envelope and the 532-THz CW laser oscillator is established by first phase-locking the rate f_o at which the pulse carrier advances with respect to the envelope from pulse to pulse. For illustrative purposes in Fig. 1, we have chosen this rate to be $f_o = f_r/10$, such that every 10th pulse is identical. The pulse envelope is then made phase coherent with the CW laser oscillator by detecting and controlling the heterodyne beat between the CW laser and the carrier field of the pulsed laser. The frequency domain description is given in the text.
47. A. Bartels, T. Dekorsy, H. Kurz, *Opt. Lett.* **24**, 996 (1999).
48. A. I. Ferguson, J. N. Eckstein, T. W. Hänsch, *Appl. Phys.* **18**, 2S7 (1979).
49. J. Reichert, R. Holzwarth, Th. Udem, T. W. Hänsch, *Opt. Commun.* **172**, S9 (1999).
S0. J. K. Ranka, R. S. Windeler, A. J. Stentz, *Opt. Lett.* **25**, 25 (2000).
S1. W. J. Wadsworth *et al.*, *Electron. Lett.* **36**, S3 (2000).
S2. We count the phase-locked beats f_o and f_b with a high-resolution counter and verify that they fluctuate about their respective phase-locked values by less than 100 mHz in 1 s. This implies that the stability of the S32-THz laser oscillator is transferred to the femtosecond comb with a relative uncertainty $<2 \times 10^{-16}$ in 1 s.
S3. S. Stein *et al.*, in *Proceedings of the 1982 IEEE International Frequency Control Symposium*, Philadelphia, PA, 2 to 4 June 1982 (IEEE, Piscataway, NJ, 1982), pp. 24–30.
S4. S. Chang, A. G. Mann, A. N. Luiten, *Electron. Lett.* **36**, 480 (2000).
55. C. W. Oates, E. A. Curtis, L. Hollberg, *Opt. Lett.* **25**, 1603 (2000).
S6. C. J. Bordé, *Phys. Lett. A* **140**, 10 (1989).
S7. L-S. Ma, P. Jungner, J. Ye, J. L Hall, *Opt. Lett.* **19**, 1777 (1994).
S8. P. Lesage, *IEEE Trans. Instrum. Meas.* **32**, 204 (1983).

S9. We are grateful to A. Bartels (GigaOptics GmbH) for assistance with the femtosecond laser. We are also indebted to R. Windeler (Lucent Technologies) for providing the microstructure optical fiber. We acknowledge many illuminating discussions with J. Hall, S. Cundiff, J. Ye, S. Karshenboim, and F. Walls. Contribution of the National Institute of Standards and Technology—not subject to U.S. copyright.

29 March 2001; accepted 11 June 2001
Published online 12 July 2001;
10.1126/science.1061171
Include this information when citing this paper.

ALL OPTICAL ATOMIC CLOCKS BASED ON A SINGLE MERCURY ION AND CALCIUM ATOMS

R.E. Drullinger, Th. Udem*, S.A. Diddams, K.R. Vogel**, C.W. Oates,
E.A. Curtis, W.D. Lee†, W.M. Itano, L. Hollberg, and J.C. Bergquist
National Institute of Standards and Technology, Boulder Colorado, USA
*Max-Planck-Institut fur Quantenoptik, Hans-Kopfermann-Str.1, Garching Germany
**Precision Photonics, Boulder, Colorado, USA
† Research Electro Optics, Boulder Colorado, USA

ABSTRACT

The frequency comb created by a femtosecond mode-locked laser and a microstructure fiber is used to phase-coherently measure the frequencies of both the Hg^+ and Ca optical frequency standards with respect to the SI second as realized at NIST. We find the transition frequencies to be f_{Hg} = 1 064 721 609 899 143(10) Hz and f_{Ca} = 455 986 240 494 158(26) Hz, respectively. This work begins to reveal the high stability and accuracy potential of optical atomic clocks based on the Hg^+ and Ca standards. Furthermore, when combined with previous measurements, we find no time variations of these atomic frequencies within the uncertainties of $|(\partial f_{Hg}/\partial t)/f_{Hg}| < 2 \times 10^{-14}$ yr^{-1} and $|(\partial f_{Ca}/\partial t)/f_{Ca}| < 8 \times 10^{-14}$ yr^{-1}.

Keywords: Optical, Atomic Clock, femtosecond, comb

INTRODUCTION

Optical frequency standards based on laser-cooled atoms and ions promise superior stability and accuracy over existing microwave standards [1–5]. However, because of their high frequencies (~ 10^{15} Hz or PHz), it has proven difficult to count cycles as required for building functioning clocks. Only recently, a reliable and convenient clockwork fast enough to count optical oscillations has been realized [6–9]. Here, we report on work toward an all-optical- clock based on a femtosecond laser that phase-coherently divides down the frequency of the visible radiation from either a Hg^+ or Ca optical-frequency standard to a countable radio frequency. We have measured the absolute frequencies of these optical transitions in terms of the SI second as realized at NIST [10]. Indeed, for the Hg^+ standard, the uncertainty in the measurement is essentially limited by our knowledge of the SI second at ~2 × 10^{-15}. Additionally, the comparison of atomic frequencies over time provides constraints on the possible time variation of fundamental constants. We now have measurements of the absolute Hg^+ frequency taken over a six month interval that differ by less than their statistical uncertainty and much less than their systematic uncertainty.

THE OPTICAL STANDARDS

The Hg^+ and Ca systems have recently been described elsewhere [1,4, 11-13], so we summarize only their basic features. The mercury optical frequency standard is based on a single, laser-cooled $^{199}Hg^+$ ion that is stored in a cryogenic, radio-frequency, spherical Paul trap. The ion is cooled and detected by driving the $^2S_{1/2}$ - $^2P_{1/2}$ cycling transition at 194 nm. The $^2S_{1/2}$ (F =0, M_F = 0) - $^2D_{5/2}$ (F =2 , M_F = 0) electric-quadrupole transition at 282 nm [Fig.1] provides the reference for the optical standard [1]. We lock the frequency-doubled output of a 563 nm dye laser with sub-hertz linewidth[12] to the quadrupole resonance. Transitions to the metastable $^2D_{5/2}$ state are detected with near unit efficiency since the absorption of a single 282 nm photon suppresses the scattering of many 194 nm photons on the strongly allowed $^2S_{1/2}$ - $^2P_{1/2}$ transition [14, 15]. In figure 2 we show an example of a normalized spectrum that was obtained from multiple, bidirectional scans through the resonance, where the probe time was 20 ms. Most often, the frequency was locked to resonance with a 10 ms interrogation period, which yielded a fractional frequency stability of 2 ×10^{-15} $\tau^{-1/2}$ for an averaging time τ measured in seconds [16].

The calcium standard starts with a collection of ~10^7 laser-cooled ^{40}Ca atoms held in a magneto-optic trap. The 423 nm $^1S_0$ - $^1P_1$ transition is used for trapping and Doppler-cooling the atoms to a residual temperature of ~2 mK. The $^1S_0$ (M_J = 0) - $^3P_1$ (M_J = 0) weakly allowed electric-dipole transition (400 Hz natural linewidth) at 657 nm is the "clock" transition for this frequency standard [Fig. 3]. We excite the transition with a four-pulse Bordé-Ramsey sequence (pulse duration =1.5 μs) with light from a continuous-wave (CW), frequency-stabilized diode laser. Using a shelving detection technique similar to that employed in the Hg^+ system, near-resonant 423 nm pulses (5 μs duration) are used before and after the 657 nm excitation to determine the fraction of atoms transferred from the ground state. Figure 4 shows the Bordé-Ramsey fringes taken at a resolution of 960 Hz. This system has demonstrated a fractional frequency stability of 4 × 10^{-15} $\tau^{-1/2}$ when probing sub-kilohertz linewidths[4]. For the measurements presented here the Ca spectrometer was operated with linewidths ranging from 0.96 to 11.55 kHz, which are integer submultiples of the recoil splitting.

THE OPTICAL COMB

The recent introduction of mode-locked lasers to optical frequency metrology greatly simplifies the task of optical-frequency measurements [6 –8, 17 –19]. The spectrum emitted by a mode-locked laser consists of a comb of regularly spaced continuous waves that are separated by the pulse repetition rate f_r. The frequency of the nth mode of the comb is given by $f_n = nf_r + f_0$ [20, 21], where f_0 is the frequency offset common to all modes. This offset is caused by the difference between the group- and the phase-velocity inside the laser cavity. f_r can be measured by direct detection of the laser's output with a photodiode. f_0 is measured by heterodyning the 2nd harmonic of mode $f_n = nf_r + f_0$ from the infrared wing of the comb with mode $f_{2n} = 2nf_r + f_0$ from the blue side of the comb [7, 8]. This self-referenced technique requires that the optical comb span at least an octave in frequency space. While an octave-spanning comb can be produced directly from a mode-locked laser [22], launching the longer pulses from a

commercially-available femtosecond laser into an air-silica microstructure fiber [23, 24] also produces a frequency comb that spans an octave. Nonlinear processes in the fiber produce the additional equally spaced and phase-coherent modes to the transmitted light. It has been demonstrated that this process of spectral broadening preserves the uniformity of spacing and spectral fidelity of the comb to at least a few parts in 10^{16} [8].

We couple approximately 200 mW average power from a femtosecond, Ti:sapphire ring laser ($f_r \approx 1$ Ghz) through a 15 cm piece of microstructure fiber that has a 1.7 μm core and group-velocity dispersion that vanishes near 770 nm [23]. This power density is sufficient to increase the spectral width of the laser from 13 THz to more than 300 THz, spanning from ~520 nm to ~1170 nm. The infrared part of the comb from the fiber (λ ~ 1060 nm) is split off by a dichroic mirror and frequency-doubled into the green portion of the visible spectrum by means of a $KNbO_3$ crystal 2 mm long. Following an adjustable delay line that matches the optical path lengths, the frequency-doubled light is spatially combined with the green part of the original comb to produce a beat note at f_0. We phase-lock both f_0 and f_r to synthesized frequencies derived from a cavity-tuned hydrogen maser that acts as the transfer standard to the NIST realization of the SI second [10]. Control of f_r is achieved with a piezo transducer driving a cavity mirror, while f_0 is controlled by adjusting the 532 nm pump beam's intensity with an electro-optic modulator [8]. When both f_0 and f_r are phase-locked, the frequency of every mode in the comb is known with the same accuracy as that of the reference maser.

The CW light from the Hg^+ (563 nm) and Ca (657 nm) standards is transferred to the mode-locked laser system via two single-mode optical fibers that are 130 m and 10 m long, respectively. Approximately 2 mW of CW light from each fiber is mode-matched with the appropriate spectral region of the frequency comb to generate a beat signal f_b with a nearby mode. This beat note is amplified and measured with a counter. The optical frequency is then expressed as $f_{opt} = mf_r + f_0 + f_b$, where m is a large integer uniquely determined for each system from previous coarse measurements of f_{opt}.

RESULTS

Figure 5 summarizes the frequency measurements of Hg^+ made between August 2000 and February 2001, while figure 6 summarizes the Ca measurements made from October 26 to November 17, 2000. The frequency of the maser is calibrated by comparing to the local NIST time scale (5 hydrogen masers and 3 commercial cesium clocks), which in turn is calibrated by the local cesium fountain standard (NIST-F1 [10]). The fractional uncertainty in the frequency of the reference maser relative to the SI second was about 1.8×10^{-15} for these measurements.

The weighted mean of our measurements of the Hg^+ clock transition is f_{Hg} =1 064 721 609 899 143 Hz. The statistical uncertainty ($\approx 4 \times 10^{-15}$) of our limited duration measurements is essentially the result of the reference-maser's short-term stability ($\sim 2 \times 10^{-13}\tau^{-1/2}$). Because we have not made a full experimental evaluation of the Hg^+ standard, we assign a very conservative value of 10 Hz for the total systematic uncertainty. The dominant contribution to the uncertainty of the *S-D* transition frequency is the electric-quadrupole shift of the $^2D_{5/2}$ state arising from coupling with the static potentials of the trap. In our spherical Paul trap, where the confinement of the ion uses no static applied fields, the maximum quadrupole shift should be less than 1 Hz (or fractional frequency shift $<10^{-15}$) [25]. In principle, it is possible to eliminate the quadrupole shift by averaging the *S-D* transition frequencies for three mutually orthogonal orientations of quantizing magnetic field of constant magnitude. In the present experiment, we have measured the *S-D* frequency for various field values, but we have made no attempt to eliminate the quadrupole shift by using three orthogonal fields of constant magnitude. No shift of the resonance frequency is observed within the precision of these measurements even under strongly varying conditions of magnetic field. We anticipate that the uncertainties of all systematic shifts in the Hg^+ system can be reduced to values approaching 1×10^{-18} [1, 25].

For the Ca data shown [Fig. 6], an additional correction is applied each day to account for frequency shift caused by residual phase chirping on the optical Ramsey pulses produced by amplitude modulating an acoustooptic modulator (AOM). The phase chirping produced resolution-dependent frequency shifts on the order of 100 Hz for fringes 11.5 kHz wide but of only 10 Hz for fringes 0.96 kHz wide. On each day, the Ca frequency was measured for ~30 minutes at each of several fringe resolutions, and the zero-intercept of a linear fit to the data was used as the corrected frequency. On the last 3 days of measurements, we were able to reduce this shift by a factor of ~3 with improvements to the RF pulses that drive the AOMs. The statistical uncertainty (typically 8 Hz) for each day's measurement is smaller than the uncontrolled systematic uncertainties in the Ca frequency. The largest systematic uncertainty stems from incomplete knowledge of the angular overlap of the counter-propagating beams in the Ca spectrometer, combined with transverse drift velocity of the cold Ca ensemble. This leads to residual first-order Doppler shift with magnitude < 15 Hz (except on November 16, where a large drift velocity led to an uncertainty of ~52 Hz). Other significant uncertainties include our lack of knowledge or control of electronic offsets and baseline symmetries (< 12 Hz), wavefront curvature (< 10 Hz), and cold-atom collisional shifts (< 10 Hz). Taking all known systematic uncertainties in quadrature gives a confidence level of ~26 Hz for the measured mean values indicated by the dashed lines in figure 6.

Figure 6 also shows the good agreement between our measurement and the most recent value measured with a harmonic frequency chain [26], which provides a degree of confidence in the reproducibility of the Ca standards. It is also in reasonable agreement with the very recent PTB measurements made with a femtosecond comb [27]. An additional measure of the Ca frequency can be made by using the present absolute measurement of Hg^+ and our earlier measurement of the 76 374 564 455 429(40) Hz gap between f_{Hg} and the Ca standard [28]. This yields a value of f_{Ca} =455 986 240 494 143(40) Hz in good agreement with the value from the present direct measurement.

Finally, these results also provide data on the relative time variability of atomic frequencies. S. Karshenboim has recently reviewed the implications of such comparisons and their

contribution toward constraining the possible time variation of fundamental constants [29]. In this regard Hg^+ and Ca are two of the most interesting cases to study. Comparing our present measurement of f_{Ca} to measurements made by PTB in 1997 [26] gives $(\partial f_{Ca}/\partial t)/f_{Ca} < 8 \times 10^{-14}$ yr^{-1}. Similarly, our August 2000 to February 2001 measurements on f_{Hg} provides an initial baseline constraint on the time variation of $(\partial f_{Hg}/\partial t)/f_{Hg} \leq 2 \times 10^{-15}$ yr^{-1}. Here we use the defined unit of time based on the frequency of the Cs hyperfine interval and assume that any time dependence is slow and dominantly linear over the relevant time scale. We believe this represents the tightest laboratory test yet of the time variability of these disparate transitions.

ACKNOWLEDGMENTS

We acknowledge the support of the Office of Naval Research. This work was also supported through a Cooperative Research and Development Agreement with Timing Solutions, Corp., Boulder, Colorado. This work is a contribution of the National Institute of Standards and Technology, and is therefore not subject to United States copyright.

REFERENCES

[1] R.Rafac, B.C. Young, J.A. Beall, W.M. Itano, D.J. Wineland and J.C. Bergquist, Phys. Rev. Lett. 85, 2462 (2000).
[2] J.E.Bernard, A. A. Madej, L. Marmet, B. G. Whitford, K. J. Siemsen, and S. Cundy , Phys. Rev. Lett. 82, 3228 (1999).
[3] H.Schnatz, B. Lipphardt, J. Helmcke, F. Riehle, and G. Zinner, Phys. Rev. Lett. 76, 18 (1996).
[4] C.W.Oates, E. A. Curtis, L. Hollberg, Opt. Lett. 25, 1603 (2000).
[5] J.von Zanthier, Th. Becker, M. Eichenseer, A. Yu. Nevsky, Ch. Schwedes, E. Peik, H. Walther, R. Holzwarth, J. Reichert, Th. Udem, T. W. Hänsch, P. V. Pokasov, M. N. Skvortsov, S. N. Bagayev, Opt. Lett. 25, 1729 (2000).
[6] S.A.Diddams, David J. Jones, Jun Ye, Steven T. Cundiff, and John L. Hall, Phys. Rev. Lett. 84, 5102 (2000).
[7] D.J.Jones, S.A. Diddams, J.K. Ranka,A. Stentz, R.S. Windeler J.L. Hall and S.T. Cundiff, Science, 288, 635 (2000).
[8] R.Holzwarth, Th. Udem, and T. W. Hänsch, Phys. Rev. Lett. 85, 2264 (2000).
[9] S.A. Diddams, Th.Udem, K.R. Vogel, C.W. Oates, E.A. Curtis, R.S. Windeler, A. Bartels, J.C. Bergquist and L. Hollberg, Proc SPIE Conf. on Laser Frequency Stabilization, Standards, Measurement, and Applications, San Jose, CA January 2001.
[10] S.R.Jefferts, *et al.*, submitted to Metrologia; S.R.Jefferts, *et al.*, IEEE International Freq.Control Symp., 714 (2000).
[11] C.W.Oates, F. Bondu, R.W. Fox and L. Hollberg, J.Phys.D, 7, 449 (1999).
[12] B.Young, F. C. Cruz, W. M. Itano, and J. C. Bergquist, Phys. Rev. Lett. 82, 3799 (1999).
[13] J.C. Bergquist, R.J. Rafac, B.C. Young, J.A. Beall, W.M. Itano, and D.J. Wineland, Proc SPIE Conf. on Laser Frequency Stabilization, Standards, Measurement, and Applications, San Jose, CA January 2001.
[14] H.Dehmelt, Bull. Am. Phys. Soc. 20, 60 (1975).
[15] J.C.Bergquist, Wayne M. Itano and D. J. Wineland, Phys. Rev. A, 36, 428 (1987).
[16] D.J.Wineland, *et al.*, *The Hydrogen Atom* ed. by T.W.Hänsch (Springer,Berlin,Heidelberg 1989) pp.123-133.
[17] Th.Udem, J. Reichert, R. Holzwarth, and T. W. Hänsch, Phys. Rev. Lett. 82, 3568 (1999).
[18] J.Reicher, M. Niering, R. Holzwarth, M. Weitz, Th. Udem, and T. W. Hänsch, Phys. Rev. Lett. 84, 3232 (2000).
[19] M.Niering, R. Holzwarth, J. Reichert, P. Pokasov, Th. Udem, M. Weitz, and T. W. Hänsch , Phys. Rev. Lett. 84, 5496 (2000).
[20] A.I.Ferguson, J.N. Echstein, T. W. Hänsch, Appl. Phys. 18, 257 (1979).
[21] J.Reicher, R. Holzwarth, Th. Udem and T. W. Hänsch, Opt. Comm. 172, 59 (1999).
[22] F.X.Kärtner, *et al.*, Opt.Lett. (in press).
[23] J.K.Rank, R. S. Windeler, A. J. Stentz , Opt. Lett. 25, 25 (2000).
[24] W.J.Wadsworth, J.C. Knight, A. Ortigosa-Blanch, J. Arriaga, E. Silvestre, P.St.J. Russell, Electron.Lett. 36, 53 (2000).
[25] W.M.Itano, J.Res.NIST (in press).
[26] F.Riehle, H. Schanatz, B.Lipphardt, G. Zinner, T. Trebst, T. Binnewies, G. Wilpers, J. Helmcke, Proceedings of EFTF-IEEE IFCS, 700 (1999).
[27] J. Stenger,T. Binnewies, G. Wilpers, F. Riehle, H.R. Telle, J.K. Ranka, R.S. Windeler, and A.J. Stentz, Phys Rev A 63 021802 (2001).
[28] K.R.Vogel, S. A. Diddams, C. W. Oates, E. A. Curtis, R. J. Rafac, W. M. Itano, J. C. Bergquist, R. W. Fox, W. D. Lee, J. S. Wells, L. Hollberg , Opt. Lett., 26, 102 (2001).
[29] S. Karshenboim, Can.J.Phys. 78, 639 (2000).

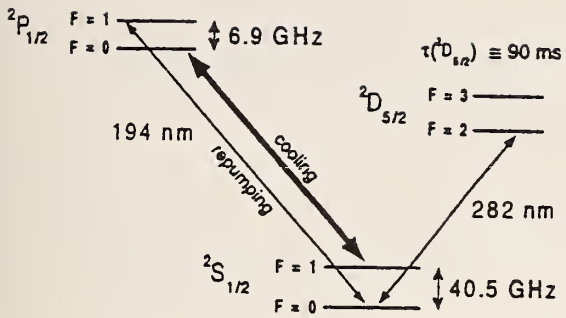

Fig. 1: Partial level scheme for $^{199}Hg^+$. The 194 nm radiation is used for Doppler cooling, state preparation and detection. The 282 nm transition from the ground state $^2S_{1/2}$ ($F=0, M_F=0$) to the metastable $^2D_{5/2}$ ($F=2, M_F=0$) state is the "clock" transition.

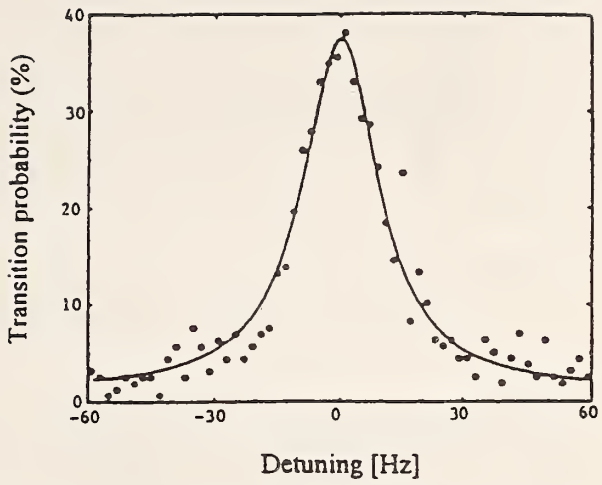

Fig. 2: A typical spectrum of the 282 nm transition . Here, the excitation pulse length was 20 ms and the measured linewidth is Fourier transform limited at about 20 Hz.

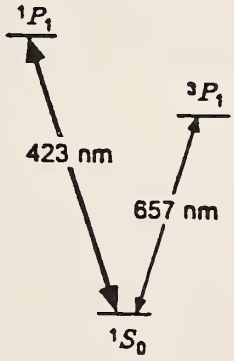

Fig. 3: Simplified diagram of the relevant energy levels in the Ca standard.

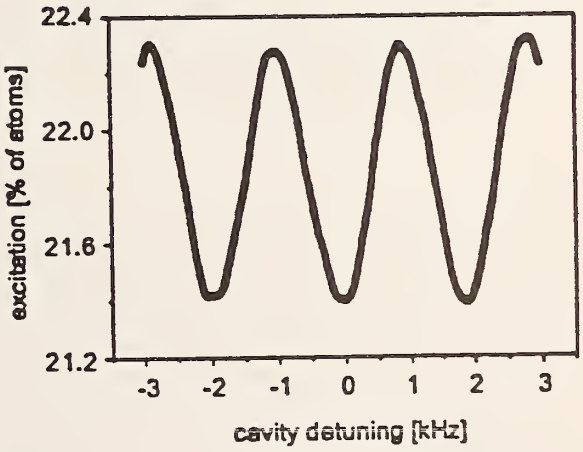

Fig. 4: Optical Bordé-Ramsey fringes with a 960 Hz (FWHM) resolution. The total averaging time to generate this figure was 20 s.

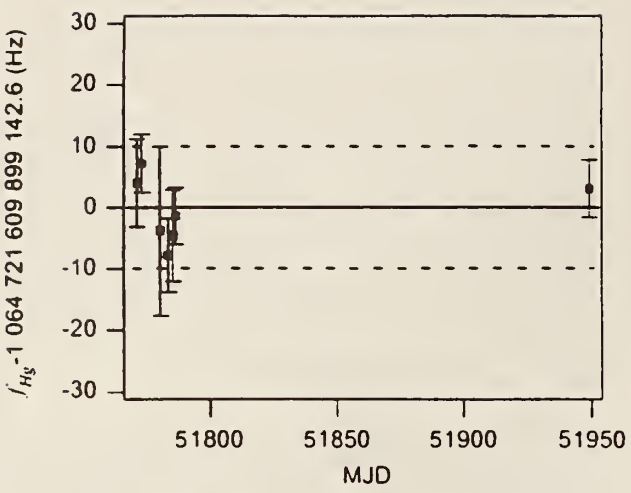

Fig. 5: A chronological record of the average daily frequency of the $^{199}Hg^{+}$ clock transition measured in August 2000 and February 2001. The error bars represent the statistical fluctuations. The dashed lines represent our assigned 10 Hz uncertainty in systematic effects.

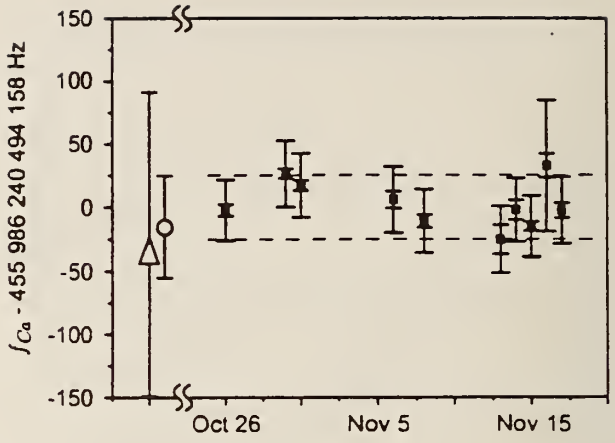

Fig. 6: The filled squares are the measured Ca frequencies on ten days over a 23-day period representing 38 787 s of total measurement time. The inner and outer error bars for each day represent the statistical and total uncertainty, respectively. The dashed lines show the 26 Hz systematic uncertainty assigned to the mean. The open triangle is the PTB measurement [26] while the open circle is the Ca frequency calculated from the present Hg^{+} result and our previous measurement of the 76 THz gap between Ca and Hg^{+} [28].

Mode and Transport Studies of Laser-Cooled Ion Plasmas in a Penning Trap*

T. B. Mitchell, J. J. Bollinger, X.-P. Huang and W. M. Itano

Time and Frequency Division, National Institute of Standards and Technology, Boulder, CO 80303

Abstract. We describe a technique and present results for imaging the modes of a laser-cooled plasma of $^9Be^+$ ions in a Penning trap. The modes are excited by sinusoidally time-varying potentials applied to the trap electrodes, or by static field errors. They are imaged by changes in the ion resonance fluorescence produced by Doppler shifts from the coherent ion velocities of the mode. For the geometry and conditions of this experiment, the mode frequencies and eigenfunctions have been calculated analytically. A comparison between theory and experiment for some of the azimuthally symmetric modes shows good agreement. Enhanced radial transport is observed where modes are resonant with static external perturbations, such as those caused by misaligning the trap with respect to the magnetic field. Similarly, the plasma angular momentum can be changed through the deliberate excitation of azimuthally asymmetric modes. The resultant torque can be much greater than that from the "rotating wall" perturbation, which is not mode-resonant.

INTRODUCTION

Non-neutral plasmas consisting exclusively of particles of a single sign of charge have been used to study many basic processes in plasma physics [1], partly because non-neutral (as opposed to neutral or quasi-neutral) plasmas can be confined by static electric and magnetic fields and also be in a state of global thermal equilibrium [2,3]. A particularly simple confinement geometry for non-neutral plasmas is the quadratic Penning trap, which uses a strong uniform magnetic field $\mathbf{B_0} = B_0\hat{\mathbf{z}}$ superimposed on a quadratic electrostatic potential

$$\phi_T(r,z) = \frac{m\omega_z^2}{2q}\left(z^2 - \frac{r^2}{2}\right). \tag{1}$$

Here m and q are the mass and charge of a trapped ion, and ω_z is the axial frequency of a single ion in the trap. The global thermal equilibrium state for a single charged species in a quadratic Penning trap has been well studied [3,4]. For sufficiently low temperatures, the plasma takes on the simple shape of a uniform density spheroid. An interesting result is that all of the electrostatic modes of a magnetized, uniform density spheroidal plasma can be calculated analytically [5,6]. This is the only finite length geometry for which exact plasma mode frequencies and eigenfunctions have been calculated for a realistic thermal equilibrium state.

In this manuscript we describe a technique for measuring these frequencies and eigenfunctions, and compare theory predictions and experimental results for some of the magnetized plasma modes. We also discuss several potential applications for the modes in Penning trap experiments. In general, the mode frequencies depend on the density and shape of the plasma spheroid. Therefore measurement of a mode frequency provides a non-destructive method for obtaining basic diagnostic information about the plasma. This is especially important in anti-matter plasmas [7,8], where conventional techniques for obtaining information about these plasmas involve ejecting the plasma from the trap. Measurement of the damping of the modes can provide information on the plasma's viscosity [9,10]. Other applications arise from the fact that the modes can strongly influence the dynamical behavior of trapped plasmas. For example, certain azimuthally asymmetric modes can have zero frequency in the laboratory frame and be excited by a static field error of the trap. These zero-frequency modes can strongly limit the achievable density in a Penning trap [11]. Similarly, the plasma angular momentum can

be changed through the deliberate excitation of azimuthally asymmetric modes [12,13], and the applied torque can be much greater than that from the "rotating wall" perturbation [14,15], which is not mode-resonant.

Previous experimental mode studies on spheroidal plasmas have been limited to frequency measurements on a small class of modes. With laser-cooled Be^+ ion plasmas, some quadrupole mode frequencies have been measured and agree well with theory [6,11]. Mode frequencies have also been measured on spheroidal cryogenic electron plasmas [16], 0.025–0.5 eV electron and positron plasmas [17], and room temperature Ar^+ ion plasmas [18]. In these cases qualitative agreement with theory was observed and the modes provided some basic diagnostic information. However, deviations from the model of a constant density spheroid in a quadratic trap limited the comparison with the ideal linear theory. Here, in addition to measuring mode frequencies, we also measure the mode eigenfunctions. The eigenfunctions permit direct identification of the modes. In addition, they contain much more information than the frequencies and therefore may be useful for observing nonlinear effects such as mode couplings. Mode eigenfunctions have been measured for low frequency, z-independent (diocotron) modes on cylindrical electron columns [19]. In that work, the mode measurements were important in identifying two coexisting modes.

EXPERIMENTAL APPARATUS

Figure 1 shows a schematic of the apparatus [20,21] used for the mode measurements. The trap consists of a 127 mm long stack of cylindrical electrodes at room temperature with an inner diameter of 40.6 mm, enclosed in a 10^{-8} Pa vacuum chamber. A uniform magnetic field $B_0 = 4.465$ T is aligned parallel to the trap axis within 0.01°, and results in a $^9Be^+$ cyclotron frequency $\Omega = qB_0/m = 2\pi \times 7.608$ MHz. The magnetic field is aligned by minimizing the excitation of zero-frequency modes produced by a tilt of the magnetic field with respect to the trap electrode symmetry axis [6,11]. Positive ions are confined in this trap by biasing the central ring electrode to a negative voltage $-V_0$ with respect to the endcaps. Because the dimensions of the Be^+ plasmas ($\lesssim 2$ mm) are small compared to the diameter of the trap electrodes, the quadratic potential of Eq. (1) is a good approximation for the trap potential. For most of the work reported here, V_0 was set at 2.00 kV which results in $\omega_z = 2\pi \times 1.13$ MHz and a single-particle magnetron frequency $\omega_m = [\Omega - (\Omega^2 - 2\omega_z^2)^{\frac{1}{2}}]/2 = 2\pi \times 84.9$ kHz.

We create a Be^+ plasma by ionizing neutral Be atoms in a separate trap (not shown) and then transferring

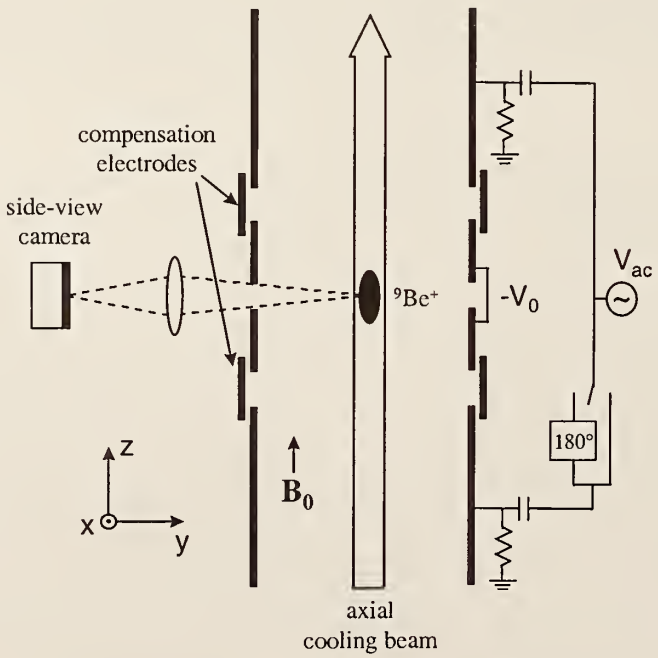

FIGURE 1. Schematic of the experimental apparatus. Azimuthally symmetric $m = 0$ modes were excited by applying in-phase or 180° out-of-phase sinusoidal potentials to the trap endcaps.

the ions to the main trap. For the work discussed here, the number of ions was typically 6×10^4. While the total charge in the trap is conserved after loading, the relative abundance of contaminant, heavier-mass ions increases, presumably due to reactions between Be^+ ions and background neutral molecules. Because we analyze our experimental results using an existing theory [5] for the electrostatic modes of a single-species plasma, we took data for mode studies only with relatively clean clouds (<3% impurity ions). The plasmas were cleaned approximately every 30 minutes by transferring the ions to the load trap where, with a shallow 3 V deep well, contaminant ions were driven out of the trap by exciting their axial frequencies. Cleaning therefore results in a decrease in the number of trapped ions. Over a 12–14 hour period, the number of ions is reduced by a factor of 2. Because the mode frequencies and eigenfunctions in a quadratic trap are independent of the number of ions, the mode measurements described here are not affected.

The trapped Be^+ ions are Doppler cooled by two laser beams at wavelength $\lambda \approx 313.11$ nm. The main cooling beam is directed parallel to $\mathbf{B_0}$ as shown in Fig. 1, and a second cooling beam propagating perpendicular to $\mathbf{B_0}$ (not shown and turned off during measurements) is also used to compress the plasma by applying a radiation pressure torque [3,11]. For mode eigenfunction measurements the axial cooling-laser frequency is fixed about one natural linewidth ($\sim$ 20 MHz) below the transition frequency. Ions which, due to excitation of a mode, have an axial velocity $v_z < 0$ therefore fluoresce more strongly than ions with $v_z > 0$. The ion temperature was not measured; however, based on previous work [3], we expect $T \lesssim 20$ mK.

An $f/5$ imaging system detects the Be^+ resonance fluorescence scattered perpendicularly from the axial cooling beam (waist ≈ 0.5 mm, power ≈ 50 μW) to produce a side-view image of the Be^+ ions. The side-view image is obtained with a photon-counting camera system which records the spatial and temporal coordinates of the detected photons. This data is processed to obtain the mode eigenfunctions by constructing side-view images as a function of the phase of the external drive used to excite the modes.

ELECTROSTATIC MODES OF A SPHEROIDAL PLASMA

A constant-density, spheroidal plasma model is a good approximation for our work. In thermal equilibrium, a Penning trap plasma rotates as a rigid body at frequency ω_r, where $\omega_m < \omega_r < \Omega - \omega_m$, about the trap's $\hat{\mathbf{z}}$ axis [2,4]. In this work the rotation frequency was precisely set by a rotating dipole electric field [14,15]. As the ions rotate through the magnetic field they experience a Lorentz force which provides the radial confining force of the trap. This ω_r-dependent confinement results in an ω_r-dependent ion density and plasma shape. At the low temperatures of this work, the plasma density is uniform over distances large compared to the interparticle spacing ($\sim$ 10 μm) and is given by $n_0 = \epsilon_0 m \omega_p^2 / q^2$ where $\omega_p = [2\omega_r(\Omega - \omega_r)]^{\frac{1}{2}}$ is the plasma frequency. With the confining potential of Eq. (1), the plasma is spheroidal with boundary $z^2/z_0^2 + x^2/r_0^2 + y^2/r_0^2 = 1$. The spheroid aspect ratio $\alpha \equiv z_0/r_0$ is determined by ω_r [3,4]. We have neglected the effect of image charges, because the plasma dimensions are small compared to the trap dimensions.

The modes of these spheroidal plasmas can be classified by integers (l, m), where $l \geq 1$ and $0 \leq m \leq l$ [5,6]. For an (l, m) mode with frequency ω_{lm} [22] the perturbed potential of the mode inside the plasma is given by a symmetric product of Legendre functions,

$$\Psi^{lm} \propto P_l^m(\bar{\xi}_1/\bar{d}) P_l^m(\bar{\xi}_2) e^{i(m\phi - \omega_{lm} t)}. \tag{2}$$

Here $\bar{\xi}_1$ and $\bar{\xi}_2$, discussed in Ref. [5], are scaled spheroidal coordinates where the scaling factor depends on the frequencies ω_r, Ω, and ω_{lm}, and $\bar{d}$ is a shape-dependent parameter which also depends on these frequencies. In general, for a given (l, m) there are many different modes. In this paper we report measurements of the mode frequencies and eigenfunctions of several magnetized plasma modes, which are defined as those modes with frequencies $|\omega_{lm}| < |\Omega - 2\omega_r|$ [5,6]. For $\omega_r \ll \Omega/2$, these modes principally consist of oscillations parallel to the magnetic field at a frequency on the order of ω_z. In the experiment we detect the axial velocity of a mode. In the linear theory, this is proportional to $\partial \Psi^{lm}/\partial z$.

We excite azimuthally symmetric ($m = 0$) plasma modes by applying sinusoidally time-varying potentials to the trap electrodes. Even-l $(l, 0)$ modes are excited by applying in-phase potentials to the endcaps (even drive), while odd-l $(l, 0)$ modes are excited by applying 180° out-of-phase potentials to the endcaps (odd drive). Azimuthally asymmetric ($m \neq 0$) modes can be excited by applying potentials to the compensation electrodes, which have 6-fold azimuthal symmetry. In Refs. [6,11] quadrupole ($l = 2$) mode frequencies were measured by observing the change in the total ion fluorescence from the plasma, averaged over the phase of the drive, which occurred when the drive frequency equaled the mode frequency. However, in order to observe such a change, the mode excitation must be large enough so that either the fluorescence from an ion nonlinearly depends on

its velocity or there is some heating of the plasma by the mode. The large amplitude drive required by this technique decreases the precision of the mode measurements.

The technique described here entails reducing the drive amplitude until the change in the phase-averaged ion fluorescence is negligible, and detecting the mode's coherent ion velocities by recording side-view images as a function of the phase and frequency of the external drive [23]. These Doppler images provide direct measurements of the mode's axial-velocity eigenfunction [24]. In addition, an accurate measurement of the mode's frequency (both real and imaginary parts) can be obtained from measurements of the mode amplitude as a function of drive frequency. High order modes have been excited and detected with this technique, such as the $(11,0)$ and $(12,1)$ modes. Imaging is not required for the (1,0) and (1,1) modes because there is no spatial variation in their eigenfunction. The driven mode amplitude and phase of these center-of-mass modes can therefore be obtained by coherently detecting the spatially integrated fluorescence as a function of the phase of the external drive [25].

EXPERIMENTAL RESULTS

Mode Frequency And Eigenfunction Measurements

In Fig. 2 we plot measured mode frequencies, along with the theoretical predictions, for several azimuthally symmetric magnetized plasma modes as a function of ω_r for $\omega_z/2\pi = 1.13$ MHz and $\Omega/2\pi = 7.608$ MHz. Many different mode frequencies at various values of ω_z have been measured with the Doppler imaging technique, and on very clean clouds agreement between the observed and predicted mode frequencies is typically better than 1%. However, as the percentage of impurity ions increases, the shift between the measured frequency and the value predicted by the single-species theory also increases. Both positive and negative frequency shifts have been observed. We think that these frequency shifts are caused by changes in the cloud shape which perturb the spheroidal geometry of the single-species cloud, arising because impurity ions centrifugally separate from the Be^+ [26].

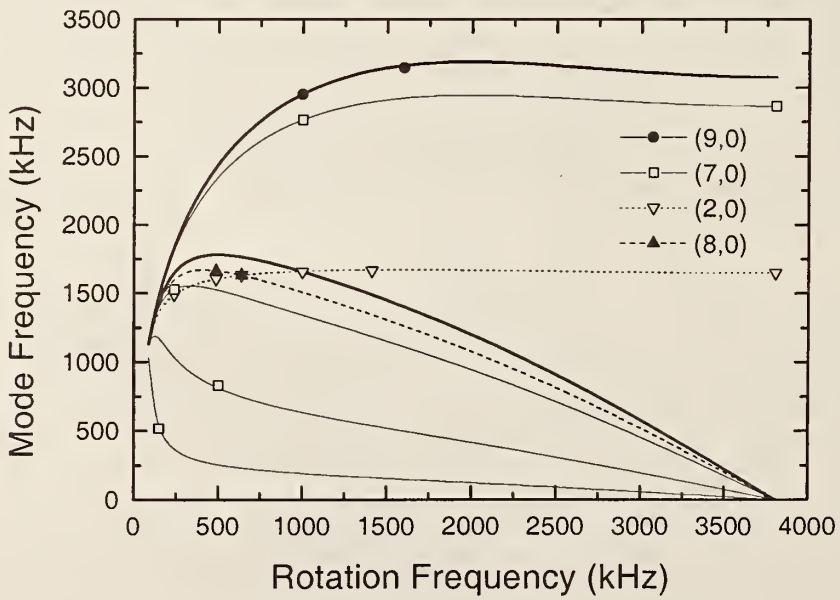

FIGURE 2. Plots of the frequencies of several $m = 0$ magnetized plasma modes as a function of rotation frequency for $\Omega/2\pi$=7.608 MHz and $\omega_z/2\pi$=1.13 MHz. The solid lines are the theoretical predictions and the symbols are experimental measurements. Only the highest frequency $(9,0)$ plasma mode and the second highest frequency $(8,0)$ plasma mode are plotted.

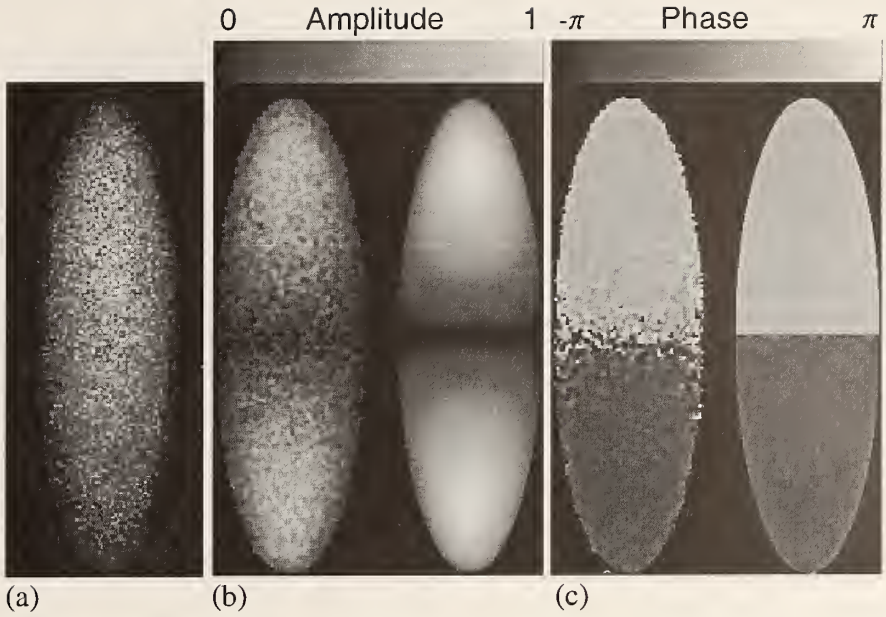

FIGURE 3. (a) Phase-coherent sideview image data obtained on a plasma with $\omega_r/2\pi = 1$ MHz while driving a (2,0) mode at $\omega_{2,0}/2\pi$=1.656 MHz. The magnetic field and axial laser beam point up. The ion cloud dimensions are $2z_0 = 0.76$ mm and $2r_0 = 0.24$ mm, and the density $n_0 = 2.70 \times 10^9$ cm^{-3}. Comparison of the amplitude (b) and phase (c) extracted from the $(2,0)$ mode in (a) with the predictions of linear theory. The theory predictions for (b) and (c) are on the right. From Ref. [23].

Figure 3 illustrates phase-coherent detection and Doppler imaging of the $(2,0)$ mode. This is one of the simplest modes that is not merely a center-of-mass oscillation of the plasma. In this mode the plasma stays spheroidal but the aspect ratio (and density) oscillate at $\omega_{2,0}$. For $\omega_r \ll \Omega/2$, the oscillation in r_0 is very small, so the mode principally consists of oscillations in z_0 at $\omega_{2,0}$. Ions above the $z = 0$ mid plane oscillate 180° out of phase with ions below $z = 0$.

Figure 3(a) shows one of a sequence of 18 side-view images taken as a function of the phase of the mode drive at $\omega_{2,0}/2\pi = 1.656$ MHz. A movie of the entire sequence is included in Ref. [23]. The plasma's rotation frequency was set to $\omega_r/2\pi = 1$ MHz and the $m = 0$ even drive rms amplitude was 7.07 mV. In the images, the magnetic field and the axial laser beam point up. As expected for the $(2,0)$ mode, the detected fluorescence in the upper half of the plasma is bright when the lower half is dark and vice versa. We analyze the data of Fig. 3(a) by performing a least-squares fit of the intensity at each point to $A_0 + A_{2,0}\cos(\omega_{2,0}t + \varphi_{2,0})$. Figures 3(b) and 3(c) show the resultant images of the measured mode amplitude $A_{2,0}(x,z)$ and phase $\varphi_{2,0}(x,z)$. These are compared with the theoretically predicted values of these quantities. Because the plasma is optically thin, the theoretical predictions were obtained by integrating $\partial\Psi^{lm}/\partial z$ over y. The amplitude of the theoretical prediction is scaled to match the experiment, and both amplitudes are normalized to 1.

From the fitted values of $A_{2,0}$ and A_0 we can estimate the coherent-ion mode velocities if the dependence of the ion fluorescence on velocity (through Doppler shifts) is known. For the low temperatures of this experiment a good approximation is to assume a Lorentzian profile with a full width at half maximum of 19 MHz due to the natural linewidth of the optical cooling transition. With the 20 MHz detuning used in this measurement, we estimate for the data of Fig. 3 that the maximum coherent mode velocity, which occurs at $z = \pm z_0$, is ~1.5 m/s. The spatial and density changes in the plasma spheroid for this excitation are too small to be resolved ($\Delta z/z_0, \Delta n/n_0 < 10^{-3}$). Therefore the observed variation in the fluorescence intensity is entirely due to Doppler shifts induced by the coherent ion velocities of the mode.

We have measured the mode eigenfunctions of a number of different azimuthally symmetric modes including the l=2,3,4,5,7, and 9 modes. Like the data of Fig. 3, good agreement with the predicted eigenfunction amplitude and phase distribution is obtained in the limit of low laser power and drive amplitude. Surprisingly high-order odd modes could be excited with the odd drive on the trap endcaps. Figure 4(a) shows one

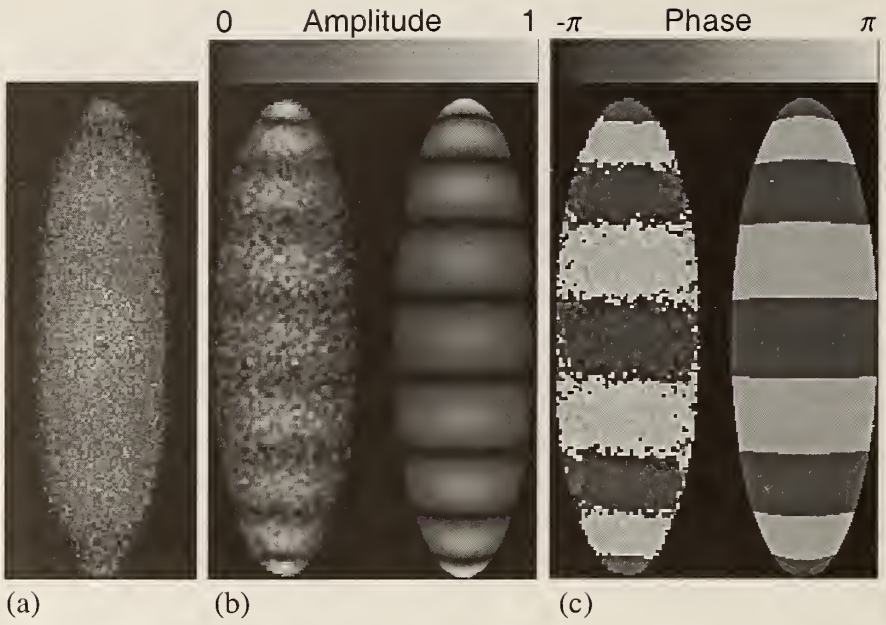

FIGURE 4. (a) Phase-coherent sideview image data obtained on the plasma of Fig. 3 with $\omega_r/2\pi$= 1.00 MHz while driving a (9,0) mode at $\omega_{9,0}/2\pi$=2.952 MHz. Comparison of the amplitude (b) and phase (c) extracted from the $(9,0)$ mode in (a) with the predictions of linear theory. The theory predictions are on the right. From Ref. [23].

of a sequence of 18 sideview images obtained with the highest frequency $(9,0)$ mode excited by a drive at $\omega_{9,0}/2\pi$ = 2.952 MHz. For a given $(l,0)$, the highest frequency magnetized plasma mode does not have any radial nodes. Figures 4(b) and 4(c) show the fitted amplitude and phase from the sequence, along with the predictions from theory. Similar high-order even $(l,0)$ modes are more difficult to excite. The mode eigenfunctions of some of the azimuthally asymmetric (m=1 and m=2) modes, such as the (1,1), (2,1), (3,1) (4,1), (6,1), (8,1) and (3,2) modes, have also been imaged. In general, the qualitative agreement with the predictions of theory is good.

Figure 5 shows images from a plasma with $\omega_r/2\pi$ = 638 kHz driven by an even drive at 1.619 MHz. This case demonstrates the utility of the Doppler imaging diagnostic. These data were initially taken during a survey of the $(2,0)$ mode eigenfunction as a function of the plasma's rotation frequency. Analysis of the phase-coherent data revealed additional, higher-order structure. An examination of the predictions for the mode frequencies revealed that at this particular rotation frequency, as shown in Fig. 2, both the $(2,0)$ mode and an $(8,0)$ mode with a radial node have similar frequencies. Characteristics of both modes are seen in the data. However, subsequent measurements of the $(2,0)$ mode frequency near this crossing indicated that any frequency shifts due to a nonlinear coupling with the $(8,0)$ mode are less than a few kilohertz. The $(2,0)$ mode driven in Fig. 3 occurs near a crossing with a $(9,0)$ mode (see Fig. 2). In this case no evidence for an excitation of a $(9,0)$ is observed, presumably because it is an odd mode which does not couple to even drives, and because there is little or no mode coupling between the $(2,0)$ and $(9,0)$.

Doppler imaging also provides a technique for measuring the damping of plasma modes. This is done by sweeping the frequency ω_{pert} of the sinusoidally time-varying perturbation through a mode frequency, while measuring the mode's resultant amplitude and phase. If the perturbation amplitude is kept low to avoid large amplitude effects the system can be modeled as a damped harmonic oscillator driven by a periodic external force, which has a characteristic lineshape for its amplitude response and a phase difference of π above and below resonance [27].

Figure 6 shows a measurement of the $(2,0)$ mode amplitude and phase response. The axial laser intensity was reduced in an attempt to make mode damping from viscous dissipation dominant over that from laser cooling, and the $z > 0$ upper half of the plasma was blocked off to permit phase-coherent detection without spatial discrimination. At each perturbation drive frequency ω_{pert} the fluorescence intensity was fitted to

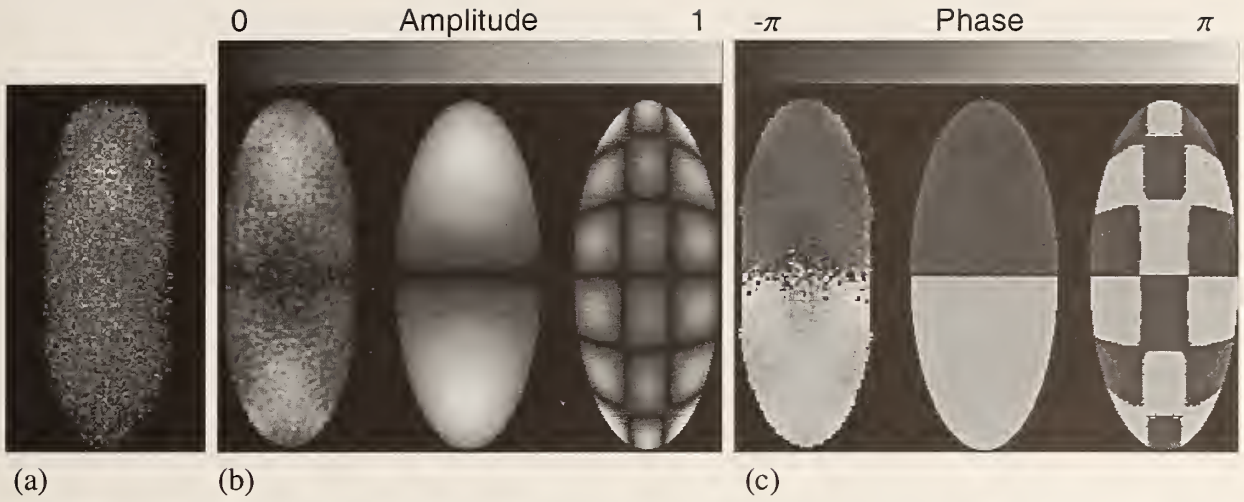

FIGURE 5. (a) Phase-coherent sideview image data obtained on a plasma with $\omega_r/2\pi$= 638 kHz while driving with an even drive at 1.619 MHz. At this rotation frequency there is a crossing of the $(2,0)$ mode and an $(8,0)$ mode with a radial node. Comparison of the amplitude (b) and phase (c) extracted from the data in (a) with the predictions of linear theory. The predictions of both the $(2,0)$ and $(8,0)$ modes are given. For this plasma $2z_0 = 0.70$ mm and $2r_0 = 0.29$ mm. From Ref. [23].

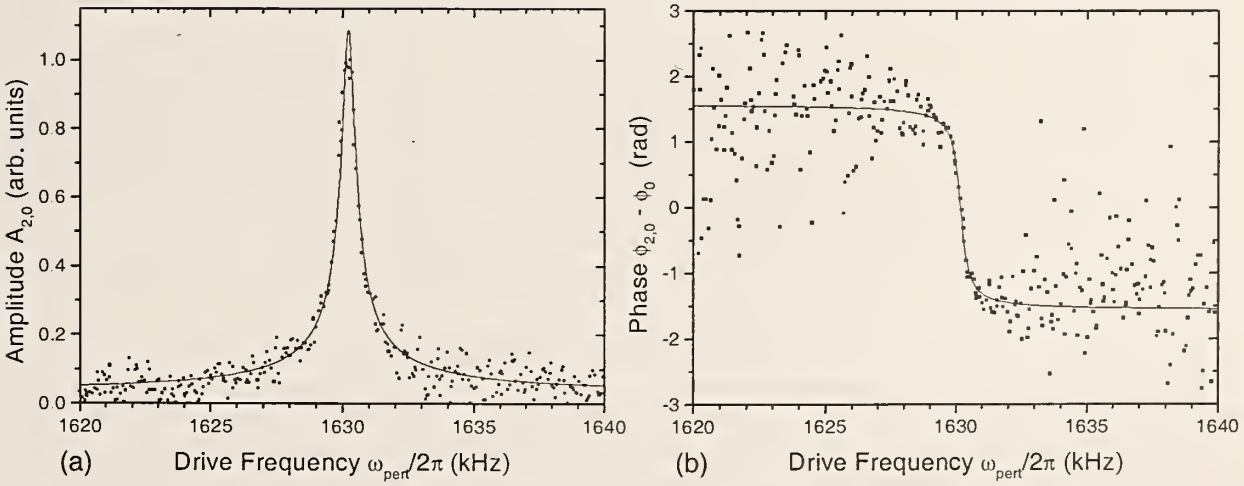

FIGURE 6. Measurement of the (2,0) mode amplitude (a) and phase (b) as a function of perturbation drive frequency. The lines are fits to theory curves for the velocity of a driven, damped harmonic oscillator [27].

$A_0 + A_{2,0}\cos(\omega_{pert}t + \varphi_{2,0})$. Figure 6(a) shows the measured amplitude $A_{2,0}$ along with a 4-parameter fit to the damped harmonic oscillator lineshape $a_0 + a_1\omega_{pert}/(\omega_{2,0}\sqrt{(\omega_{pert} - \omega_{2,0})^2 + \lambda^2})$, where λ is the damping coefficient. Figure 6(b) shows the measured phase $\varphi_{2,0}$ along with a 3-parameter fit to $\varphi_0 - \arctan((\omega_{pert} - \omega_{2,0})/\lambda)$. The two fits give damping coefficient values of $\lambda = 1405$ and 1409 s^{-1}. These are consistent with the rates of viscous damping seen in simulations [9].

Angular Momentum Transport From Resonant Modes

In principle, the confinement time of non-neutral plasmas in Penning traps is infinite because angular momentum conservation in an ideal, cylindrically symmetric trap places a constraint on the radial transport of the plasma [28]. In practice radial transport of the plasma always occurs, and at rates which, with ultrahigh vacuum, are greater than can be explained by collisions of the plasma with the neutral background gas. Because the rates of this "ambient" transport increase with increasing static field errors in the trap, it is thought to be caused by couplings between the confining field asymmetries and the plasma [29].

Although ambient transport is at present poorly understood, progress has been made on the related but simpler mechanism of mode-resonant transport. Here, torques are imparted because azimuthally asymmetric plasma modes can have zero frequency in the laboratory frame and hence be excited by the static field errors [6,11,30–32]. Because these modes need to have negative (backward) frequencies in the rotating frame of the plasma to come into resonance with a static field error, any torque they exert will slow the plasma down and hence increase transport. An analysis based on the second law of thermodynamics yields the same result [28].

When the trap walls are well away from the plasma and the ambient field errors are small, as in our experiment, it is particularly easy to study mode-resonant transport. Reference [11] demonstrated that torque and heating of the plasma occur when one of the (2,1) plasma modes is resonant with a static field error produced by a tilt between the trap symmetry axis and the magnetic field. The presence of additional heating resonances at lower rotation frequencies was also noted. We have used Doppler imaging to identify these resonances and find that they arise from $(l, 1)$ modes which come into resonance with the tilted-field error. We have also established that they exert a torque when they are resonant. Experimentally this tilt can be applied either mechanically by tilting the trap electrodes, or electrically with $m = 1$ perturbations applied to the compensation electrodes; we find no difference in the transport caused by the two methods.

Figure 7 is a plot of rotation frequency (as determined by side-view images [3]) versus time for a plasma when the trap has been electrically tilted from its aligned value by an amount equivalent to $\sim 5 \times 10^{-4}$ radians of mechanical tilt. Radial transport, which is measured here by decreases in rotation frequency (corresponding in this experimental regime to increases in the plasma radius), is enhanced by roughly a factor of 10 as compared with the aligned case. The rotation frequencies where transport is especially rapid can be identified with the mode resonances indicated on the plot. The lines show the predictions from theory for where the indicated mode has $\omega_{lm} = -\omega_r$, and Doppler imaging was used to verify the identity of these resonant zero-frequency modes. We find that the tilted-field error couples to modes with $m = 1$ and odd axial symmetry. Since with a single-species cloud only the $(2, 1)$ is predicted in linear theory to couple with a tilted-field error, the transport displayed in Fig. 7 might require the presence of impurity ions. In ion traps these are usually present at some level, and comprised $\sim$ 20% of the cloud of Fig. 7.

Because small-amplitude static field errors can be so effective in causing outward transport, it is not surprising that the process can be usefully inverted by actively driving modes which travel faster than the cloud's rotation. With the laser-cooled Be^+ plasmas, we have demonstrated mode-resonant inward transport with the (1,1), (2,1), (3,1) and (2,2) modes. The (1,1) is particularly easy to excite, as only an axially uniform rotating dipole field is required, and is useful for driving clouds into the regime where ω_r approaches Ω_c. The mode-resonant technique can do this in a few seconds, while doing the same thing with laser torque takes many seconds, and with the rotating wall perturbation at least several minutes. We note that the (1,1) mode requires an effect to break the separation between the center-of-mass and the internal degrees of freedom of the plasma. In our work, a small number of impurity ions could do this.

In comparison with the rotating wall technique for controlling an ion cloud's rotation frequency [14,15], the mode-resonant technique is less precise. The mechanism by which the rotating wall is believed to work with strongly correlated plasmas is that the plasma comes into equilibrium with rotating distortions of its surface which are imposed by the perturbation. Hence, the torque from a perturbation applied at frequency f_{RW} goes to 0 when $f_{RW} = f_r$, and changes sign about this point. In contrast, the torque imparted by a driven (l, m) mode usually has only one sign and is experimentally observed to depend sensitively upon such parameters

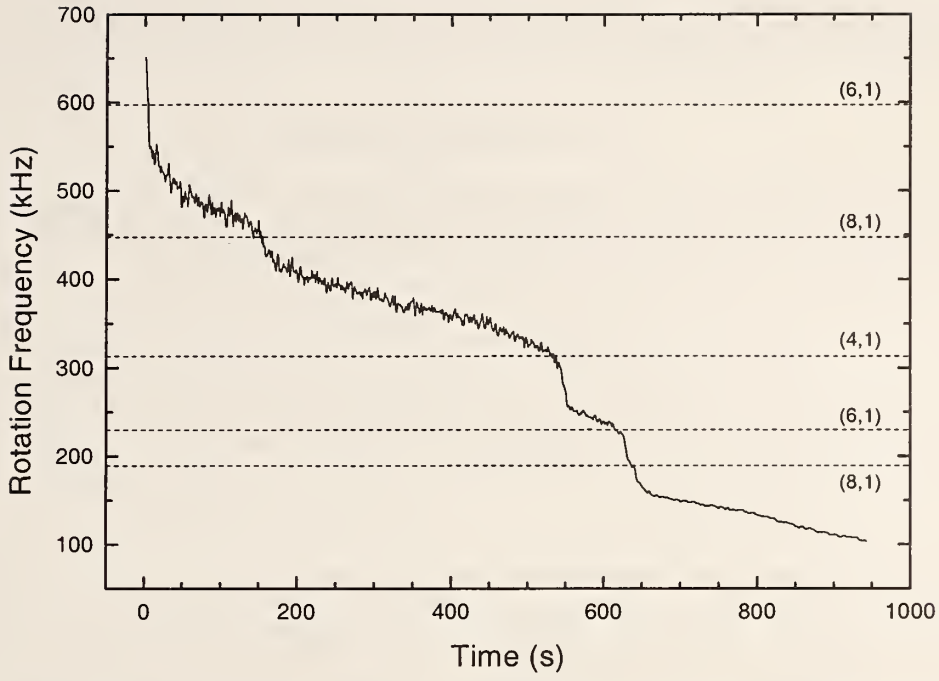

FIGURE 7. Measured plasma rotation frequency vs. time obtained when the trap was electrically tilted $\sim 5 \times 10^{-4}$ radians from its aligned value. The lines are predictions from theory for where the indicated modes have zero frequency in the lab frame.

as the temperature of the plasma. As a consequence the rotation frequency at which the cloud comes into equilibrium with the mode, which is determined by a balance between the inward mode torque and the outward ambient torque, is difficult to calculate in advance and is experimentally observed to change with variations in the cooling laser power or frequency.

However, an important advantage of mode-resonant coupling is that it can be used to transfer angular momentum to hot (uncorrelated: $\Gamma \ll 1$) plasmas. The phase-locked rotating wall control [14,15] described above has only been demonstrated with laser-cooled plasmas. In contrast, mode-resonant coupling has been used to increase angular momentum in non-neutral plasmas with temperatures up to 5 eV (which is where ionization of neutrals begins to change the density profile). Reference [12] demonstrated inward radial transport of a hot (T=0.9 eV) spheroidal electron cloud through the use of $(l, 1)$ modes. This transport was accompanied by a heating of the electrons, since there were no cooling processes in the experiment. At higher magnetic fields the heating can be balanced by cyclotron radiation cooling; steady-state confinement of uncorrelated electron plasmas in a 4 T field through the application of azimuthally asymmetric modes has recently been demonstrated [33].

SUMMARY AND FUTURE DIRECTIONS

We have described a technique, Doppler imaging, for studying the mode properties of laser-cooled ion plasmas. In general, for the magnetized plasma modes of spheroidal plasmas discussed here, good agreement is obtained between linear theory and the experimental measurements we have made to date. In the future the technique should be a useful tool for studying deviations from the linear theory such as large amplitude frequency shifts, non-linear corrections to the mode eigenfunction, and mode coupling. Because the width of the resonant lineshape of the mode amplitude as a function of the drive frequency provides a measurement of the mode damping, lineshape measurements may be able to provide information on the collisional viscosity of the strongly correlated plasma, about which little is currently known. Enhanced radial transport is observed when modes are resonant with static external perturbations, and future work may permit a quantitative

comparison to be made between experiment and theory for this basic transport process. Finally, we described how the plasma angular momentum can be usefully changed through the deliberate excitation of azimuthally asymmetric modes.

ACKNOWLEDGMENTS

We thank D. H. E. Dubin, C. F. Driscoll, E. M. Hollmann and D. J. Wineland for useful discussions, and L. B. King and B. M. Jelenković for their comments and careful reading of the manuscript. This work is supported by the Office of Naval Research.

REFERENCES

1. Fajans, J., and Dubin, D. H. E., *Non-Neutral Plasma Physics II*, New York: AIP, 1995.
2. Malmberg, J. H., and O'Neil, T. M., *Phys. Rev. Lett.* **39**, 1333–1336 (1977).
3. Brewer, L. R., *et al.*, *Phys. Rev. A* **38**, 859–873 (1988).
4. Bollinger, J. J., Wineland, D. J., , and Dubin, D. H. E., *Phys. Plasmas* **1**, 1403–1414 (1994).
5. Dubin, D. H. E., **66**, 2076–2079 (1991).
6. Bollinger, J. J., *et al.*, *Phys. Rev. A* **48**, 525–545 (1993).
7. Greaves, R. G., and Surko, C. M., *Phys. Plasmas* **4**, 1528–1543 (1997).
8. Holzscheiter, M. H., *et al.*, *Phys. Lett. A* **214**, 279–284 (1996).
9. Dubin, D. H. E., and Schiffer, J. P., *Phys. Rev. E* **53**, 5249–5267 (1996).
10. Dubin, D. H. E., *Phys. Rev. E* **53**, 5268–5290 (1996).
11. Heinzen, D. J., *et al.*, *Phys. Rev. Lett.* **66**, 2080–2083 (1991).
12. Mitchell, T. B., Ph.D. thesis, University of California at San Diego, 1993, pp. 58–61.
13. Huang, X.-P., *et al.*, *Phys. Rev. Lett.* **78**, 875–878 (1997).
14. Huang, X.-P., Bollinger, J. J., Mitchell, T. B., and Itano, W. M., *Phys. Rev. Lett.* **80**, 73–76 (1998).
15. Huang, X.-P., Bollinger, J. J., Mitchell, T. B., and Itano, W. M., *Phys. Plasmas* **5**, 1656–1663 (1998).
16. Weimer, C. S., Bollinger, J. J., Moore, F. L., and Wineland, D. J., *Phys. Rev. A* **49**, 3842–3853 (1994).
17. Tinkle, M. D., Greaves, R. G., and Surko, C. M., *Phys. Plasmas* **2**, 2880–2894 (1995).
18. Greaves, R. G., Tinkle, M. D., and Surko, C. M., *Phys. Rev. Lett.* **74**, 90–93 (1995).
19. Driscoll, C. F., *Phys. Rev. Lett.* **64**, 1528–1543 (1990).
20. Tan, J. N., Bollinger, J. J., Jelenković, B., and Wineland, D. J., *Phys. Rev. Lett.* **75**, 4198-4201 (1995).
21. Itano, W. M., *et al.*, *Science* **279**, 686–689 (1998).
22. Here ω_{lm} is the mode frequency in a frame rotating with the plasma. For the $m = 0$ modes discussed here this distinction is not necessary because their frequency is the same in either the laboratory or rotating frame.
23. Mitchell, T. B., Bollinger, J. J., Huang, X.-P., and Itano, W. M., *Opt. Exp.* **2**, 314–322 (1998).
24. Information on the mode eigenfunction can be obtained from the side-view images even when there is a change in the phase-averaged ion fluorescence. However, the images may no longer provide a linear measure of the mode axial velocity.
25. Thompson, R. C., *et al.*, *Phys. Scripta* 24–33 (1997).
26. Larson, D. J., *et al.*, *Phys. Rev. Lett.* **57**, 70–73 (1986).
27. Landau, L. D., and Lifshitz, E. M., *Mechanics and Electrodynamics*, Oxford: Pergamon Press, 1972, pp. 68–70.
28. O'Neil, T. M., and Dubin, D. H. E., *Phys. Plasmas* **5**, 2163–2193 (1998).
29. Driscoll, C. F., Fine, K. S., and Malmberg, J. H., *Phys. Fluids* **29**, 2015–2017 (1986).
30. Driscoll, C. F., and Malmberg, J. H., *Phys. Rev. Lett.* **50**, 167–170 (1983).
31. Keinigs, R., *Phys. Fluids* **27**, 1427–1433 (1984).
32. Eggleston, D. L., O'Neill, T. M., and Malmberg, J. H., *Phys. Rev. Lett.* **53**, 982–984 (1984).
33. Anderegg, F., Hollmann, E. M., and Driscoll, C. F., "Rotating Field Confinement of Pure Electron Plasmas Using Trivelpiece-Gould Modes," submitted to *Phys. Rev. Lett.*

Direct observations of the structural phases of crystallized ion plasmas*

T. B. Mitchell,[†,a)] J. J. Bollinger, X.-P. Huang, and W. M. Itano
Time and Frequency Division, National Institute of Standards and Technology, Boulder, Colorado 80303

D. H. E. Dubin
Department of Physics, University of California at San Diego, La Jolla, California 92093

(Received 13 November 1998; accepted 18 December 1998)

Laser-cooled $^9Be^+$ ions confined in a Penning trap were directly observed, and the images were used to characterize the structural phases of the ions. With the ions in two-dimensionally extended lattice planes, five different stable crystalline phases were observed, and the energetically favored structure could be sensitively tuned by changing the areal density of the confined ions. Qualitatively similar structural phase transitions occur or are predicted to occur in other planar single-component systems with a variety of interparticle interactions. Closed-shell structures were observed with small ion clouds that were spherical or prolate, and crystals with long-range order were observed in the centers of clouds with large numbers of ions. These experimental results are in good agreement with theoretical predictions for the strongly coupled one-component plasma. [S1070-664X(99)92605-8]

I. INTRODUCTION

The one-component plasma (OCP) has been a model of condensed matter in statistical physics for over 60 years, and it is used to describe such diverse systems as dense astrophysical matter[1] and electrons on the surface of liquid helium.[2] Laser-cooled trapped ions[3] are an excellent experimental realization of the OCP. The phase structures of spatially homogeneous,[4,5] cylindrical (extended in one dimension only),[6,7] and thin planar (two-dimensionally extended, with up to 5 planes)[8] OCPs have been explored recently. In this paper, images of ions that were confined in these geometries in a Penning trap are presented and used to further characterize the structural phases. The observed structures agree well with the theoretical predictions for the strongly coupled OCP.

The OCP model consists of a single charged species embedded in a uniform, neutralizing background charge. In Paul[9] or Penning[9,10] traps, which are used to confine charged particles, a (fictitious) neutralizing background is provided by the confining potentials. The thermodynamic properties of the infinite classical OCP are determined by its Coulomb coupling parameter,

$$\Gamma \equiv \frac{1}{4\pi\epsilon_0}\frac{e^2}{a_{ws}k_BT}, \tag{1}$$

which is the ratio of the Coulomb potential energy of neighboring ions to the kinetic energy per ion. Here, ϵ_0 is the permittivity of the vacuum, e is the charge of an ion, k_B is Boltzmann's constant, T is the temperature, and a_{ws} is the Wigner–Seitz radius, defined by $4\pi(a_{ws})^3/3 = 1/n_0$, where n_0 is the ion number density. The onset of short-range order for the infinite OCP is predicted[11] at $\Gamma \approx 2$, and a phase transition to a body-centered cubic (bcc) lattice is predicted[11–13] at $\Gamma \approx 170$. With an OCP in a planar geometry, boundary effects are predicted to cause the formation of a variety of additional structural phases, such as the hexagonal close-packed (hcp) and face-centered cubic (fcc) phases.[14–16] Qualitatively similar structural phase transitions occur or are predicted to occur in other planar systems with varied interparticle interactions, such as plasma dust crystals,[17,18] colloidal suspensions,[19] semiconductor electron systems,[20] and hard spheres.[21] In the case of small cylindrically- or spherically-shaped plasmas, concentric shells are predicted to form.[22]

The crystallization of small numbers (total number $N < 50$) of laser-cooled ions into Coulomb clusters[23] was first observed in Paul traps.[24,25] With larger numbers of trapped ions, concentric shells[22,26] were directly observed in Penning[27] and Paul traps.[6,7,28] Recently, Bragg diffraction has been used to detect bcc crystals (the predicted infinite volume ordering) in large spherical ($N > 2.7 \times 10^5$, radius $r_0 > 60a_{ws}$) ion plasmas confined in a Penning trap.[4,5]

In this paper we present measurements taken from direct images of the central ($r = 0$) structure of pancake-shaped (lenticular) ion plasmas (aspect ratio $\alpha \equiv z_0/r_0 < 0.1$, where $2z_0$ is the plasma center's axial extent). This region has a disk-like geometry with constant central areal density σ_0 (charge density per unit area projected onto the $z = 0$ plane), which facilitates a comparison with planar theory. We observed five different stable crystalline phases and found that the energetically favorable central structure could be tuned by changing σ_0. Both continuous and discontinuous structural phase transitions were observed. We also present direct images of the cylindrical shell structures observed in small ion clouds and of the three-dimensional (3D) periodic crystals observed in large spherical clouds, and compare our results with those obtained previously.[4,5,27]

*Paper F3I1.4 Bull. Am. Phys. Soc. 43, 1702 (1998).
[†]Invited speaker
[a)]Electronic mail: travis.mitchell@nist.gov

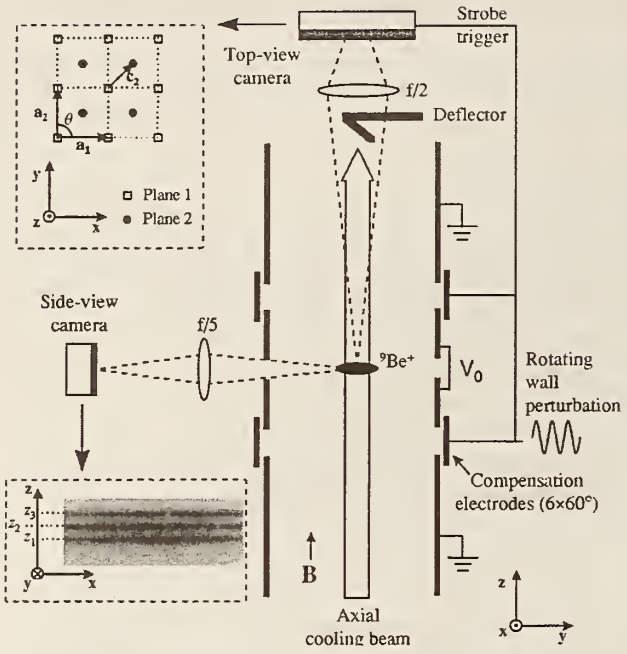

FIG. 1. Schematic side view of the cylindrical Penning trap with its side- and top-view imaging optics. The insets show the variables used to characterize the intra- and interlayer structure. The side-view inset also shows the central region of a lenticular ion plasma with three axial lattice planes.

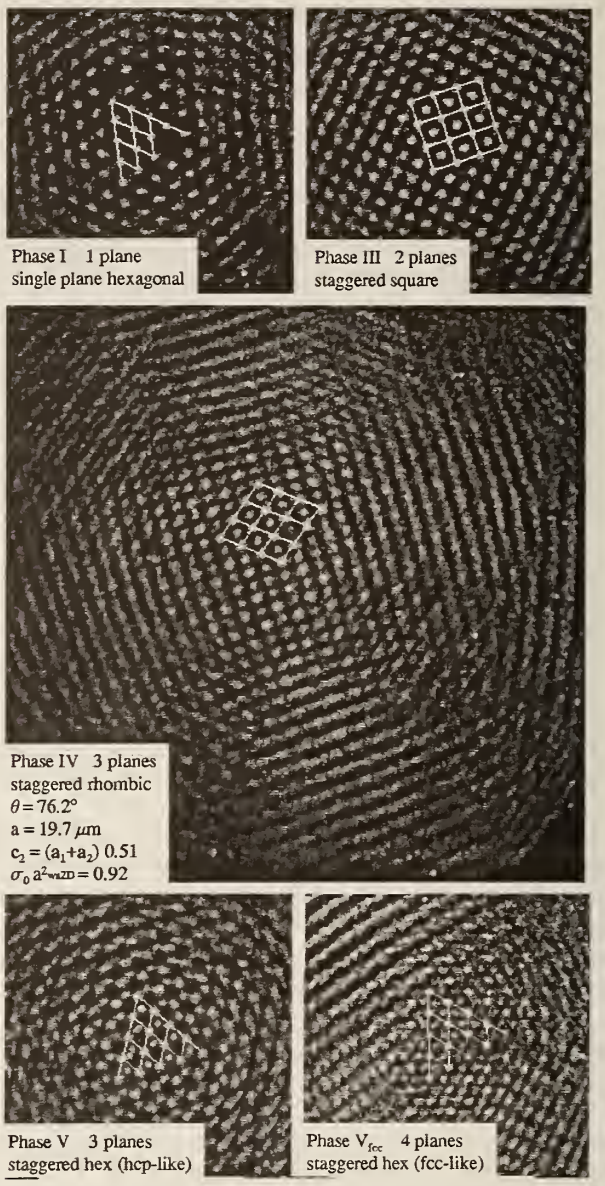

FIG. 2. Top-view (x,y) images of the five structural phases observed in the experiment, with lines showing a fit of the central ions to the indicated structure.

II. EXPERIMENTAL APPARATUS

The $^9Be^+$ ions were confined radially in a cylindrical Penning trap (Fig. 1, inner trap diameter 40.6 mm) by a uniform magnetic field $B=4.465$ T in the $\hat{\mathbf{z}}$ direction. The ions were confined axially by a potential difference of V_0 (usually -1.50 kV) applied between the center and end electrodes of the trap. Near the trap center this axial potential is quadratic and has a value of $1/2(m/e)\omega_z^2 z^2$, where the axial frequency $\omega_z/2\pi=978$ kHz for $^9Be^+$ when $V_0=-1.50$ kV. The radial electric fields of the trap, as well as the ion space charge, cause the ion plasma to undergo an $\mathbf{E}\times\mathbf{B}$ drift and thus rotate about the trap axis. In thermal equilibrium, this rotation is at a uniform frequency ω_r. The radial binding force of the trap is determined by the Lorentz force caused by the plasma's rotation through the magnetic field. Thus, low ω_r results in a weak radial binding and a lenticular plasma with a large radius. For 10^4 trapped ions with $\omega_r/2\pi=68.5$ kHz (typical for our work on thin planar clouds), the ion plasma has a density of 2.1×10^8 cm^{-3} with $2r_0\approx1.3$ mm and an aspect ratio $\alpha\approx0.05$. The rotation frequency was controlled by phase-locking the plasma rotation to an applied "rotating-wall" electric field.[29,30] At low ω_r, an increase in ω_r increases both the plasma density and z_0, providing a way to sensitively adjust σ_0.

The ions were cooled[3] by an axial laser beam propagating along the z axis and tuned 10 to 20 MHz lower in frequency than a hyperfine-Zeeman component of the $2s^2S_{1/2}\rightarrow2p^2P_{3/2}$ resonance at 313 nm with a natural linewidth of 19 MHz. The laser power was ~50 μW and was focused at the ion plasma to a diameter of ~0.5 mm. There was also a perpendicular cooling beam, derived from the same laser, which had a ~70 μm waist and variable power. The theoretical cooling limit is 0.5 mK, and an experimental upper bound of $T<10$ mK has been measured;[31] for a density of $n_0=2\times10^8$ cm^{-3}, these limits give a range of $160<\Gamma<3150$. A series of lenses form side- and top-view images of the ions, with viewing directions perpendicular and parallel to the magnetic field, respectively, on either a gateable charge-coupled device (CCD) camera, or on an imaging photomultiplier tube. The resolution of the optical systems is ~4 μm, while typical interparticle spacings are ~15 μm.

III. RESULTS AND ANALYSIS

A. Structure in thin planar OCPs: 1 to 5 planes

The side-view image inset in Fig. 1 shows the central region of a lenticular ion plasma with three axial lattice

TABLE I. Primitive and interlayer displacement vectors in the (x,y) plane for the observed phases, where $\hat{x} \equiv \mathbf{a}_1/|a_1|$.

Phase	Symmetry	Stacking	Lattice type	$\mathbf{a}_1$	$\mathbf{a}_2$	$\mathbf{c}_2$	$\mathbf{c}_3$
I	hexagonal	single plane		$(a, 0)$	$(a\cos 60°, a\sin 60°)$		
III	square	staggered	bcc(001)	$(a, 0)$	$(0, a)$	$(\mathbf{a}_1+\mathbf{a}_2)/2$	$(0, 0)$
IV	rhombic	staggered	bcc(110)	$(a, 0)$	$(a\cos\theta, a\sin\theta)$	$(\mathbf{a}_1+\mathbf{a}_2)/2$	$(0, 0)$
V	hexagonal	hcp-like	hcp	$(a, 0)$	$(a\cos 60°, a\sin 60°)$	$(\mathbf{a}_1+\mathbf{a}_2)/3$	$(0, 0)$
V_{fcc}	hexagonal	fcc-like	fcc(111)	$(a, 0)$	$(a\cos 60°, a\sin 60°)$	$(\mathbf{a}_1+\mathbf{a}_2)/3$	$2(\mathbf{a}_1+\mathbf{a}_2)/3$

planes. It is representative of the flatness and radial extent ($<10\%$ of r_0) of the plasma regions used to study the planar OCP. At a large radius, curvature of the planes can cause the side-view images of axial plane positions to blur. This effect was prevented in the planar measurements reported here by using clouds with sufficient amounts (up to 50%) of nonfluorescing impurity ions. Because these heavier ions are centrifugally separated to larger radii than the $^9Be^+$, the regions of the plasma where curvature begins to be significant can be filled with these ions, which are sympathetically cooled by the $^9Be^+$.[32,33]

With good alignment of the trap with the magnetic field (<1 mrad), the ion plasma rotation becomes phase-locked with the rotating-wall perturbation.[29,30] Direct images of the rotating ion structures can then be made by gating the top-view CCD camera synchronously with the rotating-wall perturbation for brief gate times ($<2\%$ of the plasma rotation period). Total exposure times of $\sim 3\times 10^4$ rotation periods were used in typical images (Fig. 2). For our study of the ion lattice structure we limited our analysis to the central region, where regular ordering of the ions was observed. At a larger radius we observed an increased blurring (due to the plasma rotation), occasional lattice distortions, and, ultimately, the transition to the regions filled by heavier ions.

The observed structure of the central crystallized region depended on the central areal density σ_0 of the plasma. Within a layer, the lattice is characterized by the primitive vectors $\mathbf{a}_1$ and $\mathbf{a}_2$ (which are observed to be equal in magnitude, $|\mathbf{a}_1|=|\mathbf{a}_2|\equiv a$), or, equivalently, by a and the angle θ ($\leqslant 90°$) between the primitive vectors. The interlayer structure is characterized by the axial positions z_n of the n lattice planes (measured by the side-view camera) and the interlayer displacement vector in the (x,y) plane $\mathbf{c}_n$ between layers 1 and n. Hence, the equilibrium (x,y) positions of ions in axial planes 1 and n are given by $\mathbf{R}_1(i,j)=i\mathbf{a}_1+j\mathbf{a}_2$ and $\mathbf{R}_n(i,j)=i\mathbf{a}_1+j\mathbf{a}_2+\mathbf{c}_n$, where i, j are integers. These variables are shown in the insets of Fig. 1.

Three different types of intralayer ordering were observed: hexagonal ($\theta=60°$), square ($\theta=90°$), and rhombic ($90°>\theta\geqslant 65°$). The square and rhombic layers stack in a staggered fashion, with the upper ions immediately above the centers of the parallelograms below, resulting in an interlayer displacement vector $\mathbf{c}_2=(\mathbf{a}_1+\mathbf{a}_2)/2$. Hexagonal layers also stack with ions above the centers of the triangles below, but this stacking can occur in two distinct ways: $3\mathbf{c}_2=\mathbf{a}_1+\mathbf{a}_2$ and $3\mathbf{c}_2/2=\mathbf{a}_1+\mathbf{a}_2$. With hcp-like stacking, the ions in every other plane lie directly above each other (*abab*...), while with fcc-like stacking, the ions in every third plane are so aligned (*abcabc*...). When there were 3 or more hexagonal layers, both types of stacking were observed.

The following sequence of phase structures, with their lattice parameters and types defined in Table I, were observed as the central areal density σ_0 was increased from where order was first observed: (I) one-layer hexagonal $\rightarrow$ (III) two-layer staggered square $\rightarrow$ (IV) two-layer staggered rhombic $\rightarrow$ (V) two-layer staggered hexagonal. At a critical density, a third layer was formed, resulting in (III) a three-layer staggered square. The process then repeated with minor variations, such as phase III becoming less common. In the labeling of the phases, we have used classifications from previous theoretical studies of quantum[20,34] and classical[16] electron bilayer systems. Phase II, which is a stable phase of the bilayer systems where the interlayer distance is fixed, is not listed here because it is unstable for the planar OCP, where this distance can vary.

We have performed an analytical calculation of the energies of these phase structures for the planar OCP. The theory uses Ewald summation techniques in order to minimize the energy of n parallel lattice planes confined in a harmonic potential of the form $\phi_e=1/2(m/e)\omega_z^2 z^2$. Because this potential is identical to the confinement potential of a Penning trap in the $\alpha\rightarrow 0$ planar limit,[35] the theory should predict the structures that are observed in the central region of the plasmas of the experiment. However, since only minimum energy states are determined, the theory provides the lattice structure only for the case of zero temperature ($\Gamma=\infty$).

The energy minimization was performed holding fixed n and the areal density σ of the ions. Consistent with the experimental observations, each lattice plane was assumed to have the same structure, consisting of a 2D lattice described by primitive vectors $\mathbf{a}_1$ and $\mathbf{a}_2$. Since the area $a_1 a_2 \sin\theta$ of the 2D primitive cell is equal to n/σ, the parameters that were varied in order to minimize the energy were a_2/a_1, θ, $\mathbf{c}_n$ and z_n. The functional form of the energy is given in Ref. 36.

There were several local minima in the energy function, corresponding to different minimum energy lattices. A numerical search was performed to find the true global minimum with respect to the parameters listed above. Finally, the search was repeated for several values of n at a given value of σ, and the value of n that provided the lowest energy was kept. The search was then repeated for a range of values of σ.

The correlation energy per particle E_{corr} (in units of $e^2/4\pi\epsilon_0 a_{ws2D}$) is shown in Fig. 3 as a function of the

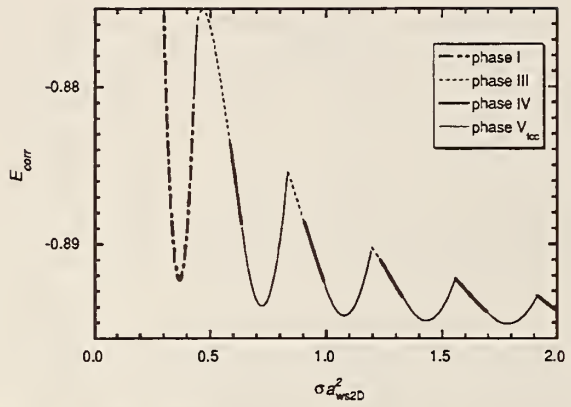

FIG. 3. The correlation energy per particle E_{corr} (in units of $e^2/4\pi\epsilon_0 a_{ws2D}$) for the minimum energy planar lattices as a function of normalized areal density.

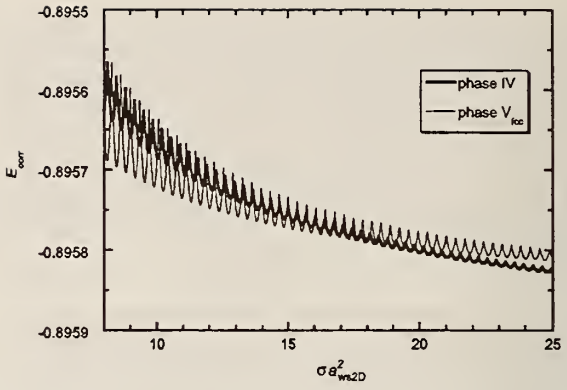

FIG. 4. The transition to the bulk bcc structure: correlation energy per particle E_{corr} for larger values of the normalized areal density.

dimensionless parameter σa_{ws2D}^2, where $a_{ws2D} = (3e^2/4\pi\epsilon_0 m\omega_z^2)^{1/3}$ is the Wigner–Seitz radius in the 2D limit. The correlation energy is the total energy of the lattice minus the energy of a uniform slab of charge with the same areal density σ. Each successive cusp in the energy function corresponds to the addition of a new lattice plane. The spacing between the planes is shown in Fig. 5(a). As σ increases, the number of lattice planes increases while the spacing between the planes is nearly constant.

The topology of the lattice planes varies as σ varies. Just as in the experiments, the minimum energy state has one of 4 separate topologies, depending on the value of σ. The structures are listed in Table I as phases I, III, IV, and V_{fcc}. In addition, there is a fifth stable phase, phase V, which has hcp-like stacking. Phase V has only a slightly higher energy than phase V_{fcc} in thin planar OCPs, and if its energy were plotted in Fig. 3 the line would overlay that of phase V_{fcc}.

The rhombic phase, phase IV, was missed in two previous publications on the minimum energy states of this system.[15,36] This is because the previous publications did not perform a full numerical minimization with respect to all of the parameters of the model. Instead, only phases I, III, V, and V_{fcc}, along with a few other symmetric phases, were considered. Although stability of these phases was checked by evaluating the normal modes of the lattices, it was not recognized that phase III becomes unstable to the rhombic phase IV deformation, since this instability was suppressed by the periodic boundary conditions. Fortunately, the energy of the rhombic phase is only slightly lower than that of phase III, so the conclusions of the previous works concerning the phase diagram of the system are only slightly altered. In particular, the maximum size of approximately 60 lattice planes required to observed bulk bcc behavior is unaffected.[37]

The transition to bulk behavior is shown in Fig. 4, which displays local minimum energy states for larger values of σ. There is a competition between the energies of the rhombic phase IV and phase V_{fcc} which implies that the lattice structure displays sensitive dependence on σ up to $\sigma a_{ws2D}^2 \sim$ 20–21, corresponding to approximately 60 lattice planes. However, beyond this range of σa_{ws2D}^2 this phase is only slightly deformed from a bcc lattice with the (110) plane oriented parallel to the surface, the deformation becoming smaller as σ increases further. This can be seen in Fig. 6 below, where the intralayer angle of the rhombic phase IV is seen to approach the bcc(110) lattice value of 70.5° as σ increases.

The predictions of the analytic planar OCP theory, which has no free parameters, were compared directly with the observations by identifying the areal density σ of the planar OCP with the directly measured central areal density σ_0 of the lenticular plasmas. For a quantitative analysis of the observed lattice structure, we performed a least-squares fit of the positions of the ions in the central region (lines in Fig. 2) to the relevant phases (shown in Table I). Using the best-fit values of the primitive vector length a and the intralayer angle θ and the observed number of lattice planes n, we calculated the central areal density $\sigma_0 = n/(a^2 \sin\theta)$.

The agreement for $n = 1$ to 5 between the planar OCP theory and experiment, with measurements taken on different plasmas with $N < 10^4$, is good (Fig. 5). This is somewhat surprising since the energy differences between competing lattices are extremely small, on the order of $10^{-2} e^2/4\pi\epsilon_0 a_{ws2D}$ per particle. As the central areal density is increased, the lattice planes move further apart axially [Fig. 5(a)]. Eventually, it becomes energetically favorable to form an additional lattice plane. However, although the phase V_{fcc} was predicted to be slightly more favorable than phase V (by energies on the order of $10^{-4} e^2/4\pi\epsilon_0 a_{ws2D}$ per particle), we rarely observed V_{fcc} ($\sim$10% of the time). These and other minor discrepancies from theory may be due to the finite radial extent or the nonzero temperature of the ion plasma; we observed a similar preference for hcp stacking in molecular dynamics simulations of small ($N = 3000$) lenticular ion plasmas with $\Gamma = 500$.

For the dependence of the angle θ (between the primitive vectors $\mathbf{a_1}$ and $\mathbf{a_2}$) on central areal density σ_0 [Fig. 5(b)], the trend was that, when a new lattice plane was formed, θ changed discontinuously from $\sim 60°$ to a higher value. As σ_0 of the crystal was further increased, θ smoothly decreased to $\sim 65°$ until there was a second discontinuous transition to a hexagonal structure. This second transition has been predicted to become continuous, with θ assuming all values $60° \leq \theta \leq 90°$, in liquid ($\Gamma < 80$) bilayer systems.[38]

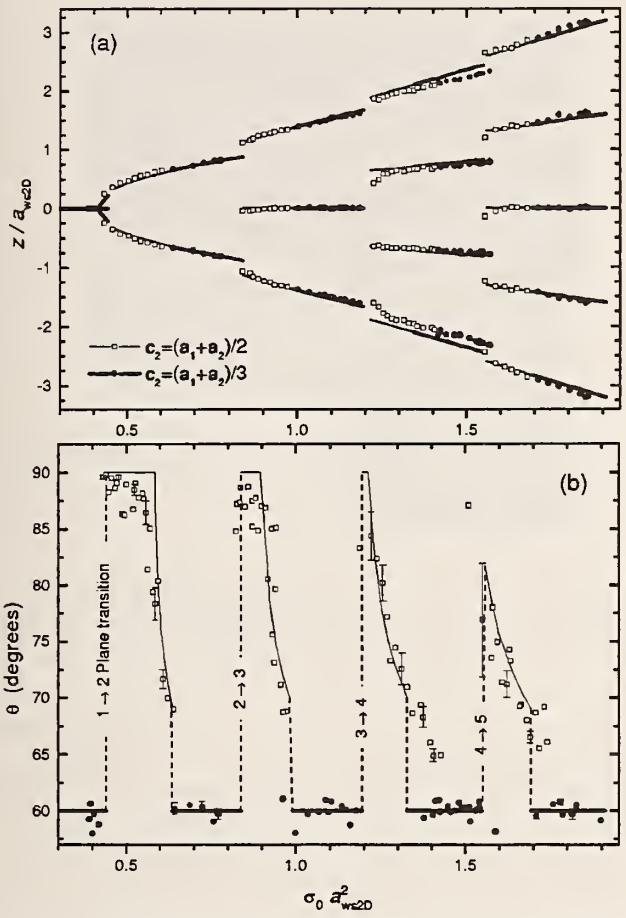

FIG. 5. (a) The interlayer structure (plane axial positions and displacement vectors) and (b) intralayer angle θ of the central region as a function of the central areal charge density. The lines show predictions from theory, and symbols show experimental measurements. Also indicated is whether the lattices have an interlattice displacement vector $\mathbf{c}_2$ characteristic of the hexagonal phases (circles, thick lines) or the square and rhombic phases (squares, thin lines). Lengths have been normalized by $a_{ws2D}=10.7\mu$m.

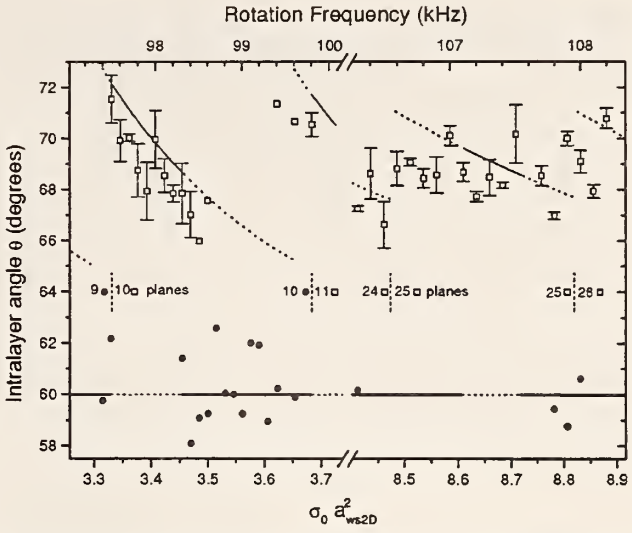

FIG. 6. Intralayer angle θ of the central region for two ion plasmas with $9\rightarrow 11$ planes (left) and $24\rightarrow 26$ planes (right). The symbols are experimental measurements as in Fig. 5, plotted versus rotation frequency. The lines are from the $T=0$ theory plotted as a function of the central areal density, with dashes indicating that the structure is not predicted to be energetically favorable. The four transitions in n used to align the two abscissas are also shown.

The lines indicate the minimum energy structures predicted by the analytic theory. At central areal charge densities near phase boundaries, both phases could be observed. In these regions, the phase which materialized after the crystal was formed was initially random, but persisted if the ions were not heated. Where there was not a strong preference for one phase over the other, both were plotted.

B. Structure in planar OCPs: 5 to 45 planes

By increasing the number of lattice planes n, we have been able to study the transition from the several plane regime where surface energy contributions are important, to one where bulk energy contributions become more important. The basic result as we increased the number of planes is that bands of alternating phase IV and phases V or V_{fcc} were observed, until ~30 planes were formed. Above this point, phase IV with θ within a few degrees of 70° and $(z_n - z_{n-1})/a$ within a few percent of 0.82 was almost exclusively seen. When $\theta=2\arctan(1/\sqrt{2})=70.53°$ and $(z_n - z_{n-1})/a=\sqrt{2/3}=0.816$, phase IV is equivalent to bcc(110) ordering, which is the predicted infinite volume ordering.

The increased axial extent of the plasmas required a modification in how the images of the structure were obtained. For plasmas with $2z_0$ greater than the depth of field of the top-view $f/2$ objective lens (~80 μm), the cooling-laser beam directed perpendicularly to **B** was used to illuminate a section of the plasma within the depth of field [see Figs. 7(b) and 8 below]. The fluorescence from the ions outside this region illuminated by the parallel beam could be made negligible by chopping the parallel beam with an optical wheel and gating the CCD camera on only when the parallel beam was blocked. This chopping technique was also occasionally used with the side-view images in order to improve their spatial resolution.

Figure 6 plots the measured and predicted intralayer angle θ of the central regions, for parameters near where the planar plasma has 10 and 25 axial lattice planes. Because the experimental uncertainties in a and θ cause the calculated σ_0 to have an unacceptably large scatter for a large number of planes, the experimental measurements have been plotted as a function of the plasma rotation frequency, which increases monotonically with σ_0. To match the observations with the theory, the range of the plotted rotation frequencies (top axis) was adjusted to make the frequencies where the $n\rightarrow n+1$ transitions shown in the figure were observed coincide with the theory predictions.

Good agreement with the analytic theory continued to be seen with 10 planes: Phases IV and V or V_{fcc} alternated as the energetically preferred structure, and the intralayer angle θ of phase IV showed the expected decrease as the central areal density of the crystal is increased. With a larger numbers of planes, however, phase IV occurred more often than

TABLE II. Incidence of phase IV (bcc-like) in planar OCPs (%).

n planes	Experiment	T=0 Theory
5	50	40
10	52	35
20	76	31
25	90	31
33	>97	26
45	>97	34
60		100

predicted (Table II). A plausible explanation for why this occurs is the ions' finite temperature. Dubin and O'Neil[38] have determined the free energy of various lattice types for the planar OCP as a function of both σ and Γ. In Fig. 9 of Ref. 37 they plot which of the two main lattices, fcc(111) and bcc(110), has the lower free energy for the regimes $200<\Gamma<5000$. They found that as Γ was decreased, the areal density above which the bcc(110) phase is exclusively favored decreases. For example, when $\Gamma=600$, bcc(110) is exclusively favored for $n>30$.

C. Shell structure in small OCPs

When the rotation frequency is increased the plasma changes shape from oblate to prolate, and the lattice planes near the plasma boundary bend in order to conform with the curvature of the boundary. The minimum energy structure at these regions consists of concentric shells, each made up of imperfect 2D hexagonal crystal sheets.[22,26] The shell curvature results in a loss of correlation between shells since the 2D lattices on different shells get out of phase as one moves along the shell surfaces.[37] With small plasmas where boundary effects are important, shell structure can be the minimum energy structure of the cloud; that is, the shell structure exists throughout the interior as well as near the plasma boundary.

Shell structure has been previously imaged in both Penning and rf trap experiments.[7,27,28] The Penning trap experiment showed differences with the simulations in that the shells were observed to be open ended cylinders (parallel to the $\hat{z}$ axis) rather than the predicted closed spheroidal shells. In order to investigate this discrepancy with the present trap, which includes the capability of taking side-view images, we returned to the geometry of the previous experiments. Figure 7 shows side- (a) and top-view (b) images of shell structure obtained on a plasma of $N=9000$ Be^+ ions and 15,000 impurity ions. Neither image was strobed with the rotating-wall perturbation.

In Fig. 7(a) the parallel beam was chopped at 1 kHz, and the side-view camera was gated on only when the parallel beam was gated off. The perpendicular laser beam was then translated up and down throughout the plasma, and the resultant ion fluorescence was integrated over many translations of the beam, producing a slice of the shell structure cutting through the plasma near the $r=0$ axis. The viewing optics are at 60° with respect to the perpendicular beam [Fig. 7(c)], which, along with the small offset of the beam from the $r=0$ axis, produced an image with the shell structure well defined on the right hand side of Fig. 7(a). In Fig. 7(b)

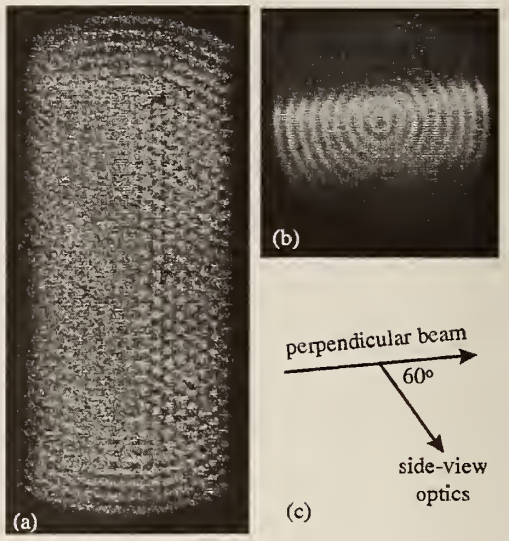

FIG. 7. Side-view (a) and topview (b) images of an ion cloud with rotation frequency $\omega_r=2\pi\times$ 63 kHz confined into a cylindrical shape due to the presence of centrifugally separated, heavier impurity ions. The viewing angle of the side-view optics is shown (top-view) in (c).

the perpendicular laser beam was held fixed near the central ($z=0$) section of the plasma and the ion fluorescence produced by both the parallel and perpendicular laser beams were integrated on the top-view camera. However, because the camera was also focused on the central section of the plasma, this figure essentially shows a cross section of the shell structure near $z=0$.

The ion plasma of Fig. 7 had 9 shells of $^9Be^+$ ions that were cylindrical near the middle ($z=0$) section of the plasma. The cylindrical shells were produced by the presence of heavier mass contaminant ions, which centrifugally separated and produced a cylindrical boundary to the lighter Be^+ ions. Figure 7(a) shows a resolved spatial structure in the axial direction and Fig. 7(b) in the radial directions. However, in agreement with the simulations, the cylindrical shells are not open ended, but are closed by a curved shell structure. The curvature of the shells near the ends of the plasma was also observed in top-view images like Fig. 7(b) when the perpendicular laser beam was directed near an axial end of the plasma. The reason for the frequent observation of open-ended cylindrical shells in the earlier Penning trap experiments is unknown, as we were not able to produce open-ended cylindrical shells in this work. For example, misaligning the trap symmetry axis with the magnetic field by up to 0.3 mrad had no apparent effect on the shell structure.

D. Crystal structure in large OCPs

The formation of a structure in spherical plasmas with many ions has been studied experimentally using Bragg diffraction.[4,5] Long-range order (3D periodic crystallization) was found to emerge in plasmas with $N>50\,000$ ions (radius $r_0\approx 37a_{ws}$). Bulk behavior (bcc crystals exclusively) was observed in plasmas with $N>270\,000$ ($r_0\approx 60a_{ws}$), and lower limits to the crystal diameters of 17 and $28a_{ws}$ were

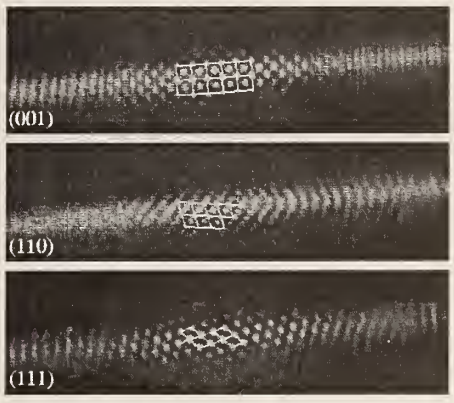

FIG. 8. Top-view images of a spherical cloud with 100 000 Be^+ ions and 60 000 impurity ions, with lines showing a fit to the bcc lattice structure with the indicated orientation. The length of the perpendicular beam in the image is $60a_{ws}$ and the axial extent is $8a_{ws}$, where $a_{ws} = 8.7$ μm.

estimated from the widths and intensities of the Bragg peaks, respectively. Theoretically, simulations have been limited in size to a 20 000 ion spherical plasma, in which was found only short range order in the form of approximately 20 spherical shells.[39]

We have used top-view images, strobed by the rotating-wall perturbation, of a large ion cloud to further investigate the structure in this regime. Of this cloud's 160 000 ions, $\sim$100 000 were $^9Be^+$ ions with a radius of $\sim 35a_{ws}$. Figure 8 shows examples of such images, along with lines showing a fit to a bcc lattice structure. Both a bcc and fcc structure were observed, with bcc occurring $\sim$70% of the time. A variety of orientations were observed, but these were usually consistent with viewing along a symmetry axis of the crystal. Evidence for preferred orientations has been previously noted.[5]

The region with the strongest regular order of individual ions was found to be a cylinder along the $r=0$ axis of the plasma. A typical diameter was $\sim 16a_{ws}$, and it extended axially throughout the sphere until significant curvature of the end planes was encountered. The transition from a crystal structure to concentric shells was not abrupt, as can be seen in Fig. 8, where the structure observed out to $r=30a_{ws}$ from the center is not regularly spaced.

IV. DISCUSSION

We have measured the correlations of strongly coupled $^9Be^+$ ion plasmas in a variety of different geometries with direct observations. The planar geometry, in particular, permits a detailed comparison with theoretical calculations, and, in general, the agreement between the observations and theory is good. We have measured the energetically preferred structures in lenticular plasmas for up to 45 lattice planes and find a gradual transition from surface-dominated to bulk behavior to occur when the ion plasma extends $\sim$30 planes axially.

Ions in a trap have been proposed as a register for a quantum computer.[40] Work in this area has focused on a string of a few ions in a linear Paul trap.[41] A single lattice plane of ions as shown in Fig. 2 could provide an alternative 2D geometry of trapped ions for studies of quantum computing or entangled quantum states.

In an approximately spherical plasma of 160 000 ions, we have observed 3D periodic crystals with long-range order. The crystals occupied the inner cylindrical core of the plasma, and outside the crystal there was a complicated transition to the shell structure. We have not observed the thermodynamic liquid–solid phase transition predicted for the bulk OCP, as our measurements have concentrated on the correlations obtained at the coldest temperatures (therefore maximum Γ) where the ion fluorescence is maximum. The study of this phase transition in the bulk and 2D geometries is an interesting direction for future studies with this system.

ACKNOWLEDGMENTS

This research was supported by the Office of Naval Research and the National Science Foundation (D. H. E. D.). We thank B. E. King, L. B. King, and D. J. Wineland for useful comments, and B. M. Jelenković and J. N. Tan for technical assistance. This manuscript is a work of the U.S. government; it is not subject to U.S. copyright.

[1] H. M. Van Horn, Science **252**, 384 (1991).
[2] C. C. Grimes and G. Adams, Phys. Rev. Lett. **42**, 795 (1979).
[3] D. J. Wineland, R. E. Drullinger, and F. L. Walls, Phys. Rev. Lett. **40**, 1639 (1978).
[4] J. N. Tan, J. J. Bollinger, B. Jelenković, and D. J. Wineland, Phys. Rev. Lett. **75**, 4198 (1995).
[5] W. M. Itano, J. J. Bollinger, J. N. Tan, B. Jelenković, X.-P. Huang, and D. J. Wineland, Science **279**, 686 (1998).
[6] I. Waki, S. Kassner, G. Birkl, and H. Walther, Phys. Rev. Lett. 68, 2007 (1992).
[7] G. Birkl, S. Kassner, and H. Walther, Nature (London) **357**, 310 (1992).
[8] T. B. Mitchell, J. J. Bollinger, D. H. E. Dubin, X.-P. Huang, W. M. Itano, and R. H. Baughman, Science **282**, 1290 (1998).
[9] P. K. Ghosh, *Ion Traps* (Clarendon, Oxford, 1995).
[10] *Non-Neutral Plasma Physics*, edited by C. W. Roberson and C. F. Driscoll (American Institute of Physics, New York, 1988).
[11] S. Ichimaru, H. Iyetomi, and S. Tanaka, Phys. Rep. **149**, 91 (1987).
[12] G. S. Stringfellow and H. E. DeWitt, Phys. Rev. A **41**, 1105 (1990).
[13] D. H. E. Dubin, Phys. Rev. A **42**, 4972 (1990).
[14] J. P. Schiffer, Phys. Rev. Lett. **70**, 818 (1993).
[15] D. H. E. Dubin, Phys. Rev. Lett. **71**, 2753 (1993).
[16] G. Goldoni and F. M. Peeters, Phys. Rev. B **53**, 4591 (1996).
[17] J. B. Pieper, J. Goree, and R. A. Quinn, J. Vac. Sci. Technol. A **14**, 519 (1996).
[18] H. Totsuji, T. Kishimoto, and C. Totsuji, Phys. Rev. Lett. **78**, 3113 (1997).
[19] D. H. Van Winkle and C. A. Murray, Phys. Rev. A **34**, 562 (1986).
[20] S. Narasimhan and T.-L. Ho, Phys. Rev. B **52**, 12291 (1995).
[21] M. Schmidt and H. Löwen, Phys. Rev. E **55**, 7228 (1997).
[22] A. Rahman and J. P. Schiffer, Phys. Rev. Lett. **57**, 1133 (1986).
[23] R. Rafac, J. P. Schiffer, J. S. Hangst, D. H. E. Dubin, and D. J. Wales, Proc. Natl. Acad. Sci. USA **88**, 483 (1991).
[24] F. Diedrich, E. Peik, J. M. Chen, W. Quint, and H. Walther, Phys. Rev. Lett. **59**, 2931 (1987).
[25] D. J. Wineland, J. C. Bergquist, W. M. Itano, J. J. Bollinger, and C. H. Manney, Phys. Rev. Lett. **59**, 2935 (1987).
[26] D. H. E. Dubin and T. M. O'Neil, Phys. Rev. Lett. **60**, 511 (1988).
[27] S. L. Gilbert, J. J. Bollinger, and D. J. Wineland, Phys. Rev. Lett. **60**, 2022 (1988).
[28] M. Drewsen, C. Brodersen, L. Hornekaer, J. S. Hangst, and J. P. Schiffer, Phys. Rev. Lett. **81**, 2878 (1998).
[29] X.-P. Huang, J. J. Bollinger, T. B. Mitchell, and W. M. Itano, Phys. Rev. Lett. **80**, 73 (1998).

[30]X.-P. Huang, J. J. Bollinger, T. B. Mitchell, and W. M. Itano, Phys. Plasmas **5**, 1656 (1998).
[31]L. R. Brewer, J. D. Prestage, J. J. Bollinger, W. M. Itano, D. J. Larson, and D. J. Wineland, Phys. Rev. A **38**, 859 (1988).
[32]T. M. O'Neil, Phys. Fluids **24**, 1447 (1981).
[33]D. J. Larson, J. C. Bergquist, J. J. Bollinger, W. M. Itano, and D. J. Wineland, Phys. Rev. Lett. **57**, 70 (1986).
[34]G. Goldoni and F. M. Peeters, Europhys. Lett. **37**, 293 (1997).
[35]T. M. O'Neil and D. H. Dubin, Phys. Plasmas **5**, 2163 (1998).
[36]D. H. E. Dubin, Phys. Rev. A **40**, 1140 (1989).
[37]D. H. E. Dubin and T. M. O'Neil, in *Strongly Coupled Plasma Physics*, edited by S. Ichimaru (Elsevier/Yamada, Osaka, 1990), p. 189.
[38]V. I. Valtchinov, G. Kalman, and K. B. Blagoev, Phys. Rev. E **56**, 4351 (1997).
[39]J. P. Schiffer, in *Non-Neutral Plasma Physics II*, edited by J. Fajans and D. H. E. Dubin (American Institute of Physics, New York, 1995), p. 191.
[40]J. I. Cirac and P. Zoller, Phys. Rev. Lett. **74**, 4091 (1995).
[41]D. J. Wineland, C. Monroe, W. M. Itano, D. Leibfried, B. King, and D. M. Meekhof, J. Res. Natl. Inst. Stand. Technol. **103**, 259 (1998).

SPECIAL TOPICS SECTION

Crystalline order in laser-cooled, non-neutral ion plasmas

J. J. Bollinger, T. B. Mitchell, X.-P. Huang, W. M. Itano, J. N. Tan,[a)]
B. M. Jelenković,[b)] and D. J. Wineland
Time and Frequency Division, National Institute of Standards and Technology, Boulder, Colorado 80303

(Received 17 May 1999; accepted 25 May 1999)

Laser-cooled trapped ions can be strongly coupled and form crystalline states. In this paper we review experimental studies that measure the spatial correlations of Be^+ ion crystals formed in Penning traps. Both Bragg scattering of the cooling-laser light and spatial imaging of the laser-induced ion fluorescence are used to measure these correlations. In spherical plasmas with more than 2×10^5 ions, body-centered-cubic (bcc) crystals, the predicted bulk structure, are the only type of crystals observed. The orientation of the ion crystals can be phase locked to a rotating electric-field perturbation. With this "rotating wall" technique and stroboscopic detection, images of individual ions in a Penning trap are obtained. The rotating wall technique also provides a precise control of the time-dilation shift due to the plasma rotation, which is important for Penning trap frequency standards. [S1070-664X(00)01501-9]

I. INTRODUCTION

In this paper we review recent progress on the study of strongly coupled ion plasmas in Penning traps. It is similar to the review in the conference proceedings of Ref. 1 and contains more background material on Bragg scattering results than Ref. 2, which focuses on results obtained from real images of the ion crystals.

Trapped ions are a good example of a one-component plasma (OCP). A OCP consists of a single charged species immersed in a neutralizing background.[3] In an ion trap, the trapping fields provide the neutralizing background.[4] Examples of OCPs include such diverse systems as the outer crust of neutron stars[5] and electrons on the surface of liquid helium.[6] The thermodynamic properties of the classical OCP of infinite spatial extent are determined by its Coulomb coupling constant,[3]

$$\Gamma \equiv \frac{1}{4\pi\epsilon_o}\frac{e^2}{a_{\mathrm{WS}}k_{\mathrm{B}}T}, \tag{1}$$

which is a measure of the ratio of the Coulomb potential energy of nearest neighbor ions to the kinetic energy per ion. Here, ϵ_0 is the permittivity of the vacuum, e is the charge of an ion, k_{B} is Boltzmann's constant, T is the temperature, and a_{WS} is the Wigner–Seitz radius, defined by $4\pi(a_{\mathrm{WS}})^3/3 = 1/n_0$, where n_0 is the ion density. For low-temperature ions in a trap, n_0 equals the equivalent neutralizing background density provided by the trapping fields. Plasmas with $\Gamma>1$ are called strongly coupled. The onset of fluid-like behavior is predicted at $\Gamma\approx2$,[3] and a phase transition to a body-centered-cubic (bcc) lattice is predicted at $\Gamma\approx170$.[3,7] From a theoretical perspective, the strongly coupled OCP has been used as a paradigm for condensed matter for decades. However, only recently has it been realized in the laboratory.[8]

Experimentally, freezing of small numbers ($N<50$) of laser-cooled atomic ions into Coulomb clusters was first observed in Paul traps.[9–11] With larger numbers of trapped ions, concentric shell structures were observed directly in Penning[12] and linear Paul[13,14] traps. The linear Paul traps provided strong confinement in the two dimensions perpendicular to the trap axis and very weak confinement along the trap axis. This resulted in cylindrically shaped plasmas whose axial lengths are large compared to their cylindrical diameters. Cylindrical-shell crystals that are periodic with distance along the trap axis were observed. The diameter of these crystals was limited to $\sim10a_{\mathrm{WS}}$ in Ref. 13 and $\sim30a_{\mathrm{WS}}$ in Ref. 14, presumably due to rf heating,[15] which is produced by the time-dependent trapping fields and increases with the plasma diameter. These plasma diameters appear to be too small to observe the three-dimensional (3-D) periodic crystals predicted for the infinite, strongly coupled OCP. Strong coupling and crystallization have also been observed with particles interacting through a screened Coulomb potential. Examples include dusty plasma crystals[16] and colloidal suspensions.[17,18]

Because Penning traps use static fields to confine charged particles, there is no rf heating. This has enabled ion plasmas that are large in all three dimensions to be laser cooled. For example, we have laser cooled $\sim10^6Be^+$ ions in an approximately spherical plasma with diameter $\sim200a_{\mathrm{WS}}$. With these large ion plasmas we have used Bragg scattering of the cooling laser light to detect the formation of bcc crystals,[19,20] the predicted state for a bulk OCP with $\Gamma>170$. In addition, we have studied the spatial correlations in

[a)]Present address: Department of Physics, Harvard University, Cambridge, Massachusetts 02138.
[b)]On leave from the Institute of Physics, University of Belgrade, Belgrade, Yugoslavia.

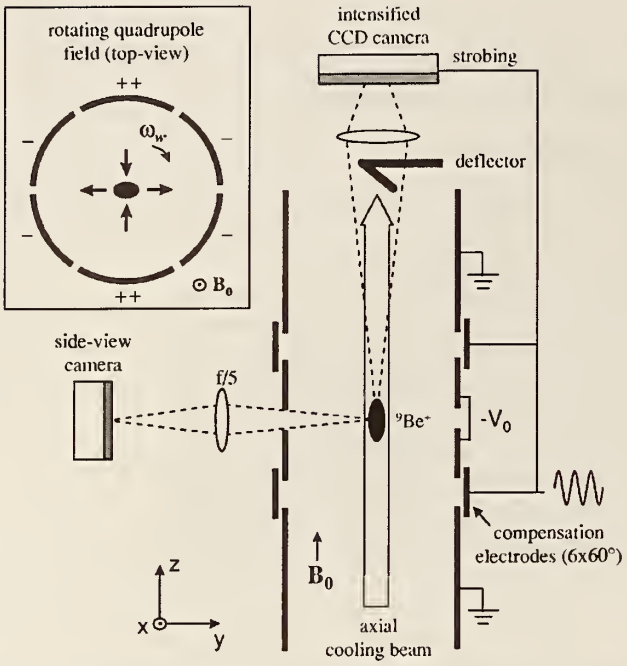

FIG. 1. Schematic view of the cylindrical trap with real space imaging optics for the side-view camera and Bragg diffraction detection system for the axial cooling beam. The size of the plasma is exaggerated. The cross section of the rotating quadrupole field (in the x-y plane) is shown in the insert. From Ref. 21.

planar, lens-shaped plasmas with axial thickness $\lesssim 10a_{WS}$. These plasmas consist of extended, two dimensionally periodic lattice planes. The importance of the plasma boundary in this case results in different crystalline structures depending on the details of the plasma shape.

A potential drawback of the Penning trap versus the rf trap is that the ions rotate about the trap magnetic field, and this has previously prevented the imaging of the ion crystals as done in Paul traps. This is because the rotation, created by the $\mathbf{E} \times \mathbf{B}$ drift due to the radial electric and the trap magnetic fields is, in general, not stable. For example, fluctuations in the plasma density or shape produce fluctuations in the ion space charge fields that change the plasma rotation. However, we are able to phase lock the rotation of the laser-cooled ion crystals to a rotating electric field perturbation.[21,22] The success of this "rotating wall" technique enables us to strobe the cameras recording the ion fluorescence synchronously with the plasma rotation and obtain images of individual ions in the plasma crystals.[23]

Figure 1 is a schematic of the cylindrical Penning trap we use to confine $^9Be^+$ ions. The trap consists of a 127 mm long vertical stack of cylindrical electrodes with an inner diameter of 40.6 mm, enclosed in a room temperature, 10^{-8} Pa vacuum chamber. The uniform magnetic field $\mathbf{B}_0 = 4.46$ T is aligned parallel to the trap axis within 0.01° and produces a $^9Be^+$ cyclotron frequency $\Omega = 2\pi \times 7.61$ MHz. A quadratic, axially symmetric potential $(m\omega_z^2/2e)(z^2 - r^2/2)$ is generated near the trap center by biasing the central electrodes to a negative voltage $-V_0$. At $V_0 = 1$ kV, the single-particle axial frequency $\omega_z = 2\pi \times 799$ kHz and the magnetron $\mathbf{E} \times \mathbf{B}$ drift frequency $\omega_m = 2\pi \times 42.2$ kHz. The trapped Be^+ ions are Doppler laser cooled by two 313 nm laser beams. The principal cooling beam (waist diameter ~0.5 mm, power ~50 μW) is directed parallel to $\mathbf{B}_0$. A second, typically weaker cooling beam with a much smaller waist (~0.08 mm) is directed perpendicularly to $\mathbf{B}_0$ (not shown in Fig. 1). This beam can also be used to vary the plasma rotation frequency by applying a torque with radiation pressure. With this configuration, ion temperatures close to the 0.5 mK Doppler laser-cooling limit are presumably achieved. However, experimentally we have only placed a rough 10 mK upper bound on the ion temperature.[24] For a typical value of $n_0 = 4 \times 10^8$ cm^{-3}, this implies $\Gamma > 200$.

Two types of imaging detectors were used. One is a charge-coupled device (CCD) camera coupled to an electronically gatable image intensifier. The other is an imaging photomultiplier tube based on a microchannel-plate electron multiplier and a multielectrode resistive anode for position sensing. For each detected photon, the position coordinates are derived from the current pulses collected by the different electrodes attached to the resistive anode. This camera therefore provides the position and time of each detected photon. However, in order to avoid saturation, we placed up to 20 dB of attenuation in front of this camera to lower the detected photon counting rate to less than ~300 kHz.

In thermal equilibrium, the trapped ion plasma rotates without shear at a frequency ω_r where $\omega_m < \omega_r < \Omega - \omega_m$.[25,26] For the low-temperature work described here, the ion density is constant and given by $n_0 = 2\epsilon_0 m\omega_r(\Omega - \omega_r)/e^2$. With a quadratic trapping potential the plasma has the simple shape of a spheroid, $z^2/z_0^2 + r^2/r_0^2 = 1$, where the aspect ratio $\alpha \equiv z_0/r_0$ depends on ω_r.[24,26] This is because the radial binding force of the trap is determined by the Lorentz force due to the plasma's rotation through the magnetic field. Thus low ω_r results in a lenticular plasma (an oblate spheroid) with a large radius. As ω_r increases, r_0 shrinks and z_0 grows, resulting in an increasing α. However, large $\omega_r (\omega_r > \Omega/2)$ produces a large centrifugal acceleration that opposes the Lorentz force and lenticular plasmas are once again obtained for $\omega_r \sim \Omega - \omega_m$. In our work, torques from a laser or a rotating electric field are used to control ω_r, and therefore the plasma density and shape. The plasma shape is observed by imaging the ion fluorescence scattered perpendicularly to $\mathbf{B}_0$ with an $f/5$ objective. (See Fig. 1.) All possible values of ω_r from ω_m to $\Omega - \omega_m$ have been accessed using both methods of applying a torque.[22,27,28] Azimuthally segmented compensation electrodes located between the main trap electrodes are used to apply the rotating electric-field perturbation. Both a rotating quadrupole (see the inset in Fig. 1) and rotating dipole field (not shown in Fig. 1) have been used to control ω_r. Below we explain how the rotating quadrupole field provides precise control of ω_r.

II. BRAGG SCATTERING

A. BCC crystals

An infinite OCP with $\Gamma \gtrsim 170$ is predicted to form a bcc lattice. However, the bulk energies per ion of the face-

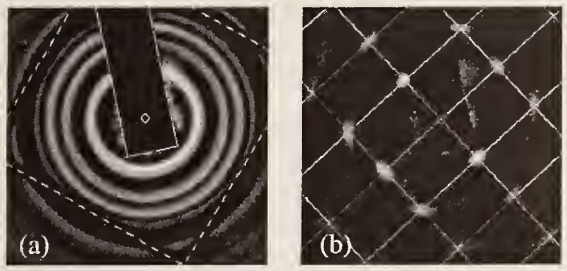

FIG. 2. Bragg diffraction patterns from a plasma phase locked to a rotating quadrupole field ($\omega_r = 2\pi \times 140$ kHz, $n_0 \approx 4.26 \times 10^8$ cm^{-3}, $\alpha \approx 1.1$). (a) A 1 s time-averaged pattern. The long rectangular shadow (highlighted by solid lines) is from the deflector for the incident beam; four line shadows (highlighted by dashed lines) that form a square are due to a wire mesh at the exit window of the vacuum chamber. The small open circle near the center of the figure marks the position of the undeflected laser beam. (b) Time-resolved pattern obtained nearly simultaneously with (a) by strobing the camera with the rotating field (integration time ≈5 s). A spot is predicted at each intersection of the rectangular grid lines for a bcc crystal with a [110] axis aligned with the laser beam. The grid spacings were determined from the n_0 calculated from ω_r and are not fitted. From Ref. 22.

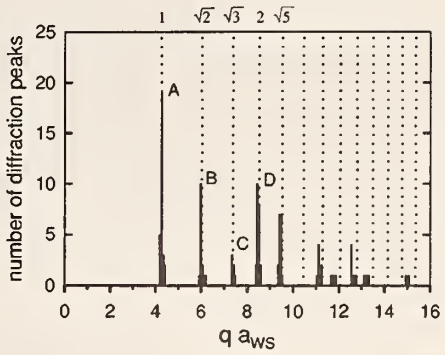

FIG. 3. Histogram showing the numbers of peaks (not intensities) observed as a function of $q \cdot a_{WS}$ (defined in the text) for 30 time-averaged Bragg scattering patterns obtained on two different spherical plasmas with $N > 2 \times 10^5$. The dotted lines show the expected peak positions for a bcc crystal, normalized to the center of gravity of the peak at A (corresponding to Bragg reflections off {110} planes). From Ref. 20.

centered-cubic (fcc) and hexagonal-close-packed (hcp) lattices differ very little from bcc ($<10^{-4}$).[29] Because some of the fcc and hcp planes have lower surface energies than any of the bcc planes, a boundary can have a strong effect on the preferred lattice structure. One calculation[29] estimates that the plasma may need to be $\gtrsim 100 a_{WS}$ across its smallest dimension to exhibit bulk behavior. For a spherical plasma this corresponds to $\sim 10^5$ ions.

We used Bragg scattering to measure the spatial correlations of approximately spherical plasmas with $N > 2 \times 10^5$ trapped Be^+ ions.[19,20] The cooling-laser beam directed along the trap axis was used for Bragg scattering, as indicated in Fig. 1. First the plasma shape was set to be approximately spherical. (In early experiments this was done with the perpendicular laser beam; more recent experiments used the rotating wall.) The parallel laser beam was then tuned approximately half a linewidth below resonance, and a Bragg scattering pattern recorded (~1–30 s integration). The plasma was then heated and recooled, and another Bragg scattering pattern was recorded. Because the 313 nm wavelength of the cooling laser is small compared to the interion separation (~10–20 μm), Bragg scattering occurs in the forward (few degree) scattering direction. In order for a diffracted beam to form, the incident and scattered wave vectors $\mathbf{k}_i$ and $\mathbf{k}_s$ must differ by a reciprocal lattice vector (Laue condition).[30] In a typical x-ray crystal diffraction case, satisfying the Laue condition for many reciprocal lattice vectors, requires that the incident radiation have a continuous range of wavelengths. Here the Laue condition is relaxed because of the small size of the crystal, so a crystalline Bragg diffraction pattern is frequently obtained, even with monochromatic radiation.

Figure 2(a) shows a time-averaged diffraction pattern obtained on a spherical plasma with $N \sim 7.5 \times 10^5$. The multiple concentric rings are due to Bragg scattering off different planes of a crystal. A concentric ring rather than a dot pattern is observed because the crystal was rotating about the laser beam. In general, many different patterns were observed, corresponding to Bragg scattering off crystals with different orientations. Figure 3 summarizes the analysis of approximately 30 time-averaged patterns obtained on two different spherical plasmas with $N > 2 \times 10^5$. It shows the number of Bragg peaks as a function of the momentum transfer $q = |\mathbf{k}_s - \mathbf{k}_i| = 2k \sin(\theta_{scatt}/2)$ ($\simeq k\theta_{scatt}$ for $\theta_{scatt} \ll 1$), where $k = 2\pi/\lambda$ is the laser wave number and θ_{scatt} is the scattering angle. The density dependence of the Bragg peak positions is removed by multiplying q by a_{WS}, which was determined from ω_r. The positions of the peaks agree with those calculated for a bcc lattice, within the 2.5% uncertainty of the angular calibration. They disagree by about 10% with the values calculated for a fcc lattice. The ratios of the peak positions of the first five peaks agree to within about 1% with the calculated ratios for a bcc lattice. This provides strong evidence for the formation of bcc crystals in spherical plasmas with $N > 2 \times 10^5$ ions. This result is significant because it is the first evidence for bulk behavior in a strongly coupled OCP in the laboratory.

B. Rotating wall

By strobing the camera recording the Bragg scattering pattern synchronously with the plasma rotation, we should be able to recover a dot pattern from the time-averaged concentric ring pattern in Fig. 2(a). Initially we used the time dependence of the Bragg scattered light to sense the phase of the plasma rotation.[20,31] More recently we used a rotating electric field perturbation to phase lock the ion plasma rotation.[21,22]

Consider the rotating quadrupolar perturbation shown in the inset of Fig. 1. This z-independent perturbation produces a small distortion in the shape of the spheroidal plasma. In particular, the plasma acquires a small elliptical cross section normal to the z axis. (In our work the distortion created by the rotating quadrupole field was typically less than 1% of the plasma diameter.) The elliptical boundary rotates at the applied rotating wall frequency ω_w. An ion near the plasma boundary experiences a torque due to this rotating boundary. If the ion is rotating slower than ω_w, the torque will speed it up. If it is rotating faster than ω_w, the torque will slow it

down. Through viscous effects, this torque is transmitted to the plasma interior. Therefore, if other external torques are small, the rotating wall perturbation will make ω_r equal ω_w. Crystallized plasmas behave more like a solid than a liquid or gas. Because the viscosity is high, the whole plasma will tend to rotate rigidly with its boundary. In particular, the orientation of the ion crystals can phase-lock to the rotating quadrupolar perturbation if the frequency difference between ω_r and ω_w is small.

To check for phase-locked control of ω_r, we strobed the camera recording the Bragg scattering pattern in Fig. 2(a) with the synthesizer used to generate the rotating wall signal. Specifically, once each $2\pi/\omega_w$ period, the rotating wall signal gated the camera on for a period $\lesssim 0.02(2\pi/\omega_w)$. The resulting Laue dot pattern in Fig. 2(b) shows that the plasma rotation was phase locked to the rotating electric-field perturbation. The dot pattern provides detailed information on the number and orientation of the crystals that contributed to the Bragg scattering signal. For example, the pattern in Fig. 2(b) was due to a single bcc crystal with a [110] axis aligned along the laser beam. For phase-locked operation of the rotating wall, other external torques must be small. For example, a misalignment of the trap magnetic field with the trap electrode symmetry axis of $>0.01°$ prevented phase-locked control of the plasma rotation. In our work, alignment to $\lesssim 0.003°$ was obtained by minimizing the excitation of zero-frequency plasma modes.[27,28]

In addition to the rotating quadrupole perturbation, phase-locked control was also achieved with a uniform rotating electric field (a "dipole" field). In fact, under many circumstances a uniform oscillating field worked equally well. In these cases the corotating component of the oscillating field controlled the plasma rotation while the perturbing effects due to the counter-rotating component were minimal. The simplicity of the oscillating dipole field makes it a convenient tool for controlling ω_r. However, in a quadratic trap, control of ω_r with a uniform rotating or oscillating electric field requires an effect that breaks the separation of center-of-mass and internal degrees of freedom of the plasma. In our work this is done by impurity ions that experience a different centrifugal potential than the $^9Be^+$ions.[22]

III. REAL-SPACE IMAGES

Bragg scattering measures the Fourier transform of the spatial correlations of the trapped ions. It provides a picture of these correlations in reciprocal-lattice space. With phase-locked control of ω_r, real-space imaging of individual ions in a Penning trap becomes possible. To obtain real-space images with high resolution, we replaced the Bragg scattering optics (see Fig. 1) with imaging optics, starting with an $f/2$ objective, which formed a real, top-view image of the ion plasma. The combined resolution limit of the optics and camera was less than 5 μm near the optimal object plane of the $f/2$ objective. This is less than the ~ 10 μm resolution limit required to resolve individual ions. However, the depth of field of an $f/2$ objective for 10 μm resolution is ~ 80 μm. For lenticular plasmas with $2z_0 \lesssim 80\,\mu$m, all of the ions within the plasma were resolvable. For plasmas with $2z_0 > 80\,\mu$m. the cooling-laser beam directed perpendicularly to $\mathbf{B_0}$ was used to illuminate a section of the plasma within the depth of field.

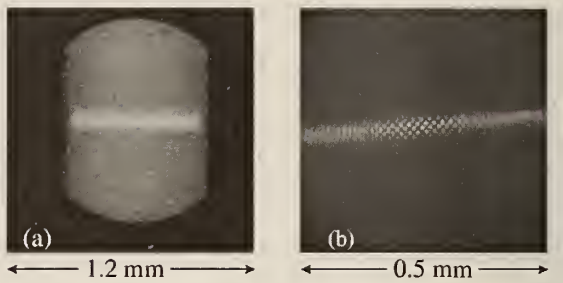

FIG. 4. Real-space images of an $N \sim 1.8 \times 10^5$ ion plasma phase locked with an oscillating dipole field at $\omega_r = 2\pi \times 120$ kHz. (a) Time-averaged side-view image showing the overall plasma shape. The bright line of fluorescence through the plasma center is due to a laser beam directed perpendicularly to $\mathbf{B_0}$. The plasma shape is approximately spherical. The presence of heavier-mass ions, which centrifugally separate from the $^9Be^+$ ions, produces the straight vertical boundaries in the image. (b) Strobed top-view image, obtained simultaneously with (a), showing the presence of a bcc crystal in the plasma center. The distance scales in (a) and (b) are different, as noted.

Figure 4 shows side-view and top-view images of an approximately spherical plasma with $N \sim 1.8 \times 10^5$. The fluorescence from the perpendicular laser beam used to highlight a small region of the plasma is clearly visible. In the top-view image, a square grid of dots is observed near the plasma center. The measured spacing between nearest neighbor dots is 12.8 ± 0.3 μm, in good agreement with the 12.5 μm spacing expected for viewing along a [100] axis of a bcc crystal with density determined by the ω_r set by the rotating field. Real-space imaging provides direct information on the location and size of the crystals. In Fig. 4 the crystal was located in the radial center of the plasma and was at least 230 μm across, or at least one-quarter of the plasma diameter.

For lenticular plasmas with $2z_0 \lesssim 80\,\mu$m, all of the ions within the plasma are resolved without the use of the perpendicular laser beam. Lenticular plasmas are obtained with ω_r slightly greater than ω_m. For small plasmas ($N \lesssim 2000$ ions) we were able to use the rotating-dipole electric field to lower ω_r and obtain a single plane while maintaining long-range order in the top-view images. Figure 5(a) shows a

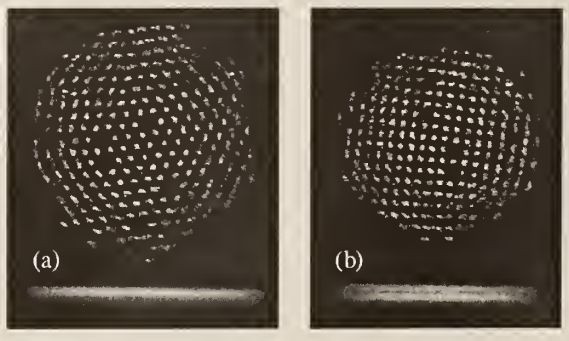

FIG. 5. Strobed top-view images of a small ($N \sim 300$) Be^+ ion plasma phase-locked with a rotating dipole field at (a) $\omega_r = 2\pi \times 65.7$ kHz and (b) 66.5 kHz. Below are unstrobed side views showing the axial lattice planes. Heavier-mass ions are located outside the $^9Be^+$ ions.

top- and side-view image of such a plasma. Near the plasma center a 2-D hexagonal lattice is observed, the preferred lattice for a 2-D system. Here each dot is the image of an individual ion.

Starting with a single plane like that shown in Fig. 5(a), we studied the structural phase transitions that occur as ω_r is increased.[23] With increasing ω_r, the radial confining force of the Penning trap increases, which decreases r_0. At a particular point, there is a structural phase transition near the plasma center from a single, hexagonal lattice plane to two lattice planes where the ions form a square grid in each plane, as shown in Fig. 5(b). Further increases in ω_r increase the number of ions per unit area of each plane as well as the spacing between the planes. During this process the square lattice planes smoothly change into rhombic lattice planes and eventually there is a sudden transition to hexagonal lattice planes. Further increases in ω_r eventually produce a structural transition to three square lattice planes, and the basic pattern repeats.

The structure of the crystallized ions depends sensitively on the projected areal density σ of the plasma. The side- and top-view images were analyzed to characterize the phase structure. Within a layer, the structural order is characterized by the primitive vectors $\mathbf{a}_1$ and $\mathbf{a}_2$ (which are observed to be equal in magnitude) and the angle θ ($\leqslant 90°$) between them. The interlayer order is characterized by the axial positions z_n of the n lattice planes (measured by the side-view camera) and the interlayer displacement vector $\mathbf{c}_n$ between layers 1 and n. Hence, the equilibrium positions in the (x,y) plane of ions in axial planes 1 and n are given by $\mathbf{R}_1 = i\mathbf{a}_1 + j\mathbf{a}_2$ and $\mathbf{R}_n = i\mathbf{a}_1 + j\mathbf{a}_2 + \mathbf{c}_n$, where i,j are integers. Three different types of intralayer ordering are observed: hexagonal ($\theta = 60°$), square ($\theta = 90°$), and rhombic ($90° > \theta \geqslant 65°$). The observations were compared to the results from Dubin,[23] who performed an analytic calculation of the energies of lattice planes that are infinite and homogeneous in the (x,y) direction but are confined in the axial direction by a harmonic external electrostatic confinement potential, $\phi_e = 1/2(m/e)\omega_z^2 z^2$. Since this potential is identical to the confinement potential of a Penning trap, as seen in the rotating frame in the $\alpha \to 0$ planar limit, the minimum energy phase structures predicted by the theory should match the structures observed in the central regions of the oblate plasmas of the experiments.

Figure 6 displays the agreement between theory and experiment for the interlayer quantities, with measurements taken on different plasmas with $N < 10^4$. Lengths have been normalized by $a_{\mathrm{WS2\text{-}D}} = (3e^2/4\pi\epsilon_0 m\omega_z^2)^{1/3} = 10.7\ \mu\mathrm{m}$, which is the Wigner–Seitz radius in the planar limit. As the central areal density is increased, the lattice planes move farther apart axially in order to match their average density to the neutralizing background. Eventually it becomes energetically favorable to form an additional lattice plane. The symbols indicate whether the lattices had an interlattice displacement vector $\mathbf{c}_2$ characteristic of the hexagonal phase (triangles) or the square and rhombic phases (squares).

Figure 7 displays the agreement between experiment and theory for the dependence of the angle θ (between the primitive vectors) on central areal charge density σ. The trend is

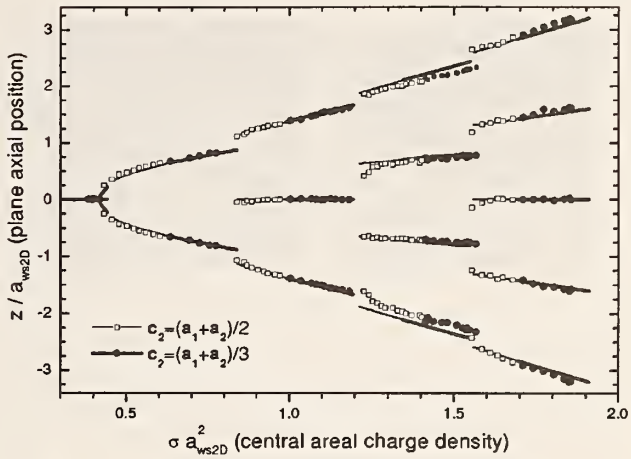

FIG. 6. Interlayer structure (plane axial positions and displacement vectors) as a function of normalized areal charge density. The lines are the predictions of theory, and the symbols are experimental measurements.

that when a new lattice plane is formed, θ changes discontinuously from $\approx 60°$ to a higher value. As the central areal density of the crystal is further increased, θ smoothly decreases to $\approx 65°$ until there is a second discontinuous transition to a hexagonal structure. This latter transition has been predicted[32] to become continuous in liquid ($\Gamma < 80$) bilayer systems. The lines indicate the minimum energy structures predicted by the 2-D theory.

IV. DISCUSSION

With Bragg scattering and spatial imaging, we have measured the correlations in both highly oblate and spherical strongly coupled $^9Be^+$ ion plasmas. The planar geometry permits a detailed comparison with theoretical calculations. We have measured the preferred lattice structures for up to five lattice planes in lenticular plasmas and obtain good agreement with theory. By increasing the number of planes (by adding more ions to the plasma), the transition from

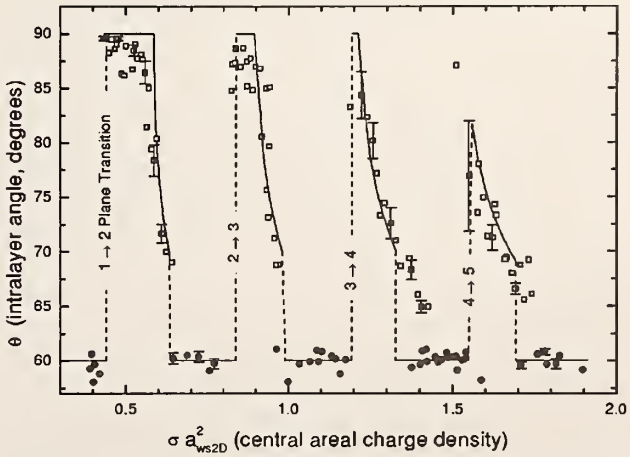

FIG. 7. Intralayer angle θ structure as a function of normalized areal charge density. The lines are the predictions of theory, and the symbols are experimental measurements. Representative error bars are included with some of the measurements.

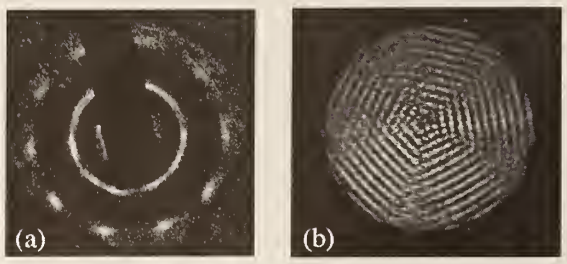

FIG. 8. Five-fold Bragg scattering and real-space patterns obtained by strobing the intensified CCD camera synchronously with the rotating electric field perturbation. (a) A Bragg scattering pattern obtained on an $N\sim 1.2\times 10^5$ ion plasma phase locked with a rotating dipole field at $\omega_r=2\pi\times 166.84$ kHz. Here $V_0=500$ V and $\alpha=2.6$. (b) Real-space image of a lenticular plasma consisting of four horizontal planes in the plasma center. The rotating dipole field was used to set $\omega_r=2\pi\times 74.35$ kHz.

surface-dominated to bulk behavior in the planar geometry can be studied. Ions in a trap have been proposed as a register for a quantum computer.[33] Work in this area has focused on a string of a few ions in a linear Paul trap.[34] A single lattice plane of ions as in Fig. 5 could provide a 2-D geometry of trapped ions for studies of quantum computing or entangled quantum states.

In spherical plasmas with more than 2×10^5 ions, we have observed the formation of bcc crystals, the predicted state for the infinite strongly coupled OCP. The crystals occupied the inner quarter of the plasma diameter. Outside the crystal there was a complicated transition to a shell structure. In this system we have not observed the thermodynamic liquid–solid phase transition predicted for the bulk OCP. Our measurements have concentrated on the correlations obtained at the coldest temperatures (therefore maximum Γ) where the ion fluorescence is maximum. The phase transition may take place in the present system, but we have experimentally missed detecting it, or possibly larger crystals (for example, where the number of ions in the crystal is large compared to the number of ions in the shells) may be required in order for a sharp phase transition to be exhibited.

We have observed structures for which we do not have a good current theoretical understanding. Figure 8(a) shows an approximate five-fold Bragg scattering pattern that was observed a number of times under different experimental circumstances. A five-fold Bragg scattering pattern is characteristic of a quasicrystal. However, more sets of dots would be present in a true quasicrystalline Bragg scattering pattern. We now think that the five-fold Bragg scattering pattern of Fig. 8(a) is due to a structure like that shown in Fig. 8(b). Figure 8(b) is a top-view image of a lenticular plasma that consisted of four horizontal planes. Even though it is difficult to distinguish individual ions in this figure, it is possible to see that there are five distinct regions where the ions resided in vertical planes. The planes from these different regions form a five-sided structure that would produce a Bragg scattering pattern like Fig. 8(a). (With the small crystals and forward Bragg scattering angles of this work, each set of vertical planes produces two Bragg peaks.) Once formed, this five-fold structure was stable and persisted for reasons that we do not understand.

In addition to enhancing studies of Coulomb crystals, the phase-locked control of ω_r has improved the prospects of a microwave frequency standard based on a hyperfine-Zeeman transition of ions stored in a Penning trap. This is because the time–dilation shift due to the plasma rotation is one of the largest known systematic shifts in such a standard. In Ref. 35, the potential frequency stability and accuracy of a microwave frequency standard based on 10^6 trapped ions is discussed. For ions such as $^{67}Zn^+$ and $^{201}Hg^+$, fractional frequency stabilities $\lesssim 10^{-14}/\tau^{1/2}$ with time–dilation shifts due to the plasma rotation of $\sim$few$\times 10^{-15}$ are possible. Here τ is the measurement time in seconds. With phase-locked operation of the rotating wall, we think it should be possible to stabilize and evaluate the rotational time–dilation shift within 1%. Therefore the inaccuracy due to this shift would contribute a few parts in 10^{-17}.

ACKNOWLEDGMENTS

We thank S. L. Gilbert and R. J. Rafac for their comments and careful reading of the manuscript. We gratefully acknowledge the support of the Office of Naval Research.

[1] J. J. Bollinger, T. B. Mitchell, X.-P. Huang, W. M. Itano, J. N. Tan, B. M. Jelenkovic, and D. J. Wineland, in *Trapped Charged Particles and Fundamental Physics*, edited by D. H. E. Dubin and D. Schneider (American Institute of Physics, New York, 1999), pp. 295–304.
[2] T. B. Mitchell, J. J. Bollinger, X.-P. Huang, W. M. Itano, and D. H. E. Dubin, Phys. Plasmas 6, 1751 (1999).
[3] S. Ichimaru, H. Iyetomi, and S. Tanaka, Phys. Rep. **149**, 91 (1987).
[4] J. H. Malmberg and T. M. O'Neil, Phys. Rev. Lett. **39**, 1333 (1977).
[5] H. M. Van Horn, Science **252**, 384 (1991).
[6] C. C. Grimes and G. Adams, Phys. Rev. Lett. **42**, 795 (1979).
[7] E. L. Pollock and J. P. Hansen, Phys. Rev. A **8**, 3110 (1973); W. L. Slattery, G. D. Doolen, and H. E. DeWitt, *ibid.* **21**, 2087 (1980); W. L. Slattery, G. D. Doolen, and H. E. DeWitt, *ibid.* **26**, 2255 (1982); S. Ogata and S. Ichimaru, *ibid.* **36**, 5451 (1987); G. S. Stringfellow and H. E. DeWitt, *ibid.* **41**, 1105 (1990); D. H. E. Dubin, *ibid.* **42**, 4972 (1990).
[8] J. P. Schiffer, Science **279**, 675 (1998).
[9] F. Diedrich, E. Peik, J. M. Chen, W. Quint, and H. Walther, Phys. Rev. Lett. **59**, 2931 (1987).
[10] D. J. Wineland, J. C. Bergquist, W. M. Itano, J. J. Bollinger, and C. H. Manney, Phys. Rev. Lett. **59**, 2935 (1987).
[11] Strongly coupled clusters of highly charged, micrometer-sized aluminum particles were previously observed in Paul traps. See R. F. Wuerker, H. Shelton, and R. V. Langmuir, J. Appl. Phys. **30**, 342 (1959).
[12] S. L. Gilbert, J. J. Bollinger, and D. J. Wineland, Phys. Rev. Lett. **60**, 2022 (1988).
[13] G. Birkl, S. Kassner, and H. Walther, Nature (London) **357**, 310 (1992).
[14] M. Drewsen, C. Broderson, L. Hornekaer, J. S. Hangst, and J. P. Schiffer, Phys. Rev. Lett. **81**, 2878 (1998).
[15] H. Walther, Adv. At., Mol., Opt. Phys. **31**, 137 (1993).
[16] A. Melzer, A. Homann, and A. Piel, Phys. Rev. E **53**, 2757 (1996).
[17] C. A. Murray and D. G. Grier, Am. Sci. **83**, 238 (1995).
[18] W. L. Vos, M. Mehens, C. M. van Kats, and P. Bösecke, Langmuir **13**, 6004 (1997).
[19] J. N. Tan, J. J. Bollinger, B. Jelenković, and D. J. Wineland, Phys. Rev. Lett. **75**, 4198 (1995).
[20] W. M. Itano, J. J. Bollinger, J. N. Tan, B. Jelenković, X.-P. Huang, and D. J. Wineland, Science **279**, 686 (1998).
[21] X.-P. Huang, J. J. Bollinger, T. B. Mitchell, and W. M. Itano, Phys. Rev. Lett. **80**, 73 (1998).
[22] X.-P. Huang, J. J. Bollinger, T. B. Mitchell, and W. M. Itano, Phys. Plasmas **5**, 1656 (1998).
[23] T. B. Mitchell, J. J. Bollinger, D. H. E. Dubin, X.-P. Huang, W. M. Itano, and R. H. Baughman, Science **282**, 1290 (1998).
[24] L. R. Brewer, J. D. Prestage, J. J. Bollinger, W. M. Itano, D. J. Larson, and D. J. Wineland, Phys. Rev. A **38**, 859 (1988).

[25]R. C. Davidson, *Physics of Non-neutral Plasmas* (Addison-Wesley, New York, 1990), pp. 39–75.
[26]T. M. O'Neil and D. H. E. Dubin, Phys. Plasmas **5**, 2163 (1998).
[27]D. J. Heinzen, J. J. Bollinger, F. L. Moore, W. M. Itano, and D. J. Wineland, Phys. Rev. Lett. **66**, 2080 (1991).
[28]J. J. Bollinger, D. J. Heinzen, F. L. Moore, W. M. Itano, D. J. Wineland, and D. H. E. Dubin, Phys. Rev. A **48**, 525 (1993).
[29]D. H. E. Dubin, Phys. Rev. A **40**, 1140 (1989).
[30]N. W. Ashcroft and N. D. Mermin, *Solid State Physics* (Saunders, Philadelphia, 1976), pp. 95–110.
[31]J. N. Tan, J. J. Bollinger, B. Jelenković, W. M. Itano, and D. J. Wineland, in *Proceedings of the International Conference on Physics of Strongly Coupled Plasmas*, edited by W. D. Kraeft and M. Schlanges (World Scientific, Singapore, 1996), pp. 387–396.
[32]V. I. Valtchinov, G. Kalman, and K. B. Blagoev, Phys. Rev. E **56**, 4351 (1997).
[33]J. I. Cirac and P. Zoller, Phys. Rev. Lett. **74**, 4091 (1995).
[34]D. J. Wineland, C. Monroe, W. M. Itano, D. Leibfried, B. E. King, and D. M. Meekhof, J. Res. Natl. Inst. Stand. Technol. **103**, 259 (1998).
[35]J. N. Tan, J. J. Bollinger, and D. J. Wineland, IEEE Trans. Instrum. Meas. **44**, 144 (1995).

Simulation of a method for forming a laser-cooled positron plasma

A. S. Newbury,* B. M. Jelenković,† J. J. Bollinger, and D. J. Wineland
Time and Frequency Division, National Institute of Standards and Technology, Boulder, Colorado 80303
(Received 13 January 2000; published 18 July 2000)

We have simulated the trapping and cooling of moderated positrons in a Penning trap in which the positrons lose energy through collisions with a simultaneously stored laser-cooled $^9Be^+$ plasma. Once the positrons are trapped, they cool through sympathetic cooling with the $^9Be^+$ plasma. After the positrons cool, their motion parallel to the magnetic field reaches a state of thermal equilibrium with the $^9Be^+$ ions and they rotate about the trap axis at the same frequency as the $^9Be^+$ ions . Therefore, a centrifugal separation will occur, forcing the positrons to coalesce into a cold column along the trap axis. A simulation which, in part, utilizes Monte Carlo techniques, indicates a capture efficiency of as high as 0.3% for 300 K moderated positrons passing through a $^9Be^+$ plasma with a density of 10^{10} atoms cm^{-3} and a column length of 1 cm. This capture efficiency leads to the positron capture rate of ~ 1000 positrons per second, assuming a 100 mCi positron source and 10^{-3} for the efficiency for moderating positrons from the source. The resulting dense reservoirs of cold positrons may be useful for antihydrogen production and for reaching a plasma state in which the mode dynamics must be treated quantum mechanically.

PACS number(s): 32.80.Pj, 52.25.Wz

I. INTRODUCTION

With advances in the use of positron moderators to produce low-energy positron beams [1–12], and in the trapping of non-neutral plasmas [13,14], attention has been focused on trapping and cooling positrons in electromagnetic traps [2–4,9–12,15–17]. Cold positron reservoirs are useful for positron-normal matter interaction studies, such as the study of resonances in low-energy positron annihilation on molecules [4]. With sufficiently high trapping rates, cold positrons can be released from electromagnetic traps to produce cold beams of high brightness for a number of different experiments [4,6,18]. A dense gas of positrons at sufficiently low temperature also provides an example of a plasma with quantized normal modes [15,16,19]. Finally, by passing cold antiprotons through a reservoir of cold positrons, one could form antihydrogen through three-body recombination [20–22].

Several groups have successfully trapped positrons in electromagnetic traps. Schwinberg, Van Dyck, and Dehmelt used resistive cooling of the positrons in a Penning trap to achieve trapping of small numbers [23]. Gabrielse, Haarsma, and Abdullah have combined this method with a 3 mCi source and a positron moderator to trap $\sim 3\times 10^4$ positrons at a rate exceeding 10^3 per hour [3]. More recently this group has been able to trap more than 10^6 positrons in 17 hours through a different method where apparently positronium in a high Rydberg state created on the surface of the moderator is field-ionized in the trap [24,25]. Conti, Ghaffari, and Steiger have also trapped positrons in a Penning trap by injecting slow positrons into the trap while ramping the trap electrostatic potential [12,26]. Mills has discussed accumulating positrons in a magnetic bottle to produce a slow positron beam [27]. Demonstration of positron trapping in a magnetic mirror by cyclotron-resonance heating has been recently demonstrated [28]. The largest number of trapped positrons ($\sim 3\times 10^8$) has been reported by Surko and coworkers [4,18,29,30]. These experiments employed collisional cooling of positrons with a room-temperature buffer gas of N_2 to provide trapping and cooling. By removing the buffer gas, the base pressure is reduced to 3×10^{-10} Torr, resulting in a positron lifetime of about one hour. With a 90 mCi positron source, a trapping rate of 3×10^8 positrons in 8 min and a trapping efficiency of moderated positrons greater than 25% were achieved.

In this paper we explore the possibility of capturing and cooling positrons in a Penning trap through collisions with a simultaneously stored laser-cooled plasma of $^9Be^+$ ions. Slow positrons become trapped through Coulomb collisions with the $^9Be^+$ plasma. Once trapped, the positrons will then be sympathetically cooled by the $^9Be^+$ plasma, which can be laser-cooled to temperatures as low as 0.5 mK [31,32]. Sympathetic cooling refers to the cooling of one species through Coulomb interactions or collisions with a second, directly cooled species [32,33]. Since this technique employs high vacuum, positron annihilation will be suppressed, permitting long trap lifetimes.

One of the simplest methods to study the transport of positrons in a $^9Be^+$ plasma is the Monte Carlo method. Unlike collisions between neutral atoms, Coulomb collision deflections at large distances are important, with each of these "distant collisions" producing a small scattering and velocity change. In Monte Carlo simulations one can treat the problem of Coulomb collisions through the cumulative effect of a large number of small angle scattering; we have used Monte Carlo simulations to calculate the scattering angle of the moderated positron after each pass through the $^9Be^+$ plasma. The simulations were based on the expression for the probability distribution for scattering of a positron into an angle θ after a large number of collisions, assumed to occur as a positron passes through the $^9Be^+$ plasma [34,35]. Recently, Nanbu used a Monte Carlo method to derive a simple

*Permanent address: MIT Lincoln Laboratory, Lexington, MA 02420.
†Permanent address: Institute of Physics, University of Belgrade, Belgrade, Yugoslavia.

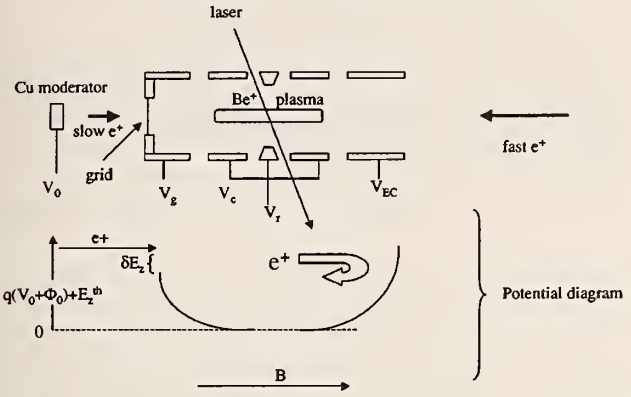

FIG. 1. Schematic diagram of a cylindrical Penning trap and of axial potentials. V_0, moderator potential; V_g, grid voltage; δE_z, positron axial kinetic energy above the grid voltage; V_r, V_c, and V_{EC}, potentials on other trap electrodes.

analytical expression for the probability density function for a deflection angle after many Coulomb collisions [36]. We also have done a number of calculations using expressions from Ref. [36] to calculate the scattering angles for positrons after passing through the plasma and obtained good agreement between the two data sets.

The basic method for capturing and cooling positrons using a $^9Be^+$ plasma, outlined previously in Ref. [16], is discussed in Sec. II. In addition, we describe here some details of a hypothetical experiment designed to trap positrons. In Sec. III we have increased the scope of the discussion by including the effects on the capture efficiency caused by the energy distribution of moderated positrons, the finite size of the positron source, the radial electric field within the plasma, and $^9Be^+$ recoil. The trap geometry, the plasma parameters, and the positron behavior described in Secs. II and III are used in the modeling of positron trapping. The Monte Carlo method used to calculate the efficiency of the proposed method [16] is described in Sec. IV. The results of the simulations and a discussion of the results are presented in Sec. V.

II. BASIC METHOD

The model assumes the $^9Be^+$ ions are first trapped in a cylindrical Penning trap contained in a room-temperature vacuum enclosure with an axial magnetic field of 6 T. Figure 1 illustrates the simple Penning trap design considered in modeling the capture of positrons. In this magnetic field, a laser-cooled $^9Be^+$ plasma in thermal equilibrium can reach a uniform density n_0 of up to 10^{10} atoms cm^{-3} [14,37]. This high density can be reached by using torques due to a laser beam [37] or due to a rotating electric-field perturbation [38,39] to control the plasma's angular momentum. A low-energy positron traversing this plasma along the magnetic-field direction will scatter off the $^9Be^+$ ions via the Coulomb interaction. The positron's parallel momentum (along the magnetic-field direction) can thus be converted to perpendicular momentum. If sufficient momentum is converted, the positron's momentum along the magnetic field can be reduced so that it will not leave the trap. In Ref. [16], it was assumed that if the positron were initially captured in this way, it would lose enough energy through cyclotron radiation to be permanently trapped. However, this is true only for a small fraction of positrons because typically, before the positron can lose enough energy through cyclotron radiation, its energy can be redistributed back by Coulomb collisions along the trap axis and it will escape [40]. In the work described here, we now include this escape process and the cooling effects of $^9Be^+$ recoil, which initially provides a more efficient cooling mechanism than cyclotron radiation.

In the Penning trap, the plasma rotates around the magnetic-field axis at a frequency ω_r. The technique of "Doppler" laser cooling [31,41,42] reduces the temperature of the plasma to less than 10 mK. The Debye length of the plasma can be expressed as $\lambda_D=(k_BT\epsilon_0/n_0q^2)^{1/2}$, where k_B is Boltzmann's constant, q is the ion's charge, and ϵ_0 is the permittivity of free space. At temperatures near 10 mK, the Debye length is small compared to plasma dimensions [31]. In this limit, the density of $^9Be^+$ ions can be expressed as a function of the $^9Be^+$ cyclotron frequency Ω, the plasma rotation frequency ω_r, and the $^9Be^+$ mass M_{Be}, as $n_0=2\epsilon_0M_{Be}\omega_r(\Omega-\omega_r)/q^2$ [14,19,31]. The maximum achievable density is the Brillouin density, which occurs when $\omega_r=\Omega/2$ and has been achieved in laser-cooled plasmas with up to a few hundred thousand $^9Be^+$ ions in magnetic fields up to 4.5 T [37,39]. For $^9Be^+$ ions confined in a 6 T magnetic field, this limit is $n_0\simeq10^{10}$ cm^{-3}. We will assume that the magnetic field is uniform along the length of the trap.

As illustrated in Fig. 1, high-energy positrons from a ^{22}Na source are injected from the right into the trap, on the trap axis, through a cylindrical endcap. The positrons have a beta-decay endpoint energy of 545 keV, and these high-energy positrons will not significantly affect the ions in the plasma (a discussion of the interactions between hot positrons and plasma is contained in the Appendix). After passing through the plasma, the positrons strike a room-temperature crystal moderator. The positrons will thermalize by interacting with electrons and phonons in the crystal. In this "reflection geometry," a small fraction (up to 10^{-3}) will avoid annihilation in the crystal and emerge as a beam of slow positrons [1,5,43] which then enter the trap [44]. At the surface of the crystal the moderated positrons have an energy determined by the crystal temperature. In addition, they are accelerated in the direction normal to the crystal surface by the work function Φ_0 of the crystal [1]. For the method of trapping positrons discussed here, the narrow distribution of thermal-energy positrons at the surface of the crystal is important. Measurements show that positrons emitted from a Cu(111) single-crystal moderator can have a narrow energy distribution whose width is reasonably consistent with thermal broadening given by the temperature of the moderator crystal [45]. In our calculations, for the purpose of the crystal work function, we assume the use of a Cu(111) crystal moderator.

After the positrons are emitted from the moderator crystal, their axial kinetic energy is assumed to be further reduced by a conducting screen with good transmission (the retarding grid of Fig. 1), which has a potential a few tenths of a volt above the moderator potential. If the moderator and

retarding grid potentials are equal, the axial energy of positrons as they pass through the grid is $\Phi_0+E_z^{th}$, where E_z^{th} is the axial component of the positron's thermal energy at the crystal surface. The positrons will then enter the $^9Be^+$ plasma with relatively little kinetic energy. At these low energies (~few eV), positron annihilation on the $^9Be^+$ ions is made negligible by Coulomb repulsion. By adjusting the potential of the rightmost cylindrical electrode, we can ensure that the moderated positrons are reflected at the end of the plasma farthest from the moderator and pass through the plasma twice. During each pass, some of the axial energy can be converted to perpendicular energy through Coulomb collisions with the $^9Be^+$ ions , thereby preventing them from escaping back through the retarding grid. Positrons that remain trapped for many passes will lose enough energy through $^9Be^+$ recoil to remain permanently trapped. The positrons that are not trapped are assumed to strike the moderator or grid and annihilate.

Once the positrons are trapped within the laser-cooled $^9Be^+$ plasma, they will be cooled through a combination of sympathetic cooling through $^9Be^+$-e^+ Coulomb collisions and cyclotron radiation. After the positrons are cooled by the $^9Be^+$ plasma, both positrons and $^9Be^+$ ions will undergo uniform rotation at the same frequency ω_r and the positrons will be forced to the center of the rotating plasma because of their smaller mass [33,46]. In the limit of zero temperature, the edges of each plasma will be sharp, and the plasmas will separate, with the positrons forming a column of uniform density along the trap axis. If the $^9Be^+$ plasma density is significantly below the Brillouin limit, the densities for confined plasmas of e^+ and $^9Be^+$ are expected to be approximately equal and the plasma separation quite small [15,46]. This implies good thermal coupling and possible positron axial temperatures less than 10 mK. The discussion of strongly magnetized plasma equilibria by Glinsky *et al.* [47] indicates that the positron plasma axial and cyclotron degrees of freedom will be strongly decoupled in a 6 T magnetic field. Therefore, cyclotron radiation may keep the positron cyclotron temperature in near-thermal equilibrium with the trap electrodes. Here we assume the electrodes are maintained at room temperature, but the equilibrium cyclotron temperature could be reduced, for example, by cooling the electrodes to 4 K with a liquid helium bath or to lower temperature with a dilution refrigerator.

One way to experimentally detect the presence of trapped positrons could be by imaging the near-resonant 313 nm fluorescence of the $^9Be^+$ plasma and looking for the absence of $^9Be^+$ ions in the center of the plasma [16]. Other ions with charge-to-mass ratios higher than $^9Be^+$, such as $^4He^+$, H_3^+, and $^9Be^{2+}$, will also be trapped in the center of the plasma. These ions will not fluoresce at 313 nm and will therefore mimic the positron signature on the imaging tube. We anticipate that these ions could be distinguished from the positrons through their resonant response to radiation applied at the cyclotron frequency. The size of the "hole" in the $^9Be^+$ plasma will yield an estimate of the number of trapped positrons. With the imaging technique we estimate we can detect the presence of a single "string" of a few tens of positrons trapped on the axis within the $^9Be^+$ plasma [48].

III. POSITRON TRAPPING

Positrons within the Cu(111) moderator crystal rapidly thermalize to a Boltzmann velocity distribution [1]. Within the crystal, the positron velocity distribution $P(v_i)$ will conform to

$$P(v_i)\propto e^{-m_e v_i^2/2k_BT}, \tag{1}$$

where the subscript i indicates the velocity direction ($i=\hat{x},\hat{y},\hat{z}$), m_e is the positron mass, and T is the temperature of the crystal moderator. Positrons emitted from the moderator are accelerated in the direction perpendicular to the moderator surface by the crystal work function Φ_0. As indicated in Fig. 1, the positron velocity is primarily along the magnetic-field axis ($\hat{z}$) since the crystal surface is oriented perpendicular to that axis. Immediately outside the crystal the slow positrons will have an axial kinetic energy distribution,

$$P(E_z)dE_z\propto e^{-E_z-\Phi_0/k_BT}dE_z, \tag{2}$$

for $E_z\geq\Phi_0$. This distribution combines the probability of effusion from the moderator surface [7,49] with the acceleration at the surface due to the work function. Equivalently, we can assume the positron axial velocity at the crystal surface is selected from the distribution

$$P(v_z)\propto v_z e^{-m_e v_z^2/2k_BT}, \tag{3}$$

and then accelerated by the potential Φ_0. The grid potential can be adjusted so that the positrons have small excess axial energy (δE_z) with respect to the grid. Before reaching the plasma, the positrons will be accelerated by the plasma potential, $V_p(r)=-n_0qr^2/(4\epsilon_0)$. [For simplicity, we have assumed that we adjust the moderator and electrode potentials to make the plasma potential along the trap axis $V_p(r=0)=0$.]

We have modeled the initial collisions of the moderated positrons with the $^9Be^+$ ions in the weakly magnetized approximation where the effects of the magnetic field on the collisions are neglected. This approximation is valid as long as the positron's cyclotron rotation is less than one cycle during the time of a collision [47]. The number of cyclotron orbits during a collision can be defined as $\kappa=\Omega_c\tau$, where Ω_c is the positron cyclotron frequency and τ is the binary collision time. Therefore, we consider collisions where $\kappa<1$ [47]. For example, the minimum collision time is $\tau=\bar{b}/v$, where $\bar{b}=q^2/2\pi\epsilon_0 m_e v^2$ is the collisional distance of closest approach. For an energy of 0.1 eV, $v\simeq1.9\times10^7$ cm s^{-1}, making $\bar{b}\simeq1.4\times10^{-6}$ cm. At 6 T, $\Omega_c\simeq1.1\times10^{12}$ s^{-1}, yielding $\kappa=0.08$.

We calculate the initial capture of positrons after one pass by using the distribution for multiple small-angle Coulomb scattering [34,35]. (The cross section for multiple small-angle Coulomb scattering is typically larger than the cross section for a single large-angle scattering [50].) Below, we define a "pass" through the plasma as a pass back and forth (or from left to right and back in Fig. 1) ending with the

positron traveling towards the moderator crystal. As seen in Fig. 1, the positron can only leak out of the trap the way it entered.

The angular distribution for multiple small-angle Coulomb scattering can be simulated by calculating an energy-dependent rms scattering angle $\sqrt{\langle\theta^2\rangle}$ according to the Rutherford scattering formula such that [50]

$$\langle\theta^2\rangle=\frac{n_0 l q^4}{2\pi\epsilon_0^2 m_e^2 v^4}\ln\left(\frac{b_{\max}}{b_{\min}}\right). \tag{4}$$

Here l represents twice the plasma length, and $b_{\max}$ and $b_{\min}$ are the maximum and minimum impact parameters, respectively. We use $b_{\max}=v/\Omega_c$, where Ω_c is the positron cyclotron frequency and v is the magnitude of the positron velocity. The quantity $b_{\max}$ is the maximum impact parameter for which we can use the weakly magnetized approximation. It is derived by setting the parameter $\kappa=1$. For the parameters used in the above discussion of κ, $b_{\max}=0.17$ μm, which is more than an order of magnitude smaller than the mean ion spacing in the $^9Be^+$ plasma. We use $b_{\min}=\bar{b}/2$ to limit the scattering to small angles [50]. The probability of multiple scattering in one pass through an angle θ can then be approximated by a Gaussian distribution in solid angle [34,35,51],

$$P_S(\theta)d\Omega\propto\sin(\theta)\exp\left(-\frac{\theta^2}{\langle\theta^2\rangle}\right)d\theta d\phi. \tag{5}$$

This distribution is valid for multiple angle scatterings where each is less than 10° [35].

The capture of positrons within the $^9Be^+$ plasma is divided into two processes. The first process is based on Coulomb collisions and traps the positrons temporarily. After a single pass a positron can be trapped if the amount of axial energy converted into perpendicular or cyclotron energy is greater than the excess axial kinetic energy of the positron. Because of the difference in the positron and $^9Be^+$ masses, positrons will actually lose very little energy by passing once through the plasma. If initially trapped, the positron will continue to make passes through the plasma until it either escapes the trap or becomes permanently trapped. To escape the trap, a positron which is "initially captured" needs to convert its perpendicular energy back to axial energy.

The second process permanently traps the positrons by depleting their excess energy primarily through $^9Be^+$ recoil cooling. A positron with energy E scattering off the ions in the plasma through an angle θ will lose an energy

$$\Delta E=4E\left(\frac{m_e}{M_{\mathrm{Be}}}\right)\sin^2(\theta/2) \tag{6}$$

to $^9Be^+$ recoil. Because of the large mass difference between a $^9Be^+$ ion and a positron, a positron will have to make many transits through the plasma in order to lose its excess energy. But once sufficient positrons are trapped, other positrons can lose axial energy through e^+-e^+ collisions. The trapping efficiency under these collisions is expected to be higher than for the e^+-$^9Be^+$ collisions because of the larger energy loss due to positron recoil. This enhanced recoil cooling is not taken into account here.

IV. SIMULATION

The Monte Carlo simulation proceeds as follows. For each positron, an initial radial coordinate is chosen according to a flat distribution over the active area of the source. The initial velocities out of the moderator in the x and y directions are chosen using velocity distribution functions $P(v_i)$ of Eq. (1). The z component of the positron velocity was obtained using a modified Boltzmann distribution [Eq. (3)]. Equivalently, the velocity v_z at the surface of the crystal is determined from the equation $v_z=v_{\mathrm{th}}[-\ln(1-R_n)]^{1/2}$, where R_n is a random number between 0 and 1. Here $v_{\mathrm{th}}=\sqrt{2kT/m}$, where T is the temperature of the crystal. We use $E_z^{\mathrm{th}}=mv_z^2/2$ to denote the axial kinetic energy. At the moderator surface the positron is further accelerated in the axial direction by the surface work function. We have used the Cu(111) work function $\Phi_0=0.4$ eV in the Monte Carlo simulation.

Figure 1 illustrates the electrical potential experienced by the positrons as they travel from the moderator, held at V_0, through the grid at potential V_g, and into the $^9Be^+$ plasma. The moderated positrons with an axial energy above the retarding grid potential, $\delta E_z[=q(V_0-V_g)+\Phi_0+E_z^{\mathrm{th}}]$, follow the magnetic-field lines and accelerate into the plasma. Their radial coordinate r with respect to the trap symmetry axis does not change until they undergo a large number of collisions inside the plasma, since their cyclotron radius is less than 10^{-4} cm. At low temperature, the electric potential inside the plasma is approximately independent of the axial coordinate, and is given by $V_p(r)=-n_0qr^2/(4\epsilon_0)$.

Coulomb scattering caused by one pass through the plasma is described by two angles, θ_s, the magnitude of the deflection angle, and ϕ_s, the orientation of the scattering around the deflection cone. The scattering angle θ_s was calculated assuming the distribution given by Eq. (5). This assumption leads to an expression for the scattering angle $\theta_s=\sqrt{\langle\theta^2\rangle[-\ln(R_\theta)]}$, where $\langle\theta^2\rangle$ is the rms scattering angle given by Eq. (4). Since the positron has no preferred azimuthal orientation, ϕ_s was obtained at the end of the pass from a uniform distribution $2\pi R_\phi$. Here R_θ and R_ϕ are random numbers between 0 and 1. At the end of each pass, the new values of the v_x, v_y, v_z were calculated from θ_s, ϕ_s, and the change of energy [Eq. (6)]. A test was then made to determine if the positron was permanently trapped. If this is not the case, the positron will either make another pass or is lost. By repeating these "runs," we determine the percentage of moderated positrons trapped within the plasma. Typically, the Monte Carlo runs had 1.5×10^5 positrons.

V. RESULTS AND DISCUSSION

Results for the efficiency of trapping positrons in a $^9Be^+$ plasma for particular conditions are shown in Fig. 2. In this case the plasma radius was 0.1 mm, and the density was 10^{10} cm^{-3}. We chose the moderator potential to be V_0

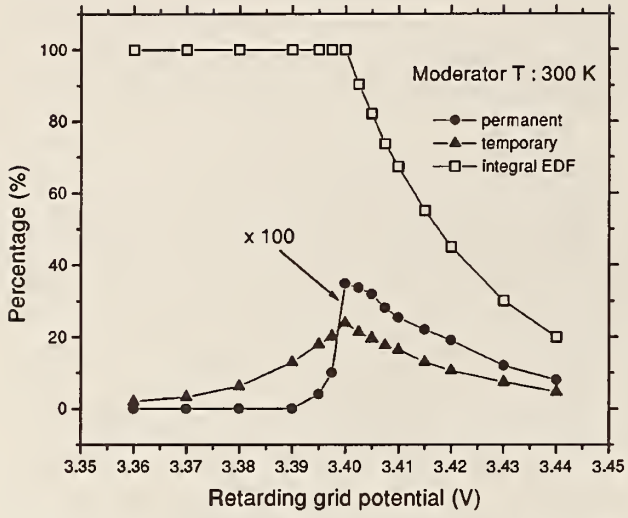

FIG. 2. Fraction of moderated positrons entering the trap (integral EDF) along with the fraction of temporarily and permanently captured positrons as a function of the retarding grid voltage for $V_0=3$ V. The crystal work function was 0.4 eV and the temperature was 300 K. The $^9Be^+$ plasma parameters were as follows: density $n_0=10^{10}$ cm^{-3}, length $l=1$ cm, and radius $r_0=0.1$ mm. Squares, integral energy distribution of positrons; circles, permanently trapped; triangles, temporarily trapped.

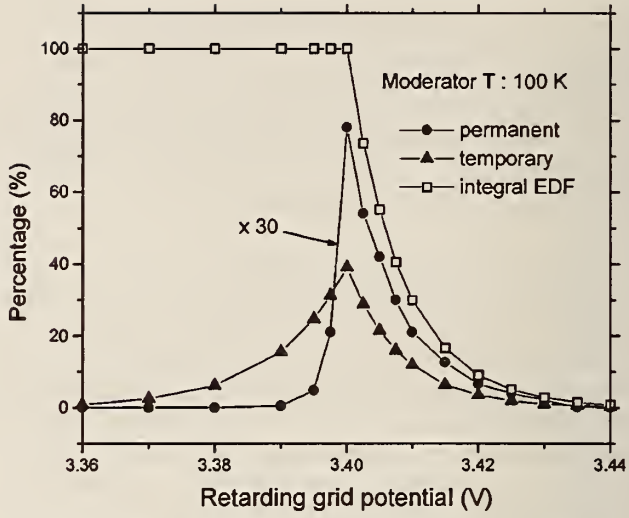

FIG. 3. Same as in Fig. 2 but for a moderator temperature of 100 K.

$=3$ V, while the grid potential V_g was varied around $V_0+\Phi_0=3.4$ V. The percentage of temporarily trapped (triangles) and permanently trapped (circles) positrons is plotted as a function of V_g. Also shown (squares) is the fraction of positrons entering the trap vs the retarding grid potential. This curve is the integral distribution of the axial component of kinetic energy, E_z. For the results of Fig. 2, the temperature of the crystal was taken to be 300 K. The maximum efficiency for positron trapping occurs at $V_g=3.4$ V and was $\sim 0.4\%$ for permanent and 24% for temporary trapping only. The results of the trapping efficiencies for the crystal cooled to 100 K are shown in Fig. 3. The width of the energy distribution is reduced by a factor of 3. Such thermal narrowing has been confirmed in experiments [7]. The efficiency for permanent trapping increases to $\sim 2.5\%$. Figures 2 and 3 indicate, as mentioned previously, that the energy spread of the moderated positrons is important for the trapping method simulated here. Experimental studies have reported near-thermal energy spreads for metal, single-crystal moderators [7,45]. In practice this condition may not be straightforward to obtain. Figure 4 shows the trapping efficiency for an energy spread of the moderated positrons corresponding to $T=2000$ K. The factor of 7 increase in the positron energy spread of Fig. 4 over Fig. 2 has resulted in a factor of 40 decrease in the efficiency for permanently trapping positrons.

In Fig. 5 we show the fraction of captured positrons for different bias potentials V_0 of the moderator while holding the crystal temperature (300 K) and plasma parameters (density, length, and radius) constant. For each value of V_0 in Fig. 5, the grid voltage was set to the value $V_g=V_0+0.4$ V which maximizes the trapping efficiency. The data show that the efficiency for permanent trapping has a maximum of $\sim 0.45\%$ when V_0 is at about 4 V. While we do not have a detailed understanding of the location of this maximum, we can describe some effects which could produce it. Once temporarily trapped, a positron will leave the plasma if it enters the loss cone θ_c about the z axis defined by $\sin(\theta_c)=\sqrt{\delta E_T/E_T}$, where E_T is the total positron kinetic energy in the plasma and δE_T is the excess kinetic energy the positron must lose to be trapped. A positron with a larger kinetic energy and the same excess energy has a smaller loss cone, which tends to increase the efficiency of trapping positrons with increasing energy. However, the energy loss per pass of a positron decreases with energy. This increases the number of passes required to permanently trap a positron (see discussions below), and will tend to decrease the trapping efficiency with increasing energy.

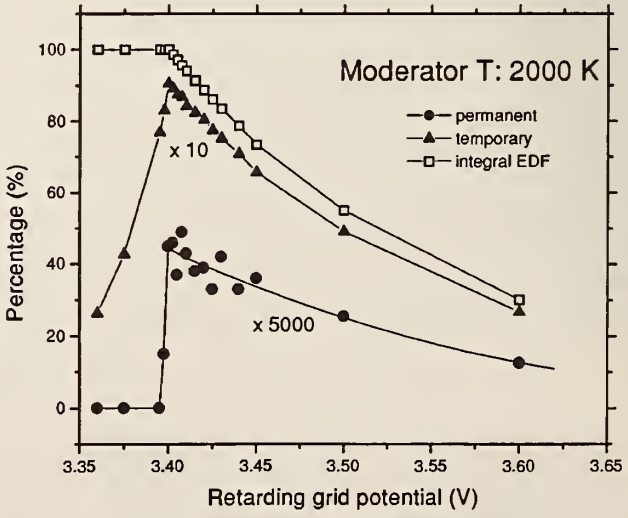

FIG. 4. Same as in Fig. 2 but for a moderator temperature of 2000 K.

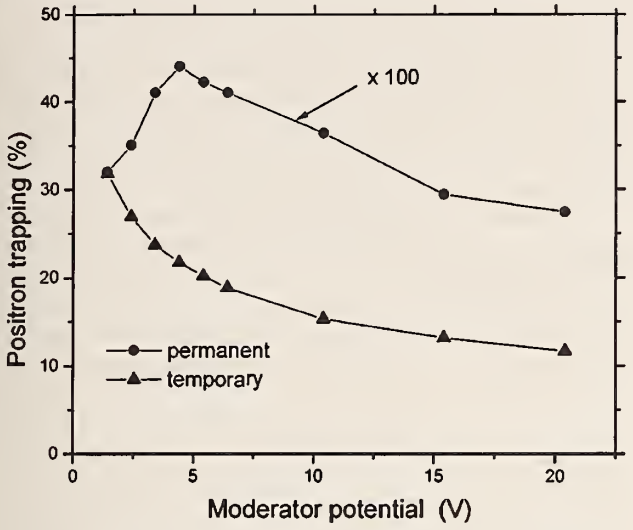

FIG. 5. Capture percentage of permanently trapped (circles) and temporarily trapped (triangles) positrons as a function of V_0. The moderator work function was 0.4 eV and grid potential was always $V_G = V_0 + 0.4$. ($n_0 = 10^{10}$ cm^{-3}, $l = 1$ cm, and $r_0 = 0.1$ mm.)

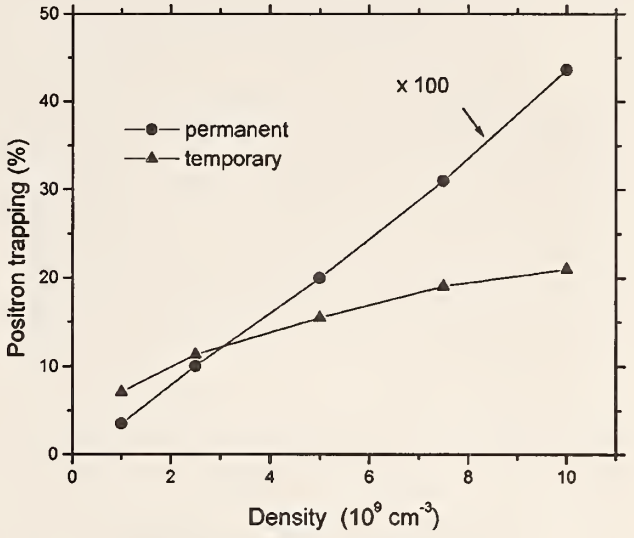

FIG. 7. Capture percentage of permanently trapped (circles) and temporarily trapped (triangles) positrons as a function of $^9Be^+$ plasma density ($r_0 = 0.1$ mm, $l = 1$ cm, $V_0 = 4$ V, and $V_g = 4.4$ V).

Shown in Figs. 6 and 7 are the variations in efficiencies for trapping positrons as the $^9Be^+$ plasma length and density were changed. The percentage of temporarily trapped positrons is increasing as a square root of both length and density. The probability for temporarily trapping positrons depends on the final scattering angle θ, which in turn is proportional to $\sqrt{\ln}$. The percentage of permanently trapped positrons is increasing linearly with n and l, possibly because the energy loss for permanent trapping [Eq. (6)] varies as the square of the rms scattering angle.

The efficiency for trapping positrons decreases with increasing plasma radius, as shown in Fig. 8, for the same reason that it decreases with increasing moderator potential V_0 for $V_0 > 4$ V (see Fig. 5). At larger radii, the positrons will have correspondingly larger energies entering the plasma. Throughout this manuscript we assume that the source radius is equal to the plasma radius.

The number of round trips in the plasma before the positron either exits back through the grid or is permanently trapped varies with the positron excess energy, values of V_0 and V_g, and the plasma radius. The histogram in Fig. 9 shows the fraction of trapped positrons vs the number of passes the positrons made through the $^9Be^+$ plasma before

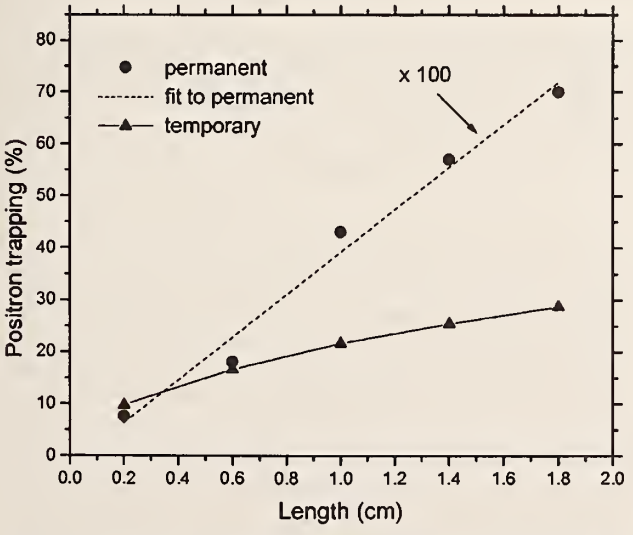

FIG. 6. Capture percentage of permanently trapped (circles) and temporarily trapped (triangles) positrons as a function of $^9Be^+$ plasma length ($n_0 = 10^{10}$ cm^{-3}, $r_0 = 0.1$ mm, $V_0 = 4$ V, and $V_g = 4.4$ V).

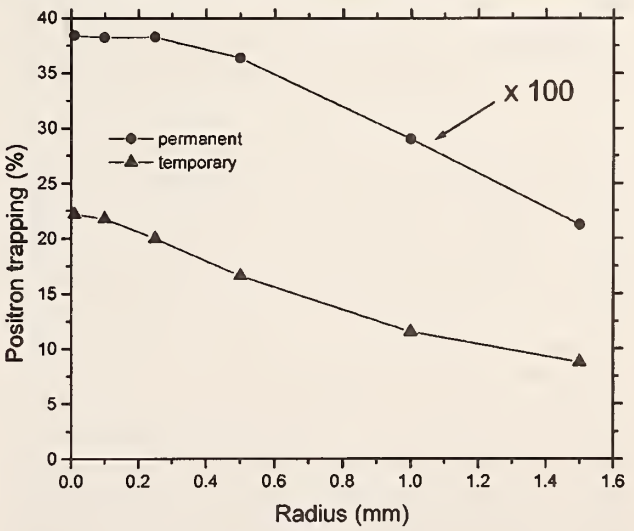

FIG. 8. Capture percentage of permanently trapped (circles) and temporarily trapped (triangles) positrons as a function of the radius of the $^9Be^+$ plasma ($n_0 = 10^{10}$ cm^{-3}, $l = 1$ cm, $V_0 = 4$ V, and $V_g = 4.4$ V). We assume the positron source radius equals the plasma radius.

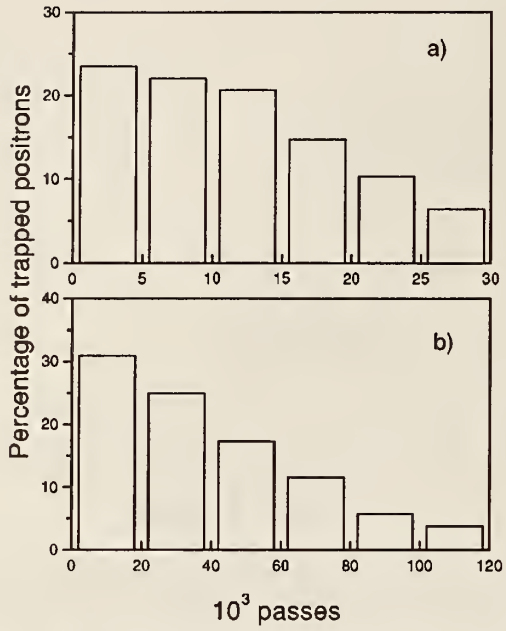

FIG. 9. Histogram showing the fraction of permanently trapped positrons vs the number of passes the positrons made through the $^9Be^+$ plasma before being trapped, for $n_0=10^{10}$ cm^{-3}, $l=1$ cm, $r_0=0.1$ mm, and $T=300$ K. (a) $V_0=4$ V, $V_G=4.4$ V; (b) $V_0=10$ V, $V_G=10.4$ V.

being permanently trapped. The results are shown for a plasma radius of 0.1 mm and for two moderator potentials, $V_0=3$ V ($V_g=3.4$ V) [Fig. 9(a)] and $V_0=10$ V ($V_g=10.4$ V) [Fig. 9(b)]. Although the positrons have the same excess energy as they pass the grid in Figs. 9(a) and 9(b), they spend different times in the trap before being captured because they enter the plasma with different kinetic energies. Similar increases in the number of passes were obtained when the plasma radius was increased to 0.5 mm. The plasma potential decreases as $-r^2$ and therefore positrons entering the plasma at larger radius have higher energies.

We can estimate the overall capture rate given the results of the simulation by including an estimate of both the source and the moderator efficiencies. A 100 mCi source will isotropically produce positrons at a rate of 3×10^9 s^{-1}. Only a fraction of the emitted positrons will reach the moderator crystal. We expect the positron flux at the Cu crystal to be $\sim4\times10^8$ s^{-1} [24]. Assuming a moderator efficiency of 10^{-3} and the trapping efficiency of 0.3%, we get a trapping rate of about 1300 positrons per second.

Using the method outlined in this paper, it should be possible to achieve a low-temperature, high-density positron plasma. In a magnetized, uncorrelated plasma, the antihydrogen recombination rate should scale as $n^2T^{-9/2}$ [20]. In a correlated plasma (plasma exhibiting liquidlike and solidlike behavior), this dependence will likely be modified. Furthermore, a pressure of 1.3×10^{-8} Pa (10^{-10} torr) may provide positron lifetimes longer than 5 days (see the Appendix). Since the Brillouin limit to the plasma density increases as the square of the magnetic field, it is possible to increase these trapping efficiencies further by going to larger magnetic fields.

We note that other electrode geometries can replace the transparent retarding grid. Any geometry which provides a potential hill between the moderator and the $^9Be^+$ plasma can mimic the effects of the retarding grid. In an experiment, a geometry other than a grid is desirable because azimuthal asymmetries in the retarding grid potential near the plasma might limit the ultimate $^9Be^+$ plasma density [14,37].

In this manuscript we assume that the $^9Be^+$ ions recoil from positron impact as if they were free particles. In fact, laser-cooled ion plasmas are often strongly coupled and exhibit liquidlike or solidlike behavior where an ion is bound in a local potential well. However, because the collision time of the weakly magnetized collisions considered here is fast compared to the period of any of the ion's plasma-mode frequencies, in considering their recoil we may treat the $^9Be^+$ ions as if they were free particles.

In addition to the importance of achieving a relatively low-temperature thermal energy spread of the moderated positrons, perhaps the largest uncertainty in an experiment designed along these lines is the ability to produce high-density, laser-cooled $^9Be^+$ plasmas of sufficient length. While large-number plasmas ($\simeq10^9$ ions [52]) and high-density plasmas ($n\simeq10^{10}$ cm^{-3} [37]) have been achieved in Penning traps, the combination of these two parameters has not yet been experimentally realized. In recent experiments we have been able to reach the Brillouin limit with $\sim10^6$ ions in a 4.5 T and 6 T magnetic field [39,53]. It may also be possible to "stack" a series of shorter plasmas in separate traps along the magnetic field, thereby maintaining high density and increasing the effective column length. However, even with a modestly sized single plasma, it should be possible to trap a sufficient number of positrons to evaluate the effectiveness of this technique.

ACKNOWLEDGMENTS

Support for this research was provided by the Office of Naval Research. We thank Travis Mitchell and Tom Heavner for their comments on the manuscript.

APPENDIX

It is important to discuss interactions between the energetic positrons from the ^{22}Na source and the cold $^9Be^+/e^+$ plasma. Here, we examine $^9Be^+$ loss due to positron impact ionization, plasma heating caused by the positron beam, and the loss of trapped positrons due to interactions with background gas. For simplicity we assume a 200 keV monoenergetic positron beam (the peak energy of the ^{22}Na beta-decay distribution) from an isotropic 2 mCi source and a $^9Be^+$ plasma of 1 cm length, with a 1 mm diameter and a density of 10^{10} ions cm^{-3} ($\sim8\times10^7$ ions).

The probability of an individual scattering event between a positron and a $^9Be^+$ ion can be expressed as $P=n_0\sigma l'$, where n_0 is the ion number density, σ is the event cross section, and l' is the effective path length through the plasma. Since positrons are emitted from the source isotro-

pically, many will have initial velocities perpendicular to the magnetic-field direction. These positrons will spiral along the magnetic-field lines. Spiraling through the plasma will increase the path length of these particular ions through the plasma. We can eliminate the positrons with the largest effective path lengths by electrically retarding the positron beam from the ^{22}Na source. By placing a potential hill of 1400 V between the source and the plasma, we can prohibit the positrons with the longest path lengths from making it to the plasma. Eliminating only $\sim 9\%$ of the positrons in this manner, we reduce the average path length through the plasma to $2.4l$. The calculations below for $^9Be^+$ heating and loss assume this effective path length.

1. $^9Be^+$ loss

The energetic positrons from the ^{22}Na source can doubly ionize the $^9Be^+$ plasma through electron impact ionization. $^9Be^{2+}$ will remain trapped but can be only sympathetically cooled; its presence can decrease the cooling capacity of the ion plasma by reducing the number of laser-cooled ions. The cross section for second ionization of Be^+ through 200 keV electron impact is approximately [54]

$$\sigma(Be^+ + e^- \rightarrow Be^{2+} + 2e^-) \simeq 3.1 \times 10^{-17} \text{ cm}^2. \quad \text{(A1)}$$

We assume the electron-impact and positron-impact ionization cross sections are approximately equal for positrons of this high energy [55]. Using this cross section and a total flux of positrons R_{e^+} of 1.3×10^7 s^{-1}, the number density of $^9Be^+$ ions n_0, and the average path length through the plasma $2.4l$, we can estimate the loss rate of $^9Be^+$ ions as

$$R_{Be^{2+}} = 2.4 \ln_0 \sigma R_{e^+} \approx 11 \text{ s}^{-1}. \quad \text{(A2)}$$

At this rate, 7% of the initial 8×10^7 $^9Be^+$ ions would be lost in about 6 days.

Another mode of $^9Be^+$ loss is through high-energy positron annihilation on the $^9Be^+$ ions. The cross section for positrons with 200 keV of kinetic energy to annihilate on $^9Be^+$ is approximately 3×10^{-25} cm^2 [56]. Thus loss of $^9Be^+$ through this mechanism caused by positrons from the ^{22}Na source is negligible.

2. $^9Be^+$ plasma heating

High-energy positrons passing through a cold dense $^9Be^+$ plasma can heat the plasma via Coulomb collisions. Since our plasma is simultaneously laser cooled, it is necessary that the rate of laser cooling be larger than that of the positron heating. To estimate the heating rate, we perform a calculation of nonrelativistic scattering. Since the heating from positron-positron collisions dominates over collisions between positron and $^9Be^+$, we estimate the heating rate due to trapped positron recoil. A high-energy positron scattering through an angle θ will impart an energy $E(\theta) = (1/2) m_e v^2 \sin^2(\theta)$ to the trapped positron. We can estimate the rate of plasma heating $\dot{E}_H$ by integrating,

$$\dot{E}_H = 2\pi n N v \int_{\theta_M}^{\pi/2} E(\theta) \frac{d\sigma}{d\theta} \sin\theta \, d\theta, \quad \text{(A3)}$$

where n is the density of positrons in the beam, v is their velocity, N is the number of positrons in the plasma, and θ_M is the minimum scattering angle for which the weakly magnetized approximation is valid [47]. This corresponds to an impact parameter approximately equal to the positron beam radius. In this limit, we estimate a heating rate of $\dot{E}_H \simeq 4.1 \times 10^{-8}$ eV/s for each positron in the plasma. If we assume a positron column plasma 1 mm in diameter and 1 cm in length containing 8×10^7 positrons, the plasma heating rate will be 3.3 eV/s.

Since the heating rate scales as $E_i^{-1/2}$, where E_i is the energy of incident positrons, the heating from moderated positrons incident on the plasma is significantly higher than that from the unmoderated ones. Taking into account the moderator efficiency, the overall heating from these positrons is comparable to that of the unmoderated ones.

It is necessary to compare this heating rate to $\dot{E}_L$, the rate at which energy is removed from the plasma through laser cooling. We assume a 313 nm laser beam directed perpendicularly to the magnetic field with a 25 μm waist perpendicular to the magnetic axis and 250 μm along the axis, centered on the ion plasma. The laser intensity is adjusted to give a resonant scatter rate of 10 MHz for an ion at the center of the beam. We assume a $^9Be^+$ cloud of 1 cm in length and 1 mm in diameter rotating at $\omega_r = 2\pi(5 \text{ MHz})$. Laser cooling is most efficient using a laser beam propagating along the trap z axis because the Doppler shift associated with the plasma rotation is absent. Experimentally, this would be difficult to realize in the apparatus described here because the positron source and moderator also lie on the z axis. We estimate the laser-cooling rate using Eq. (17) of Ref. [28]. We find that for a laser detuning of 20 MHz and a $^9Be^+$ plasma temperature of 1 K, $\dot{E}_L \simeq -1000$ eV/s. Since $|\dot{E}_L| \gg |\dot{E}_H|$, the plasma heating from positron impact should not significantly affect the plasma equilibrium.

3. Positron loss

We can estimate the rate at which trapped positrons are lost due to background collisions by scaling the results of Murphy and Surko [29]. In their experiment, positrons were trapped and cooled through collisions with a room-temperature background gas of nitrogen [29]. The trap lifetime was limited to 40 s because of annihilation and positronium formation on the 1.3×10^{-4} Pa (10^{-6} torr) N_2 background. Background gas pressures in room-temperature Penning traps approach 1.3×10^{-8} Pa (10^{-10} torr). If we assume that the cross sections for annihilation on other background gases are similar to that of N_2 [57], our trap lifetime should approach 5 days, long enough to accumulate a significant number of positrons.

We have also estimated the number of positrons ejected from the trap due to large-angle scattering by positrons from the positron source and the moderator. The Rutherford-scattering cross section for these collisions is quite small and the trap loss rate is lower than that of background collisions.

[1] P.J. Schultz and K.G. Lynn, Rev. Mod. Phys. **60**, 701 (1988), and references therein.
[2] T.J. Murphy and C.M. Surko, Phys. Rev. Lett. **67**, 2954 (1991).
[3] L.H. Haarsma, K. Abdullah, and G. Gabrielse, Phys. Rev. Lett. **75**, 806 (1995).
[4] R.G. Greaves and C.M. Surko, Phys. Plasmas **4**, 1528 (1997).
[5] A.P. Mills, Appl. Phys. Lett. **35**, 427 (1979); **37**, 667 (1980).
[6] A.P. Mills, Hyperfine Interact. **44**, 107 (1988).
[7] D.A. Fischer, K.G. Lynn, and D.W. Gidley, Phys. Rev. B **33**, 4479 (1986).
[8] N. Zafar, J. Chevallier, F.M. Jacobsen, M. Charlton, and G. Laricchia, Appl. Phys. A: Solids Surf. **47**, 409 (1988); D.M. Chen, K.G. Lynn, R. Pareja, and Bent Nielsen, Phys. Rev. B **31**, 4123 (1985).
[9] C.M. Surko, M. Leventhal, A. Passner, and F.J. Wysocki, in *Non-neutral Plasma Physics*, edited by C.W. Roberson and C.F. Driscoll (AIP, New York, 1988), p. 75; C.M. Surko, M. Leventhal, and A. Passner, Phys. Rev. Lett. **62**, 901 (1989); T.E. Cowan, J. Hartley, R.H. Howell, J.L. McDonald, R.R. Ronatgi, and J. Fajans, Mater. Sci. Forum **105-110**, 529 (1992).
[10] L. Haarsma, K. Abdullah, and G. Gabriesle, Hyperfine Interact. **76**, 143 (1993); G. Gabrielse, W. Jhe, D. Phillips, R. Kaiser, H. Kalinowsky, and J. Gröbner, Mater. Sci. Forum **105-110**, 75 (1992).
[11] J.M. Wadehra, T.S. Stein, and W.E. Kauppila, Phys. Rev. A **29**, 2912 (1984).
[12] R.S. Conti, B. Ghaffari, and T.D. Steiger, Nucl. Instrum. Methods Phys. Res. A **299**, 420 (1990).
[13] C.F. Driscoll, K.S. Fine, and J.H. Malmberg, Phys. Fluids **29**, 2015 (1986).
[14] J.J. Bollinger, D.J. Heinzen, F.L. Moore, Wayne M. Itano, D.J. Wineland, and D.H.E. Dubin, Phys. Rev. A **48**, 525 (1993).
[15] J.J. Bollinger, L.R. Brewer, J.C. Bergquist, Wayne M. Itano, D.J. Larson, S.L. Gilbert, and D.J. Wineland, in *Intense Positron Beams*, edited by E.H. Ottewitte and W. Kells (World Scientific, Singapore, 1988), p. 63.
[16] D.J. Wineland, C.S. Weimer, and J.J. Bollinger, Hyperfine Interact. **76**, 115 (1993).
[17] H. Boehmer, in *Slow Positron Beam Techniques for Solids and Surfaces*, edited by E. Ottewitte and A. Weiss, AIP Conf. Proc. 303 (AIP, New York, 1994), p. 422.
[18] S.J. Gilbert, C. Kurtz, R.G. Greaves, and C.M. Surko, Appl. Phys. Lett. **70**, 1944 (1997).
[19] J.H. Malmberg and T.M. O'Neil, Phys. Rev. Lett. **39**, 1333 (1977).
[20] G. Gabrielse, S.L. Rolston, L. Haarsma, and W. Kells, Phys. Lett. A **129**, 38 (1988).
[21] M.E. Glinsky and T.M. O'Neil, Phys. Fluids B **3**, 1279 (1991).
[22] G. Gabrielse, W. Jhe, D. Phillips, W. Quint, C. Tseng, L. Haarsma, K. Abdullah, J. Gröbner, and H. Kalinowsky, Hyperfine Interact. **76**, 81 (1993).
[23] P.B. Schwinberg, R.S. Van Dyck, and H.G. Dehmelt, Phys. Lett. **81A**, 119 (1981).
[24] D.S. Hall, Ph.D. thesis, Harvard University, Cambridge, MA, 1997.
[25] G. Gabrielse, J. Estrada. S. Peil, T. Roach. J.N. Tan, and P. Yesley, in *Non-neutral Plasma Physics III*, edited by J.J. Bollinger, R.L. Spencer, and R.C. Davidson (AIP, New York, 1999), p. 29.
[26] B. Ghaffari and R.S. Conti, Phys. Rev. Lett. **75**, 3118 (1995).
[27] A.P. Mills, Jr., in *Positron Scattering in Gases*, edited by J.W. Humberston and M.R.C. McDowell (Plenum Press, New York, 1984), p. 121.
[28] H. Boehmer, M. Adams, and N. Rynn, Phys. Plasmas **2**, 4369 (1995).
[29] T.J. Murphy and C.M. Surko, Phys. Rev. A **46**, 5696 (1992).
[30] C.M. Surko, S.J. Gilbert, and R.G. Greaves, in *Non-neutral Plasma Physics III*, edited by J.J. Bollinger, R.L. Spencer, and R.C. Davidson (AIP, New York, 1999), p. 3.
[31] L.R. Brewer, J.D. Prestage, J.J. Bollinger, Wayne M. Itano, D.J. Larson, and D.J. Wineland, Phys. Rev. A **38**, 859 (1988).
[32] For reviews, see D.J. Wineland, Wayne M. Itano, J.C. Bergquist, J.J. Bollinger, and J.D. Prestage, in *Atomic Physics 9*, edited by R.S. Van Dyck, Jr. and E.N. Fortson (World Scientific, Singapore, 1985), p. 3; W.D. Phillips, J.V. Prodan, and H. Metcalf, *ibid.*, p. 338, and references therein.
[33] D.J. Larson, J.C. Bergquist, J.J. Bollinger, Wayne M. Itano, and D.J. Wineland, Phys. Rev. Lett. **57**, 70 (1986).
[34] J.D. Jackson, *Classical Electrodynamics* (John Wiley and Sons, New York, 1975).
[35] W.R. Leo, *Techniques for Nuclear and Particle Physics Experiments* (Springer-Verlag, New York, 1987), p. 44.
[36] K. Nanbu, Phys. Rev. E **55**, 4642 (1997).
[37] D.J. Heinzen, J.J. Bollinger, F.L. Moore, Wayne M. Itano, and D.J. Wineland, Phys. Rev. Lett. 66, 2080 (1991).
[38] X.-P. Huang, J.J. Bollinger, T.B. Mitchell, and W.M. Itano, Phys. Rev. Lett. **80**, 73 (1998).
[39] X.-P. Huang, J.J. Bollinger, T.B. Mitchel, W.M. Itano, and D.H.E. Dubin, Phys. Plasmas **5**, 1656 (1998).
[40] We thank T. M. O'Neil, U. C. San Diego for pointing out this mechanism for positron loss.
[41] D.J. Wineland, R.E. Drullinger, and F.L. Walls, Phys. Rev. Lett. **40**, 1639 (1978); W.M. Itano and D.J. Wineland, Phys. Rev. A **25**, 35 (1982).
[42] W.M. Itano, L.R. Brewer, D.J. Larson, and D.J. Wineland, Phys. Rev. A **38**, 5698 (1988).
[43] D.T. Britton, P.A. Huttunen, J. Måkinen, E. Soininen, and A. Vehanen, Phys. Rev. Lett. **62**, 2413 (1989).
[44] Alternatively, the positron source and moderator could be kept on axis behind one endcap by using a thin crystal film transmission moderator. However, the transmitted positron energy spread is heavily dependent on the foil quality and thickness.
[45] C.A. Murray and A.P. Mills, Jr., Solid State Commun. **34**, 789 (1980); R.J. Wilson, Phys. Rev. B **27**, 6974 (1983).
[46] T.M. O'Neil, Phys. Fluids **24**, 1447 (1981).
[47] M.E. Glinsky, T.M. O'Neil, M.B. Rosenbluth, K. Tsuruta, and S. Ichimaru, Phys. Fluids B **4**, 1156 (1992).
[48] S.L. Gilbert, J.J. Bollinger, and D.J. Wineland, Phys. Rev. Lett. **60**, 2022 (1988).
[49] F. Reif, *Fundamentals of Statistical and Thermal Physics* (McGraw-Hill, New York, 1965), p. 273.
[50] X. Krall and X. Trivelpiece, *Principles of Plasma Physics* (McGraw-Hill, New York, 1992), p. 1156.
[51] In Ref. [16], a distribution $P(\theta)d\theta \propto \exp(\theta^2/\langle\theta^2\rangle)d\theta$ was assumed whereas the distribution $P(\theta)d\theta \propto \exp(\theta^2/\langle\theta^2\rangle)\sin\theta d\theta$ should have been used. Assuming small angles ($\sin\theta \simeq \theta$), Eq.

(9) of Ref. [16] should read $\eta_c = \exp(-\theta^2/\Delta\theta_s^2)$, where $\Delta\theta_s^2 = \langle\theta^2\rangle$. This does not significantly affect the results stated in Table 1 of Ref. [16], except for the last value of η_c, which is overestimated.

[52] C.F. Driscoll and J.H. Malmberg, Phys. Rev. Lett. **50**, 167 (1983); F. Anderegg, E. Sarid, and C.F. Driscoll, Bull. Am. Phys. Soc. **38**, 1971 (1993).

[53] B.M. Jelenkovic, T.B. Mitchell, J.J. Bollinger, X.-P. Huang, W.M. Itano, A.S. Barton, and D.J. Wineland, Bull. Am. Phys. Soc. **43**, No. 8, 1653 (1998).

[54] H. Tawara and T. Kato, At. Data Nucl. Data Tables **35**, 167 (1987).

[55] E. Morenzoni, in *Collisions of Antiparticles with Atoms*, edited by D. Berenyi and G. Hock (Springer-Verlag, Berlin, 1991), p. 173.

[56] H.S.W. Massey, E.H.S. Burhop, and H. B. Gilbody, *Electronic and Ionic Impact Phenomena* (Oxford University Press, London, 1974), Vol. V, p. 3125.

[57] P.A. Fraser, in *Advances in Atomic and Molecular Physics 4* (Academic Press, New York, 1968), p. 63.

Stick-Slip Dynamics of a Stressed Ion Crystal

T. B. Mitchell,[1] J. J. Bollinger,[2] W. M. Itano,[2] and D. H. E. Dubin[3]
[1]*Department of Physics and Astronomy, University of Delaware, Newark, Delaware 19716*
[2]*Time and Frequency Division, National Institute of Standards and Technology, Boulder, Colorado 80305*
[3]*Department of Physics, University of California at San Diego, La Jolla, California 92093*
(Received 24 May 2001; published 10 October 2001)

We study the control of the rotation of a laser-cooled ion crystal in a Penning trap by a rotating electric field perturbation. We show that application of a small torque produces sudden angular jumps or "slips" of the crystal orientation spaced by intervals when the crystal is phase locked or "stuck" relative to the rotating perturbation. The distribution of angular slips is described by a power law, where the power-law exponent depends on the applied torque. We believe this system is driven by a constant force and small perturbations or thermal effects trigger the slips.

DOI: 10.1103/PhysRevLett.87.183001 PACS numbers: 32.80.Pj, 05.65.+b, 52.27.Gr, 52.27.Jt

Non-neutral plasmas confined in Penning-Malmberg traps are used in a variety of experiments including plasma physics [1], Coulomb crystal studies [2,3], precision spectroscopy [4], antimatter research [5], and storage of highly charged ions [6]. Recently there has been a great deal of interest in using a rotating electric field perturbation to control the global $\mathbf{E} \times \mathbf{B}$ rotation of these plasmas [5,7,8]. For crystallized ion plasmas, phase-locked control of the plasma rotation has been demonstrated [8], which has important implications for atomic clocks [4] and for quantum computation with trapped ions [9]. In this Letter we study the limits to phase-locked control due to the application of a small torque produced by the radiation pressure of a weak laser beam. We observe sudden angular jumps or "slips" of the crystal orientation spaced by intervals when the crystal orientation is phase locked or "stuck" relative to the rotating perturbation. Stick-slip behavior similar to that observed here is found in many different and diverse systems: for example, in studies of friction between two surfaces [10,11], in experiments on avalanches and slips in granular systems [12–14], and as the underlying process in spring-block models of earthquakes [15,16]. Many of these systems, including the study presented here, exhibit a power-law distribution of the slip amplitudes, indicative of an underlying critical point [17,18].

Our work uses the Penning-Malmberg trap at NIST to store $\sim 15\,000$ $^9Be^+$ ions. The ions interact by unscreened Coulomb repulsion and are Doppler laser cooled [19] to millikelvin temperatures, where their thermal energy is small compared to the Coulomb potential energy between nearest neighbor ions. Under these conditions the ions are strongly coupled [20] and form a Coulomb crystal (a classical Wigner crystal) [2,3]. Structurally similar Coulomb crystals are believed to exist in dense astrophysical matter, such as the interior of white dwarfs and the outer crust of neutron stars [21]. Observations of power-law statistics of soft gamma-ray events have recently been interpreted as evidence that the Coulomb crystal comprising the outer crust of a magnetized neutron star can undergo very large-scale slips ("starquakes") [22,23]. The measured power-law exponents of the neutron starquakes lie within the range of exponents we measure here (see Fig. 3).

Figure 1(a) shows the experimental setup [3,8]. The $^9Be^+$ ions were confined radially by a uniform magnetic field $B = 4.465$ T (cyclotron frequency $\Omega_c/2\pi = 7.608$ MHz) in the $\hat{z}$ direction and axially by a potential difference of $V_0 = -500$ V applied between the center and end electrodes of the trap. Near the trap center the trap

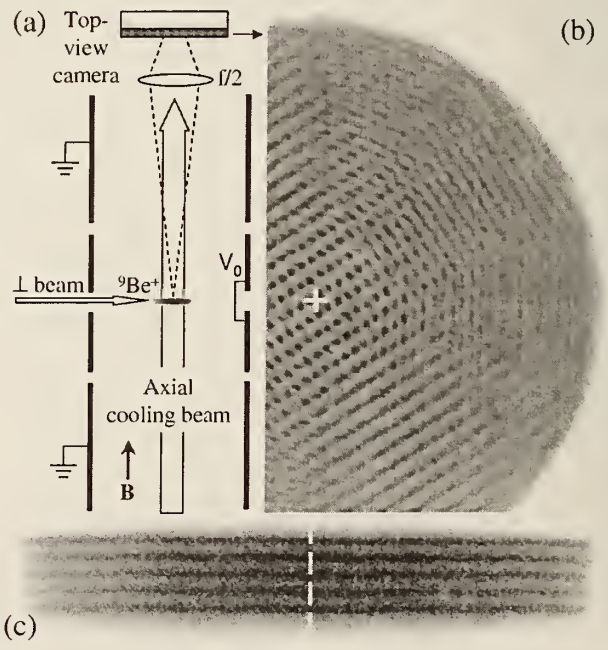

FIG. 1. (a) Schematic of the cylindrical Penning trap and the top-view imaging system. The side-view imaging system is not shown. (b) Strobed top-view image of a five-axial plane $^9Be^+$ ion crystal with a bcc structure, similar to those used in this study. (c) Side-view image (unstrobed) of the same ion crystal. The diameter ($2r_{Be}$) of the $^9Be^+$ ions is 495 μm. Ions of greater mass are located at $r > r_{Be}$ but do not fluoresce in the laser beam. The rotation axes are indicated.

potential is quadratic and given by $m\omega_z^2(z^2 - r^2/2)/(2e)$, where the axial frequency $\omega_z/2\pi = 565$ kHz for $^9Be^+$. Here r and z denote the cylindrical radial and axial coordinates. Because of the axial magnetic field and the radial components of the ion space charge and trap electric fields, the ion crystal rotates at a frequency ω_r about the trap symmetry ($\hat{z}$) axis. In addition to $^9Be^+$ ions, ions of greater mass ("heavy ions") such as BeH^+ and $BeOH^+$ are created by reactions with $^9Be^+$ ions and background neutral molecules. For the work discussed here, typically 20% to 50% of the plasma consisted of heavy impurity ions. These ions are sympathetically cooled to temperatures similar to the $^9Be^+$ ions and, due to the rotation, centrifugally separate to larger radii where they crystallize.

We applied an electric field perturbation rotating about the $\hat{z}$ axis at frequency ω_{rp} to control ω_r [8]. The rotating perturbation applies a torque on the radial boundary of the plasma (on the nonfluorescing, heavy ions) by creating a small-amplitude traveling wave. The torque due to this wave is then transferred to the plasma interior through the strong interparticle forces, which act to bring the plasma to the same rotation frequency as ω_{rp} [24]. We observe similar stick-slip motion with both dipole and quadrupole rotating fields. However, most measurements, including those we report here, were taken with a dipole rotating field. The radial binding force of the trap is due to the Lorentz force produced by the plasma's rotation through the magnetic field. Therefore, changing ω_r changes the radial binding force of the trap and provides a sensitive way to adjust the overall shape and structural phase of the plasma. In this work, $\omega_r \approx \omega_{rp} = 2\pi \times 22.8$ kHz, which produced a disk-shaped plasma consisting of five axial planes and a bcc-like crystal structure in the plasma center [3]. Because $\omega_r \ll \Omega_c$, the ion motion in a direction perpendicular to the magnetic field is determined principally by $\mathbf{E} \times \mathbf{B}$ guiding center dynamics [25].

The main cooling-laser beam ($\lambda = 313$ nm) was directed along the z axis. This beam's power was ~ 50 μW, and it was focused to a ~ 0.5 mm waist at the ion crystal. A second cooling beam [$\perp$ beam in Fig. 1(a)], derived from the same laser, was directed perpendicularly to $\hat{z}$ and had a ~ 70 μm waist and ~ 1 μW power. Both the perpendicular and parallel cooling lasers were required to form a well defined crystal in the disk-shaped plasmas discussed here. The $\perp$ beam is normally directed through the radial center ($r = 0$) of the crystal in order to minimize its applied torque while providing a low Doppler-cooling temperature [19]. In this experiment, we offset the $\perp$-beam position slightly (5–30 μm) from the plasma center to produce a torque on the $^9Be^+$ ions in the same direction as the plasma rotation [26]. The torque from the $\perp$ beam was larger than any other ambient torque due to, for example, asymmetries in the trap construction or background gas drag.

A series of lenses formed side- and top-view images of the ion fluorescence, with viewing directions perpendicular and parallel to the magnetic field, respectively, on either a gateable charge-coupled device (CCD) camera or an imaging photomultiplier tube. The resolution of the optical systems was ~ 4 μm, while typical interparticle spacings were ~ 15 μm. By detecting the ion fluorescence synchronously with the rotating perturbation drive, images of the individual ions which make up the Coulomb crystals were obtained. Figure 1(b) shows a strobed, top-view CCD camera image accumulated over 40 s of a five-axial plane crystal in the bcc structural phase. The ion positions are well localized in the plasma center; however, at larger radii they are blurred.

To investigate the blurring we used the imaging photomultiplier tube in the top-view position to record the positions and detection times of the fluorescence photons. Runs consisted of 125 ms intervals of data recorded each second over long periods of time (up to 5000 s). Images similar to those in Fig. 1(b) were created for each 125 ms interval by constructing 2D histograms of the ion fluorescence in the frame of the rotating perturbation. The orientation θ_{cry} of the central crystallized region in the rotating frame was determined (modulo π due to the bcc crystal bilateral symmetry) with an uncertainty of $\sim 0.002\pi$ rad [27].

In Fig. 2 we plot $\theta_{cry}(t)$ for two runs which differ mainly in the amount of $\perp$-beam torque. Over long time scales the $\perp$-beam torque produces a slightly faster rotation (a rotational "creep") of the $^9Be^+$ crystal relative to the rotating perturbation. For example, in run 2 $\Delta\omega \equiv \omega_r - \omega_{rp} \approx 2\pi \times 8$ mHz. Over shorter time scales, as shown in the inset in Fig. 2, much of this crystal rotation takes place with sudden jumps in θ_{cry}, slips, whose time scale is too fast to be captured by the top-view diagnostic. Intermittent behavior appears to be a common feature in the plastic deformation (creep) of many materials. (See [28] for

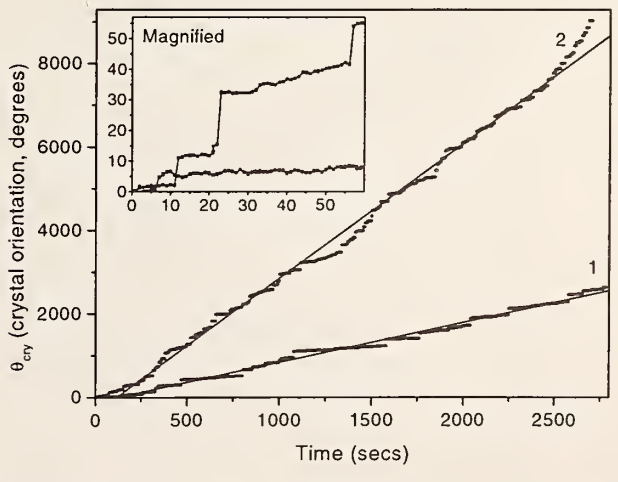

FIG. 2. Crystal orientation θ_{cry} in the frame of the rotating perturbation for two data runs with different $\perp$-beam torques. The torque is greater in run 2. The lines are from a linear regression fit. The inset shows a magnified plot of the first 60 s of data.

references.) Let $\Delta\theta_{cry}$ denote the angular displacement between two successive measurements of θ_{cry}. The statistics of $\Delta\theta_{cry}$ consists of a normal distribution (from measurement error) centered about zero with a width of $\sim 0.002\pi$, and infrequent larger slips. Because of the known sign of the $\perp$-beam torque and the π ambiguity mentioned above, we choose $\Delta\theta_{cry}$ to lie in the range $[0, \pi)$. To separate statistically significant slips from measurement error we further require $0.007\pi \leq \Delta\theta_{cry} \leq 0.97\pi$. We find that statistically significant slips account for greater than 90% of the measured change in θ_{cry}.

The $\perp$-beam torque is applied to all the $^9Be^+$ ions in the radial interior of the crystal. The rotating perturbation, however, applies its torque on the outer radial boundary of the heavy ions. We therefore believe the stress due to the competition between these torques is greatest in the region of the heavy ions and anticipate that the slips of Fig. 2 are due to ion motion between the radial boundary of the $^9Be^+$ ions, r_{Bc}, and the overall radial boundary of the plasma. This is supported by the top-view images, which show most slips occurring as approximate rigid rotations of the $^9Be^+$ ions and also by simulation work discussed below. Because the slips occur at a radius greater than r_{Be}, and r_{Be} varied from run to run, we characterize a slip amplitude A_{slip} by the linear distance $\Delta\theta_{cry} r_{Bc}$.

Figure 3 shows the distribution $f(A_{slip})$ of slips for the two data runs shown in Fig. 2. Because we cannot distinguish between slips with amplitude A_{slip} or $A_{slip} + n\pi r_{Be}$, where n is an integer, we fit to the function $f_{slip} \propto \sum_{n=0}^{n_{cut}} (A_{slip} + n\pi r_{Be})^{-\gamma}$ to determine the agreement of the data with a power-law distribution. Here n_{cut} is a cutoff that could depend on the system size, creep rate, or other factors. We obtain a good fit for

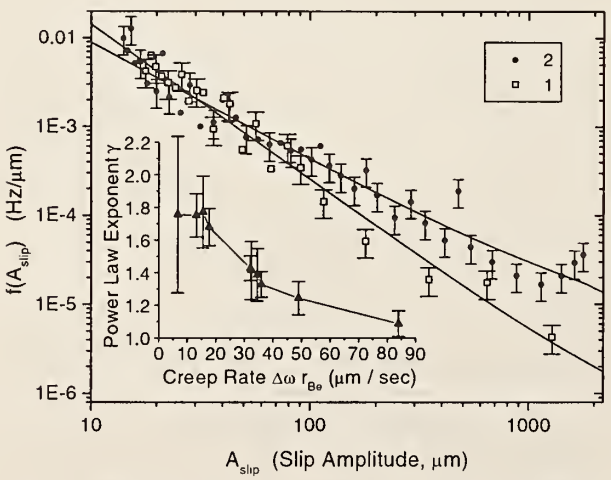

FIG. 3. Distribution $f(A_{slip})$, where $f(A_{slip})dA_{slip}$ is the frequency of slips between A_{slip} and $A_{slip} + dA_{slip}$, for the two data runs shown in Fig. 2. The lines are fits to a power law with a cutoff as described in the text. The inset shows the measured power-law exponent γ versus applied torque, as parametrized by the creep rate, for all of the data runs.

any n_{cut} but find that χ^2 goes through a weak minimum at $n_{cut} = 6$. We use $n_{cut} = 6$ in the following analysis. This results in measured γs slightly larger (<10% and within the uncertainty of the fit) than those resulting from $n_{cut} = 1$. In the inset in Fig. 3 we plot the measured power-law exponent γ as a function of the creep rate $\Delta\omega r_{Bc}$ for ten data runs with the same rotating perturbation strength but different $\perp$-beam torques. We find that γ decreases as the creep rate, a measure of the applied $\perp$-beam torque, increases. Decreases in the stick-slip exponent with increased drive have been observed in some systems [11,29,30], but not in others [28].

Most experiments exhibiting stick-slip behavior are performed with "constant-velocity driving" where the force is applied through an effective elastic coupling [11–13]. The driving force of the system is something like $F(t) = K[Vt - x(t)]$, where "x" is the "position" of an element in the system (for example, the position of a bead or slider block in a chain), K is the effective spring constant coupling the applied force to each element in the system, and V is the constant average velocity that is imposed on the system. Stick-slip motion occurs for small V and K and a critical point exists in the limit $V \to 0$ and $K \to 0$ [18,29]. If the system gets stuck, it will eventually slip again because the driving force increases linearly until slip occurs. However, this experiment is performed under conditions more similar to "constant-force driving" since the $\perp$-beam radiation-pressure force is constant in time and applied directly to the $^9Be^+$ ions. In constant-force driving the system undergoes a depinning transition at a critical force F_c and moves with constant average velocity proportional to $(F - F_c)^\beta$ for $F > F_c$ and critical exponent β [29].

Inspection of Fig. 2 shows that the time intervals between successive slips (the waiting periods) are typically many seconds. An analysis of the waiting periods shows an approximately Gaussian distribution with mean waiting periods ranging from 4 s for the highest $\perp$-beam torques to 12 s for the lowest $\perp$-beam torques. These waiting periods are long compared to any known dynamical time scales due to internal modes of the system. In constant-force driving, if the system gets stuck for such a long period, it should permanently stick, which is not what we observe. One possibility is that the slips could be excited by a perturbation. By deliberately modulating the amplitude of the cooling and torquing lasers we have established that the amplitude noise present in these beams is not high enough to trigger slips.

We have performed molecular-dynamics simulations with 1000 ions (40% $^9Be^+$, 60% heavy) with the goal of better understanding the source of the slips. About four months of computation time has been required to simulate the equivalent of $\sim$1 s of experimental time. The simulations have produced one event which can be interpreted as a slip. In that event a rearrangement of a small number of heavy ions in the vicinity of a lattice defect produced a sudden change in the orientation of the

crystal. Because it appears that the rearrangement of a few heavy ions can trigger a slip, thermal fluctuations of the ions may be responsible for starting a slip. Once started, the slip eventually stops because the driving force of the $\perp$ beam is not sufficient to sustain continuous motion.

In summary, we have observed stick-slip motion in the rotational control of laser-cooled ion crystals in a Penning trap. We believe this system is constant-force driven and may be an experimental example of a subcritical state [18] where the slips are triggered by thermal fluctuations or by other unidentified perturbations (such as collisions with neutral background atoms). The trapped-ion crystal system discussed here possesses most of the features of a self-organized critical (SOC) state [17,18]. Therefore further investigations of the stick-slip behavior over a wider range of control parameters ($\perp$-beam torque, temperature, and rotating perturbation strength) could be useful for understanding the applicability of the SOC concept to real physical systems. Finally, minimizing the occurrence of the slips is important for some applications [4,9]. This can be done by minimizing the $\perp$-beam torque, either through active control of the $\perp$-beam position or by appropriate tailoring of the $\perp$-beam profile [31]. Increasing the strength of the rotating perturbation should also decrease the frequency of slips due to small ion rearrangements. Two runs taken with half the rotating perturbation strength of the data set analyzed here showed an increase in the number of slips and rotational creep of the ion crystal.

This research was supported by the Office of Naval Research and the National Science Foundation (D. H. E. D.). We thank S. Zapperi, R. L. Kautz, J. M. Kriesel, J. P. Schiffer, and D. J. Wineland for useful comments and B. M. Jelenković and X.-P. Huang for technical assistance.

[1] *Non-Neutral Plasma Physics III,* edited by J. J. Bollinger, R. Spencer, and R. Davidson (AIP, New York, 1999).
[2] W. M. Itano, J. J. Bollinger, J. N. Tan, B. Jelenković, X.-P. Huang, and D. J. Wineland, Science **279**, 686 (1998).
[3] T. B. Mitchell, J. J. Bollinger, D. H. E. Dubin, X.-P. Huang, W. M. Itano, and R. H. Baughman, Science **282**, 1290 (1998).
[4] J. N. Tan, J. J. Bollinger, and D. J. Wineland, IEEE Trans. Instrum. Meas. **44**, 144 (1995).
[5] R. G. Greaves and C. M. Surko, Phys. Rev. Lett. **85**, 1883 (2000).
[6] L. Gruber, J. P. Holder, J. Steiger, B. R. Beck, H. E. DeWitt, J. Glassman, J. W. McDonald, D. A. Church, and D. Schneider, Phys. Rev. Lett. **86**, 636 (2001).
[7] E. M. Hollmann, F. Anderegg, and C. F. Driscoll, Phys. Plasmas **7**, 2776 (2000).
[8] X.-P. Huang, J. J. Bollinger, T. B. Mitchell, and W. M. Itano, Phys. Plasmas **5**, 1656 (1998).
[9] J. I. Cirac and P. Zoller, Phys. Rev. Lett. **74**, 4091 (1995).
[10] A. L. Demirel and S. Granick, Phys. Rev. Lett. **77**, 4330 (1996).
[11] S. Ciliberto and C. Laroche, J. Phys. I (France) **4**, 223 (1994).
[12] S. Nasuno, A. Kudrolli, and J. P. Gollub, Phys. Rev. Lett. **79**, 949 (1997).
[13] I. Albert, P. Tegzes, B. Kahnig, R. Albert, J. G. Sample, M. Pfeifer, A.-L. Barabási, T. Vicsek, and P. Schiffer, Phys. Rev. Lett. **84**, 5122 (2000).
[14] V. Frette, K. Christensen, A. Malthe-Sørenssen, J. Feder, T. Jøssang, and P. Meakin, Nature (London) **379**, 49 (1996).
[15] Z. Olami, H. J. S. Feder, and K. Christensen, Phys. Rev. Lett. **68**, 1244 (1992).
[16] R. Burridge and L. Knopoff, Bull. Seismol. Soc. Am. **57**, 341 (1967).
[17] P. Bak, C. Tang, and K. Wiesenfeld, Phys. Rev. Lett. **59**, 381 (1987).
[18] A. Vespignani and S. Zapperi, Phys. Rev. E **57**, 6345 (1998).
[19] W. M. Itano, L. R. Brewer, D. J. Larson, and D. J. Wineland, Phys. Rev. A **38**, 5698 (1988).
[20] S. Ichimaru, H. Iyetomi, and S. Tanaka, Phys. Rep. **149**, 91 (1987).
[21] H. M. Van Horn, Science **252**, 384 (1991).
[22] B. Cheng, R. I. Epstein, R. A. Guyer, and A. C. Young, Nature (London) **382**, 518 (1996).
[23] E. Göğüş, P. M. Woods, C. Kouveliotou, J. van Paradus, M. S. Briggs, R. C. Duncan, and C. Thompson, Astrophys. J. **532**, L121 (2000).
[24] D. H. E. Dubin and T. M. O'Neil, Rev. Mod. Phys. **71**, 87 (1999).
[25] D. H. E. Dubin and T. M. O'Neil, Phys. Rev. Lett. **60**, 511 (1988).
[26] D. J. Wineland, J. J. Bollinger, W. M. Itano, and J. D. Prestage, J. Opt. Soc. Am. B **2**, 1721 (1985).
[27] The crystal images occasionally showed defect lines that moved slowly across the crystal and prevented a definitive measurement of θ_{cry}. This occurred more frequently with larger torque. In this case shorter time series separated by intervals when θ_{cry} could not be unambiguously determined were appended to each other without introducing discontinuities in θ_{cry} at the junctures.
[28] M.-C. Miguel, A. Vespignani, S. Zapperi, J. Weiss, and J.-R. Grasso, Nature (London) **410**, 667 (2001).
[29] F. Lacombe, S. Zapperi, and H. J. Hermann, Phys. Rev. B **63**, 104104 (2001).
[30] S. Zapperi, P. Cizeau, G. Durin, and H. E. Stanley, Phys. Rev. B **58**, 6353 (1998).
[31] The $\perp$-beam torque can be reduced with a beam that has a large waist and frequency dispersion across the waist that matches the ion Doppler shifts due to the plasma rotation.

Quantum Coherence and Decoherence - ISQM - Tokyo '98
Y.A. Ono and K. Fujikawa (Editors)

Quantum Computation, Spectroscopy of Trapped Ions, and Schrödinger's Cat *

D.J. Wineland, C. Monroe, W.M. Itano, D. Kielpinski, B.E. King, C.J. Myatt, Q.A. Turchette, and C.S. Wood

National Institute of Standards and Technology (NIST), Boulder, CO, 80303

We summarize efforts at NIST to implement quantum computation using trapped ions, based on a scheme proposed by J.I. Cirac and P. Zoller (Innsbruck University). The use of quantum logic to create entangled states, which can maximize the quantum-limited signal-to-noise ratio in spectroscopy, is discussed.

1. INTRODUCTION

The invention by Peter Shor [1] of a quantum algorithm for factorizing large numbers has stimulated a host of theoretical and experimental investigations in the field of quantum information [2]. In the area of quantum computation, various schemes have been proposed to realize experimentally a model quantum computer [2]. In the ion storage group at NIST, we are trying to realize such a device based on the proposal by Cirac and Zoller [3].

In the Cirac-Zoller scheme, qubits are formed from two internal energy states, labeled $|\downarrow\rangle$ and $|\uparrow\rangle$, of trapped atomic ions. If the ions are laser cooled in the same trap, they form a crystalline array whose vibrations can be described in terms of normal modes. The ground and first excited states of a selected mode can also form a qubit. This qubit can serve as a data bus, since the normal modes are a *shared* property of the ions. An individual ion in the array can be coherently manipulated and coupled to the selected normal mode by using focused laser beams [3]. A universal logic operation, such as a controlled-not (CN) logic gate between ion qubit i and ion qubit j, is accomplished by (1) mapping the internal state of qubit i onto the selected motional qubit, (2) performing a CN between the motional qubit and qubit j, and (3) mapping the motional qubit state back onto qubit i. Each of these steps has been accomplished in the NIST experiments with a single ion [4,5]. We are currently devoting efforts to: (1) scaling quantum logic operations to two or more ions (Sec. 5), (2) applying quantum logic to study fundamental measurement problems on EPR and GHZ-like states, and (3) applying quantum logic to fundamentally improve the signal-to-noise ratio (SNR) in spectroscopy and atomic clocks. In this paper we briefly discuss this last application. We are aware of similar efforts to implement trapped-ion quantum logic at IBM, Almaden; Innsbruck University; Los Alamos National Laboratory; Max Planck Institute, Garching; and Oxford University.

*Contribution of NIST; not subject to U.S. copyright

2. ENTANGLED STATES FOR SPECTROSCOPY

A collection of atoms (neutral or charged) whose internal states are entangled in a specific way can improve the quantum-limited SNR in spectroscopy. This application of quantum logic to form entanglement is useful with a relatively small number of atoms and logic operations. For example, for high-accuracy, ion-based frequency standards [6], a relatively small number of trapped ions ($L \leq 100$) appears optimum due to various experimental constraints; with $L = 10 - 100$, a significant improvement in performance in atomic clocks could be expected. In contrast, factoring a number which cannot easily be factored on a classical computer would require considerably more ions and operations.

In spectroscopy experiments on L atoms, in which the observable is atomic population, we can view the problem in the following way using the spin-1/2 analog for two-level atoms. The total angular momentum of the system is given by $\mathbf{J} = \sum_{i=1}^{L} \mathbf{S}_i$, where $\mathbf{S}_i$ is the spin of the ith atom ($S_i = 1/2$). The task is to measure ω_0, the frequency of transitions between the $|\downarrow\rangle$ and $|\uparrow\rangle$ states, relative to the frequency ω_R of a reference oscillator. We first prepare an initial state for the spins. Typically, spectroscopy is performed by applying (classical) fields of frequency ω_R for a time T_R according to the method of separated fields by Ramsey [7]. We assume the same field amplitude is applied to all atoms (the phases might be different) and that the maximum value of T_R is fixed by experimental constraints (Sec. 3). After applying these fields, we measure the final state populations; for example, the number of atoms $L_\downarrow$ in the $|\downarrow\rangle$ state. In trapped-ion experiments, this has been accomplished through laser fluorescence detection with nearly 100% efficiency, which we assume here (see the discussion and references in Ref. [5]). In the spin-1/2 analog, measuring $L_\downarrow$ is equivalent to measuring the operator J_z, since $L_\downarrow = J\mathbb{I} - J_z$ where $\mathbb{I}$ is the identity operator. The SNR (for repeated measurements) is fundamentally limited by the quantum fluctuations in the number of atoms which are observed to be in the $|\downarrow\rangle$ state. These fluctuations can be called quantum projection noise [8]. Spectroscopy is typically performed on L initially unentangled atoms (for example, $\Psi(t=0) = \prod_{i=1}^{L} |\downarrow\rangle_i$) which remain unentangled after the application of the Ramsey fields. For this case, the imprecision in a determination of the frequency of the transition is limited by projection noise to the "shot noise" limit $(\Delta\omega)_{meas} = 1/\sqrt{LT_R\tau}$ where $\tau \gg T_R$ is the total averaging time [8]. If the atoms can be prepared initially in particular entangled states, it is possible to achieve $(\Delta\omega)_{meas} < 1/\sqrt{LT_R\tau}$.

In optics, squeezed states have been shown to improve the SNR in interferometers beyond the shot noise limit [9,10]. In 1986, Yurke [11] showed how particular entangled states, if they could be created, could be used as inputs to Mach-Zehnder interferometers to approach the Heisenberg limit of SNR. In 1991, Kitegawa and Ueda [12] showed how the Coulomb interaction between electrons in the two arms of an electron interferometer might be used to improve the SNR beyond the shot-noise limit. Because of the formal identity of Mach-Zehnder interferometers and Ramsey spectroscopy [13], similar ideas might be applied to the spectroscopy problem. Reference [13] showed how a Jaynes-Cummings-type coupling between trapped-ion internal states and a normal mode could be used to improve the SNR in spectroscopy beyond the shot-noise limit. The scheme in Ref. [13] has the advantage that the appropriate states can be generated by acting on all the ions at once (thus not requiring focused laser beams), but has the disadvantage that these states

are entangled with the motion, thereby requiring small motional decoherence. Reference [14] investigated the use of the generalized GHZ state, sometimes called the maximally entangled state, in spectroscopy. This state has the form

$$\psi_{max} = \frac{1}{\sqrt{2}}\Big(|\downarrow\rangle_1|\downarrow\rangle_2\cdots|\downarrow\rangle_L + e^{i\phi(t)}|\uparrow\rangle_1|\uparrow\rangle_2\cdots|\uparrow\rangle_L\Big), \tag{1}$$

where $\phi(t) = \phi_0 - L\omega_0 t$. After application of the Ramsey radiation, we measure the operator $\hat{O} \equiv \prod_{i=1}^{L} S_{zi}$. The resulting signal gives the exact Heisenberg limit of SNR ($(\Delta\omega)_{meas} = 1/L\sqrt{T_R\tau}$ where $\tau \gg T_R$) in spectroscopy (and interferometry).

The state ψ_{max} can be generated in a straightforward way by the application of L CN gates [3]. An alternative method was suggested in Ref. [14] and in Refs. [5] and [15] methods to generate ψ_{max} with a fixed number of steps (independent of L) are discussed. For all of these methods, the the motion is entangled with internal states during the creation of ψ_{max}, but is not entangled afterwards. Therefore, once ψ_{max} is created, the motion can lose coherence without affecting the entanglement of the internal states.

2.1. Schrödinger's Cat

As L becomes large and more macroscopic, states like ψ_{max} become more like Schrödinger's cat in that they represent coherent superpositions between widely separate regions of a large Hilbert space; for example, $|\uparrow\rangle_1|\uparrow\rangle_2\cdots|\uparrow\rangle_L \Longleftrightarrow$ "live cat;" $|\downarrow\rangle_1|\downarrow\rangle_2\cdots|\downarrow\rangle_L \Longleftrightarrow$ "dead cat". As has been emphasized in many discussions, as L becomes large the coherence between the two components of the cat becomes harder and harder to preserve [16]. This is apparent in Eq. (1) because if, for example, ω_0 fluctuates randomly, the two components of ψ_{max} will decohere relative to each other L times faster than for one ion (ψ_{max} for $L = 1$). Trapped ions are interesting because it may be possible to make L very large without significant decoherence. This is the same property that makes trapped ions interesting as possible frequency standards. For example, in Refs. [17] and [18], coherence times for individual ions ($L = 1$) exceeding 10 minutes were obtained.

3. Applicability

In the above, we have assumed that T_R is fixed, limited by some independent experimental factor. This assumption is warranted in many trapped-ion atomic clock experiments, where, for example, we want to limit the heating that takes place with laser cooling radiation absent. (During application of the Ramsey fields the cooling radiation must be removed to avoid perturbing the clock states.) Additionally, we may want to lock a local oscillator to the atomic reference in a practical time [6,19], thereby limiting T_R.

However, the use of entangled states may not be advantageous, given other conditions. For example, Huelga, *et al.* [20] assume that the ions are subject to a certain dephasing decoherence rate (decoherence time less than the total observation time). In this case, there is no advantage of using maximally entangled states over unentangled states. The reason is that since the maximally entangled state decoheres L times faster than the states of individual atoms, when we use the maximally entangled state, T_R must be reduced by a factor of L for optimum performance. Therefore, the gain from using the maximally entangled state is offset by the required reduced value of T_R.

Reference [5] discusses another case of practical interest. In atomic clocks, the frequency of an imperfect "local" oscillator, whose radiation drives the atomic transition, is controlled by the atom's absorption resonance. Depending on the spectrum of this oscillator's frequency fluctuations (when not controlled) the use of entangled states may or may not be beneficial.

4. Implementations

If we are able to create, with good fidelity, the state ψ_{max} (Eq. (1)), how do we perform spectroscopy? First, we note that ψ_{max} is the state we want *after* the first Ramsey $\pi/2$ pulse. Therefore, if we were to follow as closely as possible the Ramsey technique, we would take ψ_{max} and apply a $\pi/2$ pulse of radiation at frequency ω_0 to make the input state for the Ramsey radiation. However the first Ramsey $\pi/2$ pulse would only reverse this step; therefore, it is advantageous to take the creation of ψ_{max} as the first Ramsey $\pi/2$ pulse. The second Ramsey pulse (after time T_R) can be applied directly with radiation at frequency ω_R. The phase of this pulse (on each ion) must be fixed relative to the phases of the radiation used to create ψ_{max}. In general, the relation between these phases and ϕ_0 (Eq. (1)) will depend on the relative phases of the fields at the positions of each of the ions [5,21]. This will lead to a signal $S = \langle \tilde{O} \rangle \propto cos(L\Delta\omega T_R + \phi_f)$ where $\Delta\omega \equiv \omega_R - \omega_0$ and where ϕ_f depends on all of these phases.

We can extract ω_0 (relative to ω_R) by measuring $\langle \tilde{O} \rangle$ as a function of T_R, with $\Delta\omega$ fixed. This can be further simplified by measuring the signal for two values of T_R, $T_{R2} \gg T_{R1}$, where $\langle \tilde{O} \rangle \simeq 0$. Unfortunately, if the measured signal has a systematic bias as a function of T_R, an error in the determination of $\Delta\omega$ will result. This might happen, for example, if the ions heat up during application of the Ramsey radiation and a loss of signal occurs due to a reduced overlap between the ions and the laser used for fluorescence detection of the states. This problem could be overcome by measuring $\langle \tilde{O} \rangle$ for two values of ω_R, ω_{R1} and ω_{R2} such that $\omega_{R1} - \omega_0 \simeq -(\omega_{R2} - \omega_0)$ (determined by the above method), and two values of T_R, $T_{R1} \ll T_{R2}$. We then iterate the following steps: (1) we make $\langle \tilde{O}((\omega_{R1} - \omega_0)T_{R1}) \rangle \simeq \langle \tilde{O}((\omega_{R2} - \omega_0)T_{R1}) \rangle$ by adjusting the phase of the final $\pi/2$ pulse to make $\phi_f \to 0$. This will take a negligible amount of time since $T_{R1} \ll T_{R2}$. (2) We make $\langle \tilde{O}((\omega_{R1} - \omega_0)T_{R2}) \rangle \simeq \langle \tilde{O}((\omega_{R2} - \omega_0)T_{R2}) \rangle$ by adjusting ω_{R1} and/or ω_{R2} to force $\omega_{R1} - \omega_0 \to -(\omega_{R2} - \omega_0)$. This gives ω_0 relative to ω_R even if $\langle \tilde{O} \rangle$ has a systematic bias as a function of T_R.

An alternative solution is suggested by Huelga, *et al.* [20]. After T_R, instead of applying a $\pi/2$ pulse of radiation at frequency ω_R, we apply the time-reversed sequence of operations which created ψ_{max}. This has the advantage of cancelling out all of the CN phases that contribute to ϕ_0 and maps the signal ($\propto cos(L\Delta\omega T_R)$) onto a single ion (whereupon S_z is measured for that ion). This also reduces the problem of detection efficiency to one ion rather than L ions. The disadvantage of this technique is that for large values of T_R, the motional mode used for logic will, most likely, have to be recooled. This would require sympathetic cooling with the use of an ancillary ion which, to avoid the decohering effects of stray light scattering on the logic ions, might have to be another ion species [5].

A more serious limitation to the accurate determination of ω_0 is that, in practice, ψ_{max} will be realized only approximately and the state produced by the logic operations

will also be composed of states other than the $|\uparrow\rangle_1|\uparrow\rangle_2\cdots|\uparrow\rangle_L$ and $|\downarrow\rangle_1|\downarrow\rangle_2\cdots|\downarrow\rangle_L$ states; these other states will have a definite phase relation to the $|\uparrow\rangle_1|\uparrow\rangle_2\cdots|\uparrow\rangle_L$ and $|\downarrow\rangle_1|\downarrow\rangle_2\cdots|\downarrow\rangle_L$ states. Consequently, in general, the signal produced with either implemenation will be of the form

$$S = \sum_{p=1}^{L} C_p cos(p\Delta\omega T_R + \xi_p). \tag{2}$$

To accurately determine $\Delta\omega$, it will be necessary to Fourier decompose S. Since this will take more measurements, the advantages of using entangled states will be reduced.

In spite of this, in some applications, it will be useful to determine changes in ω_0 with respect to some external influence. For example, we might want to detect changes in ω_0 caused by changes in an externally applied field. In this case, as long as $|C_p| \ll 1$, for all $p < L$, we derive the benefits of entangled states (assuming the decoherence time is longer than T_R/L) by measuring changes in S for a particular value of T_R.

5. Experiments

As usual, our enthusiasm for implementing these schemes far exceeds what is accomplished in the laboratory; nevertheless, some encouraging signs are apparent from recent experiments. In Ref. [22], all motional modes for two trapped ions have been cooled to the ground state. The non-center-of-mass modes are observed to be much less susceptible to heating, suggesting the use of these modes in quantum computation or quantum state engineering. In Ref. [21], we describe logic operations which enabled ψ_{max} for $L = 2$ to be generated with modest fidelity ($\simeq 0.7$). For small L, it is only necessary to *differentially* address individual ions to create ψ_{max} and for $L = 2$, general logic can be realized even if the laser beams cannot be focused exclusively on the individual ions [21]. For general logic on more than two ions, two avenues are being pursued. For modest numbers of ions in a trap, the Cirac-Zoller scheme of individual addressing with the use of focused laser beams is the most attractive. Current efforts are devoted to obtaining sufficiently strong focusing to achieve individual ion addressing in a relatively strong trap where normal mode frequencies are relatively high ($\simeq$ 10 MHz) in order to maximize operation speed. Alternatively, general logic on many ions could be accomplished by incorporating accumulators [5], and using differential addressing on two ions at a time. This idea might be realized by scaling up a version of a linear ion trap made with lithographically deposited electrodes as we have recently demonstrated [16,23]. Concurrently, efforts are being devoted to the investigation (and hopefully, elimination) of mode heating [5] for different electrode surfaces and dimensions.

6. Acknowledgments

We gratefully acknowledge the support of the U.S. National Security Agency, U.S. Army Research Office, and the U.S. Office of Naval Research. We thank J. Bollinger, R. Blatt, D. Sullivan, and M. Young for helpful comments on the manuscript.

REFERENCES

1. P.W. Shor, *Proc. 35th Ann. Symp. Foundations of Computer Science*, S. Goldwasser ed., IEEE Computer Society Press, New York, 1994, p. 124.
2. See, for example Proc. Royal Soc., Math., Phys. and Eng. Sci., **454** (1969) (1998); Fortschritte der Physik **46** (4-5) (1998).
3. J.I. Cirac and P. Zoller, Phys. Rev. Lett. **74**, 4091 (1995).
4. C. Monroe, D.M. Meekhof, B.E. King, W.M. Itano, and D.J. Wineland, Phys. Rev. Lett. **75**, 4714 (1995).
5. D.J. Wineland, C.R. Monroe, W.M. Itano, D. Leibfried, B.E. King, and D.M. Meekhof, NIST J. Research **103** (3), 259 (1998). (available at http://nvl.nist.gov/pub/nistpubs/jres/jres.htm)
6. D.J. Berkeland, J.D. Miller, J.C. Bergquist, W.M. Itano, and D.J. Wineland, Phys. Rev. Lett. **80**, 2089 (1998).
7. N.F. Ramsey, *Molecular Beams* (Oxford Univ. Press, London, 1963).
8. W. M. Itano, J. C. Bergquist, J. J. Bollinger, J. M. Gilligan, D. J. Heinzen, F. L. Moore, M. G. Raizen, and D. J. Wineland, Phys. Rev. A**47**, 3554 (1993).
9. C.M. Caves, Phys. Rev. D**23**, 1693 (1981).
10. M. Xiao, L. -A. Wu, and H. J. Kimble, Phys. Rev. Lett. **59**, 278 (1987).
11. B. Yurke, Phys. Rev. Lett. **56**, 1515 (1986); B. Yurke, S.L. McCall, and J.R. Klauder, Phys. Rev. A**33**, 4033 (1986).
12. M. Kitagawa and M. Ueda, Phys. Rev. Lett. **67**, 1852 (1991); M. Kitagawa and M. Ueda, Phys. Rev. A**47**, 5138 (1993).
13. D.J. Wineland, J. J. Bollinger, W. M. Itano, F. L. Moore, and D. J. Heinzen, Phys. Rev. A**46**, R6797 (1992); D.J. Wineland, J. J. Bollinger, W. M. Itano, and D. J. Heinzen, Phys. Rev. A**50**, 67 (1994).
14. J.J. Bollinger, D. J. Wineland, W. M. Itano, and D. J. Heinzen, Phys. Rev. A**54**, R4649 (1996).
15. J. Steinbach and C.C. Gerry, quant-ph/9806091.
16. See, for example, S. Haroche, Physics Today **51** (7), 36 (1998).
17. J.J. Bollinger, D. J. Heinzen, W. M. Itano, S. L. Gilbert, and D. J. Wineland, IEEE Trans. on Instrum. and Measurement **40**, 126 (1991).
18. P.T.H. Fisk, M.J. Sellars, M.A. Lawn, C. Coles, A.G. Mann, and D.G. Blair, IEEE Trans. Instrum. Meas. **44**, 113 (1995).
19. J.J. Bollinger, J.D. Prestage, W.M. Itano, and D.J. Wineland, Phys. Rev. Lett. **54**, 1000 (1985).
20. S.F. Huelga, C. Macchiavello, T. Pellizzari, A.K. Ekert, M.B. Plenio, and J.I. Cirac, Phys. Rev. Lett. **79**, 3865 (1997).
21. Q.A. Turchette, C.S. Wood, B.E. King, C.J. Myatt, D. Leibfried, W.M. Itano, C. Monroe, and D.J. Wineland, submitted (quant-ph/9806012).
22. B.E. King, C.S. Wood, C.J. Myatt, Q.A. Turchette, D. Leibfried, W.M. Itano, C. Monroe, and D.J. Wineland, Phys. Rev. Lett. **81**, 1525 (1998).
23. C. Myatt, *et al.*, NIST Ion Storage Group, unpublished.

Physica Scripta. Vol. T76, 147–151, 1998

Trapped-Ion Quantum Simulator

D. J. Wineland,* C. Monroe, W. M. Itano, B. E. King, D. Leibfried, C. Myatt and C. Wood

National Institute of Standards and Technology, Boulder, CO, 80303, USA

Received September 12, 1997; accepted November 17, 1997

PACS Ref: 0365Bz, 0367Lx

Abstract

Coherent manipulations involving the quantized motional and internal states of a single trapped ion can be used to simulate the dynamics of other systems. We consider some examples, including the action of a Mach Zehnder interferometer which uses entangled input states. Coherent manipulations can also be used to create entangled states of multiple trapped ions; such states can be used to demonstrate fundamental quantum correlations.

1. Introduction

Stimulated, in part, by the interest in quantum computation and quantum communication [1], a number of papers have investigated the possibility of synthesizing or "engineering" arbitrary quantum states of trapped ions (for recent reviews, see Refs. [2] and [3]). To the extent that this can be accomplished for a large number of trapped ions, such a system would allow general quantum computations, including the factorization of large numbers [1, 4]. By anybody's reckoning, factorizing large numbers is a daunting task. Therefore, it is desirable that a quantum computer, or a system which can generate arbitrary entangled states, have wider applicability. Various possibilities have been explored in the recent literature [5–11]. Some of these proposals extend the ideas of Feynman who considered whether or not one quantum system could be used to simulate the behavior of another quantum system [12]. In this spirit, we discuss some simple examples of how a single trapped ion might be used to simulate the behavior of other quantum systems, such as entangled particles acted on by a Mach Zehnder interferometer. We also briefly discuss how the states of multiple trapped ions can be entangled; these states can be employed in fundamental demonstrations of quantum measurements.

2. Coupling of a two-level trapped ion to its motion

We first consider a single ion trapped in a 3-D harmonic well with oscillation frequencies ω_x, ω_y and ω_z along three cartesian axes. This situation is closely approximated by a single ion confined in a Paul (rf) trap. We will be interested in two internal states of the ion which we label as $|\uparrow\rangle$ and $|\downarrow\rangle$, and which are separated in energy by $\hbar\omega_0$. We apply a (classical) radiation field or fields (typically laser fields) of the form

$$E(x, t) = E_0 \cos(k \cdot x - \omega t + \phi). \tag{2.1}$$

The Hamiltonian which describes the (resonant) coupling between the ion's internal states and its motion (provided by $E(x, t)$) can be written in the rotating-wave approximation as

$$H_I = \hbar\Omega(S_+)^\varepsilon \, e^{i[k \cdot x - \delta t + \phi]} + h.c., \tag{2.2}$$

where Ω is the coupling strength (Rabi frequency), S_+ is the raising operator for the internal states ($S_+|\downarrow\rangle = |\uparrow\rangle$), x is the ion's position relative to its equilibrium position, $\delta \equiv \omega - \omega_0$, and ϕ is a phase factor of the field [3]. In eqs (2.1) and (2.2), k is the wavevector of the field for single photon transitions or k is the difference between the two wavevectors when two-photon stimulated-Raman transitions are used [13]. Similarly, ω is the frequency of the applied field for single-photon transitions, or is the difference in frequencies of the two applied fields when stimulated-Raman transitions are used. The exponent ε is equal to 1 when internal state transitions are involved and $\varepsilon = 0$ when the internal state is unchanged (stimulated-Raman transitions).

In an interaction picture of the ion's motion, this Hamiltonian becomes [3]

$$H_I = \hbar\Omega(S_+)^\varepsilon \, e^{-i(\delta t - \phi)} \prod_{j=x,y,z} \exp\left(i[\eta_j(a_j \, e^{-i\omega_j t} + a_j^\dagger \, e^{i\omega_j t})]\right) + h.c., \tag{2.3}$$

where a_j and $a_j^\dagger$ are the lowering and raising operators for harmonic motion in the jth direction, and $\eta_x \equiv k \cdot \hat{x} x_0$ is the Lamb-Dicke parameter in the x direction, where $x_0 \equiv \sqrt{\hbar/(2m\omega_x)}$ (m is the ion mass), and similarly for η_y and η_z. Now, assume that Ω is small enough, and that ω_x, ω_y and ω_z are incommensurate so that we can (resonantly) excite only one spectral component of the possible transitions induced by this interaction. For a particular resonance condition $\delta = -l_x\omega_x - l_y\omega_y - l_z\omega_z$ (l_j integers), and in the Lamb-Dicke limit, we find

$$H_I \simeq \hbar\Omega \, e^{i\phi}(S_+)^\varepsilon \prod_{j=x,y,z} \left[\delta_{l_j,|l_j|} \frac{(i\eta_j a_j)^{|l_j|}}{|l_j|!} + (1 - \delta_{l_j,|l_j|}) \frac{(i\eta_j a_j^\dagger)^{|l_j|}}{|l_j|!}\right] + h.c. \tag{2.4}$$

The two mode case where $\varepsilon = l_z = 0$, l_x, $l_y \neq 0$ is considered by Drobný and Hladký [14], and in a different excitation scheme by Steinbach, *et al.* [15]. If the Lamb-Dicke limit is not rigorously satisfied, we must consider higher-order terms in the expansion of the exponentials of eq. (2.3) [16]; specific examples are discussed by Wallentowitz and Vogel [17], and Steinbach, *et al.* [15]. These nonlinear terms appear as corrections to the Rabi frequencies for Fock states and have been observed in the experiments of Ref. [18].

* e-mail: dwineland@nist.gov

3. Simulations of processes in optics

Referring to eq. (2.4), the carrier and first red and blue (z-motion) sidebands on internal state transitions (e.g., $\varepsilon = 1$, $l_x = l_y = 0$, $l_z = 0, \pm 1$) are used in experiments to cool the ion to the ground state of motion [13, 19], for quantum logic [20], and to generate nonclassical motional states [2, 18]. The upper and lower sidebands ($l_z = \pm 1$) correspond to emission and absorption of single vibrational quanta or "phonons" associated with internal state changes; this is directly analogous to the emission and absorption of single photons into a cavity by an atom inside. An interesting system which could be simulated with these couplings is a "phonon maser" which provides vibrational amplification by stimulated emission [21]. The case $\varepsilon = 0$, $l_x = l_y = 0$, $|l_z| = 1$ has been used to create coherent [18] and Schrödinger cat [22] states of motion. Coherent states of ion motion correspond to coherent states in optics. The case $\varepsilon = 0$, $l_x = l_y = 0$, $|l_z| = 2$ has been used to create squeezed states of ion motion [18]. A realization of the Hamiltonian $H_I \propto S_+(a^\dagger)^2 + h.c.$ ($\varepsilon = 1$, $l_x = l_y = 0$, $l_z = -2$) for ions has been reported by Leibfried, *et al.* [23]. This is similar to the case of two-photon excitation in cavity QED analyzed by Buck and Sukumar [24] and Knight [25]. An example of an interesting new case would perhaps be the realization of three-phonon downconversion (e.g., $\varepsilon = 0$, $l_x = 3$, $l_y = -1$, $l_z = 0$); this is accomplished by driving a two-mode resonance using stimulated-Raman transitions where the difference in frequencies of the two laser beams is equal to $\omega_y - 3\omega_x$. This case corresponds to three-photon downconversion in quantum optics (see Refs. [15], [26], and references therein). A suggestion to realize a Hamiltonian proportional to $a_x^2 a_y^\dagger + h.c.$, ($\varepsilon = 0$, $l_z = 0$, $l_x = 2$, $l_y = -1$) is discussed by Agarwal and Banerji [27].

Clearly, a very large number of possibilities could, in principle, be realized just for a single ion; moreover, the number of possibilities increases dramatically if we consider all modes of motion for multiple trapped ions. The only limitation on how high $|l_j|$ in eq. (2.4) can be is that Ω be chosen sufficiently small that couplings to other (unwanted) resonances are avoided. This will require that decoherence be small enough to see the desired dynamical behavior before coherence is lost. Finally, the analogy to optics discussed here should not be surprising since a single ion's motion (for one mode) and a single mode of the radiation field are both described by quantized harmonic oscillators.

4. Mach Zehnder interferometer with entangled states

Realization of the various Hamiltonians indicated in eq. (2.4) can lead to simulation of various devices of practical interest. As an example, we can simulate the action of a Mach Zehnder interferometer for various input states. We consider H_I to act on two modes of ion motion; to be specific, we will assume these are the x and y modes. The analogy with a Mach-Zehnder interferometer for bosons is that the two input modes to the boson interferometer are replaced by the x and y modes of ion oscillation. The (50/50) beamsplitters in the boson interferometer are replaced by an operator [28–30]

$$B_\pm = \exp\left[\pm i\pi(a_x^\dagger a_y + a_x a_y^\dagger)/4\right] \tag{4.1}$$

This operator can be realized by applying the interaction in eq. (2.4) with $\varepsilon = l_z = 0$, and $l_x = -l_y = 1$ for a time given by $\Omega\eta_x\eta_y t = \pi/4$. A differential phase shift between the two arms of the interferometer can be simulated by shifting the relative phases of the fields in eq. (2.4) between successive applications of $B_\pm$. In a particle (e.g., boson) interferometer, one typically measures the number of particles in either one or both output modes. For single ions, the experiments so far have only one convenient observable, the internal state of the ion (either $|\downarrow\rangle$ or $|\uparrow\rangle$). Nevertheless, we can fully characterize the action of the phonon interferometer by repeating the experiment many times and measuring the density matrix of the output state [23, 31].

It will be interesting to characterize the action of the interferometer for various nonclassical input states. One interesting input state is the two-mode Fock state $|n_x\rangle_x|n_y\rangle_y$ [32]. This state could be prepared by applying the Fock state creation techniques described in Ref. [18] sequentially to the ion's x and y modes. This state is interesting because it has been shown that one could approach the Heisenberg uncertainty limit in a Mach Zehnder interferometer by measuring the distribution of bosons in the output modes [32–34]. The observable is the variance of the number of particles detected in one of the output ports when the arms of the interferometer are of approximately equal length. As the difference in length of the arms deviates from equality, the variance increases sharply. An alternative technique for studying the action of a beamsplitter on the two-mode Fock states has been suggested by Gou and Knight [35] when $\omega_x = \omega_y$. Here, a beamsplitter could be simulated by first preparing $|n_x\rangle_x|n_y\rangle_y$ along two orthogonal axes and then probing along two other axes (x' and y') which are rotated (in the xy plane) with respect to the first. This technique could also be used to analyze, for example, the $(|0\rangle_{x'}|2\rangle_{y'} + |2\rangle_{x'}|0\rangle_{y'})/\sqrt{2}$ state from an initially prepared $|1\rangle_x|1\rangle_y$ state [35].

Another interesting input state to consider is the state $B_\pm^\dagger(|N\rangle_x|0\rangle_y + |0\rangle_x|N\rangle_y)/\sqrt{2}$. (Equivalently, the state after the first beam splitter is $(|N\rangle_x|0\rangle_y + |0\rangle_x|N\rangle_y)/\sqrt{2}$.) This state has been shown to yield exactly the Heinsenberg uncertainty limit for an interferometer for any value of N and any difference of the lengths of the arms [8]. The observable is the parity of the number of particles measured in one of the output ports. For example, we could measure the number of particles $N(x)$ in the x output port. The result of this measurement is assigned the value $(-1)^{N(x)}$.

For a single ion, the state after the first beamsplitter could be prepared from the $|\downarrow\rangle|0\rangle_x|0\rangle_y$ state by the following two steps:

(1) Apply a $\pi/2$ pulse on the Nth blue sideband of mode x ($\varepsilon = 1$, $l_x = -N$, $l_y = l_z = 0$); this creates the state $(|\downarrow\rangle|0\rangle_x + |\uparrow\rangle|N\rangle_x)|0\rangle_y/\sqrt{2}$.

(2) Apply a π pulse on the Nth blue sideband of mode y ($\varepsilon = 1$, $l_x = l_z = 0$, $l_y = -N$); this creates the state $|\uparrow\rangle(|N\rangle_x|0\rangle_y + |0\rangle_x|N\rangle_y)/\sqrt{2}$.

After the second beamsplitter, we have a state which can be written as

$$\Psi_{\text{final}} = |\uparrow\rangle \sum_{n_x=0}^{N} C_{n_x}|n_x\rangle_x|N - n_x\rangle_y. \tag{4.2}$$

We now want to measure n_x, record the value $N(x)$, and assign the value $(-1)^{N(x)}$ to the overall measurement. Effec-

tively, this assignment can be accomplished if we can find interaction M which provides the mapping

$$M\Psi_{\text{final}} = |\uparrow\rangle \sum_{n_x \text{ even}}^{N} C_{n_x} e^{i\phi(n_x)} |n_x\rangle_x |N - n_x\rangle_y + |\downarrow\rangle \sum_{n_x \text{ odd}}^{N} C_{n_x} e^{i\phi(n_x)} |n_x\rangle_x |N - n_x\rangle_y. \quad (4.3)$$

After this mapping, we need only measure the internal state; if the ion is found in the $|\uparrow\rangle$ we assign the value $+1$ to the measurement; if the ion is found in the $|\downarrow\rangle$ state, we assign the value -1. The mapping M can be achieved by applying radiation with $k \| \hat{x}$ at the carrier frequency ($\varepsilon = 1$, $l_x = l_y = l_z = 0$) and insuring $\Omega_{n_x, n_x} t = 2\pi m \pm n_x \pi$ where m is an integer. Here Ω_{n_x, n_x} is the Rabi frequency for $|\downarrow\rangle \leftrightarrow |\uparrow\rangle$ which depends on n_x due to terms in the expansion of $\exp(i\boldsymbol{k} \cdot \boldsymbol{x})$ which are nonlinear in x. We find [3]

$$\Omega_{n,n} t \simeq \Omega t \, e^{-\eta_x^2/2} \left[1 - n\eta_x^2 \left(1 + \frac{\eta_x^2}{4} - n \frac{\eta_x^2}{4} \right) \right]. \quad (4.4)$$

Therefore, if we satisfy $\Omega \exp(-\eta_x^2/2) t = 2\pi m$ and $\eta_x^2(1 + \eta_x^2/4) = (2m)^{-1}$, we achieve the desired mapping as long as the contribution to the phase from the term proportional to n_x^2 in this equation is small compared to π. Therefore we require $m \gg N^2/8$ or, equivalently, $\eta_x \ll 2/N$.

If N is large and/or the Lamb-Dicke parameter is very small, creating the state $|\uparrow\rangle(|N\rangle_x|0\rangle_y + |0\rangle_x|N\rangle_y)/\sqrt{2}$ by steps (1) and (2) above may be very slow. If we use an auxiliary internal state, we can speed up this process by employing first-order sidebands. To be specific, we will assume we can realize a coupling of the form of eq. (2.4), between the $|\uparrow\rangle$ state and auxiliary state which we label $|A\rangle$. We assume state $|A\rangle$ is lower in energy than state $|\uparrow\rangle$ so that $S_{A+}|A\rangle = |\uparrow\rangle$. A particular realization of states $|\downarrow\rangle$, $|\uparrow\rangle$, and $|A\rangle$ is described in Ref. [20]. As an example, starting with the state $|\downarrow\rangle|0\rangle_x|0\rangle_y$, we can create the state $(|\uparrow\rangle(|3\rangle_x|0\rangle_y + |0\rangle_x|3\rangle_y)/\sqrt{2}$ with the following steps (and appropriate choices of ϕ):

$$|\downarrow\rangle|0\rangle_x|0\rangle_y - (S_+(\pi/2) + h.c.) \rightarrow$$

$$\frac{1}{\sqrt{2}}(|\uparrow\rangle + |\downarrow\rangle)|0\rangle_x|0\rangle_y - (S_{A+}(\pi) + h.c.) \rightarrow$$

$$\frac{1}{\sqrt{2}}(|A\rangle + |\downarrow\rangle)|0\rangle_x|0\rangle_y - (S_{A+}\, a_x^\dagger(\pi) + h.c.) \rightarrow$$

$$\frac{1}{\sqrt{2}}(|\uparrow\rangle|1\rangle_x + |\downarrow\rangle|0\rangle_x)|0\rangle_y - (S_{A+}\, a_x(\pi) + h.c.) \rightarrow$$

$$\frac{1}{\sqrt{2}}(|A\rangle|2\rangle_x + |\downarrow\rangle|0\rangle_x)|0\rangle_y - (S_+\, a_y^\dagger(\pi) + h.c.) \rightarrow$$

$$\frac{1}{\sqrt{2}}(|A\rangle|2\rangle_x|0\rangle_y + |\uparrow\rangle|0\rangle_x|1\rangle_y) - (S_+\, a_y(\pi) + h.c.) \rightarrow$$

$$\frac{1}{\sqrt{2}}(|A\rangle|2\rangle_x|0\rangle_y + |\downarrow\rangle|0\rangle_x|2\rangle_y) - (S_{A+}\, a_x^\dagger(\pi) + h.c.) \rightarrow$$

$$\frac{1}{\sqrt{2}}(|\uparrow\rangle|3\rangle_x|0\rangle_y + |\downarrow\rangle|0\rangle_x|2\rangle_y) - (S_+\, a_y^\dagger(\pi) + h.c.) \rightarrow$$

$$\frac{1}{\sqrt{2}}|\uparrow\rangle(|3\rangle_x|0\rangle_y + |0\rangle_x|3\rangle_y). \quad (4.5)$$

In this expression, the notation $S_{A+}\, a_x^\dagger(\pi) + h.c.$ means the operator $S_{A+}\, a_x^\dagger + h.c.$ is applied for a time sufficient to drive a π pulse, etc. From this, it is straightforward to see how to generate the state $|\uparrow\rangle(|N\rangle_x|0\rangle_y + |0\rangle_x|N\rangle_y)/\sqrt{2}$ for N odd. For N even, we can, for example, substitute two carrier transitions for two sideband transitions in the above steps.

One final example of a two-mode interferometer which directly yields Heisenberg $1/N$ phase sensitivity is a "beam-splitter" which creates that state $(|\downarrow\rangle|N\rangle_x|0\rangle_y + |\uparrow\rangle|0\rangle_x|N\rangle_y)/\sqrt{2}$. This state (for N even) could be created as in eq. (4.5) except the last two operations are replaced by the operation $S_{A+}(\pi) + h.c.$ For example, to create the state $(|\uparrow\rangle|2\rangle_x|0\rangle_y + |\downarrow\rangle|0\rangle_x|2\rangle_y)/\sqrt{2}$, we replace the last two steps of eq. (4.5) by

$$\frac{1}{\sqrt{2}}(|A\rangle|2\rangle_x|0\rangle_y + |\downarrow\rangle|0\rangle_x|2\rangle_y) - (S_{A+}(\pi) + h.c.) \rightarrow$$

$$\frac{1}{\sqrt{2}}(|\uparrow\rangle|2\rangle_x|0\rangle_y + |\downarrow\rangle|0\rangle_x|2\rangle_y). \quad (4.6)$$

For N odd, we can, for example, substitute two carrier transitions for two sideband transitions in the above steps. If an auxiliary state is not available, this state can be created by first making the initial dual Fock state $(|\uparrow\rangle + |\downarrow\rangle)|N/2\rangle_x|N/2\rangle_y/\sqrt{2}$ with the methods described in Ref. [18]. (In this example, we assume N is even.) Next, we apply $N/2$ π-pulses alternating between the two interaction Hamiltonians $H_1 = \Omega\eta_x\eta_y S_+ a_x^\dagger a_y + h.c.$ and $H_2 = \Omega\eta_x\eta_y S_+ a_x a_y^\dagger + h.c.$. In this way, the ion is stepped through the sequence

$$|\downarrow\rangle|N/2\rangle_x|N/2\rangle_y - (S_+(\pi/2) + h.c.) \rightarrow$$

$$\frac{1}{\sqrt{2}}(|\downarrow\rangle|N/2\rangle_x|N/2\rangle_y + |\uparrow\rangle|N/2\rangle_x|N/2\rangle_y) - (H_1) \rightarrow$$

$$\frac{1}{\sqrt{2}}(|\uparrow\rangle|N/2+1\rangle_x|N/2-1\rangle_y + |\downarrow\rangle|N/2-1\rangle_x|N/2+1\rangle_y) - (H_2) \rightarrow$$

$$\frac{1}{\sqrt{2}}(|\downarrow\rangle|N/2+2\rangle_x|N/2-2\rangle_y + |\uparrow\rangle|N/2-2\rangle_x|N/2+2\rangle_y) - (H_1) \rightarrow$$

$$\cdots - (H_2) \rightarrow \frac{1}{\sqrt{2}}(|\downarrow\rangle|N\rangle_x|0\rangle_y + |\uparrow\rangle|0\rangle_x|N\rangle_y). \quad (4.7)$$

The interactions H_1 and H_2 follow from eq. (2.4) with $\varepsilon = 1$, $l_x = -1$, $l_y = 1$, $l_z = 0$, and $\varepsilon = 1$, $l_x = 1$, $l_y = -1$, $l_z = 0$ respectively. The kth pulse has Rabi frequency $\Omega\eta_x\eta_y\sqrt{(N/2+k)(N/2-k+1)}$ in the Lamb-Dicke regime. After a relative phase is accumulated in the two "paths" of the interferometer (simulated by adjusting the phase of the

laser pulses as discussed above), then the steps in eqs (4.7) or (4.5) and (4.6) are reversed. Upon measuring the probability of occupation in state $|\downarrow\rangle$ or $|\uparrow\rangle$, the interference fringes exhibit $1/N$ phase sensitivity.

If the Lamb-Dicke criterion is not satisfied, the two components of the wavefunction superposition may experience different Rabi frequencies during each pulse, leading to undesired evolution. However, as long as $\eta_x = \eta_y$ it can be shown that the system will evolve as in eq. (4.7), even when the Lamb-Dicke criterion is not satisfied [3].

5. Quantum correlations

The coherent manipulations on single ions discussed above can be extended to multiple ions [4]. As one step towards this goal, a controlled-not quantum logic has been demonstrated [20] between qubits formed with the ground and first excited state for one mode of motion ($|n_x = 0\rangle_x \equiv |0\rangle_m$, $|n_x = 1\rangle_x \equiv |1\rangle_m$) and the ion's internal states ($|\downarrow\rangle \equiv |0\rangle$, $|\uparrow\rangle \equiv |1\rangle$). The controlled-not gate exhibited the logic

$$|\varepsilon_1\rangle_m|\varepsilon_2\rangle \rightarrow |\varepsilon_1\rangle_m|\varepsilon_1 \oplus \varepsilon_2\rangle \tag{5.1}$$

where $\oplus$ signifies addition mod 2. For a collection of ions in a trap, we select a particular mode (say the center-of-mass mode along the axis of a linear Paul trap) to comprise the motional qubit. By first mapping the internal state of ion i onto the motional qubit (which is shared by all ions), performing the logic in eq. (5.1) between the motional qubit and ion j, followed by reversing the first mapping step, we can realize a controlled-not logic operation between ion i and ion j [4]

$$|\varepsilon_1\rangle_i|\varepsilon_2\rangle_j \rightarrow |\varepsilon_1\rangle_i|\varepsilon_1 \oplus \varepsilon_2\rangle_j. \tag{5.2}$$

Application of these gates to small numbers of trapped ions can lead to interesting experiments which may shed light on the viability of local hidden-variables theories. For example, for two ions, starting with the state $|0\rangle_1|0\rangle_2$ we can apply a $\pi/2$ pulse to the internal states of ion 1 followed by a controlled-not between ions 1 and 2

$$\begin{aligned} |0\rangle_1|0\rangle_2 &\rightarrow \frac{1}{\sqrt{2}}(|0\rangle_1 + |1\rangle_1)|0\rangle_2 \\ &\rightarrow \frac{1}{\sqrt{2}}(|0\rangle_1|0\rangle_2 + |1\rangle_1|\rangle_2). \end{aligned} \tag{5.3}$$

If the states of the resulting entangled particles are detected outside of each other's light cones, then, for particular sets of measurements, we may derive Bell's inequalities [36] which local hidden-variables theories must obey, but which quantum mechanics violates. The experiments performed by Aspect and co-workers [37] (and more recent versions – see Ref. [38] and A. Zeilinger and P. Kwiat, these proceedings) provide strong evidence against local hidden-variables theories. The Aspect *et al.* experiments used polarization measurements on entangled pairs of photons. The detection of the photons' polarization states occurred outside each others' light cones. Thus, the measurement on one photon could not have affected the other measurement, which closed possible "loopholes" in the proof of quantum mechanics over other explanations.

However, some loopholes still remain open. Since the photon detection in the Aspect *et al.* experiments was not 100% efficient, the group had to make assumptions that the photons they measured were a "fair" sample of the whole population of events. Thus, their experiments do not rule out the (seemingly implausible) possibility of local hidden-variables theories in which the hidden variables cause some sub-ensemble of the photon pairs to preferentially interact with the measurement apparatus.

In the system of two ions, we may detect the state of either ion with nearly 100% efficiency through the use of "electron-shelving" (for a discussion, see Ref. [3]). On the other hand, it may be difficult to perform measurements on two ions outside each other's light cone. Such a measurement would require separating the ions by a distance larger than the speed of light times the measurement time. In principle of course, the ions could be first entangled and then placed in different traps which could be separated by large distances before measurements were performed. Alternatively, it may be possible to entangle distant pairs of ions using optical fibers [11]. Nonetheless, an experiment with two entangled ions confined in the same trap could be viewed as complementary to those of Aspect and others: the photon experiments definitively close loopholes of causality, and the ion experiments could close loopholes due to detection inefficiency. Such experiments have the additional appeal of studying EPR on massive particles (E. Fry, these proceedings). EPR states of atoms have recently been created in an atomic beam using the methods of cavity QED (S. Haroche, these proceedings); if detection efficiency can be improved, these experiments could also close loopholes due to detection inefficiency. Finally, even though measurements of quantum correlations between entangled ions cannot be easily performed outside each other's light cone, one can argue strongly that the ions cannot transfer information by any known mechanism. Therefore, if the observed correlations violate Bell's inequalities, the correlations are established by some new force of nature or are, in fact, inherent in the structure of quantum mechanics.

An intriguing possibility for ions is the possibility of making "GHZ states" [39, 40]. For three ions, the GHZ state has the form

$$\Psi = \frac{1}{\sqrt{2}}(|0\rangle_1|0\rangle_2|0\rangle_3 + e^{i\phi}|1\rangle_1|1\rangle_2|1\rangle_3). \tag{5.4}$$

This state can be made starting with the state $|0\rangle_1|0\rangle_2|0\rangle_3$, applying the first two steps shown in eq. (5.3), and following with a controlled-not gate between ions 1 and 3 [4]. For such a state, a single measurement can distinguish between the predictions of quantum mechanics and those of any local hidden-variables theory [39, 40].

Aside from these possibilities, Bell states, GHZ states, and Schrödinger-cat states are highly entangled, and are thus of inherent interest for the study of uniquely quantum behavior. As the experiments improve, it will be interesting to push the size of entangled states to be as large as possible. The question is not whether we can make states which have the attributes of Schrödinger cats, but how big can we make the cats? Certain theories which address the measurement problem will be amenable to experimental tests, for example, quantitative limits on spontaneous wavefunction

collapse theories [41, 42] can be established. The isolation from the environment exhibited by trapped ions, coupled with the control possible over their quantum state and high detection efficiency make them an interesting laboratory for the study of fundamental issues in quantum mechanics.

Acknowledgements

This work is supported by the U.S. National Security Agency, Office of Naval Research, and Army Research Office.

References

1. See, for example, Ekert, A. and Jozsa, R., Rev. Mod. Phys. **68**, 733 (1996).
2. Cirac, J. I., Parkins, A. S., Blatt, R. and Zoller, P., Adv. At. Mol. Phys. **37**, 237 (1996).
3. Wineland, D. J. *et al.*, NIST J. Research, to be published.
4. Cirac, J. I. and Zoller, P., Phys. Rev. Lett. **74**, 4091 (1995).
5. Lloyd, S., Science **261**, 1569 (1993).
6. Lloyd, S., Science **273**, 1073 (1996).
7. Grover, L. K., Proc. 28th ACM Symp. Theory of Computing (STOC), 1996, p. 212.
8. Bollinger, J. J., Wineland, D. J., Itano, W. M. and Heinzen, D. J., Phys. Rev. **A54**, R4649 (1996).
9. Boghosian, B. M. and Taylor W., 1997, unpublished.
10. Lidar, D. A. and Biham, O., Phys. Rev. **E56**, 3661 (1997).
11. van Enk, S. J., Cirac, J. I. and Zoller P., Phys. Rev. Lett. **78**, 429 (1997).
12. Feynman, R., Int. J. Theor. Phys. **21**, 467 (1982); Opt. News **11**, 11 (1985).
13. Monroe, C. *et al.*, Phys. Rev. Lett. **75**, 4011 (1995).
14. Drobný, G. and Hladký, B., Acta Phys. Slovaka **47**, 277 (1997).
15. Steinbach, J., Twamley, J. and Knight, P. L., Phys. Rev. **A56**, 4815 (1997).
16. Wineland, D. J. and Itano, W. M., Phys. Rev. **A20**, 1521 (1979).
17. Wallentowitz, S. and Vogel, W., Phys. Rev. **A55**, 4438 (1997).
18. Meekhof, D. M., Monroe, C., King, B. E., Itano, W. M. and Wineland, D. J., Phys. Rev. Lett. **76**, 1796 (1996); and erratum **77**, 2346 (1996).
19. Diedrich, F., Bergquist, J. C., Itano, W. M. and Wineland, D. J., Phys. Rev. **A62**, 403 (1989).
20. Monroe, C., Meekhof, D. M., King, B. E., Itano, W. M. and Wineland, D. J., Phys. Rev. Lett. **75**, 4714 (1995).
21. Wallentowitz, S., Vogel, W., Siemers, I. and Toschek, P. E., Phys. Rev. **A54**, 943 (1996).
22. Monroe, C., Meekhof, D. M., King, B. E. and Wineland, D. J., Science **272**, 1131 (1996).
23. Leibfried, D. *et al.*, J. Mod. Opt. **44**, 2485 (1997).
24. Buck, B. and Sukumar, C. V., Phys. Lett. **81A**, 132 (1981).
25. Knight, P. L., Physica Scripta **T12**, 51 (1986).
26. Banazek, K. and Knight, P. L., Phys. Rev. **A55**, 2368 (1997).
27. Agarwal, G. S. and Banerji, J., Phys. Rev. **A55**, R4007 (1997).
28. Yurke, B., McCall, S. L. and Klauder, J. R., Phys. Rev. **A33**, 4033 (1986).
29. Lai, W. K., Bužek, V. and Knight, P., Phys. Rev. **A43**, 6323 (1991).
30. Sanders, B. C. and Milburn, G. J., Phys. Rev. Lett. **75**, 2944 (1995).
31. Leibfried, D. *et al.*, Phys. Rev. Lett. **77**, 4281 (1996).
32. Holland, M. J. and Burnett, K., Phys. Rev. Lett. **71**, 1355 (1993).
33. Bouyer, P. and Kasevich, M., Phys. Rev. **A56**, R1083 (1997).
34. Kim, T., Phister, O., Noh, J., Holland, M. J. and Hall, J. L. (1997), unpublished.
35. Gou, S.-C. and Knight, P., Phys. Rev. **A54**, 1682 (1996).
36. Bell, J. S., Physics **1**, 195 (1964).
37. Aspect, A., Dalibard, J. and Roger, G., Phys. Rev. Lett. **49**, 1804 (1982).
38. Tittel, W. *et al.*, Europhys. Lett. **40**, 595 (1997).
39. Greenberger, D., Horne, M. A. and Zeilinger, A., in "Bell's Theorem, Quantum Theory, and Conceptions of the Universe" (edited by M. Kafatos) (Kluwer Academic, Dordrecht).
40. Greenberger, D., Horne, M. A. and Zeilinger, A., Phys. Today **46**, No. 8, 22 (1993).
41. Ghirardi, G. C., Rimini, A. and Weber, T., Phys. Rev. **D34**, 470 (1986).
42. Pearle, P., Phys. Rev. **A39**, 2277 (1989).

Decoherence of quantum superpositions through coupling to engineered reservoirs

C. J. Myatt*, B. E. King*, Q. A. Turchette, C. A. Sackett, D. Kielpinski, W. M. Itano, C. Monroe & D. J. Wineland

National Institute of Standards and Technology, Div. 847.10, 325 Broadway, Boulder, Colorado 80303, USA

The theory of quantum mechanics applies to closed systems. In such ideal situations, a single atom can, for example, exist simultaneously in a superposition of two different spatial locations. In contrast, real systems always interact with their environment, with the consequence that macroscopic quantum superpositions (as illustrated by the 'Schrödinger's cat' thought-experiment) are not observed. Moreover, macroscopic superpositions decay so quickly that even the dynamics of decoherence cannot be observed. However, mesoscopic systems offer the possibility of observing the decoherence of such quantum superpositions. Here we present measurements of the decoherence of superposed motional states of a single trapped atom. Decoherence is induced by coupling the atom to engineered reservoirs, in which the coupling and state of the environment are controllable. We perform three experiments, finding that the decoherence rate scales with the square of a quantity describing the amplitude of the superposition state.

One of the fundamental properties of quantum mechanics is the principle of superposition, a principle whose introduction was considered a "drastic" measure by Dirac[1]. The fact that quantum superpositions do not exist in the macroscopic world hinders our intuition and leads to the apparently strange behaviour dictated by quantum mechanics. A famous example of this was posed by Schrödinger in 1935 (ref. 2) who pointed out that quantum mechanics would predict bizarre situations such as a cat being simultaneously dead and alive. The existence of superpositions prescribed by quantum mechanics is valid for systems that are closed, that is, free from external influences. In contrast, real systems always couple to these external influences, the environment, which is typically composed of an extremely large number of degrees of freedom. Lack of knowledge about the environment is expressed by averaging (mathematically tracing) over the possible states of the environmental degrees of freedom. This leads to an evolution of the density matrix of the system, in which the quantum superpositions are continuously reduced to classical probability distributions, a process generally known as decoherence (see, for example, refs 3–5). One approach to describing decoherence is to treat the environment as a reservoir of quantum oscillators, each of which interacts with the quantum system in question. An example of such a reservoir–system interaction is the ensemble of empty electromagnetic field modes, each represented by a quantized harmonic oscillator, interacting with an atom in order to induce spontaneous emission. As a quantum superposition is made larger, decoherence tends to act more quickly. For truly macroscopic superpositions, such as that of 'Schrödinger's cat', decoherence occurs on such a short timescale that it is almost impossible to observe quantum coherences. However, mesoscopic systems present the possibility of studying, in a controlled way, the process of decoherence and the transition from quantum to classical behaviour.

In the past few years, techniques have been realized to generate mesoscopic superpositions, also called 'Schrödinger cats', of motional states of trapped ions[6] and of photon states in the context of cavity QED (ref. 7), where decoherence through coupling to ambient reservoirs and the sensitivity of the rate of decoherence to the size of cat were observed. Here we extend the investigations beyond the ambient reservoirs and 'engineer' the state of the reservoir, as well as the form of the system–reservoir coupling. One way this can be achieved for a system of trapped ions is by applying noisy potentials to the trap electrodes, simulating a hot resistor (reservoir) connected to the trap electrodes, with controllable temperature and spectrum. For a range of two-component superposition states, we demonstrate the expected exponential dependence of the decoherence rate on the separation of the components in Hilbert space. We also present the first, to our knowledge, study of decoherence into an engineered quantum reservoir, using laser cooling techniques to generate an effectively zero-temperature bath[8,9].

Theoretical predictions

Decoherence of specific mesoscopic quantum superpositions, with a variety of couplings to a reservoir, has been investigated extensively in theory[3–5,8,10–12]. The model in these studies is a system harmonic oscillator coupled to a bath of environment quantum oscillators. (These and other sources of decoherence in the context of trapped-ion experiments have been more recently discussed theoretically in refs 13–16.) As an illustration, we consider the system oscillator to be in a superposition of coherent states. A coherent state[17] of a harmonic oscillator is a gaussian wavepacket which oscillates back and forth while retaining its shape. In quantum mechanics, a coherent state is represented by a state vector $|\alpha\rangle$, where $\alpha = |\alpha|e^{i\theta}$ is a complex number whose magnitude $|\alpha|$ is a dimensionless amplitude of the wavepacket's motion and whose phase θ is the phase of the oscillation at some initial time $t = 0$ (the phases of all subsequent coherent manipulations are set relative to this initial phase). Coherent states are analogous to classical trajectories of a harmonic oscillator, approximated by a marble rolling back and forth in a bowl. A superposition of coherent states, $|\psi\rangle = N(|\alpha_1\rangle + |\alpha_2\rangle)$ where N is a normalization factor, can be visualized as a marble rolling in a superposition of two trajectories.

We consider the system oscillator to couple to the reservoir through an interaction proportional to the product of the amplitude of motion of the system oscillator and the amplitude of

* Present addresses: Research Electro-Optics, 1855 South 57th Court, Boulder, Colorado 80301, USA (C.J.M.); NIST, Atomic Physics Division (842), 100 Bureau Drive, Stop 8424, Gaithersburg, Maryland 20899-8424, USA (B.E.K.).

fluctuations of the reservoir. For brevity, we call this an amplitude reservoir. In the classical analogy, a hot amplitude reservoir behaves as if the bowl is subject to random displacements of its centre, resulting in a random force on the marble. For a superposition of coherent states coupled to such a reservoir, a simple scaling law may be stated: the rate of decoherence (here a dephasing between the $|\alpha_1\rangle$ and $|\alpha_2\rangle$ components of $|\psi\rangle$) scales as the square of the separation of the wave packets, $|\alpha_1 - \alpha_2|^2$. In an idealized case where, first, the superposition is created, then the amplitude reservoir is coupled to the system for a time t, and then the coupling is turned off, the remaining coherence between the two wave packets is[4]:

$$C(t) = \exp[-|\alpha_1 - \alpha_2|^2 \xi t] \quad (1)$$

Here ξ is a coupling constant between the reservoir and the system. The larger the size ($|\alpha_1 - \alpha_2|$) of the superposition, the faster the decoherence.

Another basis of quantum states for the harmonic oscillator is the energy eigenstates, also known as Fock or number states. The Fock state $|n\rangle$ has energy $\hbar\omega(n + 1/2)$ and represents a state of n units of quantized vibration, where $n \geqslant 0$ is an integer. Fock states have no classical analogue, as they are delocalized in position and uniformly distributed in phase. A superposition of two Fock states $|\psi\rangle = (|n_1\rangle + |n_2\rangle)/\sqrt{2}$ loses coherence when the modes of the reservoir couple linearly to the energy of the oscillator, which is equivalent to averaging over a gaussian distribution of phase shifts of the oscillator. We denote this case a phase reservoir. The coherence between the two Fock states decays at a rate that scales as the square of the difference between the Fock indices, $|n_1 - n_2|^2$, given by[4]:

$$C(t) = \exp[-|n_1 - n_2|^2 \kappa t] \quad (2)$$

Here κ is a coupling constant.

Trapped ions

In the experiments described here, a linear Paul trap, similar to the one described in ref. 18, confines single $^9Be^+$ atomic ions in a harmonic potential, for which we isolate the axial motion at frequency $\omega = 2\pi \times 11.3$ MHz. Within the ion's electronic ground-state hyperfine manifold we restrict our attention to two states, the $|F = 2, m_F = -2\rangle$ state, which we label $|\downarrow\rangle$, and the $|F = 1, m_F = -1\rangle$ state, which we label $|\uparrow\rangle$, separated in energy by $\hbar\omega_0$, where $\omega_0 \approx 2\pi \times 1.25$ GHz, and where F and m_F are the quantum numbers associated with the total angular momentum of the atomic state. The ion is cooled to the $n = 0$ ground state of motion, denoted $|0\rangle$, and optically pumped to the $|\downarrow\rangle$ state with resolved-sideband stimulated Raman cooling[19]. Thus, the initial state for all the experiments is $|\downarrow\rangle|0\rangle$.

We drive coherent stimulated Raman transitions with a pair of laser beams detuned approximately 12 GHz from the atomic resonance near 958 THz ($\lambda = 313$ nm). We use three types of Raman transitions, determined by the beam geometry and difference frequency of the two beams: (1) Motion-independent spin-flip transitions ($|\downarrow\rangle|n\rangle \leftrightarrow |\uparrow\rangle|n\rangle$). Here, the Raman beams are co-propagating and the difference frequency is set to ω_0. (2) Sideband transitions ($|\downarrow\rangle|n\rangle \leftrightarrow |\uparrow\rangle|n + \Delta n\rangle$). Here, the beams are orientated with their difference wavevector pointing along the trap axis and their difference frequency set to a motional sideband at $\omega_0 + \omega\Delta n$. (3) Motional displacement transitions. Here, the beams are orientated with their difference wavevector pointing along the trap axis and their difference frequency set to the trap frequency ω. This approximates the harmonic-oscillator displacement operator $D(\alpha)$, where the operator is defined[4,5] by the relation $D(\alpha)|0\rangle = |\alpha\rangle$. The displacement $|\alpha|$ is proportional to the duration of the laser pulse, and θ is set by the phase of the applied laser field[6,13]. In general, α depends on the internal state of the ion.

We can efficiently detect the $|\downarrow\rangle$ internal state of the ion by applying circularly polarized laser light resonant with the transition $|\downarrow\rangle \leftrightarrow |e\rangle$, where $|e\rangle$ is a short-lived excited electronic state that usually decays back to $|\downarrow\rangle$ by emitting a photon[19]. In contrast, the transition $|\uparrow\rangle \leftrightarrow |e\rangle$ is out of resonance, and an ion in the $|\uparrow\rangle$ state scatters negligible light.

High-temperature amplitude reservoir

The motion of a trapped ion couples to uniform electric fields **E** through the potential $U = -q\mathbf{x}\cdot\mathbf{E}$, where **x** is the displacement of the ion from its equilibrium position (proportional to the amplitude of motion) and q is the charge of the ion. This coupling is independent of the ion's internal state. Our engineered amplitude reservoir consists of random uniform electric fields applied along the axis of the trap, oscillating near the ion's axial-motion frequency ω. We generate axial fields in the trap by applying voltages to one of the trap electrodes. A commercial function generator produces

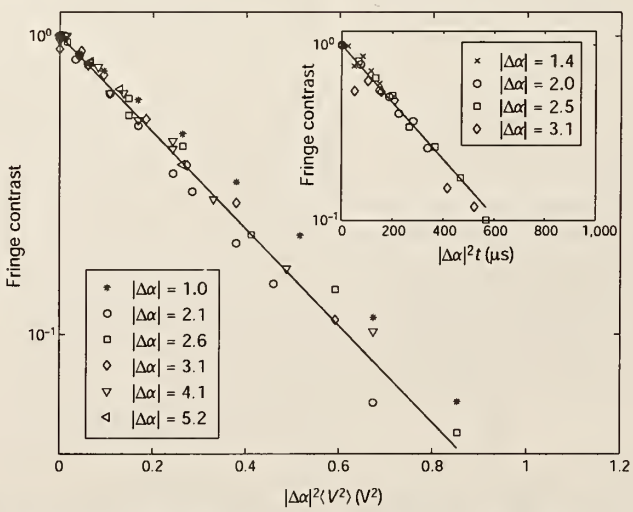

Figure 1 The decoherence of 'Schrödinger-cat' states coupled to an amplitude reservoir. In the main figure, each point is the measured contrast of the interference fringes after noisy potentials were applied to the trap electrodes. The fringe contrast at $\langle V^2\rangle = 0$ is scaled to unity in order to make comparisons between different values of $|\Delta\alpha|$. The size of the superposition, $|\Delta\alpha|$, varies linearly with the pulse time for Raman transition type (3). The applied mean-squared voltage $\langle V^2\rangle$ is scaled by $|\Delta\alpha|^2$. The solid line is a fit to an exponential. Inset, fringe contrast versus time of interaction with ambient fields is plotted. Again, the fringe contrast is scaled to unity at $t = 0$ for comparison between different values $|\Delta\alpha|$. The solid line is a fit to an exponential.

pseudo-random voltages which are applied through a band-pass filter centred near ω, defining the frequency spectrum of the reservoir.

In all the experiments reported here, we measure the coherence of the quantum superpositions with single-atom interferometry, analogous to that used in our previous work[6]. For example, to observe the effects of the amplitude reservoir, the motional state of the ion is split into a superposition of two components, each associated with a different internal state of the ion, forming a state like that of the Schrödinger cat[6]. The superposition is then coupled to the reservoir, and finally the perturbed superposition is recombined by reversing the steps which initially created it. We repeat the experiment many times, measuring the internal state of the ion as a function of the relative phase of the creation and reversal steps, and the contrast of the resulting interference fringes characterizes the amount of coherence remaining after coupling to the reservoir.

In more detail, we first form a cat state of the form:

$$|\psi_c\rangle = (|\downarrow\rangle|\alpha_\downarrow\rangle + |\uparrow\rangle|\alpha_\uparrow\rangle)/\sqrt{2} \quad (3)$$

This is created by driving a Raman transition (type (1)) to generate an equal spin superposition, $|\downarrow\rangle|0\rangle \rightarrow (|\downarrow\rangle + |\uparrow\rangle)|0\rangle/\sqrt{2}$, followed by a Raman transition (type (3)), with laser polarizations set such that $\alpha_\uparrow = -\alpha_\downarrow/2$ in equation (3).

A uniform electric field oscillating near the trap frequency ω (applied in the experiment for 3 μs) results in the displacement operator $D(\beta)$ acting equally on both $|\downarrow\rangle$ and $|\uparrow\rangle$, giving:

$$|\psi_c\rangle \rightarrow |\psi_c'\rangle = (|\downarrow\rangle|\beta + \alpha_\downarrow\rangle + e^{i\phi_m}|\uparrow\rangle|\beta + \alpha_\uparrow\rangle)/\sqrt{2} \quad (4)$$

Here $\phi_m = \mathrm{Im}\beta\Delta\alpha^*$ and $\Delta\alpha = \alpha_\downarrow - \alpha_\uparrow$. We probe the coherence by reversing the steps taken to generate the cat state. We first reverse the motional Raman transition (type (3)), resulting in the state

$$|\psi_c'\rangle \rightarrow |\psi''\rangle = (|\downarrow\rangle + e^{2i\phi_m}|\uparrow\rangle)|\beta\rangle/\sqrt{2} \quad (5)$$

A final pulse on the motion-independent spin-flip transition (1), with phase δ relative to the first pulse on transition (1), leads to interference fringes with a residual phase shift $2\phi_m$. Averaging over the gaussian random variable β, the probability of finding the ion in the $|\downarrow\rangle$ state is[21]:

$$P_\downarrow = \frac{1}{2}(1 - e^{-2|\Delta\alpha|^2\sigma^2}\cos\delta) \quad (6)$$

Interference fringes are generated by recording $P_\downarrow$ while sweeping δ. The variance σ^2 of β is proportional to the mean-squared voltage noise $\langle V^2\rangle$ (proportional to the temperature of the simulated resistor). A plot of the interference-fringe contrast as a function of the applied mean-squared voltage, scaled by the squared 'size' of the cat state $|\Delta\alpha|^2$, is shown in Fig. 1. Decay curves were recorded for a variety of superposition sizes $|\Delta\alpha|$, and all the data agree with a single exponential.

In addition to the engineered reservoir of the applied voltage noise, the ion also interacts with ambient fluctuating electric fields, which we expect to have the character of an amplitude reservoir. To examine this 'natural' decoherence, we ran the experiment outlined above without any applied voltage noise, and with a variable time t between the creation of the cat state and the recombination. The fringe visibility as a function of $|\Delta\alpha|^2 t$ is shown in the inset to Fig. 1. The decay curves are normalized to unity at $t = 0$. The decay of the fringe visibility is exponential, and the decay constant $\gamma \approx 6.7 \times 10^{-3}\,\mu s^{-1}$ is consistent with the measured heating rate[13] of $\gamma \approx 5.9 \times 10^{-3}\,\mu s^{-1}$ for this apparatus. The effects of this ambient reservoir were negligible during the time (3 μs) that the engineered amplitude reservoir was coupled to the ion.

High-temperature phase reservoir

A phase reservoir coupled to the ion is simulated by random variations in the trap frequency ω, changing the phase of the ion oscillation without changing its energy. We realize this coupling experimentally by modulating the trap frequency. A random voltage noise source is passed through a low-pass filter network with a cut-off frequency well below ω to maintain adiabaticity. The fluctuations in potential are applied symmetrically to the trap electrodes so as to produce linear field gradients and negligible uniform fields. This in turn perturbs the trap frequency, by $\delta\omega(t)$. When integrated over the time (20 μs) of the applied noise, the ion's motion is phase-shifted by $\phi = \int\delta\omega(t)\mathrm{d}t$. This technique yields a gaussian-distributed ensemble of phase shifts with variance σ^2 proportional to the applied mean-squared voltage noise $\langle V^2\rangle$.

Motional decoherence caused by a phase reservoir is clearly illustrated with a superposition of two Fock states. We generate superpositions of Fock states of the form $|\psi\rangle = |s\rangle(|n\rangle + |n'\rangle)/\sqrt{2}$, where $s = \downarrow$ or $\uparrow$, with pulses on the Raman motional sidebands (case (2) above) as in ref. 20. The trap frequency is then perturbed by the

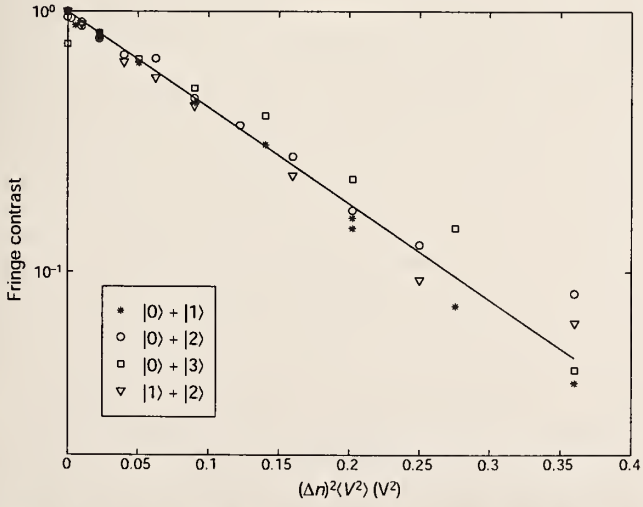

Figure 2 Decoherence of superpositions of Fock states coupled to the phase reservoir. The data points are the measured fringe contrast. The fringe contrast is normalized to unity at $\langle V^2\rangle = 0$. The mean squared voltage applied to the trap electrodes is scaled by the squared size of the superposition $|\Delta n|^2$. The solid line is a fit to an exponential.

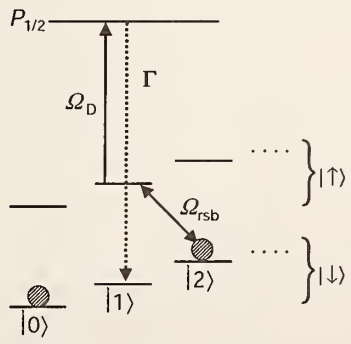

Figure 3 Implementation of an engineered zero-temperature reservoir. The states $|\downarrow\rangle|n\rangle$ and $|\uparrow\rangle|n-1\rangle$ are coupled by driving Raman motion-sensitive transitions (case (2) in the text). The state $|\uparrow\rangle$ is coupled to the environment by applying a weak optical pumping beam. The circles represent the superposition generated before applying this zero-temperature reservoir. The arrows show how the population in the $|\downarrow\rangle|2\rangle$ state is driven to the $|\uparrow\rangle|1\rangle$ state, and subsequently to the $|\downarrow\rangle|1\rangle$ state, through spontaneous Raman scattering.

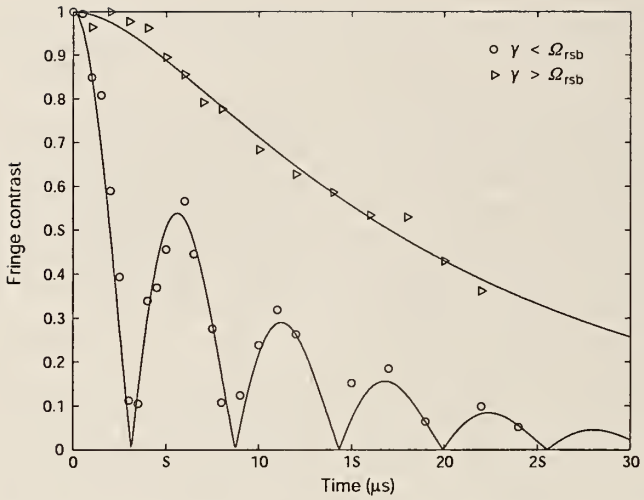

Figure 4 Decoherence of a Fock state superposition into the engineered zero-temperature reservoir. Fringe contrast is plotted as a function of the time the system is coupled to the zero temperature reservoir. The only difference in the two cases shown was the intensity of the optical pumping beam (see Fig. 3).

applied random potentials, and the Fock states of the superposition acquire a relative phase factor $e^{i\psi\Delta n}$, where $\Delta n = n - n'$. The steps that created the superposition are then reversed, with a relative phase difference δ between the creation and reversal pulses, leading to a probability of detecting the ion in the $|\downarrow\rangle$ state[21]:

$$P_{\downarrow} = \frac{1}{2}[1 + e^{-|\Delta n|^2\sigma^2/2}\cos\delta] \qquad (7)$$

Interference fringes are recorded by varying δ as in the Schrödinger-cat interferometer. The fringe contrast is plotted as a function of $|\Delta n|^2\langle V^2\rangle$ in Fig. 2. As with the Schrödinger-cat states and amplitude reservoir, the data were fitted by a single exponential in $|\Delta n|^2\langle V\rangle^2$.

Zero-temperature reservoir

A third type of engineered reservoir requires a quantum mechanical description. This is a bath of laser cooling light plus optical spontaneous emission, an engineered (nearly) zero-temperature reservoir following the suggestion of Poyatos *et al.*[8]. Our implementation, shown in Fig. 3, is essentially a continuous Raman cooling technique. A pair of Raman beams (case (2)), tuned to the first red sideband, couples the states $|\downarrow\rangle|n\rangle \leftrightarrow |\uparrow\rangle|n-1\rangle$. Concurrently, an optical pumping beam causes spontaneous Raman transitions from $|\uparrow\rangle$ to $|\downarrow\rangle$ through an unstable excited state $|e\rangle$, which decays at rate Γ. The Raman coupling strength is characterized by the Rabi frequency Ω_{rsb}, a function of the intensity and detuning of the Raman beams[13]. If the Rabi frequency of the optical pumping beam is Ω_D, then we can define an effective damping rate for the $|\uparrow\rangle$ state of $\gamma = \Omega_D^2/\Gamma$, valid for our case of $\Omega_D \ll \Gamma$. From the diagram in Fig. 3 we see that all populations are driven towards the state $|\downarrow\rangle|0\rangle$, the defining property of a zero-temperature reservoir. By varying the strength of the Raman and optical pumping couplings, we can control the reservoir parameters.

In the experiment, we examine the time evolution of the coherence of the Fock state superposition $\psi = |\downarrow\rangle(|0\rangle + |2\rangle)/\sqrt{2}$ for varying lengths of reservoir-interaction time. The interferometry is the same as in the study of the phase reservoir, where the Fock superposition is created, coupled to the reservoir, recombined, and probed, generating interference fringes. The data are shown in Fig. 4. Each data point represents the contrast of the fringes after the system interacts with the reservoir. We show two cases, $\gamma < \Omega_{rbs}$ and $\gamma > \Omega_{rsb}$. In the former case, the coherence between the $|0\rangle$ and $|2\rangle$ state disappears and reappears over time, with an overall decay of the fringe contrast. The underlying effect is population transfer back and forth (Rabi flopping) between the states $|\downarrow\rangle|2\rangle$ and $|\uparrow\rangle|1\rangle$ with a coupling of the $|\uparrow\rangle|1\rangle$ state to the outside environment through spontaneous Raman scattering. In effect, we have restricted the size of the environment (here the manifold of $|\uparrow\rangle|n\rangle$ states, weakly coupled to the outside environment) to an extent where we can reverse the effects of decoherence (of the $\psi = |\downarrow\rangle(|0\rangle + |2\rangle)/\sqrt{2}$ state) in a way similar to that proposed in ref. 22. This is also a striking example of non-exponential decay[23] in a context that is investigated in ref. 24. For the case $\gamma > \Omega_{rsb}$, the fringe contrast decreases monotonically to zero. Even in the case of monotonic decay, a deviation from exponential is observed, a manifestation of the quantum Zeno effect[24,25].

Although the data with $\gamma < \Omega_{rsb}$ illustrate how coherence transferred to the environment can be recovered, an alternative explanation would say that by transferring the $|\downarrow\rangle|2\rangle$ component of the superposition to the $|\uparrow\rangle|1\rangle$ state, we gain 'which-path' information in our interferometer—the paths being the $|\downarrow\rangle|0\rangle$ and $|\downarrow\rangle|2\rangle$ parts of the superposition. The oscillation in which-path information is analogous to that illustrated by other experiments[26,27].

Conclusions

The decoherence caused by the engineered high-temperature reservoirs described above can be explained by ensemble-averaging over random classical fields applied to the ion[21,28]. From previous experiments[20], we know that we can undo the effects of this decoherence by applying, in each experiment, a pulse of radiation that reverses the 'random' displacement. Similarly, the experiments here could also be carried out by coupling a hot resistor (with appropriate spectral filtering) between the trap electrodes (our case would correspond to a limit where the temperature $T \to \infty$ and the damping resistance $R \to 0$) (ref. 10). However, even in this case we could, subject to both practical and fundamental measurement uncertainties, record the voltages applied to the electrodes and reverse the effects of the random noise in each experiment. If we choose to ignore any knowledge of the electrical potentials applied to the trap electrodes, we can account for the observations just as well by considering the ion to be coupled to a large number of quantum oscillators, forming a heat bath. In the latter case, the state of the ion is entangled with that of the environment oscillators. After tracing over the environment variables, we are left with a reduced system, involving only the ion. The behaviour is the same as that obtained in the former case, in which the decoherence is caused by a deliberately applied external potential, but the environment is not considered to be a dynamical system itself[3,4]. Loosely speaking, the effect of an environment oscillator in the latter case is replaced by that of a single Fourier component of the electrical potential in the former case. Therefore, in the high-temperature limit simulated

by the first two experiments, one need not consider the entanglement with the environment because the environment noise can be sensed (classically) and its effects reversed. This is in contrast to the decay of ion motion into a zero-temperature reservoir described above, similar to that seen in cavity-QED experiments[7]. In this case, after the quantum system couples to the environment through spontaneous emission, a measurement of the environment is not sufficient to reverse the effects of decoherence.

The methods of engineering reservoirs that are presented here begin to broaden the field of experimental investigations of decoherence. With control over the reservoir parameters combined with non-classical motional states of trapped ions, detailed comparisons between theory and experiment are possible. Here we have simulated the decoherence caused by coupling a charged atom to a hot resistor (reservoir) by applying noisy voltages to the ion-trap electrodes. The cases considered demonstrate a quadratic dependence of the rate of decoherence on the size of the superpositions, demonstrating the difficulty in generating truly macroscopic superpositions, such as that of 'Schrödinger's cat'. As a practical matter, these 'high-temperature' sources of noise are important because they currently limit the performance of a trapped-ion quantum computer[13]. We have also simulated a zero-temperature reservoir by using laser cooling to damp the ion motion. Extensions of the technique used to generate this zero-temperature bath should permit some interesting system–bath interactions that would be difficult to realize in any other way. One possibility is generating a squeezed reservoir, where all initial states asymptotically relax to a squeezed state of motion[8]. Other couplings can be tailored to relax the system into a 'Schrödinger-cat' state[29,30]. □

Received 24 September; accepted 30 November 1999.

1. Dirac, P. A. M. *The Principles of Quantum Mechanics* (Oxford Univ. Press, Clarendon, 1958).
2. Schrödinger, E. Die gegenwärtige situation in der quantenmechanik. *Naturwissenschaften* **23**, 807–812, 823–828, 844–849 (1935).
3. Zurek, W. H. Decoherence and the transition from quantum to classical. *Phys. Today* **44**, 36–44 (1991).
4. Walls, D. F. & Milburn, G. J. *Quantum Optics* (Springer, Berlin, 1994).
5. Bužek, V. & Knight, P. L. Quantum interference, superposition states of light, and nonclassical effects. *Prog. Opt.* **XXXIV**, 1–158 (1995).
6. Monroe, C., Meekhof, D. M., King, B. E. & Wineland, D. J. A "Schrödinger cat" superposition state of an atom. *Science* **272**, 1131–1136 (1996).
7. Brune, M. *et al.* Observing the progressive decoherence of the "meter" in a quantum measurement. *Phys. Rev. Lett.* **77**, 4887–4890 (1996).
8. Poyatos, J. F., Cirac, J. I. & Zoller, P. Quantum reservoir engineering with laser cooled trapped ions. *Phys. Rev. Lett.* **77**, 4728–4731 (1996).
9. Marzoli, I., Cirac, J. I., Blatt, R. & Zoller, P. Laser cooling of trapped three-level ions: designing two-level systems for sideband cooling. *Phys. Rev. A* **49**, 2771–2779 (1994).
10. Caldeira, A. O. & Leggett, A. J. Influence of damping on quantum interference: an exactly soluble model. *Phys. Rev. A* **31**, 1059–1066 (1985).
11. Walls, D. F. & Milburn, G. J. Effect of dissipation on quantum coherence. *Phys. Rev. A* **31**, 2403–2408 (1985).
12. Collett, M. J. Exact density-matrix calculations for simple open systems. *Phys. Rev. A* **38**, 2233–2247 (1988).
13. Wineland, D. J. *et al.* Experimental issues in coherent quantum-state manipulations of trapped atomic ions. *J. Res. NIST* **103**, 259–328 (1998).
14. Schneider, S. & Milburn, G. J. Decoherence in ion traps due to laser intensity and phase fluctuations. *Phys. Rev. A* **57**, 3748–3752 (1998).
15. Murao, M. & Knight, P. L. Decoherence in nonclassical motional states of a trapped ion. *Phys. Rev. A* **58**, 663–669 (1998).
16. Schneider, S. & Milburn, G. J. Decoherence and fidelity in ion traps with fluctuating trap parameters. *Phys. Rev. A* **59**, 3766–3774 (1999).
17. Glauber, R. J. Coherent and incoherent states of the radiation field. *Phys. Rev.* **131**, 2766–2788 (1963).
18. Raizen, M. G., Gilligan, J. M., Bergquist, J. C., Itano, W. M. & Wineland, D. J. Ionic crystals in a linear Paul trap. *Phys. Rev. A* **45**, 6493–6501 (1992).
19. Monroe, C. *et al.* Resolved-sideband Raman cooling of a bound atom to the 3D zero-point energy. *Phys. Rev. Lett.* **75**, 4011–4014 (1995).
20. Meekhof, D. M., Monroe, C., King, B. E., Itano, W. M. & Wineland, D. J. Generation of nonclassical motional states of a trapped atom. *Phys. Rev. Lett.* **76**, 1796–1799 (1996).
21. Myatt, C. J. *et al.* in *Laser Spectroscopy 13* (ed. Blatt, R., Eschner, J., Leibfried, D. & Schmidt-Kaler, F.) (World Scientific, Singapore, in the press).
22. Raimond, J. M., Brune, M. & Haroche, S. Reversible decoherence of a mesoscopic superposition of field states. *Phys. Rev. Lett.* **79**, 1964–1967 (1997).
23. Wilkinson, S. R. *et al.* Experimental evidence for non-exponential decay in quantum tunnelling. *Nature* **387**, 575–577 (1997).
24. Thompson, R. C., Hernandez-Pozos, J.-L., Höffges, J., Segal, D. M. & Vincent, J. R. in *Trapped Charged Particles and Fundamental Physics* (eds Dubin, D. H. E. & Schneider, D.) 388–392 (American Institute of Physics Conf. Proc. 457, AIP Press, Woodbury, New York, 1999).
25. Itano, W. M., Heizen, D. J., Bollinger, J. J. & Wineland, D. J. Quantum Zeno effect. *Phys. Rev. A* **41**, 2295–2300 (1990).
26. Chapman, M. S. *et al.* Photon scattering from atoms in an interferometer: coherence lost and regained. *Phys. Rev. Lett.* **75**, 3783–3787 (1995).
27. Dürr, S., Nonn, T. & Rempe, G. Fringe visibility and which-way information in an atom interferometer. *Phys. Rev. Lett.* **81**, 5705–5709 (1998).
28. Itano, W. M. *et al.* Quantum harmonic oscillator state synthesis and analysis. *Proc. SPIE* **2995**, 43–55 (1997).
29. de Matos Filho, R. L. & Vogel, W. Even and odd coherent states of the motion of a trapped ion. *Phys. Rev. Lett.* **76**, 608–611 (1996).
30. Garraway, B. M., Knight, P. L. & Plenio, M. B. Generation and preservation of coherence in dissipative quantum optical environments. *Phys. Scr.* **T76**, 152–158 (1998).

Acknowledgements

We thank the US National Security Agency, Army Research Office, and Office of Naval Research for support. We thank P. Zoller, H. Mabuchi and W. Zurek for discussions. We thank them, D. Leibfried, M. Rowe, D. Sullivan and M. Lombardi for comments on the manuscript.

Correspondence and requests for materials should be addressed to D.J.W. (e-mail: dwineland@nist.gov).

Experimental entanglement of four particles

C. A. Sackett*, D. Kielpinski*, B. E. King*†, C. Langer*, V. Meyer*, C. J. Myatt*‡, M. Rowe*, Q. A. Turchette*‡, W. M. Itano*, D. J. Wineland* & C. Monroe*

* *Time and Frequency Division, National Institute of Standards and Technology, Boulder, Colorado 80303, USA*
† *Atomic Physics Division, NIST, Gaithersburg, Maryland 20899, USA*
‡ *Research Electro-Optics, 1855 S. 57th Ct., Boulder, Colorado 80301, USA*

Quantum mechanics allows for many-particle wavefunctions that cannot be factorized into a product of single-particle wavefunctions, even when the constituent particles are entirely distinct. Such 'entangled' states explicitly demonstrate the non-local character of quantum theory[1], having potential applications in high-precision spectroscopy[2], quantum communication, cryptography and computation[3]. In general, the more particles that can be entangled, the more clearly nonclassical effects are exhibited[4,5]—and the more useful the states are for quantum applications. Here we implement a recently proposed entanglement technique[6] to generate entangled states of two and four trapped ions. Coupling between the ions is provided through their collective motional degrees of freedom, but actual motional excitation is minimized. Entanglement is achieved using a single laser pulse, and the method can in principle be applied to any number of ions.

Most experimental demonstrations of entanglement to date have relied on the selection of data from random processes, such as the preparation and detection of photon pairs in parametric down-conversion[7–9] or of atoms in a thermal beam[10]. All methods of this type suffer from inescapable signal degradation when entanglement of larger numbers of particles is attempted, as the probability of randomly generating the appropriate conditions decreases exponentially. For instance, in the experiment of ref. 7, two-photon entangled states could be generated and detected at a rate of roughly 1,000 per second, three-photon states at a rate of 30 per hour, and four-photon states at an extrapolated rate of several per year. Trapped ions have been suggested as a system in which such effects might be avoided[11], and we have demonstrated two-particle entanglement in a deterministic way[12]. By 'deterministic' we mean that the desired state could be produced with a high degree of certainty at a user-specified time[13], which is necessary for avoiding the degradation described above. However, that experiment relied on the particular behaviour of two ions in a quadrupole radio-frequency trap, and could not easily be applied to larger numbers of particles.

The entanglement technique proposed by Mølmer and Sørensen[6,14] can be understood by considering a pair of spin-half charged particles confined together in a harmonic potential. The energy levels of this system are illustrated in Fig. 1, where $\hbar\omega_0$ is the internal energy splitting of each particle, and ν is the oscillation frequency of a particular collective mode of the particles in the trap. Using laser-cooling and optical-pumping techniques[15], the particles are initially prepared in their spin-down internal state and in the ground state of their collective motion: $|\psi\rangle = |\downarrow\downarrow 0\rangle$. By applying optical fields oscillating at $\omega_0 + \nu - \delta$ and $\omega_0 - \nu + \delta$, the two-step transition from $|\downarrow\downarrow 0\rangle$ to $|\uparrow\uparrow 0\rangle$ is driven. For sufficiently large δ, the intermediate states $|\uparrow\downarrow 1\rangle$ and $|\downarrow\uparrow 1\rangle$ are negligibly occupied, so that no motional excitation occurs. The resulting interaction hamiltonian, in the rotating-wave approximation and the Lamb–Dicke limit, is then

$$H = \frac{\hbar\bar{\Omega}}{2}(|\uparrow\uparrow\rangle\langle\downarrow\downarrow| + |\downarrow\downarrow\rangle\langle\uparrow\uparrow| + |\uparrow\downarrow\rangle\langle\downarrow\uparrow| + |\downarrow\uparrow\rangle\langle\uparrow\downarrow|) \qquad (1)$$

with $\bar{\Omega} = \eta^2\Omega^2/\delta$ when the single particle $|\downarrow\rangle \leftrightarrow |\uparrow\rangle$ transition has Rabi frequency Ω and the Lamb–Dicke parameter is η. For an excitation involving momentum transfer $\hbar k$ and a total particle mass of M, η is given by $(\hbar k^2/2M\nu)^{1/2}$. Entanglement is achieved by applying H for a time $t = \pi/2\bar{\Omega}$, making the spin wavefunction $|\psi_2\rangle = (|\uparrow\uparrow\rangle - i|\downarrow\downarrow\rangle)/\sqrt{2}$. This spin state is in fact created for any initial motional state $|n\rangle$, so long as the Lamb–Dicke criterion $\eta^2 n \ll 1$ is satisfied.

In order for the intermediate states $|\uparrow\downarrow 1\rangle$ and $|\downarrow\uparrow 1\rangle$ to be negligibly occupied, the detuning δ must be large compared to the transition linewidth $\eta\Omega$. However, it is clear from the expression for $\bar{\Omega}$ that the entanglement speed is maximized for small δ, and in fact the technique can still be applied for $\delta \approx \eta\Omega$ (refs 14, 16). Although motional excitation does then occur to some degree, for select values of δ the excitation vanishes at precisely the time that the entangled spin state is created. The condition for this to occur is

$$\delta/\eta\Omega = 2\sqrt{m} \qquad (2)$$

for any integer m, and the maximum excitation during the pulse then has mean quantum number $\bar{n} = 1/2m$. Our experiment is operated with $m = 1$.

As discussed in ref. 6, the entanglement method is scalable in the sense that precisely the same operation can be used to generate the N-particle entangled state

$$|\psi_N\rangle = (|\uparrow\uparrow\ldots\uparrow\rangle + i^{N+1}|\downarrow\downarrow\ldots\downarrow\rangle)/\sqrt{2} \qquad (3)$$

if N is any even number, while for N odd, $|\psi_N\rangle$ can be generated using one entanglement pulse accompanied by a separate independent rotation of each particle's spin.

If the ions are uniformly illuminated, the Mølmer and Sørensen scheme[6,14] requires that they all participate equally in the intermediate motional excitation, which implies that the only suitable mode for arbitrary N is the centre-of-mass mode. However, this mode has a practical disadvantage because in our experiments fluctuating ambient electric fields cause it to heat at a significant rate. Although for large δ the entanglement operation is largely independent of the motion, so that heating is unimportant, in the small-δ case it is necessary that motional decoherence be avoided. Modes involving only relative ion motion couple to higher moments of the field, so heating of these modes is negligible[15]. For $N = 2$ and $N = 4$, such modes do exist in which each particle participates with equal amplitude[17]. In both cases, they are symmetric 'stretch' modes, in which alternating ions oscillate out of

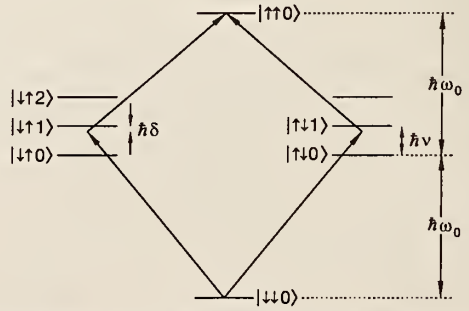

Figure 1 Entanglement scheme for two particles. Each ion is initially prepared in the $|\downarrow\rangle$ internal state, and the collective motion of the pair is cooled to its ground state $|0\rangle$. Laser fields oscillating near $\omega_0 + \nu$ and $\omega_0 - \nu$ couple the $|\downarrow\downarrow\rangle$ and $|\uparrow\uparrow\rangle$ states as shown. By detuning the single transition frequencies by a small amount δ, the populations of the $|\downarrow\uparrow 1\rangle$ and $|\uparrow\downarrow 1\rangle$ states are kept small. Then, by driving the double transition for the appropriate time, the entangled state $(|\uparrow\uparrow\rangle - i|\downarrow\downarrow\rangle)/\sqrt{2}$ is created. For four ions, the same procedure generates the state $(|\uparrow\uparrow\uparrow\uparrow\rangle + i|\downarrow\downarrow\downarrow\downarrow\rangle)/\sqrt{2}$. We note that in the actual experiment, each of the single transitions shown is itself a two-photon Raman transition, driven by a pair of laser beams; the entire process therefore consists of a four-photon transition.

phase. We use these modes here. Excitation of the centre-of-mass mode still affects the experiment, as the motion in spectator modes modifies the coupling strength to the mode of interest[14,15]. For this reason, we initially cool both the centre-of-mass and stretch modes to near their ground state.

The experiment was performed using $^9Be^+$ ions confined in a miniature linear radio-frequency trap[18], with the N ions lying in a line along the trap's weak axis. Two spectrally resolved ground-state hyperfine levels comprise the effective spin-half system, with $|\downarrow\rangle \equiv |F = 2, m_F = -2\rangle$ and $|\uparrow\rangle \equiv |F = 1, m_F = -1\rangle$, where F is the total angular momentum quantum number, and $\hbar m_F$ is the projection of the angular momentum along the quantization axis defined by an externally applied magnetic field. The hyperfine splitting $\omega_0/2\pi$ is approximately 1.25 GHz. Coherent coupling between $|\downarrow\rangle$ and $|\uparrow\rangle$ is provided by stimulated Raman transitions. The two Raman laser beams have a wavelength of 313 nm with a difference frequency near ω_0, and are perpendicular, with their difference wave-vector lying along the line of ions. They are detuned ~80 GHz blue of the $2P_{1/2}$ excited state, with intensities giving $\Omega/2\pi \approx 500$ kHz. For both the two- and four-ion experiments, the desired stretch-mode frequency $\nu/2\pi$ was 8.8 MHz, giving $\eta = 0.23/N^{1/2}$. The two driving frequencies required for the entanglement operation are generated by frequency-modulating one of the Raman beams using an electro-optic modulator.

After the entanglement operation, the ions are probed by illuminating them with a circularly polarized laser beam tuned to the $2S_{1/2}(F = 2, m_F = -2) \leftrightarrow 2P_{3/2}(F = 3, m_F = -3)$ cycling transition. Each ion in $|\downarrow\rangle$ fluoresces brightly, leading to the detection of ~15 photons per ion on a photomultiplier tube during a 200-μs detection period. In contrast, an ion in $|\uparrow\rangle$ remains nearly dark. Because the number of photons detected from a spin-down ion fluctuates according to Poisson statistics, in a single experiment the number of spin-down ions can be determined with only a limited accuracy. For the data reported, each experiment was repeated 1,000 times under the same conditions, and the resulting photon–number distribution fitted to a sum of poissonians to determine the probabilities P_j for j ions to be in $|\downarrow\rangle$. The results are given in Table 1, and show that in both cases, the probabilities for all N ions to be in the same state are large compared to the probabilities for the other cases. This is characteristic of the states $|\psi_N\rangle$, although the fact that the middle probabilities are non-zero indicates that we do not generate the entangled states with perfect accuracy.

Table 1 Characterization of two-ion and four-ion states

N	P_0	P_1	P_2	P_3	P_4	$\rho_{(\downarrow\uparrow)}$
2	0.43	0.11	0.46	–	–	0.385
4	0.35	0.10	0.10	0.10	0.35	0.215

N is the number of ions, P_j denotes the probability that j ions were measured to be in $|\downarrow\rangle$, and $\rho_{(\downarrow\uparrow)}$ denotes the amplitude of the density matrix element $\rho_{\downarrow\ldots\downarrow\uparrow\downarrow\ldots\downarrow}$. Uncertainties in $\rho_{(\downarrow\uparrow)}$ and the $N = 2$ populations are ±0.01, and uncertainties in the $N = 4$ populations are ±0.02.

In order to prove that we are generating a reasonable approximation to $|\psi_N\rangle$, it is necessary to prove that the populations of $|\uparrow\ldots\uparrow\rangle$ and $|\downarrow\ldots\downarrow\rangle$ are coherent. In terms of the density matrix for the system, ρ, we must measure the far off-diagonal element $\rho_{\uparrow\ldots\uparrow\downarrow\ldots\downarrow}$, whose amplitude will be abbreviated $\rho_{(\downarrow\downarrow)}$. This can be achieved by applying a simple analysis pulse to the ions before observing them. If the Raman difference frequency is set to ω_0 (and the frequency modulator turned off), each ion i undergoes ordinary Rabi oscillations, evolving according to the hamiltonian

$$H_i = \frac{\hbar\Omega}{2}(e^{i\phi}|\uparrow\rangle_i\langle\downarrow|_i + e^{-i\phi}|\downarrow\rangle_i\langle\uparrow|_i) \tag{4}$$

where ϕ is the phase of the difference frequency relative to that of the entanglement pulse. This hamiltonian is applied for time $\pi/2\Omega$ (a $\pi/2$ pulse), and the parity

$$\Pi \equiv \sum_{j=0}^{N}(-1)^j P_j \tag{5}$$

is observed while ϕ is varied. As seen in Fig. 2, for N ions Π oscillates as $\cos N\phi$, and the amplitude of this oscillation is in fact $2\rho_{(\downarrow\downarrow)}$ (ref. 2). The resulting values are given in Table 1. From the data shown in the table, our state preparation fidelity

$$F \equiv \langle\psi_N|\rho|\psi_N\rangle = \frac{1}{2}(P_{(\uparrow)} + P_{(\downarrow)}) + \rho_{(\downarrow\downarrow)} \tag{6}$$

can be determined, where $P_{(\uparrow)}$ is the population of $|\uparrow\ldots\uparrow\rangle$ and $P_{(\downarrow)}$ is the population of $|\downarrow\ldots\downarrow\rangle$. For $N = 2$ we achieve $F = 0.83 \pm 0.01$, while for $N = 4$, $F = 0.57 \pm 0.02$.

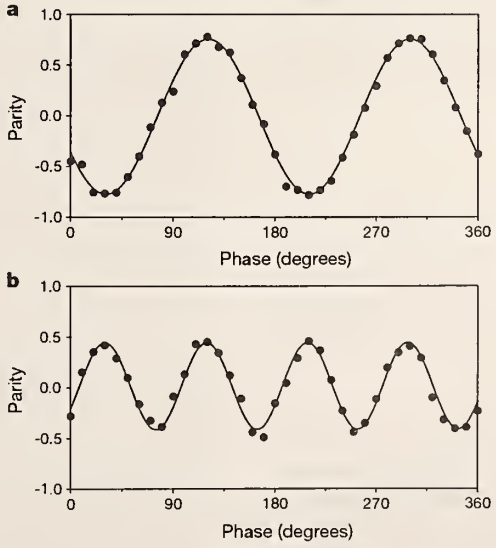

Figure 2 Determination of $\rho_{(\downarrow\downarrow)}$. **a**, Interference signal for two ions; **b**, four ions. After the entanglement operation of Fig. 1, an analysis pulse with relative phase ϕ is applied on the single-ion $|\downarrow\rangle \leftrightarrow |\uparrow\rangle$ transition. As ϕ is varied, the parity of the N ions oscillates as $\cos N\phi$, and the amplitude of the oscillation is twice the magnitude of the density-matrix element $\rho_{(\downarrow\downarrow)}$. Each data point represents an average of 1,000 experiments, corresponding to a total integration time of roughly 10 s for each graph.

The fact that $\rho_{(\uparrow\downarrow)}$ is non-zero is still insufficient to guarantee entanglement. To be explicit, a system with density matrix ρ exhibits N-particle entanglement only if no decomposition $\rho = \Sigma_k p_k |\psi_k\rangle\langle\psi_k|$ exists with all the $\{|\psi_k\rangle\}$ factorizable into products of wavefunctions that depend on fewer than N particles. For example, if $|\psi\rangle_i = (|\uparrow\rangle_i + |\downarrow\rangle_i)/\sqrt{2}$ is a state of ion i, then the four-particle state $|\psi\rangle_1|\psi\rangle_2|\psi\rangle_3|\psi\rangle_4$ is not entangled, but still has $\rho_{(\uparrow\downarrow)} = 1/16$. We note that these are the types of states studied in liquid-state nuclear magnetic resonance experiments[19]. Alternatively, for $|\psi\rangle_{12} = (|\uparrow\rangle_1|\uparrow\rangle_2 + |\downarrow\rangle_1|\downarrow\rangle_2)/\sqrt{2}$ and $|\psi\rangle_{34} = (|\uparrow\rangle_3|\uparrow\rangle_4 + |\downarrow\rangle_3|\downarrow\rangle_4)/\sqrt{2}$, the state $|\psi\rangle_{12}|\psi\rangle_{34}$ exhibits two-particle, but not four-particle entanglement, and has $\rho_{(\uparrow\downarrow)} = 1/4$.

To establish that we are actually observing N-particle entanglement, consider an arbitrary factorizable wavefunction

$$|\psi_F\rangle = [a|\uparrow \ldots \uparrow\rangle_X + b|\downarrow \ldots \downarrow\rangle_X + \ldots][c|\uparrow \ldots \uparrow\rangle_Y + d|\downarrow \ldots \downarrow\rangle_Y + \ldots] \quad (7)$$

where X and Y refer to two distinct subsets of the N particles, with $|\uparrow\ldots\uparrow\rangle_X$ indicating the state with all particles in subset X spin-up, and similarly for the other terms. Normalization of the factor wavefunctions requires $|a|^2 + |b|^2 \leq 1$ and $|c|^2 + |d|^2 \leq 1$, which can be combined and rewritten as

$$(|a| - |c|)^2 + 2|ac| + (|b| - |d|)^2 + 2|bd| \leq 2 \quad (8)$$

Since the squared terms on the left are positive, equation (8) implies that $|ac| + |bd| \leq 1$, and in turn that $(|ac| + |bd|)^2 \leq 1$. Expanding the square yields the desired relation[20]:

$$P_{(\uparrow)} + P_{(\downarrow)} + 2\rho_{(\uparrow\downarrow)} = 2F \leq 1 \quad (9)$$

where $P_{(\uparrow)} = |ac|^2$, $P_{(\downarrow)} = |bd|^2$, and $\rho_{(\uparrow\downarrow)} = |abcd|$ are the previously defined quantities. Since equation (9) holds for any separable wavefunction, it must also hold for any separable density matrix. Both our $N = 2$ and $N = 4$ experiments give $F > 1/2$, so the states they produce exhibit N-particle entanglement.

Quantifying the amount of entanglement present is a more difficult question. A variety of measures of entanglement have been proposed, but most are difficult to calculate even numerically[21,22]. For $N = 2$, there is an explicit formula for the "entanglement of formation" E as a function of ρ (ref. 23). Although we have not reconstructed the entire two-particle density matrix, the populations measured place sufficient bounds on the unmeasured elements to determine that $E \approx 0.5$. This indicates that roughly two pairs of our ions would be required to carry the same quantum information as a single perfectly entangled pair.

In the four-ion case, no explicit formula for entanglement is known. The data do indicate that our density matrix can be expressed approximately as

$$\rho = 0.43|\psi_4\rangle\langle\psi_4| + 0.57\rho_{\text{incoh}} \quad (10)$$

where $|\psi_4\rangle$ is the desired state and ρ_{incoh} is completely incoherent (that is, diagonal). These coefficients are determined directly from the value of $\rho_{(\uparrow\downarrow)}$ in Table 1, together with the fact that no evidence for other off-diagonal matrix elements was observed. To determine a measure of entanglement, however, it is necessary to decompose ρ as a sum of $|\psi_4\rangle$ and a 'worst-case' factorizable matrix ρ_F, which can be accomplished as

$$\rho = 0.13|\psi_4\rangle\langle\psi_4| + 0.87\rho_F. \quad (11)$$

Note that equations (10) and (11) both describe the same physical state, but that in equation (11), ρ_F consists of a specific mixture of two- and three-particle entangled states that is highly unlikely to occur in our experiments. In either description, it is clear that our state-preparation accuracy is limited.

The source of decoherence in our experiments is not entirely clear, but evidence suggests that it is related to intensity fluctuations in the Raman laser beams, a problem we are working to understand and correct[24]. The presence of decoherence, and the fact that it affects the four-ion experiment more strongly than the two-ion one, illustrates the need to carefully define the sense in which our entanglement operation is 'scalable'. Any entanglement experiment is more sensitive to decoherence as the number of particles involved is increased, unless sufficient accuracy can be achieved for error-correction schemes to be usefully applied. Such schemes are thought to require an error rate of the order of 10^{-4} per operation[25], and we are certainly far from this regime. However, even if such a level of fidelity were to be achieved, applications such as quantum computing still require very large entangled states to be generated in a reasonable amount of time and using a reasonable amount of resources. The method demonstrated here is important in this regard, since it uses only a single operation and requires a time that scales roughly as $N^{1/2}$.

In the language of quantum information science, we have realized a four-quantum-bit logic gate. This system is relevant for the future development of quantum information technology, as such states may be used to implement quantum error-detection schemes[26] or to make rudimentary demonstrations of quantum algorithms[27,28]. Entanglement of four particles is also interesting in its own right, as such states can show strong violations of local realism[5]. Even the two-particle Bell's inequality measurement would be interesting to implement, as the near-perfect detection efficiency for ions would eliminate the "fair sampling" hypothesis which has been required in other experiments[29]. In addition to improved fidelity, applications such as these do require the ability to perform individual manipulation and detection of each ion, but this is not expected to be a severe experimental challenge[30]. □

Received 11 February; accepted 15 February 2000.

1. Bell, J. *Speakable and Unspeakable in Quantum Mechanics* (Cambridge Univ. Press, 1987).
2. Bollinger, J., Itano, W. M., Wineland, D. & Heinzen, D. Optimal frequency measurements with maximally correlated states. *Phys. Rev. A* **54**, R4649–R4652 (1996).
3. Lo, H.-K., Popescu, S. & Spiller, T. (eds) *Introduction to Quantum Computation and Information* (World Scientific, Singapore, 1997).
4. Pan, J.-W., Bouwmeester, D., Daniell, M., Weinfurter, H. & Zeilinger, A. Experimental test of quantum non-locality in three-photon Greenberger–Horne–Zeilinger entanglement. *Nature* **403**, 515–519 (2000).
5. Mermin, N. D. Extreme quantum entanglement in a superposition of macroscopically distinct states. *Phys. Rev. Lett.* **65**, 1838–1840 (1990).
6. Mølmer, K. & Sørensen, A. Multiparticle entanglement of hot trapped ions. *Phys. Rev. Lett.* **82**, 1835–1838 (1999).
7. Bouwmeester, D., Pan, J.-W., Daniell, M., Weinfurter, H. & Zeilinger, A. Observation of three-photon Greenberger-Horne-Zeilinger entanglement. *Phys. Rev. Lett.* **82**, 1345–1349 (1999).
8. Kwiat, P. *et al.* New high-intensity source of polarization-entangled photon pairs. *Phys. Rev. Lett.* **75**, 4337–4341 (1995).
9. Tittle, W., Brendel, J., Zbinden, H. & Gisin, N. Violation of Bell inequalities by photons more than 10 km apart. *Phys. Rev. Lett.* **81**, 3565–3566 (1998).
10. Hagley, E. *et al.* Generation of Einstein-Podolsky-Rosen pairs of atoms. *Phys. Rev. Lett.* **79**, 1–5 (1997).
11. Cirac, J. & Zoller, P. Quantum computations with cold trapped ions. *Phys. Rev. Lett.* **74**, 4091–4094 (1995).
12. Turchette, Q. *et al.* Deterministic entanglement of two trapped ions. *Phys. Rev. Lett.* **81**, 3631–3634 (1998).
13. Law, C. & Kimble, J. Deterministic generation of a bit-stream of single-photon pulses. *J. Mod. Opt.* **44**, 2067–2074 (1997).
14. Mølmer, K. & Sørensen, A. Entanglement and quantum computation with ions in thermal motion. Pre-print quant-ph/0002024 at ⟨xxx.lanl.gov⟩ (2000).
15. King, B. *et al.* Cooling the collective motion of trapped ions to initialize a quantum register. *Phys. Rev. Lett.* **81**, 1525–2528 (1998).
16. Milburn, G. Simulating nonlinear spin models in an ion trap. Pre-print quant-ph/9908037 at ⟨xxx.lanl.gov⟩ (1999).
17. James, D. Quantum dynamics of cold trapped ions with applications to quantum computation. *Appl. Phys. B* **66**, 181–190 (1998).
18. Turchette, Q. *et al.* Heating of trapped ions from the quantum ground state. Pre-print quant-ph/0002040 at ⟨xxx.lanl.gov⟩ (2000).
19. Fitzgerald, R. What really gives a quantum computer its power? *Phys. Today* **53**, 20–22 (2000).
20. Bennett, C. *et al.* Purification of noisy entanglement and faithful teleportation via noisy channels. *Phys. Rev. Lett.* **76**, 722–725 (1996).
21. Vedral, V., Plenio, M., Rippin, M. & Knight, P. Quantifying entanglement. *Phys. Rev. Lett.* **78**, 2275–2279 (1997).
22. Lewenstein, M. & Sanpera, A. Separability and entanglement of composite quantum systems. *Phys. Rev. Lett.* **80**, 2261–2264 (1998).
23. Wootters, W. K. Entanglement of formation of an arbitrary state of two qubits. *Phys. Rev. Lett.* **80**, 2245–2248 (1998).
24. Wineland, D. *et al.* Experimental issues in coherent quantum-state manipulation of trapped atomic ions. *J. Res. NIST* **103**, 259–328 (1998).

25. Preskill, J. Battling decoherence: the fault tolerant quantum computer. *Phys. Today* **52**, 24–30 (1999).
26. Vaidman, L., Goldenberg, L. & Wiesner, S. Error prevention scheme with four particles. *Phys. Rev. A* **54**, R1745–R1748 (1996).
27. Shor, P. Polynomial-time algorithms for prime factorization and discrete logarithms on a quantum computer. *SIAM J. Comput.* **26**, 1484–1509 (1997).
28. Grover, L. Quantum mechanics helps in searching for a needle in a haystack. *Phys. Rev. Lett.* **79**, 325–328 (1997).
29. Eberhard, P. Background level and counter efficiencies required for a loophole-free Einstein-Podolsky-Rosen experiment. *Phys. Rev. A* **47**, R747–R750 (1993).
30. Nägerl, H. *et al.* Laser addressing of individual ions in a linear ion trap. *Phys. Rev. A* **60**, 145–148 (1999).

Acknowledgements

We thank J. Bollinger and E. A. Cornell for comments on the manuscript. This work was supported by the US National Security Agency, Army Research Office and Office of Naval Research.

Correspondence and requests for materials should be addressed to C. M. (e-mail: monroe@boulder.nist.gov).

Quantum distribution of protons in solid molecular hydrogen at megabar pressures

Hikaru Kitamura*†‡, Shinji Tsuneyuki*, Tadashi Ogitsu*§ & Takashi Miyake‖

* *Institute for Solid State Physics, University of Tokyo, Roppongi, Tokyo 106-8666, Japan*
† *Department of Space Physics and Astronomy, Rice University, Houston, Texas 77251-1892, USA*
‡ *Applied Theoretical and Computational Physics Division, Los Alamos National Laboratory, Los Alamos, New Mexico 87545, USA*
§ *National Center for Supercomputing Applications, University of Illinois at Urbana-Champaign, Urbana, Illinois 61801, USA*
‖ *Joint Research Center for Atom Technology, Tsukuba, Ibaraki 305-0046, Japan*

Solid hydrogen, a simple system consisting only of protons and electrons, exhibits a variety of structural phase transitions at high pressures. Experimental studies[1] based on static compression up to about 230 GPa revealed three relevant phases of solid molecular hydrogen: phase I (high-temperature, low-pressure phase), phase II (low-temperature phase) and phase III (high-pressure phase). Spectroscopic data suggest that symmetry breaking, possibly related to orientational ordering[1,2], accompanies the transition into phases II and III. The boundaries dividing the three phases exhibit a strong isotope effect[3], indicating that the quantum-mechanical properties of hydrogen nuclei are important. Here we report the quantum distributions of protons in the three phases of solid hydrogen, obtained by a first-principles path-integral molecular dynamics method. We show that quantum fluctuations of protons effectively hinder molecular rotation—that is, a quantum localization occurs. The obtained crystal structures have entirely different symmetries from those predicted by the conventional simulations which treat protons classically.

The structures of these broken-symmetry phases have been extensively investigated both by experimental[1–3] and by theoretical[4–9] studies, though the results are still controversial. In most theoretical studies, even when they precisely compare total energies of model structures on the basis of electronic-structure calculations, quantum fluctuations of protons are usually neglected, or roughly discussed, perhaps due to some technical reason. But as shown by our previous study on impurity muonium (a bound state comprising a positive muon and an electron) and hydrogen in crystalline silicon[10], quantum states of light particles may exhibit distributions significantly different from those expected from stability analyses based on the classical potential-energy surface. It is therefore desirable to examine quantitatively the quantum-mechanical properties of protons in solid hydrogen, especially when we are concerned with its symmetry breaking under high pressure. Natoli *et al.*[11] treated both electrons and protons with quantum Monte Carlo methods; their simulations were, however, performed with trial wavefunctions based on the fixed static configuration of the protons, and were restricted to the molecules centred on the hexagonal close packed (h.c.p.) lattice sites.

The first-principles path-integral molecular dynamics (FP-PIMD) method enables us to incorporate quantum-mechanical properties of protons in conventional Car–Parrinello-type first-principles simulations. The basic formalism was first presented by Marx and Parrinello[12]. Recently this scheme was further developed by the present authors[10], and we use this in the present study. We consider a supercell containing N (= 64) atoms, which is subject to the periodic boundary conditions. To represent the quantum properties of protons in the path-integral formalism, imaginary time $\beta\hbar$ (where β is the inverse temperature in units of Boltzmann constant) is divided into P finite time slices; each proton is thus represented by a polymer consisting of P 'beads' interacting via intrapolymeric harmonic forces[13]. Exchange effects between protons are neglected in this study. Assuming the Born–Oppenheimer approximation, interatomic forces between protons at each atomic configuration and at each time slice are determined by electronic-structure calculation based on the density-functional theory (DFT). The resultant classical system of NP particles is simulated by molecular dynamics (MD) at constant volume and temperature with the aid of the Nosé–Hoover chain thermostat[14]. In the evaluation of the exchange-correlation potential in the DFT calculation, we adopt the generalized gradient approximation (GGA)[15]. The interaction between a proton and an electron has been described by the norm-conserving non-local pseudopotential of the Troullier–Martins type[16]; the electronic wavefunctions have been expanded in plane waves with a cut-off energy of 50 Ry. Integration over the first Brillouin zone has been achieved by sampling 8 uniform k-points. Energy eigenvalues of the lowest 32 occupied bands have been explicitly calculated, since the system should remain an insulator in the relevant pressure range[1]. The ground-state electron density has been obtained by minimizing the total energy functional through the conjugated-gradient method[17]. We have verified, through static DFT calculations with these parameter conditions, that the potential energy surface associated with molecular rotation in the $Pca2_1$ structure obtained earlier by

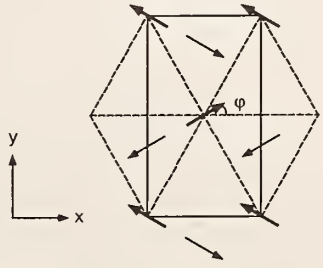

Figure 1 Illustration of the $Pca2_1$ structure projected onto the x–y plane. Thick arrows represent molecules on the α-plane and thin arrows depict those on the β-plane, both pointing towards the positive-z hemisphere. These two planes are apart from each other by $c/2$ in the z-direction. The quantity θ measures the angle between a molecular axis and the $c(z)$-axis of the crystal: φ is the corresponding azimuthal angle. The $Cmc2_1$ structure is obtained by setting $\varphi = 90°$.

Sympathetic cooling of trapped ions for quantum logic

D. Kielpinski, B. E. King, C. J. Myatt, C. A. Sackett, Q. A. Turchette, W. M. Itano, C. Monroe, and D. J. Wineland
Time and Frequency Division, National Institute of Standards and Technology, Boulder, Colorado 80303

W. H. Zurek
T-6 (Theoretical Astrophysics), MS B288, Los Alamos National Laboratory, Los Alamos, New Mexico 87545
(Received 27 August 1999; published 16 February 2000)

One limit to the fidelity of quantum logic operations on trapped ions arises from heating of the ions' collective modes of motion. Sympathetic cooling of the ions during the logic operations may eliminate this source of errors. We discuss the benefits and drawbacks of this proposal, and describe possible experimental implementations. We also present an overview of trapped-ion dynamics in this scheme.

PACS number(s): 03.67.−a, 32.80.Pj

I. INTRODUCTION

One of the most attractive physical systems for generating large entangled states and realizing a quantum computer [1] is a collection of cold trapped atomic ions [2]. The ion trap quantum computer stores one or more quantum bits (qubits) in the internal states of each trapped ion, and quantum logic gates (implemented by interactions with externally applied laser beams) can couple qubits through a collective quantized mode of motion of the ion Coulomb crystal. Loss of coherence of the internal states of trapped ions is negligible under proper conditions but heating of the motion of the ion crystal may ultimately limit the fidelity of logic gates of this type. In fact, such heating is currently a limiting factor in the National Institute of Standards and Technology (NIST) ion-trap quantum logic experiments [3,4].

Electric fields from the environment readily couple to the motion of the ions, heating the ion crystal [3–7]. If the ion trap is much larger than the ion crystal size, we expect these electric fields to be nearly uniform across the crystal. Uniform fields will heat only modes that involve center-of-mass motion (COM motion), in which the crystal moves as a rigid body. Motional modes orthogonal to the COM motion, for instance, the collective breathing mode, require field gradients to excite their motion. The heating of these modes is therefore suppressed [4]. However, even if quantum logic operations use such a "cold" mode, the heating of the COM motion can still indirectly limit the fidelity of logic operations. Since the laser coupling of an internal qubit and a motional mode depends on the total wave-packet spread of the ion containing the qubit, the thermal COM motion can reduce the logic fidelity [3,4].

In this paper, we examine sympathetic cooling [8] in a particular scheme for which we can continuously laser cool the COM motion while leaving undisturbed the coherences of both the internal qubits and the mode used for quantum logic. In this method, one applies continuous laser cooling to only the center ion of a Coulomb-coupled string of an odd number of ions. One can address the center ion alone if the center ion is of a different ion species than that composing the rest of the string [9]. Alternatively, one can simply focus the cooling beams so that they affect only the center ion. In either case, the cooling affects only the internal states of the center ion, leaving all other internal coherences intact. If the logic operations use a mode in which the center ion remains at rest, the motional coherences in that mode are also unaffected by the cooling. On the other hand, the sympathetic cooling keeps the COM motion cold, reducing the thermal wave packet spread of the ions. In the following, we will discuss the dynamics of an ion string in which all ions are identical except the center ion, assuming heating by a uniform electric field. Our results give guidelines for implementing the sympathetic cooling scheme. Similar results would apply to two- and three-dimensional ion crystals [10–13].

II. AXIAL MODES OF MOTION

We consider a crystal of N ions, all of charge q, in a linear radiofrequency (RF) trap [10,11]. The linear RF trap is essentially an RF quadrupole mass filter with a static confining potential along the filter axis $\hat{z}$. If the radial confinement is sufficiently strong compared to the axial confinement, the ions will line up along the z axis in a string configuration [10,11]. There is no RF electric field along $\hat{z}$, so we can write the axial confining potential as $\phi(z)=\mathrm{q}a_0 z^2/2$ for a_0 a constant. The potential energy of the string is then given by

$$V(z_1,\ldots,z_n)=\frac{1}{2}\mathrm{q}a_0\sum_{i=1}^{N} z_i^2+\frac{\mathrm{q}^2}{8\pi\epsilon_0}\sum_{\substack{i,j=1\\ i\neq j}}^{N}\frac{1}{|z_i-z_j|} \quad (1)$$

for z_i the position of the ith ion in the string (counting from the end of the string). The first term in the potential energy expresses the influence of the static confining potential along the z axis, while the second arises from the mutual Coulomb repulsion of the ions. For a single ion of mass m, the trap frequency along z is just $\omega_z=\sqrt{\mathrm{q}a_0/m}$.

We can compute the equilibrium positions of the ions in the string by minimizing the potential energy of Eq. (1). Defining a length scale ℓ by $\ell^3=\mathrm{q}/(4\pi\epsilon_0 a_0)$ and normalizing the ion positions by $u_i=z_i/\ell$ gives a set of equations for the u_i as

$$u_i-\sum_{j=1}^{i-1}\frac{1}{(u_i-u_j)^2}+\sum_{j=i+1}^{N}\frac{1}{(u_i-u_j)^2}=0,\quad i=1,\ldots,N, \tag{2}$$

which has analytic solutions only up to $N=3$. Steane [1] and James [14] have computed the equilibrium positions of ions in strings with N up to 10. The potential energy is independent of the mass, so the equilibrium positions of ions in a string are independent of the elemental composition of the string if all the ions have the same charge.

In a real ion trap the ions will have some nonzero temperature and will move about their equilibrium positions. If the ions are sufficiently cold, we can write their positions as a function of time as $z_i(t)=\ell u_i+q_i(t)$, where $q_i(t)$ is small enough to allow linearizing all forces. We focus on the case of an odd number of ions N, where all ions have mass m, except for the one at the center of the string which has mass M. The ions are numbered $1,\ldots,N$, with the center ion labeled by $n_c=(N+1)/2$. Following James [14], the Lagrangian for the resulting small oscillations is

$$L=\frac{m}{2}\sum_{\substack{i=1\\ i\neq n_c}}^{N}\dot{q}_i^2+\frac{M}{2}\dot{q}_{n_c}^2-\frac{1}{2}\sum_{i,j=1}^{N}\left.\frac{\partial^2 V}{\partial z_i\partial z_j}\right|_{\{q_i\}=0}q_iq_j \tag{3}$$

$$=\frac{m}{2}\sum_{\substack{i=1\\ i\neq n_c}}^{N}\dot{q}_i^2+\frac{M}{2}\dot{q}_{n_c}^2-\frac{1}{2}\mathrm{q}a_0\sum_{i,j=1}^{N}A_{ij}q_iq_j, \tag{4}$$

where

$$A_{ij}=\begin{cases}1+2\displaystyle\sum_{\substack{k=1\\ k\neq i}}^{N}\frac{1}{|u_i-u_k|^3} & i=j\\ -2\dfrac{1}{|u_i-u_j|^3} & i\neq j.\end{cases} \tag{5}$$

We define a normalized time as $T=\omega_z t$. In treating the case of two ion species, we write $\mu=M/m$ for the mass ratio of the two species and normalize the amplitude of the ion vibrations $q_i(t)$ as $Q_i=q_i\sqrt{\mathrm{q}a_0}$, $i\neq n_c$, $Q_{n_c}=q_{n_c}\sqrt{\mathrm{q}a_0\mu}$. The Lagrangian becomes

$$L=\frac{1}{2}\sum_{i=1}^{N}\left(\frac{dQ_i}{dT}\right)^2-\frac{1}{2}\sum_{i,j=1}^{N}A'_{ij}Q_iQ_j, \tag{6}$$

where

$$A'_{ij}=\begin{cases}A_{ij} & i,j\neq n_c\\ A_{ij}/\sqrt{\mu} & i \text{ or } j=n_c, i\neq j\\ A_{ij}/\mu & i=j=n_c\end{cases} \tag{7}$$

generalizing the result of James [14].

The Lagrangian is now cast in the canonical form for small oscillations in the coordinates $Q_i(t)$. To find the normal modes, we solve the eigenvalue equation

$$\mathbf{A}'\cdot\vec{v}^{(k)}=\zeta_k^2\vec{v}^{(k)}\quad k=1,\ldots,N \tag{8}$$

for the frequencies ζ_k and (orthonormal) eigenvectors $\vec{v}^{(k)}$ of the N normal modes. Because of our normalization of the Lagrangian (6), the ζ_k are normalized to ω_z and the $\vec{v}^{(k)}$ are expressed in terms of the normalized coordinates $Q_i(t)$. In terms of the physical time t, the frequency of the kth mode is $\zeta_k\omega_z$. If the kth mode is excited with an amplitude C, we have

$$q_i(t)=\mathrm{Re}[Cv_i^{(k)}e^{i(\zeta_k\omega_z t+\phi_k)}]\quad i\neq n_c, \tag{9}$$

$$q_{n_c}(t)=\mathrm{Re}\left[C\frac{1}{\sqrt{\mu}}v_{n_c}^{(k)}e^{i(\zeta_k\omega_z t+\phi_k)}\right] \tag{10}$$

in terms of the physical coordinates $q_i(t)$.

We can solve for the normal modes analytically for $N=3$. Exact expressions for the normal-mode frequencies are

$$\zeta_1=\left[\frac{13}{10}+\frac{1}{10\mu}(21-\sqrt{441-34\mu+169\mu^2})\right]^{1/2}, \tag{11}$$

$$\zeta_2=\sqrt{3}, \tag{12}$$

$$\zeta_3=\left[\frac{13}{10}+\frac{1}{10\mu}(21+\sqrt{441-34\mu+169\mu^2})\right]^{1/2}, \tag{13}$$

normalized to ω_z. The mode eigenvectors are

$$\vec{v}^{(1)}=N_1\left(1,\frac{\sqrt{\mu}}{8}(13-5\zeta_1^2),1\right), \tag{14}$$

$$\vec{v}^{(2)}=N_2(1,0,-1), \tag{15}$$

$$\vec{v}^{(3)}=N_3\left(1,\frac{\sqrt{\mu}}{8}(13-5\zeta_3^2),1\right), \tag{16}$$

in terms of $Q_i(t)$. Here N_1, N_2, and N_3 are normalization factors. In the case of three identical ions ($\mu=1$), we can express the mode eigenvectors in terms of the $Q_i(t)$ as $\vec{v}^{(1)}=(1,1,1)/\sqrt{3}$, $\vec{v}^{(2)}=(1,0,-1)/\sqrt{2}$, and $\vec{v}^{(3)}=(1,-2,1)/\sqrt{6}$. The mode eigenvectors, in this special case, also give the ion oscillation amplitudes in terms of the physical coordinates $q_i(t)$. For three identical ions, then, pure axial COM motion constitutes a normal mode. (This result holds for an arbitrary number of identical ions.) We also note that the center ion does not move in mode #2; hence the frequency and eigenvector of mode #2 are independent of μ. For any odd number N of ions there are $(N-1)/2$ modes for which the center ion does not move. These modes will likewise have frequencies and eigenvectors independent of μ. Moreover, they have $v_{n_c-m}^{(k)}=-v_{n_c+m}^{(k)}$ and so they are orthogonal to the COM motion and do not couple to uniform electric fields. The center ion moves in the other $(N+1)/2$ modes, and unless $\mu=1$, each of these $(N+1)/2$ modes has a component of axial COM motion and therefore couples to uniform electric fields.

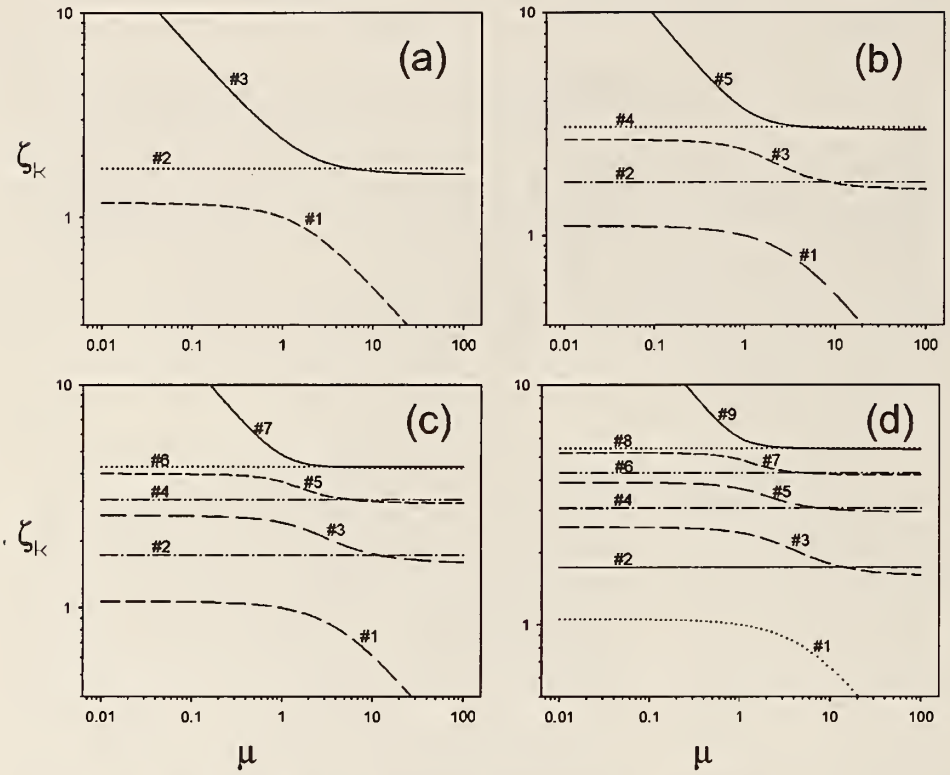

FIG. 1. Normalized axial mode frequencies as a function of μ for (a) 3, (b) 5, (c) 7, and (d) 9 ions.

For $N=5$ and higher, the normal mode frequencies depend on μ in a complicated way. However, it is easy to find the frequencies numerically. Figure 1 shows the mode frequencies for $N=3$, 5, 7, and 9 as a function of μ for $0.01 < \mu < 100$. The modes are numbered in order of increasing frequency (at $\mu=1$), and are normalized to ω_z. In each case, the lowest-lying mode has all ions moving in the same direction and consists of pure COM motion for $\mu=1$. The even-numbered modes correspond to the $(N-1)/2$ modes for which the center ion does not move. Their frequencies are therefore independent of μ. For both very large and very small μ the modes pair up, as shown in Fig. 1. For each pair there is some value $\mu>1$ for which the modes become degenerate. The relative spacing between modes in a pair is also smaller in the large-μ limit than in the small-μ limit.

If the static confining potential of the trap is not perfectly harmonic, the normal modes of motion will exchange energy with each other. This problem is addressed in Ref. [3] (Sec. 4.1.8). These effects are small if all modes are reasonably cold. Moreover, mode cross-coupling is a resonant process which requires the mode frequencies to be related as sums or differences. Avoiding such resonances by tuning the trap potentials reduces the rate of energy transfer by a large factor.

The Rabi frequency of the laser-ion interaction sets the speed of quantum logic gates and the linewidths of transitions between vibrational states of the ion crystal. If we perform quantum logic on a normal mode whose frequency is too close to that of another "spectator" mode, we must reduce our Rabi frequency, and thus our gate speed, to avoid driving transitions on the spectator mode; otherwise we suffer a loss of fidelity. Only the lowest-frequency mode is well separated from all other modes for μ very large. We will show below (Sec. IV) that this mode is undesirable for use in quantum logic. Hence, in order to maximize gate speed, it is best to use a cooling ion that is of the same mass as, or lighter than, the logic ions. In this case mode 2 is well separated from all other modes, as shown in Fig. 1.

III. TRANSVERSE MODES OF MOTION

We now consider the motion of the ions transverse to the z axis. The ions experience an RF potential $\chi\cos(\Omega t)(x^2-y^2)/2$ for a suitable choice of axes x and y perpendicular to z, where Ω is the frequency of the RF field and χ is a constant. The static confining potential can be written $(qa_0/2)(z^2-\alpha x^2-(1-\alpha)y^2)$ at the position of the ions (with α a constant), so there is also a transverse static electric field. To analyze the ion motion, we work in the pseudopotential approximation [15], in which one time averages the motion over a period of the RF drive to find the ponderomotive force on the ion. If the static potential is negligible, the RF drive gives rise to an effective transverse confining potential of $\frac{1}{2}m\omega_{r0}^2(x^2+y^2)$, where $\omega_{r0}=q\chi/(\sqrt{2}\Omega m)$ for an ion of mass m. If we include the effects of the static field, the transverse potential becomes $\frac{1}{2}m(\omega_x^2x^2+\omega_y^2y^2)$, where $\omega_x=\omega_{r0}\sqrt{1-\alpha\omega_z^2/\omega_{r0}^2}$, $\omega_y=\omega_{r0}\sqrt{1-(1-\alpha)\omega_z^2/\omega_{r0}^2}$. Below we will assume $\alpha=1/2$, so that $\omega_y=\omega_x$. In any case, the transverse potential is that of a simple harmonic oscillator, as we saw also for the axial potential. However, the transverse potential depends directly on the ion's mass, so the center ion of a string feels a different trap potential than the others for $\mu\neq1$.

We define $\epsilon=\omega_{r0}/\omega_z$, so that $\omega_x=\omega_z\sqrt{\epsilon^2-1/2}$. Then the

normalized Lagrangian for the motion along x is

$$L=\frac{1}{2}\sum_{i=1}^{N}\left(\frac{dX_i}{dT}\right)^2-\frac{1}{2}\sum_{i,j=1}^{N}B'_{ij}X_iX_j, \tag{17}$$

where $X_i=x_i\sqrt{qa_0}$ for $i\neq n_c$ and $X_{n_c}=x_i\sqrt{qa_0\mu}$ are normalized ion vibration amplitudes along x. Here

$$B'_{ij}=\begin{cases} B_{ij} & i,j\neq n_c \\ B_{ij}/\sqrt{\mu} & i \text{ or } j=n_c, i\neq j \\ B_{ij}/\mu & i=j=n_c \end{cases} \tag{18}$$

and

$$B_{ij}=\begin{cases} \epsilon^2-\frac{1}{2}-\sum\limits_{\substack{k=1\\k\neq i}}^{N}\frac{1}{|u_i-u_k|^3} & i=j, j\neq n_c \\ \frac{\epsilon^2}{\mu}-\frac{1}{2}-\sum\limits_{\substack{k=1\\k\neq i}}^{N}\frac{1}{|u_i-u_k|^3} & i=j=n_c \\ \frac{1}{|u_i-u_j|^3} & i\neq j. \end{cases} \tag{19}$$

We can describe the normal mode frequencies and oscillation amplitudes in terms of the eigenvectors and eigenvalues of B'_{ij}, just as for the axial case above. The normalizations of the time and position coordinates remain the same as in the axial case.

In the previous section, we assumed that the radial confinement of the ions was strong enough that the configuration of ions in a string along the z axis was always stable. However, for sufficiently small ϵ, the string configuration becomes unstable. The stable configurations for different values of ϵ can be calculated [16,17], and several of these configurations have been observed for small numbers of ions [10,11]. Rather than review the theory of these configurations, we will simply find the range of validity of our small-oscillation Lagrangian for the string configuration. The string will remain stable for all ϵ greater than some $\epsilon_s=\epsilon_s(\mu)$; ϵ_s also varies with N. On the boundary between stable and unstable regions, the frequency of some mode goes to zero. Recalling that the determinant of a matrix is equal to the product of its eigenvalues, we see that $\epsilon_s(\mu)$ is the maximum value of ϵ satisfying $\det B'(\epsilon,\mu)=0$ for μ fixed. Figure 2 shows $\epsilon_s(\mu)$ as a function of μ for 3, 5, 7, and 9 ions. In each case, there is a cusp in $\epsilon_s(\mu)$ corresponding to the crossing of the two largest solutions to $\det B'(\epsilon,\mu)=0$. The position of the cusp varies with the number of ions, but lies between $\mu=0.1$ and $\mu=1$ for $N\leq 9$. The positions of the cusps are labeled with arrows in Fig. 2. For μ greater than the value at the cusp, $\epsilon<\epsilon_s(\mu)$ corresponds to instability of the zigzag mode, so that the string breaks into a configuration in which each ion is displaced in the opposite direction to its neighbors [16,17]. For μ smaller than the value at the cusp, ϵ_s is independent of μ. In this regime, $\epsilon<\epsilon_s$ creates an instability in a mode similar to the zigzag mode, except that the center ion remains fixed.

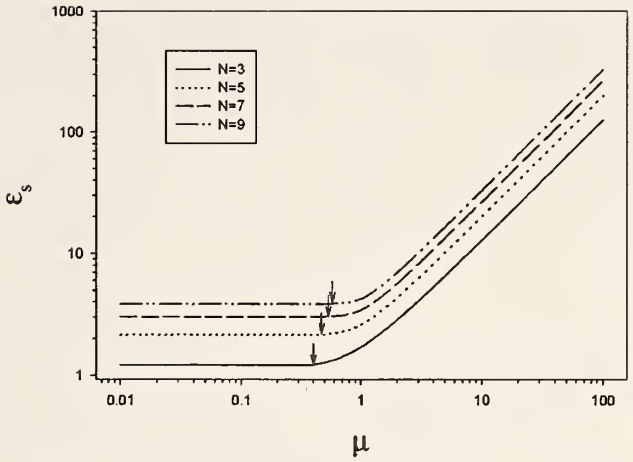

FIG. 2. Trap anisotropy at instability of the string configuration as a function of μ for 3, 5, 7, and 9 ions. Arrows indicate the cusps discussed in the text.

We can proceed to calculate the frequencies of the transverse modes for values $\epsilon>\epsilon_s(\mu)$. Again, these frequencies are normalized to the axial frequency of a single ion of mass m. Figure 3 shows the transverse mode frequencies for 3, 5, 7, and 9 ions as a function of μ, where ϵ is taken equal to $1.1\epsilon_s(\mu)$. The modes are numbered in order of increasing frequency at $\mu=1$ (all ions identical). In this numbering scheme, the central ion moves in odd-numbered modes but not in even-numbered modes. The frequencies of the even-numbered modes appear to depend on μ because they are calculated at a multiple of $\epsilon_s(\mu)$; for constant ϵ these frequencies are independent of μ. The cusps in the mode frequencies in Fig. 3 arise from the cusps of $\epsilon_s(\mu)$ at the crossover points between the two relevant solutions of $\det B'=0$. Mode frequencies plotted for a constant value of ϵ do not exhibit these cusps. As in the case of axial motion, the mode frequencies form pairs of one even- and one odd-numbered mode for small μ. However, for large μ all but one of the transverse modes become degenerate. The only nondegenerate transverse mode in this case is the zigzag mode. In general, the modes are most easily resolved from their neighbors for $\mu=1$, as in the case of axial motion. Increasing ϵ reduces the frequency spacing between nearly degenerate modes. At $\epsilon=1.1\epsilon_s(\mu)$ and $\mu=1$, for instance, the fractional spacing between the cold transverse mode of 3 ions and its nearest neighbor is 0.20, but for $\epsilon=1.5\epsilon_s(\mu)$ the same spacing is 0.09.

The near degeneracy of the modes for large or small μ and for ϵ/ϵ_s significantly greater than 1 limits the usefulness of these modes because of possible mode cross-coupling, just as for the axial modes. Resolving a particular transverse mode requires operating the trap near the point at which the string configuration becomes unstable, i.e., ϵ near $\epsilon_0(\mu)$. In this regime, the collective motion of the ions is quite sensi-

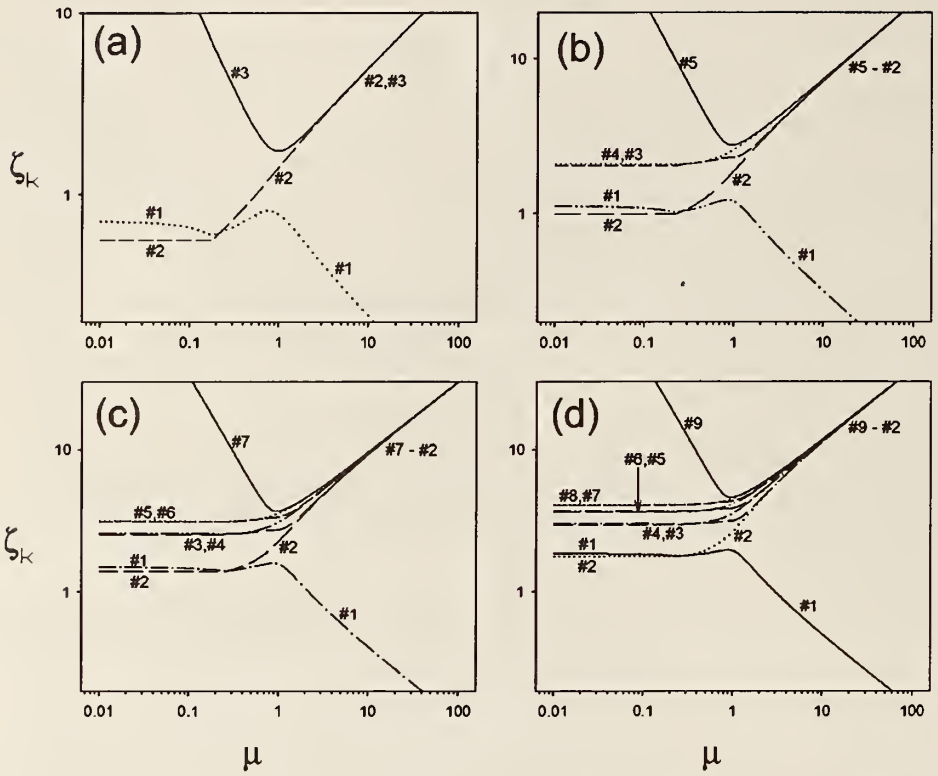

FIG. 3. Normalized frequencies of the transverse modes as a function of μ with $\epsilon = 1.1\epsilon_0(\mu)$ for (a) 3, (b) 5, (c) 7, and (d) 9 ions.

tive to uncontrolled perturbations, which may pose significant technical problems for using a transverse mode in quantum logic operations.

IV. MODE HEATING

Stochastic electric fields present on the ion trap electrodes, for instance, from fluctuating surface potentials, can heat the various normal modes of motion incoherently. For ion trap characteristic dimension d_{trap} much larger than the size of the ion crystal d_{ions}, these fields are approximately uniform across the ion crystal, so they couple only to the COM motion. The $(N-1)/2$ even-numbered modes are orthogonal to the COM motion, so they are only heated by fluctuating electric-field gradients. The heating rates of these modes are reduced by a factor of at least $(d_{ions}/d_{trap})^2 \ll 1$ as compared to the heating of the other modes [4]. In the following, therefore, we will neglect the effects of fluctuating field gradients, so that the even-numbered modes do not heat at all.

The analysis of Secs. II and III shows that the motion of a crystal of N ions is separable into the $3N$ normal modes, each of which is equivalent to a simple harmonic oscillator. Hence we can quantize the crystal motion by quantizing the normal modes. The kth normal mode gives rise to a ladder of energy levels spaced by $\hbar\zeta_k\omega_z$, with $3N$ such ladders in all. If we now write the uniform electric-field power spectral density as $S_E(\omega)$, we can generalize the result of Ref. [18] to give

$$\dot{\bar{n}}_k = \frac{q^2 S_E(\zeta_k\omega_z)}{4m\hbar\zeta_k\omega_z}\left(\frac{v_{n_c}^{(k)}}{\sqrt{\mu}} + \sum_{\substack{j=1 \\ j\neq n_c}}^{N} v_j^{(k)}\right)^2 \qquad (20)$$

for the heating rate of the kth mode, expressed in terms of the average number of quanta gained per second. Recall that $v_i^{(k)}$ is the oscillation amplitude of the ith ion in the kth normal mode, expressed in the normalized coordinates. It is useful to normalize the heating rate in Eq. (20) to the heating rate of the lowest-lying axial mode of a string of identical ions. This normal mode consists entirely of COM motion and we write $v_j^{COM} = 1/\sqrt{N}$ for all ions. The normalized heating rate of the kth mode is then

$$\frac{\dot{\bar{n}}_k}{\dot{\bar{n}}_{COM}} = \frac{1}{N\zeta_k}\left(\frac{v_{n_c}^{(k)}}{\sqrt{\mu}} + \sum_{\substack{j=1 \\ j\neq n_c}}^{N} v_j^{(k)}\right)^2, \qquad (21)$$

where we have assumed that the spectral density $S_E(\omega)$ is constant over the frequency range of the normal modes, i.e., $S_E(\omega_z) = S_E(\zeta_k\omega_z)$.

Figure 4 shows plots of the normalized heating rates of the axial modes for $N=3$, 5, 7, and 9 as a function of μ. Figure 5 is the same, but for the transverse modes, with $\epsilon = 1.1\epsilon_s$. The numbering of modes on the plots of heating rate matches the numbering on the corresponding plots of mode frequency (Figs 1 and 2).

In both axial-mode and transverse-mode plots, the even-numbered modes have the center ion at rest, while the center ion moves for all odd-numbered modes. We see from Figs. 4 and 5 that the modes for which the center ion is fixed can never heat, while all the other modes always heat to some extent for $\mu \neq 1$. We will refer to these modes as "cold" and "hot" modes, respectively. If the ions are identical, only the modes with all ions moving with the same amplitude (COM

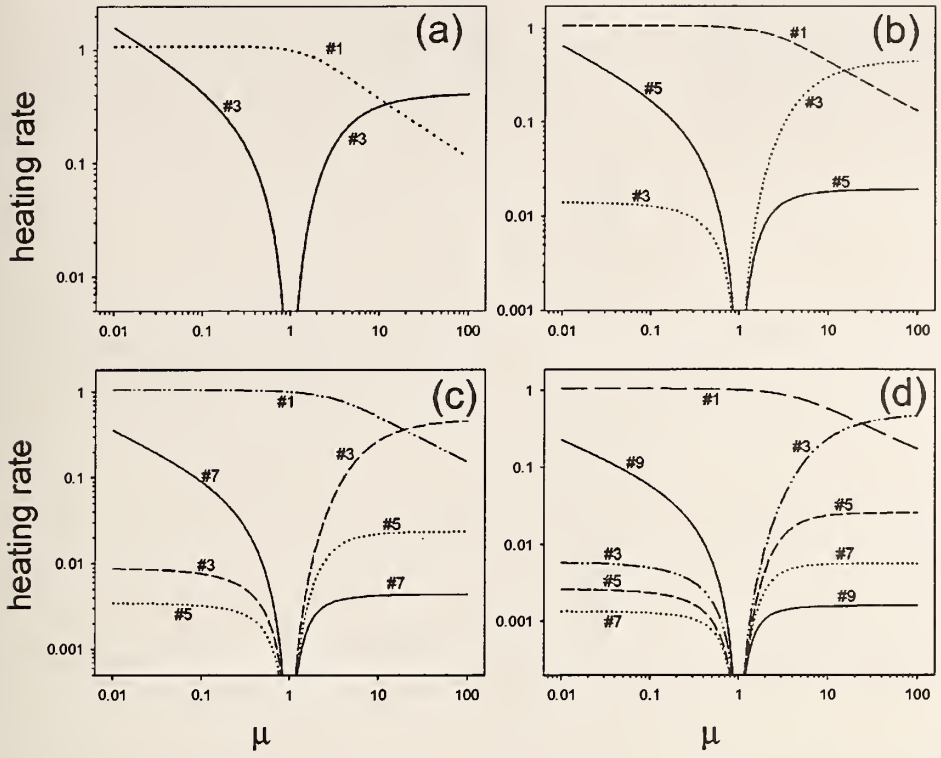

FIG. 4. Normalized heating rates for the axial modes as a function of μ for (a) 3, (b) 5, (c) 7, and (d) 9 ions.

modes) can heat. There are three such modes, one along $\hat{x}$, one along $\hat{y}$, and one along $\hat{z}$. In interpreting Figs. 4 and 5, it is important to recall that the normalized heating rate defined in Eq. (21) is inversely proportional to the mode frequency. For instance, the μ dependence of the heating rate of the highest-frequency transverse mode can be largely ascribed to variations in the mode frequency, rather than to changes in the coupling of the mode to the electric field.

V. PROSPECTS FOR SYMPATHETIC COOLING

Heating reduces logic gate fidelity in two ways. The logic mode itself can be heated, but by choosing a cold mode, we can render this effect negligible. On the other hand, the Rabi frequency of the transition between logic-mode motional states depends on the total wave-packet spread of the ion involved in the transition [3,4]. Heating on modes other than the logic mode can thus lead to unknown, uncontrolled changes in this Rabi frequency, resulting in overdriving or underdriving of the transition. The purpose of sympathetic cooling is to remove this effect by cooling the center ion and thus all hot modes.

In the foregoing, we have chosen to consider only the case of a crystal of an odd number of ions, with the cooling ion at the center. We now see that this is the only case suitable for sympathetic cooling, since only in this case do we find both (a) cold modes for arbitrary μ and (b) isolation of motion of the cold modes from motion of the cooling ion. As long as the crystal is symmetric under inversion in $\vec{z}$, the normal modes must be either symmetric (hot) or antisymmetric (cold) under inversion in $\vec{z}$. If the cooling ion is not at the center of the crystal, the crystal symmetry is broken and cold modes will only appear for particular values of μ. The case of a crystal of an even number of ions, with two cooling ions at the center, will again yield cold modes. However, excitation of any mode will cause the cooling ions to move, so that the cold modes are not well isolated from the sympathetic cooling in this case.

For sympathetic cooling to be useful, we must find a cold mode suitable for use in quantum logic. The cold mode must be spectrally well separated from any other modes in order to maximize gate speed. We can use the lowest-lying cold axial mode as the logic mode for $\mu \lesssim 3$. In this mode, called the breathing mode, the center ion remains fixed and the spacings between ions expand and contract in unison. Unless the trap is operated very close to the instability point of the string configuration, the breathing mode is better separated from its neighbors than are any of the cold transverse modes. For $\mu \gtrsim 3$ any cold mode, either axial or transverse, is nearly degenerate with a hot mode. In this regime one must make a specific calculation of mode frequencies in order to find the best-resolved cold mode. Even so, the cold axial modes are again better separated from their neighbors than are the cold transverse modes, except for ϵ very close to $\epsilon_s(\mu)$. It seems best to select a cold axial mode as the logic mode in most cases.

By selecting our laser-beam geometry appropriately, we can ensure that the Rabi frequency of the motional transition on the axial mode used for logic depends chiefly on the spread of the ion wave packet along z. In this case, heating of the axial modes will affect logic-gate fidelity, but heating of the transverse modes will have little effect. If the mass of the central ion is nearly the same as that of the others ($\mu \approx 1$), only the lowest axial mode will heat significantly, and we

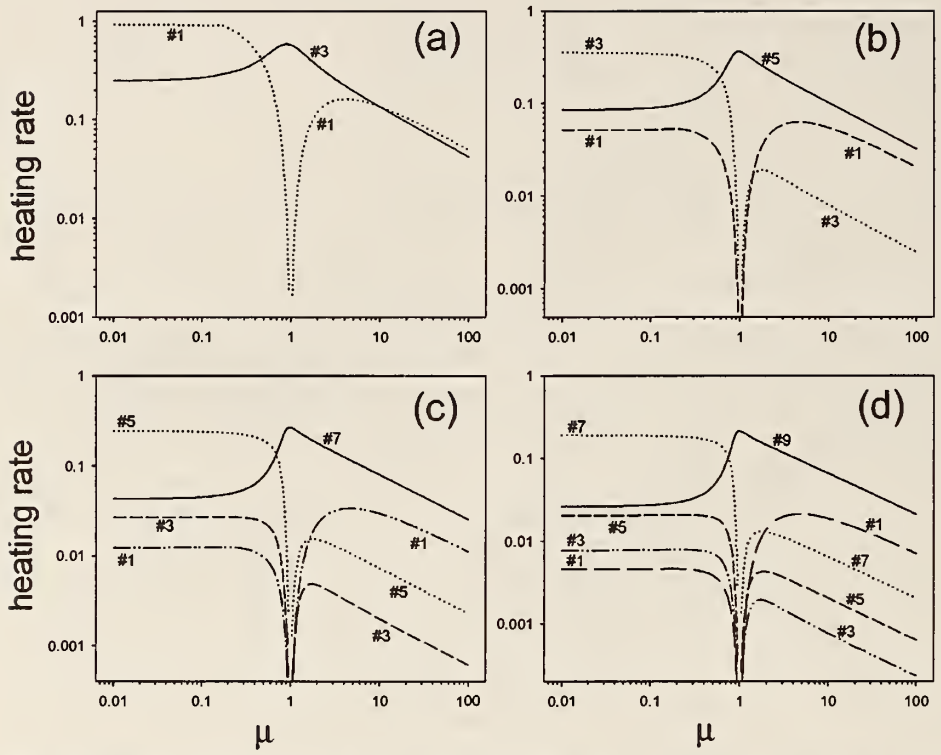

FIG. 5. Normalized heating rates for the transverse modes as a function of μ with $\epsilon = 1.1\epsilon_0(\mu)$ for (a) 3, (b) 5, (c) 7, and (d) 9 ions.

can continuously cool this mode by cooling only the central ion, ensuring that all ions remain in the Lamb-Dicke limit [3]. If μ is not near 1, we must cool all $(N+1)/2$ hot modes (again by addressing the central ion) to keep all ions in the Lamb-Dicke limit.

The analysis above indicates that, all other things being equal, we are best off if our substituted ion is identical to, or is an isotope of, the logic ions. However, sympathetic cooling can still be useful if the two ion species have different masses. For example, we can consider sympathetic cooling using the species $^9Be^+$ and $^{24}Mg^+$. Linear traps constructed at NIST have demonstrated axial secular frequencies of over 10 MHz for single trapped $^9Be^+$ ions. For three ions with $^{24}Mg^+$ as the central ion, $\omega_z(Be^+) = 2\pi \times 10$ MHz yields a spacing of 1.6 MHz between the cold axial breathing mode and its nearest neighbor. If we reverse the roles of the ions [$\omega_z(Mg^+) = 2\pi \times 10$ MHz], the spacing increases to 6.2 MHz. The transverse modes are much harder to resolve from each other. For three ions with $^{24}Mg^+$ in the center, we require $\omega_{r0}(Be^+) = 2\pi \times 27.6$ MHz to obtain $\epsilon = 1.1\epsilon_s$, and the spacing between the cold transverse zigzag mode and its nearest neighbor is only 560 kHz. Reversing the roles of the ions, we find $\epsilon = 1.1\epsilon_s$ at $\omega_{r0}(Mg^+) = 2\pi \times 14.7$ MHz with a spacing of 1.1 MHz. For this combination of ion species, the cold axial breathing mode seems most appropriate for logic. For a string of 3 or 5 ions, sympathetic cooling would require driving transitions on 2 or 3 axial-mode sidebands, respectively. From this example we see that sympathetic cooling can be useful even for ion mass ratios of nearly 3 to 1.

VI. CONCLUSION

We have investigated a particular sympathetic cooling scheme for the case of an ion string confined in a linear RF trap. We have numerically calculated the mode frequencies of the axial and transverse modes as functions of the mass ratio μ and trap anisotropy ϵ for 3, 5, 7, and 9 ions. We have also calculated the heating rates of these modes relative to the heating rate of a single ion, assuming that the heating is driven by a uniform stochastic electric field. The results indicate that the scheme is feasible for many choices of ion species if we use a cold axial mode as the logic mode. The optimal implementation of the scheme employs two ion species of nearly equal mass. However, a demonstration of sympathetic cooling using $^9Be^+$ and $^{24}Mg^+$ appears well within the reach of current experimental technique.

ACKNOWLEDGMENTS

This research was supported by NSA, ONR, and ARO.

[1] A. Steane, Appl. Phys. B: Lasers Opt. **64**, 623 (1997).
[2] J.I. Cirac and P. Zoller, Phys. Rev. Lett. **74**, 4091 (1995).
[3] D.J. Wineland *et al.*, J. Res. Natl. Inst. Stand. Technol. **103**, 259 (1998).
[4] B.E. King *et al.*, Phys. Rev. Lett. **81**, 1525 (1998).
[5] S.K. Lamoreaux, Phys. Rev. A **56**, 4970 (1997).
[6] D.F.V. James, Phys. Rev. Lett. **81**, 317 (1998).
[7] C. Henkel and M. Wilkins, e-print quant-ph/9902009.
[8] D.J. Larson *et al.*, Phys. Rev. Lett. **57**, 70 (1986).
[9] We assume that the cooling transitions of the center ion are

well resolved from all relevant transitions of the logic ions.
[10] M.G. Raizen *et al.*, Phys. Rev. A **45**, 6493 (1992).
[11] H. Walther, Adv. At., Mol., Opt. Phys. **31**, 137 (1993).
[12] M. Drewsen *et al.*, Phys. Rev. Lett. **81**, 2878 (1998).
[13] T.B. Mitchell *et al.*, Science **282**, 1290 (1998).
[14] D.F.V. James, Appl. Phys. B: Lasers Opt. **66**, 181 (1998).
[15] P. K. Ghosh, *Ion Traps* (Oxford, Clarendon, 1995).
[16] R. Rafac *et al.*, Proc. Natl. Acad. Sci. USA **88**, 483 (1991).
[17] J.P. Schiffer, Phys. Rev. Lett. **70**, 818 (1993).
[18] D.J. Wineland *et al.*, Fortschr. Phys. **46**, 363 (1998).

Scalable Entanglement of Trapped Ions

C. Monroe, C.A. Sackett, D. Kielpinski, B.E. King,
C. Langer, V. Meyer, C.J. Myatt, M. Rowe,
Q.A. Turchette, W.M. Itano, and D.J. Wineland

Time and Frequency Division, National Institute of Standards and Technology[1]
Boulder Colorado 80303

Abstract. Entangled states are a crucial component in quantum computers, and are of great interest in their own right, highlighting the inherent nonlocality of quantum mechanics. As part of the drive toward larger entangled states for quantum computing, we have engineered the most complex entangled state so far in a collection of four trapped atomic ions. Notably, we employ a technique which is readily scalable to much larger numbers of atoms. Limits to the current experiment and plans to circumvent these limitations are presented.

INTRODUCTION

At the heart of quantum mechanics lies the principle of superposition, where physical properties of a system can exist in two or more states simultaneously. When a system is composed of more than one degree of freedom, superpositions can be prepared where distinct degrees of freedom are perfectly correlated, yet the state of each degree of freedom is by itself in superposition. The prototypical example is Bohm's version [1] of the Einstein-Podolsky-Rosen paradox [2], where a spin-zero particle decays into a pair of spin-1/2 daughters, resulting in the singlet state

$$|\Psi_{EPR}\rangle = \frac{|\uparrow\rangle_1|\downarrow\rangle_2 - |\downarrow\rangle_1|\uparrow\rangle_2}{\sqrt{2}}. \quad (1)$$

This state is *entangled*, since it cannot be expressed as a direct product of states representing each particle. When one of the subsystems in such a state is measured,

[1] This work was supported in part by the U.S. National Security Agency and the Advanced Research and Development Activity under contract MOD7037.00, the U.S. Army Research Office, and the U.S. Office of Naval Research.

CP551, *Atomic Physics 17*, edited by E. Arimondo, P. DeNatale, and M. Inguscio
2001 American Institute of Physics 1-56396-982-3

the other subsystem is also determined, even when the particles are not in physical contact or outside each other's lightcones. In general, entangled states such as $|\Psi_{EPR}\rangle$ highlight the nonlocal character of quantum mechanics. Quantitatively, this is usually expressed in terms of Bell's inequality violations [3], where measured correlations between the entangled subsystems can be shown to be incompatible with what would be expected under conditions of local realism.

Although the correlation in the above state cannot be used for superluminal communication, it can be harnessed for enhanced communication rates over what can be obtained classically [4,5]. Furthermore, such states are useful in a variety of quantum communication schemes such as quantum cryptography [6] and quantum "teleportation" [7–10].

Entangled states of larger systems are a defining feature of a quantum computer. Here, for example, a collection of N spin-1/2 particles are prepared in an arbitrary entangled state of the form

$$|\Psi_{QC}\rangle = a_0|000\ldots0\rangle + a_1|000\ldots1\rangle + \ldots + a_{2^N-1}|111\ldots1\rangle, \qquad (2)$$

where $|0\rangle$ and $|1\rangle$ refer to the two spin states of each particle, and the a_k are the amplitudes of the number k being stored by the register of particles. By choosing appropriate entangled states and making appropriate state measurements of the particles, quantum computers can solve certain problems much faster than any classical computer [11,12]. The reason quantum computers are mere speculation at this point is that $|\Psi_{QC}\rangle$ is very difficult to produce in the laboratory.

SCALABLE ENTANGLEMENT WITH TRAPPED IONS

Nearly every demonstration of entanglement to date has relied upon a random or selection process which prohibits scaling to large numbers of particles. This can be quantified in terms of the *entanglement efficiency* parameter ϵ, or the probability per unit time that a perfect entangled pair is created [13]. The probability of realizing a perfect N-particle entangled state typically scales as ϵ^{cN}, where c is of order unity and depends on the particular experiment.

The first measured Bell's inequality violations were seen in atomic cascade experiments involving the entanglement of a pair of spontaneously-emitted photons [14,15]. Spontaneous parametric downconversion is now a popular source of entangled photons, where typically ultraviolet photons traverse a nonlinear crystal and downconvert into a pair of polarization-entangled infrared beams [16,17]. Unfortunately, the probability of each input photon being converted leads to an efficiency $\epsilon \simeq 10^{-4}$, so the probability of entangling larger numbers of photons becomes very small. (Nevertheless, by waiting long enough, three-photon entangled states were recently observed from simultaneous downconversion into two pairs [18]). Experiments in cavity-QED have recently shown entanglement of two atoms [19] and two atoms with a photon [20], where a thermal (random) source of atoms traverse a common microwave cavity. In these experiments, $\epsilon \simeq 0.005$. Experiments with

optical parametric oscillators can also entangle the continuous quadratures of two optical field modes [21]. Although this source has near-unit entanglement efficiency, scaling to larger numbers of degrees of freedom appears difficult.

The Cirac-Zoller Scheme

In 1995, Cirac and Zoller showed that a collection of trapped ions may be suitable for storing large-scale entangled states such as $|\Psi_{QC}\rangle$ [22]. In their proposal, each atomic ion stores a quantum bit (qubit) of information in a pair of electronic energy levels, and a collective mode of harmonic vibration is used to entangle any pair of ion qubits. By applying laser beams to an individual ion in the collection, its internal qubit state can be mapped onto the collective ion motion, and subsequent quantum logic gates can be applied between the motion and a second ion, effectively entangling the two ions. The entanglement can be extended to any number of ions by repeating these steps on other pairs of ions. When accompanied by single-ion rotations, the Cirac-Zoller scheme allows the creation of an arbitrary entangled state [Eq. (2)], and therefore forms a set of universal quantum logic gates.

The basic elements of the Cirac-Zoller scheme were demonstrated on a single trapped ion in 1995 [23]. A variation of this scheme was later used to entangle a pair of trapped ions [24] with entanglement efficiency $\epsilon \simeq 0.8$, representing the first scalable entanglement source with near-unit efficiency.

The Mølmer-Sørensen Scheme

Instead of entangling the ions sequentially, Mølmer and Sørensen showed how to create the N-ion entangled state

$$|\Psi_N\rangle = \frac{|\uparrow\rangle_1|\uparrow\rangle_2 \cdots |\uparrow\rangle_N + e^{i\phi_N}|\downarrow\rangle_1|\downarrow\rangle_2 \cdots |\downarrow\rangle_N}{\sqrt{2}} \tag{3}$$

with a single pulse of laser radiation [25]. The Mølmer-Sørensen operation applied to any pair of qubits in a collection of ions (accompanied by single ion rotations) allows the creation of any entangled state [Eq. (2)], and thus forms a set of universal quantum logic gates alternative to the Cirac-Zoller scheme [26]. We have employed the Mølmer-Sørensen scheme to create the entangled state of Eq. (3) for $N = 2$ and $N = 4$ trapped ions [27]. In both cases, the entanglement efficiency was $\epsilon \simeq 0.8$, as discussed below.

The Mølmer-Sørensen entanglement technique can be understood by considering a pair of identical spin-1/2 charged particles confined together in a harmonic potential [28]. The energy levels of this system are illustrated in Fig. 1, where $\hbar\omega_0$ is the internal energy splitting of each qubit, and ν is the oscillation frequency of a particular collective mode of the particles in the trap.

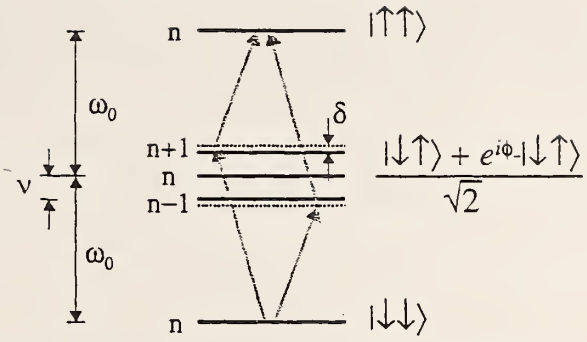

FIGURE 1. Entanglement scheme for two particles. Each ion is initially prepared in the $|\downarrow\downarrow\rangle$ internal state, and the collective motion of the pair initially contains exactly n quanta. Laser fields equally illuminating the two ions and oscillating near $\omega_0 + \nu + \delta$ and $\omega_0 - \nu - \delta$ couple the $|\downarrow\downarrow\rangle$ and $|\uparrow\uparrow\rangle$ states as shown. For sufficient detuning δ, the populations of the middle states are kept small. By driving the double transition for the appropriate time, the entangled state $(|\uparrow\uparrow\rangle + e^{i\phi_2}|\downarrow\downarrow\rangle)/\sqrt{2}$ is generated. For four ions, the same procedure generates the state $(|\uparrow\uparrow\uparrow\uparrow\rangle + e^{i\phi_4}|\downarrow\downarrow\downarrow\downarrow\rangle)/\sqrt{2}$.

The ions are initially prepared in the $|\downarrow\downarrow\rangle$ internal state, and we assume the ions are in a collective motional eigenstate $|n\rangle$. By simultaneously applying optical fields near the first upper and lower motional sidebands (oscillating at $\omega_0 + \nu + \delta$ and $\omega_0 - \nu - \delta$ respectively) with equal illumination on the two ions, the two-step transition from $|\downarrow\downarrow\rangle|n\rangle$ to $|\uparrow\uparrow\rangle|n\rangle$ is driven through the intermediate states

$$|\Psi_{int}\rangle_{\pm} = \frac{|\downarrow\rangle|\uparrow\rangle|n \pm 1\rangle + e^{i\phi_-}|\uparrow\rangle|\downarrow\rangle|n \pm 1\rangle}{\sqrt{2}}, \tag{4}$$

where ϕ_- is the phase difference of the field at the two ion positions. For sufficiently large detuning δ from the sidebands, these intermediate states are negligibly occupied, so that the motional state is not altered. We also assume $\delta \ll \nu$ so that intermediate states involving other motional modes are not involved in the coupling. As shown in Fig. 1, there are two paths from $|\downarrow\downarrow\rangle$ to $|\uparrow\uparrow\rangle$, and their respective couplings are given by the product of the two resonant sideband Rabi frequencies divided by the detuning $\pm\delta$ from the relevant virtual intermediate level. For the upper- then lower-sideband path (arrows on left side of Fig. 1), this coupling is $(\eta g\sqrt{n+1})^2/\delta$, and for the lower- then upper-sideband path (arrows on right side of Fig. 1), it is $-(\eta g\sqrt{n})^2/\delta$, where g is the single ion resonant carrier Rabi frequency and η is the Lamb-Dicke parameter of the motional mode involved. (These expressions are valid only in the Lamb-Dicke limit $\eta^2(n+1) \ll 1$.) Adding the couplings from these two paths results in a net Rabi frequency from $|\downarrow\downarrow\rangle$ to $|\uparrow\uparrow\rangle$ of $\Omega = \eta^2 g^2/\delta$, independent of the motional state $|n\rangle$ within the Lamb-Dicke regime. The net interaction Hamiltonian is proportional to $\sigma_x^{(1)}\sigma_x^{(2)}$, where $\sigma_x^{(i)}$ is

the transverse Pauli spin-1/2 operator of ion i. Entanglement is achieved by simply applying these beams for a time $\tau = \pi/2\Omega$, creating the desired spin state

$$|\Psi_2\rangle = \frac{|\uparrow\uparrow\rangle + e^{i\phi_+}|\downarrow\downarrow\rangle}{\sqrt{2}}, \tag{5}$$

where ϕ_- is the sum of the field phases at the two ion positions.

1 Fast Entanglement

In order for the intermediate states $|\Psi_{int}\rangle_\pm$ to be negligibly occupied, the detuning δ must be large compared to both single-spin sideband Rabi frequencies $\eta g\sqrt{n+1}$ and $\eta g\sqrt{n}$, meaning the entangling operation must be much slower than the resonant sideband operations. (This is the characteristic slowdown of driving higher-order transitions through virtual levels.) However, it is possible to violate this condition and still generate the state $|\Psi_2\rangle$ [29,30]. In this case, the intermediate states $|\Psi_{int}\rangle_\pm$ are occupied during the operation (and the motional state becomes entangled with the spins), but this occupation can vanish at exactly the moment the desired entangled spin state $|\Psi_2\rangle$ is created. Without regard to the the spin states, we find that for arbitrarily small δ (and within the Lamb-Dicke limit), the motion evolves during the operation as a coherent superposition of its original state $\rho_m(0)$ and an oscillating displaced state [29]

$$\rho_m^{dis}(t) = \mathcal{D}\left[\sqrt{\frac{\Omega}{\delta}}(e^{i\delta t}-1)\right]\rho_m(0)\mathcal{D}\left[\sqrt{\frac{\Omega}{\delta}}(e^{i\delta t}-1)\right]^\dagger, \tag{6}$$

where $\mathcal{D}(\alpha)$ is the displacement operator with phase space argument α [31]. The overall motion is thus in a "Schrödinger Cat"-type superposition state [32], with maximum separation in phase space $2\sqrt{\Omega/\delta}$. The phase space trajectory of the displaced component $\rho_m^{dis}(t)$ follows a circle from its original state with radius $\sqrt{\Omega/\delta}$, returning to the initial motional state $\rho_m(0)$ at times $t_m = 2\pi m/\delta$, where the positive integer m is the number of complete circular cycles of the displacement [29]. Setting the entanglement pulse time τ defined above equal to t_m, we find that the condition for a return to the initial motional state following the entanglement step is $\Omega/\delta = 1/(4m)$. The entangling time can thus be rewritten as $\tau = \pi\sqrt{m}/(\eta g)$, which is only a factor of $2\sqrt{m}$ slower than an analogous resonant sideband transition. To maximize the speed of the Mølmer-Sørensen operation in the experiment, we operate with $m = 1$.

2 Scalable Entanglement

Surprisingly, the Mølmer-Sørensen entangling scheme is scalable in the sense that precisely the same operation can be used to generate the N-particle entangled state

of Eq. (3) for any even number of ions N. (For N odd, $|\Psi_N\rangle$ can be generated using one entanglement pulse accompanied by a separate independent rotation of each particle's spin.) The Mølmer-Sørensen interaction is proportional to J_x^2, where J_x is the transverse spin operator for the effective spin-$N/2$ particle. Physically, this interaction simultaneously flips all pairs of ions in the collection. Through the properties of angular momentum rotations [25], this results in the desired entangled state $|\Psi_N\rangle$. In scaling to larger numbers of ions, the only difference (for a given motional mode frequency) is that the operation is $\sqrt{N}$ times slower, since the Lamb-Dicke parameter is proportional to $1/\sqrt{N}$. In addition, the phase which appears in Eq. (3) is the sum of the field phases at each ion position.

If the ions are uniformly illuminated, the Mølmer-Sørensen scheme requires that they all participate equally in the intermediate motional excitation, which implies that the only suitable mode for arbitrary N is the center-of-mass mode. However, this mode has a practical disadvantage that fluctuating ambient electric fields cause it to heat at a significant rate [33]. For large δ, the entanglement operation is independent of the motion, so that heating is unimportant, so long as the ions remain in the Lamb-Dicke regime [29]. In the small-δ case however, motional decoherence of the Schrödinger-Cat state discussed above must be avoided. Modes involving only relative ion motion couple to higher moments of the field, so heating of them is negligible [34]. For $N = 2$ and $N = 4$ ions, such modes do exist in which each particle participates with equal amplitude [35]. In both cases, they are uniform "stretch" modes, in which alternating ions oscillate out of phase; we use these modes here. Excitation of the center-of-mass mode does still affect the experiment, as the ion eventually can get heated out of the Lamb-Dicke regime. For this reason, we initially sideband cool both the center-of-mass and uniform stretch modes to near their ground state. We note that other modes of motion can also be used for entanglement, as long as the laser intensity on each ion is adjusted to compensate for the difference in mode amplitude of that ion, resulting in equal sideband couplings for all ions.

EXPERIMENT

The experiment was performed using $^9Be^+$ ions confined in a miniature linear RF trap [33], with the N ions lying in a line along the trap's weak axis. Two spectrally resolved ground-state hyperfine levels compose the effective spin-1/2 system, with $|\downarrow\rangle \equiv |F = 2, m_F = -2\rangle$, $|\uparrow\rangle \equiv |F = 1, m_F = -1\rangle$. The hyperfine splitting between these states is $\omega_0/2\pi \simeq 1.25$ GHz.

Coherent coupling between $|\downarrow\rangle$ and $|\uparrow\rangle$ is provided via stimulated Raman transitions. The two Raman laser beams have a wavelength of $\lambda \simeq 313$ nm with a difference frequency near ω_0. Their wave-vectors are perpendicular with their difference wave-vector lying along the line of ions with magnitude $\delta k = 2\pi\sqrt{2}/\lambda$. They are detuned $\sim$80 GHz blue of the $2P_{1/2}$ excited state, with intensities giving $g/2\pi \simeq 500$ kHz.

The Raman beam frequencies can also be tuned to coherently flip the spins while simultaneously affecting the collective motional state of the ions. For modes considered here (having equal amplitudes of motion for all the ions), the spin-motional coupling is determined by the Lamb-Dicke parameter $\eta = \delta k(\hbar/2Nm_1\nu)^{1/2}$ of the mode with frequency ν, where m_1 is the mass of a single particle in the collection.

Fig. 2 displays a stimulated-Raman absorption spectrum of four trapped ions in a linear array, with the four axial modes as well as higher-order features clearly visible. For both the two- and four-ion experiments, the desired stretch-mode frequency was set to $\nu/2\pi \simeq 8.8$ MHz, giving a Lamb-Dicke parameter of $\eta_{STR} = 0.23/N^{1/2}$. For the Mølmer-Sørensen operation, the two driving frequencies required to generate a coupling near the first blue- and first red-sidebands are generated by frequency modulating one of the Raman beams using an electro-optic modulator. The spectral positions of the relevant difference frequencies of the Raman beam pairs is indicated by the two arrows and dashed vertical lines in Fig. 2.

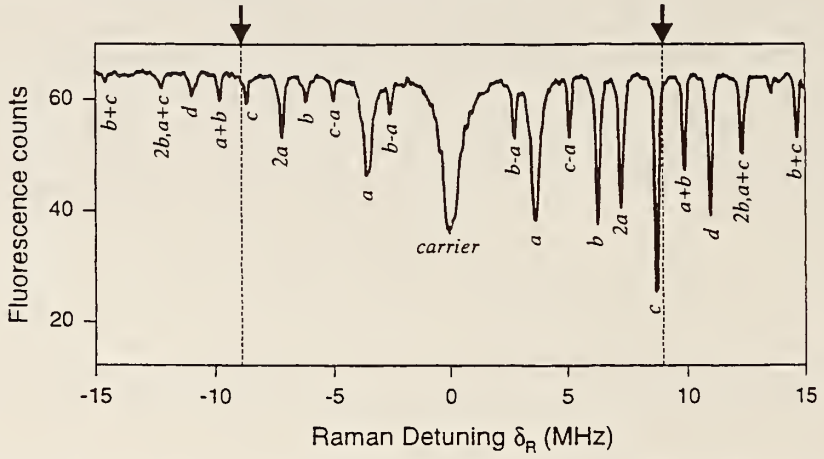

FIGURE 2. Raman absorption spectrum of four ions confined in a linear crystal and Doppler laser-cooled. The ordinate is the detuning δ_R of the Raman beams' difference frequency from the carrier and the abscissa shows the average counts of ion fluorescence per experiment ($200\mu s$ integration time), proportional to the number of ions in the state $|\downarrow\rangle$ (the ions are initially prepared in state $|\downarrow\downarrow\downarrow\downarrow\rangle$). The carrier appears at $\delta_R = 0$, and the first sidebands of the four axial normal modes of motion (labelled by letters *a*-*d*) appear at $\delta_R = \pm 3.62, \pm 6.23, \pm 8.67$ MHz, and ± 11.02 MHz in agreement with the theoretical frequency ratios $1 : \sqrt{3} : 2.410 : 3.051$. Several higher order sidebands also appear at sums and differences of harmonics of the normal mode frequencies, as indicated. The sideband asymmetry (upper sidebands are always stronger) indicates cooling to the quantum regime with not-too-many thermal phonons. The two arrows and the dashed lines, just outside the first upper and lower stretch sidebands, indicate the frequencies used for the four ion Mølmer-Sørensen scheme.

After an interaction with the stimulated Raman beams, the ion internal states

TABLE 1. Characterization of two-ion and four-ion states. P_j denotes the probability that j ions were measured to be in $|\downarrow\rangle$, and $|\rho_{\uparrow\ldots\uparrow,\downarrow\ldots\downarrow}|$ denotes the coherence between $|\uparrow\ldots\uparrow\rangle$ and $|\downarrow\ldots\downarrow\rangle$. Uncertainties in the $N = 2$ measurements are ± 0.01; uncertainties in the $N = 4$ populations are ± 0.02.

N	P_0	P_1	P_2	P_3	P_4	$\lvert\rho_{\uparrow\ldots\uparrow,\downarrow\ldots\downarrow}\rvert$
2	0.43	0.11	0.46	-	-	0.385
4	0.35	0.10	0.10	0.10	0.35	0.215

are measured by illuminating them with a circularly-polarized laser beam tuned to the $2S_{1/2}(F = 2, m_F = -2) \leftrightarrow 2P_{3/2}(F = 3, m_F = -3)$ cycling transition. Each ion in $|\downarrow\rangle$ fluoresces brightly, leading to the detection of ~15 photons/ion on a photomultiplier tube during a 200 μs detection period. In contrast, an ion in $|\uparrow\rangle$ remains nearly dark. For a single ion, we are able to discriminate between $|\uparrow\rangle$ and $|\downarrow\rangle$ with approximately 99% accuracy, as shown in the histograms of Figs. 3a and 3b. This accuracy is limited by off-resonant optical pumping which causes the dark state $|\downarrow\rangle$ to eventually partake in the cycling transition and fluoresce [24]. This 1% error rate could be improved considerably by appropriately weighting the photon counts by their arrival time, as this optical pumping will contaminate later counts more so than earlier counts. Fig. 3c shows a histogram of four ions prepared in an initial state with incoherent populations in all five possible states of excitation without distinguishing the individual ions. Here, the number of ions in state $|\downarrow\rangle$ can be determined with an accuracy of about 80% on any a given experiment, although this number could be improved to better than 95% by weighting the counts as discussed above. These statistical detection errors can be averaged away by repeating the experiment many times and fitting the resulting photon-number distribution to a sum of Poissonians to determine the probability distribution P_j of having exactly j ions in the state $|\downarrow\rangle$ [24].

N-particle entanglement results

Following the Mølmer-Sørensen entangling procedure, the probability distribution P_j is measured. The results are given in Table 1, and show that in both cases, the probabilities for all N ions to be in the same state are large compared to the probabilities for the other cases. This is characteristic of the state $|\Psi_N\rangle$ [Eq. (3)], although the fact that the middle probabilities are nonzero indicates that we do not generate the entangled states with perfect accuracy.

In order to prove that we are generating a reasonable approximation to $|\Psi_N\rangle$, it is necessary to prove that the populations of $|\uparrow\uparrow\uparrow\uparrow\rangle$ and $|\downarrow\downarrow\downarrow\downarrow\rangle$ are coherent. In terms of the N-spin density matrix ρ_N, we must measure the far off-diagonal

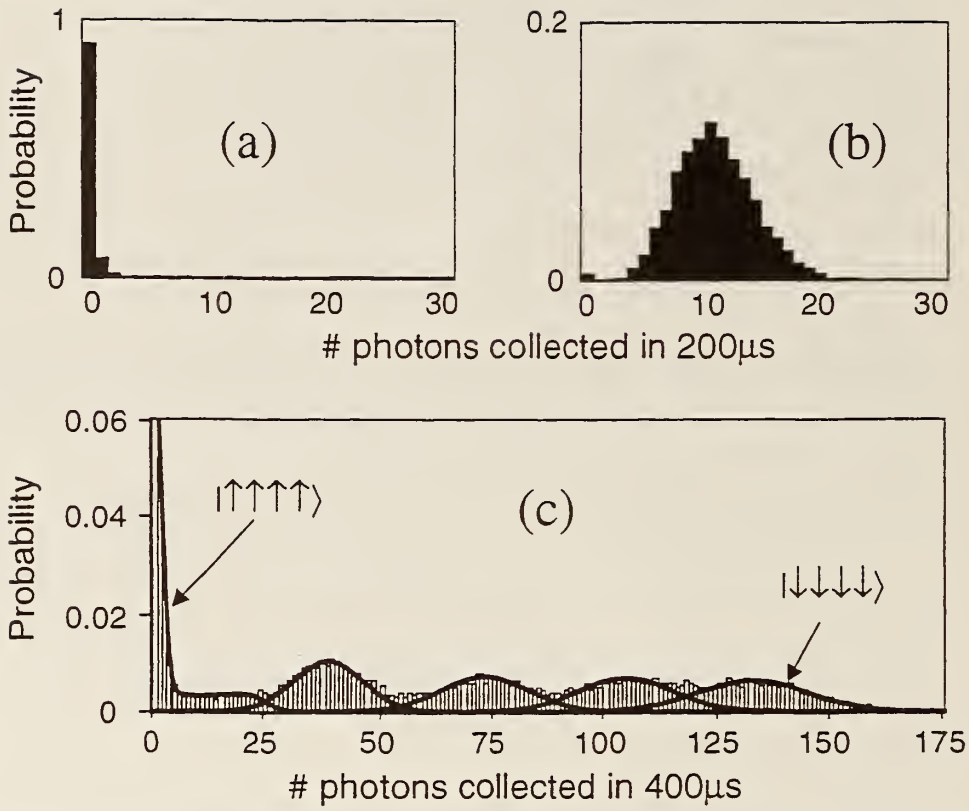

FIGURE 3. Measured probability distribution of detected fluorescence counts of a single trapped ion in (a) state $|\uparrow\rangle$ and (b) state $|\downarrow\rangle$ after 200 μs of integration (1000 measurements). (c) Measured probability distribution of detected fluorescence counts of four trapped ions after 400 μs of integration (1000 measurements). The lines are least-squares fits to reference distributions for having anywhere from 0 ions (leftmost curve) to 4 ions (rightmost curve) in state $|\downarrow\rangle$, providing relative probabilities P_j of j ions in state $|\downarrow\rangle$.

element $\rho_{\uparrow\ldots\uparrow,\downarrow\ldots\downarrow}$. This can be achieved by viewing the first entanglement pulse as the first pulse in a Ramsey experiment [36], and applying a second (non-entangling) $\pi/2$ pulse to the ions before observing them, closing the Ramsey interferometer. The relevant observable after this modified Ramsey experiment is the parity of the number of ions in state $|\downarrow\rangle$ [37]

$$\Pi(\phi) \equiv \sum_{j=0}^{N} (-1)^j P_j(\phi). \tag{7}$$

As the parity is measured while ϕ is varied, the resulting Ramsey fringes oscillate as

$\cos N\phi$ for N ions, as seen in Fig. 4. The amplitude of the fringes is just twice the

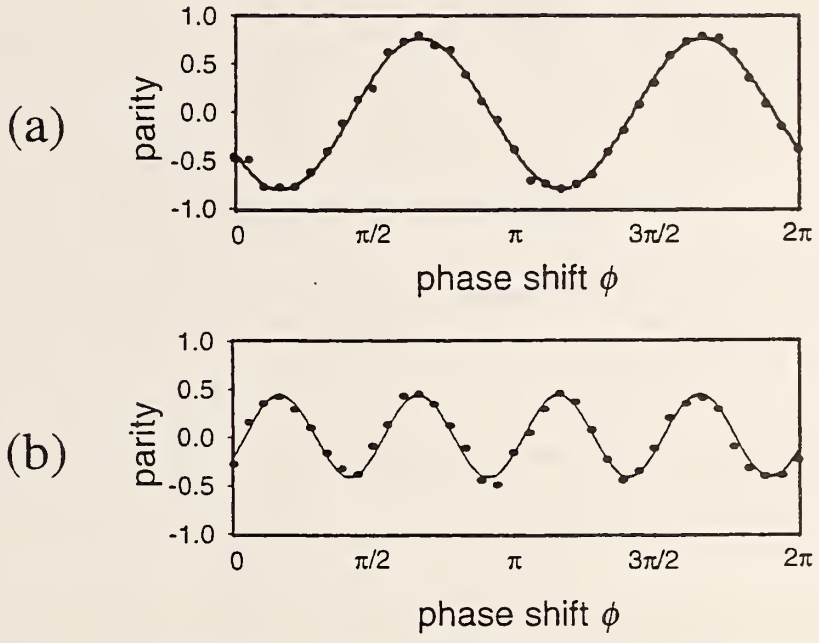

FIGURE 4. Determination of $\rho_{\uparrow\ldots\uparrow,\downarrow\ldots\downarrow}$ for (a) two ions and (b) four ions. After the entanglement operation, a non-entanling $\pi/2$ pulse with relative phase ϕ drives the $|\downarrow\rangle \leftrightarrow |\uparrow\rangle$ transition in each ion. As ϕ is varied, the parity of the N ions oscillates as $\cos N\phi$, and the amplitude of the oscillation is twice the magnitude of the density-matrix element $\rho_{\uparrow\ldots\uparrow,\downarrow\ldots\downarrow}$. Each data point represents an average of 1000 experiments, corresponding to a total integration time of roughly 10 s for each graph.

desired coherence $2|\rho_{\uparrow\ldots\uparrow,\downarrow\ldots\downarrow}|$. This compression of the Ramsey fringes by a factor of N is the basis for extracting Heisenberg-limited signal-to-noise in spectroscopy of entangled states, where the frequency uncertainty $\Delta\omega$ is limited by the N-particle Heisenberg uncertainty relation $\Delta\omega\Delta t \geq 1/N$ for observation time Δt [37]. Fig. 5 shows an analog of this effect in a Mach-Zender interferomer.

The measurements of $|\rho_{\uparrow\ldots\uparrow,\downarrow\ldots\downarrow}|$ are listed in the last column of Table 1 for both 2- and 4-ion cases. The fidelity of our state generation, or the overlap between the idealized state $|\Psi_N\rangle$ in Eq. (3) and the observed density matrix, is

$$\mathcal{F}_N \equiv \langle|\Psi_N\rangle|\rho_N|\Psi_N\rangle = \frac{P_0 + P_N}{2} + |\rho_{\uparrow\ldots\uparrow,\downarrow\ldots\downarrow}|. \tag{8}$$

For $N = 2$ we achieve $\mathcal{F}_2 = 0.83 \pm 0.01$, while for $N = 4$, $\mathcal{F}_4 = 0.57 \pm 0.02$. In both cases the fidelity is above 0.5, indicating N-particle entanglement [27].

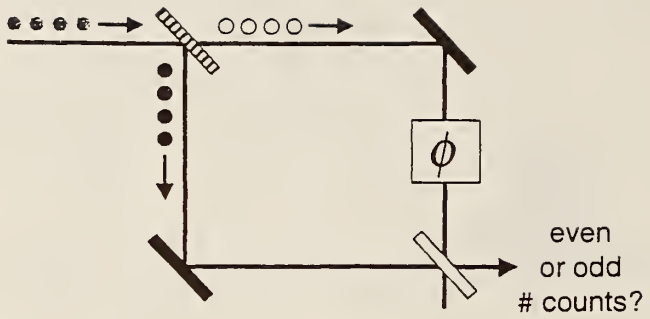

FIGURE 5. Mach-Zender interferometer analog for four-particle entanglement observation. Four photons propagate through a "super-beamsplitter," which sends the photons in a superposition of all going through and all reflecting. One arm contains a phase shifter, and the two paths are recombined on a normal beamsplitter. The parity of the number of photons received in one of the output ports is measured as the interferometer phase is scanned. Because the photons all take the same path, the measured phase shift is amplified by a factor of four (fringe period $= \pi/2$), providing enhanced interferometric sensitivity.

Quantifying the *amount* of entanglement is a more difficult question. A variety of measures of entanglement have been proposed, but most are difficult to calculate even numerically [38,39]. For $N = 2$, Wootters has given an explicit formula for the *entanglement of formation*, $\mathcal{E}(\rho_2)$ [40]. Although we have not reconstructed the entire two-particle density matrix, the populations measured place sufficient bounds on the unmeasured elements to determine that $\mathcal{E}(\rho_2) \approx 0.5$. This indicates that roughly two pairs of our ions would be required to carry the same quantum information as a single perfectly entangled pair.

In the four-ion case, no explicit formula for entanglement is known. The data does indicate that our density matrix can be expressed as

$$\rho_4 \simeq 0.43|\Psi_4\rangle\langle\Psi_4| + 0.57\rho_4^{incoh}, \tag{9}$$

where $|\Psi_4\rangle$ is the desired state of Eq. (3) and ρ_4^{incoh} is completely incoherent (ie., diagonal). The coefficients of Eq. (9) are determined directly from the value of $\rho_{\uparrow\uparrow\uparrow\uparrow,\downarrow\downarrow\downarrow\downarrow}$ in Table I, together with the fact that no evidence for other off-diagonal matrix elements was observed. (Other coherences involving less than four ions would have given fringes varying as $cos\phi$, $cos2\phi$, or $cos3\phi$ in the measured populations $P_j(\phi)$ and parity $\Pi(\phi)$).

A measurement of $|\rho_{\uparrow\ldots\uparrow,\downarrow\ldots\downarrow}| > 0$ does not by itself guarantee N-particle entanglement. For instance, consider the four-particle states

$$|\Psi_A\rangle = \left(\frac{|\downarrow\downarrow\downarrow\downarrow\rangle + |\uparrow\uparrow\uparrow\uparrow\rangle}{\sqrt{2}}\right) \otimes \left(\frac{|\downarrow\rangle + |\uparrow\rangle}{\sqrt{2}}\right) \tag{10}$$

and

$$|\Psi_B\rangle = \left(\frac{|\downarrow\downarrow\downarrow\rangle + i|\uparrow\uparrow\uparrow\rangle}{\sqrt{2}}\right) \otimes \left(\frac{|\downarrow\rangle - i|\uparrow\rangle}{\sqrt{2}}\right). \tag{11}$$

An equally weighted statistical mixture of Ψ_A and Ψ_B exhibits only three-particle entanglement, yet has $|\rho_{\uparrow\ldots\uparrow,\downarrow\ldots\downarrow}| = 0.25$ (larger than our observed value) without any other coherences. A similar mixed state with pairs of two-particle entangled states also has $|\rho_{\uparrow\ldots\uparrow,\downarrow\ldots\downarrow}| = 0.25$ without other coherences. However, these states significantly differ from $|\Psi_4\rangle\langle\Psi_4|$ along the diagonals, so the observed populations P_j following the entanglement procedure (Table 1) can set an upper bound on how much these states can contribute to the measured density matrix. We decompose ρ_4 as a sum of the desired state $|\Psi_4\rangle\langle\Psi_4|$ and a "worst-case" factorizable density matrix ρ_4^F which includes mixed states such as above. We find that an upper bound on the amount of four-particle coherence in ρ_4^F is

$$\rho^F_{\uparrow\uparrow\uparrow\uparrow,\downarrow\downarrow\downarrow\downarrow}(max) = Min\left[P_0, P_4, \frac{P_2}{2} + Min(P_1, P_3)\right]. \tag{12}$$

From the data in Table (1), we find that $\rho^F_{\uparrow\uparrow\uparrow\uparrow,\downarrow\downarrow\downarrow\downarrow}(max) = 0.15$, leaving the remainder of the observed four-particle coherence (0.065) to be unambiguously associated with the four-particle entangled state $|\Psi_4\rangle$. This gives the worst-case decomposition

$$\rho_4 = 0.13|\psi_4\rangle\langle\psi_4| + 0.87\rho_4^F, \tag{13}$$

where ρ_4^F contains mixtures of particular two- and three-particle entangled states (such as Eqs. (10) and (11)) which are very unlikely to occur in the experiment.

OUTLOOK

The data on two-ion and four-ion entanglement are consistent with an entanglement efficiency of $\epsilon \approx 0.8$. Although this represents the only demonstrated source of 4-particle entanglement and uses a scalable method, the imperfect contrast of (Fig. 4) indicates that even this efficiency will limit how many particles can be entangled in this experiment. It may be required to achieve entanglement efficiencies $\epsilon > 0.9999$ in order to implement fault-tolerant error correction schemes which may allow entanglement of arbitrarily large numbers of particles [41].

Several technical noise sources degrade the observed efficiency, including laser intensity and beam-pointing noise, nonuniform illumination of the ions during the Mølmer-Sørensen operation, and magnetic field noise. The chief limitation in the current experiment appears to be stochastic heating of the ions to outside the Lamb-Dicke regime. The center-of-mass (CM) motion of the ions is observed to heat at a rate of $\langle\dot{n}_{CM}\rangle \approx 0.02N\ \mu s^{-1}$ [33], so after a 10 μs four-ion entangling operation, $\langle n_{CM}\rangle$ approaches ≈ 10 thermal quanta. This invalidates the Lamb-Dicke criterion $\eta^2_{CM}\langle n_{CM}\rangle \ll 1$, and severely limits the fidelity of the operation. Mølmer and Sørensen have shown [29] that the expected fidelity of the entangled state $|\Psi_N\rangle$ of N ions is

$$\mathcal{F} \approx 1 - N(N-1)\eta_{CM}^4 \langle n_{CM} \rangle^2, \tag{14}$$

to lowest order in the center-of-mass Lamb-Dicke parameter η_{CM} with $N \gg 1$ and $\langle n_{CM} \rangle \gg 1$. The factor $N(N-1)/2$ comes from the number of pairs of N ions which are simultaneously flipped during the Mølmer-Sørensen entangling operation. We find for the $N = 4$ experiment, the above expression is consistent with the observations.

The source of ion heating has not been pinpointed, but it appears to be related to fluctuating microscopic potentials on the electrodes. The observed heating is not a fundamental limitation, as it has been observed to be orders of magnitude smaller under some conditions [33]. Moreover, by trapping multiple ion species and continuously laser-cooling one, the other qubit ions can be sympathetically cooled to remain in the Lamb-Dicke regime while not disturbing the qubit coherence [42].

Producing entangled states of very large numbers of ions (tens or hundreds) for relevance to large-scale quantum computing will require a different approach. This is because a trap confining more than several ions will have low oscillation frequencies, and mode cross-coupling from the complicated mode structure will be unavoidable. A promising path to large numbers is to use a multiplexed ion trap structure of many separated ion traps [43]. Here, entangling operations are done only in traps holding a few $(2-5)$ ions, and the ions are be shuttled between traps to extend the entanglement to larger numbers. Because the quantum bits are stored in magnetic dipole (hyperfine) internal states and the ions are moved around with electric fields acting on their charge, the coherence of the qubits should not be disturbed. Peeling away an ion from or introducing an ion to other ions in a trap will obviously introduce a significant amount of motional energy, but this energy can be removed again by trapping multiple species and relying on sympatheic cooling to return the motion to well inside the Lamb-Dicke regime for subsequent entangling operations.

REFERENCES

1. D. Bohm, *Quantum theory* (Prentice Hall, Engelwood Cliffs, NJ, 1951).
2. A. Einstein, B. Podolsky. and N. Rosen, Phys. Rev. **47**, 777 (1935).
3. J. S. Bell, Physics **1**, 195 (1964).
4. C. H. Bennett and S. J. Weisner, Phys. Rev. Lett. **69**, 2881 (1996).
5. K. Mattle, H. Weinfurter, P. G. Kwiat, and A. Zeilinger, Phys. Rev. Lett. **76**, 4656 (1996).
6. A. K. Ekert, Phys. Rev. Lett. **67**, 661 (1991).
7. C. H. Bennett *et al.*, Phys. Rev. Lett. **70**, 1895 (1993).
8. D. Bouwmeester *et al.*, Nature **390**, 575 (1997).
9. D. Boschi *et al.*, Phys. Rev. Lett. **80**, 1121 (1998).
10. A. Furusawa *et al.*, Science **282**, 706 (1998).
11. P. W. Shor, *Proceedings of the 35th Annual Symposium on the Foundations of Computer Science* (IEEE Computer Society Press, New York, 1994), p. 124.

12. L. K. Grover, Phys. Rev. Lett. **79**, 325 (1997).
13. A. M. Steane and D. M. Lucas, quant-ph/0004053 (2000).
14. S. J. Freedman and J. F. Clauser, Phys. Rev. Lett. **28**, 938 (1972).
15. A. Aspect, P. Grangier, and G. Roger, Phys. Rev. Lett. **49**, 91 (1982).
16. Z. Y. Ou and L. Mandel, Phys. Rev. Lett. **61**, 50 (1988).
17. Y. H. Shih and C. O. Alley, Phys. Rev. Lett. **61**, 2921 (1988).
18. D. Bouwmeester *et al.*, Phys. Rev. Lett. **82**, 1345 (1999).
19. E. Hagley *et al.*, Phys. Rev. Lett. **79**, 1 (1997).
20. A. Rauschenbeutel *et al.*, Science **288**, 2024 (2000).
21. Z. Y. Ou, S. F. Pereira, H. J. Kimble, and K. C. Peng, Phys. Rev. Lett. **68**, 3663 (1992).
22. J. I. Cirac and P. Zoller, Phys. Rev. Lett. **74**, 4091 (1995).
23. C. Monroe *et al.*, Phys. Rev. Lett. **75**, 4714 (1995).
24. Q. A. Turchette *et al.*, Phys. Rev. Lett. **81**, 1525 (1998).
25. K. Mølmer and A. Sørensen, Phys. Rev. Lett. **82**, 1835 (1999).
26. K. Mølmer and A. Sørensen, Phys. Rev. Lett. **82**, 1971 (1999).
27. C. A. Sackett *et al.*, Nature **404**, 256 (2000).
28. E. Solano, R. L. de Matos Filho, and N. Zagury, Phys. Rev. A **59**, 2539 (1999).
29. A. Sørensen and K. Mølmer, quant-ph/0002024 (2000).
30. G. J. Milburn, quant-ph/9908037 (1999).
31. D. F. Walls and G. J. Milburn, *Quantum Optics* (Springer Verlag, Berlin, 1994).
32. C. Monroe, D. M. Meekhof, B. E. King, and D. J. Wineland, Science **272**, 1131 (1996).
33. Q. A. Turchette *et al.*, Phys. Rev. A **61**, 063418 (2000).
34. B. E. King *et al.*, Phys. Rev. Lett. **81**, 1525 (1998).
35. D. James, Appl. Phys. B **66**, 181 (1998).
36. N. F. Ramsey, *Molecular Beams* (Oxford University Press, London, 1963).
37. J. J. Bollinger, W. M. Itano, D. J. Wineland, and D. J. Heinzen, Phys. Rev. A **54**, R4649 (1996).
38. V. Vedral, M. Plenio, M. Rippin, and P. Knight, Phys. Rev. Lett. **78**, 2275 (1997).
39. M. Lewenstein and A. Sanpera, Phys. Rev. Lett. **80**, 2261 (1998).
40. W. K. Wootters, Phys. Rev. Lett. **80**, 2245 (1998).
41. W. H. Zurek, Physics Today **52**, 24 (1999).
42. D. Kielpinski *et al.*, Phys. Rev. A **61**, 032310 (2000).
43. D. J. Wineland *et al.*, J. Res. Nat. Inst. Stand. Tech. **103**, 259 (1998).

Heating of trapped ions from the quantum ground state

Q. A. Turchette,*,† D. Kielpinski, B. E. King,‡ D. Leibfried,§ D. M. Meekhof, C. J. Myatt,† M. A. Rowe, C. A. Sackett, C. S. Wood,‖ W. M. Itano, C. Monroe, and D. J. Wineland
Time and Frequency Division, National Institute of Standards and Technology, Boulder, Colorado 80303
(Received 14 October 1999; published 17 May 2000)

We have investigated motional heating of laser-cooled $^9Be^+$ ions held in radio-frequency (Paul) traps. We have measured heating rates in a variety of traps with different geometries, electrode materials, and characteristic sizes. The results show that heating is due to electric-field noise from the trap electrodes that exerts a stochastic fluctuating force on the ion. The scaling of the heating rate with trap size is much stronger than that expected from a spatially uniform noise source on the electrodes (such as Johnson noise from external circuits), indicating that a microscopic uncorrelated noise source on the electrodes (such as fluctuating patch-potential fields) is a more likely candidate for the source of heating.

PACS number(s): 32.80.Pj, 39.10.+j, 42.50.Vk

I. INTRODUCTION

Cold trapped ions have been proposed as a physical implementation for quantum computation (QC) [1], and experiments on one [2–5] and two [6,7] ions have demonstrated proof of the principle. Work is currently underway to extend these results. In ion trap QC, ion-laser interactions prepare, manipulate, and entangle atomic states in ways dependent on the quantum motional state of the ions. A limiting factor in the fidelity of an operation is uncontrolled heating of the motion during manipulations. Heating leads to decoherence of the quantum superposition states involved in the computation [8,9], and can ultimately limit the number of elementary gate operations that can be strung together. Speculations have been made about the mechanisms that lead to heating [8,10–14], but measurements are scarce since the necessary sensitivity can be achieved only through laser cooling to near the ground state of motion. Additionally, systematic studies of the dependence of heating rate on various trap properties are difficult, since often this requires the construction and operation of an entirely new trap apparatus, which may have different values of properties not under study. Indeed, the data presented here pose several interpretational difficulties for this reason.

Heating of a single trapped ion (or the center-of-mass motion of a collection of trapped ions) occurs when noisy electric fields at the position of the ion couple to its charge, giving rise to fluctuating forces. If the spectrum of fluctuations overlaps the trap secular motion frequency or its micromotion sidebands, the fluctuating forces can impart significant energy to the secular motion of the ion. Here, we express the heating rate as the average number of quanta of energy gained by the secular motion in a given time. There are several candidates worth considering for sources of the noisy fields that give rise to heating. Some of these are [8–14] Johnson noise from the resistance in the trap electrodes or external circuitry (the manifestation of thermal electronic noise or black body radiation consistent with the boundary conditions imposed by the trap electrode structure), fluctuating patch potentials (due, for example, to randomly oriented domains at the surface of the electrodes or adsorbed materials on the electrodes), ambient electric fields from injected electronic noise, fields generated by fluctuating currents such as electron currents from field-emitter points on the trap electrodes, and collisions with background atoms. Only the first two mechanisms will be considered here since the remaining mechanisms (and others) are unlikely contributors [8] or can be eliminated by comparing the measured heating rates of the center of mass and differential modes of two ions [6]. As will be shown below, the Johnson noise and patch-potential mechanisms give rise to heating rates, which scale differently with the distance between the ion and the trap electrodes.

II. TWO MODELS FOR SOURCES OF HEATING

A. Preliminaries

The heating rate caused by a fluctuating uniform field can be derived as in Savard *et al.* [15] and agrees with a classical calculation [8]. The Hamiltonian for a particle of charge q and mass m trapped in an harmonic well subject to a fluctuating, uniform (nongradient) electric field drive $\epsilon(t)$ is

$$H(t)=H_0-q\epsilon(t)x, \tag{1}$$

where $H_0=p^2/2m+m\omega_m^2x^2/2$ is the usual, stationary harmonic oscillator Hamiltonian with trap frequency ω_m. From first-order perturbation theory, the rate of transition from the ground state of the well ($|n=0\rangle$) to the first excited state ($|n=1\rangle$) is [15]

$$\Gamma_{0\to1}=\frac{1}{\hbar^2}\int_{-\infty}^{\infty}d\tau\, e^{i\omega_m\tau}\langle\epsilon(t)\epsilon(t+\tau)\rangle|\langle 0|qx|1\rangle|^2. \tag{2}$$

Evaluating the motional matrix element gives

*Electronic address: quentint@reoinc.com
†Present address: Research Electro-optics, Boulder, CO.
‡Present address: NIST, Gaithersburg, MD.
§Present address: University of Innsbruck, Austria.
‖Present address: ILX Lightwave, Boulder, CO.

$$\Gamma_{0\to 1}=\frac{q^2}{4m\hbar\omega_m}S_E(\omega_m), \tag{3}$$

where $S_E(\omega)\equiv 2\int_{-\infty}^{\infty}d\tau e^{i\omega\tau}\langle\epsilon(t)\epsilon(t+\tau)\rangle$ is the spectral density of electric-field fluctuations in units of $(\mathrm{V/cm})^2\mathrm{Hz}^{-1}$.

For an ion trapped by a combination of (assumed noiseless) static fields and inhomogeneous rf fields (Paul trap) the heating rate can be generalized to [11]

$$\dot{\bar{n}}=\frac{q^2}{4m\hbar\omega_m}\left(S_E(\omega_m)+\frac{\omega_m^2}{2\Omega_T^2}S_E(\Omega_T\pm\omega_m)\right), \tag{4}$$

where $\dot{\bar{n}}$ is the rate of change of the average thermal occupation number, ω_m is now the secular frequency of the mode of motion under consideration, and Ω_T is the trap rf drive frequency. The second term on the right-hand side (RHS) of Eq. (4) is due to a cross coupling between the rf and noise fields; it will not be present for the axial motion of a linear trap, which is confined only by static fields. Even for motion confined by rf pondermotive forces, this second term will be negligible in the absence of spurious resonances in $S_E(\omega)$ or increasing $S_E(\omega)$ (since $\omega_m^2/\Omega_T^2\sim 10^{-4}$) and is neglected in what follows [8].

We differentiate two sources of the noise that gives rise to heating. The first is thermal electronic noise in the imperfectly conducting trap electrodes and elsewhere in the trap circuitry. Though this source of noise is ultimately microscopic in origin, for our purposes here it can be treated adequately by use of lumped circuit models. Thermal noise has been considered in the context of ion-trap heating in several places [8,11–14]. The second source of noise considered here is due to "microscopic" regions of material (small compared to the size of the trap electrodes) with fluctuating, discontinuous potentials established, for example, at the interface of different materials or crystalline domains. We call this patch-potential noise, and its microscopic origin leads to manifestly different heating behavior from that for the thermal electronic noise case. Static patch potentials are a well-known phenomenon, but little is known about the high-frequency (MHz) fluctuating patches, which are required to account for our observed heating rates [16–18].

B. Thermal electronic noise

Heating rates in the case of thermal electronic noise (Johnson noise) can be obtained simply through the use of lumped-circuit models, which are justified by the fact that the wavelength of the relevant fields (at typical trap secular or drive frequencies) is significantly larger than the size of the trap electrodes. Such an analysis has been carried out elsewhere [8,11,19], and only the major results will be quoted here. Resistances in the trap electrodes and connecting circuits give rise to an electric-field noise spectral density $S_E(\omega)=4k_BTR(\omega)/d^2$, where d is the characteristic distance from the trap electrodes to the ion, T is the temperature (near room temperature for all of our experiments), k_B is Boltzmann's constant, and $R(\omega)$ is the effective (lumped-circuit) resistance between trap electrodes. The heating rate is given by

$$\dot{\bar{n}}_{\mathrm{R}}=\frac{q^2k_BTR(\omega_m)}{m\hbar\omega_md^2}. \tag{5}$$

A numerical estimate of the heating rate for typical trap parameters gives $0.1/\mathrm{s}<\dot{\bar{n}}_{\mathrm{R}}<1/\mathrm{s}$ [8,11], which is significantly slower than our observed rates. As a final note, the lumped-circuit approach is convenient, but not necessary. In the Appendix, we present a microscopic model that is valid for arbitrary ion-electrode distances and reproduces Eq. (5) for all the traps considered here (and for all realistic traps where $d\gg\delta$, where δ is the skin depth of the electrode material at the trap secular frequency).

C. Fluctuating patch-potential noise

To derive the heating rate for the case of microscopic patch potentials we use the following approximate model. We assume that the trap electrodes form a spherical conducting shell of radius a around the ion. Each of the patches is a disc on the inner surface of the sphere with radius $r_p\ll a$ and electric potential noise $V_p(\omega)$. Alternatively, each patch is assumed to have power noise spectral density $S_V(\omega)$. The electric field noise at the ion due to a single patch is $E_p(\omega)=-3V_p(\omega)r_p^2/4a^3$ in the direction of the patch. There are $N\approx 4Ca^2/r_p^2$ such patches distributed over the sphere with coverage $C\leqslant 1$. Averaging over a random distribution of patches on the sphere, we find that the power spectral density of the electric field at the ion (along a single direction) is

$$S_E(\omega)=N\left(\frac{\partial E_p(\omega)}{\partial V_p(\omega)}\right)^2S_V(\omega)=\frac{3CS_V(\omega)r_p^2}{4a^4}. \tag{6}$$

This gives a heating rate

$$\dot{\bar{n}}_{\mathrm{P}}=\frac{3q^2Cr_p^2S_V(\omega_m)}{16m\hbar\omega_md^4}, \tag{7}$$

in which the association $d\sim a$ is made. Note the difference in scaling with electrode size between Eqs. (5) and (7). The thermal electronic noise model gives a scaling $\dot{\bar{n}}_{\mathrm{R}}\propto d^{-2}$, while the patch-potential model gives $\dot{\bar{n}}_{\mathrm{P}}\propto d^{-4}$. In fact, a d^{-4} dependence also arises from a random distribution of fluctuating charges or dipoles.

III. MEASUREMENTS

A. Measuring the heating rate

To determine the heating rate, we first cool the ion to near the ground state. In sufficiently strong traps, this is achieved simply by laser cooling with light, red detuned from a fast cycling transition ($\gamma\approx\omega_m$, where γ is the radiative linewidth of the upper state) propagating in a direction such that

its k vector has a component along the direction of the mode of interest. In weaker traps, additional sideband Raman cooling is utilized to cool to the ground state [3]. Typical starting values of $\bar{n}$, the average number of thermal phonons in the mode of interest, are between 0 and 2.

After cooling and optically pumping the ion to its internal ground state (denoted $|\downarrow\rangle$), we drive Raman transitions between atomic and motional levels [2–4]. Tuning the Raman difference frequency $\Delta\omega$ to the kth motional blue sideband (bsb) at $\Delta\omega=\omega_0+k\omega_m$ drives the transition $|\downarrow\rangle|n\rangle \leftrightarrow|\uparrow\rangle|n+k\rangle$ where $|\uparrow\rangle,|\downarrow\rangle$ refer to the internal (spin) states of the atom that are separated by ω_0. The kth red sideband (rsb) at $\Delta\omega=\omega_0-k\omega_m$ drives $|\downarrow\rangle|n\rangle\leftrightarrow|\uparrow\rangle|n-k\rangle$. The measurement utilizes asymmetry in the strengths of the red and blue motional sidebands to extract $\bar{n}$. The strengths of the sidebands are defined as the probability of making a transition $|\downarrow\rangle\leftrightarrow|\uparrow\rangle$, which depends on the occupation number of the motional levels. The strengths are probed by a Raman pulse of duration t tuned to either kth sideband. The probability $P_\downarrow$ of remaining in $|\downarrow\rangle$ after probing is measured and the strengths $I_k^{\mathrm{rsb}}=1-P_{\downarrow,\mathrm{rsb}}$ and $I_k^{\mathrm{bsb}}=1-P_{\downarrow,\mathrm{bsb}}$ are extracted. For thermal motional states, the strengths of the red and blue sidebands are related by [3,8]

$$I_k^{\mathrm{rsb}}=\sum_{m=k}^{\infty} P_m \sin^2 \Omega_{m,m-k}t \tag{8}$$

$$=\left(\frac{\bar{n}}{1+\bar{n}}\right)^k \sum_{m=0}^{\infty} P_m \sin^2 \Omega_{m+k,m}t \tag{9}$$

$$=\left(\frac{\bar{n}}{1+\bar{n}}\right)^k I_k^{\mathrm{bsb}}, \tag{10}$$

where $\Omega_{m+k,m}=\Omega_{m,m+k}$ is the Rabi frequency of the kth sideband between levels m and $m+k$, and $P_m=\bar{n}^m/(1+\bar{n})^{m+1}$ is the probability of the mth level being occupied for a thermal distribution of mean number $\bar{n}$. The ratio of the sidebands $R_k\equiv I_k^{\mathrm{rsb}}/I_k^{\mathrm{bsb}}$ is independent of drive time t and immediately gives the mean occupation number $\bar{n}$,

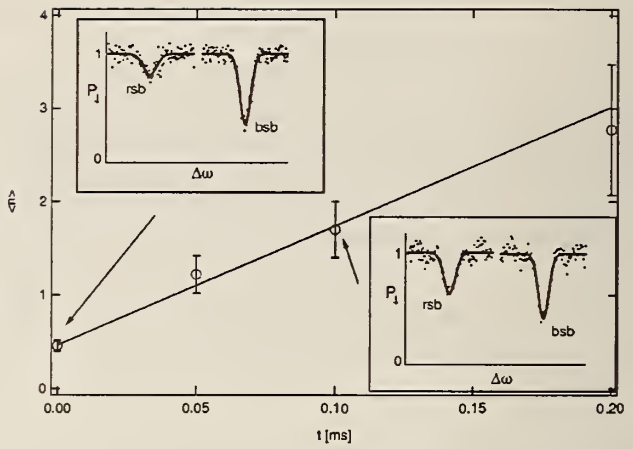

FIG. 1. An example of heating rate data. The main graph shows $\bar{n}$ ($\equiv\langle n\rangle$) vs t, the delay between cooling and probing. The insets show Raman spectra from which $\bar{n}$ is extracted, according to Eq. (11). For the insets, $P_\downarrow$ is the probability that the ion remains in the $|\downarrow\rangle$ state after application of a Raman probe of fixed duration with difference frequency $\Delta\omega$; rsb, red motional sideband; bsb, blue motional sideband. The sidebands shown are the first sidebands. The data are for trap 5 from Table I at 5 MHz secular frequency and $\dot{\bar{n}}=12\pm2$/ms.

$$\bar{n}=\frac{(R_k)^{1/k}}{1-(R_k)^{1/k}}, \tag{11}$$

which is valid even if the Lamb-Dicke criterion is not satisfied. In principle, k should be chosen to be the positive integer nearest to $\bar{n}$ in order to maximize sensitivity. In practice we use $k=1$, 2, or 3 in most cases. Note that Eq. (11) is valid only for thermal states; this is adequate since Doppler cooling leaves the motion in a thermal state [4,20], as does any cooling to near the ground state.

In order to determine the heating rate $\dot{\bar{n}}$, delays with no laser interaction are added between the cooling cycle and the probing cycle. An example of a data set at a fixed trap secular frequency is shown in Fig. 1. The error bars are determined as follows: The raw data of Raman scans over the

TABLE I. Summary of traps. The size column is approximately the distance between the ion and the nearest electrode surface. Ω_T is the trap rf drive frequency. The heating rate ($\dot{\bar{n}}$) is for a trap secular frequency of 10 MHz, which in the case of traps 3a and 3b had to be extrapolated from data at lower trap secular frequencies. The two numbers quoted for 3a and 3b are for two different versions of the trap. See the text for a further discussion of the parameters.

Trap	Type	Material	Size (μm)	$\Omega_T/2\pi$ [MHz]	$\dot{\bar{n}}$ (ms^{-1})	Refs.
1	circular ring	Mo	170	250	1	[3,4]
2	elliptical ring	Be	175	250	10	[6,7]
3a	circular ring	Mo	175	150	10,10^{-2}	
3b	circular ring	Mo	395	150	0.5,10^{-5}	
4	linear	Au	~~280~~ 160	150	2.3	[9]
5	linear	Au	~~280~~ 160	230	3.5	[22]
6	linear	Au	~~365~~ 220	230	1.1	[22]

correction

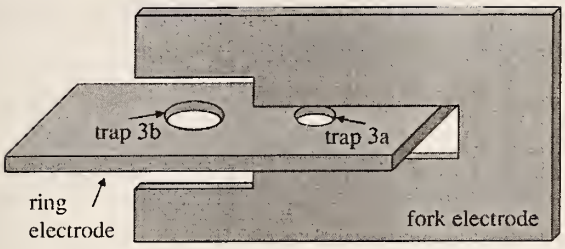

FIG. 2. Schematic diagram of the electrodes of trap 3 (from Table I). The distance between traps 3a and 3b is 1.7 mm. Not to scale.

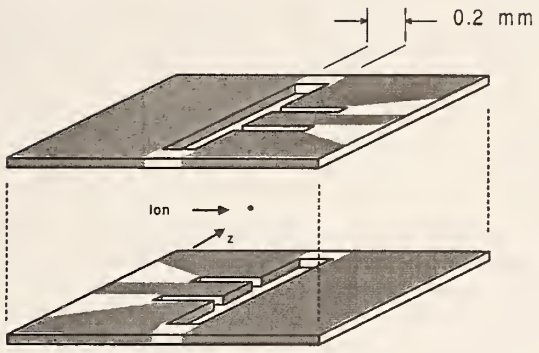

FIG. 3. Schematic diagram of the electrodes of the linear traps (traps 4, 5, and 6 from Table I). The traps are formed by evaporating gold (approximately 0.75 μm thick) on an alumina substrate. The outer segmented electrodes are the endcaps, while the long unbroken electrodes carry rf. The axial direction (labeled z) is parallel to the rf electrode. The two separate trap wafers are spaced by 200 μm for traps 4 and 5 and 280 μm for trap 6 (spacers not shown). Schematic diagram not to scale.

sidebands (such as is those shown in the insets of Fig. 1) are fit to Gaussians, from which the depths of the sidebands are extracted, with error on the parameter estimate calculated assuming normal distribution of the data. The errors from the rsb and bsb strengths are propagated through Eq. (11) for an error on $\bar{n}$. The error bars shown are 1σ, and include only statistical factors. These errors are incorporated in the linear regression to extract $\bar{\bar{n}}$ with appropriate error. Many such data sets are taken for various types of traps and at different secular frequencies.

B. The traps

The measurements of heating rate in this paper extend over a five year period and utilize six different traps. The traps are summarized in Table I. The traps are described in the references listed; here only a brief discussion is included. The "ring" traps are approximate quadrupole configurations consisting of a flat electrode (125 μm thick) with a hole drilled through it (the ring) and an independent "fork" electrode (100 μm thick) that forms end caps on either side of the electrode, centered with the hole, similar to the trap shown in Fig. 2. In trap 1, the ring and endcap electrodes were at the same average potential; in traps 2 and 3 a static bias field could be added between the fork and ring to change the distribution of binding strengths along the three principle axes of the trap. The size of these traps is stated as the hole radius, with the end cap spacing approximately 70% of the hole diameter. For the elliptical ring trap (trap 2) the stated size is the radius along the minor axis and the aspect ratio is 3:2; the fork tines are parallel to the major axis of the ellipse. Traps 3a and 3b were drilled into a single flat electrode with a single graded fork electrode (see Fig. 2). The rings are circular and the size stated is the radius. This was the trap used for the size-scaling measurements. The heating in all of the ring traps was measured in a direction in the plane of the ring electrode, parallel to the tines of the fork electrode. Traps 4, 5, and 6 are similar linear traps with geometry indicated in Fig. 3. Trap 6 was made slightly larger than traps 4 and 5 by increasing the space between the two electrode wafers. Heating was measured along the axial direction, which has only a static confining potential. The size quoted in Table I for the linear traps is the distance between the ion and the nearest electrode. All traps are mounted at the end of a coaxial $\lambda/4$ resonator for rf voltage buildup [21]. Typical resonator quality factors are around 500 and rf voltage at the open end is approximately 500 V with a few watts of input power. In all traps except for traps 3a and 3b the resonator is inside the vacuum chamber with the trap. In traps 3a and 3b, the resonator is outside the chamber, with the high-voltage rf applied to the trap through a standard vacuum feedthrough.

Since we believe that surface effects are an important factor in heating, we cleaned the electrode surfaces before using a trap. When trap electrodes were recycled, they were first cleaned with HCl in order to remove the Be coating deposited by the atomic source. For the molybdenum traps an electropolish in phosphoric acid was then used. For the beryllium electrodes electropolishing in a variety of acids was ineffective, so abrasive polishing was used. Finally, the traps were rinsed in distilled water followed by methanol. The gold electrodes of the linear traps were cleaned with solvents after being evaporatively deposited on their alumina substrates. The time of exposure of clean trap electrodes to the atmosphere before the vacuum chamber was evacuated was typically less than one day. The traps were then vacuum baked at $\sim$350° C for approximately three days.

C. Data

Our longest-term heating measurements were made on trap 1. In Fig. 4 we plot the heating rate as a function of date of data acquisition for a fixed trap frequency (11 MHz). The heating rate is on the order of 1 quantum per millisecond with a basic trend upwards of $\sim$1 quantum per millisecond per year. Over this time the electrodes were coated with Be from the source ovens, but beyond this, nothing was changed in the vacuum envelope, which was closed for this entire period of time. The cause of the increase in heating rate is unknown, but may be related to increased Be deposition on the electrodes. Be plating on the trap electrodes could be a source of patch-potential noise.

Figure 5 shows heating rates in the linear traps (traps 4, 5, and 6) and the elliptical ring trap (trap 2) as a function of trap secular frequency. The frequency dependence of the heating

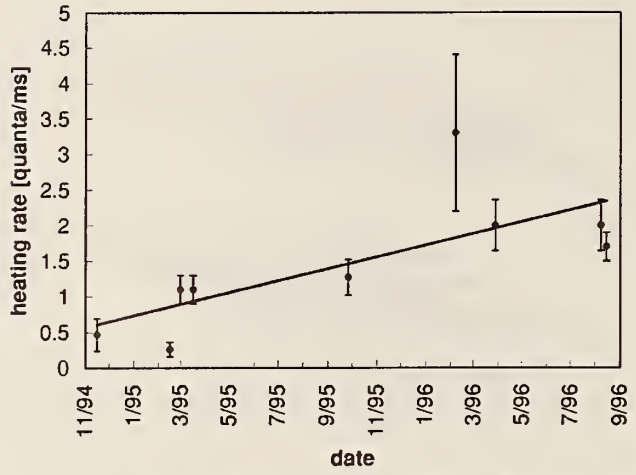

FIG. 4. Heating rate in ring trap 1 vs time. The secular frequency for all measurements was ~11 MHz. The solid line shows a trend, which does not account for the weights of the data points.

rate is expected to scale as $S_E(\omega_m)/\omega_m$ [Eq. (4)]. For example, a trap electrode with a flat noise spectrum [$S_E(\omega)$ = const] will have a heating rate that scales as ω_m^{-1}. The actual spectrum of fluctuations is impossible to know *a priori*, but in principle the data can be used to extract a spectrum over a limited frequency range given the model leading to Eq. (4). For the three linear traps, the heating rate data are most consistent with a ω_m^{-2} scaling, implying $S_E \propto \omega^{-1}$. This

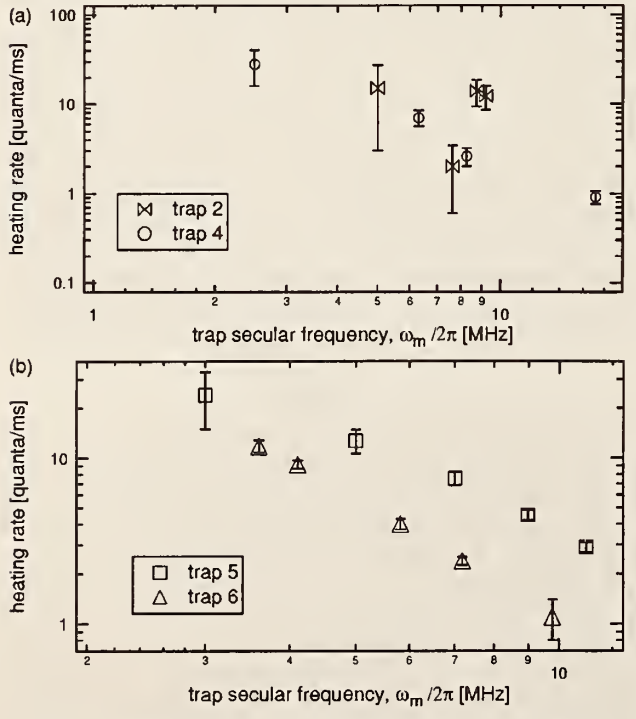

FIG. 5. Heating rates vs trap secular frequency in (a) the elliptical ring trap 2 and in the microlinear trap 4 and in (b) linear traps 5 and 6. The only intended difference between traps 5 and 6 is the size. In all four data sets, the secular frequency was varied by changing a static potential only.

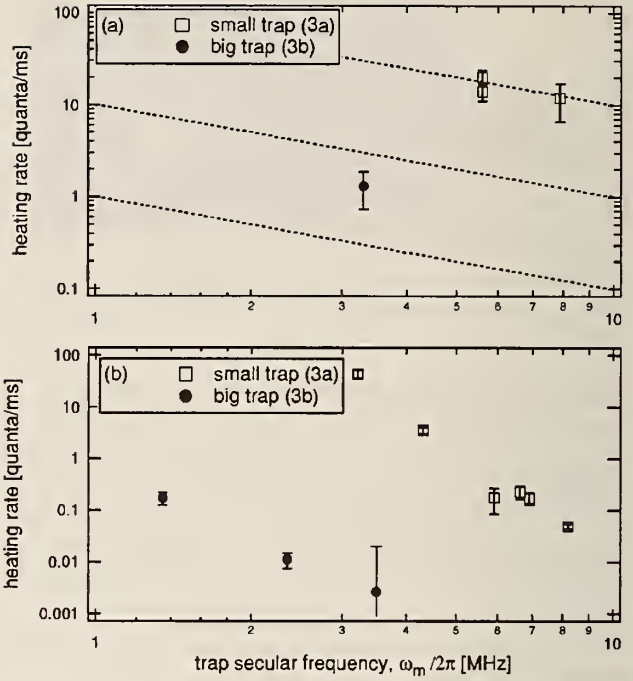

FIG. 6. Data from trap 3, showing heating rates vs trap secular frequency. (a) Data set number 1. The two points on the small trap at $\omega_m/2\pi = 5.3$ MHz were taken with Raman cooling to $\bar{n}(t=0) \sim 0$ and with Doppler cooling only to $\bar{n}(t=0) \sim 2$. Note that they give comparable results, as they should. The dashed lines show ω_m^{-1} scaling. (b) Data set number 2. The small trap data were taken with an rf voltage of ~400 V and the big trap with ~600 V. The secular frequency was changed by tuning the dc bias between fork and ring electrodes.

does not greatly assist us in identifying a physical mechanism for the heating. For example, pure Johnson noise will have a flat spectrum, low-pass-filtered Johnson noise will have a spectrum that decreases with increasing frequency, and the spectrum of fluctuations in the patch-potential case is entirely unknown. In addition to the theoretical ambiguity, there is evidence in other data sets of different frequency scalings (though they are always power-law scalings). This measurement certainly cannot be used to pinpoint a heating mechanism; it is presented here only for completeness.

The data of Fig. 5(b) provide a first indication of the scaling of the heating rate with trap size. Trap 6 is about 1.3 times larger than trap 5, while its heating rate (at 10 MHz) was a factor of 3 slower. This indicates that the dependence of heating rate on trap size is stronger than d^{-2}, but is consistent with d^{-4}. Of course, this comparison is to be taken with some caution, since these are two separate traps measured several weeks apart, and therefore likely had different microscopic electrode environments. However, a comparison is warranted since the traps were identical apart from their sizes. In particular, all the associated electronics were the same and the rf drive voltage was very nearly the same. In fact, the rf voltage was slightly larger for the measurements on trap 6, which showed the lower heating rate. This is important to note because we observe a slight dependence of the heating rate on the applied rf trapping voltage. Though

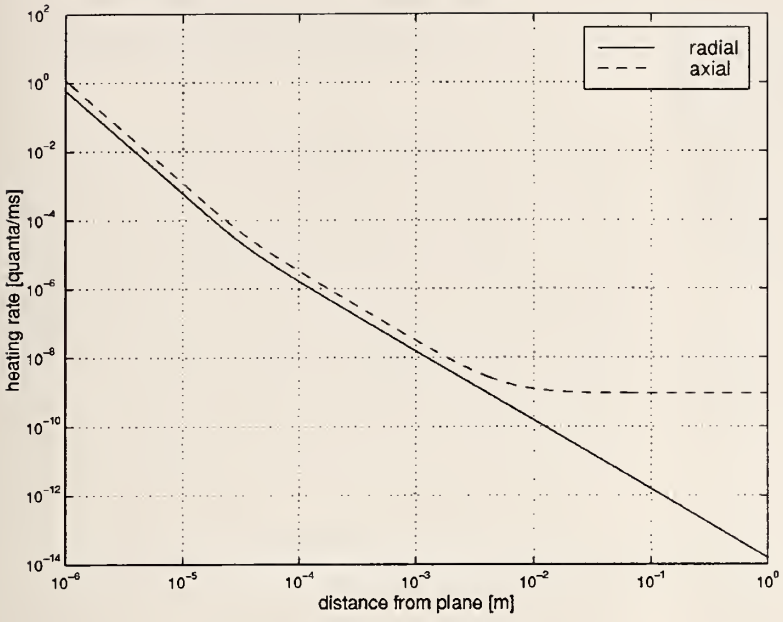

FIG. 7. Expected heating rate vs distance from electrode for thermal electronic noise, from Eqs. (A6), (A7), and (4). The numerical parameters are those for $^9Be^+$ with molybdenum electrodes at 10 MHz secular frequency and room temperature.

we have only a qualitative sense of this dependence at present, it seems that heating rates increase with rf voltage, up to a point, at which the effect levels off. This rf-voltage dependence is observed along directions where the ion is confined both by static fields and by pondermotive fields. It may not be unreasonable that the increased rf voltage increases the intensity of the noise source (possibly due to an increase of temperature of the electrodes), even when it does not affect the trap secular frequency, as in the axial direction of the linear traps.

Trap 3 was designed to give a controlled measure of the heating rate as a function of trap size, while all other parameters were held fixed. The trap electrodes were made from the same substrates, the electrodes were subjected to the same preuse cleaning, the traps were in the same vacuum envelope, driven by the same rf electronics (simultaneously), and data for both traps were acquired with minimal delay. For direct comparison at the same secular frequency in both traps, it was necessary to change the applied rf voltage since $\omega_m \propto 1/d^2$. (A static bias between ring and endcap can be added, as discussed above, but this was not sufficient to measure heating at identical secular frequencies for the same rf drive.) There are two data sets to be discussed for this trap, shown in Fig. 6.

In the first set, shown in Fig. 6(a), we have data points at two different secular frequencies for the "small trap" (trap 3a) and one point for the "big trap" (trap 3b). The heating rates of the small trap are comparable to the heating rates for other traps and show a ω_m^{-1} scaling of the heating rate. The single point on the big trap is at a lower secular frequency, yet has a much *slower* heating rate. In fact, if we extrapolate the data from the small trap to the same secular frequency (using ω_m^{-1}), the heating rate is over an order of magnitude lower in the big trap. The ratio of the heating rate in the small trap to that of the big trap is 20 ± 6. This is a much stronger scaling than that predicted by a Johnson noise heating mechanism [Eq. (5) predicts a $d^2 \sim 4.8$ scaling], but is consistent with the scaling in the patch-potential case [Eq. (7) predicts a $d^4 \sim 23$ scaling]. When these data are used to predict an exponent for the size scaling, the result is $d^{3.8 \pm 0.6}$.

For the second data set, shown in Fig. 6(b), the trap was removed from the vacuum enclosure, given the usual cleaning (as discussed above), and replaced for the measurements. In this data set, the trap behaved quite differently from all other traps, with heating rates significantly below those of other traps. Also, S_E must have been a strong function of ω for this trap since the scaling with trap frequency was rather pronounced. The scaling with size was also strong: the heating rate was 16 000 times smaller in the big trap. When these data are used to predict an exponent for the size scaling, the result is $d^{12 \pm 2}$. Needless to say, it is difficult to draw general conclusions from the data for this particular trap, but the difference in heating rates between the two traps seems to strongly indicate, again, that Johnson noise is not the source of the heating. We cannot be sure why this trap had such anomalous heating behavior, but we speculate that it is due to a less-than-usual deposition of Be on the trap electrodes prior to the measurements, because the trap was loaded with minimal exposure to the Be source atomic beam.

At this point it is useful to compare the present results to heating rates in other experiments. There are two other measurements. The first was done with $^{198}Hg^+$ [10]. For that experiment $\omega_m/2\pi \approx 3$ MHz and $d \approx 450$ μm and the heating rate was 0.006/ms. Accounting for scalings with trap frequency (ω_m^{-1}) [23] and mass (m^{-1}), these results are consistent with the present results for a size scaling of d^{-4}. Another measurement has been made with $^{40}Ca^+$ [5]. For that experiment $\omega_m/2\pi \approx 4$ MHz and $d \approx 700$ μm and the heating rate was 0.005/ms. Compared to the present experiments and the Hg experiment, this is also consistent with a d^{-4} scaling, although it is certainly unlikely that all systems had the same patch field environment.

IV. CONCLUSIONS AND OUTLOOK

We have measured heating from the ground state of trapped ions in different traps. The magnitude of heating rates and the results of the size-scaling measurements are inconsistent with thermal electronic noise as the source of the heating. The results do not indicate any strong dependence on trap-electrode material or on the type of trap potential (pondermotive or static). The rf voltage applied to the electrodes may play a role in heating, in as much as it may have an influence on patch potentials.

Since we have not identified the mechanism for the observed heating, it is difficult to say what path should be taken to correct it. If fluctuating patch potentials on the surface of the electrodes are the cause, then further cleaning may be appropriate. Additionally, better masking of the trap electrodes from the Be source ovens may help.

The results coupled with those of other experiments [10,5] strongly indicate that bigger traps have smaller heating rates. This is not a surprise, but the strength of the scaling may be. With little sacrifice in the trap secular frequency (which ultimately determines the fastest rate of coherent manipulation) a dramatic decrease in the heating rate vs logic gate speed appears possible using larger traps.

ACKNOWLEDGMENTS

We acknowledge support from the U.S. National Security Agency, Office of Naval Research, and Army Research Office. We thank Chris Langer, Pin Chen, and Mike Lombardi for critical readings of the manuscript. We thank J. Beall for help in construction of the linear traps (Fig. 3).

APPENDIX: THERMAL ELECTRIC FIELDS

We are interested in the thermal electric field power spectral density $S_{E_i}(\boldsymbol{r},\omega)$ generated from a specified volume of conductor. The conductor can be decomposed into a web of resistors each carrying current spectral density $S_{I_i}=4k_BT/R_i$ (where we assume $k_BT\gg\hbar\omega$). The resistance along the ith direction of an infinitesimal volume element is $R_i=dl/(\sigma dA)$, where σ is the conductivity, dl is the length along i, and dA is the cross-sectional area. A Fourier component of current $I_i(\omega)$ through the volume $dV=dldA$ gives rise to an electric dipole $P_i(\omega)=I_i(\omega)dl/\omega$. Thus the equivalent spectral density of electric dipole of the infinitesimal resistor is isotropic: $S_{P_i}(\omega)=4k_BT\sigma\, dV/\omega^2$.

The electric field from an electric dipole $\boldsymbol{P}(\boldsymbol{r}',\omega)$ oscillating at frequency ω and position $\boldsymbol{r}'$ is

$$E_i(\boldsymbol{r},\omega)=\sum_{j=x,y,z} P_j(\boldsymbol{r}',\omega)G_{ij}(\boldsymbol{r},\boldsymbol{r}',\omega). \tag{A1}$$

In this expression, $G_{ij}(\boldsymbol{r},\boldsymbol{r}',\omega)$ is a Green function matrix, representing the ith component of electric field at position $\boldsymbol{r}$ due to the jth component of a point dipole at $\boldsymbol{r}'$, which satisfies the appropriate boundary conditions of the geometry. The electric-field spectral density at position $\boldsymbol{r}$ is an integral over the dipoles in the conductor volume:

$$S_{E_i}(\boldsymbol{r},\omega)=\frac{4k_BT}{\omega^2}\int \sigma(\boldsymbol{r}')\sum_{j=x,y,z}|G_{ij}(\boldsymbol{r},\boldsymbol{r}',\omega)|^2\, dV'. \tag{A2}$$

The Green function satisfies $G_{ij}(\boldsymbol{r},\boldsymbol{r}',\omega)=G_{ij}(\boldsymbol{r}',\boldsymbol{r},\omega)$, so the above integral can be interpreted as the Ohmic power absorbed by the conductor from the electric fields generated by a point dipole at position $\boldsymbol{r}$. By energy conservation, this must be equivalent to the time-averaged power dissipated by a point dipole at $\boldsymbol{r}$, which is related to the imaginary part of the Green function matrix $G_{ij}(\boldsymbol{r},\boldsymbol{r},\omega)$ [24]. This simplifies Eq. (A2), leaving the fluctuation-dissipation theorem

$$S_{E_i}(\boldsymbol{r},\omega)=\frac{2k_BT}{\omega}\sum_{j=x,y,z}\mathrm{Im}\, G_{ij}(\boldsymbol{r},\boldsymbol{r},\omega). \tag{A3}$$

Agarwal solved Maxwell's equations for $G_{ij}(\boldsymbol{r}',\boldsymbol{r},\omega)$ for the simple geometry of an infinite sheet of conductor, filling the space $z\leqslant 0$ with the conductor-vacuum interface in the $z=0$ plane [25]. Although this idealized geometry is far from any real ion-trap electrode structure, rough scalings of the thermal fields can be relevant to real ion-trap geometries. From Ref. [25], the Green function matrix for this problem is diagonal with axial (z) and radial (ρ) components

$$G_{zz}(z,z,\omega)=G^{free}(\omega)+i\int_0^\infty \frac{q^3}{w_0}\left(\frac{w_0\varepsilon-w}{w_0\varepsilon+w}\right)e^{2iw_0z}\, dq, \tag{A4}$$

$$G_{\rho\rho}(z,z,\omega)=G^{free}(\omega)-\frac{i}{2}\int_0^\infty q\left[w_0\left(\frac{w_0\varepsilon-w}{w_0\varepsilon+w}\right)+\frac{k^2}{w_0}\left(\frac{w-w_0}{w+w_0}\right)\right]e^{2iw_0z}\, dq. \tag{A5}$$

In the above expressions, $\varepsilon(\omega)=\varepsilon_0+i\sigma/\varepsilon_0\omega$ is the dielectric function of the conductor (in the low frequency limit), $k=\omega/c$, and wave vectors w_0 and w (generally complex) are defined by $w_0^2=k^2-q^2$ and $w^2=k^2\varepsilon-q^2$ with $\mathrm{Im}\, w_0\geqslant 0$ and $\mathrm{Im}\, w\geqslant 0$. The free-space Green's function $G^{free}(\omega)$ has imaginary part $\mathrm{Im}\, G^{free}(\omega)=k^3/6\pi\varepsilon_0$ and gives rise to the isotropic free-space black body electric-field fluctuations when substituted into Eq. (A3).

The above integrals are significantly simplified in the "quasistatic" limit, where $kz\ll 1$ and the conductivity is sufficiently high so that $k\delta\ll 1$, where $\delta=\sqrt{2c^2\varepsilon_0/\omega\sigma}$ is the skin depth of the conductor. Despite these conditions, no restriction is placed on the value of z/δ. We break the above integrals into two pieces. The first piece $\int_0^k$ has $q\leqslant k$ with w_0 real. In the quasistatic limit, this piece can be shown to cancel the free-space contribution to the transverse Green function $\mathrm{Im}\, G_{\rho\rho}(z,z,\omega)$, while doubling the free-space contribution to the axial Green function $\mathrm{Im}\, G_{zz}(z,z,\omega)$. Physically, the presence of the conductor negates the transverse free-space black body field while it doubles the axial black body field due to a near-perfect reflection. The second piece of the integrals $\int_k^\infty$ has $q\geqslant k$ with w_0 imaginary. These pieces of the integral can be solved to lowest order in kz and $k\delta$. Com-

bining terms and substituting the results into Eq. (A3), the thermal electric-field spectral density is

$$S_{E_z}(z,\omega)=\frac{2k_BT\omega^2}{3\pi\varepsilon_0c^3}+\frac{k_BT}{4\pi\sigma z^3}\left(\frac{1}{2}+\sqrt{\frac{1}{4}+\frac{z^4}{\delta^4}}\right)^{1/2}, \tag{A6}$$

$$S_{E_\rho}(z,\omega)=\frac{k_BT}{8\pi\sigma z^3}\left(\frac{1}{2}+\sqrt{\frac{1}{4}+\frac{z^4}{\delta^4}}\right)^{1/2}. \tag{A7}$$

These expressions show that the thermal electric-field noise scales as $1/z^3$ for $z\ll\delta$ [14], but scales as $1/z^2$ for $z\gg\delta$ [8,11]. At large distances $z>\sqrt{\delta/k}$ (with $kz\ll1$), the axial field noise settles toward twice the free-space black body value while the radial field vanishes. This result is also reported in Ref. [26]. The behavior is shown in Fig. 7, where Eqs. (A6) and (A7) have been substituted into Eq. (4), giving the expected thermal heating rate for a ^{9}Be ion trapped with molybdenum electrodes at room temperature. Note that the predicted heating rate at trap sizes typical in our experiments is significantly slower than the 0.1-1 quanta/s rate predicted in [8,11]. This difference comes from the choice of the value of the resistance in Eq. (5), which was chosen in [8,11] as an absolute upper limit.

When interpreting these results, only the rough scaling should be considered. Realistic ion-trap electrode geometries are more complicated than a single infinite conducting plane, involving a more closed electrode structure. This generally requires a full numerical solution to the relevant boundary value problem. Moreover, we are usually interested in the electric-field fluctuations at the center of the trap, where these fluctuations will be substantially different from those above an infinite plate.

[1] J. 1. Cirac and P. Zoller, Phys. Rev. Lett. **74**, 4091 (1995).
[2] C. Monroe, D. M. Meekhof, B. E. King, W. M. 1tano, and D. J. Wineland, Phys. Rev. Lett. **75**, 4714 (1995).
[3] C. Monroe, D. M. Meekhof, B. E. King, S. R. Jefferts, W. M. Itano, D. J. Wineland, and P. Gould, Phys. Rev. Lett. **75**, 4011 (1995).
[4] D. M. Meekhof, C. Monroe, B. E. King, W. M. 1tano, and D. J. Wineland, Phys. Rev. Lett. **76**, 1796 (1996).
[5] Ch. Roos, Th. Zeiger, H. Rohde, H. C. Nägerl, J. Eschner, D. Leibfried, F. Schmidt-Kaler, and R. Blatt, Phys. Rev. Lett. **83**, 4713 (1999).
[6] B. E. King, C. S. Wood, C. J. Myatt, Q. A. Turchette, D. Leibfried, W. M. 1tano, C. Monroe, and D. J. Wineland, Phys. Rev. Lett. **81**, 1525 (1998).
[7] Q. A. Turchette, C. S. Wood, B. E. King, C. J. Myatt, D. Leibfried, W. M. 1tano, C. Monroe, and D. J. Wineland, Phys. Rev. Lett. **81**, 3631 (1998).
[8] D. J. Wineland, C. Monroe, W. M. 1tano, D. Leibfried, B. E. King, and D. M. Meekhof, J. Res. Natl. 1nst. Stand. Technol. **103**, 259 (1998).
[9] C. J. Myatt, B. E. King, Q. A. Turchette, C. A. Sackett, D. Kielpinski, W. M. 1tano, C. Monroe, and D. J. Wineland, Nature (London) **403**, 269 (2000).
[10] F. Diedrich, J. C. Bergquist, W. M. 1tano, D. J. Wineland, Phys. Rev. Lett. **62**, 403 (1989).
[11] D. J. Wineland, C. Monroe, W. M. Itano, B. E. King, D. Leibfried, D. M. Meekhof, C. Myatt, and C. Wood, Fortschr. Phys. **46**, 363 (1998).
[12] S. K. Lamoreaux, Phys. Rev. A **56**, 4970 (1997).
[13] D. F. V. James, Phys. Rev. Lett. **81**, 317 (1998).
[14] C. Henkel and M. Wilkens, Europhys. Lett. **47**, 414 (1999).
[15] T. A. Savard, K. M. O'Hara, and J. E. Thomas, Phys. Rev. A **56**, R1095 (1997).
[16] J. B. Camp, T. W. Darling, and R. E. Brown, J. Appl. Phys. **69**, 7126 (1991).
[17] C. Kleint, Ann. Phys. (Leipzig) **10**, 309 (1963).
[18] G. W. Timm and A. Van der Ziel, Physica (Utrecht) **32**, 1333 (1966).
[19] D. J. Wineland and H. G. Dehmelt, J. Appl. Phys. **46**, 919 (1975).
[20] S. Stenholm, Rev. Mod. Phys. **58**, 699 (1986).
[21] S. R. Jefferts, C. Monroe, E. W. Bell, and D. J. Wineland, Phys. Rev. A **51**, 3112 (1995).
[22] C. A. Sackett, D. Kielpinski, B. E. King, C. Langer, V. Meyer, C. J. Myatt, M. Rowe, Q. A. Turchette, W. M. Itano, D. J. Wineland, and C. Monroe, Nature (London) **404**, 256 (2000).
[23] There is no way to know if ω_m^{-1} is the proper way to scale for trap frequency, but it is a reasonable first assumption.
[24] L. D. Landau and E. M. Lifshitz, *Statistical Physics, Part I 3rd ed.* (Pergamon, Oxford, 1980), Chap. Xll.
[25] G. S. Agarwal, Phys. Rev. A **11**, 230 (1975).
[26] C. Henkel, S. Potting, and M. Wilkens, Appl. Phys. B: Lasers Opt. **B69**, 379 (1999).

Decoherence and decay of motional quantum states of a trapped atom coupled to engineered reservoirs

Q. A. Turchette,* C. J. Myatt,† B. E. King,‡ C. A. Sackett, D. Kielpinski, W. M. Itano, C. Monroe,§ and D. J. Wineland
Time and Frequency Division, National Institute of Standards and Technology, Boulder, Colorado 80303
(Received 28 February 2000; published 16 October 2000)

We present results from an experimental study of the decoherence and decay of quantum states of a trapped atomic ion's harmonic motion interacting with several types of *engineered* reservoirs. We experimentally simulate three types of reservoirs: a high-temperature amplitude reservoir, a zero-temperature amplitude reservoir, and a high-temperature phase reservoir. Interaction with these environments causes the ion's motional state to decay or heat, and in the case of superposition states, to lose coherence. We report measurements of the decoherence of superpositions of coherent states and two-Fock-state superpositions into these reservoirs, as well as the decay and heating of Fock states. We confirm the theoretically well-known scaling laws that predict that the decoherence rate of superposition states scales with the square of the "size" of the state.

PACS number(s): 42.50.−p, 03.67.Lx, 03.65.−w, 32.80.Pj

I. INTRODUCTION

The decoherence and decay of quantum states coupled to a variety of reservoirs have been investigated extensively in theory [1–8]. The model in these studies is typically a system harmonic oscillator coupled to a bath of environment harmonic oscillators. One of the most interesting results has been the realization that macroscopic superposition states decay at extremely fast rates. As an illustration, consider a charged harmonic-oscillator system in a superposition of coherent states $\psi \propto |\alpha_1\rangle + |\alpha_2\rangle$ coupled to the noisy electric field $\mathbf{E}$ of the environment. The interaction potential is $V = -q\mathbf{x}\cdot\mathbf{E}$, where $\mathbf{x}$ is the position and q is the charge of the particle. Regardless of the temperature of the reservoir, $\langle \mathbf{E}^2 \rangle \neq 0$, so that the system is always subject to some level of noise from the environment. For a superposition of coherent states coupled to a reservoir of fluctuating fields, a simple scaling law may be stated [3]: the rate of decoherence scales as the square of the separation of the wave packets, $|\Delta\alpha|^2 = |\alpha_1 - \alpha_2|^2$. In an idealized case, the superposition is created, the amplitude reservoir is coupled to the system for a time t, and the coupling is then turned off. The remaining coherence C between the two wave packets, expressed for instance as the magnitude of the off-diagonal components of the system density matrix, is

$$C(t) = C(0)\exp\left[-|\Delta\alpha|^2 \frac{\gamma}{2} t\right], \tag{1}$$

where γ is a coupling constant between the reservoir and the system. For the same interaction, the energy H of the system decays like

$$H(t) = H(0)\exp[-\gamma t], \tag{2}$$

at a rate independent of the size of the initial state. For superpositions of macroscopic-sized wave packets, the quantum coherence may be obliterated in a time over which the energy of the system does not change appreciably.

Significant attention has been paid to the role of decoherence in the classical/quantum correspondence and in fundamental issues of physics. Recently, decoherence has also been studied in a more pragmatic role: as a primary impediment to quantum computing. Quantum computation relies on entanglement of large quantum states to perform efficient calculations. Such states, separated by large distances in Hilbert space, will be very susceptible to the detrimental effects of decoherence. Any system will interact with its environment, so the nature of the interaction and the time scales over which it acts are of critical import in implementations of quantum information processing. Since trapped ions are a leading technology for investigations in quantum computing, a study of decoherence in an ion trap quantum computer system [9], as presented here, is particularly relevant.

Over the past several years, techniques have been described to generate mesoscopic superpositions, called "Schrödinger cats," of motional states of trapped ions [10] and of photon states in cavity quantum electrodynamics [11]. In both cases decoherence through coupling to ambient reservoirs was observed, and sensitivity to the size of the superposition was demonstrated [10,11]. In more recent work with trapped ions [12], we extended the investigations beyond ambient reservoirs and "engineered" the form, bandwidth, and strength of coupling to the reservoir. We observed the quantitative scaling laws of the decoherence of superpositions of coherent states and superpositions of Fock states into a variety of reservoirs for a range of parameters. This paper is a more detailed discussion of the experiments of Ref. [12] with additional theoretical development and additional data.

The paper is arranged as follows. In Sec. II we review the theory of the damping of a harmonic oscillator coupled to several types of reservoirs. In particular, we derive specific formulas for the time evolution of the density matrix for several types of system-reservoir interactions. In Sec. III we discuss the experimental apparatus and techniques, and in Sec. IV we analyze the data.

*Electronic address: quentint@boulder.nist.gov
†Present address: Research Electro-Optics, Boulder, CO.
‡Present address: NIST, Gaithersburg, MD.
§Present address: Department of Physics, University of Michigan, Ann Arbor, MI.

II. THEORETICAL SUMMARY

A. Damping of harmonic oscillators

1. Thermal amplitude reservoir

We begin by reminding the reader of some formal results in the theory of damping of harmonic oscillators coupled to two types of baths. In this section we consider the case in which the reservoir is a bath of oscillators, and the coupling is to the position of the oscillator via the interaction Hamiltonian

$$H_I=\hbar\sum_i (\Gamma_i \hat{b}_i \hat{a}^\dagger+\Gamma_i^* \hat{b}_i^\dagger \hat{a}), \tag{3}$$

where Γ_i is the coupling rate of the ith bath oscillator to the system, $\hat{b}_i$ is the lowering operator of this reservoir oscillator, and $\hat{a}$ is the lowering operator of the system oscillator. This is known as an amplitude coupling. If furthermore, the reservoir oscillators are in thermal equilibrium at temperature T, then the system exchanges energy with the reservoir in a process leading to overall thermal equilibrium. The time evolution of this process is described by the following master equation for the system density matrix formed by tracing over the reservoir degrees of freedom [5]:

$$\dot{\rho}(t)=\frac{\gamma}{2}(\bar{n}+1)(2\hat{a}\rho\hat{a}^\dagger-\hat{a}^\dagger\hat{a}\rho-\rho\hat{a}^\dagger\hat{a}) +\frac{\gamma}{2}\bar{n}(2\hat{a}^\dagger\rho\hat{a}-\hat{a}\hat{a}^\dagger\rho-\rho\hat{a}\hat{a}^\dagger), \tag{4}$$

where γ is the system decay rate and $\bar{n}$ is the average number of quanta in the reservoir at the resonance frequency of the system oscillator ω_0:

$$\bar{n}=\frac{e^{-\hbar\omega_0/k_BT}}{1-e^{-\hbar\omega_0/k_BT}} \tag{5}$$

and k_B is Boltzmann's constant. The zero-temperature reservoir ($\bar{n}=0$) is a special case of the thermal amplitude reservoir in which the inescapable quantum noise dominates the classical thermal noise of fluctuating oscillators.

a. Amplitude damping, Fock states. The solution of Eq. (4) is nontrivial, and has been discussed at some length in the literature (which is reviewed in Ref. [8]). We first consider its solution in a Fock-state basis. In this basis, the decomposition of $\rho(t)$ is given by

$$\rho(t)=\sum_{n,m}\rho_{nm}(t)|n\rangle\langle m|. \tag{6}$$

Based on calculations presented in Ref. [13], we state the solution to Eq. (4) with the expansion of Eq. (6) as:

$$\rho_{nm}(t)=\frac{1}{1+N(t)}\sum_{j=0}^{\min(n,m)}\left(\frac{N(t)}{1+N(t)}\right)^j\left(\frac{e^{-\gamma t/2}}{1+N(t)}\right)^{n+m-2j} \times\sum_{l=0}^{\infty}\left(1-\frac{e^{-\gamma t}}{1+N(t)}\right)^l \times\sqrt{\binom{n+l-j}{n-j}\binom{m+l-j}{m-j}\binom{n}{j}\binom{m}{j}} \times\rho_{n+l-j,m+l-j}(0), \tag{7}$$

where $\rho_{nm}(0)$ is the initial density matrix and

$$N(t)=\bar{n}(1-e^{-\gamma t}) \tag{8}$$

can be interpreted as the average number of quanta in the *system* at time t for an initial ground-state system [$\rho(0)=|0\rangle\langle 0|$]. The form of Eq. (7) is qualitatively illuminating: the evolution of a given density-matrix element depends only on neighbors along its own diagonal. We note that this calculation has been performed in Refs. [13] and [14]. We used Ref. [13] to derive Eq. (7); in this reference the final form [Ref. [13], Eq. (37)] seems to be written incorrectly, though the correct result can be derived from earlier equations. In Ref. [14] the result is written in terms of the Q function, and agrees with Ref. [13], and therefore not with our result.

In some cases, we are interested in the time evolution of the diagonal elements only, which are given by:

$$\rho_{nn}(t)=\frac{1}{1+N(t)}\sum_{j=0}^{n}\left(\frac{N(t)}{1+N(t)}\right)^j\left(\frac{e^{-\gamma t/2}}{1+N(t)}\right)^{2n-2j} \tag{9}$$

$$\times\sum_{l=0}^{\infty}\left(1-\frac{e^{-\gamma t}}{1+N(t)}\right)^l\binom{n+l-j}{n-j} \times\binom{n}{j}\rho_{n+l-j,n+l-j}(0). \tag{10}$$

As stated above, the zero-temperature reservoir is a special case of the amplitude reservoir. We write the solution in this case as:

$$\rho_{nm}(t)=e^{-(n+m)\gamma t/2}\sum_{l=0}^{\infty}(1-e^{-\gamma t})^l \times\sqrt{\binom{n+l}{n}\binom{m+l}{m}}\rho_{n+l,m+l}(0). \tag{11}$$

For the diagonals only,

$$\rho_{nn}(t)=e^{-n\gamma t}\sum_{l=0}^{\infty}(1-e^{-\gamma t})^l\binom{n+l}{n}\rho_{n+l,n+l}(0). \tag{12}$$

b. Amplitude damping, coherent states. In this paragraph we consider the solution of Eq. (4) in a situation appropriate to coherent-state evolution. We follow exactly the results of Ref. [4]. For coherent states the density matrix is expanded as:

$$\rho(t)=\int d^2\mu d^2\nu P(\mu,\nu^*)\frac{|\nu\rangle\langle\mu|}{\langle\nu|\mu\rangle}, \tag{13}$$

where $P(\mu,\nu^*)$ is the positive-P representation [5–7]. The solution to Eq. (4) is written [4]

$$\rho(t)=\int d^2\mu d^2\nu P_0(\mu,\nu^*) \times\langle\nu|\mu\rangle^{-e^{-\gamma t/1+2N(t)}}\hat{\mathcal{D}}(\bar{\mu})\rho_T(t)\hat{\mathcal{D}}^\dagger(\bar{\nu}), \tag{14}$$

where $P_0(\mu,\nu^*)$ describes the initial system density matrix through Eq. (13),

$$\bar{\mu}=\frac{e^{-\gamma t/2}}{1+2N(t)}\{[(1+N(t)]\mu+N(t)\nu\}, \tag{15}$$

$$\bar{\nu}=\frac{e^{-\gamma t/2}}{1+2N(t)}\{[1+N(t)]\nu+N(t)\mu\}, \tag{16}$$

and $\rho_T(t)$ is a thermal state density matrix with $N(t)$ quanta:

$$\rho_T(t)=\frac{1}{1+N(t)}\sum_{m=0}^{\infty}\left[\frac{N(t)}{1+N(t)}\right]^m|m\rangle\langle m|. \tag{17}$$

$N(t)$ is defined in Eq. (8). $\hat{\mathcal{D}}$ is the displacement operator $\hat{\mathcal{D}}(\alpha)|0\rangle=|\alpha\rangle$. The form of this solution makes it difficult to see the simple result for the off-diagonal elements of the density matrix as presented in the Introduction. The appropriate experimental measurement will reveal it when we apply this formal result below.

2. Phase reservoir

Here we consider a reservoir whose coupling preserves the energy of the system, with interaction Hamiltonian

$$H_I=\hbar\sum_i(\Gamma_i\hat{b}_i\hat{a}^\dagger\hat{a}+\Gamma_i^*\hat{b}_i^\dagger\hat{a}^\dagger\hat{a}). \tag{18}$$

This is known as a phase-damping reservoir.

For the system-reservoir interaction described by Eq. (18) and a reservoir in thermal equilibrium at a temperature corresponding to a mean occupation number $\bar{n}$ [as in Eq. (5)], the master equation is given by [6]:

$$\dot{\rho}(t)=\frac{\kappa}{2}[2\hat{a}^\dagger\hat{a}\rho\hat{a}^\dagger\hat{a}-(\hat{a}^\dagger\hat{a})^2\rho-\rho(\hat{a}^\dagger\hat{a})^2]. \tag{19}$$

Here $\kappa=K(2\bar{n}+1)$, is the system decay rate with K the coupling to the reservoir of oscillators.

a. Phase damping, Fock states. For initial Fock states, the solution of Eq. (19) is straightforward. Using the expansion of Eq. (6),

$$\dot{\rho}_{nm}=-\frac{\kappa}{2}(n-m)^2\rho_{nm}, \tag{20}$$

with solution

$$\rho_{nm}(t)=e^{-(\kappa/2)(n-m)^2t}\rho_{mn}(0). \tag{21}$$

Here it is clear that the off-diagonal density-matrix elements decay exponentially at a rate proportional to the square of their distance from the diagonal.

b. Phase damping, coherent states. For the coherent state basis, the solution of Eq. (19) is rather complicated. We will forego its solution in favor of the technique presented in the next section.

B. Interferometry

This section presents an experimentally motivated approach to calculating the decay of quantum coherences. Here the off-diagonal matrix elements are measured as the contrast of an ion interferometry experiment. This section is adapted from Ref. [15].

1. Ion states and transitions

First we review a few details necessary to understand the ion interferometer analysis. For the purposes of this section, a trapped ion has an external degree of freedom that is a perfect one-dimensional (1D) harmonic oscillator (along $\hat{z}$) of frequency ω. The internal degree of freedom is assumed to be a perfect two-state system, the states of which we label in analogy with a spin-1/2 system by $|\downarrow\rangle$ and $|\uparrow\rangle$. The states $|\downarrow\rangle$ and $|\uparrow\rangle$ are coupled to the motional harmonic-oscillator states $|n\rangle$ via a classical optical laser field. The interaction Hamiltonian has resonant couplings between internal states $|s\rangle$ ($|s\rangle=|\downarrow\rangle$ or $|\uparrow\rangle$) and motional states $|n\rangle$ whose matrix elements are [16,17]

$$\langle s',n'|\hat{H}_I|s,n\rangle=\hbar\Omega\langle s',n'|\sigma_+e^{i\eta(\hat{a}+\hat{a}^\dagger)} +\sigma_-e^{-i\eta(\hat{a}+\hat{a}^\dagger)}|s,n\rangle, \tag{22}$$

where σ_+ (σ_-) is the atomic raising (lowering) operator, $\hat{a}^\dagger$ ($\hat{a}$) is the harmonic-oscillator creation (annihilation) operator, Ω is the laser-atom coupling strength, or Rabi frequency, and $\eta=\delta k\, z_0$ is the Lamb-Dicke parameter, where δk is the $\hat{z}$ component of the applied field wave vector and $z_0=\sqrt{\hbar/2m\omega}$ is the harmonic-oscillator characteristic length [16].

The excitation spectrum of the ion consists of a carrier transition ($|\downarrow\rangle|n\rangle\leftrightarrow|\uparrow\rangle|n\rangle$) and motional sideband transitions ($|\downarrow\rangle|n\rangle\leftrightarrow|\uparrow\rangle|m\rangle n\neq m$). The sideband transition frequencies differ from that of the carrier by a frequency of $(n-m)\omega$, where $|n-m|$ is the order (first, second, etc.) of the sideband. With resolved sideband cooling [18] and optical pumping we prepare the ion in the $|\downarrow\rangle|0\rangle$ state before each repetition of the experiment.

At the end of any experiment, there is one observable: the probability that the ion is found in the $|\downarrow\rangle$ state, denoted by $P_\downarrow$. The measurement is not sensitive to the motional state of the ion, so a trace over the motion is required to calculate this probability. The final density matrix at the end of an

experiment is written ρ_f, and in general is not separable between spin and motion parts [19]. The detection signal is given by

$$P_{\downarrow}=\langle\downarrow|\mathrm{Tr}_M\rho_f|\downarrow\rangle=\sum_n \langle n|\langle\downarrow|\rho_f|\downarrow\rangle|n\rangle. \tag{23}$$

For pure states $\rho_f=|\psi_f\rangle\langle\psi_f|$, this reduces to

$$P_{\downarrow}=\sum_n |\langle\downarrow|\langle n|\psi_f\rangle|^2. \tag{24}$$

In experiments in which a coherence is measured, we employ a type of Ramsey interferometry. Generically, the procedure is to embed the coupling to the reservoir between the initial and final "beam splitters" of a Ramsey interferometer. The beam splitters create and undo a motional quantum state. As the coherence of the quantum state is degraded (due to interaction with the reservoir) the contrast of the Ramsey fringes decreases, giving a measure of the remaining coherence.

2. Amplitude reservoirs

a. Schrödinger cat interferometer and amplitude reservoir. The first type of interferometer that we employ uses the Schrödinger cat state [10]

$$|\psi\rangle=\frac{1}{\sqrt{2}}(|\downarrow\rangle|\alpha_{\downarrow}\rangle+|\uparrow\rangle|\alpha_{\uparrow}\rangle), \tag{25}$$

where $|\uparrow\rangle$ and $|\downarrow\rangle$ are internal states of the ion, and $|\alpha_{\downarrow,\uparrow}\rangle$ are coherent states of the ion's motion in the harmonic well of the trap. As will be seen, the action of an amplitude reservoir on this Schrödinger cat interferometer clearly illustrates the scaling of the decoherence as a function of the size of the superposition.

A diagram of the Schrödinger cat interferometer is presented in Fig. 1. Initially the ion is prepared in the state $|\psi\rangle=|\downarrow\rangle|0\rangle$. Next, we generate the spin superposition $|\psi\rangle=(|\downarrow\rangle+|\uparrow\rangle)|0\rangle/\sqrt{2}$, as shown in panel 1. The motional superposition is created by applying a spin-dependent optical dipole force that approximates the coherent displacement operators [10,19] $\mathcal{D}(\alpha_{\downarrow})$ and $\mathcal{D}(\alpha_{\uparrow})$ acting on the states $|\downarrow\rangle$ and $|\uparrow\rangle$. The resulting state (with constant phase factors suppressed), shown in panel 2, is that of Eq. (25). These two operations constitute the first "beam splitter," or Ramsey zone of the interferometer. During the Ramsey waiting time, the amplitude reservoir [with coupling shown in Eq. (3)] is applied, by placing noisy fields on the trap electrodes (this will be discussed in Sec. III C 1 below). The application of the amplitude reservoir for a fixed time results in a random displacement β that displaces both spin states equally. Since

$$\mathcal{D}(\lambda)|\kappa\rangle=e^{-i\mathrm{Im}[\lambda^*\kappa]}|\lambda+\kappa\rangle, \tag{26}$$

where $|\kappa\rangle$ and $|\lambda+\kappa\rangle$ are coherent states, after application of the operator $\mathcal{D}(\beta)$ to the wave function from Eq. (25)

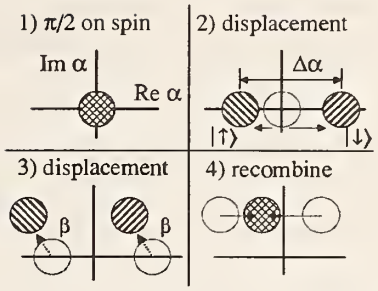

FIG. 1. Pictorial representation of the Schrodinger-cat interferometer with coupling to an amplitude reservoir. The coherent states are represented by minimum uncertainty circles in phase space, while the different spin states are indicated by the hatching. In panel 1, a spin superposition $|\psi\rangle=(|\downarrow\rangle+|\uparrow\rangle)|0\rangle/\sqrt{2}$ is created with a $\pi/2$ pulse on the carrier transition. The cat state $|\psi\rangle=(|\downarrow\rangle|\alpha_{\downarrow}\rangle+|\uparrow\rangle|\alpha_{\uparrow}\rangle)/\sqrt{2}$ is completed with a spin dependent dipole force, as shown in panel 2. The effects of coupling to an engineered amplitude reservoir are shown in panel 3. A random displacement by β in panel 3 displaces both spin states equally, but with different phase factors. After the reversal of the initial displacement in panel 4 the motion may again be factored out, but leaving a relative phase shift $2\,\mathrm{Im}[\beta\Delta\alpha^*]$ between the spin components. An ensemble average over β leads to a loss of contrast (decoherence) that scales with the size of the superposition $|\Delta\alpha|$.

$$|\psi\rangle=\frac{1}{\sqrt{2}}(|\downarrow\rangle|\alpha_{\downarrow}+\beta\rangle+e^{i\,\mathrm{Im}[\beta\Delta\alpha^*]}|\uparrow\rangle|\alpha_{\uparrow}+\beta\rangle), \tag{27}$$

where $\Delta\alpha=\alpha_{\uparrow}-\alpha_{\downarrow}$ and an overall phase factor has been removed. The motional superposition is reversed by applying $\mathcal{D}(-\alpha_{\downarrow})$ and $\mathcal{D}(-\alpha_{\uparrow})$, resulting in

$$|\psi\rangle=\frac{1}{\sqrt{2}}(|\downarrow\rangle+e^{2i\,\mathrm{Im}[\beta\Delta\alpha^*]}|\uparrow\rangle)|\beta\rangle. \tag{28}$$

A final $\pi/2$ pulse transforms the spins as

$$|\downarrow\rangle\rightarrow\frac{1}{\sqrt{2}}(|\downarrow\rangle+e^{-i\delta}|\uparrow\rangle), \tag{29}$$

$$|\uparrow\rangle\rightarrow\frac{1}{\sqrt{2}}(|\uparrow\rangle-e^{i\delta}|\downarrow\rangle), \tag{30}$$

and yields the state

$$|\psi\rangle=\frac{1}{2}[(1+e^{i(\delta+2\,\mathrm{Im}[\beta\Delta\alpha^*])})|\downarrow\rangle + (e^{2i\,\mathrm{Im}[\beta\Delta\alpha^*]}-e^{i\delta})|\uparrow\rangle]|\beta\rangle, \tag{31}$$

where δ is the Ramsey phase, i.e., the phase difference between the initial and final $\pi/2$ spin flips. These last two steps constitute the second, recombining beam splitter of the interferometer.

In a single experiment the probability that the ion is in the $|\downarrow\rangle$ state is

$$P_{\downarrow}(\beta)=|\langle\downarrow|\psi\rangle|^2=\frac{1}{2}[1+\cos(\delta+2\,\mathrm{Im}[\beta\Delta\alpha^*])]. \tag{32}$$

If β were fixed on each repetition of the experiment, as the Ramsey phase δ is swept, the signal would be a perfect cosine with phase dictated by the displacement β. The decoherence (and loss of contrast in this picture) enters, because β is a random variable that fluctuates to a different value on each repetition of the experiment, giving rise to a random-phase shift of the fringe that averages the contrast away from unity. In the experiment, we force β to be a Gaussian distributed random variable, as, for example, realized by a hot resistor coupled to the trap electrodes. We take both $\mathrm{Re}\,\beta$ and $\mathrm{Im}\,\beta$ to have a standard deviation σ. An ensemble average of $P_{\downarrow}(\beta)$ yields the form of the Ramsey fringes:

$$P_{\downarrow}=\frac{1}{2}[1+e^{-2|\Delta\alpha|^2\sigma^2}\cos\delta]. \tag{33}$$

We see that the contrast of the fringes is exponentially sensitive to (the square of) the "size" $|\Delta\alpha|$ of the superposition. This scaling [3,7,20] is one of the key results that is demonstrated experimentally in a later section.

(b) Fock state interferometer and amplitude reservoir. A second type of interferometer generates a superposition of two Fock states with the first beam splitter using the technique described in Ref. [17]. For example, consider the interferometer that generates the superposition $(|0\rangle+|2\rangle)/\sqrt{2}$ and then recombines the two parts of the wave function to produce interference fringes. Starting from the state $|\downarrow\rangle|0\rangle$, a $\pi/2$ pulse on the first blue sideband generates the state $|\psi\rangle=(|\downarrow\rangle|0\rangle+|\uparrow\rangle|1\rangle)/\sqrt{2}$. A π pulse, tuned to the first red sideband, drives the transition $|\uparrow\rangle|1\rangle\rightarrow|\downarrow\rangle|2\rangle$ while leaving the population in the $|\downarrow\rangle|0\rangle$ state unperturbed. This combination of pulses generates the superposition

$$|\psi\rangle=\frac{1}{\sqrt{2}}|\downarrow\rangle(|0\rangle+|2\rangle). \tag{34}$$

The second beam splitter of the interferometer is realized by reversing the above procedure—driving a π pulse on the first red sideband followed by a $\pi/2$ pulse on the first blue sideband. When the phase of the second $\pi/2$ pulse is swept, the spin state at the end of the experiment oscillates between $|\downarrow\rangle$ and $|\uparrow\rangle$.

For the experiments reported here, we use two pulses to generate the beam splitters in the Fock state interferometer. For the first beam splitter, the first pulse is a $\pi/2$ pulse on the n'th order blue sideband, generating the state

$$|\psi\rangle=\frac{1}{\sqrt{2}}(|\downarrow\rangle|0\rangle+|\uparrow\rangle|n'\rangle). \tag{35}$$

A second pulse selectively drives only one of the spin components, resulting in the Fock state superposition

TABLE I. The stimulated Raman pulses required for the first beam splitter of the Fock state interferometer where the initial state is always $|\downarrow\rangle|0\rangle$. To reverse the superposition in the second beam splitter, first the π pulse is applied, followed by the $\pi/2$ pulse with a phase added with respect to the first $\pi/2$. RSB and BSB stand for red sideband and blue sideband, respectively.

$\pi/2$ pulse	π pulse	State
carrier	1st RSB	$\|\downarrow\rangle(\|0\rangle+\|1\rangle)/\sqrt{2}$
1st BSB	1st RSB	$\|\downarrow\rangle(\|0\rangle+\|2\rangle)/\sqrt{2}$
2nd BSB	1st RSB	$\|\downarrow\rangle(\|0\rangle+\|3\rangle)/\sqrt{2}$
1st BSB	2nd BSB	$\|\uparrow\rangle(\|1\rangle+\|2\rangle)/\sqrt{2}$

$$|\psi\rangle=\frac{1}{\sqrt{2}}|s\rangle(|m\rangle+|n\rangle), \tag{36}$$

where $|s\rangle$ denotes one of the spin states $|\downarrow\rangle$ or $|\uparrow\rangle$. The four pairs of Fock states generated in the experiments, along with the pulses used to generate the superpositions, are shown in Table I.

The Fock state interferometer can be coupled to an amplitude reservoir. For simplicity, we restrict ourselves to Fock state superpositions of the form

$$|\psi\rangle=\frac{1}{\sqrt{2}}|\downarrow\rangle(|0\rangle+|m\rangle). \tag{37}$$

It is an extended exercise to calculate results for the entire interferometer in the manner of the preceding case (coherent states in amplitude reservoir). The complication is twofold: First, displacing Fock states leads to cumbersome expressions. Second, there is a problem with the beam splitters: the pulses of the second beam splitter are π and $\pi/2$ pulses strictly for the transitions $|\downarrow\rangle|m\rangle\leftrightarrow|\uparrow\rangle|m-1\rangle$ and $|\downarrow\rangle|0\rangle\leftrightarrow|\uparrow\rangle|m-1\rangle$, respectively. Thus applying these pulses to an ion in a motional state that has changed from its original form does not result in full spatial overlap. It turns out that while the calculation is complicated, the details are not important to the actual experiment, which is performed only for small m, and in the limit $\gamma t\ll 1$. Rather than present the full calculation, we will merely state a simple result based on the master-equation approach. For states of the type shown in Eq. (37), the time evolution of the relevant density-matrix elements predicted by Eq. (7) reduces to the simple form

$$\rho_{0,m}\approx\frac{1}{2(1+\bar{n}\gamma t)^{1+m}} \tag{38}$$

for $\gamma t\ll 1$. The measured contrast is simply twice this matrix element. For the range of m and $\bar{n}\gamma t$ studied in the experiment, this expression differs by less than 5% from an exact treatment of the imperfect spatial overlap.

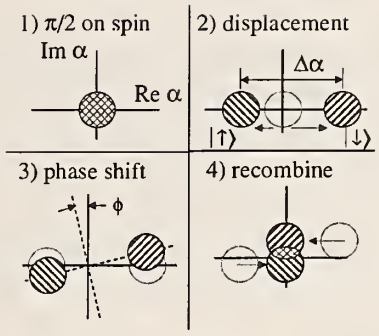

FIG. 2. Pictorial representation of the Schrodinger-cat interferometer with coupling to a phase reservoir. The coherent states are represented by minimum uncertainty circles in phase space, while the different spin states are indicated by the hatching. In panel 1, a spin superposition $|\psi\rangle=(|\downarrow\rangle+|\uparrow\rangle)|0\rangle/\sqrt{2}$ is created with a $\pi/2$ pulse on the carrier transition. The cat state $|\psi\rangle=(|\downarrow\rangle|\alpha_\downarrow\rangle+|\uparrow\rangle|\alpha_\uparrow\rangle)/\sqrt{2}$ is completed with a spin dependent dipole force, as shown in panel 2. Coupling to a phase reservoir is depicted in panel 3. The random-phase shift in panel 3 prevents the correct reversing of the initial creation of the cat, resulting in a loss of contrast due to both the phase shift ϕ as well as the reduced spatial overlap.

3. Phase reservoirs

(a) Schrödinger cat interferometer and phase reservoir. A second reservoir that we apply is a phase reservoir. A phase reservoir is realized by adiabatically changing the trap frequency for a period of time and then restoring the original trap frequency. If the deviation of the trap frequency is $\delta\omega(t)$, then the phase shift of the ion oscillation in time T is

$$\phi=\int_0^T \delta\omega(t)\,dt. \tag{39}$$

The potentials required to change the trap frequency are applied to the trap electrodes during the Ramsey time between the beam splitter pulses (see Sec. III C 2).

The effect of a phase reservoir on a Schrödinger cat state is diagrammed in Fig. 2. The generation of the Schrödinger cat state $|\psi\rangle=(|\downarrow\rangle|\alpha_\downarrow\rangle+|\uparrow\rangle|\alpha_\uparrow\rangle)/\sqrt{2}$ is accomplished as discussed previously. A phase shift of the ion oscillation by the random variable ϕ introduces complex phase factors to the coherent states,

$$|\psi\rangle=\frac{1}{\sqrt{2}}(|\downarrow\rangle|\alpha_\downarrow e^{i\phi}\rangle+|\uparrow\rangle|\alpha_\uparrow e^{i\phi}\rangle). \tag{40}$$

Due to these phase factors $e^{i\phi}$, the motional superposition is not correctly reversed, as shown in Fig. 2, panel 4. The second beam splitter consists of the displacements $\mathcal{D}(-\alpha_\downarrow)$ and $\mathcal{D}(-\alpha_\uparrow)$ followed by a second $\pi/2$ pulse on the carrier, yielding

$$|\psi\rangle=\frac{1}{2}[e^{i|\alpha_\downarrow|^2\sin\phi}(|\downarrow\rangle+e^{i\delta}|\uparrow\rangle)|\alpha_\downarrow(e^{i\phi}-1)\rangle$$
$$+e^{i|\alpha_\uparrow|^2\sin\phi}(|\downarrow\rangle-e^{i\delta}|\uparrow\rangle)|\alpha_\uparrow(e^{i\phi}-1)\rangle]. \tag{41}$$

In a single run of the experiment, the probability to find the ion in the $|\downarrow\rangle$ state is

$$P_\downarrow(\phi)=|\langle\downarrow|\psi\rangle|^2=\frac{1}{2}\{1-\exp[-|\Delta\alpha|^2(1-\cos\phi)]$$
$$\times\cos[\delta+(|\alpha_\downarrow|^2-|\alpha_\uparrow|^2)\sin\phi$$
$$+2(1-\cos\phi)\mathrm{Im}\,\alpha_\downarrow^*\alpha_\uparrow]\}. \tag{42}$$

The phase shift ϕ is taken to be a Gaussian distributed random variable with standard deviation σ. The average of $P_\downarrow(\phi)$ is

$$P_\downarrow=\frac{1}{2}\left\{1-\frac{1}{\sqrt{2\pi\sigma^2}}\int_{-\infty}^{\infty}\exp\left(-\frac{\phi^2}{2\sigma^2}-|\Delta\alpha|^2(1-\cos\phi)\right)\right.$$
$$\times\cos[(|\alpha_\downarrow|^2-|\alpha_\uparrow|^2)\sin\phi]$$
$$\left.\times\cos[\delta+2(1-\cos\phi)\mathrm{Im}\,\alpha_\downarrow^*\alpha_\uparrow]d\phi\right\}, \tag{43}$$

where the odd part of the integrand vanishes. We note that in general there is a phase shift to the fringes even though the distribution of ϕ is symmetric. In general this integral does not simplify. However, in the case of experimental interest, $\alpha_\downarrow\propto\alpha_\uparrow$ (specifically, $\alpha_\downarrow=-2\alpha_\uparrow$) in which case $\mathrm{Im}\,\alpha_\downarrow^*\alpha_\uparrow=0$. We further make the small-angle approximation in the integrand, which is valid if $\sigma^2\ll1$, when the term $e^{-\phi^2/2\sigma^2}$ dominates; or, if $|\Delta\alpha|\gg1$ and $\sigma\leqslant\pi$, when the term $e^{-|\Delta\alpha|^2(1-\cos\phi)}$ dominates. In these regimes, the integral can be evaluated analytically to yield the signal

$$P_\downarrow=\frac{1}{2}\left\{1-\frac{\cos\delta}{\sqrt{1+|\Delta\alpha|^2\sigma^2}}\exp\left[\frac{-(|\alpha_\downarrow|^2-|\alpha_\uparrow|^2)^2\sigma^2}{2(1+|\Delta\alpha|^2\sigma^2)}\right]\right\}. \tag{44}$$

This approximate expression provides a good guide to the behavior and can be used for a simplified comparison to the data. We note that in the experimentally accessible regime of $|\Delta\alpha|\sim1$–4 and $\sigma\leqslant2$, Eq. (44) is accurate to about 10% even though the small angle approximation is not strictly valid.

(b) Fock state interferometer and phase reservoir. We start in the state $[|n\rangle+|m\rangle]|\downarrow\rangle/\sqrt{2}$. We again denote the ion oscillation phase shift by ϕ, and the phase shifted superposition is

$$|\psi\rangle=\frac{1}{\sqrt{2}}|\downarrow\rangle(e^{-im\phi}|m\rangle+e^{-in\phi}|n\rangle). \tag{45}$$

In the second beam splitter a $-\pi$ pulse again entangles the spins with the motion, as

$$|\psi\rangle=\frac{1}{\sqrt{2}}(e^{-im\phi}|\downarrow\rangle|0\rangle+e^{-in\phi}|\uparrow\rangle|n'\rangle). \tag{46}$$

A final $\pi/2$ pulse generates the state

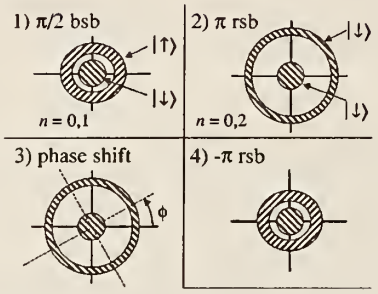

FIG. 3. Pictorial representation of the action of a phase reservoir on a Fock state interferometer. Here we consider the interferometer that generates the state $|\psi\rangle=|\downarrow\rangle(|0\rangle+|2\rangle)/\sqrt{2}$. A $\pi/2$ pulse on the first blue sideband generates the state $|\psi\rangle=(|\downarrow\rangle|0\rangle+|\uparrow\rangle|1\rangle)/\sqrt{2}$ depicted in panel 1, where the different spin states are indicated by the shading. A π pulse tuned to the first red sideband drives the transition $|\uparrow\rangle|1\rangle\rightarrow|\downarrow\rangle|2\rangle$ and generates the desired superposition. The random motional phase shift ϕ in panel 3 adds a relative phase factor, $|\psi\rangle=|\downarrow\rangle(|0\rangle+e^{-2i\phi}|2\rangle)/\sqrt{2}$, where the phase is scaled by the difference in indices of the Fock states (2 in this case). A second π pulse generates the state $|\psi\rangle=(|\downarrow\rangle|0\rangle+e^{-2i\phi}|\uparrow\rangle|1\rangle)/\sqrt{2}$ (panel 4). The result of the final $\pi/2$ pulse depends on the phase ϕ. Random fluctuations in ϕ result in decreased contrast of the Ramsey fringes.

$$|\psi\rangle=\frac{1}{2}[(e^{-im\phi}-e^{i(\delta-n\phi)})|\downarrow\rangle|0\rangle + (e^{-in\phi}+e^{i(\delta-m\phi)})|\uparrow\rangle|n'\rangle]. \quad (47)$$

The projection onto $|\downarrow\rangle$ yields

$$P_{\downarrow}(\phi)=|\langle\downarrow|\psi\rangle|^2=\frac{1}{2}\{1+\cos[\delta+(n-m)\phi]\}. \quad (48)$$

Again, the phase shift introduced between the beam splitter pulses results in a shift of the fringes. The random-phase shifts ϕ are assumed to be Gaussian distributed with standard deviation σ, and the ensemble average of $P_{\downarrow}(\phi)$ is

$$P_{\downarrow}=\frac{1}{2}[1+e^{-(n-m)^2\sigma^2/2}\cos\delta]. \quad (49)$$

The decoherence scales exponentially with the square of the difference in the Fock state indices $n-m$, so that "larger" superpositions lose coherence exponentially faster. Compare the scaling of the decay of the fringe contrast as a function of $n-m$ in Eq. (49) with the decay of the off-diagonal elements of the density matrix ρ_{mn} given in Eq. (21). The results are equivalent. (See Fig. 3.)

C. Connection of averaged interferometer approach and master equation

It is reasonable to ask in what sense the interferometer experiments of Sec. II B directly probe the relevant off-diagonal matrix elements as calculated in Sec. II A. In the case of Fock states interacting with the phase reservoir (Secs. II A 2 and II B 3), the connection is quite simple, in other cases, the connection is not as straightforward.

1. Spin coherence

In this section we argue that the contrast of the interference fringes is a measure of the coherence of the combined spin and motional quantum state, and that the spin part can be negligible or can be removed. To address this issue, we consider the interferometer experiment in the case of no added noise. We take the example of the cat state interferometer discussed in Sec. II B and write the cat state of the system after the first $\pi/2$ and displacement pulses (assumed to be short) as a density matrix [the wave function for $\mathcal{C}=1$ is given in Eq. 25]:

$$\rho=\frac{1}{2}[|\alpha_{\downarrow}\rangle|\downarrow\rangle\langle\downarrow|\langle\alpha_{\downarrow}|+|\alpha_{\uparrow}\rangle|\uparrow\rangle\langle\uparrow|\langle\alpha_{\uparrow}| + \mathcal{C}|\alpha_{\downarrow}\rangle|\downarrow\rangle\langle\uparrow|\langle\alpha_{\uparrow}|+\mathcal{C}^*|\alpha_{\uparrow}\rangle|\uparrow\rangle\langle\downarrow|\langle\alpha_{\downarrow}|], \quad (50)$$

where $\mathcal{C}=\mathcal{C}_s\mathcal{C}_m$ quantifies the coherence that has contributions from both the spin ($\mathcal{C}_s$) and motion ($\mathcal{C}_m$). This separation of the contrast into a product of spin and motion contributions is valid for reservoirs in which the spin and motion are not coupled, such as the amplitude, natural, and phase reservoirs. Moreover, separate experiments verify that the spin is not disturbed by or during the time of application of our engineered phase, amplitude, and zero-temperature reservoirs, so that in these experiments the fringe contrast is a simple probe of the change in motional coherence. The only reservoir experiments in which the spin decoherence is not negligible are the natural reservoir experiments, since for all of our applied reservoirs the time of application is short. For the natural reservoir experiments, we are forced to simply wait a time t for the ambient noise to act on the system. Note that the separation of coherences is valid if the spin undergoes only phase decay, with no random spin-flip transitions, which is verified in our experiments. To within experimental errors, we can adequately characterize spin decoherence as exponential, $\mathcal{C}_s=\exp(-\gamma_s t)$.

In the second part of the cat state interferometer, the second displacement is applied, undoing the first displacement, leaving

$$\rho=\frac{1}{2}[|0\rangle|\downarrow\rangle\langle\downarrow|\langle 0|+|0\rangle|\uparrow\rangle\langle\uparrow|\langle 0| + \mathcal{C}|0\rangle|\downarrow\rangle\langle\uparrow|\langle 0|+\mathcal{C}^*|0\rangle|\uparrow\rangle\langle\downarrow|\langle 0|]. \quad (51)$$

The final $\pi/2$-pulse with phase δ transforms the spins as in Eqs. (30), and the detection of $|\downarrow\rangle$ with trace over the motion leaves:

$$P_{\downarrow}=\frac{1-\mathrm{Re}(\mathcal{C})\cos\delta}{2}. \quad (52)$$

Thus the contrast of the Ramsey fringes depends directly on the coherence.

2. Cats, amplitude noise

The interferometer calculations presented in Sec. II B predict the outcome of particular experiments. The master-

equation solutions in Sec. II A do not. In this section, we take the solution of the master equation, in terms of the time evolution of a density matrix and derive a prediction for an interferometer experiment. The result is shown to be equivalent to the average-over-classical-variables approach in Sec. II B. We do this for the Schrödinger cat interferometer subject to amplitude noise. The solution to the master equation was given in Sec. II A 1. It is a straightforward matter to add the spin part to this solution, which must be done for the interferometer calculation. Starting from Eq. (14), we divide the initial density matrix [written as an initial P function $P_0(\mu,\nu^*)$] into four parts, corresponding to the initial state $|\psi\rangle=(|\downarrow\rangle|\alpha_\downarrow\rangle+|\uparrow\rangle|\alpha_\uparrow\rangle)/\sqrt{2}$:

$$P_0(\mu,\nu^*)=P_0^{(1)}(\mu,\nu^*)+P_0^{(2)}(\mu,\nu^*)+P_0^{(3)}(\mu,\nu^*)+P_0^{(4)}(\mu,\nu^*) \tag{53}$$

with

$$P_0^{(1)}(\mu,\nu^*)=\frac{1}{2}\delta(\mu-\alpha_\downarrow)\delta(\nu-\alpha_\downarrow)|\downarrow\rangle\langle\downarrow|, \tag{54}$$

$$P_0^{(2)}(\mu,\nu^*)=\frac{1}{2}\delta(\mu-\alpha_\uparrow)\delta(\nu-\alpha_\uparrow)|\uparrow\rangle\langle\uparrow|, \tag{55}$$

$$P_0^{(3)}(\mu,\nu^*)=\frac{1}{2}\langle\alpha_\uparrow|\alpha_\downarrow\rangle\delta(\mu-\alpha_\downarrow)\delta(\nu-\alpha_\uparrow)|\downarrow\rangle\langle\uparrow|, \tag{56}$$

$$P_0^{(4)}(\mu,\nu^*)=[P_0^{(3)}(\mu,\nu^*)]^\dagger. \tag{57}$$

From Eq. (14) this leads to four contributions to $\rho(t)$

$$\rho(t)=\rho^{(1)}(t)+\rho^{(2)}(t)+\rho^{(3)}(t)+\rho^{(4)}(t) \tag{58}$$

with

$$\rho^{(1)}(t)=\frac{1}{2}\mathcal{D}(\bar{\alpha}_\downarrow)\rho_T(t)\mathcal{D}^\dagger(\bar{\alpha}_\downarrow)|\downarrow\rangle\langle\downarrow|, \tag{59}$$

$$\rho^{(2)}(t)=\frac{1}{2}\mathcal{D}(\bar{\alpha}_\uparrow)\rho_T(t)\mathcal{D}^\dagger(\bar{\alpha}_\uparrow)|\uparrow\rangle\langle\uparrow|, \tag{60}$$

$$\rho^{(3)}(t)=\frac{1}{2}\langle\alpha_\uparrow|\alpha_\downarrow\rangle^{1-[e^{-\gamma t}/1+2N(t)]}\mathcal{D}(\bar{\alpha}_\downarrow)\rho_T(t)\mathcal{D}^\dagger(\bar{\alpha}_\uparrow)|\downarrow\rangle\langle\uparrow|, \tag{61}$$

$$\rho^{(4)}(t)=[\rho^{(3)}(t)]^\dagger, \tag{62}$$

where $\bar{\alpha}_{\downarrow,\uparrow}$ are defined as in Eqs. (15) and (16). To complete the experiment, we apply a second displacement, which is given by the operator

$$|\downarrow\rangle\langle\downarrow|\mathcal{D}(\alpha_\downarrow e^{-i\theta})+|\uparrow\rangle\langle\uparrow|\mathcal{D}(\alpha_\uparrow e^{-i\theta}), \tag{63}$$

where θ is the phase of the second displacement with respect to that of the first. We then apply the final $\pi/2$ Ramsey pulse that transforms the spins as in Eq. (30) and measure the probability that the ion is in the spin-down state, as discussed in the context of Eq. (23). Thus we are interested only in the component of ρ given by $\rho_\downarrow\equiv\langle\downarrow|\rho_f|\downarrow\rangle$, where ρ_f is the density matrix after the final displacement and Ramsey pulses. Furthermore, since we do not measure the motional state, a trace over the motional degrees of freedom is required:

$$P_\downarrow(t)=\mathrm{Tr}_n\rho_\downarrow(t)=\sum_n\langle n|\rho_\downarrow(t)|n\rangle. \tag{64}$$

The quantity $\rho_\downarrow$ is given by

$$\rho_\downarrow(t)=\rho_\downarrow^{(1)}(t)+\rho_\downarrow^{(2)}(t)+\rho_\downarrow^{(3)}(t)+\rho_\downarrow^{(4)}(t) \tag{65}$$

with

$$\rho_\downarrow^{(1)}(t)=\frac{1}{4}\mathcal{D}(\alpha_\downarrow e^{-i\theta})\mathcal{D}(\bar{\alpha}_\downarrow)\rho_T(t)\mathcal{D}^\dagger(\bar{\alpha}_\downarrow)\mathcal{D}^\dagger(\alpha_\downarrow e^{-i\theta}), \tag{66}$$

$$\rho_\downarrow^{(2)}(t)=\frac{1}{4}\mathcal{D}(\alpha_\uparrow e^{-i\theta})\mathcal{D}(\bar{\alpha}_\uparrow)\rho_T(t)\mathcal{D}^\dagger(\bar{\alpha}_\uparrow)\mathcal{D}^\dagger(\alpha_\uparrow e^{-i\theta}), \tag{67}$$

$$\rho_\downarrow^{(3)}(t)=-\frac{1}{4}e^{i\delta}\langle\alpha_\uparrow|\alpha_\downarrow\rangle^{1-[e^{-\gamma t}/1+2N(t)]}\mathcal{D}(\alpha_\downarrow e^{-i\theta})\times\mathcal{D}(\bar{\alpha}_\downarrow)\rho_T(t)\mathcal{D}^\dagger(\bar{\alpha}_\uparrow)\mathcal{D}^\dagger(\alpha_\uparrow e^{-i\theta}), \tag{68}$$

$$\rho_\downarrow^{(4)}(t)=[\rho_\downarrow^{(3)}(t)]^\dagger. \tag{69}$$

In what follows, we assume that $\alpha_{\downarrow,\uparrow}$ are real. Performing the trace, we find that $\mathrm{Tr}_n\rho_\downarrow^{(1)}=\mathrm{Tr}_n\rho_\downarrow^{(2)}=1/4$ and that $\mathrm{Tr}_n\rho_\downarrow^{(3,4)}$ gives rise to the interference. Using the identity

$$\mathcal{D}(\kappa)\mathcal{D}(\lambda)=e^{\frac{1}{2}(\kappa\lambda^*-\kappa^*\lambda)}\mathcal{D}(\kappa+\lambda), \tag{70}$$

substituting for ρ_T from Eq. (17) and using the closure relation $\Sigma_m|m\rangle\langle m|=1$,

$$\mathrm{Tr}_n\rho_\downarrow^{(3)}(t)=\frac{1}{1+N(t)}e^{i(\alpha_\uparrow-\alpha_\downarrow)(\bar{\alpha}_\downarrow+\bar{\alpha}_\uparrow)\sin\theta}\times\sum_m\left(\frac{N(t)}{1+N(t)}\right)^m\mathcal{L}_m(|\beta|^2)e^{-\frac{1}{2}|\beta|^2}, \tag{71}$$

where $\beta=\alpha_\uparrow e^{-i\theta}+\bar{\alpha}_\uparrow-\alpha_\downarrow e^{-i\theta}-\bar{\alpha}_\downarrow$ and $\mathcal{L}$ is a Laguerre polynomial which comes from $\langle m|\mathcal{D}(\kappa)|m\rangle=\exp(-|\kappa|^2/2)\mathcal{L}_m(|\kappa|^2)$. Using $\Sigma_m\epsilon^m\mathcal{L}_m(x)=(1-\epsilon)^{-1}\exp[-\epsilon x/(1-\epsilon)]$ and further simplifying,

$$P_\downarrow(t)=\frac{1}{2}-\frac{1}{2}e^{-(\alpha_\downarrow-\alpha_\uparrow)^2[1+\bar{n}(1-e^{-\gamma t})+e^{-\gamma t/2}\cos\theta]}\times\cos[\delta+e^{-\gamma t/2}(\alpha_\uparrow^2-\alpha_\downarrow^2)\sin\theta]. \tag{72}$$

For all of our experiments we can consider the high-temperature, short-time limits: $\bar{n}\gg1$ and $\gamma t\ll1$. In this limit,

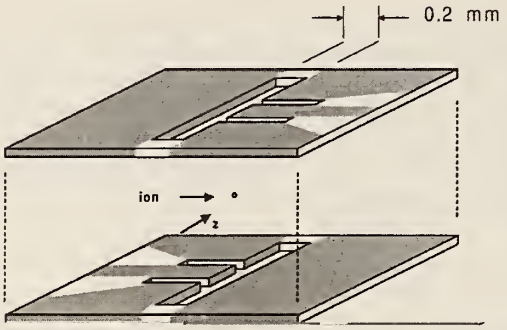

FIG. 4. Schematic diagram of the electrodes of the linear trap (not to scale). The trap electrodes are formed by evaporating gold onto alumina substrates. The outer segmented electrodes are the endcaps, while the long unbroken electrodes carry rf. The axial ($\hat{z}$) direction is parallel to the rf electrode. The two separate trap wafers are separated by 200 μm with alumina spacers (not shown).

$$P_{\downarrow}(t)=\frac{1}{2}\{1-e^{-(\alpha_{\downarrow}-\alpha_{\uparrow})^2[1+\bar{n}\gamma t+\cos\theta]} \times\cos[\delta+(1-\gamma t/2)(\alpha_{\uparrow}^2-\alpha_{\downarrow}^2)\sin\theta]\}. \quad (73)$$

Normally, the second displacement is the reverse of the first ($\theta=\pi$) and the Ramsey fringes in Eq. (33) are recovered with the association $\bar{n}\gamma t\rightarrow 2\sigma^2$. The scaling with the square of the size of the initial state is evident. The constant term in the exponential measures a residual overlap between the initial state and the final state, present even in the infinite time limit.

Similar procedures to this for other types of initial states and reservoirs yield results that agree with those from the interferometer averaging over random displacements/phases approach given in Sec. II B.

III. EXPERIMENT

A. Ion trap

We use a miniaturized version of the linear Paul trap [21]. A diagram of the trap structure is shown in Fig. 4. It consists of two alumina wafers separated by 200 μm with alumina spacers (not shown). Each wafer has a slot 2 mm long by 200 μm wide. Gold is deposited onto the edges of the slot to form electrodes. One side of the slot is the rf electrode, and the other side is divided into three segments to which different static potentials are applied to make a static well along the z axis. The segmented electrodes are formed by cutting two side slots of width 20 μm. The side slots are separated by 200 μm, forming two "endcaps" and one "middle" electrode. When the wafers are sandwiched together with the spacers, the four interior edges of the main slots approximate the four wires of a linear quadrupole trap. The microfabricated structure described here allows miniaturization of the linear trap and correspondingly high-trap strength.

The linear trap is mounted at the end of an rf quarter-wave coaxial resonator that supplies the required rf voltage [22]. The trap and coaxial resonator are contained within an UHV enclosure, as in Ref. [22]. The two rf electrodes are connected to the tip of the coaxial center conductor. Each of the static-potential segments are connected to UHV feedthroughs through a pair of 200 kHz RC low-pass filters in series. The coaxial resonator is 30 cm long and partially filled with alumina to lower its resonance frequency to $\Omega_T/2\pi=113$ MHz. With 8 W of rf power, the radial secular frequencies are approximately 13 MHz. The axial potential is controlled by the static potentials applied to the segmented electrodes. Positive potentials are applied to the endcaps to confine positive ions in the middle of the trap. For the data presented in this paper, we restrict our attention to the axial mode of motion. With 30 V applied to the endcap segments and the middle segments and rf electrodes held at static ground potential, the axial frequency is $\omega_z/2\pi=11.3$ MHz.

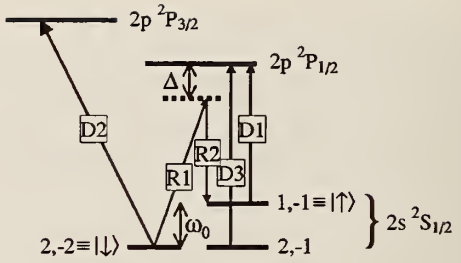

FIG. 5. Simplified level diagram of $^9Be^+$ (not to scale). The transitions labeled D are: D1: optical pumping (also called red Doppler), D2: detection/cooling, D3: repumping. The transitions labeled R are the two arms of the two-photon stimulated-Raman transition. Δ is the detuning between the $2p\ ^2P_{1/2}$ and the Raman virtual level and $\omega_0/2\pi=1.25$ GHz is the $2s\ ^2S_{1/2}$ hyperfine splitting. The fine-structure splitting of the P state is 197 GHz. The transition wavelength from the S to P state is 313 nm.

B. Raman transitions and cooling the ion

The level structure of $^9Be^+$ is shown in Fig. 5. We select two states from the ground-state hyperfine manifold: the $|F=2,m_F=-2\rangle$ state, which we label $|\downarrow\rangle$, and the $|F=1,m_F=-1\rangle$ state, which we label $|\uparrow\rangle$. The ion is Doppler cooled by applying circularly polarized light detuned ~ 8 MHz below the strongly-allowed ($\Gamma/2\pi=19$ MHz) cycling transition $2s\ ^2S_{1/2}|2,-2\rangle\rightarrow 2p\ ^2P_{3/2}|3,-3\rangle$ (beam D2 of Fig. 5). Due to imperfect σ^- polarization the ion optically pumps to the $|1,-1\rangle$ state with a probability $\sim 1\times 10^{-4}$. To prevent a loss of cooling from these decay events, we apply laser light resonant with the transition $2s\ ^2S_{1/2}|1,-1\rangle\rightarrow 2p\ ^2P_{1/2}|2,-2\rangle$. This transition is labeled D1 in Fig. 5. After Doppler cooling, the mean occupation number of the axial mode of motion is $\langle n\rangle\approx 1$.

We efficiently detect (Fig. 6) the $|\downarrow\rangle$ internal state of the ion by applying Doppler beam D2 with no D1 light [18]. The fluorescence collection system has a $f/1.2$ aperture, and the light is transferred onto the photocathode of a photomultiplier tube (PMT). The PMT quantum efficiency is $\approx 30\%$. After all losses at windows and filters, the overall scattered-photon detection efficiency is measured to be $\approx 1.5\times 10^{-3}$. For detection, the laser is at the same detuning as for Doppler cooling and the intensity is kept well below saturation $I\sim 0.1 I_{\rm sat}$. During a 200-μs-detection period, we collect an

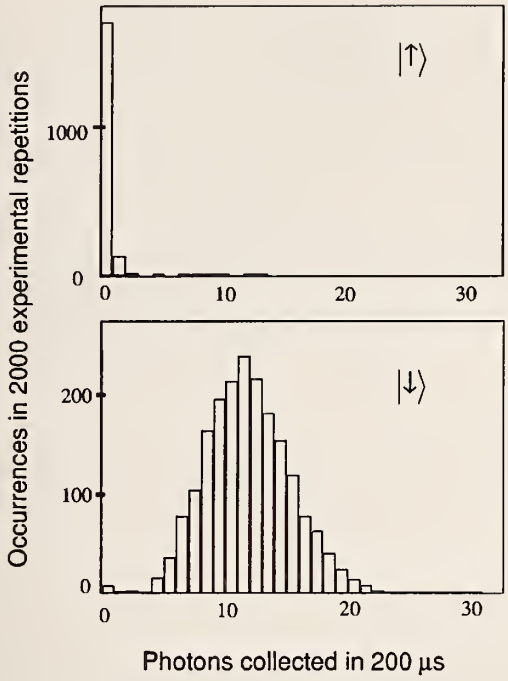

FIG. 6. Detection efficiency. The graphs show histograms of photons collected in a 200 μs interval for 2000 repetitions of the experiment for the two initial states $|\downarrow\rangle$ and $|\uparrow\rangle$. Note that if a discriminator were placed at the bin associated with $n=3$ photons, then, *on a per experiment basis*, the state of the ion would be distinguishable with a 97% quantum efficiency.

average of 10 photons if the ion is in the $|\downarrow\rangle$ state, and 0.1 photons if it is in the $|\uparrow\rangle$ state. The photon distributions are Poissonian. By averaging the number of photons detected in successive repetitions of a given experiment and normalizing to the count rate when the ion is prepared in a control experiment in the $|\downarrow\rangle$ state (by simple optical pumping), we determine the probability $P_{\downarrow}$.

In previous experiments using miniature spherical quadrupole ion traps (see e.g., Ref. [24]), ion internal state discrimination was limited by sidebands on the $2s\ ^2S_{1/2}F=1 \rightarrow 2p\ ^2P_{1/2}$, $F=2$ transition due to ion micromotion at frequency Ω_T. Thus a laser tuned to transition D2 would weakly drive an ion in the $|\uparrow\rangle$ state. The miniature linear trap addresses the issue of micromotion in two ways. First, there is negligible micromotion associated with the confinement along the axis of the trap. Second, the close proximity of the static-potential electrodes permits accurate cancellation of stray static fields, resulting in negligible sidebands on the transitions from micromotion. This permits state discrimination of 97% in a single experiment. This is shown in Fig. 6. Even in the absence of micromotion, detection efficiency is limited by off-resonant optical pumping of the $|\uparrow\rangle$ state by the detection laser [23].

We drive coherent stimulated Raman transitions with a pair of laser beams (such as R1 and R2 shown in Fig. 5) detuned $\Delta/2\pi \approx 10$ to 20 GHz from the $2s\ ^2S_{1/2} \rightarrow 2p\ ^2P_{1/2}$ transition near $\lambda = 313$ nm. The Raman beams are derived from a single dye laser beam that is frequency doubled, and the difference frequency between the two Raman beams is generated with several acousto-optic modulators in series. We employ three types of Raman transitions, distinguished by beam geometry and difference frequency [16,25]. The beam geometry sets the projection of photon momentum onto the axis of the trap ($\hat{z}$), characterized by the wave vector difference $\delta k = (\mathbf{k}_1 - \mathbf{k}_2)\cdot\hat{z}$. The coupling of this photon momentum to the motion of the ion is parametrized by the Lamb-Dicke parameter $\eta = \delta k\, z_0$, where $z_0 = \sqrt{\hbar/2m\omega} \approx 7$ nm is the harmonic-oscillator characteristic length for axial motion.

The three types of Raman transitions are as follows. (i) Copropagating beams ($\delta k \approx 0$) drive a motion-independent "spin-flip" transition, $|\uparrow\rangle|n\rangle \leftrightarrow |\downarrow\rangle|n\rangle$. The frequency difference between the Raman beams is set equal to the frequency difference between the states, $\omega_0 = \omega_{hf} + \omega_Z$, where $\omega_{hf}/2\pi \approx 1.25$ GHz is the hyperfine splitting and $\omega_Z/2\pi \approx 12$ MHz is the Zeeman splitting due to an applied magnetic field $|\mathbf{B}| \approx 0.57$ mT. (ii) Beams oriented 45° to the trap axis and 90° to each other result in a wave vector difference pointing along the trap axis with $\delta k = 2\sqrt{2}\pi/\lambda$ and couple to the axial motion. For the conditions of this experiment, $\eta \approx 0.20$. These beams at difference frequencies $\omega_0 + \omega\Delta n$, couple the states $|\downarrow\rangle|n\rangle$ and $|\uparrow\rangle|n+\Delta n\rangle$. In the Lamb-Dicke limit, ($\eta^2\langle n\rangle \ll 1$), the strength of the sideband coupling is proportional to $\eta^{|\Delta n|}$. The Raman beams in cases (i) and (ii) are linearly polarized, with one beam polarized parallel to the quantization axis ($\Delta m = 0$) and the other polarized perpendicular ($\Delta m = \pm 1$). Note that only the σ^- component of the latter beam is required to drive the Raman transition, but the use of linear polarized light reduces the Stark shifts relative to the case of using circularly polarized light. (iii) Beams oriented as in (ii), with difference frequency set equal to the axial secular motion frequency ω approximate the harmonic-oscillator displacement operator $\mathcal{D}(\alpha)$, defined by the relation $\mathcal{D}(\alpha)|0\rangle = |\alpha\rangle$, and $|\alpha\rangle$ is a coherent state. In the Lamb-Dicke limit, the displacement $|\alpha| = \eta\Omega_{\mathcal{D}}t$ is proportional to the duration of the laser pulse t and the Rabi frequency $\Omega_{\mathcal{D}}$, and θ is set by the phase and polarization of the applied laser fields. In this case, the two Raman beams are linearly polarized such that the polarization vectors are mutually orthogonal to both each other and to the quantization axis. This cancels Stark shifts to a high degree and results in the two spin states being simultaneously displaced in opposite directions such that $\alpha_{\uparrow} = -\alpha_{\downarrow}/2$.

The ion is first prepared in the ground state of motion with resolved sideband Raman cooling [18]. Raman cooling consists of repeatedly driving the first red-Raman sideband of the axial-motion-sensitive transition, case (ii) with $\Delta n = -1$, followed by optical pumping to the $|\downarrow\rangle$ state after each Raman pulse. The optical pumping is achieved by applying beams D1 and D3 (see Fig. 5). The rate at which the ion undergoes the red sideband Raman transition depends on the initial state of motion as $\Omega_{\mathrm{rsb}} \propto \sqrt{n}$. The duration of the successive Raman pulses is progressively lengthened, so as to successively drive π pulses on the $n_i \rightarrow n_i - 1, n_i - 1 \rightarrow n_i - 2$, etc., transitions, where n_i is the total number of cooling pulses. The final pulse of this sequence is selected to drive a π pulse on the $|\downarrow\rangle|1\rangle \rightarrow |\uparrow\rangle|0\rangle$ transition. After each Raman

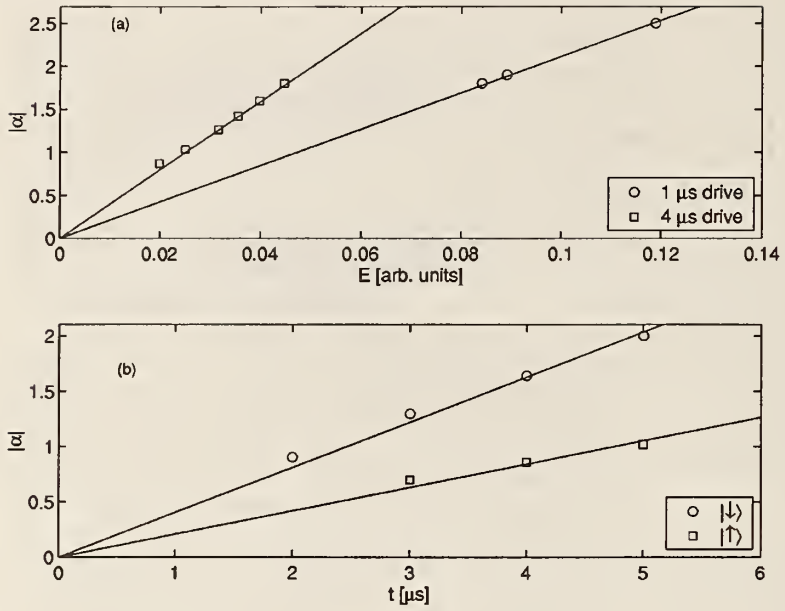

FIG. 7. Calibration of displacement amplitude for (a) uniform electric-field drive and (b) laser drive. The y axis is in terms of the coherent-state amplitude α, determined as described in the text.

pulse, we drive the $D1$ and $D3$ transitions for 5 μs, optically pumping any population in the $|\uparrow\rangle$ state, or the $(2,-1)$ state to the $|\downarrow\rangle$ state. Typically, after 6 cycles of Raman cooling, the ion has a probability of 95% to be in the ground state $|\downarrow\rangle|0\rangle$.

C. Ion interferometry: techniques

In the experiments reported here, we measure the coherence of quantum superpositions with single-atom interferometry, analogous to that used in our previous work [10] and discussed in Sec. II B. The motional state of the ion is split into a superposition of two parts. The "beam splitters" of our interferometers consist of a pair of stimulated Raman pulses. We employ two types of interferometers, both discussed in Sec. II B.

1. Ion interferometry: Cat states

The Schrödinger-cat interferometer starts with the usual ground-state ($|\downarrow\rangle|0\rangle$) preparation. The first pulse is then a $\pi/2$ pulse on the motion-independent transition (i), with drive time typically $T_{\pi/2}\approx 0.3$ μs, which generates an equal spin superposition, $|\downarrow\rangle|0\rangle\rightarrow(|\downarrow\rangle+|\uparrow\rangle)|0\rangle/\sqrt{2}$ as indicated schematically in Fig. 1, panel (1).

We drive Raman transition (iii) to excite the motion associated with each spin state into a coherent state, resulting in the state of Eq. (25). We call this the displacement pulse [Fig. 1, panel (2)]. We vary the length of the Raman drive pulse in order to vary $|\alpha_\downarrow|$ and $|\alpha_\uparrow|$. We independently measure $|\alpha_\downarrow|$ and $|\alpha_\uparrow|$ in the following manner [17] [which is also discussed in the context of Eqs. (85) and (86), below]. The ion is prepared in a coherent state, and then Raman transition (ii), tuned to the first blue sideband, is driven for a variable time t_p. After this "probe" Raman transition, we determine the probability $P_\downarrow(t_p)$. The resulting curve may be decomposed into sums of sinusoids that correspond to $\Delta n = 1$ transitions between Fock states. The Fock state distribution is then fit to that of a coherent state, thereby extracting $|\alpha|$ [17]. The values of $|\alpha_\downarrow|$ and $|\alpha_\uparrow|$ are measured separately, by preparing the ion in either the $|\downarrow\rangle|0\rangle$ state or in the $|\uparrow\rangle|0\rangle$ state, applying the coherent drive pulse, and then probing and detecting as just described. Curves of $|\alpha_{\downarrow,\uparrow}|$ vs the length t of the displacement pulse are shown in Fig. 7(b). The ratio $|\alpha_\downarrow|/|\alpha_\uparrow|=2.0\pm0.1$, averaged over the data set, is consistent with the expected value of 2. The slope $d|\Delta\alpha|/dt=\eta\Omega$ is consistent with the expected value.

The Schrödinger-cat interferometer is completed by applying a second coherent displacement pulse 180° out of phase from the first displacement pulse [Fig. 1, panel (4)]. The phase of the displacement is set by the phase of an oscillator that drives an acousto-optic modulator that is in one of the Raman beams. All phases are referenced to a master oscillator by phase locking to that oscillator. If the motion was unperturbed during the time between the displacement pulses, then the inverse displacement would restore the motion associated with each spin state to the ground state of motion. The wave function would return to $|\psi\rangle=(|\downarrow\rangle+|\uparrow\rangle)|0\rangle/\sqrt{2}$. A second $\pi/2$ pulse on the motion-independent spin-flip transition, with phase δ relative to the first $\pi/2$ pulse, interferes with the spin components. The probability $P_\downarrow(\delta)$ varies sinusoidally with δ. To record $P_\downarrow(\delta)$, we step the frequency of the oscillator controlling the $\pi/2$ pulses and bin the fluorescence counts at each step. Here, δ is the accumulated phase difference caused by the frequency difference between the oscillator frequency ν and ν_0 as in normal Ramsey spectroscopy. We typically repeat the experiment 100 times at each step. Note that the resulting fringe spacing is much smaller than the width of the Rabi pedestal, meaning that the predominant effect is a change in phase, without introducing significant inaccuracy in the $\pi/2$ pulse. We typically record three oscillations of $P_\downarrow$. The fringes are fit with a sinusoid $A+B\cos(\omega-\omega_0)T$, where T is the time between spin pulses. The contrast of the fringes is

defined as B/A. For the basic interferometer just described, with no perturbations of the motion between the "beam splitter" pulses, the contrast is typically 0.6–0.8. This contrast differs from unity for several reasons. (1) Errors in the $\pi/2$ spin-flip pulses, primarily due to laser power fluctuations. (2) Fluctuating magnetic fields that reduce the spin coherence through fluctuating Zeeman shifts. (3) Motional heating during and between the displacement pulses, with further small contributions due to inaccuracies in reversing the initial displacement pulse. These effects are expected to be random and should not influence the additional decoherence caused by the applied reservoir (see Sec. II C).

2. Interferometry: Fock state interferometer

The Fock state interferometer beam splitters combine a $\pi/2$ pulse with a π pulse on transitions of either type (i) or (ii), as shown in Table I. As an example, consider the generation of the superposition $|\downarrow\rangle(|0\rangle+|2\rangle)/\sqrt{2}$. A $\pi/2$-pulse on the first blue sideband, transition type (ii) with $\Delta n=+1$ and duration $T_{\pi/2}\approx 1$ μs, drives the transition $|\downarrow\rangle|0\rangle \rightarrow(|\downarrow\rangle|0\rangle+|\uparrow\rangle|1\rangle)/\sqrt{2}$. A π pulse on the first red sideband, transition type (ii) with $\Delta n=-1$ and duration $T_{\pi}\approx 1.5$ μs, drives the transition $|\uparrow\rangle|1\rangle\rightarrow|\downarrow\rangle|2\rangle$. This second pulse does not affect the population in the $|\downarrow\rangle|0\rangle$ state. The result of these two pulses is the desired state $|\psi\rangle=|\downarrow\rangle(|0\rangle+|2\rangle)/\sqrt{2}$. The second beam splitter recombines the two parts of the wave function by driving a second π pulse on the red sideband followed by a $\pi/2$ pulse on the blue sideband. By sweeping the frequency of the blue sideband oscillator we generate Ramsey fringes in the probability $P_{\downarrow}$. Contrast (without coupling to the reservoir) is limited by the same mechanisms as in the Schrödinger-cat interferometer.

D. Engineering reservoirs: techniques

1. High-temperature amplitude reservoir

As discussed in the Introduction, the motion of a trapped ion couples to environmental electric fields $\mathbf{E}$ through the potential $U=-q\mathbf{x}\cdot\mathbf{E}$, where $\mathbf{x}$ is the position of the ion relative to its equilibrium position (proportional to the amplitude of motion) and q is the charge of the ion. If $\mathbf{E}$ is due to a reservoir of fluctuating field modes, then $\mathbf{E}\propto\Sigma_i\boldsymbol{\epsilon}_i(\hat{b}_i+\hat{b}_i^{\dagger})$, where $\hat{b}_i$, $\hat{b}_i^{\dagger}$ are the lowering and raising operators of the field modes (as in Sec. II A 1). A classical coherent drive (for which $\mathbf{E}$ is a narrow-band sine-wave) applied to the trap electrodes at the ion axial motional frequency ω results in a displacement of the motional state proportional to the size and duration of the applied field. This is shown in Fig. 7(a) for two different durations of the applied field. We simulate the effects of the high-temperature amplitude reservoir discussed in Sec. II A 1 by applying *random* electric fields along the axis of the trap, whose spectrum is centered on the ion axial motion frequency ω.

To generate the required axial fields, we apply a potential to one of the endcap electrodes. This generates both an axial field and a small radial field. We ignore the effect of the radial field since we are insensitive to motion in the radial direction. This field also modulates the axial potential and gives rise to an accompanying (random) phase shift; however, for the experimental conditions this phase shift is negligible. We start with a 10 MHz bandwidth noise source that rolls off at 6 dB/octave starting at 10 MHz. We filter the noise such that the resulting noise spectrum has 3 dB points at 9 MHz and 11.5 MHz, and the noise rolls off at 6 dB/octave above and below these points. This spectral noise is applied to the trap electrodes through a network of RC low-pass filters designed to prevent such fields from reaching the static trap electrodes. The filters effectively limit ambient noise from reaching the electrodes, but large deliberately applied fields can still be effective. The noise is applied for 3 μs between the Ramsey zones. The total time for the Ramsey experiment (the time between the $\pi/2$ spin-pulses) is about $T=20$ μs and is held fixed. For these filters, trap geometry and application time, it can be shown that this type of drive correctly simulates an infinite-bandwidth, amplitude-only reservoir.

2. Phase reservoir

A phase reservoir, as described in Sec. II A 2, is simulated by random variations in the trap frequency ω, changing the phase of the ion oscillation without changing its energy. We realize this coupling experimentally by adiabatically modulating the trap frequency. The random potential fluctuations are filtered through a low-pass network with a cutoff frequency well below ω to maintain adiabaticity and to avoid any power at the trap secular frequency, which may cause amplitude noise. The potential fluctuations are applied to one of the middle electrodes, which is symmetric with respect to the axial direction, so as to produce field gradients and minimize any applied uniform axial fields further reducing the possibility of changing the motional energy. Applying a potential to just one middle electrode does result in a radial field, but as before, we isolate the axial motion and ignore any radial motion.

In the phase reservoir, the ion follows the change in trap frequency in the sense that there is no change in the energy of the trap motion, however the phase is either advanced or retarded relative to the unperturbed motion. We start with a 10 MHz pseudorandom noise source and filter the noise, creating a spectrum that is flat between 1 kHz and 100 kHz with a roll-off of 12 dB/octave above 100 kHz and 6 dB/octave below 1 kHz. The phase deviation of the ion motion is related to the voltage deviation on the electrodes. The trap axial frequency is related to the voltage difference between the endcap and middle segments by the relation $\omega_z\propto\sqrt{V_0}$. The deviation of the trap frequency is given by $\delta\omega/\omega_z \approx \delta V/4V_0$ since only one electrode is driven. The phase shift of the ion motion is the integral of the frequency deviation over the time of the noise pulse T_n, $\delta\phi\equiv\int_0^{T_n}\delta\omega_z dt =\int_0^{T_n}\omega_z(\delta V/4V_0)dt$. Typically $T_n=10$ μs. We cannot directly measure the voltage on the trap electrodes since some of the filters between our noise generator and the electrodes are within the vacuum enclosure. However, on a mock up of the trap electrodes and the associated filters, we measured the voltage deviations with an integrating circuit. These measurements verified that the phase deviations are Gaussian

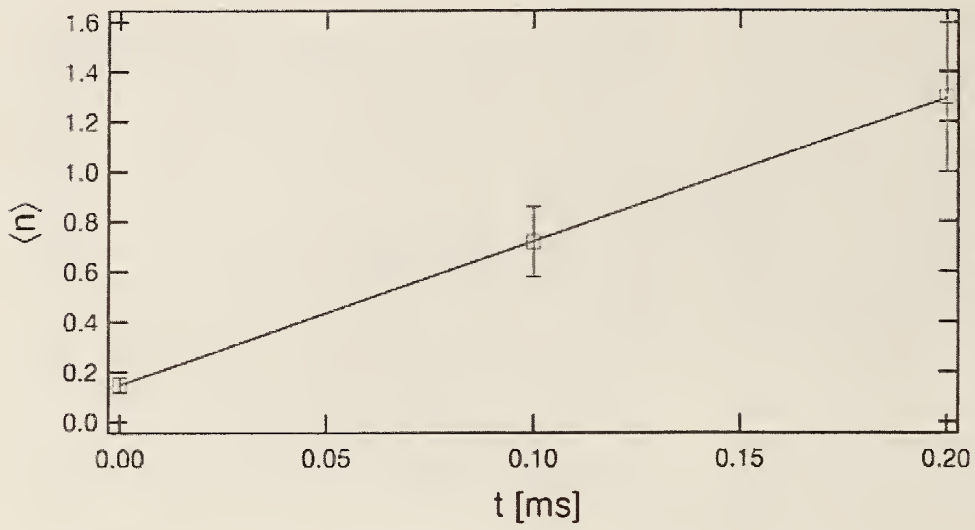

FIG. 8. (Color) Heating of the motional state. At $t=0$ the ion is prepared in a state near the ground state $|0\rangle$. As time passes, the ion heats out of the ground state, as measured by the energy in the motional state, which is proportional to the average occupation number $\langle n\rangle$.

distributed, with a width that varies with the applied noise voltage, and that negligible voltage noise is added at the trap secular frequency. In separate experiments, we verified that the change in motional energy was negligible during the application of the phase reservoir.

3. Natural reservoir

The third type of reservoir is not engineered, but is the ambient, or "natural" noise in our trap. We have previously observed heating in miniaturized Paul traps [26]. We have further determined that this ambient noise is dominated by uniform field fluctuations rather than field-gradient fluctuations [27]. We do not currently have an explanation of the heating mechanism. However, thermal or Johnson noise, background gas collisions, and several other sources are too small to explain the heating rate. We do know that this ambient noise source adds energy to the ion (amplitude noise), and that the state of the ion evolves into a thermal state with steadily increasing temperature. The suspected cause is fluctuating patch potentials at the trap electrodes, a problem that is exacerbated by the small size of our trap [26]. To observe the effects of this heating on quantum coherences, we simply run the Ramsey interferometer experiment with varying time between the Ramsey pulses.

We can also observe the effect of the heating on the energy of the motional state. We find that due to our unknown environmental source of noisy electric fields, the ion heats from the ground state at a rate linear in time with $\partial\langle n\rangle/\partial t \sim 5.7\pm 1$ quanta per ms. Shown in Fig. 8 are data for the mean quantum number in the motion as a function of delay time. That is, the ground state is prepared and the average quantum number is measured after a fixed delay time t. At each point the motional state is thermal as determined by the method of Refs. [17] and [26].

4. Zero-temperature reservoir

The fourth type of engineered reservoir was a zero-temperature reservoir realized by laser cooling. Some theoretical results for this reservoir were mentioned briefly in Sec. II A 1a. The experimental scheme is outlined in Fig. 9 and follows a proposal by Poyatos *et al.* [28]. The goal is to simulate decay of the states $|\downarrow\rangle|n\rangle$ into a $T=0$ reservoir. To do this, we simultaneously drive on the first red sideband transitions $|\downarrow\rangle|n\rangle \rightarrow |\uparrow\rangle|n-1\rangle$ at a Rabi frequency $\Omega_{\rm rsb}$ and the red-Doppler (D1 from Fig. 5) from $|\uparrow\rangle$ to the $P_{1/2}$ level at a rate $\Omega_D (\ll\Gamma)$. This is effectively a continuous Raman

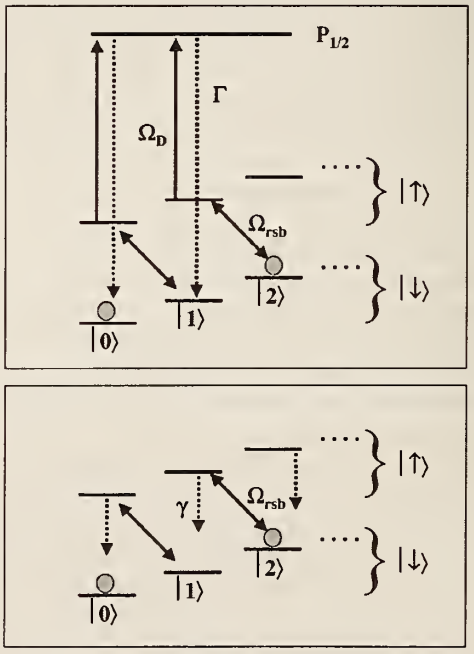

FIG. 9. Engineering a $T=0$ reservoir with laser cooling: schematic diagram of the levels. The top panel shows the full three-(internal) level system (dressed by the motional states), while the bottom panel shows the equivalent two-level system. The red Doppler beam with resonant Rabi frequency Ω_D is used to give the $|\uparrow\rangle$ state an effective linewidth $\gamma \equiv \gamma_{\rm eff} \approx \Omega_D^2/\Gamma$. Simultaneously the red sideband (rsb) is driven coherently at rate $\Omega_{\rm rsb}$ to drive population out of the $|\downarrow\rangle$ state. The sum of the two applied fields simulates a variable bandwidth zero temperature reservoir.

cooling process (in contrast to the stepwise Raman cooling process described at the end of Sec. III B) which eventually relaxes the system to a state in which all population is in the ground state $|0\rangle|\downarrow\rangle$ [29,30]. The $|\uparrow\rangle$ level is given an effective decay rate $\gamma_{\rm eff}\sim\Omega_D^2/\Gamma$. We begin by preparing an initial state $|\downarrow\rangle(|0\rangle+|2\rangle)/\sqrt{2}$. The point of the experiment is to follow the time evolution of the coherence of this state ($\rho_{0\downarrow,2\downarrow}$ as we label the relevant off-diagonal element of the density matrix) as it decoheres during the cooling process. To gain a qualitative understanding of the experiment we can consider a reduced problem, as follows.

We are simulating a $T=0$ reservoir by simultaneously driving (resonantly) on the red sideband and red-Doppler transitions. The red-Doppler drive gives the $|\uparrow\rangle$ state an effective linewidth $\gamma_{\rm eff}$ (see Fig. 9). The system density matrix obeys the following time evolution:

$$\dot{\rho}=i[\rho,H]+\frac{\gamma_{\rm eff}}{2}[2\sigma_-\rho\sigma_+-\sigma_+\sigma_-\rho-\rho\sigma_+\sigma_-] \quad (74)$$

with interaction-picture Hamiltonian

$$H=g(a^\dagger\sigma_-+a\sigma_+), \quad (75)$$

where $g\equiv\Omega_{\rm rsb}$ is the Rabi rate of the red sideband drive (assumed real) and σ_+ (σ_-) is the raising (lowering) operator of the atom. Here we have neglected the effects of recoil heating, valid for $\eta^2\ll 1$. This is simply the master equation for a driven, decaying two-state atom dressed by coupling to a harmonic-oscillator system [familiar to cavity QED as the Jaynes-Cummings model [31] with atomic (but no cavity) decay]. We consider the experiment in which we make an initial state

$$\psi_0=|\downarrow\rangle(|0\rangle+|m\rangle)/\sqrt{2} \quad (76)$$

and we measure the coherence that we call $\rho_{m\downarrow,0\downarrow}$. Equation (74) leads to:

$$\dot{\rho}_{m\downarrow,0\downarrow}=-i\sqrt{m}g\,\rho_{m-1\uparrow,0\downarrow}, \quad (77)$$

$$\dot{\rho}_{m-1\uparrow,0\downarrow}=-i\sqrt{m}g\,\rho_{m\downarrow,0\downarrow}-\frac{\gamma_{\rm eff}}{2}\rho_{m-1\uparrow,0\downarrow}. \quad (78)$$

The solution to this set of differential equations [with initial conditions specified by Eq. (76)] is

$$\rho_{m-1\uparrow,0\downarrow}=\frac{-i\sqrt{m}g}{2(\lambda_+-\lambda_-)}[e^{\lambda_+t}-e^{\lambda_-t}], \quad (79)$$

$$\rho_{m\downarrow,0\downarrow}=\frac{1}{2(\lambda_+-\lambda_-)}\left[\left(\lambda_++\frac{\gamma_{\rm eff}}{2}\right)e^{\lambda_+t}-\left(\lambda_-+\frac{\gamma_{\rm eff}}{2}\right)e^{\lambda_-t}\right] \quad (80)$$

with

$$\lambda_\pm=-\frac{\gamma_{\rm eff}}{4}\pm\frac{1}{2}\sqrt{\frac{\gamma_{\rm eff}^2}{4}-4mg^2}. \quad (81)$$

Consider two limiting cases. In the first $g\gg\gamma_{\rm eff}$, so that $\lambda_\pm$ have an imaginary part. Here the time evolution of the coherence is an exponentially decaying cosine, reflecting the fact that the coherent drive is faster than the decay rate:

$$\rho_{m\downarrow,0\downarrow}(t)\rightarrow\frac{e^{-\gamma_{\rm eff}t/4}}{2}\cos(\sqrt{m}gt). \quad (82)$$

In the second case $g\ll\gamma_{\rm eff}$, so that $\lambda_\pm$ are strictly real. In this case,

$$\rho_{m\downarrow,0\downarrow}(t)\rightarrow\frac{1}{2}\exp\left(-m\frac{2g^2}{\gamma_{\rm eff}}t\right), \quad (83)$$

and we have simple exponential decay of the off-diagonal density-matrix element. It is instructive to compare this to the $T=0$ limit of the amplitude reservoir presented in Sec. II A 1a. From Eq. (11), with $\rho_{om}(0)=1/2$

$$\rho_{0m}=\frac{1}{2}\exp\left(-m\frac{\gamma}{2}t\right). \quad (84)$$

With the identification $\gamma/2\rightarrow 2g^2/\gamma_{\rm eff}$, Eqs. (83) and (84) are identical. This is the anticipated result, since the effective linewidth of the $|\uparrow\rangle$ state is simply the square of the Rabi frequency divided by the bare decay rate, and in the case of the red sideband the Rabi frequency scales as $g\sqrt{m}$.

IV. DATA

To reiterate, the experiments consist of a Ramsey type interferometer experiment in which the ion is coupled to one of the engineered reservoirs between the initial and final "beam splitter" pulses. The experiment proceeds as follows. The ion is first Doppler cooled and then Raman cooled, preparing the ion in the $|\downarrow\rangle|0\rangle$ state. The state preparation pulses are then applied to generate the desired superposition (first beam splitter). A period of time elapses during which the ion is coupled to the reservoir. After this time, we reverse the sequence of pulses used in state preparation (second beam splitter). The resulting internal state of the ion depends on the frequency and phase of the oscillators used in the preparation and reversal pulse sequences. The ion internal state is detected as described in Sec. III B. The contrast of the resulting Ramsey fringes is a measure of the motional state coherence, which decreases with increasing interaction with the reservoir, either in time or in strength (applied voltage noise).

A. Schrödinger-cat decoherence

1. Cat states, applied amplitude noise

The effect of coupling the Schrödinger-cat interferometer to the engineered amplitude reservoir is shown in Fig. 10. The reservoir is simulated by driving particular trap electrodes with a noisy potential V near the trap secular frequency as discussed in Sec. III D 1. The amplitude reservoir

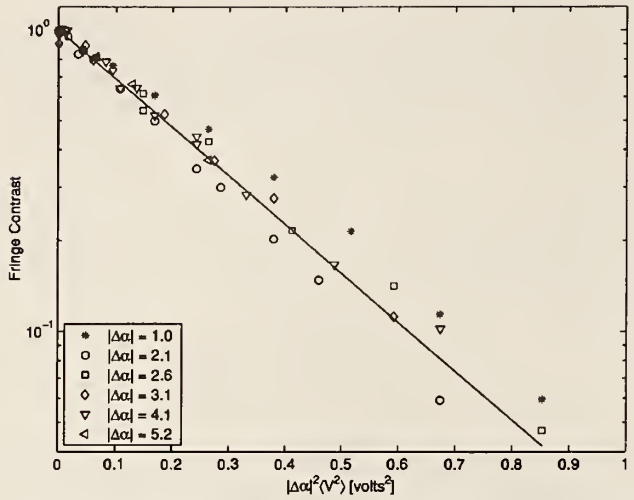

FIG. 10. Decay of Schrödinger-cat state coherences with applied amplitude noise. Note the universal scaling of the states to an exponential with decay constant proportional to $|\Delta\alpha|^2$. The reservoir was applied for 3 μs.

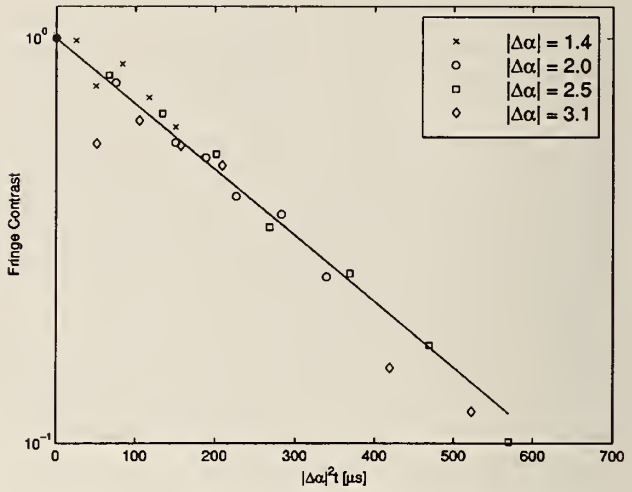

FIG. 11. Decay of Schrödinger-cat state coherences in natural amplitude noise. Note again the universal scaling of the states to an exponential with decay constant proportional to $|\Delta\alpha|^2$, and that the decay constant is the same as that derived from the heating data of Fig. 8. This is discussed further in the text.

is coupled to the ion for 3 μs between the beam splitter pulses of the interferometer. The variance σ^2 of β (Sec. II B 2a) is proportional to the mean-squared voltage noise $\langle V^2\rangle$. Figure 10 shows a plot of the interference fringe contrast as a function of the applied mean-squared voltage, scaled by the squared "size" of the cat state $|\Delta\alpha|^2$. Decay curves were recorded for a variety of superposition sizes $|\Delta\alpha|$, and all the data agree with a single exponential, as in Eq. (33). The initial contrast for each value of $|\Delta\alpha|$ is normalized to unity at $\langle V^2\rangle=0$.

2. Cat states, natural noise

The natural noise that gives rise to the heating described in Sec. III D 3 causes decoherence. For this experiment, we simply wait for some amount of time between the Ramsey zones and measure the fringe contrast as a function of this time. The results are shown in Fig. 11. As in the previous case, the results are consistent with a single exponential. This time, the decay constant has meaning relative to another experimental quantity: it should be the same as that measured for the heating. For example, the mean quantum number in the system is given by Eq. (8), from which γ is interpreted as the heating rate of Sec. III D 3. The decay constant relevant to the decoherence measured in Fig. 11 is given by Eq. (73), with the same coupling constant γ appearing. The measured numbers for γ agree reasonably well. We find a decay rate of $\gamma/2\pi=5.7\pm1$ quanta/ms from the heating data (Fig. 8) and $\gamma/2\pi=7.5\pm0.7$ quanta/ms from the decoherence data (Fig. 11). Discrepancies can easily arise due to variations in heating rate from day to day and other systematic errors that are not included in the error quoted on γ, such as miscalibration of the size of the coherent states $\Delta\alpha$. In addition, there is some spin decoherence during the 80 μs of Ramsey time used for the longest data points (see the discussion of Sec. II C). The contrast is normalized to unity at $t=0$.

3. Cat states, phase noise

Results from coupling of the Schrödinger-cat interferometer to the engineered phase reservoir are shown in Fig. 12. The theory has only one free parameter, which is a scaling to convert voltage noise to phase deviation (see below for a discussion of this). The theory curves are from Eq. (44), all with the same scaling parameter. Note that there is no simple universal scaling law for the functional form of the decoherence as there is in the case of Schrödinger cats subject to amplitude noise. The contrasts at $\langle V^2\rangle=0$ are normalized to unity. The phase noise reservoir is applied for $\sim$10 μs.

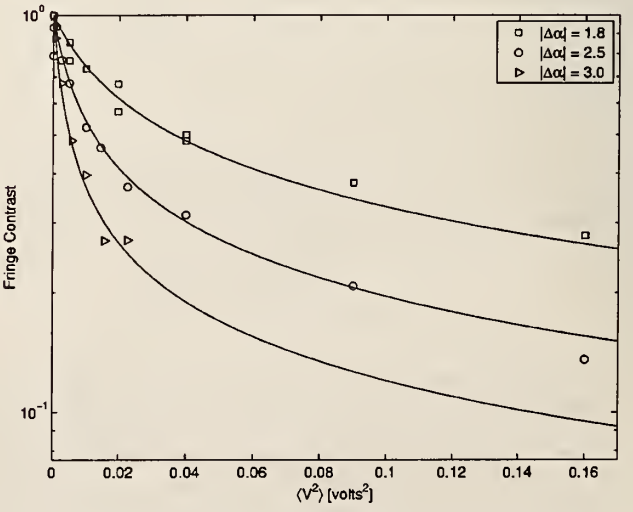

FIG. 12. Decay of Schrödinger-cat state coherences in an applied phase noise reservoir. Several sizes of cats are shown. The reservoir was applied for 20 μs.

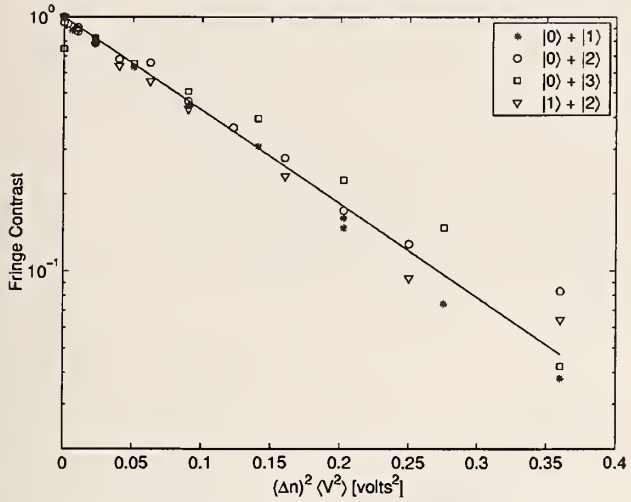

FIG. 13. Decay of Fock state coherences in applied phase noise. Note the universal scaling of the states to an exponential with decay constant proportional to $|\Delta n|^2$. The reservoir was applied for 10 μs.

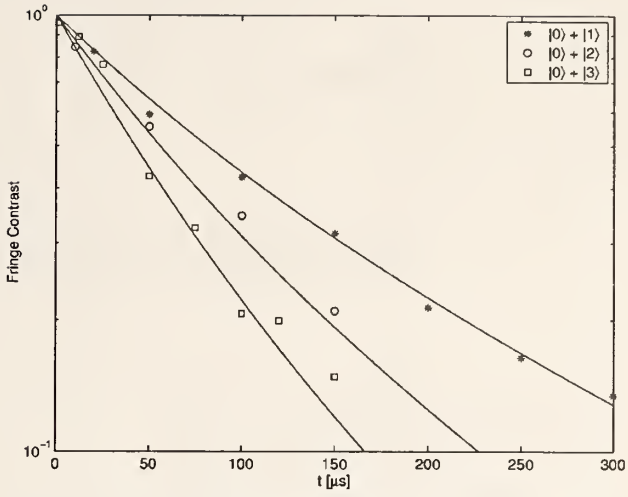

FIG. 14. Decay of Fock state coherences in natural amplitude noise. The theory curves are to the functional form of Eq. (38) with an additional exponential decay to account for spin decoherence. The horizontal scaling is forced to be the same for the three states, and the data are normalized to unit contrast at $t=0$.

B. Decoherence of superpositions of Fock states and decay of Fock states

1. Fock states, phase noise

Coupling the Fock state interferometer to phase noise results in the simple behavior predicted by Eq. (21). This is confirmed in the data of Fig. 13 in which the fringe contrast of the interferometer is measured for different values of the applied phase noise reservoir. The data for different initial Fock state superpositions are scaled by the squared "size" $(\Delta n)^2$ of the superposition in order to show the universal scaling law of Eq. (21). The scaling of the x axis of the graph is a free parameter in the theory. In principle, the size of the noise measured in radians could be known from the variance of the applied noise $\langle V^2 \rangle$. However, in practice, unknown geometrical factors in converting voltage on a subset of the trap electrodes to change in trap secular frequency, prevents a direct comparison. A rough estimate, nonetheless, gives a correspondence of about π radians of phase noise at 0.1 V^2, which is in rough agreement with the fit parameters from the data. The voltage noise was applied for a 10 μs interval.

2. Fock states, amplitude noise: decoherence and decay

The coupling of superpositions of two Fock states to an amplitude reservoir is particularly relevant to quantum logic with trapped ions: Fock state superpositions are generated during quantum logic gates, and the natural decoherence is due to coupling to a hot thermal amplitude reservoir. Decoherence of superpositions of Fock states and heating (decay) of Fock states limit the fidelity of quantum operations.

a. Decoherence. To simplify analysis, we restricted our attention to superpositions of the form $(|0\rangle+|n\rangle)/\sqrt{2}$ in which Eq. (38) in Sec. II B 2b applies to a good approximation. Data for $n=1,2$, and 3 are shown in Fig. 14, where the amplitude reservoir is the natural noise on the trap electrodes discussed in Sec. III D 3. Using Eq. (38) the fits F_n for states $(|0\rangle+|n\rangle)/\sqrt{2}$ are given by $F_n=\exp(-\gamma_s t)/(1+s_n t)^{1+n}$ with s_n the scaling factor forced to be the same for all n. The exponential decay accounts for the loss of spin coherence due, for example, to fluctuating magnetic fields, with $\gamma_s/2\pi \sim 0.01\ \mu\text{s}^{-1}$. The best overall fit to the data gives $s_n=5$/ms, which is consistent with the decay rates quoted in Sec. IV A 2.

b. Decay of populations; purity and entropy. In order to study this case more completely, we performed measurements directly on the populations (diagonal elements of the system density matrix). Starting from a Fock state $|n\rangle$, we applied the amplitude reservoir and observed the evolution of the system. The procedure was as follows. We generated the state $|n\rangle$ [17], waited a time t, during which the Fock state $|n\rangle$ would evolve to a distribution over Fock states $\{|n'\rangle\}$. We then drove transitions on the blue sideband (bsb) for various Raman probe times t_p. Following this, $P_\downarrow$ was measured from the fluorescence signal. The resulting signal has contributions from all possible transitions $|\downarrow\rangle|n'\rangle \rightarrow|\uparrow\rangle|n'+1\rangle$, each of which is at a well-defined frequency. The bsb curve thus generated is described by:

$$P_\downarrow(t_p)=\frac{1}{2}+\sum_n \frac{1}{2}P_n[\cos(2\Omega_j t_p)e^{-\gamma_n t_p}] \qquad (85)$$

with the Rabi frequency given by

$$\Omega_n=|\langle n|e^{-i\eta(a+a^\dagger)}|n+1\rangle|=\Omega_0 e^{-\eta^2/2}(n+1)^{-1/2}\eta\mathcal{L}_n^1(\eta^2), \qquad (86)$$

where $\mathcal{L}$ are Laguerre polynomials. The phenomenological decay rate $\gamma_n=-(n+1)^{0.7}\gamma_0$ is used to model decay in the data due to Raman beam intensity fluctuations and other sources [17]. We perform a singular value decomposition (svd) [32] on the data to extract the populations P_n of the various $|n\rangle$-states at the end of the reservoir application time t. The time evolution of the populations is shown in Fig. 15

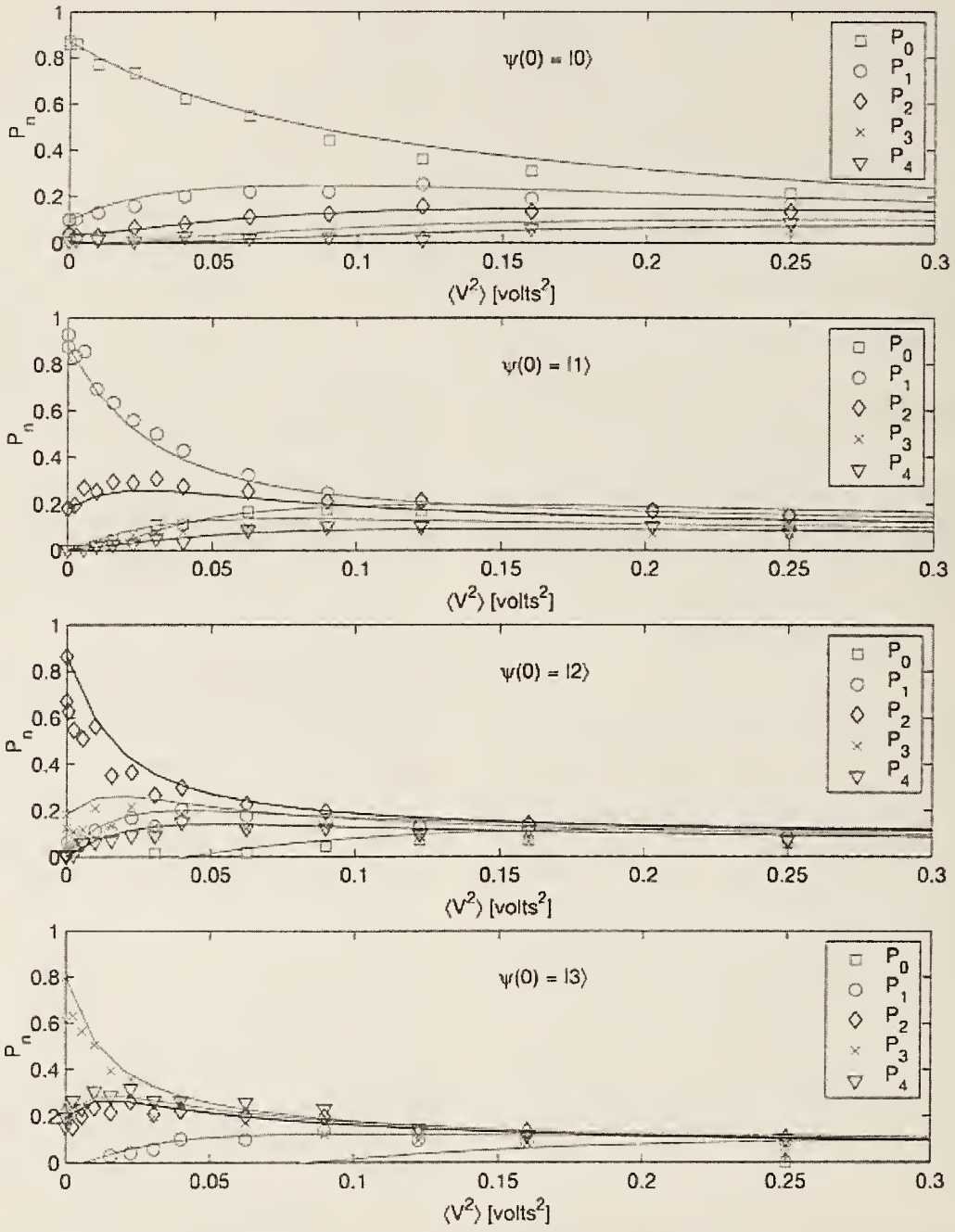

FIG. 15. (Color) Decay of Fock states in a hot amplitude reservoir. Each graph shows the time evolution of the populations P_n in state $|n\rangle$ of the motional state for an experiment starting in the initial state $\psi(0)$ indicated. [The initial states are not perfectly generated, as can be seen by $P_n(0)$.] The populations are given in Eq. (10), from which the solid lines are derived.

for different initial starting states $\psi(0)=|n_0\rangle$. The theory curves are given in Eq. (10) which describe the evolution of the diagonals of the density matrix. From these data, the expected qualitative effects are evident. The theory for all the data of Fig. 15 has only a single free parameter, which is the scaling of the x axis. Additionally, we use the svd populations from the initial experimental state for the initial state of the calculations [$\rho_{nn}(0)$ from Eq. (10)].

An interesting way to further quantify the progression to thermal equilibrium of the system is via the purity and entropy of the (mixed) states. The time evolution of the purity is shown in Fig. 16 and of the entropy in Fig. 17. It should be noted that we use the terms entropy and purity in an approximate sense: the svd is in practice only useful to $n\approx 4$, so we assign a cutoff to the calculations on the data. Additionally, only the diagonal elements $P_n \equiv \rho_{nn}$ are used. This is valid for initial Fock states and thermal states (to which the ground state evolves under the amplitude reservoir) since the coher-

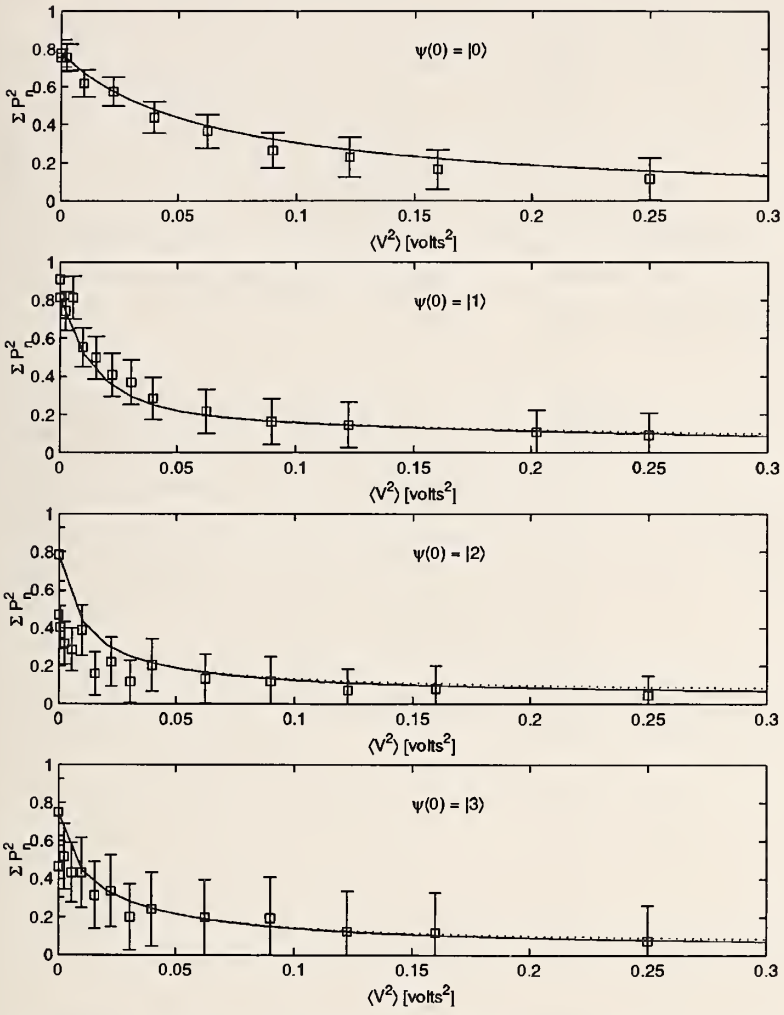

FIG. 16. Evolution of purity for initial Fock states in hot amplitude reservoir. Each graph shows the time evolution of the purity of the motional state for an experiment starting in the initial state indicated. The purity is defined in Eq. (87), from which the solid curves are derived. The dotted lines are an untruncated theory, whereas the solid lines are truncated at a maximum value of $n=n_{\max}$.

ences are absent. However, imperfections in state preparation could lead to unwanted coherences in the experimental states. In practice, we assume that such effects are small, but we have not experimentally verified this assumption. Some of the discrepancies between theory and data may result from this. The definitions under these constraints are, for the purity,

$$\mathcal{P}(t)\equiv \mathrm{Tr}\,\rho^2(t)\simeq \sum_{n=0}^{n_{\max}} P_n^2(t) \tag{87}$$

and for the entropy,

$$\mathcal{S}(t)\equiv \mathrm{Tr}\,\rho(t)\ln\rho(t)\simeq \sum_{n=0}^{n_{\max}} P_n(t)\ln P_n(t), \tag{88}$$

where $n_{\max}$ is the value of n at which the series is truncated. As stated above, since preparation of individual Fock states is not perfect, it is necessary to take into account the imperfections in the initial-state populations, especially as the initial state gets large. To match the data to the theory, the initial diagonal elements of the density matrix are measured and used as an initial condition in the theory curves. The theory that is compared to the data is also truncated at $n_{\max}$. This has only a minor effect on the purity calculation, but does change the qualitative result of the entropy, which for a limited basis set saturates much more quickly and to a lower value than it otherwise would. The predicted entropy and purity curves (with no truncation, that is, as $n_{\max}\to\infty$) are shown as the dotted lines in their respective figures.

C. Zero-temperature reservoir

a. Decoherence. Here we discuss the effect of the variable-bandwidth zero-temperature reservoir presented in Sec. III D 4 on a superposition of Fock states. As before, we prepare the superposition state, apply the reservoir, and undo the state preparation forming a Ramsey interferometer to measure the coherence. In this case, the only state considered was the superposition state $|\downarrow\rangle[|0\rangle+|2\rangle]/\sqrt{2}$.

We distinguish the two limiting cases discussed in Sec. III D 4. In the first, the effective decay rate γ_{eff} is much faster than the coherent Rabi rate Ω_{rsb}. This regime leads to exponential decay of the coherence and is a simulation of a broad bandwidth $T=0$ reservoir. In the other, the effective decay rate is slow compared to the coherent Rabi rate. Here, the system is driven coherently before appreciable decay sets

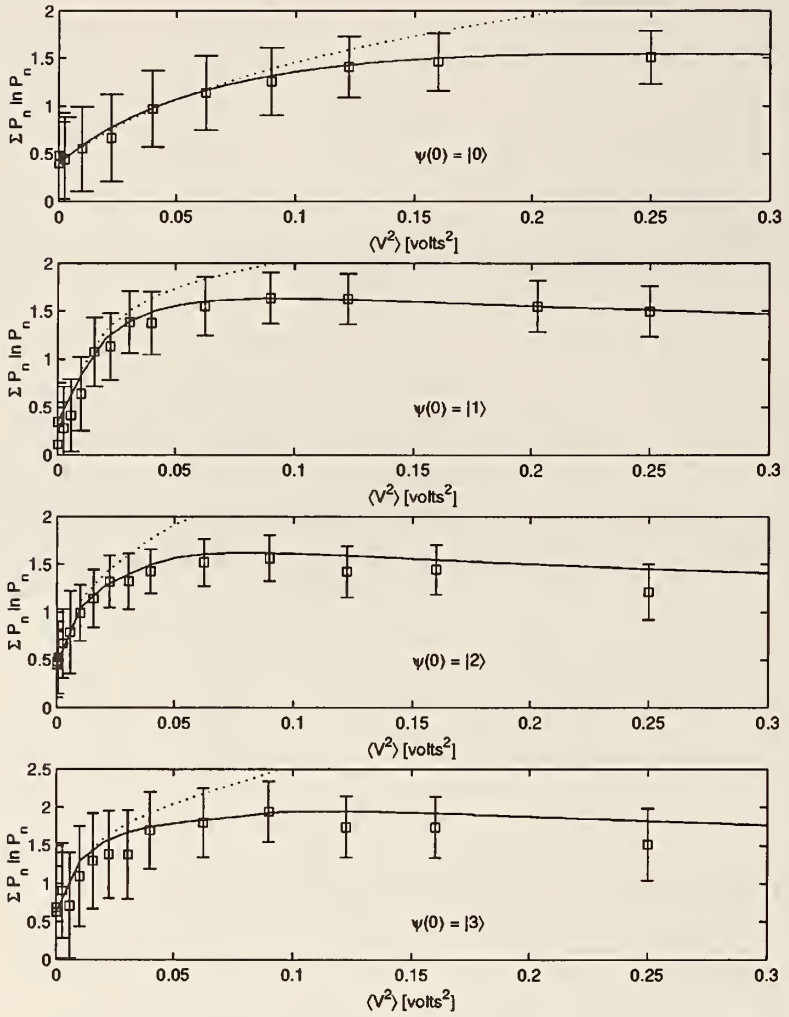

FIG. 17. Evolution of entropy for initial Fock states in hot amplitude reservoir. Each graph shows the time evolution of the entropy of the motional state for an experiment starting in the initial state indicated. The entropy is defined in Eq. (88), from which the solid curves are derived. The dotted lines are an untruncated theory, whereas the solid lines are truncated at a maximum value of $n=n_{\max}$.

in. Thus the coherent drive [on the red side band (rsb)] is capable of completing several Rabi oscillations of the spin. The evolution of fringe contrast shows that the coherence goes to zero (as a π pulse transfers most of the population out of $|\downarrow\rangle|2\rangle$ into $|\uparrow\rangle|1\rangle$ and therefore destroys all coherence between $|2\rangle$ and $|0\rangle$) but then comes back (with opposite sign) as a reservoir pulse with area greater than π is applied. During this time, the coherence is decaying due to dissipation on $|\uparrow\rangle$. The evolution between the two regimes is shown in Fig. 18. Note that the first graph has almost no decay. Here the red Doppler was absent ($\gamma_{\text{eff}} \propto \Omega_D = 0$) so that the residual decay is dominated by natural heating and Rabi frequency fluctuations. In the subsequent graphs, either the strength of the red Doppler laser, or the Rabi frequency of the rsb drive, or both were changed in such a way as to increase the ratio of dissipation to coherent drive, $\gamma_{\text{eff}}/\Omega_{\text{rsb}}$.

The experiment has an additional parameter that must be accounted for. The application of the red Doppler beam causes a Stark shift of the level $|\uparrow\rangle$. In the data of Fig. 18 this effect was corrected for during the experiment simply by changing the detuning of the Raman beams to compensate for the level shift; this must be done anew for each value of Ω_{rsb}. It is more convenient to perform the experiment not compensating for the Stark shift Δ. The theory for this is only slightly more complicated than that associated with Eq. (80), which can be generalized to:

$$\rho_{m\downarrow,0\downarrow} = \frac{1}{2}\exp(-\gamma_{\text{eff}}t/4)\left[\cos\frac{\Omega_R t}{2} - i\frac{\bar{\Delta}}{\Omega_R}\sin\frac{\Omega_R t}{2}\right], \quad (89)$$

$$\bar{\Delta} = \Delta + \frac{i\gamma_{\text{eff}}}{2}, \quad (90)$$

$$\Omega_R = \sqrt{4mg^2 + \bar{\Delta}^2}. \quad (91)$$

A progression of increasing $\gamma_{\text{eff}}/\Omega_R$ with Stark-shift detunings is shown in Fig. 19.

b. Decay. For completeness, we also consider the decay subject to the zero temperature reservoir of the diagonals of the density matrix (with no detunings, $\Delta = 0$). We measure the time evolution of these populations starting from an initial state of $\psi(0) = |\downarrow\rangle|2\rangle$. The predicted time evolution is given by Eq. (12). The data are shown in Fig. 20. One will immediately notice the negative "populations." This results from population left in the $|\uparrow\rangle$ state after the continuous

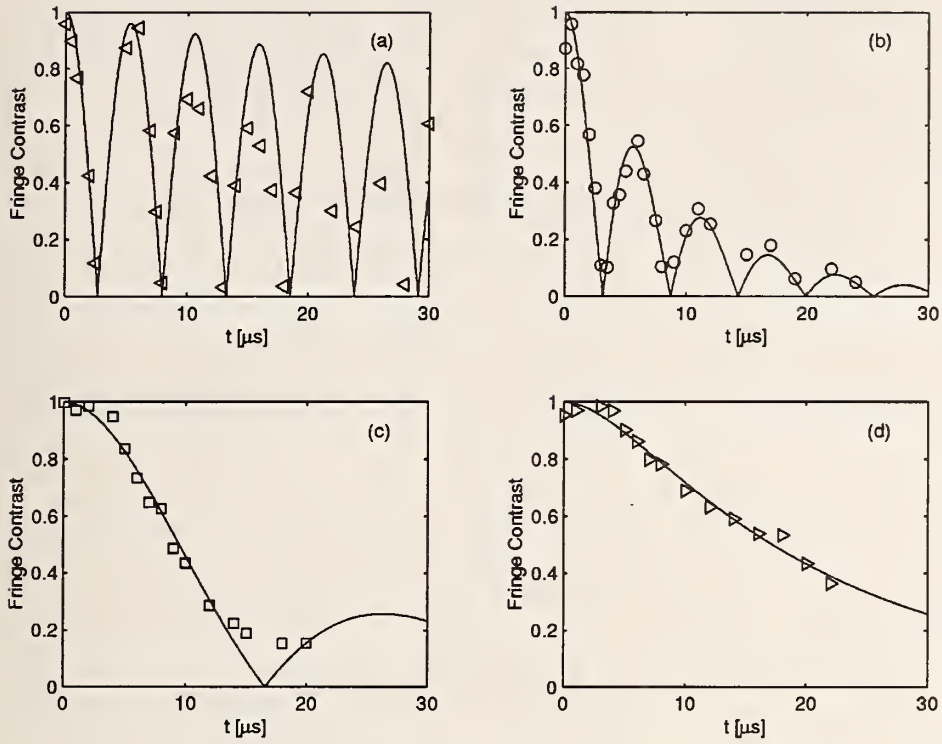

FIG. 18. Decay of Fock state coherences coupled to an engineered $T=0$ reservoir. The points in each graph are the contrast of a Ramsey fringe that measures the coherence between the $|0\rangle$ and $|2\rangle$ motional states as the time t of continuous Raman cooling ($T=0$ reservoir) is varied. The graphs have progressively larger ratios of $r \equiv \gamma_{\text{eff}}/g$: (a) $r=0.23$, (b) $r=1.1$, (c) $r=2.3$, and (d) $r=8$. The Stark-induced detunings are corrected experimentally, that is, the position of the RSB and its drive laser are made coincident. The theory curves are fits to Eq. (80), from which r is quoted.

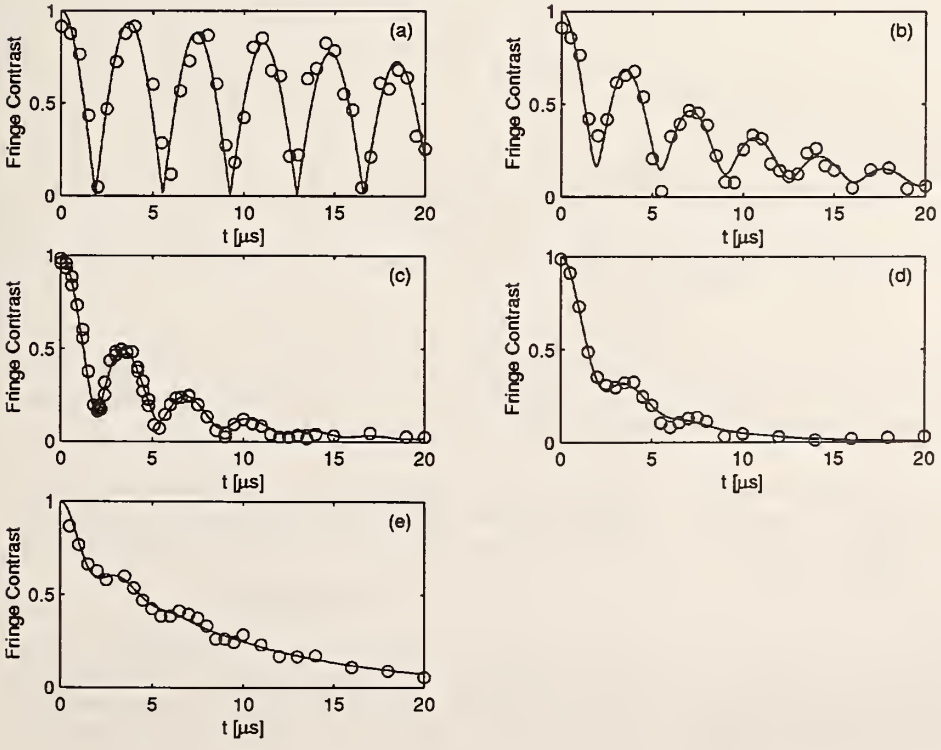

FIG. 19. Decay of Fock state coherences in $T=0$ reservoir. Same as Fig. 18, except the Stark-induced detunings are not corrected experimentally, but are accounted for in the theory curves, which are fits to Eq. (89). From the fits, $\gamma_{\text{eff}}/g=(0.1,0.7,1.3,2.7, 2.2)$ and $\Delta/g=(0,0.5,0.4,1,2)$ for graphs (a)–(e), respectively. See the text for a discussion.

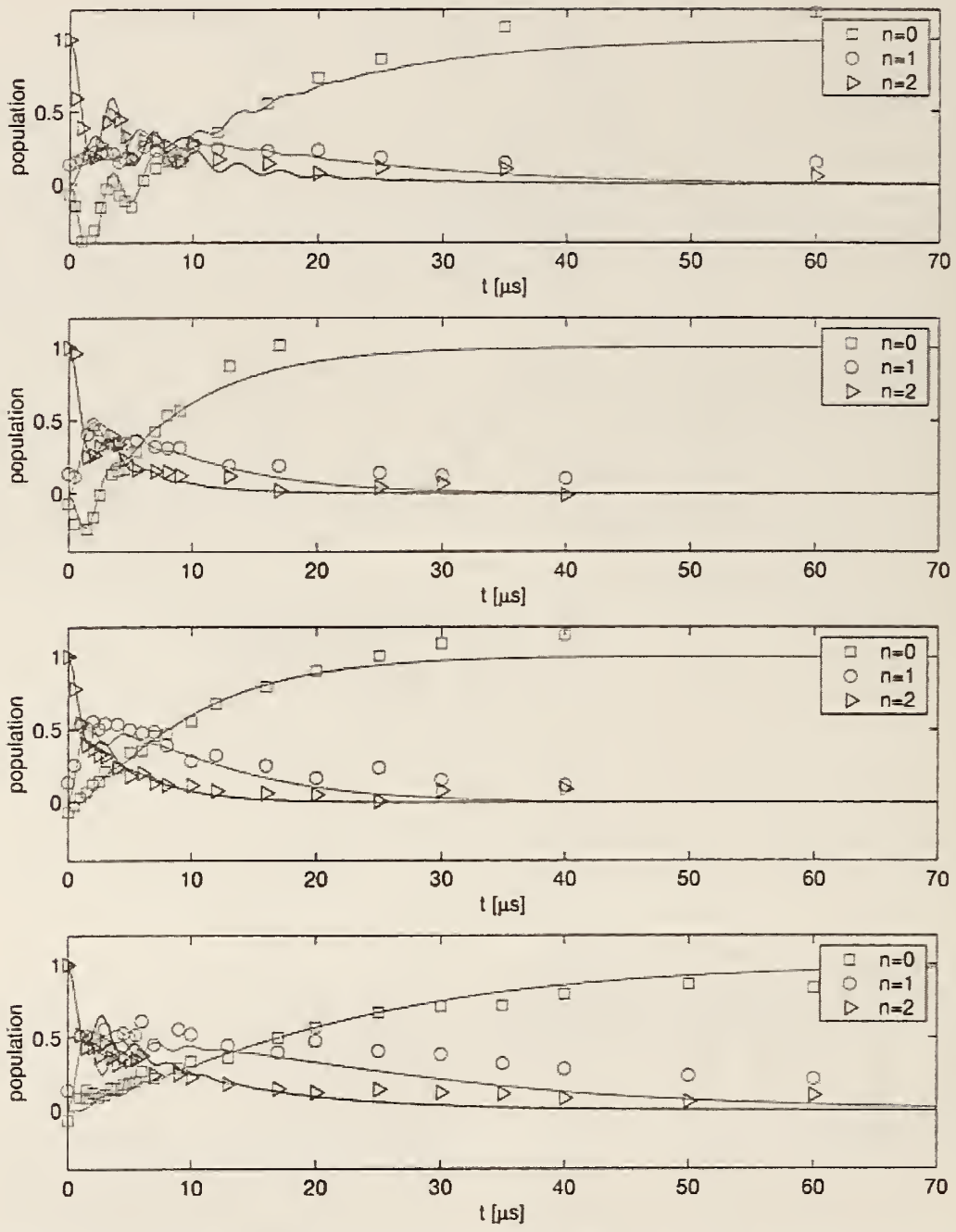

FIG. 20. (Color) Decay of Fock state populations in a $T=0$ reservoir starting from $\psi(0)=|2\rangle$. The strength of the red Doppler (which provides dissipation) is increased starting from the upper graph. Theory curves are from Eq. (12) with a modification to account for residual population left in $|\uparrow\rangle$ at the end of the continuous cooling cycle. See the text for a discussion.

Raman cooling. For weak enough red Doppler power, the optical pumping does not entirely depump the $|\uparrow\rangle$ state. This appears as a negative contribution to the flopping state analysis seen in the first two panels of Fig. 20 [see Eq. (85)].

V. CONCLUSION

We have presented a detailed study of the interaction of several types of quantum states with several types of engineered reservoirs. The results compare favorably with theoretical predictions, and for several cases, we have confirmed predicted scalings for a range of experimental conditions.

ACKNOWLEDGMENTS

We acknowledge support from the U. S. National Security Agency, Office of Naval Research and Army Research Office. We thank Chris Langer, Mary Rowe, Mike Lombardi, and Don Sullivan for critical readings of the manuscript.

[1] W.H. Zurek, Phys. Today **44**, 36 (1991), and references therein.
[2] A.O. Caldeira and A.J. Leggett, Phys. Rev. A **31**, 1059 (1985).
[3] D.F. Walls and G.J. Milburn, Phys. Rev. A **31**, 2403 (1985).
[4] M. Collet, Phys. Rev. A **38**, 2233 (1988).
[5] H. J. Carmichael, *An Open Systems Approach to Quantum Optics* (Springer-Verlag, Berlin, 1993).
[6] C. W. Gardiner, *Quantum Noise* (Springer-Verlag, Berlin, 1991).
[7] D. F. Walls and G. J. Milburn, *Quantum Optics* (Springer-Verlag, Berlin, 1994).
[8] V. Bužek and P. L. Knight in *Progress in Optics XXXIV* (Elsevier, Amsterdam, 1995), pp. 1–158.
[9] J.I. Cirac and P. Zoller, Phys. Rev. Lett. **74**, 4091 (1995).
[10] C. Monroe, D.M. Meekhof, B.E. King, and D.J. Wineland, Science **272**, 1131 (1996).
[11] M. Brune, E. Hagley, J. Dreyer, X. Maître, A. Maali, C. Wunderlich, J.M. Raimond, and S. Haroche, Phys. Rev. Lett. **77**, 4887 (1996).
[12] C.J. Myatt, B.E. King, Q.A. Turchette, C.A. Sackett, D. Kielpinski, W.M. Itano, C. Monroe, and D.J. Wineland, Nature (London) **403**, 269 (2000).
[13] V. Peřinová and A. Lukš, Phys. Rev. A **41**, 414 (1990).
[14] M.S. Kim and V. Bužek, Phys. Rev. A **46**, 4239 (1992).
[15] C. J. Myatt, B. E. King, Q. A. Turchette, C. A. Sackett, D. Kielpinski, W. M. Itano, C. Monroe, and D. J. Wineland, in *Laser Spectroscopy, XIV International Conference, Innsbruck, June, 1999*, edited by R. Blatt, J. Eschner, D. Leibfried, F. Schmidt-Kaler (World Scientific, Singapore, 1999), pp. 237–245.
[16] D.J. Wineland, C. Monroe, W.M. Itano, D. Leibfried, B.E. King, and D.M. Meekhof, J. Res. NIST **103**, 259 (1998).
[17] D.M. Meekhof, C. Monroe, B.E. King, W.M. Itano, and D.J. Wineland, Phys. Rev. Lett. **76**, 1796 (1996).
[18] C. Monroe, D.M. Meekhof, B.E. King, S.R. Jefferts, W.M. Itano, D.J. Wineland, and P. Gould, Phys. Rev. Lett. **75**, 4011 (1995).
[19] S. Wallentowitz and W. Vogel, Phys. Rev. A **58**, 679 (1998).
[20] W.M. Itano, C. Monroe, D.M. Meekhof, D. Leibfried, B.E. King, and D.J. Wineland, SPIE Proc. **2995**, 43 (1997).
[21] M.G. Raizen, J.M. Gilligan, J.C. Bergquist, W.M. Itano, and D.J. Wineland, Phys. Rev. A **45**, 6493 (1992).
[22] S.R. Jefferts, C. Monroe, E.W. Bell, and D.J. Wineland, Phys. Rev. A **51**, 3112 (1995).
[23] B. E. King, Ph.D. thesis, University of Colorado, 1999 (unpublished).
[24] Q.A. Turchette, C.S. Wood, B.E. King, C.J. Myatt, D. Leibfried, W.M. Itano, C. Monroe, and D.J. Wineland, Phys. Rev. Lett. **81**, 3631 (1998).
[25] D.J. Wineland, C. Monroe, W.M. Itano, B.E. King, D. Leibfried, D.M. Meekhof, C. Myatt, and C. Wood, Fortschr. Phys. **46**, 363 (1998).
[26] Q. A. Turchette, D. Kielpinski, D. Leibfried, D. M. Meekhof, C. J. Myatt, M. A. Rowe, C. A. Sackett, C. S. Wood, W. Itano, C. Monroe, and D. Wineland, Phys. Rev. A **61**, 063418 (2000).
[27] B.E. King, C.S. Wood, C.J. Myatt, Q.A. Turchette, D. Leibfried, W.M. Itano, C. Monroe, and D.J. Wineland, Phys. Rev. Lett. **81**, 1525 (1998).
[28] J.F. Poyatos, J.I. Cirac, and P. Zoller, Phys. Rev. Lett. **77**, 4728 (1996).
[29] F. Diedrich, J.C. Bergquist, W.M. Itano, and D.J. Wineland, Phys. Rev. Lett. **62**, 403 (1989).
[30] I. Marzoli, J.I. Cirac, R. Blatt, and P. Zoller, Phys. Rev. A **49**, 2771 (1994).
[31] E.T. Jaynes and F.W. Cummings, Proc. IEEE **51**, 89 (1963).
[32] W. H. Press, S. A. Teukolsky, W. T. Vetterling, and B. P. Flannery, *Numerical Recipes in C* (Cambridge University Press, New York, 1996).

A Decoherence-Free Quantum Memory Using Trapped Ions

D. Kielpinski,[1]* V. Meyer,[1] M. A. Rowe,[1] C. A. Sackett,[1]
W. M. Itano,[1] C. Monroe,[2] D. J. Wineland[1]

We demonstrate a decoherence-free quantum memory of one qubit. By encoding the qubit into the decoherence-free subspace (DFS) of a pair of trapped $^9Be^+$ ions, we protect the qubit from environment-induced dephasing that limits the storage time of a qubit composed of a single ion. We measured the storage time under ambient conditions and under interaction with an engineered noisy environment and observed that encoding into the DFS increases the storage time by up to an order of magnitude. The encoding reversibly transfers an arbitrary qubit stored in a single ion to the DFS of two ions.

A quantum memory stores information in superposition states of a collection of two-level systems called "qubits." Quantum computation, which may provide a substantial speedup in factoring large numbers (*1*) and in searching databases (*2*), works by operating on information in the form of such superpositions. Robust quantum memories are therefore essential to realizing the potential gains of quantum computing (*3*). However, interaction of a quantum memory with its environment destroys the stored information, a process called "decoherence" (*4, 5*). Many proposed quantum memories decohere because of an environment that has the same coupling to each qubit (*6–12*). Encoding the stored information into a decoherence-free subspace, or DFS, allows the memory to retain information, even in the presence of this type of decoherence (*10–12*). The DFS states are invariant under the coupling to such an environment, protecting the encoded "logical qubit" from the decoherence affecting general superpositions of the "physical qubits" that make up the full state space. DFSs have been shown to require an asymptotically small overhead for large systems (*10*) and to support universal fault-tolerant quantum logic (*13, 14*). These properties suggest that DFSs will be intrinsic to future quantum computing architectures. Logic gates on DFS-encoded qubits have been proposed in the context of cavity quantum electrodynamics (*15*) and solid state quantum logic schemes (*14*). Also, a recent experiment has demonstrated the immunity of a DFS of two photons to collective noise (*16*). Here we demonstrate the immunity of a DFS of two atoms to collective dephasing and implement a technique for encoding an arbitrary physical qubit state into the DFS.

[1]Time and Frequency Division, National Institute of Standards and Technology, Boulder, CO 80305, USA. [2]Department of Physics, University of Michigan, Ann Arbor, MI 48109, USA.

*To whom correspondence should be addressed. E-mail: davidk@boulder.nist.gov

Our physical qubits are $^9Be^+$ ions confined along the axis of a miniature linear radio-frequency (RF) trap (*17*). We choose two $^9Be^+$ hyperfine states, denoted $|\downarrow\rangle$ and $|\uparrow\rangle$, as our physical qubit basis states. We detect logic states by applying laser light resonant with a $^9Be^+$ cycling transition (*18*). The detection laser causes ions in $|\downarrow\rangle$ to fluoresce, whereas ions in $|\uparrow\rangle$ fluoresce negligibly, allowing discrimination of logic states with high efficiency (*19*). Applying nonresonant laser beams BR (blue Raman) and RR (red Raman) with frequency difference $\omega_{BR} - \omega_{RR}$ equal to the $|\uparrow\rangle \leftrightarrow |\downarrow\rangle$ transition frequency ω_0 drives stimulated Raman transitions between $|\downarrow\rangle$ and $|\uparrow\rangle$. This "carrier" transition implements rotation of a single physical qubit, one of the fundamental quantum logic gates (*19*). The corresponding evolution is

$$|\downarrow\rangle \rightarrow \cos\theta|\downarrow\rangle + e^{i\phi}\sin\theta\,|\uparrow\rangle$$
$$|\uparrow\rangle \rightarrow \cos\theta|\uparrow\rangle - e^{-i\phi}\sin\theta\,|\downarrow\rangle \quad (1)$$

where θ is proportional to the carrier drive duration and ϕ is the phase difference between the BR and RR beams at the position of the ion, referred to as the "ion phase." For two ions, we write the ion phases ϕ_i for each ion as ϕ_1, ϕ_2 (*20*).

The experiments reported here use two trapped ions. The ions are strongly coupled by the Coulomb interaction, so that the motion of the ions along the axis decomposes into symmetric and antisymmetric normal modes at frequencies of 5.0 and 8.8 MHz, respectively. The wave vector difference between BR and RR lies along the trap axis, so we can drive transitions that couple the internal and motional states of the ions. Driving these transitions as described in (*21*), we perform the two-ion logic gate of Sørensen and Mølmer (*22*), which entangles the two ions. The evolution under this gate is

$$|\downarrow\downarrow\rangle \rightarrow (|\downarrow\downarrow\rangle + i|\uparrow\uparrow\rangle)/\sqrt{2}$$
$$|\uparrow\uparrow\rangle \rightarrow (|\uparrow\uparrow\rangle + i|\downarrow\downarrow\rangle)/\sqrt{2}$$
$$|\downarrow\uparrow\rangle \rightarrow (|\downarrow\uparrow\rangle + i|\uparrow\downarrow\rangle)/\sqrt{2}$$
$$|\uparrow\downarrow\rangle \rightarrow (|\uparrow\downarrow\rangle + i|\downarrow\uparrow\rangle)/\sqrt{2} \quad (2)$$

We can also realize the inverse of this gate by performing the gate three times in succession. In general, the evolution under the two-ion gate depends on the ion phases, but we choose a phase convention in which $\phi_1 = \phi_2 = 0$ during application of the two-ion gate, yielding the evolution of Eq. 2. This gate, in combination with single-qubit rotations, implements universal quantum logic (*23*), in the sense that these gates suffice to transform any superposition of the states $|\downarrow\downarrow\rangle$, $|\uparrow\downarrow\rangle$, $|\downarrow\uparrow\rangle$, and $|\uparrow\uparrow\rangle$ into any other superposition of those states.

The DFS realized here is spanned by $|\psi_-\rangle = (|\downarrow\uparrow\rangle - i|\uparrow\downarrow\rangle)/\sqrt{2}$ and $|\psi_+\rangle = (|\downarrow\uparrow\rangle + i|\uparrow\downarrow\rangle)/\sqrt{2}$, which form the basis states for our logical qubit. These states are clearly invariant under collective dephasing; the transformation $|\uparrow\rangle \rightarrow e^{i\zeta}|\uparrow\rangle$, applied simultaneously to both ions, leaves any superposition of $|\psi_-\rangle$ and $|\psi_+\rangle$ invariant. Such collective dephasing is expected to be a major source of qubit decoherence for quantum information processing using trapped atoms. The encoding method demonstrated below reversibly transfers information between one physical qubit (one ion) and one decoherence-free logical qubit. The encoding works even if we have no information about the initial state of the physical qubit. This fact is essential for the use of our method in quantum information processing, in which the state to be encoded may be entangled with the state of another system.

To demonstrate the general character of the encoding method, we show that the encoding works for arbitrary states of form

$$|\downarrow\rangle(a|\downarrow\rangle + b|\uparrow\rangle)$$
$$|a|^2 + |b|^2 = 1 \quad a,b \text{ complex} \quad (3)$$

To prepare a state of this form, we first initialize the ions in the logic state $|\downarrow\downarrow\rangle$ by optical pumping. We then drive the carrier transition of Eq. 1 on both ions simultaneously, once with $\theta = \beta$, and again with $\theta = \beta$ and ϕ_1, shifted by π. We set $\phi_2 = \alpha$ for both pulses. The final state has $a = \cos 2\beta$, $b = e^{i\alpha}\sin 2\beta$. In a classical picture of spin with $\beta = \pi/8$, the first drive takes $\downarrow\downarrow$ to $\searrow\searrow$. The second drive reverses the sense of rotation on ion 1 while keeping it the same on ion 2, so the second drive takes $\searrow\searrow$ to $\downarrow\rightarrow$ The net effect is to rotate ion 2 alone, without changing the state of ion 1 (*24*).

We encode the state of Eq. 3 into the DFS in two steps. First, we apply the inverse of the two-ion gate of Eq. 2, yielding $a(|\downarrow\downarrow\rangle - i|\uparrow\uparrow\rangle) + b(|\downarrow\uparrow\rangle - i|\uparrow\downarrow\rangle)$. Then, we drive the carrier with $\theta = \pi/4$, $\phi_1 = \pi/2$, $\phi_2 = 0$ to

obtain $|\psi_{DFS}\rangle = a\,|\psi_+\rangle + b|\psi_-\rangle$. The information stored in the physical qubit of ion 2 is now encoded in the logical qubit of the DFS. In the experiment, we take $|a| = |b|$, though our method permits preparation and encoding of any state of the more general form.

To read out the encoded information, we reverse the carrier pulse in the encoding and apply the two-ion gate of Eq. 2 to decode $|\psi_{DFS}\rangle$ into $|\downarrow\rangle(a|\downarrow\rangle + b|\uparrow\rangle)$. After decoding, we rotate ion 2 as in preparing the state of Eq. 3 but with the phase on ion 2 changed to α'. We then measure the probability P_2 of finding both ions in $|\downarrow\rangle$. P_2 varies sinusoidally with $\alpha - \alpha'$, and the magnitude of oscillation is equal to the coherence C of ion 2 (*25*). Because we set $|a| = |b| = 1/\sqrt{2}$, ideally $C = 1$. Departures from $C = 1$ measure the effects of both decoherence and imperfect logic. We verified that C is independent of α, thus showing that our encoding method works even if we have no information about the phase of the input state.

To study the effects of decoherence on the DFS-encoded state, we leave a fixed delay time between the encoding and decoding steps and apply an engineered noisy environment for some fraction of the delay time. The engineered environment consists of an off-resonant laser beam with a randomly varying intensity. The beam induces a shift of ω_0 through the ac Stark effect, causing the $|\uparrow\rangle$ component of each ion to acquire a random phase relative to the $|\downarrow\rangle$ component. The two ions are nearly equally illuminated by the beam, so the random phase is nearly the same on both ions, leading to collective dephasing. The DFS state should resist the dephasing effect of this environment. The coherence of ion 2 in the test state $|\downarrow\rangle(|\downarrow\rangle + e^{i\Phi}|\uparrow\rangle)/\sqrt{2}$, however, should be sensitive to collective dephasing. We measure the decay of the test state by simply turning off the encoding and decoding sequences in the procedure used to measure the decay of the DFS-encoded state.

We applied decoherence to the test and encoded states during a delay time of ~25 μs (Fig. 1). The coherence without applied noise is ~0.69 for the test state and ~0.43 for the encoded state; they depart from 1 because of imperfect logic gates and detection, due in part to laser intensity fluctuations and heating of the ions (*17, 21*). For white-noise intensity fluctuations of the Stark-shifting beam, we expect C to decay exponentially for the test state, as shown by the fit line. The small decay rate of the test state between 0 and 2.5-μs noise duration arises because the intensity fluctuations of the noise beam have finite bandwidth (dc to 100 kHz) (*6*). We therefore extract the decay rate of the test state by excluding the point with zero applied noise from the fit. We also fit the coherence of the DFS state to an exponential decay for comparison. The decay rate of the test state is 0.18 ± 0.01 μs^{-1}, whereas the decay rate of the DFS state is 0.0035 ± 0.0050 μs^{-1}, consistent with zero decay. To investigate the eventual decay of the DFS state, we increased the delay time to ~200 μs and applied decoherence for up to 100 μs during the delay time. The DFS state coherence dropped by 50% for 100-μs applied noise relative to its value for the same delay time and no applied noise, but we think that this decay was not due to collective dephasing. The decay was Gaussian, rather than exponential, and is consistent with the effect of differential dephasing due to small departures from equal illumination by the Stark-shifting beam. We think that ambient sources of differential dephasing are much weaker than the differential dephasing caused by the Stark-shifting beam.

We also measured the storage times of the encoded and test states under ambient conditions in our laboratory (Fig. 2). Here we measure the coherence as a function of the delay time between encoding and decoding to give the ambient noise a variable time to act, rather than leaving a fixed delay time and applying noise for some fraction of the delay time. The coherence data for this case are normalized in the same way as the data with applied noise. The decoherence of the test state is dominated by ambient fluctuating magnetic fields whose frequencies lie primarily at 60 Hz and its harmonics. These fields randomly shift ω_0 through the Zeeman effect. Because these fields are roughly uniform across the ion string, they induce collective dephasing similar to that created by the engineered environment. We empirically find the decay of both test and encoded states to be roughly exponential, as indicated by the fit lines. The decay rate of the test state is (7.9 ± 1.5) × 10^{-3} μs^{-1}, whereas the decay rate of the DFS state is (2.2 ± 0.3) × 10^{-3} μs^{-1}. Although Fig. 1 presents only normalized contrasts, the data show that the unnormalized contrast of the DFS state is higher than that of the test state for delay times exceeding 150 μs. The DFS-encoded state maintains coherence much longer than the test state, so we conclude that collective dephasing from magnetic field noise is the major ambient source of decoherence for the test state (*26*). The loss of coherence of the encoded state is consistent with degradation of the decoding pulses (*19, 22, 27*), due to heating of the ion motional state over the delay time (*17*).

We have demonstrated reversible encoding of a qubit stored in one ion into a DFS of

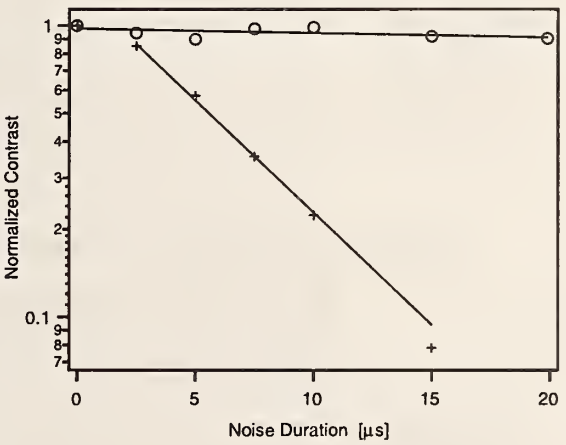

Fig. 1. Decay of the DFS-encoded state (circles) and the test state (crosses) under engineered dephasing noise. The noise is applied for a fraction of the delay time of ~25 μs between encoding and decoding. Coherence data are normalized to their values for zero applied noise. The fit lines are exponential decay curves. The test data are predicted to decay exponentially for white noise, so we exclude the point with zero applied noise from the fit. The DFS data are fit for comparison. The decay rate of the test state is 0.18 ± 0.01 μs^{-1}, whereas the decay rate of the DFS state is 0.0035 ± 0.0050 μs^{-1}, consistent with zero decay.

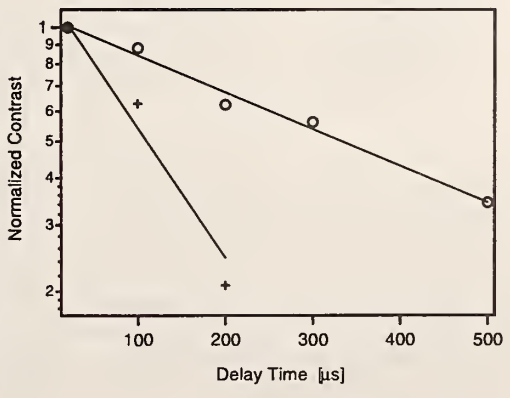

Fig. 2. Decay of the DFS-encoded state (circles) and the test state (crosses) under ambient decoherence. We vary the delay time between encoding and decoding to give the ambient noise a variable time to act. Coherence data are normalized to their values for zero applied noise. The fit lines are exponential decay curves for purposes of comparison and are not theoretical predictions. The decay rate of the test state is (7.9 ± 1.5) × 10^{-3} μs^{-1}, whereas the decay rate of the DFS state is (2.2 ± 0.3) × 10^{-3} μs^{-1}. Because the coherence time of the DFS-encoded state is much longer than that of the test state, we see that the chief source of ambient decoherence is collective dephasing.

two ions. The DFS-encoded state can store a qubit at least 10 times as long under applied noise as a single ion can, and appears immune to collective dephasing. Under typical ambient conditions, the DFS encoding also improves storage time considerably, showing that collective dephasing is indeed the limit to quantum memory using our physical qubits. Even without normalizing for the overhead incurred in encoding and decoding, the encoded state retains more coherence than the test state for long storage times in ambient conditions. The DFS encoding therefore currently provides an improved single-qubit quantum memory for ion-trap quantum computing applications. The loss of coherence incurred in encoding and decoding is a drawback to our scheme, but in the future, practical quantum computing will in any case require logic gates of a much higher fidelity than those used in this work. We therefore expect that, once the technical problems of ion heating and laser fluctuations are solved, the scheme presented here should be a practical method for long-term storage of qubits with near-perfect fidelity.

Our results suggest applications in quantum communication and large-scale quantum computing. Single photons have already been shown to transmit quantum information over long distances with high fidelity (*8, 9*), and the information in a single photon can be mapped onto a single atom (*28, 29*). With our encoding technique, the quantum information received by a single ion can be mapped into a DFS for robust storage. Our encoding technique will also be essential in scaling up ion-trap quantum computers. In one model of large-scale ion-trap quantum computing (*19*), qubits reside in a large array of interconnected ion traps. To perform one- or two-qubit logic gates, the relevant ions are moved into "accumulator" regions where they interact with lasers that drive the gates. One obstacle to this quantum computing architecture is that the magnetic field strength must be well-characterized across the entire device. Otherwise, the ions will constantly accumulate unknown relative phase during transport, leading to decoherence. Encoding into the DFS solves this problem, because the phase of a logical qubit in the DFS does not depend on the local magnetic field strength as long as the field strength is the same at each physical qubit. Thus, we can entangle two logical qubits, move them far apart, and perform operations on them in separate accumulators without losing phase information.

References and Notes

1. P. W. Shor, in *Proceedings of the 35th Annual Symposium on Foundations of Computer Science*, S. Goldwasser, Ed. (IEEE Computer Society, Los Alamitos, CA, 1994), p. 116.
2. L. K. Grover, *Phys. Rev. Lett.* **79**, 325 (1997).
3. A. Steane, paper presented at the Fifth International Conference on Quantum Communication, Measurement, and Computing, Capri, Italy, 3 to 8 July 2000.
4. W. H. Zurek, *Phys. Today* **44** (no. 10), 36 (1991).
5. D. Giulini *et al.*, *Decoherence and the Appearance of a Classical World in Quantum Theory* (Springer, Berlin, 1996).
6. G. M. Palma, K.-A. Suominen, A. K. Ekert, *Proc. R. Soc. London Ser. A* **452**, 567 (1996).
7. P. Zanardi, F. Rossi, *Phys. Rev. Lett.* **81**, 4752 (1998).
8. *Fortschr. Phys.* **46** (no. 4-8) (1998).
9. *Fortschr. Phys.* **48** (no. 9-11) (2000).
10. D. A. Lidar, I. L. Chuang, K. B. Whaley, *Phys. Rev. Lett.* **81**, 2594 (1998).
11. P. Zanardi, M. Rasetti, *Phys. Rev. Lett.* **79**, 3306 (1997).
12. L. M. Duan, G. C. Guo, *Phys. Rev. A* **57**, 737 (1998).
13. D. A. Lidar, D. Bacon, K. B. Whaley, *Phys. Rev. Lett.* **82**, 4556 (1999).
14. D. Bacon, J. Kempe, D. A. Lidar, K. B. Whaley, *Phys. Rev. Lett.* **85**, 1758 (2000).
15. A. Beige, D. Braun, B. Tregenna, P. L. Knight, *Phys. Rev. Lett.* **85**, 1762 (2000).
16. P. G. Kwiat, A. J. Berglund, J. B. Altepeter, A. G. White, *Science* **290**, 498 (2000).
17. Q. A. Turchette *et al.*, *Phys. Rev. A* **61**, 063418 (2000) (available at http://publish.aps.org/abstract/PRA/v61/e063418).
18. The hyperfine states corresponding to $|\downarrow\rangle$ and $|\uparrow\rangle$ are the $|F = 2, m_F = -2\rangle$ and $|F = 1, m_F = -1\rangle$ sublevels of the ground $^2S_{1/2}$ state, respectively. The cycling transition is excited by left circularly polarized light and connects $|\downarrow\rangle$ to the $|F = 3, m_F = -3\rangle$ sublevel of the excited $^2P_{3/2}$ state.
19. D. J. Wineland *et al.*, *J. Res. NIST* **103**, 259 (1998).
20. For two ions, we effect common-mode changes of ϕ_1 and ϕ_2 by changing the phase of the RF synthesizer that controls the difference frequency $\omega_{BR} - \omega_{RR}$. By changing the oscillation frequency of the trap, we can control the ion spacing precisely, allowing us to make differential changes to ϕ_1 and ϕ_2. These two techniques combined allow us to control ϕ_1 and ϕ_2 independently for two ions.
21. C. A. Sackett *et al.*, *Nature* **404**, 256 (2000).
22. A. Sørensen, K. Mølmer, *Phys. Rev. A* **62**, 022311 (2000) (available at http://publish.aps.org/abstract/PRA/v62/e022311).
23. ———, *Phys. Rev. Lett.* **82**, 1971 (1999).
24. Individual optical addressing of the ions can prepare the desired state with only one carrier pulse [H. C. Nägerl *et al.*, *Phys. Rev. A* **60**, 145 (1998)], but it is technically more challenging in our experiment because our ions are separated by only ~2.5 μm.
25. The decoding and final rotation can give rise to coherence in ion 2 even if the state before decoding is completely incoherent. We avoid this eventuality by detuning the RF synthesizer used for the initial and final rotations of ion 2 from the synthesizers used for encoding and decoding. The phases α and α' then change from shot to shot of the experiment, and the spurious coherences average out over many shots. No trace of this effect then remains in the data.
26. We can also reduce the dephasing from this mechanism by using the $^2S_{1/2}$ hyperfine sublevels $|F = 1, m_F = 0\rangle$ and $|F = 2, m_F = 0\rangle$ to represent the two levels of a qubit. In a separate experiment, we measured the coherence time of superpositions of these two states at a static magnetic field of $\sim 1.6 \times 10^{-3}$ T to be an order of magnitude longer than the coherence time between the qubit basis states used here. Magnetic field dephasing still limits the coherence time between the $m_F = 0$ states through the quadratic Zeeman shift. We expect the DFS encoding to improve coherence time in this case as well, because the encoding protects against purely collective dephasing to all orders. A practical ion-trap quantum computer will probably use the $m_F = 0$ states as qubit basis states but will also encode qubits into the DFS.
27. B. E. King *et al.*, *Phys. Rev. Lett.* **81**, 1525 (1998).
28. X. Maitre *et al.*, *Phys. Rev. Lett.* **79**, 769 (1997).
29. J. I. Cirac, P. Zoller, H. J. Kimble, H. Mabuchi, *Phys. Rev. Lett.* **78**, 3221 (1997).

30. This work was supported by the U.S. National Security Agency and the Advanced Research and Development Activity under contract MOD-7171.00 and by the U.S. Office of Naval Research. We thank J. Bergquist and A. Ben-Kish for comments on the manuscript. This paper is a contribution of the National Institute of Standards and Technology and is not subject to U.S. copyright.

10 November 2000; accepted 22 December 2000
Published online 5 January 2001;
10.1126/science.1057357
Include this information when citing this paper.

Magnetization Precession by Hot Spin Injection

W. Weber,[1]* S. Riesen,[1] H. C. Siegmann[2]

As electrons are injected at various energies into ferromagnetic material with their spin polarization vector perpendicular to the axis of the magnetization, we observe precessional motion of the spin polarization on the femtosecond time scale. Because of angular momentum conservation, the magnetization vector must precess as well. We show that spin injection will generate the precessional magnetization reversal in nanosized ferromagnetic bits. At reasonable injected current densities this occurs on the picosecond time scale.

Electrons injected into ferromagnetic material experience exchange coupling to the magnetization and spin-dependent scattering, leading to excitations of the magnetization (*1–4*). By injecting currents of high density, these excitations have been observed through the occurrence of spin waves (*5–7*), permanent changes of the micromagnetic structure (*8, 9*), or even a reversal of the magnetization (*10–12*). However, to date, the injection of electrons from a ferromagnetic emitter through nanocontacts occurs continously or in pulses that are long compared with the relaxation

[1]Laboratorium für Festkörperphysik, ETH Zürich, CH-8093 Zürich, Switzerland. [2]Stanford Linear Accelerator Center, Stanford University, Stanford, CA 94309, USA.

*To whom correspondence should be addressed. E-mail: weber@solid.phys.ethz.ch

Experimental violation of a Bell's inequality with efficient detection

M. A. Rowe*, D. Kielpinski*, V. Meyer*, C. A. Sackett*, W. M. Itano*, C. Monroe† & D. J. Wineland*

* *Time and Frequency Division, National Institute of Standards and Technology, Boulder, Colorado 80305, USA*
† *Department of Physics, University of Michigan, Ann Arbor, Michigan 48109, USA*

Local realism is the idea that objects have definite properties whether or not they are measured, and that measurements of these properties are not affected by events taking place sufficiently far away[1]. Einstein, Podolsky and Rosen[2] used these reasonable assumptions to conclude that quantum mechanics is incomplete. Starting in 1965, Bell and others constructed mathematical inequalities whereby experimental tests could distinguish between quantum mechanics and local realistic theories[1,3–5]. Many experiments[1,6–15] have since been done that are consistent with quantum mechanics and inconsistent with local realism. But these conclusions remain the subject of considerable interest and debate, and experiments are still being refined to overcome 'loopholes' that might allow a local realistic interpretation. Here we have measured correlations in the classical properties of massive entangled particles ($^9Be^+$ ions): these correlations violate a form of Bell's inequality. Our measured value of the appropriate Bell's 'signal' is 2.25 ± 0.03, whereas a value of 2 is the maximum allowed by local realistic theories of nature. In contrast to previous measurements with massive particles, this violation of Bell's inequality was obtained by use of a complete set of measurements. Moreover, the high detection efficiency of our apparatus eliminates the so-called 'detection' loophole.

Early experiments to test Bell's inequalities were subject to two primary, although seemingly implausible, loopholes. The first might be termed the locality or 'lightcone' loophole, in which the correlations of apparently separate events could result from unknown subluminal signals propagating between different regions of the apparatus. Aspect[16] has given a brief history of this issue, starting with the experiments of ref. 8 and highlighting the strict relativistic separation between measurements reported by the Innsbruck group[15]. Similar results have also been reported for the Geneva experiment[14,17]. The second loophole is usually referred to as the detection loophole. All experiments up to now have had detection efficiencies low enough to allow the possibility that the subensemble of detected events agrees with quantum mechanics even though the entire ensemble satisfies Bell's inequalities. Therefore it must be assumed that the detected events represent the entire ensemble; a fair-sampling hypothesis. Several proposals for closing this loophole have been made[18–24]; we believe the experiment that we report here is the first to do so. Another feature of our experiment is that it uses massive particles. A previous test of Bell's inequality was carried out on protons[25], but the interpretation of the detected events relied on quantum mechanics, as symmetries valid given quantum mechanics were used to extrapolate the data to a complete set of Bell's angles. Here we do not make such assumptions.

A Bell measurement of the type suggested by Clauser, Horne, Shimony and Holt[5] (CHSH) consists of three basic ingredients (Fig. 1a). First is the preparation of a pair of particles in a repeatable starting configuration (the output of the 'magic' box in Fig. 1a). Second, a variable classical manipulation is applied independently to each particle; these manipulations are labelled ϕ_1 and ϕ_2. Finally, in the detection phase, a classical property with two possible outcomes is measured for each of the particles. The correlation of these outcomes

$$q(\phi_1,\phi_2)=\frac{N_{\text{same}}(\phi_1,\phi_2)-N_{\text{different}}(\phi_1,\phi_2)}{N_{\text{same}}+N_{\text{different}}} \quad (1)$$

is measured by repeating the experiment many times. Here N_{same} and $N_{\text{different}}$ are the number of measurements where the two results were the same and different, respectively. The CHSH form of Bell's inequalities states that the correlations resulting from local realistic theories must obey:

$$B(\alpha_1,\delta_1,\beta_2,\gamma_2)=|q(\delta_1,\gamma_2)-q(\alpha_1,\gamma_2)| + |q(\delta_1,\beta_2)+q(\alpha_1,\beta_2)|\leqslant 2 \quad (2)$$

where α_1 and δ_1 (β_2 and γ_2) are specific values of ϕ_1 (ϕ_2). For example, in a photon experiment[15], parametric down-conversion prepares a pair of photons in a singlet Einstein–Podolsky–Rosen (EPR) pair. After this, a variable rotation of the photon polarization is applied to each photon. Finally, the photons' polarization states, vertical or horizontal, are determined.

Our experiment prepares a pair of two-level atomic ions in a repeatable configuration (entangled state). Next, a laser field is applied to the particles; the classical manipulation variables are the

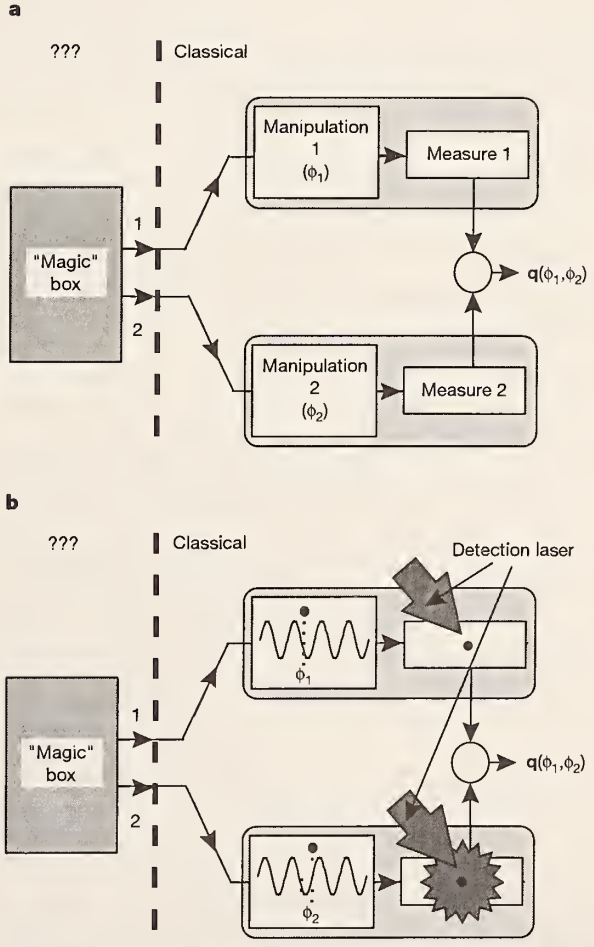

Figure 1 Illustration of how Bell's inequality experiments work. The idea is that a 'magic box' emits a pair of particles. We attempt to determine the joint properties of these particles by applying various classical manipulations to them and observing the correlations of the measurement outputs. **a**, A general CHSH type of Bell's inequality experiment. **b**, Our experiment. The manipulation is a laser wave applied with phases ϕ_1 and ϕ_2 to ion 1 and ion 2 respectively. The measurement is the detection of photons emanating from the ions upon application of a detection laser. Two possible measurement outcomes are possible, detection of few photons (as depicted for ion 1 in the figure) or the detection of many photons (as depicted for ion 2 in the figure).

phases of this field at each ion's position. Finally, upon application of a detection laser beam, the classical property measured is the number of scattered photons emanating from the particles (which effectively measures their atomic states). Figure 1b shows how our experiment maps onto the general case. Entangled atoms produced in the context of cavity-quantum-electrodynamics[26] could similarly be used to measure Bell's inequalities.

The experimental apparatus is as described in ref. 27. Two $^9Be^+$ ions are confined along the axis of a linear Paul trap with an axial centre-of-mass frequency of 5 MHz. We select two resolved levels of the $2S_{1/2}$ ground state, $|\downarrow\rangle \equiv |F = 2, m_F = -2\rangle$ and $|\uparrow\rangle \equiv |F = 1, m_F = -1\rangle$, where F and m_F are the quantum numbers of the total angular momentum. These states are coupled by a coherent stimulated Raman transition. The two laser beams used to drive the transition have a wavelength of 313 nm and a difference frequency near the hyperfine splitting of the states, $\omega_0 \cong 2\pi \times 1.25$ GHz. The beams are aligned perpendicular to each other, with their difference wavevector $\Delta\mathbf{k}$ along the trap axis. As described in ref. 27, it is possible in this configuration to produce the entangled state

$$|\psi_2\rangle = \frac{1}{\sqrt{2}}(|\uparrow\uparrow\rangle - |\downarrow\downarrow\rangle) \quad (3)$$

The fidelity $F = \langle\psi_2|\rho|\psi_2\rangle$, where ρ is the density matrix for the state we make, was about 88% for the data runs. In the discussion below we assume $|\psi_2\rangle$ as the starting condition for the experiment.

After making the state $|\psi_2\rangle$, we again apply Raman beams for a pulse of short duration (~400 ns) so that the state of each ion j is transformed in the interaction picture as

$$|\uparrow_j\rangle \rightarrow \frac{1}{\sqrt{2}}(|\uparrow_j\rangle - ie^{-i\phi_j}|\downarrow_j\rangle); |\downarrow_j\rangle \rightarrow \frac{1}{\sqrt{2}}(|\downarrow_j\rangle - ie^{i\phi_j}|\uparrow_j\rangle) \quad (4)$$

The phase, ϕ_j, is the phase of the field driving the Raman transitions (more specifically, the phase difference between the two Raman beams) at the position of ion j and corresponds to the inputs ϕ_1 and ϕ_2 in Fig. 1. We set this phase in two ways in the experiment. First, as an ion is moved along the trap axis this phase changes by $\Delta\mathbf{k}\cdot\Delta\mathbf{x}_j$. For example, a translation of $\lambda/\sqrt{2}$ along the trap axis corresponds to a phase shift of 2π. In addition, the laser phase on both ions is changed by a common amount by varying the phase, ϕ_s, of the radio-frequency synthesizer that determines the Raman difference frequency. The phase on ion j is therefore

$$\phi_j = \phi_s + \Delta\mathbf{k}\cdot\mathbf{x}_j \quad (5)$$

In the experiment, the axial trap strength is changed so that the ions move about the centre of the trap symmetrically, giving $\Delta x_1 = -\Delta x_2$. Therefore the trap strength controls the differential phase, $\Delta\phi \equiv \phi_1 - \phi_2 = \Delta\mathbf{k}\cdot(\mathbf{x}_1 - \mathbf{x}_2)$, and the synthesizer controls the total phase, $\phi_{tot} \equiv \phi_1 + \phi_2 = 2\phi_s$. The calibration of these relations is discussed in the Methods.

The state of an ion, $|\downarrow\rangle$ or $|\uparrow\rangle$, is determined by probing the ion with circularly polarized light from a 'detection' laser beam[27]. During this detection pulse, ions in the $|\downarrow\rangle$ or bright state scatter many photons, and on average about 64 of these are detected with a photomultiplier tube, while ions in the $|\uparrow\rangle$ or dark state scatter very few photons. For two ions, three cases can occur: zero ions bright, one ion bright, or two ions bright. In the one-ion-bright case it is not necessary to know which ion is bright because the Bell's measurement requires only knowledge of whether or not the ions' states are different. Figure 2 shows histograms, each with 20,000 detection measurements. The three cases are distinguished from each other with simple discriminator levels in the number of photons collected with the phototube.

An alternative description of our experiment can be made in the language of spin-one-half magnetic moments in a magnetic field (directed in the $\hat{z}$ direction). The dynamics of the spin system are the same as for our two-level system[28]. Combining the manipulation (equation (4)) and measurement steps, we effectively measure the spin projection of each ion j in the $\hat{r}_j$ direction, where the vector $\hat{r}_j$ is in the $\hat{x} - \hat{y}$ plane at an angle ϕ_j to the $\hat{y}$ axis. Although we have used quantum-mechanical language to describe the manipulation and measurement steps, we emphasize that both are procedures completely analogous to the classical rotations of wave-plates and measurements of polarization in an optical apparatus.

Here we calculate the quantum-mechanical prediction for the correlation function. Our manipulation step transforms the starting

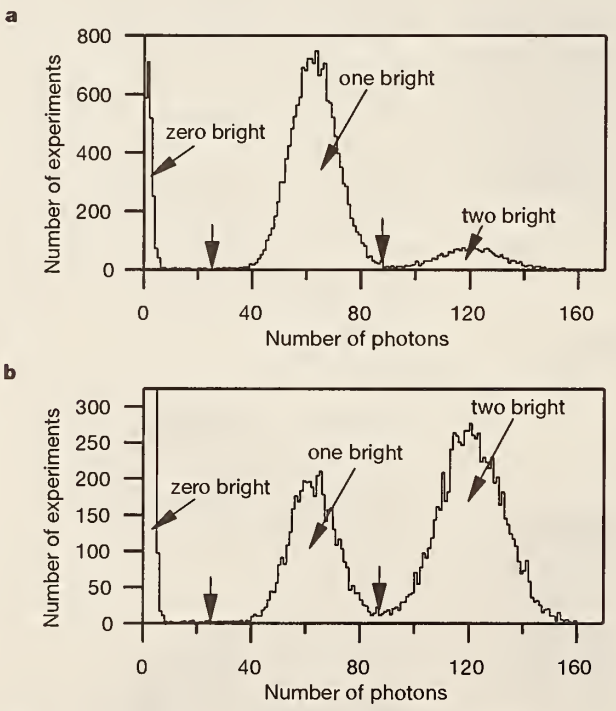

Figure 2 Typical data histograms comprising the detection measurements of 20,000 experiments taking a total time of about 20 s. In each experiment the population in the $|\uparrow\rangle$ state is first coherently transferred to the $|F = 1, M_F = +1\rangle$ to make it even less likely to fluoresce upon application of the detection laser. The detection laser is turned on and the number of fluorescence photons detected by the phototube in 1 ms is recorded. The cut between the one bright and two bright cases is made so that the fractions of two equal distributions which extend past the cut points are equal. The vertical arrows indicate the location of the cut between the 0 (1) bright and 1 (2) bright peaks at 25 (86) counts. **a**, Data histogram with a negative correlation using $\phi_1 = 3\pi/8$ and $\phi_2 = 3\pi/8$. For these data $N_0 \cong 2{,}200$, $N_1 \cong 15{,}500$ and $N_2 \cong 2{,}300$. **b**, Data histogram with a positive correlation using $\phi_1 = 3\pi/8$ and $\phi_2 = -\pi/8$. For these data $N_0 \cong 7{,}700$, $N_1 \cong 4{,}400$ and $N_2 \cong 7{,}900$. The zero bright peak extends vertically to 2,551.

Table 1 The four sets of phase angles used for the Bell's experiment

Experiment input	ϕ_1	ϕ_2	$\Delta\phi$	ϕ_{tot}
$\alpha_1\beta_2$	$-\pi/8$	$-\pi/8$	0	$-\pi/4$
$\alpha_1\gamma_2$	$-\pi/8$	$3\pi/8$	$-\pi/2$	$+\pi/4$
$\delta_1\beta_2$	$3\pi/8$	$-\pi/8$	$+\pi/2$	$+\pi/4$
$\delta_1\gamma_2$	$3\pi/8$	$3\pi/8$	0	$+3\pi/4$

Table 2 Correlation values and resulting Bell's signals for five experimental runs

Run number	$q(\alpha_1, \beta_2)$	$q(\alpha_1, \gamma_2)$	$q(\delta_1, \beta_2)$	$q(\delta_1, \gamma_2)$	$B(\alpha_1, \delta_1, \beta_2, \gamma_2)$
1	0.541	0.539	0.569	−0.573	2.222
2	0.575	0.570	0.530	−0.600	2.275
3	0.551	0.634	0.590	−0.487	2.262
4	0.575	0.561	0.559	−0.551	2.246
5	0.541	0.596	0.537	−0.571	2.245

The experimental angle values were $\alpha_1 = -(\pi/8)$, $\delta_1 = 3\pi/8$, $\beta_2 = -(\pi/8)$, and $\gamma_2 = 3\pi/8$. The statistical errors are 0.006 and 0.012 for the q and B values respectively. The systematic errors (see text) are 0.03 and 0.06 for the q and B values respectively.

state, $|\psi_2\rangle$, to

$$|\psi_2'\rangle = \frac{1}{2\sqrt{2}}\{(1+e^{i(\phi_1+\phi_2)})(|\uparrow\uparrow\rangle - e^{-i(\phi_1+\phi_2)}|\downarrow\downarrow\rangle) - i(1-e^{i(\phi_1+\phi_2)})(e^{-i\phi_2}|\uparrow\downarrow\rangle + e^{-i\phi_1}|\downarrow\uparrow\rangle)\} \quad (6)$$

Using the measurement operators $\hat{N}_{\text{same}} = N_{\text{tot}}[|\uparrow\uparrow\rangle\langle\uparrow\uparrow| + |\downarrow\downarrow\rangle\langle\downarrow\downarrow|]$ and $\hat{N}_{\text{different}} = N_{\text{tot}}[|\uparrow\downarrow\rangle\langle\uparrow\downarrow| + |\downarrow\uparrow\rangle\langle\downarrow\uparrow|]$, the correlation function is calculated to be

$$q(\phi_1,\phi_2) = \frac{1}{8}[2|1+e^{i(\phi_1+\phi_2)}|^2 - 2|1-e^{i(\phi_1+\phi_2)}|^2] = \cos(\phi_1+\phi_2) \quad (7)$$

The CHSH inequality (equation (2)) is maximally violated by quantum mechanics at certain sets of phase angles. One such set is $\alpha_1 = -(\pi/8)$, $\delta_1 = 3\pi/8$, $\beta_2 = -(\pi/8)$ and $\gamma_2 = 3\pi/8$. With these phase angles quantum mechanics predicts

$$B\left(-\frac{\pi}{8},\frac{3\pi}{8},-\frac{\pi}{8},\frac{3\pi}{8}\right) = 2\sqrt{2} \quad (8)$$

This violates the local realism condition, which requires that $B \leqslant 2$.

The correlation function is measured experimentally at four sets of phase angles, listed in Table 1. The experiment is repeated $N_{\text{tot}} = 20{,}000$ times at each of the four sets of phases. For each set of phases the correlation function is calculated using

$$q = \frac{(N_0+N_2)-N_1}{N_{\text{tot}}} \quad (9)$$

Here N_0, N_1 and N_2 are the number of events with zero, one and two ions bright, respectively. The correlation values from the four sets of phase angles are combined into the Bell's signal, $B(\alpha_1,\delta_1,\beta_2,\gamma_2)$, using equation (2). The correlation values and resulting Bell's signals from five data runs are given in Table 2.

So far we have described the experiment in terms of perfect implementation of the phase angles. In the actual experiment, however, α_1, δ_1, β_2 and γ_2 are not quite the same angles both times they occur in the Bell's inequality. In our experiment the dominant reason for this error results from the phase instability of the synthesizer, which can cause the angles to drift appreciably during four minutes, the time required to take a complete set of measurements. This random drift causes a root-mean-squared error for the correlation function of ± 0.03 on this timescale, which propagates to an error of ± 0.06 for the Bell's signal. The error for the Bell's signal from the five combined data sets is then ± 0.03, consistent with the run-to-run variation observed. Averaging the five Bell's signals from Table 2, we arrive at our experimental result, which is

$$B\left(-\frac{\pi}{8},\frac{3\pi}{8},-\frac{\pi}{8},\frac{3\pi}{8}\right) = 2.25 \pm 0.03 \quad (10)$$

If we take into account the imperfections of our experiment (imperfect state fidelity, manipulations, and detection), this value agrees with the prediction of quantum mechanics.

The result above was obtained using the outcomes of every experiment, so that no fair-sampling hypothesis is required. In this case, the issue of detection efficiency is replaced by detection accuracy. The dominant cause of inaccuracy in our state detection comes from the bright state becoming dark because of optical pumping effects. For example, imperfect circular polarization of the detection light allows an ion in the $|\downarrow\rangle$ state to be pumped to $|\uparrow\rangle$, resulting in fewer collected photons from a bright ion. Because of such errors, a bright ion is misidentified 2% of the time as being dark. This imperfect detection accuracy decreases the magnitude of the measured correlations. We estimate that our Bell's signal would be 2.37 with perfect detection accuracy.

We have thus presented experimental results of a Bell's inequality measurement where a measurement outcome was recorded for every experiment. Our detection efficiency was high enough for a Bell's inequality to be violated without requiring the assumption of fair sampling, thereby closing the detection loophole in this experiment. The ions were separated by a distance large enough that no known interaction could affect the results; however, the lightcone loophole remains open here. Further details of this experiment will be published elsewhere. □

Methods

Phase calibration

The experiment was run with specific phase differences of the Raman laser beam fields at each ion. In order to implement a complete set of laser phases, a calibration of the phase on each ion as a function of axial trap strength was made. We emphasize that the calibration method is classical in nature. Although quantum mechanics guided the choice of calibration method, no quantum mechanics was used to interpret the signal. General arguments are used to describe the signal resulting from a sequence of laser pulses and its dependence on the classical physical parameters of the system, the laser phase at the ion, and the ion's position.

In the calibration procedure, a Ramsey experiment was performed on two ions. The first $\pi/2$ Rabi rotation was performed identically each time. The laser phases at the ions' positions for the second $\pi/2$ Rabi rotation were varied, ϕ_1 for ion 1 and ϕ_2 for ion 2. The detection signal is the total number of photons counted during detection. With an auxiliary one-ion experiment we first established empirically that the individual signal depends only on the laser phase at an individual ion and is $C + A\cos\phi_j$. Here C and A are the offset and amplitude of the one-ion signal. We measure the detector to be linear, so that the detection signal is the sum of the two ions' individual signals. The two-ion signal is therefore

$$C + A\cos\phi_1 + C + A\cos\phi_2 = 2C + 2A\cos\left[\frac{1}{2}(\phi_1+\phi_2)\right]\cos\left[\frac{1}{2}(\phi_1-\phi_2)\right] \quad (11)$$

By measuring the fringe amplitude and phase as $\phi_+ = (\phi_1+\phi_2)/2$ is swept, we calibrate $\phi_1 - \phi_2$ as a function of trap strength and ensure that $\phi_1 + \phi_2$ is independent of trap strength.

We use the phase convention that at the ion separation used for the entanglement preparation pulse the maximum of the correlation function is at $\phi_1 = \phi_2 = 0$ (or $\Delta\phi = \phi_{\text{tot}} = 0$). Our measurement procedure begins by experimentally finding this condition of $\phi_1 = \phi_2 = 0$ by keeping $\Delta\phi = 0$ and scanning the synthesizer phase to find the maximum correlation. The experiment is then adjusted to the phase angles specified above by switching the axial trap strength to set $\Delta\phi$ and incrementing the synthesizer phase to set ϕ_{tot}.

Locality issues

The ions are separated by a distance of approximately 3 μm, which is greater than 100 times the size of the wavepacket of each ion. Although the Coulomb interaction strongly couples the ions' motion it does not affect the ions' internal states. At this distance, all known relevant interactions are expected to be small. For example, dipole–dipole interactions between the ions slightly modify the light-scattering intensity, but this effect is negligible for the ion–ion separations used[29]. Also, the detection solid angle is large enough that Young's interference fringes, if present, are averaged out[30]. Even though all known interactions would cause negligible correlations in the measurement outcomes, the ion separation is not large enough to eliminate the lightcone loophole.

We note that the experiment would be conceptually simpler if, after creating the entangled state, we separated the ions so that the input manipulations and measurements were done individually. However, unless we separated the ions by a distance large enough to overcome the lightcone loophole, this is only a matter of convenience of description and does not change the conclusions that can be drawn from the results.

Received 25 October; accepted 30 November 2000.

1. Clauser, J. F. & Shimony, A. Bell's theorem: experimental tests and implications. *Rep. Prog. Phys.* **41**, 1883–1927 (1978).
2. Einstein, A., Podolsky, B. & Rosen, N. Can quantum-mechanical description of reality be considered complete? *Phys. Rev.* **47**, 777–780 (1935).
3. Bell, J. S. On the Einstein-Podolsky-Rosen paradox. *Physics* **1**, 195–200 (1965).
4. Bell, J. S. in *Foundations of Quantum Mechanics* (ed. d'Espagnat, B.) 171–181 (Academic, New York, 1971).
5. Clauser, J. F., Horne, M. A., Shimony, A. & Holt, R. A. Proposed experiment to test local hidden-variable theories. *Phys. Rev. Lett.* **23**, 880–884 (1969).
6. Freedman, S. J. & Clauser, J. F. Experimental test of local hidden-variable theories. *Phys. Rev. Lett.* **28**, 938–941 (1972).
7. Fry, E. S. & Thompson, R. C. Experimental test of local hidden-variable theories. *Phys. Rev. Lett.* **37**, 465–468 (1976).
8. Aspect, A., Grangier, P. & Roger, G. Experimental realization of Einstein-Podolsky-Rosen-Bohm *Gedankenexperiment*: a new violation of Bell's inequalities. *Phys. Rev. Lett.* **49**, 91–94 (1982).
9. Aspect, A., Dalibard, J. & Roger, G. Experimental test of Bell's inequalities using time-varying analyzers. *Phys. Rev. Lett.* **49**, 1804–1807 (1982).
10. Ou, Z. Y. & Mandel, L. Violation of Bell's inequality and classical probability in a two-photon correlation experiment. *Phys. Rev. Lett.* **61**, 50–53 (1988).
11. Shih, Y. H. & Alley, C. O. New type of Einstein-Podolsky-Rosen-Bohm experiment using pairs of light

quanta produced by optical parametric down conversion. *Phys. Rev. Lett.* **61**, 2921–2924 (1988).
12. Tapster, P. R., Rarity, J. G. & Owens, P. C. M. Violation of Bell's inequality over 4 km of optical fiber. *Phys. Rev. Lett.* **73**, 1923–1926 (1994).
13. Kwiat, P. G., Mattle, K., Weinfurter, H. & Zeilinger, A. New high-intensity source of polarization-entangled photon pairs. *Phys. Rev. Lett.* **75**, 4337–4341 (1995).
14. Tittel, W., Brendel, J., Zbinden, H. & Gisin, N. Violation of Bell inequalities by photons more than 10 km apart. *Phys. Rev. Lett.* **81**, 3563–3566 (1998).
15. Weihs, G. *et al.* Violation of Bell's inequality under strict Einstein locality conditions. *Phys. Rev. Lett.* **81**, 5039–5043 (1998).
16. Aspect, A. Bell's inequality test: more ideal than ever. *Nature* **398**, 189–190 (1999).
17. Gisin, N. & Zbinden, H. Bell inequality and the locality loophole: active versus passive switches. *Phys. Lett. A* **264**, 103–107 (1999).
18. Lo, T. K. & Shimony, A. Proposed molecular test of local hidden-variable theories. *Phys. Rev. A* **23**, 3003–3012 (1981).
19. Kwiat, P. G., Eberhard, P. H., Steinberg, A. M. & Chiao, R. Y. Proposal for a loophole-free Bell inequality experiment. *Phys. Rev. A* **49**, 3209–3220 (1994).
20. Huelga, S. F., Ferrero, M. & Santos, E. Loophole-free test of the Bell inequality. *Phys. Rev. A* **51**, 5008–5011 (1995).
21. Fry, E. S., Walther, T. & Li, S. Proposal for a loophole free test of the Bell inequalities. *Phys. Rev. A* **52**, 4381–4395 (1995).
22. Freyberger, M., Aravind, P. K., Horne, M. A. & Shimony, A. Proposed test of Bell's inequality without a detection loophole by using entangled Rydberg atoms. *Phys. Rev. A* **53**, 1232–1244 (1996).
23. Brif, C. & Mann, A. Testing Bell's inequality with two-level atoms via population spectroscopy. *Europhys. Lett.* **49**, 1–7 (2000).
24. Beige, A., Munro, W. J. & Knight, P. L. A Bell's inequality test with entangled atoms. *Phys. Rev. A* **62**, 052102-1–052102-9 (2000).
25. Lamehi-Rachti, M. & Mittig, W. Quantum mechanics and hidden variables: a test of Bell's inequality by the measurement of the spin correlation in low-energy proton–proton scattering. *Phys. Rev. D* **14**, 2543–2555 (1976).
26. Hagley, E. *et al.* Generation of Einstein-Podolsky-Rosen pairs of atoms. *Phys. Rev. Lett.* **79**, 1–5 (1997).
27. Sackett, C. A. *et al.* Experimental entanglement of four particles. *Nature* **404**, 256–259 (2000).
28. Feynman, R. P., Vernon, F. L. & Hellwarth, R. W. Geometrical representation of the Schrödinger equation for solving maser problems. *J. Appl. Phys.* **28**, 49–52 (1957).
29. Richter, T. Cooperative resonance fluorescence from two atoms experiencing different driving fields. *Optica Acta* **30**, 1769–1780 (1983).
30. Eichmann, U. *et al.* Young's interference experiment with light scattered from two atoms. *Phys. Rev. Lett.* **70**, 2359–2362 (1993).

Acknowledgements

We thank A. Ben-Kish, J. Bollinger, J. Britton, N. Gisin, P. Knight, P. Kwiat and I. Percival for useful discussions and comments on the manuscript. This work was supported by the US National Security Agency (NSA) and the Advanced Research and Development Activity (ARDA), the US Office of Naval Research, and the US Army Research Office. This paper is a contribution of the National Institute of Standards and Technology and is not subject to US copyright.

Correspondence and requests for materials should be addressed to D.J.W. (e-mail: david.wineland@boulder.nist.gov).

Autonomic healing of polymer composites

S. R. White*, N. R. Sottos†, P. H. Geubelle*, J. S. Moore‡, M. R. Kessler†, S. R. Sriram‡, E. N. Brown† & S. Viswanathan*

** Department of Aeronautical and Astronautical Engineering, † Department of Theoretical and Applied Mechanics, ‡ Department of Chemistry, University of Illinois at Urbana-Champaign, Urbana, Illinois 61801, USA*

Structural polymers are susceptible to damage in the form of cracks, which form deep within the structure where detection is difficult and repair is almost impossible. Cracking leads to mechanical degradation[1–3] of fibre-reinforced polymer composites; in microelectronic polymeric components it can also lead to electrical failure[4]. Microcracking induced by thermal and mechanical fatigue is also a long-standing problem in polymer adhesives[5]. Regardless of the application, once cracks have formed within polymeric materials, the integrity of the structure is significantly compromised. Experiments exploring the concept of self-repair have been previously reported[6–8], but the only successful crack-healing methods that have been reported so far require some form of manual intervention[10–18]. Here we report a structural polymeric material with the ability to autonomically heal cracks. The material incorporates a microencapsulated healing agent that is released upon crack intrusion. Polymerization of the healing agent is then triggered by contact with an embedded catalyst, bonding the crack faces. Our fracture experiments yield as much as 75% recovery in toughness, and we expect that our approach will be applicable to other brittle materials systems (including ceramics and glasses).

Figure 1 illustrates our autonomic healing concept. Healing is accomplished by incorporating a microencapsulated healing agent and a catalytic chemical trigger within an epoxy matrix. An approaching crack ruptures embedded microcapsules, releasing healing agent into the crack plane through capillary action. Polymerization of the healing agent is triggered by contact with the embedded catalyst, bonding the crack faces. The damage-induced triggering mechanism provides site-specific autonomic control of repair. An additional unique feature of our healing concept is the use of living (that is, having unterminated chain-ends) polymerization catalysts, thus enabling multiple healing events. Engineering this self-healing composite involves the challenge of combining polymer science, experimental and analytical mechanics, and composites processing principles.

We began by analysing the effects of microcapsule geometry and properties on the mechanical triggering process. For example, capsule walls that are too thick will not rupture when the crack approaches, whereas capsules with very thin walls will break during processing. Other relevant design parameters are the toughness and the relative stiffness of the microcapsules, and the strength of the interface between the microcapsule and the matrix. Micromechanical modelling with the aid of the Eshelby–Mura equivalent inclusion method[19] has been used to study various aspects of the complex three-dimensional interaction between a crack and a microcapsule. An illustrative result from these studies is presented in Fig. 2a, which shows the effect of the relative stiffness of the microcapsule on the propagation path of an approaching crack. The crack, the sphere and the surrounding matrix are subjected to a far-field tensile loading, σ_∞, perpendicular to the crack plane.

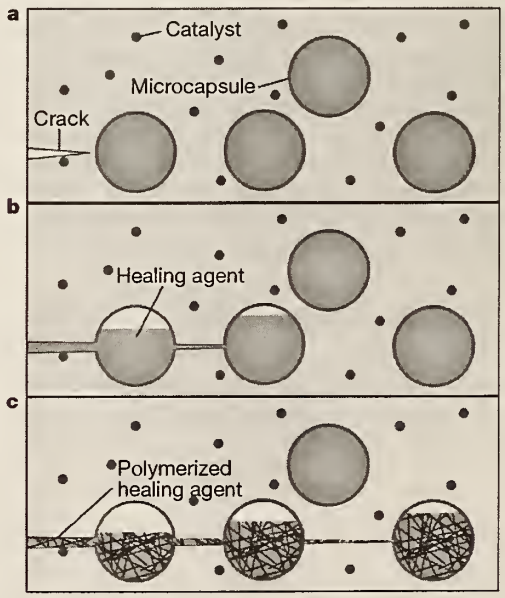

Figure 1 The autonomic healing concept. A microencapsulated healing agent is embedded in a structural composite matrix containing a catalyst capable of polymerizing the healing agent. **a**, Cracks form in the matrix wherever damage occurs; **b**, the crack ruptures the microcapsules, releasing the healing agent into the crack plane through capillary action; **c**, the healing agent contacts the catalyst, triggering polymerization that bonds the crack faces closed.

Experimental Demonstration of Entanglement-Enhanced Rotation Angle Estimation Using Trapped Ions

V. Meyer,[1] M. A. Rowe,[1] D. Kielpinski,[1] C. A. Sackett,[2] W. M. Itano,[1] C. Monroe,[3] and D. J. Wineland[1]
[1]*Time and Frequency Division, National Institute of Standards and Technology, Boulder, Colorado 80305-3328*
[2]*Physics Department, University of Virginia, Charlottesville, Virginia 22904*
[3]*Department of Physics, University of Michigan, Ann Arbor, Michigan 48109*
(Received 26 February 2001)

We experimentally investigate three methods, utilizing different atomic observables and entangled states, to increase the sensitivity of rotation angle measurements beyond the "standard quantum limit" for nonentangled states. All methods use a form of quantum mechanical "squeezing." In a system of two entangled trapped $^9Be^+$ ions we observe a reduction in uncertainty of rotation angle below the standard quantum limit for all three methods including all sources of noise. As an application, we demonstrate an increase in precision of frequency measurement in a Ramsey spectroscopy experiment.

DOI: 10.1103/PhysRevLett.86.5870 PACS numbers: 42.50.Dv, 03.65.Ud, 32.80.Pj, 39.30.+w

Entanglement has played an important role in elucidating fundamental, and sometimes apparently mysterious, aspects of quantum mechanics [1]. It is an integral part of quantum information processing [2], where potential applications include efficient algorithms for problems that are computationally hard on classical computers. Entanglement can also provide increased sensitivity in quantum-limited measurements; here we report experimental measurements of rotation angle in an atomic ensemble where the observed uncertainty is smaller than can possibly be obtained without entanglement.

Generally, we assume a quantum system where an observable $\tilde{O}$ depends on a system parameter ζ. Using measurements of $\tilde{O}(\zeta)$ to determine ζ, the uncertainty in our determination of ζ for a single measurement is given by

$$\delta\zeta = \frac{\Delta\tilde{O}}{|\partial\langle\tilde{O}\rangle/\partial\zeta|}, \tag{1}$$

where $(\Delta\tilde{O})^2 \equiv \langle\tilde{O}^2\rangle - \langle\tilde{O}\rangle^2$ is a measure of the rms fluctuations in repeated measurements of $\tilde{O}$. The specific problem we investigate is efficient estimation of spin rotation angle. We consider a system of N spin-1/2 particles with total angular momentum $\boldsymbol{J} = \sum_{i=1}^{N} \boldsymbol{S}_i$, where $\boldsymbol{S}_i$ is the spin of the ith particle. For each spin, $|\downarrow\rangle_i$ and $|\uparrow\rangle_i$ are spin eigenstates with respect to a chosen axis. Rotations of the entire system are characterized by the operator $R = \exp(-i\zeta \boldsymbol{J}\cdot\hat{\boldsymbol{u}})$ for ζ an angle and $\hat{\boldsymbol{u}}$ the axis of rotation. To make the best estimate of ζ, we want to prepare an input state and choose an observable $\tilde{O}$ that will minimize $\delta\zeta$. This problem is analogous to measurements of path-dependent phase differences in a Mach-Zehnder interferometer [3–5] or transition frequencies in spectroscopy [6–8].

For nonentangled spin-1/2 particles, the states which minimize $\delta\zeta$ are (angular momentum) coherent states [9]. Coherent states can be obtained from the state $|\Psi_0\rangle = |\downarrow\rangle_1|\downarrow\rangle_2\cdots|\downarrow\rangle_N = |J = N/2, m_J = -N/2\rangle$ by an overall rotation. In this case $\tilde{O} = \tilde{J}_\perp$ minimizes $\delta\zeta$, where $\tilde{J}_\perp$ is the angular momentum operator perpendicular to $\langle\boldsymbol{J}\rangle$ in the plane of rotation (Fig. 1). Then, $\delta\zeta = \Delta J_\perp/|\langle J\rangle|$ [10]. Assuming no additional sources of error, for coherent states we obtain $\delta\zeta = \delta\zeta_c = 1/\sqrt{N}$, the standard quantum limit (SQL) [3–8].

We examine three proposed methods to reduce $\delta\zeta$ using entangled states. The first uses states well described by "spin squeezing" [3,4,6], as depicted in Fig. 1b. Here, we take $\tilde{O} = \tilde{J}_\perp$ and $\delta\zeta = \Delta J_\perp/|\langle J\rangle|$ as for coherent states. A second method [11–13] has been discussed in the context of a Mach-Zehnder interferometer for bosons, where the angle ζ to be measured is the interferometer phase offset due to unequal arm length. In the spin context here, a state of the form $|\Psi\rangle = |J = N/2, m_J = 0\rangle$ is rotated and subsequently measured with the variance operator $\tilde{V} = \tilde{J}_z^2 - \langle\tilde{J}_z\rangle^2$. A third method [8] uses states of the form $|\Psi\rangle = [|J,-J\rangle + e^{i\beta}|J,+J\rangle]/\sqrt{2} = [|\downarrow\rangle_1|\downarrow\rangle_2\cdots|\downarrow\rangle_N + e^{i\beta}|\uparrow\rangle_1|\uparrow\rangle_2\cdots|\uparrow\rangle_N]/\sqrt{2}$ that are rotated and subsequently measured with the parity operator $\tilde{O} = \tilde{P} = \prod_{i=1}^{N}\sigma_{zi}$, where $\sigma_{zi} = 2S_{zi}/\hbar$ is the Pauli spin operator in the z direction for the ith particle. In experiments

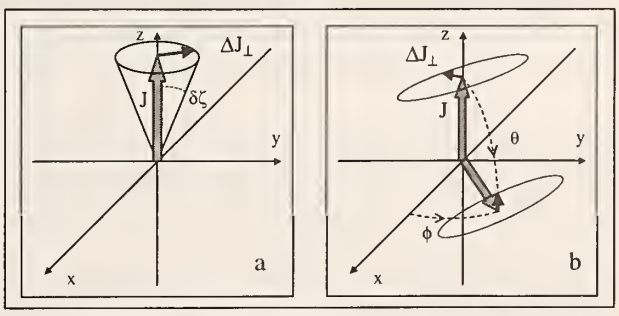

FIG. 1. (a) For spins in a coherent state the uncertainty distribution of the perpendicular spin components $\Delta J_\perp$ is uniform and forms a circle of radius $\sqrt{J/2}$, whereas for entangled spins (b) the distribution of $\Delta J_\perp$ can be "squeezed" in one direction, forming an ellipse. To measure $\Delta J_\perp$, we rotate the spin J into the x-y plane and measure ΔJ_z, observing its oscillation with respect to the phase angle ϕ. From this and the measured value of $|\langle J\rangle|$ we determine $\delta\theta$ (Fig. 2).

 0031-9007/01/86(26)/5870(4)$15.00

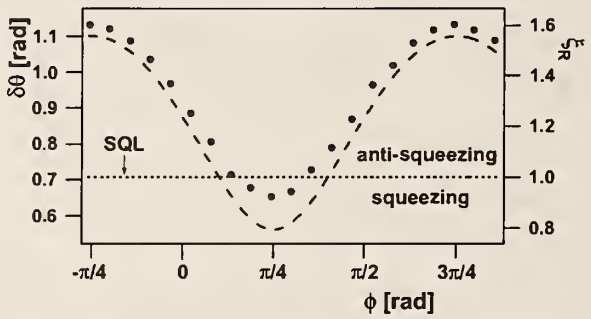

FIG. 2. The ideal phase sensitivity of the state $|\Psi\rangle = \cos(\pi/10)|\downarrow\downarrow\rangle + i\sin(\pi/10)|\uparrow\uparrow\rangle$ is shown as the dashed curve [Eq. (4)]. The full circles are the values determined from 10 000 experiments ($\simeq$1 ms per experiment) per data point. Error bars are smaller than the marker size. The dotted line marks the standard quantum limit $\delta\theta_c = 1/\sqrt{2}$, which is independent of ϕ [7].

with two ions, we use each of these methods and measure a value of $\delta\zeta < \delta\zeta_c$. We quantify these results with the parameter $\xi_R = \delta\zeta/\delta\zeta_c$ [6], related to the entanglement of the system [14]. The minimum possible value of ξ_R is $1/\sqrt{N}$ ($\delta\zeta = 1/N$), the Heisenberg limit [3–8].

The experiments use two $^9Be^+$ ions that are confined along the axis of a miniature linear radio frequency trap [15]. The spectrally resolved $|F = 1, m_F = -1\rangle \equiv |\uparrow\rangle$ and $|F = 2, m_F = -2\rangle \equiv |\downarrow\rangle$ $^2S_{1/2}$ ground-state hyperfine levels of $^9Be^+$ form the basis of an effective spin-1/2 system. Coherent superpositions between $|\downarrow\rangle$ and $|\uparrow\rangle$ are generated by laser-driven two-photon stimulated-Raman transitions [16]. Defining the quantization axis to be the z axis, these operations are equivalent to the spin rotation R for $\hat{u}$ in the x-y plane:

$$|\downarrow\rangle \rightarrow \cos\tfrac{\theta}{2}|\downarrow\rangle - \sin\tfrac{\theta}{2}e^{-i\phi}|\uparrow\rangle, \quad (2a)$$

$$|\uparrow\rangle \rightarrow \cos\tfrac{\theta}{2}|\uparrow\rangle + \sin\tfrac{\theta}{2}e^{i\phi}|\downarrow\rangle, \quad (2b)$$

where ϕ is the laser phase and θ is proportional to the duration the laser pulses are applied (Fig. 1b). Using stimulated-Raman transitions that couple to the ions' motion [17,18], we can also realize the entangling operation:

$$|\downarrow\downarrow\rangle \rightarrow |\Psi\rangle \equiv \cos\alpha|\downarrow\downarrow\rangle + i\sin\alpha|\uparrow\uparrow\rangle, \quad (3)$$

where α is proportional to the laser pulses' duration. At the end of each experiment, we detect the number of ions in the $|\downarrow\rangle$ or $|\uparrow\rangle$ state with state-sensitive fluorescence [19].

For spin squeezing, we take $|\Psi\rangle$ with values of $\alpha \neq M\pi/4$ (M odd) in which case $\langle J\rangle = \langle J_z\rangle = -\cos(2\alpha)$ does not vanish. In the experiment, we extract $\langle J\rangle$ by applying the rotation of Eqs. (2), varying θ, and recording $\langle J_z\rangle$ ("Rabi flopping"). In general $\Delta J_\perp$ depends on ϕ, as indicated in Fig. 1b. To determine $\Delta J_\perp(\phi)$, we rotate $|\Psi\rangle$ into the x-y plane by driving a "$\pi/2$-pulse" on both ions [Eqs. (2) with $\theta = \pi/2$] and measure ΔJ_z for different values of ϕ. This operation preserves the expectation values of $\langle J\rangle$ and $\Delta J_\perp$ in the rotated frame. Therefore we can regard the experiment as measuring the precision of our $\zeta = \theta = \pi/2$ rotation of the spins for the initial state $|\Psi\rangle$; this precision will be optimized for certain values of ϕ. For the ideal case, we have

$$\delta\theta(\phi) = \frac{\Delta J_\perp(\phi)}{|\langle J\rangle|} = \frac{\sqrt{\frac{1}{2}[1 - \sin(2\alpha)\sin(2\phi)]}}{|\cos(2\alpha)|}. \quad (4)$$

We performed experiments for several values of α, obtaining the highest sensitivity for $\alpha = \pi/10$ (Fig. 2). From the Rabi flopping curves we measure $|\langle J\rangle|$ to be 0.768(2) in this case (ideally, we expect 0.809). The highest measured sensitivities achieved are $\delta\theta_{\min} = 0.65(1)$, or $\xi_R = 0.92(1)$. [Ideally $\delta\theta_{\min} = 0.561$ ($\xi_R = 0.794$)]. An increase in sensitivity over the SQL for two nonentangled spins ($\delta\theta_c = 1/\sqrt{2}$) is visible for a range of about $\pi/4$ rad. The discrepancy with the theoretically expected minimal values is caused primarily by imperfect entangled-state preparation. Note that ideally, for two spins, $\delta\theta_{\min} \rightarrow 1/2$ (the Heisenberg limit) as $\alpha \rightarrow \pi/4$. However, then $\langle J\rangle \rightarrow 0$ so that any added noise prevents achieving this limit.

The improvements in phase sensitivity over the SQL arise from spin squeezing. For angular momentum states, the uncertainty relation $(\Delta J_i)^2(\Delta J_j)^2 \geq \frac{1}{4}\hbar^2|\langle J_k\rangle|^2$ allows for one of the variances $(\Delta J_i)^2$ to be reduced (squeezing) at the cost of $(\Delta J_j)^2$ increasing (antisqueezing). $|\langle J_k\rangle|$ must also shrink. The Hamiltonian $H = \chi J_x^2$ which carries the state $|\downarrow\downarrow\rangle$ into $|\Psi\rangle$ [Eq. (3)] [4,17,20] establishes a correlation between the spins of both particles that results in spin squeezing [4]. The redistributed variances of the spins are indicated as an ellipse in Fig. 1b and allow us to obtain values of $\xi_R < 1$ when ΔJ_i shrinks more than $|\langle J_k\rangle|$. Recently, observations of spin squeezing have been reported in Refs. [21] and [22], but the results were not cast in terms of measured $\delta\zeta$ or ξ_R; therefore, a direct comparison is precluded.

For the maximally entangled state $|\Psi_M\rangle = (|\downarrow\downarrow\rangle + i|\uparrow\uparrow\rangle)/\sqrt{2}$ [$\alpha = \pi/4$ in Eq. (3)], or the state $|J = 1, m_J = 0\rangle$, $\langle J\rangle = 0$ [23] so that the above method is experimentally inaccessible. In these cases, the parity operator $\tilde{P}$ or the variance $\tilde{V}$ can be used to increase the sensitivity of a phase measurement. For two ions, $|J = 1, m_J = 0\rangle = (|\downarrow\uparrow\rangle + |\uparrow\downarrow\rangle)/\sqrt{2}$ can be obtained from $|\Psi_M\rangle$ by a rotation [Eqs. (2) with $\theta = \pi/2$ and $\phi = \pi/4$]. For two ions, we have $\tilde{V} = (1 + \tilde{P})/2 - \langle\tilde{J}_z\rangle^2$, so that, except for an offset and scale factor, the measured values of $\tilde{V}$ and $\tilde{P}$ are the same. Therefore we can explore the second and third methods cited in the introduction with the same experiment. Here, we cast the experiment in terms of $|\Psi_M\rangle$ and the parity operator $\tilde{P}$.

We view the experiment as performing a $\pi/2$ rotation of the state $|\Psi_M\rangle$ [Eqs. (2) with $\theta = \pi/2$] and desire to determine $\zeta = \phi$ with maximum sensitivity. To do this, we prepare the state $|\Psi_M\rangle$, perform a $\pi/2$ rotation for various values of ϕ, and measure $\tilde{P}(\phi)$, in which case $\delta\phi = \Delta\tilde{P}/|\partial\langle\tilde{P}\rangle/\partial\phi|$. The measurements

are displayed in Fig. 3b. The amplitude of the observed sinusoidal oscillation is 0.845(2) rather than the theoretical maximum of 1, due primarily to imperfections in state creation. Because of these imperfections, $\delta\phi$ also depends on ϕ as shown in Fig. 3c. Ideally, we have $\delta\phi = 1/2$ ($\xi_R = 1/\sqrt{2}$), the Heisenberg limit, independent of ϕ [8]. In the experiment, we observe $\delta\phi < \delta\phi_c$ for a limited range of ϕ values. The minimal uncertainty observed is $\delta\phi = 0.59(1) < 1/\sqrt{2} = \delta\phi_c$ [$\xi_R = 0.83(1)$]. Note that the period of the oscillation of $\langle\tilde{P}\rangle$ with respect to ϕ is half (in general $1/N$ [8]) that of the period when the observable is J_z (Fig. 1b). This results in a relative increase in $|\partial\langle\tilde{O}\rangle/\partial\phi|$, which is the main reason we can find values of $\xi_R < 1$. The analog of this experiment using entangled photon pairs has been reported in Ref. [24].

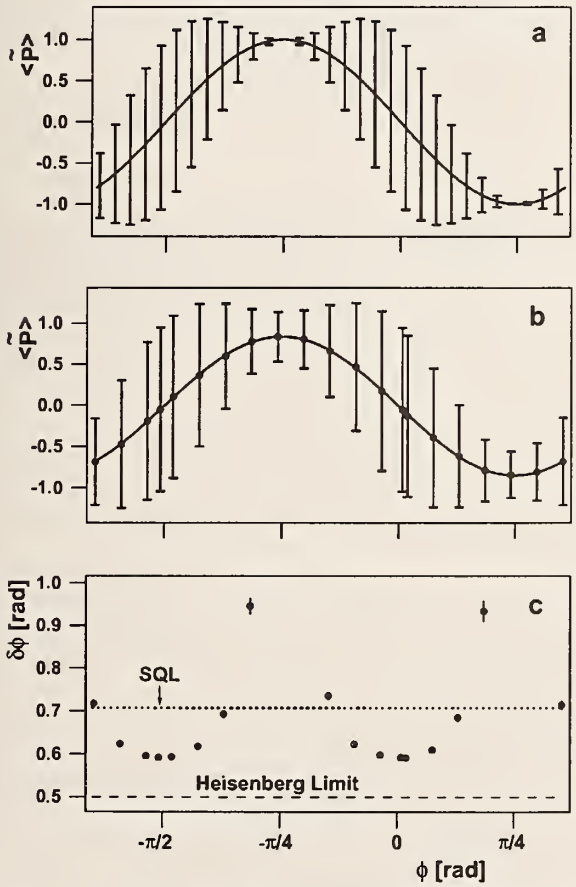

FIG. 3. In (a), we plot the theoretical value $\langle\tilde{P}(\phi)\rangle$ for an initial state $|\Psi_M\rangle = (|\downarrow\downarrow\rangle + i|\uparrow\uparrow\rangle)/\sqrt{2}$ which has been rotated through angles $\theta = \pi/2$, ϕ [Eqs. (2)]. The bars represent the variance $(\Delta\tilde{P})^2$ of the parity. In (b), we show the corresponding measured values from 10 000 experiments (experiment duration $\simeq$1 ms) per data point and a fit to the expected sinusoidal dependence. (c) The resulting phase sensitivity $\delta\phi = \Delta\tilde{P}/|\frac{\partial\langle\tilde{P}\rangle}{\partial\phi}|$, as determined from the data of (b). For the idealized experiment $\delta\phi = 1/2$, independent of ϕ [8], the Heisenberg limit. The dotted line at $1/\sqrt{2}$ represents the SQL. All figures share the same abscissa [shown in (c)].

These methods are of interest for improved frequency measurements [6,8]. Here, we consider use of the parity operator $\tilde{P}$ in combination with maximally entangled states [8]. In Ramsey separated-field spectroscopy [25], if the state after the first Ramsey pulse is of the form $|\Psi\rangle = [|\downarrow\rangle_1|\downarrow\rangle_2\cdots|\downarrow\rangle_N + e^{i\beta}|\uparrow\rangle_1|\uparrow\rangle_2\cdots|\uparrow\rangle_N]/\sqrt{2}$, the transition frequency between the states $|\downarrow\rangle$ and $|\uparrow\rangle$ can be determined with a precision of $\delta(\omega - \omega_0) = \delta\zeta/T = 1/(NT)$ [8]. In this expression, T is the time difference between the first and the second Ramsey pulse and $\delta(\omega - \omega_0)$ is the uncertainty in the measured frequency difference between the atoms' transition frequency ω_0 and the frequency ω of the applied radiation. Therefore, here phase sensitivity translates into frequency sensitivity through the relation $\delta\zeta = \delta(\omega - \omega_0)T$. The gain of a factor of $1/\sqrt{N}$ compared to spectroscopy of atoms in coherent states is of particular interest for precision spectroscopy, which has come close to the SQL [7,26].

To demonstrate the use of entangled states for spectroscopy, we prepare an initial state of two ions of the form $|\Psi_R\rangle \cong (|\downarrow\uparrow\rangle + |\uparrow\downarrow\rangle)/\sqrt{2}$. The Ramsey experiment was performed on $|\downarrow\rangle \leftrightarrow |\uparrow\rangle$ transitions using stimulated Raman excitation with $\omega/2\pi$ detuned by about 10 kHz from $\omega_0/2\pi \cong 1.25$ GHz. We varied the time T between the two Ramsey pulses to change the phase difference $\zeta = (\omega - \omega_0)T$ for the experiments; that is, we determine $\omega - \omega_0$ by varying T and measuring $\tilde{P}$. In Fig. 4 the maximal gain in precision is a factor of 1.14(1) [$\xi_R = 0.88(1)$], compared to an idealized Ramsey experiment using two ions in a coherent state where preparation and detection are perfect.

In summary, we have demonstrated a fundamental increase in sensitivity of rotation angle measurement benefiting from entanglement. The reported measurements include all sources of noise (no noise subtraction)

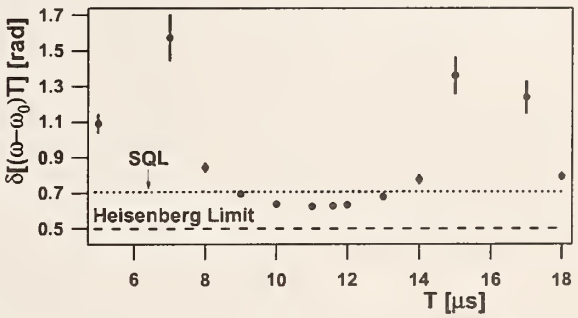

FIG. 4. Uncertainty in frequency determination in a Ramsey experiment using the input state $|\Psi_R\rangle = (|\downarrow\uparrow\rangle + |\uparrow\downarrow\rangle)/\sqrt{2}$. We vary the time T between the Ramsey pulses for fixed frequency detuning $|\omega - \omega_0|/2\pi \cong 10$ kHz. We performed 10 000 experiments (experiment duration $\simeq$1 ms) per data point. The dotted line represents the SQL for two ions in a coherent spin state [7]. The dashed line marks the Heisenberg limit.

and demonstrate a sensitivity better than that which can be obtained without entanglement under ideal conditions. The most important limitation of our experiments is the imperfection of initial state preparation induced by heating of the ions to higher motional states [15], which reduces the degree of entanglement. Maintaining the ions close to their motional ground state should significantly reduce these effects [17]. In an application to a Ramsey spectroscopy experiment, we achieved an increased precision in frequency measurement compared to an idealized experiment using unentangled particles. This may be of significance for the construction of more precise atomic clocks.

We thank J. J. Bollinger and B. E. King for helpful comments on the manuscript. This work was supported by the U.S. National Security Agency (NSA) and the Advanced Research and Development Activity (ARDA) under Contract No. MOD-7171.00, the U.S. Office of Naval Research, and the U.S. Army Research Office. This paper is a contribution of the National Institute of Standards and Technology and is not subject to U.S. copyright.

Note in proof.—Since our submission, number-squeezed atomic states have been reported [27]. Such states are analogous to the $|J = 1, m_J = 0\rangle$ state of our experiment [3–5] and are an important step toward sub-shot-noise atom interferometry [12].

[1] See, for example, J. S. Bell, *Speakable and Unspeakable in Quantum Mechanics* (Cambridge University Press, Cambridge, 1987); N. D. Mermin, Phys. Today **38**, No. (4), 38 (1985).

[2] See, for example, M. A. Nielsen and I. L. Chuang, *Quantum Computation and Quantum Information* (Cambridge University Press, Cambridge, 2000).

[3] B. Yurke, Phys. Rev. Lett. **56**, 1515 (1986); B. Yurke, S. L. McCall, and J. R. Klauder, Phys. Rev. A **33**, 4033 (1986).

[4] M. Kitagawa and M. Ueda, Phys. Rev. A **47**, 5138 (1993).

[5] B. C. Sanders and G. J. Milburn, Phys. Rev. Lett. **75**, 2944 (1995).

[6] D. J. Wineland, J. J. Bollinger, W. M. Itano, F. L. Moore, and D. J. Heinzen, Phys. Rev. A **46**, R6797 (1992); D. J. Wineland, J. J. Bollinger, W. M. Itano, and D. J. Heinzen, Phys. Rev. A **50**, 67 (1994).

[7] W. M. Itano, J. C. Bergquist, J. J. Bollinger, J. M. Gilligan, D. J. Heinzen, F. L. Moore, M. G. Raizen, and D. J. Wineland, Phys. Rev. A **47**, 3554 (1993).

[8] J. J. Bollinger, W. M. Itano, D. J. Wineland, and D. J. Heinzen, Phys. Rev. A **54**, R4649 (1996).

[9] F. T. Arecci, E. Courtens, R. Gilmore, and H. Thomas, Phys. Rev. A **6**, 2211 (1972).

[10] More precisely, $\delta\zeta = \arctan(\Delta J_\perp/|\langle J\rangle|)$ (Fig. 1a). Following convention, we use instead $\delta\zeta = \Delta J_\perp/|\langle J\rangle|$ given by Eq. (1). In typical situations, where measurements of $\tilde{O}$ are repeated M times ($M \gg 1$), $\Delta J_\perp \to \Delta J_\perp/\sqrt{M}$ and this distinction is not important.

[11] M. J. Holland and K. Burnett, Phys. Rev. Lett. **71**, 1355 (1993).

[12] P. Bouyer and M. A. Kasevich, Phys. Rev. A **56**, R1083 (1997).

[13] T. Kim, O. Pfister, M. J. Holland, J. Noh, and J. L. Hall, Phys. Rev. A **57**, 4004 (1998).

[14] A. Sørensen, L.-M. Duan, J. I. Cirac, and P. Zoller, Nature (London) **409**, 63 (2001).

[15] Q. A. Turchette, D. Kielpinski, B. E. King, D. Leibfried, D. M. Meekhof, C. J. Myatt, M. A. Rowe, C. A. Sackett, C. S. Wood, W. M. Itano, C. Monroe, and D. J. Wineland, Phys. Rev. A **61**, 063418 (2000).

[16] C. Monroe, D. M. Meekhof, B. E. King, S. R. Jefferts, W. M. Itano, D. J. Wineland, and P. Gould, Phys. Rev. Lett. **75**, 4011 (1995).

[17] A. Sørensen and K. Mølmer, Phys. Rev. A **62**, 022311 (2000).

[18] C. A. Sackett, D. Kielpinski, B. E. King, C. Langer, V. Meyer, C. J. Myatt, M. Rowe, Q. A. Turchette, W. M. Itano, D. J. Wineland, and C. Monroe, Nature (London) **404**, 256 (2000).

[19] M. A. Rowe, D. Kielpinski, V. Meyer, C. A. Sackett, W. M. Itano, C. Monroe, and D. J. Wineland, Nature (London) **409**, 791 (2001).

[20] B. C. Sanders, Phys. Rev. A **40**, 2417 (1989).

[21] J. Hald, J. L. Sørensen, C. Schori, and E. S. Polzik, Phys. Rev. Lett. **83**, 1319 (1999).

[22] A. Kuzmich, L. Mandel, and N. P. Bigelow, Phys. Rev. Lett. **85**, 1594 (2000).

[23] In the context of Fig. 1, $|\Psi_M\rangle$ is a circle of unit radius in the plane defined by the $\hat{z}$ and $(\hat{x} - \hat{y})/\sqrt{2}$ directions and centered at the origin.

[24] A. Kuzmich and L. Mandel, Quantum Semiclass. Opt. **10**, 493 (1998).

[25] N. F. Ramsey, *Molecular Beams* (Oxford University Press, London, 1963), p. 124.

[26] G. Santarelli, Ph. Laurent, P. Lemonde, A. Clairon, A. G. Mann, S. Chang, A. N. Luiten, and C. Salomon, Phys. Rev. Lett. **82**, 4619 (1999).

[27] C. Orzel, A. K. Tuchman, M. L. Fenselau, M. Yasuda, and M. A. Kasevich, Science **291**, 2386 (2001).

Diode-pumped Nd:FAP laser at 1.126 μm: a possible local oscillator for a Hg^+ optical frequency standard

Flavio C. Cruz, Brenton C. Young, and James C. Bergquist

We report the efficient operation of a continuous-wave, single-frequency, diode-pumped Nd:FAP laser at 1.126 μm. When frequency quadrupled, such a laser might be used as a local oscillator for an optical frequency standard based on the single-photon $^2S_{1/2}$–$^2D_{5/2}$ electric quadrupole transition of a trapped and laser-cooled $^{199}Hg^+$ ion. Since the frequencies of the atomic transition and the laser are harmonically related, this scheme helps to simplify the measurement of the *S–D* clock transition frequency by a phase-coherent chain to the cesium primary frequency standard.

OCIS codes: 020.7010, 140.3480, 140.3580, 190.4160, 300.6520.

Trapped and laser-cooled ions have great potential for optical frequency and time standards.[1–6] High resolution is possible because perturbations can be made small[7] and interrogation times long.[8,9] In addition, laser cooling reduces first- and second-order Doppler shifts to extremely low levels.[10] Among proposed standards that use trapped and laser-cooled ions,[6] a $^{199}Hg^+$ ion standard is attractive because it offers both a microwave transition[9] and a narrow optical transition that promise high performance. The optical standard is based on the $^2S_{1/2}$–$^2D_{5/2}$, 281.5-nm electric quadrupole transition.[11] Optical frequency standards are attractive since the potential fractional frequency instability of a standard is inversely proportional to its frequency. An optical clock can have a fractional frequency instability less than 1×10^{-15} at 1 s even for a single laser-cooled ion. However, for reaching such low instabilities it is necessary to have a laser (local oscillator) whose frequency fluctuations are less than 1 Hz for times as long as a few seconds.

The inherent frequency stability of solid-state lasers makes them attractive for metrological applications and precision spectroscopy. In addition, a solid-state laser can be compact, reliable, and long-lived. Reliable, commercial diode lasers do not yet exist in the UV, near the transition needed for the Hg^+ system, but high-power, near-infrared diode lasers are available. Consequently, some groups have frequency-quadrupled the output of near-infrared diode lasers that oscillate at a single frequency and in a single spatial mode to obtain cw, single-frequency UV sources.[12,13] An alternative approach is to frequency-quadruple the output of a cw, solid-state laser that is pumped with high-power multimode diode lasers, such as has previously been done with Nd:YAG and Nd:YVO_4 lasers.[14] Here we report the development of a diode-pumped solid-state Nd:FAP laser that operates in a single spatial and single-frequency mode at 1.126 μm. The frequency of the output radiation from this laser was quadrupled and might be used as a local oscillator in an optical frequency standard based on the *S–D* quadrupole transition of trapped and laser-cooled $^{199}Hg^+$ ions at 282 nm. Because the free-running frequency instability of this laser is dominated by low-frequency acoustical and mechanical noise, only a moderate-speed servo system is needed to lock the laser frequency tightly to the resonance of a high-finesse cavity.[11,15] In addition, since the frequency of the Nd:FAP laser is quadrupled to reach the atomic transition, we have completed the first steps in a frequency chain from the optical to the microwave.

The spectral analysis and lasing performance of Nd:FAP at 1.06 μm have been reported elsewhere.[16,17] The absorption spectrum of Nd:FAP, like Nd:YAG, has a strong line near 808 nm, approximately 2.5 nm wide, which is well suited to optical pumping by a diode laser. In addition to a strong emission peak at 1.06 μm, weaker features near 1.12 and 0.93 μm are also observed. We make the Nd:

When this research was performed, all the authors were with the Time and Frequency Division, National Institute of Standards and Technology, 325 Broadway, Boulder, Colorado 80303. F. C. Cruz is now with the Universidade Estadual de Campinas (UNICAMP), Instituto de Fisica "Gleb Wataghin," CP.6165, Campinas, SP 13083-970, Brazil. The email address for B. C. Young is byoung@boulder.nist.gov.

Received 24 June 1998.

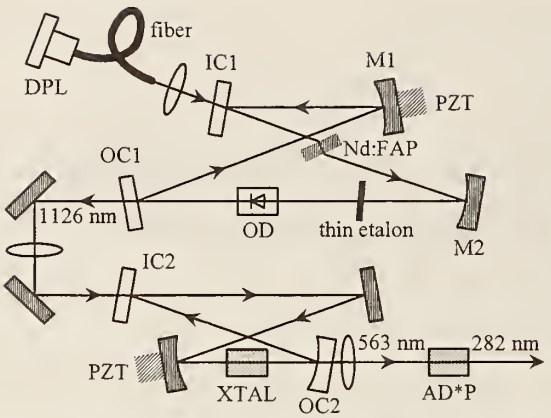

Fig. 1. Experimental setup for the frequency-quadrupled, diode-pumped Nd:FAP laser: DPL, diode pump laser at 808 nm; IC1, flat input coupler for the Nd:FAP laser (HR at 1126 nm, $T \approx 90\%$ at 808 nm); PZT, piezoelectric transducer; M1 and M2, 15-cm radius-of-curvature mirrors (HR at 1126 nm); OD, optical diode; OC1, flat output coupler ($T = 0.4\%$ at 1126 nm, $T \approx 50\%$ at 1064 nm); IC2, flat input coupler for doubling cavity ($T = 1.7\%$ at 1126 nm); XTAL, $KNbO_3$ or $LiNbO_3$ doubling crystal; OC2, flat output coupler (HR at 1126 nm, $T \approx 80\%$ at 563 nm for $KNbO_3$ or 94% for $LiNbO_3$); AD*P, deuterated ammonium dihydrogen phosphate.

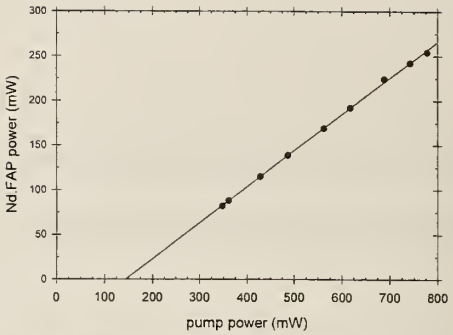

Fig. 2. Output power of the Nd:FAP laser at 1.126 μm as a function of pump power from a Ti:sapphire laser.

FAP laser oscillate at 1.126 μm by strongly suppressing the higher-gain oscillation at 1.06 μm. Our crystal is cut, polished, and oriented at Brewster's angle to avoid the need for any antireflection coatings. The c axis lies in a plane parallel to the polished surfaces and is oriented perpendicular to the polarization of the radiation of both the pump laser and the Nd:FAP laser. The thickness of the crystal is 2 mm, and the diameter is 6.3 mm. The Nd concentration gives approximately 80% absorption of the light from a diode laser at 808 nm. Absorption is nearly 100% when a narrow-band Ti:sapphire laser is used. We largely eliminate thermal problems for pump powers as high as 1 W by heat sinking the crystal in a tightly fitting copper support piece. Maximum output powers are achieved for cavity waists ω_0 between 80 and 100 μm. The diode laser used for pumping emits as high as 1 W at 808 nm, which is coupled into a fiber with a 100-μm core diameter. Approximately 750 mW is available after the fiber. A 3.5-cm focal-length lens collimates the beam diverging from the fiber, and a 6.7-cm lens focuses the light through the Nd:FAP crystal.

The 1.126-μm laser is built as a ring cavity formed by two flat mirrors (input and output couplers) and two 15-cm radius-of-curvature mirrors that are highly reflecting (HR) at 1.126 μm (M1 and M2 in Fig. 1). The Nd:FAP crystal is positioned midway between the 15-cm mirrors at a nearly optimum cavity waist of $\omega_0 \approx 80$ μm. The flat input coupler IC1 transmits 90% of the pump light at 808 nm and is HR at 1.126 μm. The output coupler OC1 was coated to transmit 0.4% of the radiation at 1.126 μm and 50% at 1.06 μm, which eliminates lasing on the strong line at 1.06 μm. The pump beam is focused into the crystal with a beam waist of $\omega_0 \approx 100$ μm. The astigmatism introduced by the crystal is compensated by the off-axis orientation of the 15-cm mirrors. Unidirectional oscillation is enforced by an optical diode formed by a terbium–gallium garnet Faraday rotator and a quartz compensating plate. The laser oscillates at 1.126 μm in a single-frequency TEM_{00} mode without any frequency-selective elements inside the cavity. However, a thin etalon improves the mode stability and makes it possible to tune the wavelength. Tuning of the laser from approximately 1.118 to 1.128 μm was verified by use of an interferometric wavemeter and an optical spectrum analyzer. When frequency quadrupled, the Nd:FAP laser reaches the Hg^+ S–D transition at 281.5 nm. The tuning range also includes the $A_2\,\Sigma(n'' = 1) \leftarrow X_2\,\Pi(n' = 0)$ transition of OH molecules at 281.93 nm, which could possibly be used for remote sensing of OH in the atmosphere.[18]

The output power of the 1.126-μm laser as a function of pump power from the Ti:sapphire laser is plotted in Fig. 2. The slope efficiency is approximately 40%. For an input power of 780 mW, an output power of 260 mW is achieved, corresponding to an overall efficiency of 33%. When pumped by the diode laser, the efficiency is reduced to approximately 20% owing to the poorer spatial mode quality of the diode laser beam and to the lower absorption of the pump power by the crystal.

We double the fundamental radiation at 1126 nm using either $KNbO_3$ or $LiNbO_3$. Noncritically phase-matched harmonic generation in $KNbO_3$, which would be highly efficient, is predicted to occur for 1126-nm light at a phase-matching temperature[19] of 268 °C. Unfortunately, this is precluded since $KNbO_3$ experiences a phase transition near 220 °C. However, less efficient type-I angle-tuned critical phase matching at room temperature is still possible for b-cut $KNbO_3$ at a phase-matching angle of $\theta_{pm} \approx 23.9°$. The calculated effective nonlinear coefficient d_{eff} is 11.8 pm/V and the walkoff angle is approximately 60 mrad, which implies an efficiency per unit crystal length of 2×10^{-3} W^{-1} cm^{-1}. For 2-mm-long crystals we measure single-pass efficiencies η slightly higher than 1×10^{-4} W^{-1} under optimum focusing conditions, which is less than predicted. We increase the harmonic power by using

antireflection-coated $KNbO_3$ in an external build-up cavity (Fig. 1). The cavity is locked to resonance with the frequency of the laser by the Hänsch–Couillaud polarization technique.[20] The power-enhancement cavity is formed by two flat mirrors and two spherical mirrors (7.5-cm radius of curvature) that produce a waist of 14 μm, nearly optimum[21] for the 2-mm-long $KNbO_3$. The input coupler IC2 transmits 1.7% of the radiation at 1126 nm. This transmittance gives nearly 100% coupling into the cavity for 100 mW of incident radiation when light at the second harmonic is generated. The output coupler OC2 is one of the 7.5-cm mirrors, which is HR at 1126 nm and 80% transmitting at 563 nm. The other mirrors are HR at 1126 nm. The crystal is positioned in the tight focus between the two curved mirrors, and the fundamental beam is mode matched into the softer waist between the two flat mirrors. We keep the cavity angles as small as possible to minimize the astigmatism introduced by the curved mirrors. The cavity losses (excluding the input coupler) are 0.1% and the crystal losses are 0.3%, as determined from the measured finesse and build-up factors of the cavity with and without the crystal. The crystal losses are dominated by surface scattering. For an input power of 100 mW at 1126 nm and an enhancement factor of 150, we achieve an output power of 10 mW at 563 nm.

We also verified that generation of the second harmonic of 1126-nm radiation is possible in congruent $LiNbO_3$ at $T_{pm} \approx 142$ °C. At this temperature we observe no indication of optical damage. At 1126 nm, d_{eff} is 4.3 pm/V, which gives $\eta \approx 1.9 \times 10^{-3}$ W^{-1} for our 11.3-mm-long crystal. However, we measure a single-pass efficiency of only 8.0×10^{-4} W^{-1} for optimum focusing conditions ($\omega_0 \approx 20$ μm). We again use a power-enhancement cavity, but the size of our oven restricts us to focusing mirrors with longer radii of curvature. Hence the waist in the crystal is larger than optimum, limiting η to approximately 3.7×10^{-4} W^{-1}. The power-enhancement factor in the presence of the crystal is only 76, largely because of scattering from the Brewster-cut crystal surfaces. Even so, we again attain an output power of approximately 10 mW at 563 nm. This corresponds to approximately 22 mW of harmonic radiation generated in the crystal when the power is corrected for the 94% transmittance of the output coupler and the 60% transmittance of the Brewster face of the crystal. Since the usable power is nearly the same in both cases, we find it easier and more practical to use $KNbO_3$.

For the second stage of harmonic generation we use deuterated ammonium dihydrogen phosphate (AD*P) to double 563 to 281.5 nm.[22] Since less than 1 pW can be enough to saturate the narrow *S–D* transition,[22] we simply double the radiation at 563 nm in a single-pass configuration (Fig. 1). Type-I noncritical phase matching is possible for doubling 563 nm with AD*P at $T_{pm} \approx 128$ °C. The measured single-pass efficiency is approximately 10^{-3} W^{-1} for our 3-cm-long crystal. Approximately 0.1 μW is generated at 281.5 nm for 10 mW of input power at 563 nm. If more power is needed, then another option could be β-barium borate (BBO) in an external build-up cavity. Type-I angle-tuned critical phase matching at $\theta_{pm} \approx 44°$ is possible with $d_{eff} \approx 1.64$ pm/V. The walkoff angle is 77 mrad, which gives $\eta \approx 1.3 \times 10^{-4}$ W^{-1} for a 6-mm-long crystal.

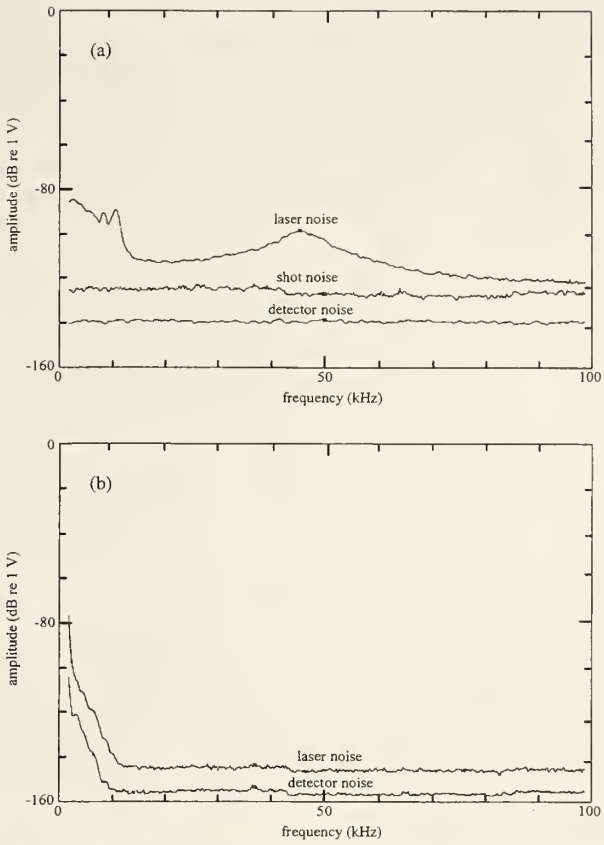

Fig. 3. (a) AM and (b) FM noise spectral densities in a 1-kHz bandwidth for the Nd:FAP laser at 563 nm. The peak at approximately 50 kHz in (a) caused by relaxation oscillations.

Figure 3 shows the power spectral densities of AM and FM noise for the radiation from the Nd:FAP laser at 563 nm. Also shown are the shot noise and detector noise. For the AM noise measurements part of the laser power is directed onto a fast photodetector. The amplitude noise spectrum of the Nd:FAP laser is obtained by a fast Fourier transform of the detected signal. The FM noise measurements are similar, except that a Fabry–Perot cavity is used as a frequency discriminator, converting frequency fluctuations into intensity fluctuations. The spectral distributions of amplitude and frequency noise of the Nd:FAP laser are dominated by contributions at low frequencies (<12 kHz). The pump diode laser, the elements in the Nd:FAP laser cavity, and the components in the external doubling cavity were all mounted in aluminum supports connected by Invar bars to improve the passive stability. A broad peak caused by relaxation oscillations at several tens of kilohertz (depending on the pump power) is observed in the spectral density of AM noise, which is shot-

noise limited above 100 kHz. The relaxation-oscillation peak is nearly absent in the FM spectral density at 563 nm. Both the AM and FM noise are lower when the Nd:FAP laser is diode pumped than when it is pumped by a Ti:sapphire laser. The free-running rms frequency excursions of the Nd:FAP laser are measured to be smaller than 100 kHz for periods of a few seconds. Therefore we anticipate that a moderate-speed servo system would be sufficient to lock its frequency to the resonance of a quiet reference cavity. When the frequency of the laser is locked to the cavity, one can measure the laser linewidth by heterodyning two independent systems[11] and by probing the narrow *S–D* atomic transition in $^{199}Hg^{+}$. The quadrupled Nd:FAP laser should also facilitate the implementation of a frequency chain to the cesium standard at 9.2 GHz. One can directly compare the Nd:FAP fundamental frequency to a secondary frequency standard such as the methane-stabilized He–Ne laser at 3.39 μm by using a recently demonstrated 3:1 optical divider.[23]

This study is partially supported by the Office of Naval Research. F. C. Cruz acknowledges the support of Fundação Coordenação de Aperfeiçoamento de Pessoal de Nivel Superior (Brazil). We thank R. Byer, T. Y. Fan, and D. Nabors for providing the Nd:FAP crystal and for their useful comments.

References and Notes

1. H. G. Dehmelt, "Mono-ion oscillator as potential ultimate laser frequency standard," IEEE Trans. Instrum. Meas. **31,** 83–87 (1982).
2. E. Peik, G. Hollemann, and H. Walther, "Laser cooling and quantum jumps of a single indium ion," Phys. Rev. A **49,** 402–408 (1994).
3. P. Taylor, M. Roberts, G. P. Barwood, and P. Gill, "Combined optical–infrared single-ion frequency standard," Opt. Lett. **23,** 298–300 (1998).
4. L. Marmet, A. A. Madej, K. J. Siemsen, J. E. Bernard, and B. G. Whitford, "Precision frequency measurement of the $^2S_{1/2}$–$^2D_{5/2}$ transition of Sr^+ with a 674-nm diode laser locked to an ultrastable cavity," IEEE Trans. Intrum. Meas. **46,** 169–173 (1997).
5. S. Urabe, M. Watanabe, H. Imajo, and K. Hayasaka, "Laser cooling of trapped Ca^+ and measurement of the 3 $^2D_{5/2}$ state lifetime," Opt. Lett. **17,** 1140–1142 (1992).
6. See, for example, *Proceedings of the Fifth Symposium on Frequency Standards and Metrology*, J. C. Bergquist, ed. (World Scientific, Singapore, 1996).
7. D. J. Wineland, J. C. Bergquist, R. E. Drullinger, H. Hemmati, W. M. Itano, and F. L. Walls, "Laser cooled, stored ion experiments at NBS and possible applications to microwave and optical frequency standards," J. Phys. **42,** C8-307–C8-313 (1981).
8. J. J. Bollinger, J. D. Prestage, W. M. Itano, and D. J. Wineland, "Laser-cooled-atomic frequency standard," Phys. Rev. Lett. **54,** 1000–1003 (1985); J. J. Bollinger, D. J. Heinzen, W. M. Itano, S. L. Gilbert, and D. J. Wineland, "A 303-MHz frequency standard based on trapped Be^+ ions," IEEE Trans. Instrum. Meas. **40,** 126–128 (1991).
9. D. J. Berkeland, J. D. Miller, J. C. Bergquist, W. M. Itano, and D. J. Wineland, "Laser-cooled mercury ion frequency standard," Phys. Rev. Lett. **80,** 2089–2092 (1998).
10. D. J. Wineland, J. C. Bergquist, W. M. Itano, F. Diedrich, and C. S. Weimer, "Frequency standards in the optical spectrum," in *The Hydrogen Atom*, G. F. Bassani, M. Inguscio, and T. W. Hänsch, eds. (Springer-Verlag, Berlin, 1989), pp. 123–133.
11. J. C. Bergquist, W. M. Itano, and D. J. Wineland, "Laser stabilization to a single ion," in *Frontiers in Laser Spectroscopy*, T. W. Hänsch and M. Inguscio, eds. (North Holland, Amsterdam, 1994), pp. 359–376.
12. C. Zimmermann, V. Vuletic, A. Hemmerich, and T. W. Hänsch, "All solid state laser source for tunable blue and ultraviolet radiation," Appl. Phys. Lett. **66,** 2318–2320 (1995).
13. K. Matsubara, U. Tanaka, H. Imajo, K. Hayasaka, R. Ohmukai, M. Watanabe, and S. Urabe, "An all-solid-state tunable 214.5-nm continuous-wave light source by using two-stage frequency doubling of a diode laser," Appl. Phys. B **67,** 1–4 (1998).
14. See, for example, G. Hollemann, E. Peik, and H. Walther, "Frequency-stabilized diode-pumped Nd:YAG laser at 946 nm with harmonics at 473 and 237 nm," Opt. Lett. **19,** 192–194 (1994); K. Kondo, M. Oka, H. Wada, T. Fukui, N. Umezu, K. Tatsuki, and S. Kubota, "Demonstration of long-term reliability of a 266-nm, continuous-wave, frequency-quadrupled solid-state laser using β-BaB_2O_4," Opt. Lett. **23,** 195–197 (1998).
15. M. Zhu and J. L. Hall, "Frequency stabilization of tunable lasers," in *Experimental Methods in the Physical Sciences*, F. B. Dunning and R. G. Hulet, eds. (Academic, San Diego, 1996), Vol. 29C, pp. 103–136, and references therein.
16. R. C. Ohlmann, K. B. Steinbruegge, and R. Mazelsky, "Spectroscopic and laser characteristics of neodymium-doped calcium fluorophosphate," Appl. Opt. **7,** 905–914 (1968).
17. X. X. Zhang, A. B. Villaverde, M. Bass, G. Lutts, and B. H. T. Chai, "Spectroscopy and lasing performance of Nd^{3+} doped $Ca_5(PO_4)_3F$," in *Growth, Characterization, and Applications of Laser Host and Nonlinear Crystals II*, B. H. T. Chai, ed., Proc. SPIE **1863,** 35–38 (1993).
18. D. D. Davis, W. S. Heaps, D. Philen, M. Rodgers, T. McGee, A. Nelson, and A. J. Moriarty, "Airborne laser induced fluorescence system for measuring OH and other trace gases in the parts-per-quadrillion to parts-per-trillion range," Rev. Sci. Instrum. **50,** 1505–1516 (1979); G. L. Vaghjiani and A. R. Ravishankara, "Kinetics and mechanism of OH reaction with CH_3OOH," J. Phys. Chem. **93,** 1948–1959 (1989).
19. I. Biaggio, P. Kerkoc, L.-S. Wu, P. Günter, and B. Zysset, "Refractive indices of orthorhombic $KNbO_3$. II. Phase-matching configurations for nonlinear-optical interactions," J. Opt. Soc. Am. B **9,** 507–517 (1992).
20. T. W. Hänsch and B. Couillaud, "Laser frequency stabilization by polarization spectroscopy of a reflecting reference cavity," Opt. Commun. **35,** 441–444 (1980).
21. G. D. Boyd and D. A. Kleinman, "Parametric interaction of focused Gaussian light beams," J. Appl. Phys. **39,** 3597–3639 (1968).
22. J. C. Bergquist, R. G. Hulet, W. M. Itano, and D. J. Wineland, "Observation of quantum jumps in a single atom," Phys. Rev. Lett. **57,** 1699–1702 (1986).
23. O. Pfister, M. Mürtz, J. S. Wells, L. Hollberg, and J. T. Murray, "Division by 3 of optical frequencies by use of difference-frequency generation in noncritically phase-matched $RbTiOAsO_4$," Opt. Lett. **21,** 1387–1389 (1996).

Visible Lasers with Subhertz Linewidths

B. C. Young, F. C. Cruz,* W. M. Itano, and J. C. Bergquist
Time & Frequency Division, National Institute of Standards and Technology, 325 Broadway, Boulder, Colorado 80303
(Received 5 January 1999)

We report a visible laser with a subhertz linewidth for use in precision spectroscopy and as a local oscillator for an optical frequency standard. The laser derives its stability from a well-isolated, high-finesse, Fabry-Pérot cavity. For a 563 nm laser beam locked to our stable cavity, we measure a linewidth of 0.6 Hz for averaging times up to 32 s. The fractional frequency instability for the light locked to the cavity is typically 3×10^{-16} at 1 s. Both the linewidth and fractional frequency instability are approximately an order of magnitude less than previously published results for stabilized lasers. [S0031-9007(99)09100-0]

PACS numbers: 42.55.–f, 06.30.Ft, 07.10.Fq, 42.60.Da

Stable and spectrally narrow lasers are important for optical frequency standards and also for measurements of fundamental constants, high-resolution spectroscopy, and fundamental tests of physics [1,2]. It has already been demonstrated that the frequencies of several types of lasers can be locked to resonances of Fabry-Pérot cavities with precisions better than 0.1 Hz [3]. What remained to be demonstrated, however, was that the resonance frequency of a reference cavity could have a stability better than 1 Hz. Previously, the narrowest reported visible-laser linewidth was 10 Hz for a 1 s averaging time [4]. Here we report a linewidth of 0.6 Hz for averaging times up to 32 s. Previous results from our group (21 Hz linewidth for 70 s averaging times [5]) were limited by cavity length changes caused by vibrational noise. The improvement reported here derives from modifications that include cavities with more stable material properties and better isolation of the cavities from mechanical vibrations.

The central component of our stabilized laser is a high-finesse ($\mathcal{F} > 150\,000$) Fabry-Pérot cavity [5]. We use a dye laser at 563 nm as the optical source that is locked to this reference cavity. Rather than locking the laser directly to the high-finesse cavity, we first prestabilize it to a cavity with a finesse of $\approx$800 using a Pound-Drever-Hall frequency modulation (FM) lock [6]. An intracavity electro-optic modulator (EOM) in the dye laser provides high-frequency correction of laser frequency noise. A piezoelectric transducer (PZT) behind one of the dye-laser cavity mirrors eliminates long-term frequency drifts between the dye laser and the low-finesse cavity. A loop bandwidth of $\approx$2 MHz in this prestabilization stage narrows the dye-laser short-term ($\tau < 1$ s) linewidth to $\approx$1 kHz.

An optical fiber delivers light from the dye-laser table to a vibrationally isolated table that supports the high-finesse cavity. An acousto-optic modulator (AOM) mounted on the isolated table shifts the frequency of the incoming light to match a cavity resonance. Again, we implement the lock using the Pound-Drever-Hall technique. The feedback loop performs corrections at frequencies as high as $\approx$90 kHz by varying the AOM drive frequency and at low frequencies by adjusting a PZT on the prestabilization cavity.

The high-finesse cavity must have intrinsically low sensitivity to temperature variations and must be well protected from environmental perturbations. The spacer between the cavity mirrors is composed of a low-thermal-expansion material. While we have used both Zerodur and ULE spacers [7,8], the data reported here were collected using ULE spacers. Our spacer is cylindrical with a 15 cm outer diameter and a 24 cm length. The spacer is tapered at both ends to provide greater stiffness than that of a cylinder with the same length and mass. A 1 cm diameter core is drilled through the center of the cylinder. A second core is drilled from the side of the cylinder into the center to allow evacuation of the intracavity region. The cavity mirrors are made with ULE substrates and are optically contacted onto the ends of the spacer.

The cavity is supported inside an evacuated chamber by an aluminum v-block. Four cylindrical pieces of Viton embedded in the v-block serve as the contact points with the cavity. The Viton contacts help to provide high-frequency vibration isolation, damping for mechanical motion, and thermal isolation for the cavity (the thermal time constant between the cavity and the vacuum chamber is $\approx$14 h). Evacuating the chamber reduces shifts of the cavity resonance caused by index-of-refraction changes in the intracavity volume and thermally insulates the cavity from the environment. The temperature of the vacuum chamber is held at $\approx$30 °C, which is near the temperature at which the coefficient of thermal expansion for the cavity spacer is zero. The residual temperature fluctuations of the vacuum chamber are $\approx$10 mK.

We protect the cavity from vibrational noise by mounting the vacuum chamber on a passively isolated optical table. The table is suspended by vertical strands of surgical tubing stretched to $\approx$3 m. The fundamental stretch mode and the pendulum mode of the suspension both have

frequencies of ≈0.3 Hz. This suspension system reduces the amplitude of the transmitted vibrational noise at frequencies greater than 3 Hz by more than a factor of 50. In many systems the cavity is isolated by using a pendulum suspension inside the vacuum chamber, but our table suspension is sufficiently good so that we can semirigidly mount the cavity inside the vacuum chamber. Dashpots filled with grease at each corner of the table provide viscous damping (damping time constant ≈1 s). Proximity detectors at three corners of the table serve as sensors for stabilizing the table position relative to the floor. A servo system drives heaters surrounding the surgical tubing so as to stabilize the table position with a time constant of ≈100 s. To prevent the coupling of acoustic noise into the cavity, we enclose the optical table in a wooden box lined internally with lead foam [9].

The intracavity light heats the mirror coatings, thereby shifting the cavity resonance by ≈1 Hz/μW. We minimize this shift by coupling only 100 μW to 200 μW of 563 nm light into the cavity and controlling the circulating optical power by monitoring the light transmitted through the cavity. Active control of the rf power driving the AOM (also used for frequency control) stabilizes the output power from the cavity to ≈0.1%.

To characterize the cavity's stability, we constructed a second cavity and vibrationally isolated table similar to that described above. The dye-laser output is split into two parts, each of which couples through an optical fiber onto one of the reference cavity tables. Since the prestabilized dye-laser light has a linewidth of ≈1 kHz and the rf lock to the reference cavity has a loop bandwidth of ≈50 kHz, very little correlation exists between the frequency fluctuations in the two beams at frequencies ≲10 kHz, which contribute dominantly to the linewidth. Consequently, it is appropriate to consider beams locked to the two cavities as independent sources when measuring noise at frequencies ≲10 kHz.

We expect negligible correlation between environmental perturbations of the two reference cavities. The masses of the two vibrationally isolated tables differ by a factor of 4, and the spring supports for one table are attached to the ceiling, while the spring supports for the other table are supported by posts resting on the laboratory floor. These differences cause the coupling of mechanical vibrations to differ for the two tables. Additionally, the separate vacuum chambers, temperature control systems, and acoustic-isolation boxes provide further decoupling between the two cavities. The largest common-mode variations probably arise from long-term drifts of the room temperature. Temperature-induced effects should occur dominantly at very low frequencies, so they should not degrade the short- and medium-term stabilities observed here. (Long-term drifts will be removed when the laser is locked to an atomic reference.)

Part of the beam locked to one of the cavities is split off and travels from one isolated platform to the other. There, it is heterodyned with part of the beam that is stabilized to the second cavity, providing a measure of the relative frequency deviations between the two optical beams. The beams locked to the two cavities differ in frequency by ≈400 MHz. Mixing the beat note with a precision rf source translates the beat-note frequency lower to facilitate high-resolution analysis. A fairly uniform drift of the beat-note frequency (≲2 Hz/s), which may be caused by a slow temperature drift of one of the cavities, is removed by mixing the beat note against an rf source with a matching linear frequency chirp.

Residual relative motion between the two isolated optical tables makes Doppler-shift contributions to the beat-note frequency width. We measure these contributions using an auxiliary beam sent between the tables [5]. On one of the tables, a beam is split into two parts—one of which is given a precise frequency offset for use as a frequency reference. The second beam travels from one table to the other along a path very near (≈1 cm) the beam path used for the intercavity beat note and then retroreflects back to the initial table. The heterodyne beat note between the auxiliary beam and the reference beam contains frequency fluctuations from relative table motion twice as large as the corresponding fluctuations on the intercavity beat signal. We digitally divide the frequency of this Doppler-shift beat signal by a factor of 2. The resulting signal can then be mixed with the intercavity beat signal to remove contributions to the noise from the relative table motion. Typically, relative table motion is not the dominant source of frequency noise, so we often omit this correction. A similar Doppler-cancellation technique will be critical for avoiding linewidth degradation while transporting light from the vibrationally isolated table to an atomic reference [5,10].

We have analyzed the beat signal between the beams locked to the two cavities using both frequency-domain and time-domain techniques. We use a fast Fourier transform (FFT) spectrum analyzer to measure the spectrum of the beat note, as shown in Fig. 1. The width of the spectrum at its half-power point is 0.9 Hz. Correcting for the 0.477 Hz resolution bandwidth of the spectrum analyzer, we infer that at least one of the beams has a frequency width less than 0.6 Hz at 563 nm for averaging times up to 32 s. This fractional linewidth of 1×10^{-15} is more than an order of magnitude smaller than previously published results.

An additional measurement in the frequency domain involves using a spectrum analyzer as a frequency discriminator [11]. The resolution bandwidth of the spectrum analyzer is set wide enough to include all noise frequencies of interest. The frequency span is zeroed, and the center frequency is set at the −3 dB point of the beat note. This arrangement converts frequency noise of the beat note into amplitude noise on the intermediate frequency output from the spectrum analyzer, which is then analyzed on an FFT spectrum analyzer. This technique

directly reveals the noise power spectral density. Hence, it was a particularly useful diagnostic in the early stages of the work as we searched for the dominant contributions to the laser linewidth. Conversion of the noise power spectral density to a laser linewidth gives a result consistent with the more direct linewidth measurement.

For time-domain measurements, we mix the beat signal down to dc and record the phase evolution using a computer-based data acquisition system. Figure 2(a) shows a typical time record. The extreme values of the mixer output correspond to phase differences between the two beams of $\Delta\phi = 0$ rad and π rad. Typically, $\Delta\phi$ varies less than π rad for times on the order of 1 s, consistent with our subhertz linewidth measurement. Unfortunately, the relative phase differs sufficiently from the in-quadrature condition ($\Delta\phi = \pi/2$ rad) so that the conversion from beat-signal amplitude to $\Delta\phi$ is nonlinear and indeterminate at the extrema. We can, however, frequency divide the beat note by a factor of 20 and measure similar time records of $\Delta\phi/20$ [see Fig. 2(b)]. In this case, the in-quadrature condition is maintained for time durations long enough to facilitate easy determination of the phase noise for averaging times less than a few seconds. For time intervals $\geq$0.5 s, we perform time-domain measurements using an automated dual-mixer time-difference measurement system [12]. The fractional frequency instabilities, or Allan deviations $\sigma_y(\tau)$, determined using these two measurement techniques are plotted in Fig. 3, alongside the reported Allan deviations for a number of other stable laser systems. For the 30 ms to several second time scale relevant for our proposed optical standard [5], the Allan deviation of our laser is approximately an order of magnitude less than that of the other stable lasers.

We have made preliminary investigations of the sensitivity of the laser-beam frequencies to various environmental perturbations of the reference cavity or laser locking system. For example, we have examined the tilt and acceleration sensitivity of the cavities by using solenoids to apply sinusoidal driving forces to the vibrationally isolated optical tables. Tilting a cavity modifies the optical resonance frequencies because of distortions of the cavity caused by the redistribution or reorientation of the support forces. Accelerations modify the resonance frequencies because the support forces change to balance inertial forces, again distorting the cavity. For fixed drive amplitude, inertial forces vary with the square of the drive frequency. Cavity distortions due to accelerations dominate in our system at drive frequencies $\geq$0.1 Hz.

Driving one of the tables at a low frequency of 0.01 Hz tests predominantly the tilt sensitivity of the cavity resonance. For table tilts as large as 20 μrad, frequency shifts are less than 2 Hz. Consequently, driving the table with similar amplitude at a higher frequency of 1 Hz mainly probes the acceleration sensitivity of the cavity systems. At higher motional frequencies, we observe considerable broadening of the beat-note frequency width. Much of this broadening is caused by Doppler shifts from the component of the table motion along the direction of the beam traveling between the two tables. Generally, applying the Doppler-shift correction described earlier reduces the beat-note width by a factor of 5 to 10. Assuming the residual broadening is caused by inertial forces on the cavities gives an acceleration sensitivity of $\approx$100 kHz/(m/s^2). Theoretical estimates of the sensitivity of our cavity to accelerations suggest that the dominant shifts should be caused by vertical accelerations, which is consistent with

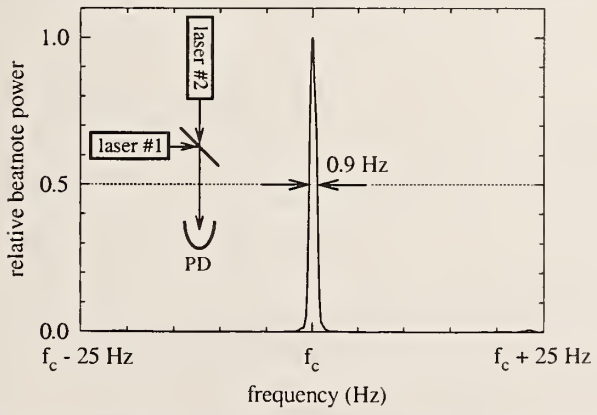

FIG. 1. Power spectrum of the beat note between two laser beams stabilized to two independent cavities. The averaging time is 32 s. The resolution bandwidth of the spectrum analyzer is 0.447 Hz. A nearly uniform relative cavity drift of 2.4 Hz/s is suppressed by mixing the beat note with a swept synthesizer. (PD) photodiode.

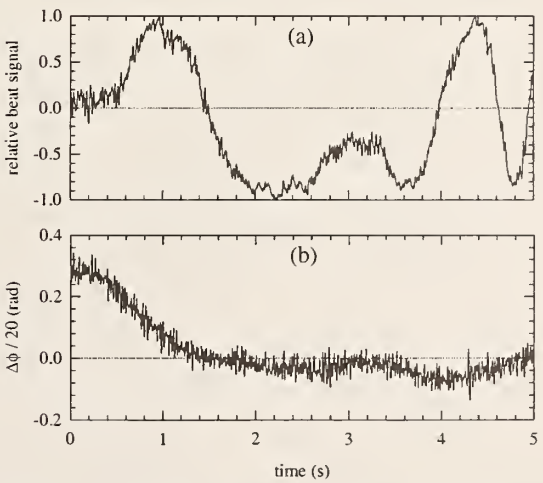

FIG. 2. Two time records of the beat signal between two stable 563 nm laser beams. The waveform sampling rate is 2 kHz. (a) The extrema of the mixer output of $\pm$1 correspond to relative phases $\Delta\phi = 0$ rad and π rad. For clarity, an 8 Hz, first-order, low-pass filter on the mixer output suppresses some high-frequency noise components. (b) Frequency division of the beat signal by 20 facilitates conversion from the mixer output amplitude to a phase for sample periods of many seconds, and allows calculation of the Allan deviation between 2 ms and 2 s. The signal bandwidth exceeds 50 kHz.

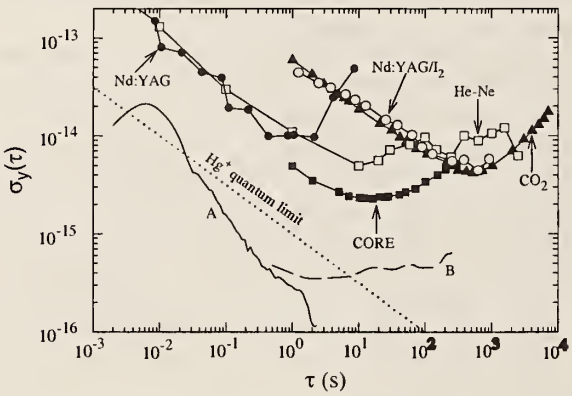

FIG. 3. Allan deviation curves for stabilized lasers. We calculate $\sigma_y(\tau)$ for one of our sources from an analog-to-digital sample of the beat signal (curve *A*) and using a dual-mixer measurement system (curve *B*). The dotted line shows the quantum noise limit for a Hg^+ optical frequency standard with one ion and a 30 ms Ramsey interrogation time [13]. Results for other stabilized lasers: (Nd:YAG) Nd:YAG lasers locked to Fabry-Pérot cavities [14]; (Nd:YAG/I_2) iodine-stabilized Nd:YAG lasers [15]; (He-Ne) methane-stabilized He-Ne lasers [16]; (CO_2) CO_2 lasers locked to OsO_4 [17] (see comparable results in Ref. [18]); (CORE) Nd:YAG lasers locked to cryogenic resonator oscillators [19].

our observations for various motional modes of the tables. The estimated sizes of the shifts agree within an order of magnitude with the experimental results.

Our laser is suitable for precision spectroscopy and for optical frequency standards. It has a linewidth of less than 0.6 Hz at 563 nm for averaging times up to 32 s. Future efforts will involve more detailed study of the sensitivity of the laser frequency to environmental perturbations such as temperature, acoustic noise, optical-power fluctuations, and laser-beam misalignment. The frequency instability of our laser is still approximately an order of magnitude higher than the linewidth limit set by the lock to the Fabry-Pérot cavity. Consequently, further improvement may be achieved. Although the results presented here are sufficiently good for the Hg^+ optical standard that we are assembling [5], lasers with lower linewidths could be beneficial for other standards based on longer-lifetime metastable states in atoms or ions. One possible route to more reliable laser operation is the development of an all-solid-state replacement for the dye laser [20]. Finally, we are assembling a cryogenic Hg^+ ion trap [21] for our proposed optical frequency standard. This system, coupled with a frequency chain to microwave frequencies, may eventually provide a time standard with an accuracy near 10^{-18}.

We thank C. N. Man for the use of her high-finesse cavity design and R. Lalezari, M. Lauer, and D. Willis of Research Electro-Optics for its fabrication; W. D. Lee and C. Nelson for the use of their digital servo software in stabilizing one of our isolation tables; F. Walls for assistance with the dual-mixer measurement system; and D. J. Wineland, L. Hollberg, J. Hall, M. Young, and D. Sullivan for useful comments. This work is supported by the Office of Naval Research and the National Institute of Standards and Technology.

*Present address: Universidade Estadual de Campinas, Campinas, SP, 13083-970, Brazil.

[1] *Laser Spectroscopy XII,* edited by M. Inguscio, M. Allegrini, and A. Sasso (World Scientific, Singapore, 1996).
[2] *Proceedings of the Workshop on the Scientific Applications of Clocks in Space,* edited by L. Maleki (Jet Propulsion Laboratory, Pasadena, 1997).
[3] C. Salomon, D. Hils, and J. L. Hall, J. Opt. Soc. Am. B **5**, 1576 (1988).
[4] J. Dirscherl, B. Neizert, T. Wegener, and H. Walther, Opt. Commun. **91**, 131 (1992).
[5] J. C. Bergquist, W. M. Itano, and D. J. Wineland, in *Frontiers in Laser Spectroscopy, Proceedings of the International School of Physics "Enrico Fermi": Course 120,* edited by T. W. Hänsch and M. Inguscio (North-Holland, Amsterdam, 1994), pp. 359–376.
[6] R. W. P. Drever *et al.,* Appl. Phys. B **31**, 97 (1983).
[7] Commercial products are identified in order to adequately specify the experimental procedure. Such identification does not imply recommendation or endorsement by the National Institute of Standards and Technology.
[8] S. F. Jacobs, Opt. Acta **33**, 1377 (1986).
[9] D. Hils, J. E. Faller, and J. L. Hall, Rev. Sci. Instrum. **57**, 2532 (1986).
[10] L.-S. Ma, P. Jungner, J. Ye, and J. L. Hall, Opt. Lett. **19**, 1777 (1994).
[11] J. Hough *et al.,* Appl. Phys. B **33**, 179 (1984).
[12] S. Stein *et al.,* in *Proceedings, 36th Annual Frequency Control Symposium* (U.S. Army Electronics Command, Ft. Monmouth, NJ, 1982), pp. 314–320.
[13] D. J. Wineland *et al.,* in *Frequency Standards and Metrology: Proceedings of the Fourth Symposium,* edited by A. De Marchi (Springer-Verlag, Berlin, 1989), pp. 71–77.
[14] N. M. Sampas, E. K. Gustafson, and R. L. Byer, Opt. Lett. **18**, 947 (1993).
[15] J. L. Hall *et al.,* in *1998 Conference on Precision Electromagnetic Measurements Digest,* edited by T. L. Nelson (IEEE, New York, 1998), pp. 151–152.
[16] S. N. Bagayev, A. K. Dmitriyev, P. V. Pokasov, and B. N. Skvortsov, in *Proceedings of the Fifth Symposium on Frequency Standards and Metrology,* edited by J. C. Bergquist (World Scientific, Singapore, 1996), pp. 289–296.
[17] O. Acef, Opt. Commun. **134**, 479 (1997).
[18] V. Bernard *et al.,* IEEE J. Quantum Electron. **33**, 1282 (1997).
[19] S. Seel *et al.,* Phys. Rev. Lett. **78**, 4741 (1997).
[20] F. C. Cruz, B. C. Young, and J. C. Bergquist, Appl. Opt. **37**, 7801 (1998).
[21] D. J. Berkeland *et al.,* Phys. Rev. Lett. **80**, 2089 (1998).

The National Institute of Standards and Technology was established in 1988 by Congress to "assist industry in the development of technology . . . needed to improve product quality, to modernize manufacturing processes, to ensure product reliability . . . and to facilitate rapid commercialization . . . of products based on new scientific discoveries."

NIST, originally founded as the National Bureau of Standards in 1901, works to strengthen U.S. industry's competitiveness; advance science and engineering; and improve public health, safety, and the environment. One of the agency's basic functions is to develop, maintain, and retain custody of the national standards of measurement, and provide the means and methods for comparing standards used in science, engineering, manufacturing, commerce, industry, and education with the standards adopted or recognized by the Federal Government.

As an agency of the U.S. Commerce Department's Technology Administration, NIST conducts basic and applied research in the physical sciences and engineering, and develops measurement techniques, test methods, standards, and related services. The Institute does generic and precompetitive work on new and advanced technologies. NIST's research facilities are located at Gaithersburg, MD 20899, and at Boulder, CO 80303. Major technical operating units and their principal activities are listed below. For more information contact the Publications and Program Inquiries Desk, 301-975-3058.

Office of the Director
- National Quality Program
- International and Academic Affairs

Technology Services
- Standards Services
- Technology Partnerships
- Measurement Services
- Information Services

Advanced Technology Program
- Economic Assessment
- Information Technology and Applications
- Chemistry and Life Sciences
- Electronics and Photonics Technology

Manufacturing Extension Partnership Program
- Regional Programs
- National Programs
- Program Development

Electronics and Electrical Engineering Laboratory
- Microelectronics
- Law Enforcement Standards
- Electricity
- Semiconductor Electronics
- Radio-Frequency Technology[1]
- Electromagnetic Technology[1]
- Optoelectronics[1]
- Magnetic Technology[1]

Materials Science and Engineering Laboratory
- Intelligent Processing of Materials
- Ceramics
- Materials Reliability[1]
- Polymers
- Metallurgy
- NIST Center for Neutron Research

Chemical Science and Technology Laboratory
- Biotechnology
- Physical and Chemical Properties[2]
- Analytical Chemistry
- Process Measurements
- Surface and Microanalysis Science

Physics Laboratory
- Electron and Optical Physics
- Atomic Physics
- Optical Technology
- Ionizing Radiation
- Time and Frequency[1]
- Quantum Physics[1]

Manufacturing Engineering Laboratory
- Precision Engineering
- Manufacturing Metrology
- Intelligent Systems
- Fabrication Technology
- Manufacturing Systems Integration

Building and Fire Research Laboratory
- Applied Economics
- Structures
- Building Materials
- Building Environment
- Fire Research

Information Technology Laboratory
- Mathematical and Computational Sciences[2]
- Advanced Network Technologies
- Computer Security
- Information Access
- Convergent Information Systems
- Information Services and Computing
- Software Diagnostics and Conformance Testing
- Statistical Engineering

[1]At Boulder, CO 80303.
[2]Some elements at Boulder, CO.

U.S. Department of Commerce
National Institute of Standards and Technology
325 Broadway
Boulder, CO 80305

Official Business
Penalty for Private Use $300